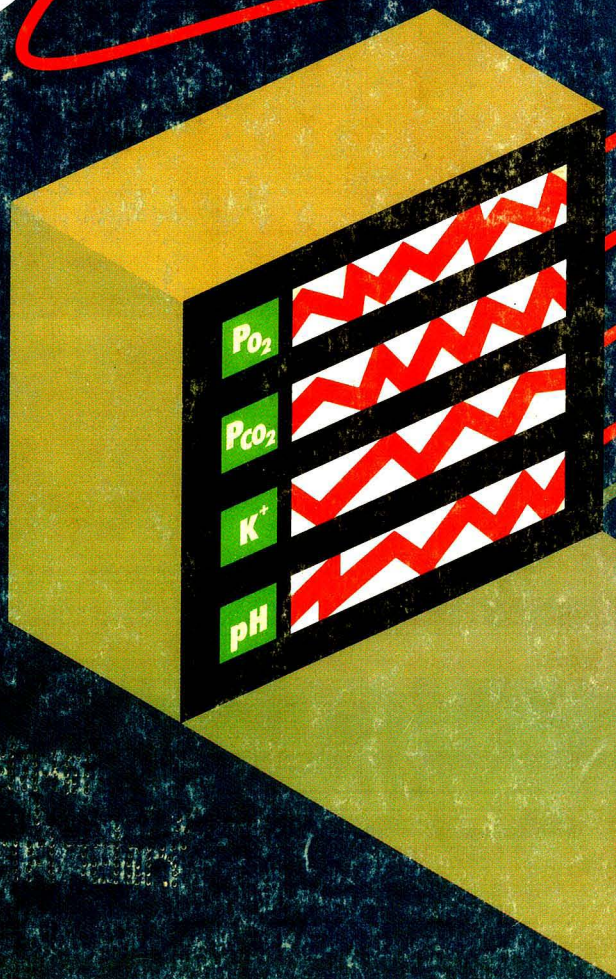
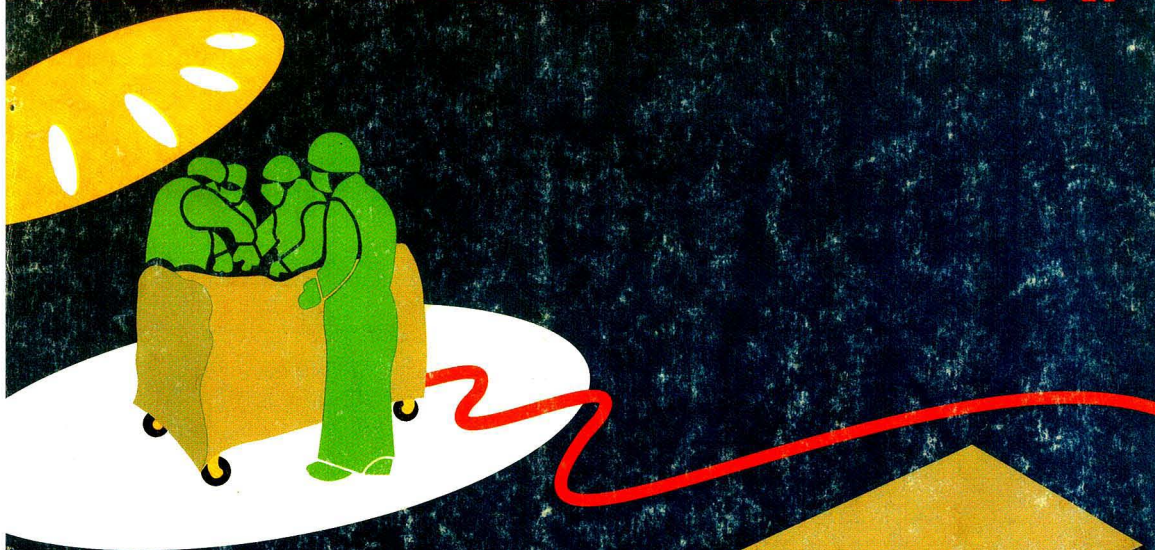


APRIL 1, 1990

# Analytical CHEMISTRY



## Chemical Sensors for Bedside Monitoring of Critically Ill Patients

425A



**Model PHH-30**  
Handheld  
pH/ORP Meter  
**\$194**

**Models PHE-4580**  
and **PHE-6510**  
Electrodes  
**\$95 each**

**CDH-X Series**  
Conductivity Testers  
**\$44 each**

**PHH-1X**  
pH Tester  
**\$44**

For more information on these products,  
circle reader service number 101

You'll Find It All  
In This Free Handbook!!

**NEW! FREE! FASCINATING!**  
**AND NOW WITH HARDCOVER...**  
**FOR YOUR TECHNICAL LIBRARY!**

- ✓ Over 300 Full Color Pages
- ✓ All Prices Listed
- ✓ Thousands of Products
- ✓ Complete with Technical Data
- ✓ Fast "Off-The-Shelf" Delivery

in a Hurry for Your Handbooks?  
Dial **(203) 359-RUSH**  
**(203) 359-7874**

Or Circle the Reader Service No. 102  
for Your Handbook Qualification Form.  
(OMEGA Offers 6 Technical Handbooks,  
with Over 3500 Pages.)

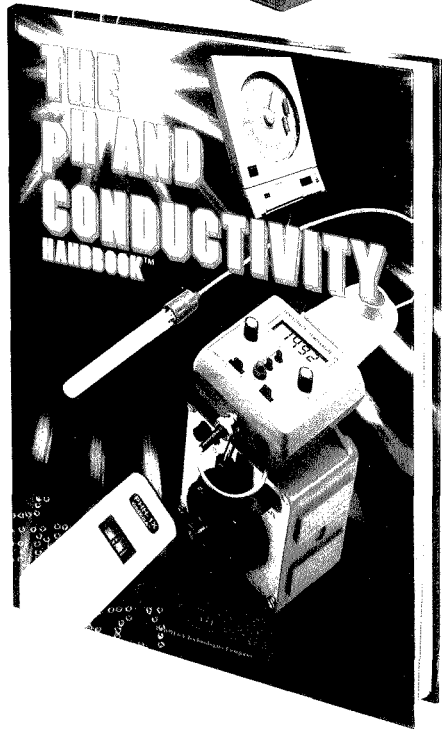
pH and Conductivity • Temperature • Pressure, Strain and Force  
Flow and Level • Data Acquisition • Electric Heaters

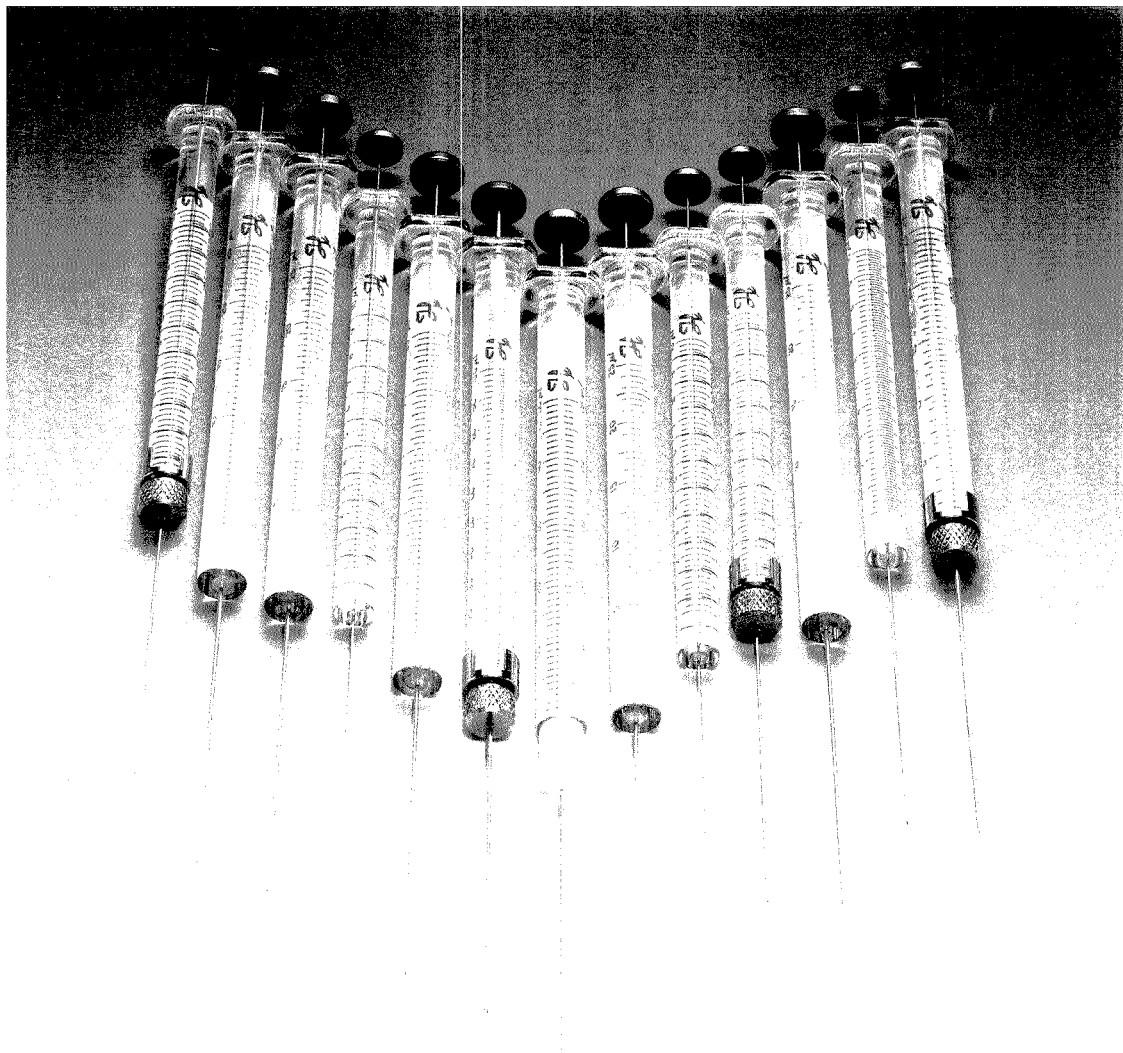
For More Information,  
Dial **(203) 359-1660**



An OMEGA Technologies Company  
One Omega Drive, Box 4047, Stamford, CT 06907  
Telex 996404 Cable OMEGA FAX (203) 359-7900

© COPYRIGHT 1990, OMEGA ENGINEERING, INC. ALL RIGHTS RESERVED





## WHICH IS THE MOST IMPORTANT POINT TO A CHROMATOGRAPHER?

Is it the Hamilton Microliter<sup>®</sup> 700 Series syringe? You might think so. After all, it's the world standard for measuring up to 500 $\mu$ l. Or is it the 7000 Series ultramicro syringe? Not a bad guess if you do capillary GC or TLC. Then again, it might be our Gastight<sup>®</sup> 1000 Series syringe.

The most important point here is not any one particular syringe. It's the confidence that comes with every Hamilton syringe—confidence in quality, precision and accuracy.

**HAMILTON**

The measure of excellence.

Call or write for your free copy of the Hamilton product catalog, Hamilton Company, P.O. Box 10030, Reno, NV 89520, (800) 648-5950.

CIRCLE 62 ON READER SERVICE CARD

# DIALOG INTRODUCES ANOTHER TABLE OF BASIC ELEMENTS FOR YOUR LAB.



There's no symbol for *information* in the Periodic Table. Yet nothing could be more crucial to your research than complete, accurate technical and business information.

That's why many chemists consider DIALOG<sup>®</sup> an essential element in the modern lab.

As the world's largest online knowledgebank, DIALOG gives you access to a whole world of critical information. Right in your own lab.

For starters, you can tap into the crucial scientific data. DIALOG has detailed information on everything from

compound identification to chemical safety data, property data, substance and substructure.

Then you can expand your focus by accessing important, related data that will enable you to look at your work in a broader context.

For example, you can investigate patents, competitive projects, new product markets, and worldwide industry trends. In fact, you can investigate any topic, anytime.

And you won't have to sacrifice depth for the sake of breadth. DIALOG is updated continuously, so the data is

always comprehensive and current. And many citations can be conveniently retrieved in full text.

Call today for more information and a free Periodic Table Reference Card. Once you've examined them, you'll see how DIALOG can become a basic element of all your research.

Call us toll free at 800-3-DIALOG, (800-334-2564). Or request information by Fax at 415-858-7069.

**DIALOG** INFORMATION SERVICES, INC.  
A Knight-Ridder Company 

*The world's largest online knowledgebank.*

© 1989 Dialog Information Services, Inc., 3460 Hillview Avenue, Palo Alto, California 94304. All rights reserved. DIALOG is a service mark of Dialog Information Services, Inc. Registered U.S. Patent and Trademark Office.

CIRCLE 30 ON READER SERVICE CARD

**A** The ANCHAM  
Audit Bureau 62(7) 401A-464A/657-784 (1990)  
ISSN 0003-2700

Registered in U.S. Patent and Trademark Office;  
Copyright 1990 by the American Chemical Society

ANALYTICAL CHEMISTRY (ISSN 0003-2700) is published semi-monthly by the American Chemical Society at 1155 16th St., N.W., Washington, DC 20036. Editorial offices are located at the same ACS address (202-872-4570; FAX 202-872-4574; TDD 202-872-8733). Second-class postage paid at Washington, DC, and additional mailing offices. Postmaster: Send address changes to ANALYTICAL CHEMISTRY Member & Subscriber Services, P.O. Box 3337, Columbus, OH 43210.

Claims for missing numbers will not be allowed if loss was due to failure of notice of change of address to be received in the time specified; if claim is dated (a) North America: more than 90 days beyond issue date, (b) all other foreign: more than one year beyond issue date, or if the reason given is "missing from files."

**Copyright Permission:** An individual may make a single reprographic copy of an article in this publication for personal use. Reprographic copying beyond that permitted by Section 107 or 108 of the U.S. Copyright Law is allowed, provided that the appropriate per-copy fee is paid through the Copyright Clearance Center, Inc., 27 Congress St., Salem, MA 01970. For reprint permission, write Copyright Administrator, Publications Division, ACS, 1155 16th St., N.W., Washington, DC 20036.

Registered names and trademarks, etc., used in this publication, even without specific indication thereof, are not to be considered unprotected by law.

**Advertising Management:** Centcom, Ltd., 500 Post Rd. East, Westport, CT 06880 (203-226-7131)

1990 subscription rates include air delivery outside the U.S., Canada, and Mexico

	1 yr	2 yr
<b>Members</b>		
Domestic	\$ 29	\$ 49
Canada and Mexico	64	119
Europe	96	183
All Other Countries	118	227
<b>Nonmembers</b>		
Domestic	59	100
Canada and Mexico	94	170
Europe	186	336
All Other Countries	208	380

Three-year and other rates contact: Member & Subscriber Services, ACS, P.O. Box 3337, Columbus, OH 43210 (614-447-3776 or 800-333-9511).

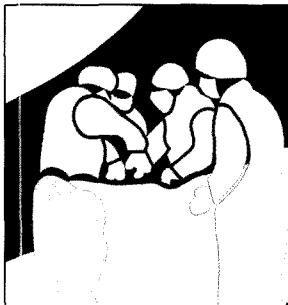
**Subscription orders by phone** may be charged to VISA, MasterCard, Barclay card, Access, or American Express. Call toll free 800-ACS-5558 in the continental United States; in the Washington, DC, metropolitan area and outside the continental United States, call 202-872-8065. Mail orders for new and renewal subscriptions should be sent with payment to the Business Management Division, ACS, P.O. Box 28597, Central Station, Washington, DC 20005.

**Subscription service inquiries and changes of address** (include both old and new addresses with ZIP code and *recent mailing label*) should be directed to the ACS Columbus address noted above. Please allow six weeks for changes to become effective.

**ACS membership information:** Lorraine Bowlin (202-872-4567)

**Single issues,** current year, \$8.00 except review issue, \$14.00, and LabGuide, \$49.00; **back issues and volumes and microform editions** available by single volume or back issue collection. For information or to order, call the number listed for subscription orders by phone; or write the Microform & Back Issues Office at the Washington address.

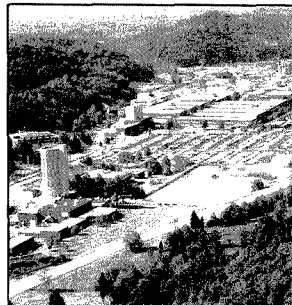
**Nonmembers rates in Japan:** Rates above do not apply to nonmember subscribers in Japan, who must enter subscription orders with Maruzen Company Ltd., 3-10 Nihonbashi 2-chome, Chuo-ku, Tokyo 103, Japan. Tel: (03) 272-7211.



## REPORT

425 A

**On the cover. Chemical sensing for bedside monitoring of critically ill patients.** Modern clinicians are increasingly dependent on reliable measurements of key chemical variables in blood for proper clinical diagnosis and therapy. Michael E. Collison and Mark E. Meyerhoff of the University of Michigan discuss recent efforts to develop and implement modern sensing technologies for measuring blood gases and electrolytes



## MEETINGS

439 A

"Analytical Mass Spectrometry" is the subject of the 1990 Summer Symposium on Analytical Chemistry to be held July 24-27 at Oak Ridge National Laboratory. Eight of this year's **Gordon Research Conferences** are of particular interest to analytical chemists. The Analytical Chemistry conference will be held August 6-10 at the New Hampton School, New Hampton, NH

## BRIEFS

408 A

## EDITORIAL

417 A

**Real science.** Science is strengthened by the interconnections within the various scientific disciplines and weakened by those promoting their own importance

## LETTERS

418 A

## NEWS

421 A

Chemist for **NIST director.** ▶ Into the ozone by pilotless plane. ▶ Most cited ANALYTICAL CHEMISTRY articles

## FOCUS

449 A

**Chemistry on wheels.** Chemists at Juniata College, working with local high school teachers, are bringing sophisticated equipment such as gas chromatographs and spectrophotometers to high school laboratories

455 A

**International Symposium on Detection in Liquid Chromatography and Flow Injection Analysis.** Recognizing that the essential features of continuous detection in HPLC and FIA are remarkably similar, chemists from Spain's University of Cordoba organized an international symposium last year. Gary Christian, Ira Krull, and Julian Tyson report on the highlights of this unique meeting

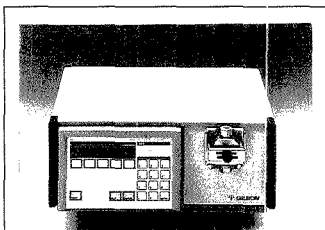
## NEW PRODUCTS & MANUFACTURERS' LITERATURE

460 A

## AUTHOR INDEX

657

GILSON  
LIQUID CHROMATOGRAPHY



**The Master Pump**

*HPLC Pump and System Controller*

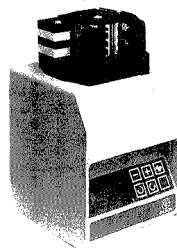
Operating across a wide range of pressures and flowrates, the 305 Master Pump directly controls all other modules in a Gilson HPLC system.

Circle no. 161

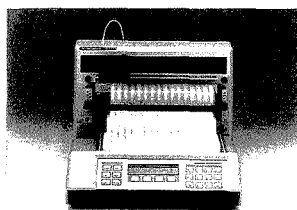
**Minipuls 3**

*Versatile Peristaltic Pump*

Equipped with interchangeable heads, this peristaltic pump operates at high pressures while producing a remarkably smooth flow.



Circle no. 164



**FC 203 Fraction Collector**

*Special Low Pressure LC*

The FC 203 is a multi-mode unit for 128 fractions. A built-in keyboard allows easy parameter selection, and a special HELP key provides on-line instruction.

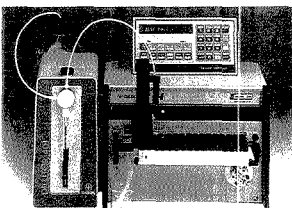
Circle no. 160

**231-401 Auto-Sampling Injector**

*Flexible Automation*

The 231-401 automates HPLC sampling and injection procedures. Fully programmable, the unit accepts up to 128 vials with or without caps.

Circle no. 162

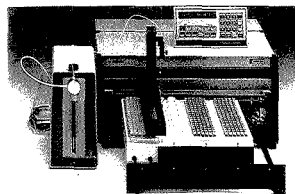


**232-401 Sample Processor and Injector**

*High Capacity*

The 232-401 completely automates preparation and injection of up to 560 samples for unattended HPLC. Options include thermostatted racks and a column switching valve.

Circle no. 165



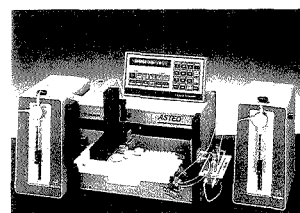
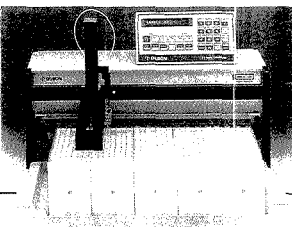
GILSON  
SAMPLE PROCESSORS

**221 and 222 Auto Samplers**

*Automate Sample Preparation and Sample Transfer*

Adaptable to a wide variety of applications, these samplers dispense, pipette, dilute and mix liquids, and then transfer the prepared samples to an analytical instrument.

Circle no. 163

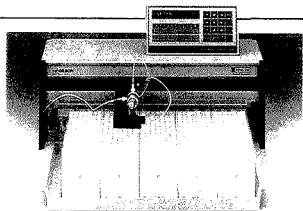


**ASTED Sample Preparation**

*Increases HPLC Throughput*

This patented system uses dialysis and trace enrichment to isolate low molecular weight analytes from samples prior to HPLC analysis.

Circle no. 166

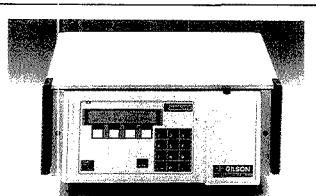


### 202 Fraction Collector

*With 15 Operating Modes*

The 202 offers 540-tube collection in a versatile five-rack configuration. 15 operating modes permit complex fractionation schemes including double column collection.

Circle no. 167

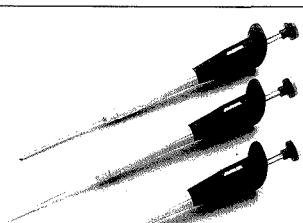


### 116 UV Detector

*Programmable for Variable Wavelengths*

The 116 UV detects in a range of 190-380 nm. Choose the single wavelength, dual wavelength or scan operating mode. Sensitivity (0.001-200 AUFS) depends on the flow cell used.

Circle no. 170

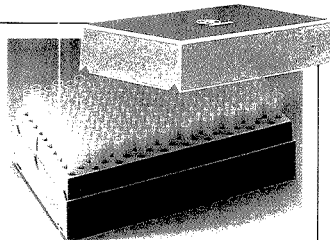


### Microman™

*Pipette for Problem Liquids*

Microman measures viscous, volatile, or high-density samples. Capillaries and pistons can be ejected safely without hand contact, for hazardous samples.

Circle no. 168



### Pipetman Tips

*Guaranteed Performance*

Manufactured by Gilson for Pipetman, these tips are your assurance of performance according to specifications.

Circle no. 171

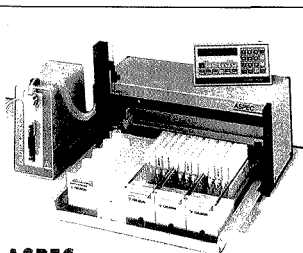


### Pipetman™

*Continuously Adjustable Digital Pipette*

Pipetman is the instrument you know you can depend on for critical research applications. Pipetman is the world's standard for microliter pipetting.

Circle no. 173

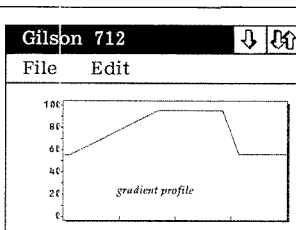


### ASPEC

*Automatic Solid Phase Extraction*

For clean-up or trace enrichment, ASPEC automates all liquid handling in solid phase extraction. ASPEC accepts standard extraction columns.

Circle no. 169

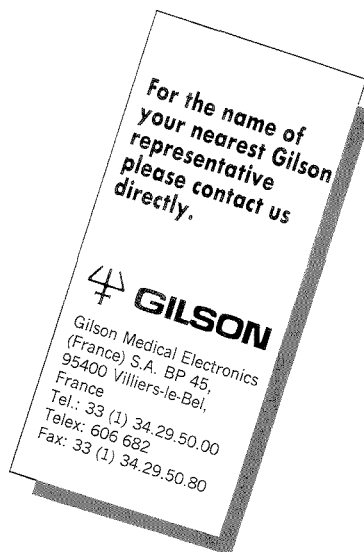


### HPLC Software

*System Control and Data Analysis*

Gilson 712 and 714 HPLC system controllers offer ternary or quaternary gradient control and single or multiple channel data analysis.

Circle no. 172



## Articles

### Resolution of Severely Overlapped Spectra from Matrix-Formatted Spectral Data Using Constrained Nonlinear Optimization 658

A three-step scheme for estimating severely overlapping component spectra from bilinear matrix-formatted spectral data is described. The performance of the scheme is evaluated using synthetic fluorescence excitation-emission matrices exhibiting various levels of spectral overlap and random noise. Experimental EEMs of four-component mixtures are resolved.

Sharon L. Neal, Ernest R. Davidson, and Isiah M. Warner\*, Department of Chemistry, Emory University, Atlanta, GA 30322, and Department of Chemistry, Indiana University, Bloomington, IN 47405

### Locally Weighted Regression and Scatter Correction for Near-Infrared Reflectance Data 664

The effects of multiplicative scatter correction and nonlinear regression, based on the first two and three principal components for near-IR reflectance spectroscopy data, are investigated. The theory is illustrated by three examples.

Tormod Naes\* and Tomas Isaksson, MATFORSK, Oslovegen 1, 1430 Ås, Norway and Bruce Kowalski, Laboratory of Chemometrics, University of Washington, Seattle, WA 98195

### In Vitro Percutaneous Absorptiometry by Simultaneous Measurement Using the Photoacoustic Method and Absorbance 674

A photoacoustic cell is used to measure the decreasing concentration of a drug applied to the outside of a membrane while the increasing concentration of the drug on the inside of the membrane is measured simultaneously by absorption.

Ryuichi Takamoto, Ryujiro Namba, Okitsugu Nakata, and Tsuguo Sawada\*, Shiseido Co., Ltd., Toxicological & Analytical Research Center, 1050 Nippa-cho, Kohoku-ku, Yokohama 223, Japan

### Surface-Enhanced Raman Spectroscopy at a Silver Electrode as a Detection System in Flowing Streams 678

SERS of selected DNA bases are recorded in a flow cell. Components are adsorbed and desorbed at an Ag electrode in < 10 s as a function of applied potential. The DNA bases yield a detection limit of 175–225 pmol.

Neil J. Pothier and R. Ken Forcé\*, Department of Chemistry, University of Rhode Island, Kingston, RI 02881

### Laser-Induced-Fluorescence Detection of Sodium Atomized by a Microwave-Induced Plasma with Tungsten Filament Vaporization 680

The laser-induced-fluorescence technique is used to detect Na in pure water at a concentration range down to pg/cm<sup>3</sup>. The absolute atomizing efficiency is determined.

Yuji Oki\*, Hisanori Uda, Chikahisa Honda, Mitsuo Maeda, Jun Izumi, Takashi Morimoto, and Masazumi Tanoura, Department of Electrical Engineering, Kyushu University, Hakozaki, Fukuoka 812, Japan

### Prediction of Gas Chromatography Flame Ionization Detector Response Factors from Molecular Structures 683

The FID response of 71 compounds is analyzed in terms of structural components using effective carbon numbers. Response is predicted to within an average of 1.7% for single functional group compounds in the study.

Andrew D. Jorgensen\*, Department of Chemistry, University of Toledo, Toledo, OH 43606 and Kurt C. Picel and Vassilis C. Stamoudis, Argonne National Laboratory, Argonne, IL 60439

### Surface-Enhanced Raman Analysis of Sulfa Drugs on Colloidal Silver Dispersion 689

Spectral fingerprinting of sulfadiazine, sulfamerazine, and sulfamethazine by SERS is described. Limits of detection in the low-ng mL<sup>-1</sup> range are obtained.

W. S. Sutherland, J. J. Laserna, M. J. Angebrannt, and J. D. Winefordner\*, Department of Chemistry, University of Florida, Gainesville, FL 32611

### Effect of Reducing Disulfide-Containing Proteins on Electrospray Ionization Mass Spectra 693

An increase in maximum charge state is observed in the electrospray ionization mass spectra of multiply charged ions for proteins with molecular weights up to 133 kDa due to the reduction of disulfide bonds.

Joseph A. Loo, Charles G. Edmonds, Harold R. Udseth, and Richard D. Smith\*, Chemical Methods and Separations Group, Chemical Sciences Department, Pacific Northwest Laboratory, Richland, WA 99352

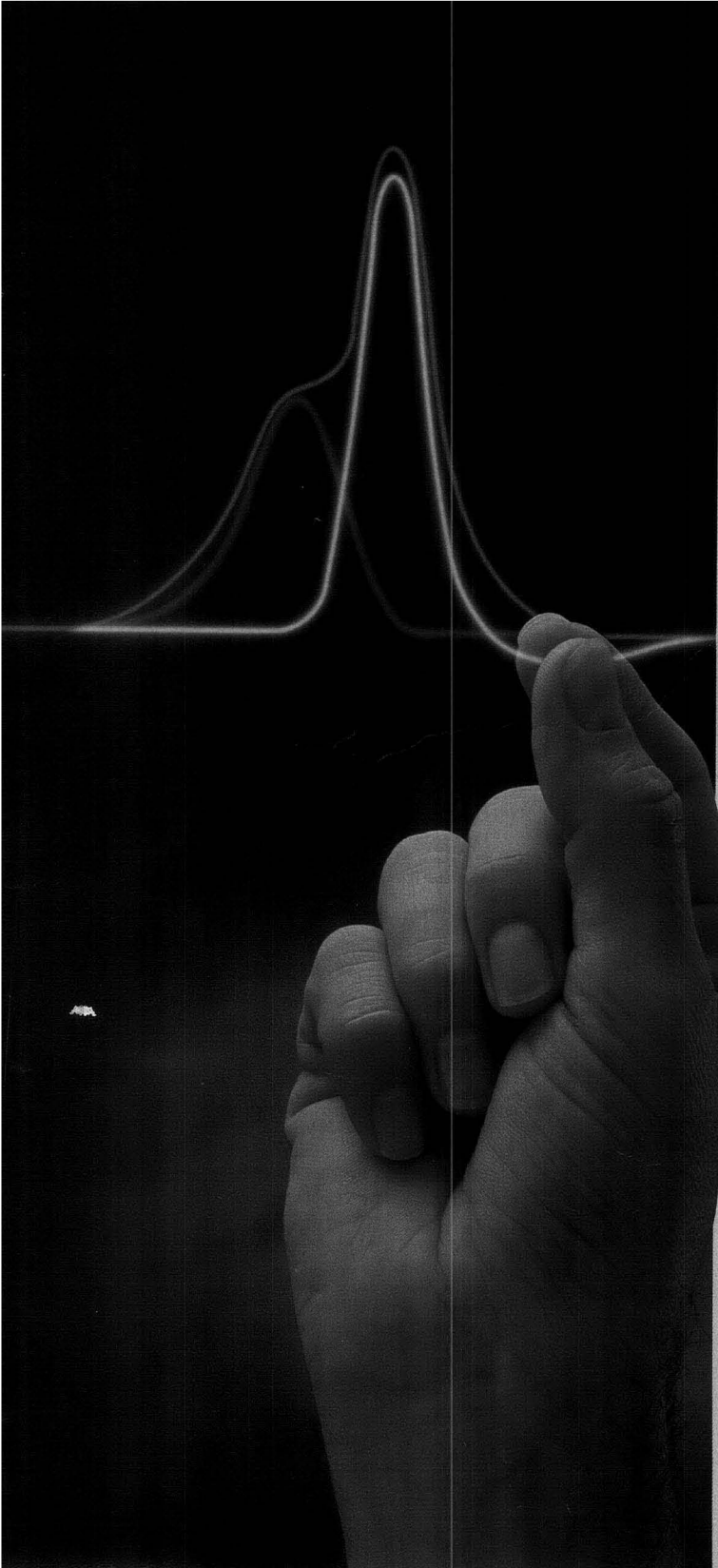
### Hadamard Transform Measurement of Tandem Fourier-Transform Mass Spectra 698

Simultaneous Hadamard transform collection of 11 tandem mass spectra yields the expected 1.8X S/N improvement. A proposed Hadamard differences method provides all MS<sup>n</sup> spectra from the sample required for one spectrum.

Evan R. Williams, Stanton Y. Loh, and Fred W. McLafferty\*, Chemistry Department, Baker Laboratory, Cornell University, Ithaca, NY 14853-1301 and Robert B. Cody, Nicolet Analytical Instruments, 6416 Schroeder Road, Madison, WI 53711

\*Corresponding author



A black and white photograph of a hand with the index finger pointing towards a prominent peak in a chromatogram. The chromatogram shows a baseline with several peaks, the most prominent being a sharp, narrow peak that the hand is pointing to. The background is dark, making the white lines of the chromatogram stand out.

# Now, advanced methods development is System Gold™ easy.

System Gold™ the Personal™ Chromatograph, is the most advanced, easiest-to-learn, easiest-to-use HPLC.



And now it offers the fully automated convenience of our new Model 168 Diode Array Detector Module and new Model 507 Autosampler.

You get rapid acquisition of complete UV/VIS spectra through diode array detection. And you get the programmable versatility of the 507 Autosampler.

All with a level of convenience and automation never before available with *any* HPLC.

And it's System Gold easy.

Find out for yourself how easy methods development can be with System Gold. Contact your local Beckman representative. Offices in major cities worldwide.

Call 800/742-2345 in the US. Or write Beckman Instruments, Inc., Altex Division, 2350 Camino Ramon, P.O. Box 5101, San Ramon, CA 94583.

## BECKMAN

Australia, Sydney Austria, Vienna Canada, Toronto  
France, Gagny Germany, Munich Hong Kong, Aberdeen  
Italy, Milano Japan, Tokyo Mexico, Mexico City  
Netherlands, Mijdrecht Puerto Rico, Carolina  
Singapore, South Africa, Johannesburg Spain, Madrid  
Sweden, Bromma Switzerland, Nyon Taiwan, Taipei  
United Kingdom, High Wycombe ©1989, Beckman  
Instruments, Inc. AX88-1043A

CIRCLE 16 FOR REPRESENTATIVE  
& LITERATURE.  
CIRCLE 17 FOR LITERATURE ONLY.

### Interlaboratory Comparison of Different Analytical Techniques for the Determination of Oxygen-18 Abundance 703

A series of six artificially enriched water samples, containing between 2500 and 6500 ppm oxygen-18, are prepared by adding weighed portions of distilled water and highly enriched  $H_2^{18}O$  and analyzed using proton activation analysis and gas isotope ratio MS.

J. R. Speakman\*, K. A. Nagy, D. Masman, W. G. Mook, S. D. Poppitt, G. E. Strathearn, and P. A. Racey, Department of Zoology, University of Aberdeen, Aberdeen, Scotland, U.K. AB9 2TN, Laboratory of Biomedical and Environmental Sciences, University of California, Los Angeles, 900 Veteran Avenue, Los Angeles, CA 90024, and Rijksuniversiteit Groningen, Centrum voor Isotopen Onderzoek, Westersingel 34, 9718 CM Groningen, The Netherlands

### Flow Injection Analysis of L-Lactate with Enzyme Amplification and Amperometric Detection 708

Experimental conditions for determining lactate anion are studied using the simplex and univariate methods. Detection limits are  $1.19 \times 10^{-7}$  M and  $3.29 \times 10^{-7}$  M lactate, respectively. An oxygen electrode is used to monitor the changing oxygen concentration in the flow stream.

Moore U. Asouzu, William K. Nonidez\*, and Mat H. Ho, Department of Chemistry, University of Alabama at Birmingham, Birmingham, AL 35294

### Stereoselective Determination of Free Warfarin Concentration in Protein Binding Equilibrium Using Direct Sample Injection and an On-Line Liquid Chromatographic System 712

An internal-surface, reversed-phase silica column and a chiral separation column are used together to determine free warfarin enantiomers. The results agree well with those obtained by the conventional ultrafiltration method.

Akimasu Shibukawa\*, Miwa Nagao, Yoshihiro Kuroda, and Terumichi Nakagawa, Faculty of Pharmaceutical Sciences, Kyoto University, Sakyo-ku, Kyoto-shi 606, Japan

### Characterization of Overlapped Chromatographic Peaks by Their Second Derivative. The Limit of the Method 717

The second-derivative approach to integration limits in chromatography is limited by the height ratio of the two components in the composite and by the S/N ratio. A method is described that allows derivatives to be used for noisy chromatograms.

Eli Grushka\* and Dror Israeli, Department of Inorganic and Analytical Chemistry, The Hebrew University, Jerusalem, Israel

### Calibration of the Ion Microprobe for the Quantitative Determination of Strontium, Iron, Manganese, and Magnesium in Carbonate Minerals 722

Detection limits for the determination of Sr, Mn, and Mg in carbonate materials using the ion microprobe are as low as 1 ppm. For Fe, these limits are approximately an order of magnitude higher.

Peter K. Swart, Rosenstiel School of Marine and Atmospheric Science, Marine Geology and Geophysics, University of Miami, Miami, FL 33149

### Multivariate Rule Building Expert System 729

A multivariate rule building expert system, MuRES, is developed that performs supervised classification of multivariate data by combining the advantages of conventional expert systems with multivariate linear classifiers.

Peter de B. Harrington\* and Kent J. Voorhees, Department of Chemistry & Geochemistry, Colorado School of Mines, Golden, CO 80401

### Indirect Conductometric Detection of Poly(oxyethylenes) after Chromatographic Separation 734

A detection method for compounds containing poly(oxyethylenes) separated on a  $K^+$ -loaded cation-exchange resin is described. A quantitation scheme for oligomers is presented.

Tetsuo Okada, Faculty of Liberal Arts, Shizuoka University, Shizuoka 422, Japan

### Design of a Calcium-Selective Optode Membrane Based on Neutral Ionophores 738

A PVC membrane that incorporates a conventional  $Ca^{2+}$ -selective neutral ionophore and a  $H^+$ -selective chromoionophore is used to optically measure  $Ca^{2+}$  activities in pH buffered solutions.

Werner E. Morf, Kurt Seiler, Bruno Rusterholz, and Wilhelm Simon\*, Swiss Federal Institute of Technology (ETH), Department of Organic Chemistry, Universitätstrasse 16, CH-8092 Zürich, Switzerland

### Fabrication of Pyrolytic Carbon Film Electrodes by Pyrolysis of Methane on a Machinable Glass Ceramic 742

Electrodes are fabricated at 850 °C and 1000 °C. As indicated by cyclic voltammetry, favorable charge-transfer characteristics are obtained for ferrocyanide, dopamine, and methyl viologen. Surface morphologies are examined via SEM.

Christopher F. McFadden and Paula Rossi Melaragno\*, Department of Chemistry, Ebaugh Laboratories, Denison University, Granville, OH 43023 and James A. Davis, Owens/Corning Fiberglass, Technical Center, Granville, OH 43023

### Voltammetric Measurement of Ultraslow Diffusion Rates in Polymeric Media with Microdisk Electrodes 747

Potential sweep and step experiments are used to measure diffusion coefficients of electroactive molecules in polymeric solvents as small as  $10^{-12}$  cm<sup>2</sup>/s.

M. L. Longmire, M. Watanabe, H. Zhang, T. T. Wooster, and Royce W. Murray\*, Kenan Laboratories of Chemistry, University of North Carolina, Chapel Hill, NC 27514-3290

### Constant Potential Amperometric Detection at a Copper-Based Electrode: Electrode Formation and Operation 752

The formation of copper-based electrodes for the detection of carbohydrate compounds in flow systems appears to involve the galvanic deposition of CuCl onto the glassy carbon substrate. Electrodes possessing similar activity can also be prepared by direct electrodeposition of metallic copper.

Peifang Luo, Sunil V. Prabhu, and Richard P. Baldwin\*, Department of Chemistry, University of Louisville, Louisville, KY 40292

# Acrodisc: The Difference is Clear.

## **Clearly the Widest Selection.**

Gelman Sciences Acrodiscs® are available in a wide variety of membrane types, with 0.2 $\mu$ m or 0.45 $\mu$ m pore sizes and 13mm or 25mm diameters.

## **Clearly Identified.**

Acrodiscs are printed with identifying information, and are color-coded to the product packaging. Convenient tube containers allow you to see their contents at a glance.

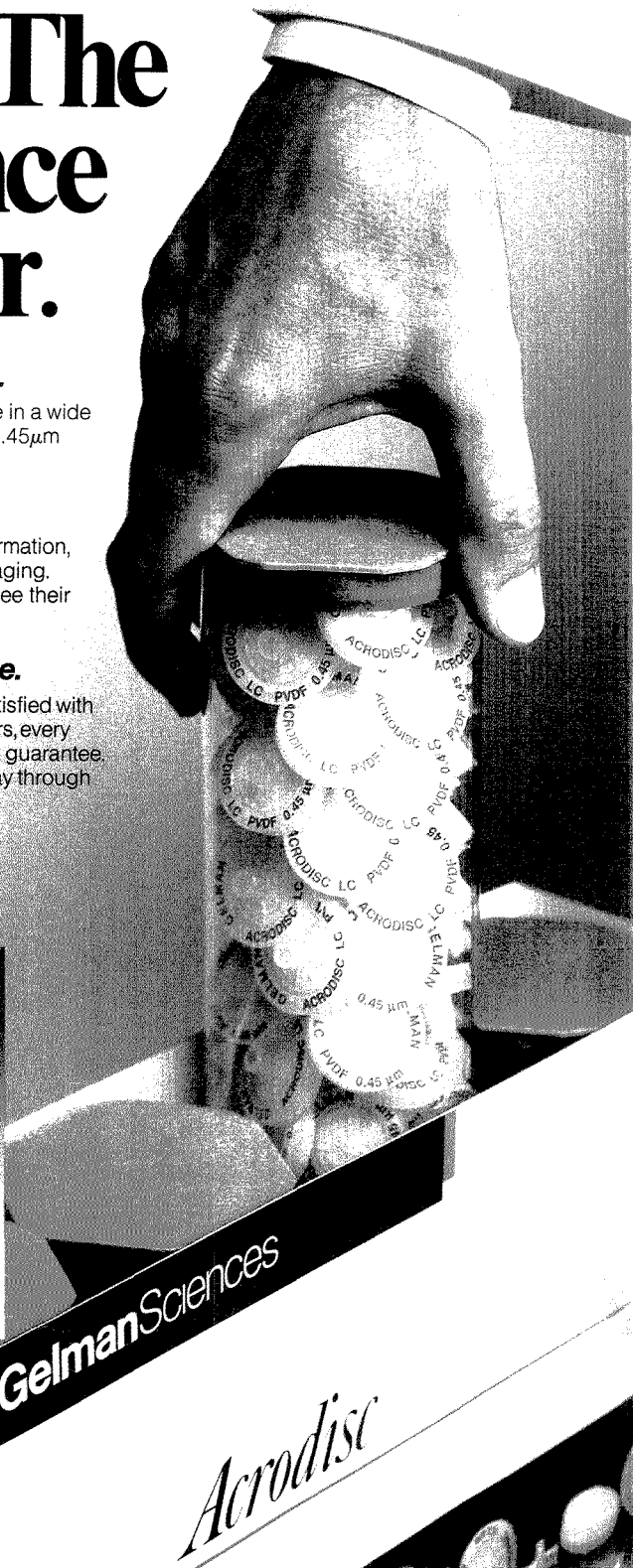
## **Clearly the Best Performance.**

Gelman Sciences is so certain you'll be satisfied with the performance of its Acrodisc syringe filters, every package is covered by a free-replacement guarantee. So order Gelman Sciences Acrodiscs today through your local laboratory products distributor.



**Gelman Sciences**

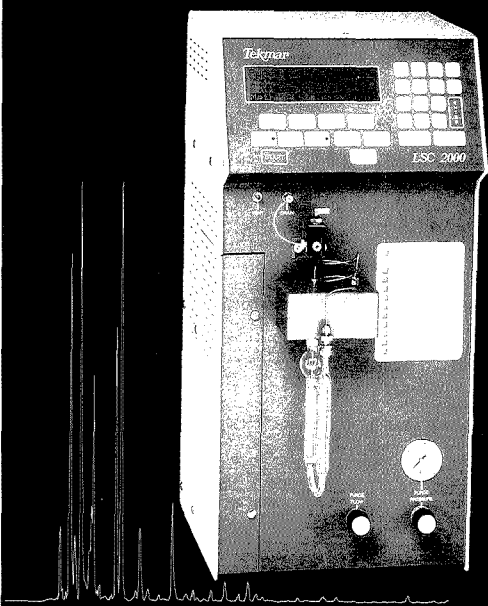
600 S. Wagner Rd. • Ann Arbor, MI 48106-1448 • 313-665-0611  
CIRCLE 48 ON READER SERVICE CARD



**Gelman Sciences**

*Acrodisc*

**MAXIMIZE YOUR  
SENSITIVITY...  
for Volatile Organic  
Compounds by Dynamic  
Headspace Concentration**



5 ml Coffee on Tekmar's LSC 2000 and Capillary Interface

**Flavor/Fragrance  
Competitive Analysis  
Off Flavor/Odor Analysis  
Packaging Materials  
Pharmaceuticals/Residual Solvents  
Building Products/Outgassing Studies  
Polymers  
Residual Monomers/Solvents**

Ask for our **FREE** bibliography of reprints  
on a wide range of applications

P.O. Box 371856 • Cincinnati, OH 45222-1856  
(800) 543-4461 Sales • (800) 874-2004 Service  
Fax (513) 761-5183 • Telex 21-4221

CIRCLE 135 ON READER SERVICE CARD

**BRIEFS**

**Fiber-Optic Glucose Sensor with Electrochemical Generation of Indicator Reagent 755**

A reversible indicator reagent for a glucose fiber-optic sensor is provided by electrochemically regenerating a redox mediator, tetrathiafulvalene. The fiber-optic sensor is compared with an amperometric enzyme electrode.

Hari Gunasingham\*, Chin-Huat Tan, and Jimmy K. L. Seow, Department of Chemistry, National University of Singapore, Kent Ridge, Singapore 0511

**Poly(vitamin B<sub>12</sub>)-Modified Carbon Electrodes Used as a Preconcentration-Type Sensor for Alkylating Agents 759**

The B<sub>12</sub>-CME, a multiple-use preconcentration-type electrochemical sensor for alkylating agents (RX), is related to organometallic adduct formation (B<sub>12</sub>-CME-R). Primary alkyl iodides are detected at 10<sup>-7</sup> M < [RI] < 10<sup>-3</sup> M, depending on R.

Beat Steiger, Annette Ruhe, and Lorenz Walder\*, Institute of Organic Chemistry, University of Berne, Freiestrasse 3, CH-3012 Berne, Switzerland

**Photodissociation/Gas Diffusion/Ion Chromatography System for Determination of Total and Labile Cyanide in Waters 766**

Complexed cyanide is photodecomposed to release free cyanide in an acidic solution. The free cyanide is separated from interferences with a gas diffusion ion chromatography separation scheme. The detection limit for cyanide is 0.1 µg/L.

Yan Liu\*, Roy D. Rocklin, Robert J. Joyce, and Michael J. Doyle, Dionex Corporation, 1228 Titan Way, Sunnyvale, CA 94088-3603

**Correspondence**

**Computational Analysis of Chiral Recognition in Pirkle Phases 770**

Kenny B. Lipkowitz\* and Brian Baker, Department of Chemistry, Purdue University School of Science at Indianapolis (PUSSD), 1125 East 38th Street, Indianapolis, IN 46205

**Technical Notes**

**Maleic Acid/Ammonium Hydroxide Buffer System for Preconcentration of Trace Metals from Seawater 774**

Su-Cheng Pai\*, Tsai-Chu Chen, and George T. F. Wong, Institute of Oceanography, National Taiwan University, Taipei, Taiwan, R.O.C. and Chin-Chang Hung, Department of Oceanography, National Taiwan Ocean University, Keelung, Taiwan, R.O.C.

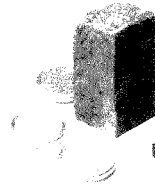
# SIEMENS

## Universal elemental analysis with the SRS 303 Sequential X-ray Spectrometer



Copper  $67.8 \pm 0.08\%$

Zinc  $0.5 \pm 0.1$  ppm



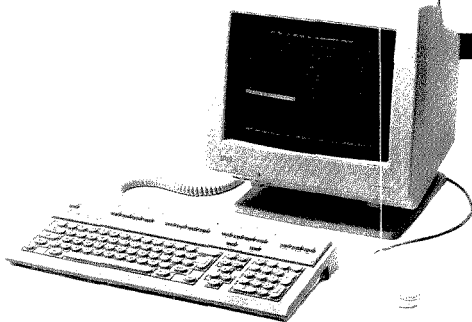
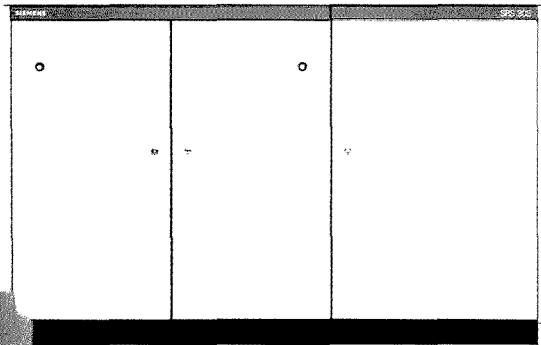
Uranium  $34 \pm 1$  ppm

### All elements from boron to uranium

- From ppm to 100% concentrations.
- Minimal sample preparation.
- Quantitative, qualitative, semi-quantitative.



Boron  $4.0 \pm 0.1\%$



The SRS 303 X-ray Spectrometer provides optimal excitation for all elements using a Siemens AG Rh 66 end-window tube.

Analyses are automated using fully integrated sample changers with 10 or 72 positions by means of easy-to-use PC software. Additional programs for the system support fundamental parameters and semi-quantitative analysis, with comprehensive facilities for storing and processing data, as well as for integration in computer networks.

In USA & Canada contact: Siemens Analytical X-Ray Instruments, Inc. • 6300 Enterprise Lane • Madison, WI 53719 • (608) 276-3000 • FAX (608) 276-3006  
Worldwide contact: Siemens AG, Analytical Systems AUT V 353 • D 7500 Karlsruhe 21 • P.O. Box 21 1262 • Federal Republic of Germany • (0721) 595-4295

CIRCLE 133 ON READER SERVICE CARD



**The GOW-MAC Series  
580 Gas Chromatograph  
Lets You Set the  
Specifications**

**Custom modifications insure optimum performance for your dedicated applications**

- Select one of seven different detector options for isothermal analyses
- Specific TC detectors designed for corrosion, trace, preparative scale, and high O<sub>2</sub> content analysis
- Select either packed, capillary, or widebore capillary columns
- Complete selection of manual or automatic valves for gas/liquid sampling, backflush, column switching, and series bypass operations
- Select injection ports for either gas or liquid samples

Send your specifications to P.O. Box 32, Bound Brook, New Jersey 08805 or call 201/560-0600, FAX: 201/271-2782 and we will provide a Gas Chromatograph custom tailored for the job.

**GOW-MAC**  
INSTRUMENT CO.

The World's Leading Manufacturer of Thermal Conductivity Detectors  
CIRCLE 50 ON READER SERVICE CARD

414 A • ANALYTICAL CHEMISTRY, VOL. 62, NO. 7, APRIL 1, 1990

**BRIEFS**

**Design for Field-Flow Fractionation Channels and Split-Flow Lateral-Transport Thin Separation Cells 777**

Lori Koch, Central Analytical Department, CIBA-GEIGY Ltd., CH-4002 Basel, Switzerland

**Ultrasonic Hydrodynamic Modulation Voltammetry 779**

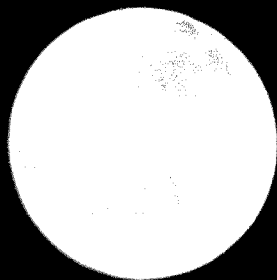
Howard D. Dewald\* and Brock A. Peterson, Department of Chemistry, Ohio University, Athens, OH 45701-2979

**Construction of Submicrometer Voltammetric Electrodes 782**

Bradford D. Pendley and Héctor D. Abruña\*, Department of Chemistry, Baker Laboratory, Cornell University, Ithaca, NY 14853-1301

**Correction. Random-Walk Theory of Nonequilibrium Plate Height in Micellar Electrokinetic Capillary Chromatography 784**

Joe M. Davis, Department of Chemistry and Biochemistry, Southern Illinois University, Carbondale, IL 62901



## If the moon can move oceans, imagine what it can do to a 1 gram sample.

Little did Newton know what problems would befall future scientists due to gravity. But fortunately, we've come up with a solution. The METTLER AT Analytical Balance.

As a matter of FACT (that's Fully Automatic Calibration Technology), it does everything in its power to combat the forces of nature.

FACT gives the METTLER AT a mind of its own. It actually adjusts itself to the unsettling influences of gravity, temperature and humidity. So no matter where in the world you use the AT, you get the absolute precision you expect from a METTLER instrument.

What's more, FACT decides when a calibration is needed. And even does it automatically.

All things considered, when it comes to adjusting to your lab's environment, the METTLER AT is a natural.

METTLER balances are available only from Fisher Scientific or VWR Scientific.

All products are backed by METTLER Service Plus®. Call 1-800-METTLER for information.

CIRCLE 90 ON READER SERVICE CARD

**Mettler Instrument Corporation**

Box 71

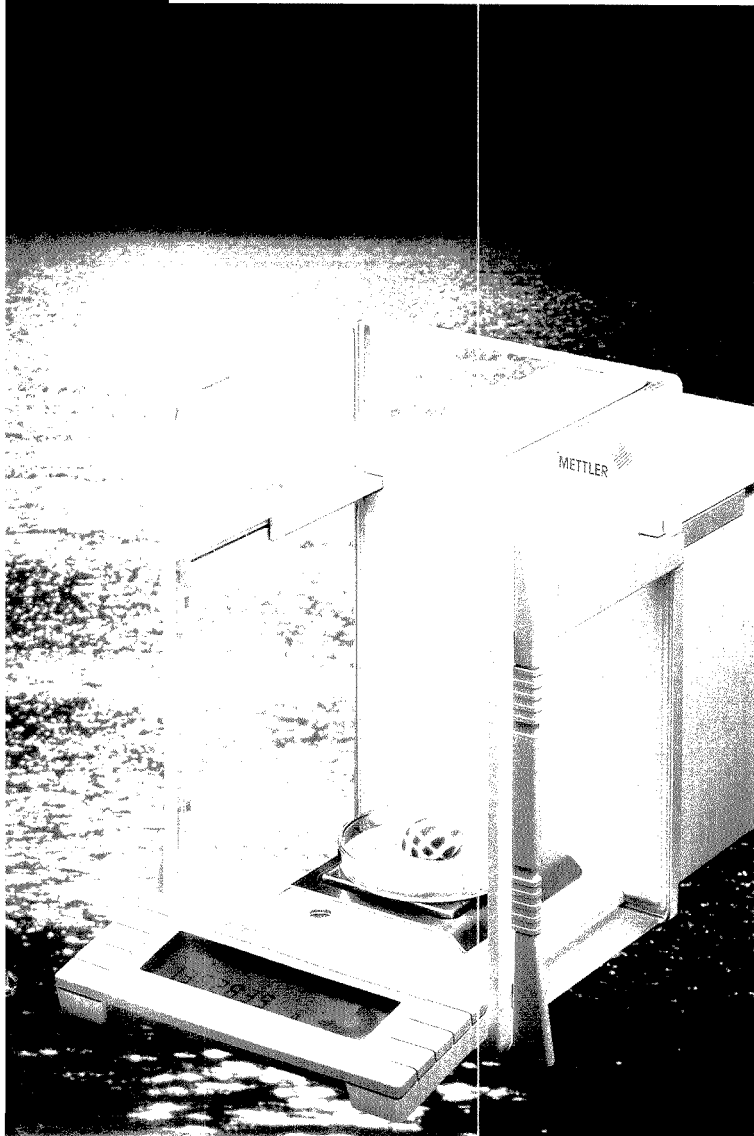
Highstown, NJ 08520

1-800-METTLER

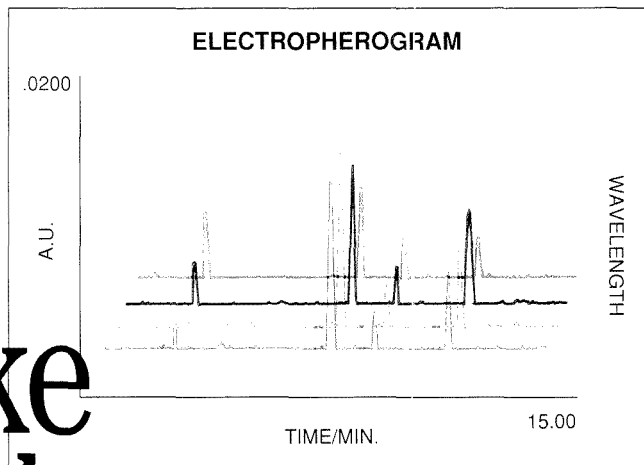
(NJ 1-609-448-3000)

# METTLER

We understand.  
Precisely.



# Take a better look at your CE data.



See what's been missing in capillary electrophoresis.

Spectra! The benefits of multi-dimensional detection are yours with the Spectra PHORESIS™ 1000 capillary electrophoresis (CE) system now from Spectra-Physics.

Spectra will authenticate your data. Peak purity and spectral scans conform to the latest regulatory requirements. Separation reproducibility is guaranteed by our unique design which cools the entire capillary. Analyze up to 80 samples on our autosampler.

Advanced detector technology gives you three detection modes—single- $\lambda$ , multi- $\lambda$  and spectral scanning. If you want to know more call us toll-free at 800-424-7666. Take a better look at your CE data. Now see what you've been missing!

VISIT US AT F.A.S.E.B. — BOOTH 1605

 **Spectra-Physics**

Discover the Quality

Circle 130 for literature. Circle 131 for a sales representative.



# EDITORIAL

## Real Science

The perceived hierarchy and bias among scientists (mathematician vs. physicist vs. chemist vs. biologist) have received attention in this column before (June 1986). However, in the past four years little has changed to alter anyone's feelings on the subject. The branches of science and even the divisions within chemistry are competing for media attention and branding each other with stereotypes.

The type of prejudice that gives rise to superiority and inferiority labels based on field of endeavor is having a very negative effect on science. Competition is healthy and promotes achievement, but discrimination and snobbery result in poor relationships and reinforce a negative view of science among outside observers.

The reality of this class structure can be seen in almost everything we do, and it is disturbing that such opinions affect the attitudes of graduate students. The prevailing notion of "good science" versus "bad science" has led to a simplistic view of the real world. Certain areas of science are looked down upon with regard to the significance of the work and the quality of the people involved. There should be no place for such thinking, and as scientists who are normally proud of our objective views, we should be particularly sensitive to such misconceptions.

A good example of the absurdity of stereotypes and the class system in science can be found in the discovery and implementation of a new drug. Is the contribution of the organic chemist who discovered the molecule more significant than that of the biologist who determined its activity? What about the process chemist who made the bulk synthesis of the drug a reality? Without this contribution there would be no drug. And the analytical chemist who developed techniques to ensure an effective and contaminant-free product? The chemical engineer who turned a bulk

process into an on-line manufacturing plant? Each step alone is significant, but each step cannot stand alone; it is only after combining these steps that we see the true overall accomplishment.

A student of mine related the friendly competition between two of his former professors, one an inorganic chemist and the other an organic chemist. Their argument was based on the question of the classification of ferrocene. Is this an inorganic or organic molecule? They both used a pastrami sandwich as a model for their theory. The organic chemist stated that a pastrami sandwich is not a sandwich without the rye bread above and below the meat. No one eats pastrami alone or on white bread. Therefore it is the organic component of the molecule, the rings above and below the iron, that is critical. Conclusion: Ferrocene is an organic molecule. The inorganic chemist pointed out that a pastrami sandwich without pastrami is no more than two slices of bread. The central iron atom gives ferrocene its importance and is therefore an inorganic molecule.

The absurdity and humor of their friendly debate sheds light on the absurdity of the scientific class system. No one branch of science is more important than another; in fact, no one area of science can stand alone. Mathematics is not better than physics; physics utilizes the discipline of mathematics and can provide math with a connection to the world. The importance of science is in its interconnections, the way in which disciplines overlap. The contributions of all fields and investigators make the whole of science important in this world. This is the unbiased view that we as participants in science must take. If we do not, we can never expect outside observers to take an unbiased view of us.

*G. H. Morrison*

# PEAK QUALITY

with

# Claisse Fluxes

(Borates and Phosphates)

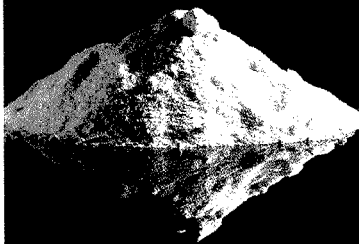
Get a new perspective on analysis and better results. The CLAISSÉ FLUXES have exceptional qualities due to their PURITY and COARSE texture. Claisse Fluxes are Tip-Top.

#### FEATURES

- ▶ free-flowing crystals
- ▶ low surface area
- ▶ high density
- ▶ fused, not mixed
- ▶ popular and special compositions

#### CONSEQUENT ADVANTAGES

- ▶ no loss from static electricity
- ▶ no loss by splattering or foaming on heating
- ▶ very low water absorption
- ▶ no uncertainty on quantity weighed
- ▶ no segregation in containers
- ▶ FREE SAMPLE upon request



For world-wide sales, address of local agents and service information please call or write to:



corporation  
scientifique  
claisse inc.

2522, chemin Sainte-Foy  
Sainte-Foy (Québec)  
Canada G1V 1T5  
Tel: (418) 856-8453  
Fax: (418) 856-1189  
Telex: 051-31731

**The First and Finest in Fusion.**

CIRCLE 22 ON READER SERVICE CARD

418 A • ANALYTICAL CHEMISTRY, VOL. 62, NO. 7, APRIL 1, 1990

## LETTERS

### Early Analytical Automation

Sir: The article by H. M. Kingston (*Anal. Chem.* 1989, 61(24), 1381 A-1384 A) brought back memories of the early 1950s. At that time, I would have had much interest in the proposed Consortium on Automated Analytical Laboratory Systems. Although I am now 96 and in the process of giving up my office, I still have some interest in the subject.

As a member of ASTM Committee E-3 and a close watcher of Committee E-2 on atomic emission spectroscopy, I became interested in the efforts of the two Churchills, H. V. and J. R., to speed up the analysis of aluminum alloys. Also, I had been suggesting to my junior students in chemical engineering a possible development of a balance that would stamp mass values, in indelible ink, in their laboratory notebooks. Several did report efforts in this direction after they joined industrial laboratories.

In the course of preparing our reviews on molecular absorption spectroscopy, I noticed many abstracts on various kinds of automation and suggested to the editor the possibility of publishing a review of these developments. He agreed, and we published three reviews in 1950, 1951, and 1952. These were mostly written by my student, G. D. Patterson, Jr., who worked for Du Pont. As they did not see much advantage to the company in continuing the reviews, we did no more. Later, I published a report on automation (*Anal. Chem.* 1958, 30(12), 25 A).

I also gave a talk entitled "Analytical Automations" to a number of ACS local sections. I tried to get the Chur-

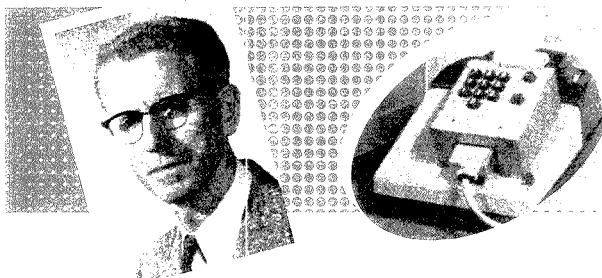
chills to prepare a film showing what they were doing. I recall a talk by H. V. Churchill in which he stated that an automatic method's primary use is in highly repetitive work, such as analyzing blood and urine in the Mayo Clinic laboratories.

As an indication of my practical interest in the subject, we purchased the first General Electric recording spectrophotometer in 1934. I had started our course on physicochemical methods in 1921. (I never use the word instrumental as I consider all measurement instrumental.) My student H. W. Swank in 1936 devised the first manual calculator for determining tristimulus values from spectrophotometric curves.

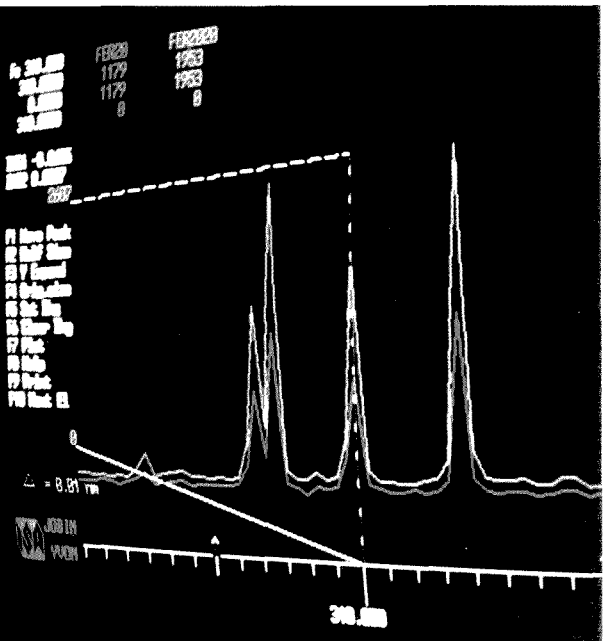
Then, around 1960, at a Pittsburgh Conference, I persuaded Howard Cary to try to make an instrument with which one could determine either absorbance or transmittance. Six months later he wrote that he had solved the problem, and we bought what I presume was the first Model 10-11. I am just completing the transfer of my historical collection of some 20 photometers (both filter and spectrophotometers) to the Instrument Museum of the University of Cincinnati.

I should like to survive long enough to learn how the consortium develops.

M. G. Mellon  
Professor Emeritus  
Analytical Chemistry  
Department of Chemistry  
Purdue University  
West Lafayette, IN 47907



# ICP SPECTROMETERS FROM J-Y DIVISION, ISA



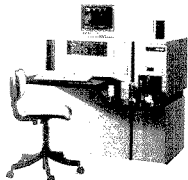
## MEANINGFUL FEATURES—MEANINGFUL RESULTS

From the World Leader in ICP Spectroscopy

The Jobin Yvon family of ICP's give you the widest choice of systems available... one ideally suited for your application. Choose from two sequential systems, two simultaneous systems, or the world's most powerful ICP... The J-Y Combination System.

But perhaps more important than the wide range of products are the features. *The best detection limits. Interchangeable cassettes for different types of samples. Computer controlled slits to maximize detection for dif-*

*ferent elements... even in the same method.* Highest performance, fast efficient service and applications support, and a continuing commitment to technical innovations... all are meaningful features included with every Jobin Yvon System. They assure you of meaningful results not only now, but also in the future. For more information use the reader service card, or write or call (201) 494-8660 today.



**JY 24 Sequential**  
The affordably priced JY 24 gives you high performance and flexibility in a compact design.



**JY 38 Sequential**  
Unequaled resolution and stray light rejection combine to give you superior limits of detection.



**JY 50 Polyscan Simultaneous**  
The unique REST concept provides the advantages of simultaneous, multi-element speed and the flexibility of sequential scanning.



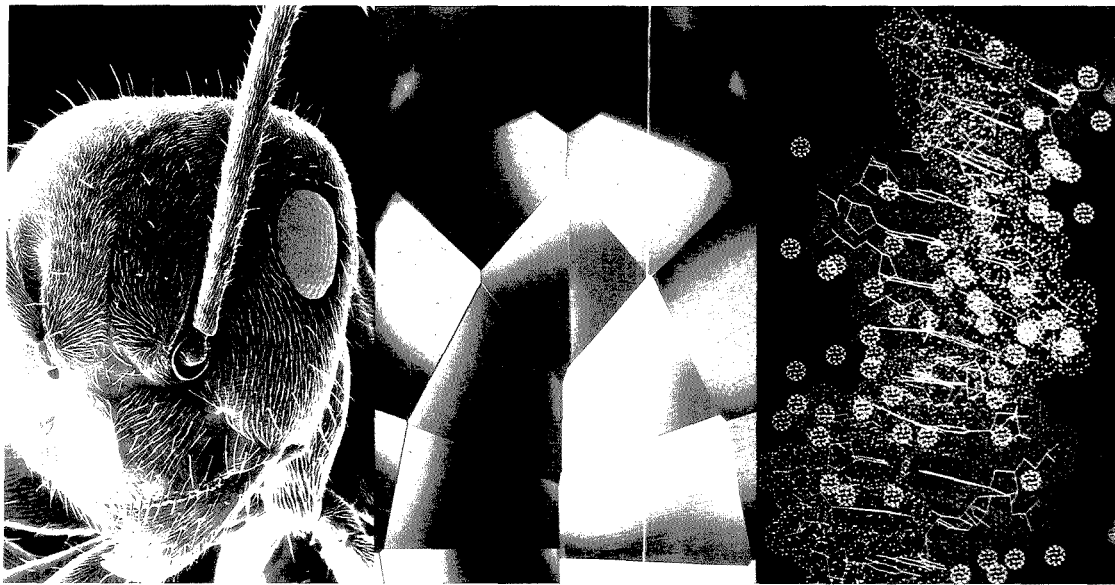
**JY 70 Combination Simultaneous Sequential** — The JY 70 combines all the advantages of the JY Family of ICP's for the ultimate in speed, precision and versatility.



**J-Y DIVISION**  
Instruments SA, Inc.

6 Olsen Avenue, Edison, New Jersey 08820-2419  
Tel. (201) 494-8660, Telex 844516 FAX (201) 494-8796  
In Europe: Jobin Yvon, 16-18 Rue du Canal 91163 Longjumeau, France.  
Tel. (33) 1 69 09 34 93 Telex JOBYVON 602992F FAX (33) 1 69 09 07 21

# VARIAN NMR FLEXIBILITY NOW RESOLVES PROBLEM DIVERSITY



MICROIMAGING

SOLIDS

LIQUIDS

## UNITY lets you switch from one to the other with ease

Combine high performance capabilities with unparalleled flexibility using Varian's new UNITY™ NMR spectrometer. This unique spectrometer is a true, multi-capability instrument that performs high resolution microimaging as easily as it analyzes liquid and solid samples.

UNITY's revolutionary system architecture employs a modular design that addresses all NMR applications with a single instrument.

Analyze liquid samples using a variety of techniques over a wide range of nuclei. Perform CP/MAS, wideline and multipulse for solid samples.

Examine microimaging samples with ease. Maximum flexibility has been built in to cover future experimental capabilities for every application.

Resolve problem diversity: invest in the most flexible technology of today to better address the research of tomorrow. Invest in a UNITY NMR spectrometer. For additional information, please call **800-231-8134**. In Canada, call **416-457-4130**.

Varian is your full-line  
company for analytical  
instrumentation

UV-Visible-NIR

LIMS

Atomic Absorption

NMR

Liquid Chromatography

Gas Chromatography

CIRCLE 140 ON READER SERVICE CARD

## NMR WITH A FUTURE

## Ozone Plane

Working with researchers at Harvard University, engineers at Aurora Flight Sciences in Alexandria, VA, have begun constructing a remote-controlled plane for studying the ozone hole over Antarctica. The pilotless plane, named *Perseus*, will reach altitudes as high as 25 km carrying instrument payloads of up to 50 kg for analyzing upper atmosphere constituents. "Such flights can gather the data we need to understand what controls the depletion of ozone over the polar regions," explains James Anderson, Harvard professor of atmospheric chemistry.

The plane's construction is being directed by John Langford, who also developed *Project Daedalus*, the human-powered aircraft that flew 120 km between the Mediterranean islands of Crete and Santorini. "The advantage of the plane," explains Langford, "is lower cost and increased scientific utility."

At present, ozone researchers rely on balloon-carried instruments to collect in situ data at 25 km. The balloon payloads return by parachute but often are damaged or even lost in the process. Given the demand for more monitoring of the ozone hole, the plane should save money by eliminating the cost of replacing balloon payloads.

The greater scientific utility results from the increased flexibility of the plane. According to Langford, weather and wind conditions are right to launch balloons on about 35% of the days, but the plane should be able to fly as much as 70% of the time. In addition, balloon-borne instruments only take measurements on the way down because of the balloon's initial outgassing. The plane, on the other hand, will collect data nearly continuously. Finally, the plane offers better control of location than do free-floating balloons.

Like *Project Daedalus*, *Perseus* will be constructed with lightweight composite materials. The plane (see illustration) will be battery-powered and will have a 17.5-m wingspan and an aft-mounted propeller. Instrument payloads are simply bolted in and can be changed as required. The estimated \$200,000 cost is being financed by the Weld Foundation.

*Perseus*'s maiden flight should occur later this year. Antarctica missions are expected to begin late in 1992—the region's spring season—when ozone levels have generally been at their lowest. The plane could also be employed to monitor greenhouse gases that may be collecting over mid-latitude regions.

## Cited Articles

According to the latest survey by *Science Citation Index*, which covers the period from 1945 to 1989, three of the top 100 most cited articles were printed in ANALYTICAL CHEMISTRY. The three articles are a 1956 paper by Chen, Toribara, and Warner on the microdetermination of P;

another 1956 paper by Dubois, Gilles, Hamilton, Rebers, and Smith describing the coulometric method for determining sugars and related substances; and the Spackman, Stein, and Moore 1958 report of a system for continuous-flow detection of amino acids. The most cited article is the 1975 introduction by Ames, McCann, and Yamasaki of a screening method for carcinogens and mutagens known as the Ames Test.

The Ames article was published in the *Journal of Biological Chemistry*, which is the most cited publication in the list with 17 references. However, ANALYTICAL CHEMISTRY's three papers compared favorably with two for *Science* and one for the *Journal of the American Chemical Society*.

## New NIST Director

The U.S. Senate has confirmed physical chemist **John Lyons** as the ninth director of the National Institute of Standards and Technology (NIST). He succeeds Ernest Ambler, who retired last spring.

Lyons received his A.B. degree from Harvard (1952) and his A.M. degree (1963) and Ph.D. (1964) from Washington University. After 18 years with Monsanto, he joined the then National Bureau of Standards as head of the Center for Fire Research in 1973. Lyons is the author of three books and the recipient of several awards, including the Presidential Rank Award of Distinguished Executive and the 1986 Edward Uhler Condon Award for his book *Fire*.



## For Your Information

The National Institute of Standards and Technology has just released *Standard Reference Data Publications 1987-1989*, which updates the 1964-1984 directory of publications and databases dealing with physical and chemical properties of substances prepared through the National Standard Reference Data System. For more information, contact Standard Reference Data Program, A323 Physics Bldg., NIST, Gaithersburg, MD 20899 (301-975-2208).

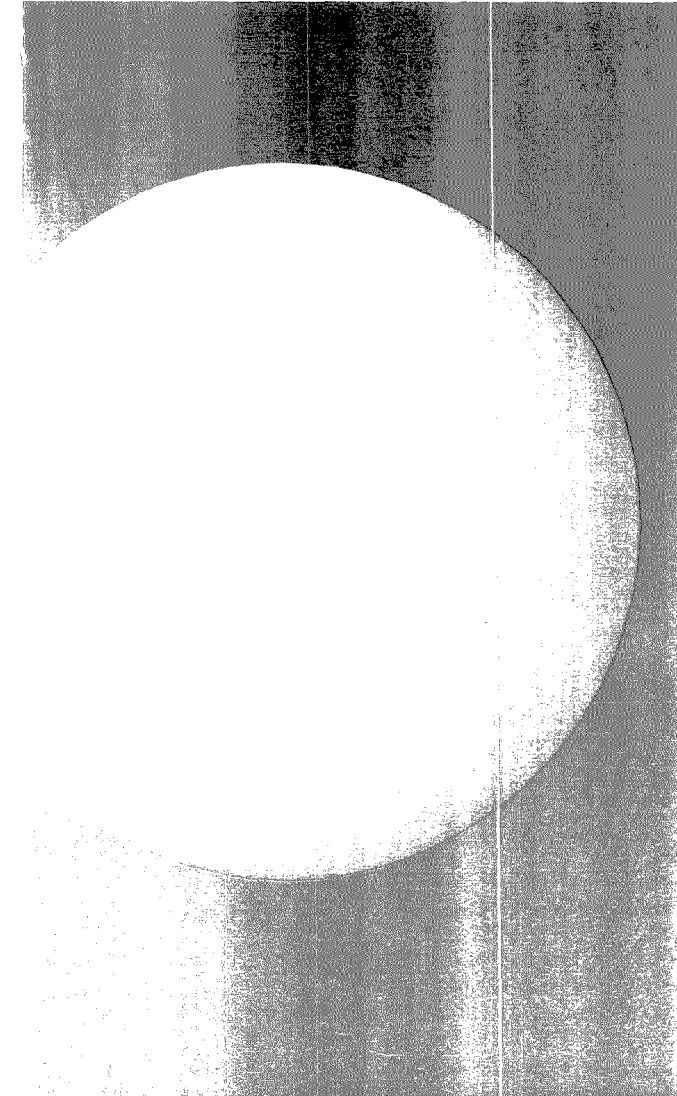
The National Science Foundation has announced that elementary school teachers are now eligible for Presidential Awards for Excellence in Science and Mathematics Teaching. Nominations should be sent by April 23 to: Elementary PAEMST, National Science Teachers Association, 1742 Connecticut Ave, N.W., Washington, DC 20009.



VIG INSTRUMENTS

**F U S I O N : A S O U R**

A R L    C A R L O   E R B A   I N S T R U M E N T S    H A A K E



There is a new, vibrant source of energy in the world of analytical instrumentation. The VG Group has just joined forces with a company that has a proven record in fostering the talents and services of innovative, specialised companies. That company is Fisons and with this important acquisition Fisons Instruments is now among the very largest analytical instrumentation enterprises in the world.

VG is the most recent instrument company to join this highly successful parent. Among its companies Fisons Instruments already counts other well-known market leaders like ARL, Carlo Erba Instruments and Haake.

What did companies with marked success in their own right stand to gain from this fusion?

Simply, more energy for their business and their customers. A new dynamic environment that promotes the fusion of ideas from many technologies, producing rapid advancements in hyphenated techniques. A huge pool of expertise and resources to promote creativity and turn concepts into realities. And the power of one of the largest customer support networks in the scientific world behind them.

The VG Group is known worldwide as the leading innovator in mass and X-ray spectrometry, surface analysis and ultra-high vacuum technology. Fisons is internationally respected as the company that really helps its customers to benefit from the latest advances in analytical instrumentation.

Together they become your indispensable partners in scientific endeavour.

Whatever your own field of work, let us tell you more about the choices now open to you through the new Fisons Instruments. Contact us for a copy of our brochure.

**C E O F N E W E N E R G Y**

**FISONS**  
Instruments

Fisons Instruments, 24911 Avenue Stanford, Valencia,  
CA 91355, USA  
Telephone: (800) 551-8741 Interstate  
(800) 631-6841 California

K E V E X      V G   I N S T R U M E N T S

CIRCLE 45 ON READER SERVICE CARD



**Joe Harland, Ph.D.**  
Senior Research Chemist

Has developed many new and unique phase chemistries, including J&W's Alumina for C<sub>18</sub> isomers, and Cyclodex-B™ for chiral separations.

**Michi Lee**  
QC Lead Technician

Tests hundreds of GC columns each week; a signed column performance summary, included with each product she approves, is her personal guarantee of quality.

**Mark Dinnauer**  
Technical Support Chemist

Answers applications questions for J&W customers, drawing on his expertise in pharmaceutical and pesticide chemistry.

# Three smart reasons to choose J&W.

**Great chemistry.** The results you get out of a column depend on the chemistry you put in—polymer chemistry, that is. Polymers are the basis of all GC, HPLC and SPE phases. That's why J&W has a team of Ph.D. chemists who specialize in novel polymer synthesis, from silane building blocks to unique surface chemistries.

Their ingenuity made J&W a world leader in gas chromatography. Now, that same expertise is applied to our new Accusphere™ HPLC columns and Accubond™ SPE cartridges. Remember, chromatography begins at the molecular level—long before pumps and detectors. So if you're working with HPLC or GC, give J&W a call. It could be the smartest move you'll ever make.

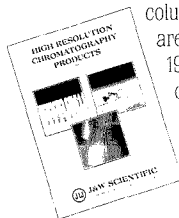
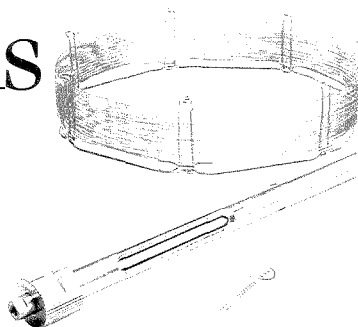
**Reliability.** J&W chemists control every detail of the manufacturing process, from the very start. They synthesize the phases that bond to HPLC and SPE silica, and the silanes that make up each GC

stationary phase. This ensures a high level of consistency, with excellent batch-to-batch reproducibility. Our QC technicians personally test and guarantee every column we sell. You can depend on J&W for the very best—both in our products, and your results.

**Convenience.** J&W is your central source for GC and HPLC columns and SPE cartridges. All our products are optimized for performance. And when you have questions, there's just one place to call for technical support and applications advice.

Chemistry. Reliability. Convenience. Three smart reasons to choose J&W for columns and cartridges. There are dozens more. Send for our 1990–91 catalog and find out for yourself.

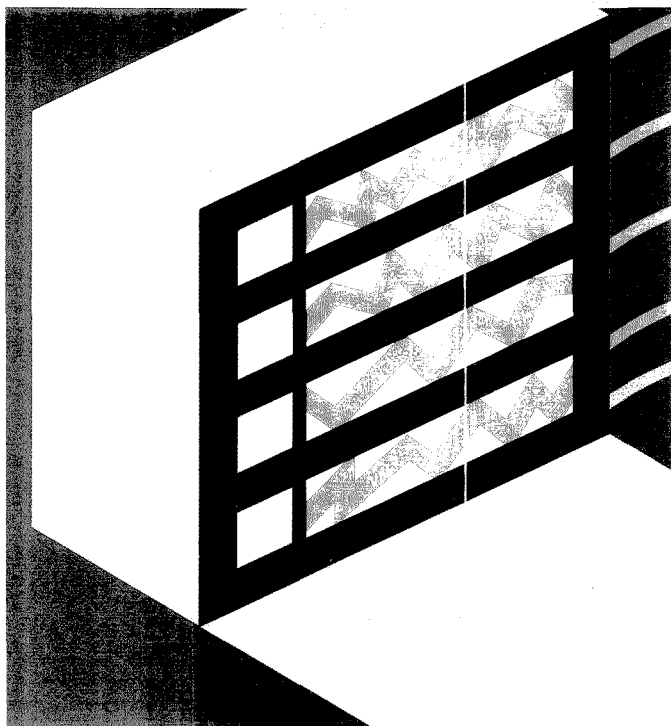
It's free. Which may be the best reason of all.



## FISONS

J&W Scientific  
91 Blue Ravine Road  
Folsom, CA 95630  
(916) 985-7888  
Fax (916) 985-1101





# Chemical Sensors for Bedside Monitoring of Critically Ill Patients

---

## Michael E. Collison

Analytical Development Division  
Lilly Research Laboratories  
Lilly Corporate Center  
Indianapolis, IN 46285

## Mark E. Meyerhoff

Department of Chemistry  
University of Michigan  
Ann Arbor, Michigan 48109

---

"He will manage the cure best who has foreseen what is to happen from the present state of matters."

*The Book of Prognostics* by  
Hippocrates (ca. 460-377 B.C.)

Empedocles (ca. 500-430 B.C.), the "Father of Greek Chemistry," originated the theory of elements and compounds in which all substances derive from combinations of the four "elements": earth, air, fire, and water. Hippocrates adapted Empedocles' view of nature to a similar theory of human physiology (1), in which health existed when four humors, or body fluids (blood, phlegm, yellow bile, and black bile), were present in proper proportion to each other. Thus Hippocrates' call to assess "the present state of matters" may have been the first historical recognition of the need to monitor closely the physiological state of the human body in order to manage a more effective cure.

In the two and a half millennia since the Hippocratic doctrine, models of human physiology have grown in complexity, and the need for physiological monitoring has progressed beyond the balancing of the four humors. Indeed, modern clinicians are increasingly dependent on reliable measurements of key chemical variables in blood for proper clinical diagnosis and therapy.

Until recently, physiological monitoring has been accomplished by analyzing discrete blood samples at centralized clinical chemistry laboratories remote from the patient's bedside.

---

## REPORT

---

This conventional approach, however, provides only "historical" measurement values because it takes precious time to transport the sample to the main lab, have the lab perform the appropriate test, and then return the test results to the clinician or nurse. In some hospitals, this so-called turnaround time can be 30 min or more. These inherent delays may prevent early detection of rapidly changing blood chemistries, particularly for critically ill, surgical, and other unstable patients. Moreover, for certain key analytes (e.g., blood gases), test values measured in remote laboratories may

not reflect the true physiological levels of the analyte because of errors induced by the required sample transport process (2).

As the number of highly specialized and sophisticated critical care/surgical units at hospitals has grown, there has been an increase in the demand for measurement technologies that can monitor changes in a select list of critical care analytes (see Table I) at the bedside of seriously ill and surgical patients. Devices capable of continuously or semicontinuously monitoring blood gases, electrolytes, and certain metabolites can provide real-time information that can result in improved diagnosis and more timely therapeutic intervention. This growing demand for convenient critical care chemical testing technology challenges the analytical chemist to bring conventional analytical techniques from the clinical laboratory directly to the patient's bedside without compromising measurement accuracy and reliability.

Although various complex technologies can be used to determine blood levels of the species listed in Table I, bedside analysis requires inexpensive and rugged testing instrumentation. In addition, the equipment should be simple to operate, ideally by nonlaboratory personnel with little or no training in analytical chemistry. We will discuss recent efforts to develop and imple-

ment modern chemical sensing technologies (both electrochemical and optical) for measuring blood gases (and related parameters) and electrolytes. Enzyme-based biosensors suitable for bedside testing are not described here; their current state of development has

been discussed extensively in recent reviews and monographs (3, 4).

**Blood gas and electrolyte measurements**

$P_{O_2}$  and  $P_{CO_2}$ . Blood gas analysis mandates simultaneous measurement of

pH and the partial pressures of oxygen and carbon dioxide ( $P_{O_2}$  and  $P_{CO_2}$ ) directly in undiluted whole blood samples. Almost all laboratory blood gas and electrolyte determinations are performed on commercial instruments that employ conventional Clark-style polarographic oxygen sensors for  $P_{O_2}$  measurements (Figure 1a). Such sensors operate in an amperometric mode and consist of a microplatinum cathode, a Ag/AgCl anode, an inert electrolyte, and an outer gas-permeable membrane.

A negative voltage applied to the cathode forces the reduction of oxygen to water, hydrogen peroxide, or hydroxide ions. The outer oxygen-permeable membrane protects the platinum surface from protein fouling. This membrane also controls the rate of diffusion of oxygen from the sample to the surface of the platinum and thus the rate of electrochemical reaction (measured as a current flow). The flux of  $O_2$  to the cathode is directly related to sample  $P_{O_2}$  levels. Measured currents are also dependent on membrane thickness, diffusivity of  $O_2$  through the membranes, and cathode size. Because these parameters can change with time, the output of such nonequilibrium devices tends to drift, necessitating frequent recalibration. This has hampered efforts to devise reliable catheter-type polarographic  $P_{O_2}$  sensors that are suitable for continuous *in vivo* measurements over extended time periods (5).

Newer optical  $P_{O_2}$  sensors (Figure 1b), already used in commercial extracorporeal bedside measurement systems, employ fluorescent dyes that are trapped or chemically immobilized in a thin layer adjacent to an optical fiber(s) (6, 7). In the presence of oxygen, the fluorescence intensity of the dye is quenched in an amount proportional to the  $P_{O_2}$  level in the sample. Such sensors are equilibrium devices in that no oxygen is consumed during the measurement. In principle, optical oxygen sensors offer the advantage of potential long-term stability over conventional polarographic  $O_2$  sensors, particularly for continuous *in vivo* measurements. In practice, however, such improved stability can be difficult to achieve because of the low degree of quenching that is actually observed (20%), the instability of source and detector, and the photodegradation of the immobilized dyes.

Both optical and potentiometric  $P_{CO_2}$  sensors are based on detection of equilibrium pH values in a small volume of electrolyte held behind an outer gas-permeable membrane (Figure 1c). When the partial pressure of  $CO_2$  is

**Table I. Critical care analytes and their normal ranges in blood**

Blood gases and related parameters		Electrolytes		Metabolites	
$P_{O_2}$	80–104 Torr	$Na^+$	135–155 mmol/L	Glucose	70–110 mg/100 mL
$P_{CO_2}$	33–48 Torr	$K^+$	3.6–5.5 mmol/L	Lactate	3–7 mg/100 mL
pH	7.31–7.45	$Ca^{2+}$	1.14–1.31 mmol/L	Creatinine	0.9–1.4 mg/100 mL
Hematocrit	40–54 %	$Cl^-$	98–109 mmol/L	Urea	8–26 mg/100 mL
Total hemoglobin	13–18 g/100 mL				
$O_2$ -saturated hemoglobin	95–100 %				

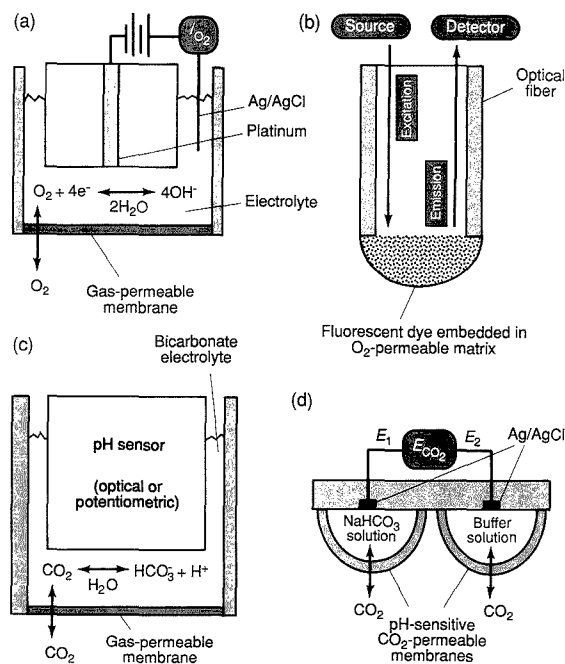
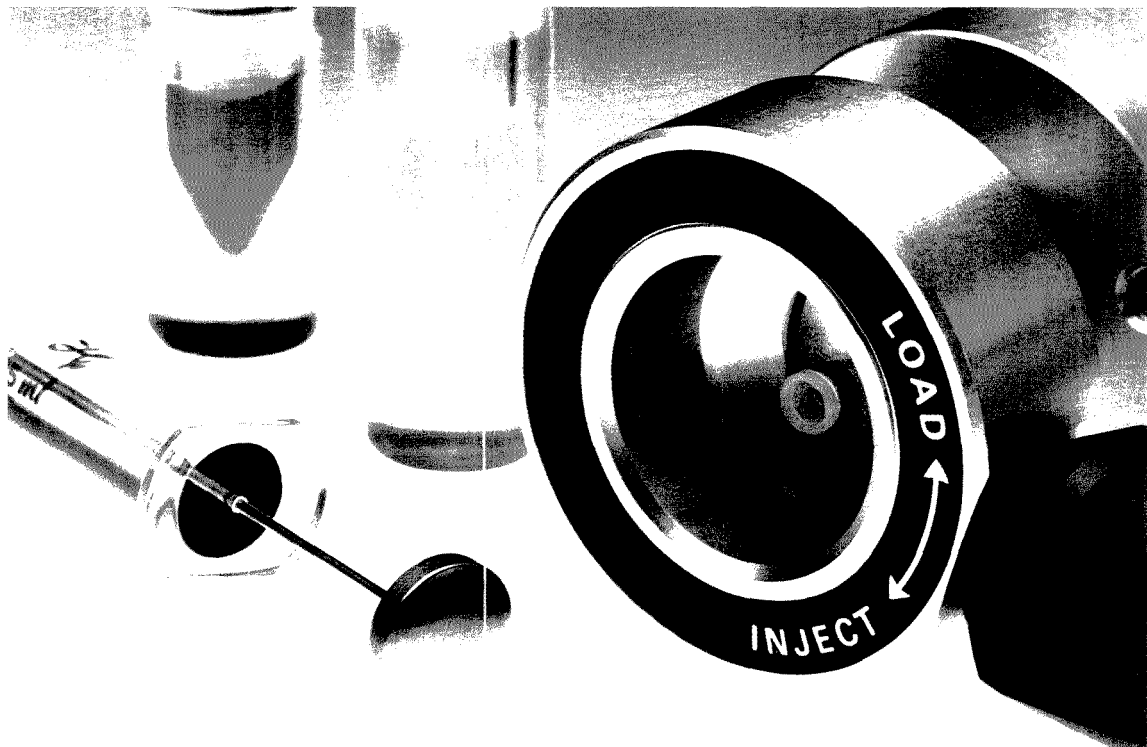


**Figure 1.** Gas sensor designs suitable for whole blood measurements. (a) Clark-style amperometric  $P_{O_2}$  sensor, (b) optical  $P_{O_2}$  sensor based on fluorescence quenching, (c) optical and potentiometric  $P_{CO_2}$  sensors, and (d) differential potentiometric  $P_{CO_2}$  sensing arrangement using dual polymeric  $H^+$ -selective sensors.

# TASK MASTER.



The Rheodyne 7125 LC sample injector is equipped with two operating modes to master every injection task.

In the "partial-fill" mode, the sample from a syringe fills a sample loop only partially. No sample is lost. The amount injected is the exact volume dispensed from the syringe.

You use this mode when you need to conserve sample or change sample volume frequently. You can inject from 1  $\mu\text{L}$  to 2.5 mL with a precision of 1%.

In the "complete-fill" mode, sample

from a syringe fills the loop completely—using excess sample. The amount injected is the exact volume of the loop.

You use this mode when you need the maximum volumetric precision of 0.1%, or you wish to load sample without having to read syringe calibrations carefully. You can inject from 5  $\mu\text{L}$  to 5 mL using one of ten interchangeable sample loops.

Variations of the Model 7125 perform yet other tasks. Model 8125 minimizes sample dispersion with micro columns. And Model 9125

uses inert plastic flow passages to prevent the mobile phase from contacting metal.

For more information about these versatile injectors, phone your Rheodyne dealer. Or contact Rheodyne, Inc., P.O. Box 996, Cotati, California, 94931, U.S.A. Phone (707) 664-9050.

**RHEODYNE**  
THE LC CONNECTION COMPANY

CIRCLE 120 ON READER SERVICE CARD

# GOOD NEWS FOR ATOMIC ABSORPTION SPECTROSCOPY



## Hamamatsu Hollow Cathode Lamps are now available from major lab suppliers.

Hamamatsu single and multi-element Hollow Cathode Lamps offer superior stability, spectral purity and output intensity, even for such elements as arsenic and selenium. They are compatible with most commercial spectrophotometers, including Beckman, Zeiss and Perkin-Elmer. And best of all, they're available from your local lab supplier.

**For Application Information, Call 1-800-524-0504**  
1-201-231-0960 in New Jersey

## HAMAMATSU

HAMAMATSU CORPORATION  
360 FOOTHILL ROAD  
P. O. BOX 6910  
BRIDGEWATER, NJ 08807  
PHONE: 201/231-0960  
International Offices in  
Major Countries of  
Europe and Asia.

© Hamamatsu Photonics, 1986

CIRCLE 60 ON READER SERVICE CARD

## REPORT

equal on both sides of the membrane, the pH of the inner electrolyte is governed by the dissociation of carbonic acid formed from diffusing  $\text{CO}_2$  in accordance with the well-known Henderson-Haselbach equation:

$$\text{pH}_{(\text{thin layer})} = \log (a_{\text{HCO}_3^-} / K_1 \cdot P_{\text{CO}_2}) \quad (1)$$

where  $K_1$  is the first dissociation constant for carbonic acid. In practice, the activity of bicarbonate in the inner electrolyte is held constant by using a high concentration of sodium bicarbonate (e.g., 50 mmol/L) such that

$$\text{pH}_{(\text{thin layer})} = K' - \log P_{\text{CO}_2} \quad (2)$$

$K'$  takes into account both the fixed amount of bicarbonate and the dissociation constant for carbonic acid. In traditional blood gas instruments, the pH of the inner bicarbonate solution is monitored by a standard glass membrane combination electrode that provides a wide dynamic  $P_{\text{CO}_2}$  measuring range. Optical  $P_{\text{CO}_2}$  sensors for extracorporeal and in vivo sensing employ optical pH probes as inner transducers. Because these devices use pH-sensitive indicator dyes (6, 7), the dynamic measuring range of the resultant  $P_{\text{CO}_2}$  probes is more restricted but still quite adequate for most biomedical situations.

With the advent of solvent/polymeric membrane electrodes for measurement of specific ionic species, including protons, a novel differential detection scheme can also be used to measure  $P_{\text{CO}_2}$  levels reliably in whole blood (Figure 1d). The analyte  $\text{CO}_2$  diffuses through the  $\text{H}^+$ -selective polymeric membranes of two "pH sensors" prepared by doping the membranes with neutral trialkylamine species (e.g., tridodecylamine). A small volume of bicarbonate/NaCl solution is used as the inner solution behind one pH membrane, and the inner solution of the second electrode is composed of a strong buffer. If both polymeric membranes respond to the proton activity of the sample identically, then at equilibrium this sample pH will cancel in the differential measurement mode, yielding:

$$E_{\text{cell}} = E_1 - E_2 \\ = K - 0.059 \log P_{\text{CO}_2(\text{sample})} \quad (3)$$

The cell constant,  $K$ , is dependent on the pH of the strong buffer used as the inner reference fill of pH electrode  $E_2$  (Figure 1d). This differential  $P_{\text{CO}_2}$  measurement is an attractive approach for systems that require disposable/planar-sensing elements.

**pH and electrolytes.** Potentiometric ion-selective membrane electrodes are the dominant methodology employed for determining pH and electro-

lytes in whole blood. Although pH and  $\text{Na}^+$ -selective glass membrane electrodes are still used in many laboratory instruments, newer bedside testing instrumentation, including some prototype in vivo sensors, rely on modern solvent/polymeric membrane electrode technology to measure  $\text{H}^+$ ,  $\text{Na}^+$ , and other important ionic species such as  $\text{Ca}^{2+}$  and  $\text{K}^+$  (8). Solvent/polymeric membranes function as ion-selective transducers only when an appropriate ionophore is incorporated within the polymeric film. The ionophore serves as a reversible and reusable binding reagent that selectively extracts the analyte ion into the organic membrane phase, thereby creating a charge separation or phase boundary potential at the membrane sample/interface.

In the differential  $\text{CO}_2$  sensor described above, the alkylamine compounds doped into the polymer membrane are the proton-selective ionophores. Indeed, the potential  $E_2$  in Figure 1d, when measured against a conventional reference electrode in contact with the sample, can be used to measure the pH of undiluted blood.

In general, sensors with membranes doped with different ionophores are used to detect pH as well as  $\text{Na}^+$ ,  $\text{K}^+$ ,  $\text{Ca}^{2+}$ , and  $\text{Cl}^-$ . The response of such sensors is proportional to the activity of the specific analyte ion in the blood sample, as described by a form of the Nernst equation:

$$E_{\text{cell}} = K + 0.059 \log a_i(\text{sample}) \quad (4)$$

The logarithmic response of these devices creates problems because very small uncertainties in the measured cell potential can only be achieved if proper attention is given to minimizing changes in the cell constant  $K$  (which includes reference electrode liquid junction potentials) when switching from calibration solutions to the unknown blood sample. Drift in cell constants can also create significant accuracy problems when trying to use miniaturized forms of these polymer membrane-based sensors for continuous in vivo pH and electrolyte whole blood measurements, because frequent recalibration is not possible under such measurement conditions.

Optical sensors for determining pH and electrolytes in blood have received considerable attention (6, 9). Optical pH sensors are based on immobilized indicator dyes that have acid-base functional groups in their structures. Changes in the absorption spectra as a function of the protonation or deprotonation of these groups are sensed directly or via more sensitive fluorescence detection schemes. As in the case of the optical  $P_{\text{CO}_2}$  sensors, the ratio of

signals at two wavelengths can be used to improve sensor output stability (i.e., to compensate for photobleaching of the dye). However, the effect of variations in blood ionic strength on the accuracy of this type of pH measurement is a concern (10).

The development of truly reversible multiuse optical electrolyte sensors that can be used for whole blood measurements (i.e., similar to the optical pH sensors) remains a significant challenge. Although advances have been made in the design of organic colorimetric/fluorescent reagents that selectively interact with the desired electrolyte species (11), immobilizing these species in a true sensing configuration has been hampered by the slow kinetics of the ion-ionophore reactions. Moreover, many of the most selective ionophores are electrically neutral; thus, extraction of the electrolyte ion into an ionophore-doped membrane, or onto a surface possessing immobilized ionophore sites, requires the concomitant extraction of an oppositely charged ion to maintain charge neutrality in the immobilized reagent layer that provides the optical signal. In some instances, the actual optical signal is generated from the addition of a fixed concentration of this "indicator" counter ion to the sample (usually serum, not whole blood) (12). Such reagent additions/sample dilutions preclude the use of electrolyte sensing methods in undiluted whole blood, making these methods less attractive for incorporation into bedside testing systems.

**Hematocrit, hemoglobin, and O<sub>2</sub> saturation.** Conventional microcentrifuge and modern cell-counting cytometry methods for measuring blood hematocrit (volume of red blood cells per unit volume of whole blood) are not amenable to the design of convenient or continuous bedside monitoring instrumentation. The simplest and most practical approach for determining hematocrit involves the measurement of blood conductivity ( $1/R_{\text{blood}}$ ). This is accomplished by using two platinum black electrodes in a standard AC impedance measurement arrangement. The spherical erythrocytes are essentially nonconducting relative to the extracellular plasma electrolyte medium, and thus increasing hematocrit decreases the current flow in the circuit. Hematocrit is calculated using the following equation (13):

$$\text{Hematocrit}(\%) = a \ln R - b \quad (5)$$

where  $a$  and  $b$  are constants and  $R$  is the specific resistance (in ohm · cm) of the blood, corrected for variations in the activity of sodium ions in the plasma phase. For the most accurate he-

# The Art... of Measuring TOC



*OI Analytical's Model 700 Total Organic Carbon Analyzer can, with just the touch of a button perform tests accurately and with the highest sensitivity available.*

*If your testing volume has expanded beyond your current capabilities or you wish to enhance your data quality... the Model 700 provides a fundamental solution with an array of intelligent accessories.*

OI Analytical views measuring impurities in ultra-high purity and drinking water as an art form; one that we have mastered.

We have gone beyond the obvious to develop a fundamental solution to the limitations of other instrumentation.



Data Handling System

OI Analytical's Model 700 TOC Analyzer has a wide range of sampling capabilities to provide today's testing laboratories with:

- Effortless automated operation
- Sophisticated data handling
- Broad-based versatility

Based on its classic methodology as described in scientific literature, the Model 700 utilizes the most preferred means of measuring total organic carbon.

Easy to operate, easy to interface and easy to purchase, the Model 700 TOC Analyzer is an attainable masterpiece.

OI Analytical 

P.O. Box 2980 · College Station, TX 77841-2980

Tel: (409) 690-1711 · Fax: 409-690-0440

CIRCLE 106 ON READER SERVICE CARD

matocrit measurements, simultaneous determination of whole blood sodium activity by a suitable ion-selective electrode is required.

The determination of hematocrit provides an indirect measure of total hemoglobin. Indeed, instruments that measure hematocrit via conductivity cells can compute a hemoglobin value by using an appropriate algorithm.

However, the only reliable and direct method to determine total hemoglobin requires lysing of red blood cells, either by ultrasound or by dilution with a lysing reagent (surfactant), and subsequent photometric measurement of the blood's absorption at an isobestic point in the visible absorption spectrum of hemoglobin (506.5 or 810 nm).

Small, dedicated instruments per-

form such tests on discrete whole blood samples and also calculate the percent of hemoglobin containing bound  $O_2$  ( $O_2$ -saturation) by monitoring blood absorption at a second wavelength corresponding to the maximum absorbance of oxyhemoglobin. However, the various optical methods for detecting  $O_2$ -saturation, either in vivo using optical fiber catheters or noninvasively through the skin (see below), cannot provide a quantitative direct measure of the total hemoglobin; they provide only the ratio of the oxy to deoxy forms.

**Adapting analytical detection methods to bedside testing and monitoring**

A variety of approaches can be used to adapt the chemical sensing methods described above to the bedside of critically ill and surgical patients (Figure 2). These approaches are discrete sample analyzers, noninvasive monitors, extracorporeal in-line and on-line sensing systems, and continuous in vivo sensing methods. Each technique offers a potentially different menu of critical care analytes because of the nature of the sensing technologies involved. In addition, the absolute analytical accuracies vary because of calibration and quality control limitations associated with each method. Such limitations closely relate to whether a given approach functions as a viable analytical test method (i.e., an acceptable alternative to conventional laboratory test values) or simply a trend-monitoring technique that can aid in the management of critical care patients but cannot substitute for frequent laboratory blood tests.

**Discrete sample analyzers.** For the most part, these analyzers are adaptations of systems already being used in high-volume clinical chemistry laboratories. Samples of blood must be withdrawn from the patient and injected or aspirated into an instrument positioned at or near the patient's bedside. Although they cannot be considered true real-time or continuous measurement systems, they do allow clinicians and nurses to obtain blood chemistry information more rapidly and frequently. A variety of such analyzers are available commercially with capabilities ranging from one to nine critical care analytes, using the measurement technologies described above.

The more attractive multiuse-multi-parameter test systems employ an array of chemical sensors positioned in a flow-through channel (Figure 3). In most instances the actual measurement signals are acquired with the sample or standard stagnant in the

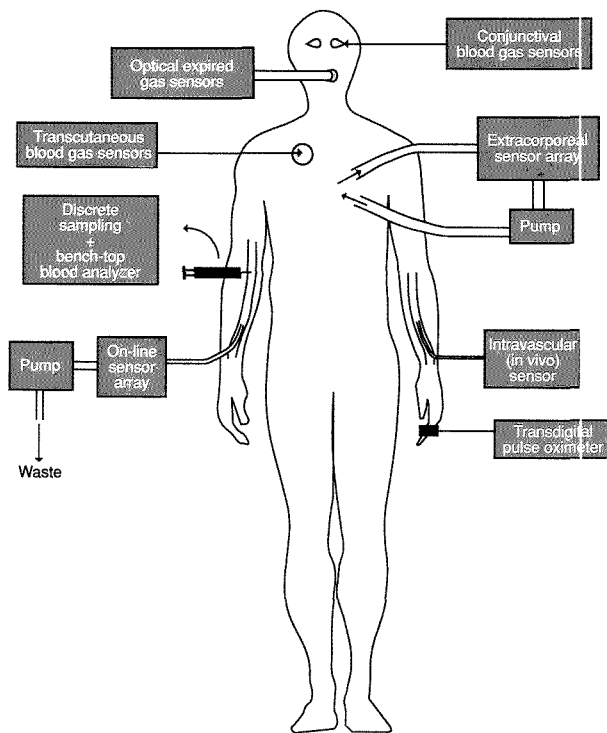


**Figure 2.** Approaches for using chemical sensing methods to monitor key analytes at the bedside of critically ill and surgical patients.

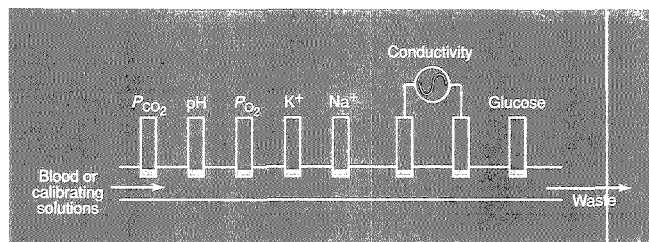
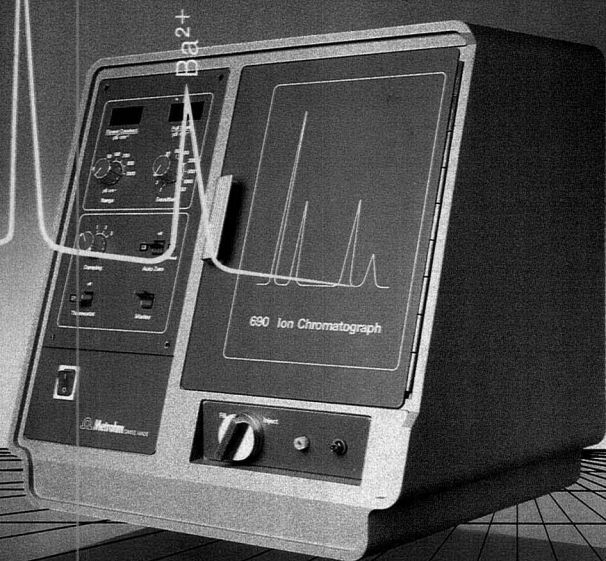


**Figure 3.** Typical flow-through sensor array used in modern discrete sample multi-parameter bedside testing instruments.

# Your LC to IC converter

If you already own HPLC instrumentation, you can easily convert it to a fully fledged IC system by the simple addition of the Metrohm 690 Ion Chromatograph. It comprises a high performance conductivity detector second to none, a thermally insulated and electrically isolated column compartment and a manual or automatic injector. Add to this the full range of Metrohm IC columns, components and accessories and we can accommodate your every needs. Outstanding are the Metrohm range of «Super Sep» columns for anion and cation separations. The «Super Sep» cation column (according to Schomburg) gives the analytical chemist the power to separate both mono- and divalent cations for the first time using a simple isocratic system. No need for extra pumps and gradient programmers.

Metrohm gives you all the applications, service and support you need. Ion chromatography — quite simply with Metrohm.



**Metrohm**

Measurement in Chemistry  
Worldwide with Metrohm  
METROHM Ltd.  
CH-9101 Herisau Switzerland  
Phone 071 / 53 11 33  
Telefax 071 / 52 11 14  
Telex 88 27 12 metr ch

 Metrohm

**BRINKMANN** Quality products for research and control  
INSTRUMENTS, INC.  
Cantiague Rd., Westbury, New York 11590  
(516) 334-7500 (800) 645-3050

CIRCLE 92 ON READER SERVICE CARD

flow-through channel. After sample measurements, the entire array is flushed with a calibrating solution, which enables the instrument to compensate continuously for any drift in the sensors' output signal. Periodic two-point calibrations allow instruments to update the sensors' calibration sensitivities (slopes) to help assure accuracy for each parameter measured.

Several manufacturers have designed systems that enable simultaneous measurement of blood gases and electrolytes using a single sample (100–500  $\mu\text{L}$ ) of undiluted whole blood with sensor arrays consisting of conventional blood gas and ion-selective electrodes. However, such systems tend to require periodic maintenance of the electrodes and assorted pump tubing. One manufacturer has designed a bedside multiparameter test system that requires minimal operator interaction and no routine maintenance. This advance is achieved by packaging the appropriate blood gas and electrolyte sensor array along with calibrating and flush solutions, within a single disposable cartridge. Once the cartridge is placed into the instrument, the user can run 50 samples over a period of up to 48 h. Unlike other blood gas analyzers that calibrate by tonometry with tanks of gas (i.e., equilibrating solutions with precise partial pressures of gas) or by using the gas tanks to calibrate in the gas phase, calibration of the disposable blood gas sensors is achieved with pretonometered solutions stored in disposable foil pouches. This eliminates the need for gas tanks and reduces the complexity and size of the resultant bedside instrument.

**Noninvasive monitors.** Noninvasive chemical sensing approaches are considered by many to be the ideal measurement technology for bedside testing of critically ill and surgical patients. These methods can provide more desirable real-time or continuous measurement without the risks associated with invasive *in vivo* methods (see below) or the time delays associated with approaches requiring specimen withdrawal. Unfortunately, the only species that currently can be determined via noninvasive techniques are  $\text{O}_2$ -saturation,  $P_{\text{O}_2}$ , and  $P_{\text{CO}_2}$ . The latter gas measurements are made through the skin using transcutaneous devices, in exhaled breath via IR absorbance (capnography) and mass spectrometry, or through the inner lining of the eyelid using conjunctival optical or electrochemical sensors (14, 15).

The more common transcutaneous oxygen and carbon dioxide sensors are quite similar in design to the electrochemical devices used in conventional

blood gas instruments except that the electrodes are more easily attached directly to the surface of the skin (Figure 4a). In this arrangement, the skin acts essentially as the outer gas-permeable membrane of the conventional gas-sensing designs illustrated in Figures 1a and 1c.

Both individual and combination oxygen and carbon dioxide sensors are commercially available. These sensors, and the sensing areas of the skin beneath them, are heated to ensure full arterialization of the underlying capillaries (Figure 4a) and faster response times. Nonetheless, the values obtained via transcutaneous oxygen and carbon dioxide measurements (termed  $P_{\text{tcO}_2}$  and  $P_{\text{tcCO}_2}$ , respectively) are subject to a number of physiological variables, including thickness of skin, peripheral blood perfusion, shunting, and other circulatory conditions. Consequently, such measurements tend to correlate more closely with actual

whole blood  $P_{\text{O}_2}$  and  $P_{\text{CO}_2}$  values only for infants and neonates. Contradictory results are obtained with adult patients, and this inconsistency has prevented widespread use of this noninvasive measurement technique (14). At best, for either patient population, transcutaneous blood gas measurements provide only trend-monitoring information and cannot substitute for regular *in vitro* whole blood tests (16).

A much greater level of routine clinical use has been attained with very simple pulse oximeters that measure  $\text{O}_2$ -saturation noninvasively. As shown in Figure 4b, the measurement is made by attaching a probe monitor consisting of two light-emitting diodes and a photodiode detector on opposite sides of a vascular bed (usually a finger). The wavelengths used correspond to the absorbance maxima for the two forms of hemoglobin, oxy and deoxy. Optical measurements at both wavelengths are taken during each pulse to ensure arte-

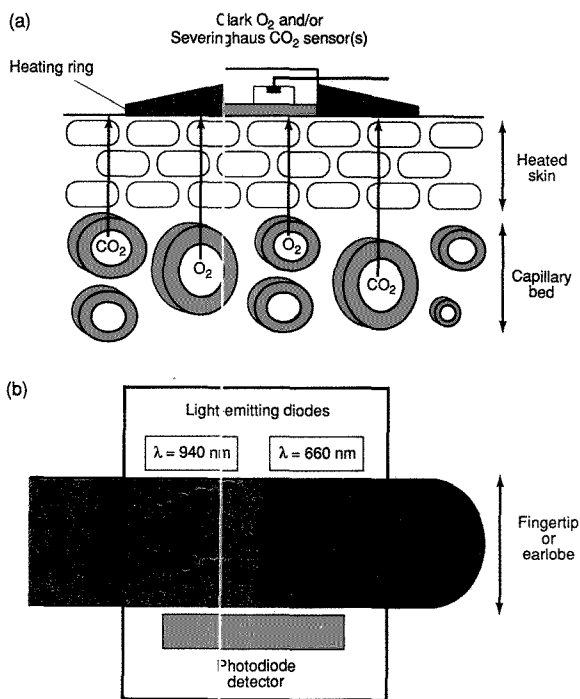
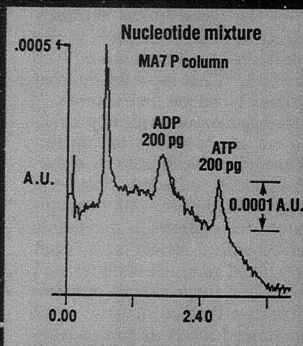
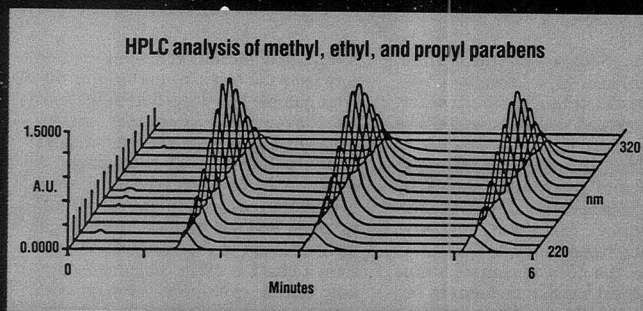


**Figure 4.** Noninvasive monitors.

(a) Sensing arrangement for transcutaneous monitoring of  $P_{\text{CO}_2}$  and/or  $P_{\text{O}_2}$  and (b) optical sensing arrangement used to monitor percent saturated  $\text{O}_2$  via noninvasive oximetry.





Make sure your  
UV-Vis detector  
has all these  
capabilities...

Not just some of them!

- Unsurpassed sensitivity—detect picograms of biomolecules
- Complete spectral scans in a fraction of a second
- Full UV-Vis operation, 190 to 800 nm
- High sensitivity using true dual-beam optics
- Wide range of flow cells for any HPLC application
- Powerful Microsoft® Windows® software for complete data handling including 3-D, ratioing and derivative plots
- Real time data acquisition and display

As you can see, the Bio-Dimension™ UV-Vis detector combines the best capabilities of a fixed wavelength detector with those of a photo diode array. As such, it's the perfect choice for methods development—or any application demanding superior sensitivity.

Don't wait. Call now for details.

**BIO-RAD**

**Chemical  
Division**

3300 Regatta Blvd.  
Richmond, CA 94804  
(415) 232-7000  
1-800-4 BIORAD

Also in Rockville Centre, NY; Hornsby, Australia; Vienna, Austria; Brussels, Belgium; Mississauga, Canada; Hemel Hempstead, England; Paris, France; Munich, Germany; Hong Kong; Milan, Italy; Tokyo, Japan; Veenedaal, The Netherlands; and Glattbrugg, Switzerland.

CIRCLE 14 ON READER SERVICE CARD

rialization of the blood in the vascular region being sensed. Typical instruments average the values obtained from five successive heartbeats before displaying calculated O<sub>2</sub>-saturation values. Good correlation between this noninvasive approach and the standard laboratory method (optical measurement of a lysed blood sample) is observed at O<sub>2</sub>-saturated values greater than 70%. Below this value, considerable error has been documented (17). Nonetheless, the use of pulse oximetry is now commonplace in critical care and surgical units, providing reliable and vital continuous monitoring information.

**Extracorporeal in-line and on-line sensing systems.** A third approach for performing bedside chemical testing is to recirculate the blood via extracorporeal tubing to a sensor, or an array of sensors, placed outside the body. To be considered a closed-loop "in-line" system, the blood that passes from the patient must return through an appropriate vein. Alternatively, "on-line" systems may be used to classify arrangements in which blood is continuously or intermittently sampled (either directly from an in-dwelling sampling probe inserted into the

patient or from an extracorporeal blood loop such as a heart-lung machine), passed through the measurement system, and then on to waste. The latter approach makes it possible to perform frequent one- and two-point calibrations of the sensors simply by diverting appropriate calibrating solutions and/or gas-phase mixtures through the sensor array.

To date, the development of in-line extracorporeal sensing techniques has focused primarily on the continuous measurement of P<sub>O<sub>2</sub></sub>, P<sub>CO<sub>2</sub></sub>, and pH. For example, a disposable optical sensor-based system intended for use during cardiopulmonary bypass procedures is now available. This three-sensor system is calibrated prior to insertion into the blood line of a heart-lung machine. The stability of the sensors' calibration is critical to the long-term analytical performance of the system. However, because this in-line system is intended primarily for short-term heart bypass procedures (4-5 h), reasonably good correlation with conventional methods can be obtained over this finite period without a repeated two-point calibration of the optical sensors (18).

To compensate for sensor drift, periodic one-point calibrations can be ac-

complished (without removing the sensors from the loop) by performing discrete sample blood gas determinations on conventional laboratory instruments and updating the output display of the in-line monitor accordingly. A similar system involves the use of a hybrid detection system; optical sensors for P<sub>CO<sub>2</sub></sub> and pH and electrochemical measurement of P<sub>O<sub>2</sub></sub>. Because the patient's blood is often cooled considerably during open-heart surgery, both systems allow simultaneous measurement of the temperature (via a thermocouple) of the blood in the extracorporeal loop so that, if desired, values can be corrected to those that would be obtained at 37 °C, as reported by most conventional blood gas instruments.

The on-line measurement approaches are more accurate than in-line systems. The ability to calibrate these systems frequently enhances long-term analytical performance. One commercial system incorporates a disposable all-electrochemical sensor array that measures blood gases, electrolytes, and hematocrit in a single sample of whole blood drawn either on demand or at preprogrammed intervals from a sampling device placed in the blood loop of a heart-lung machine. Between sam-

# Capture that elusive document with CAS Document Delivery Service®

- photocopies or loans of documents
- most documents on their way within 24 hours
- documents since 1975, many even earlier
- fast service — mail, fax, or courier
- competitive prices, no copyright worries



Return this coupon to:

Chemical Abstracts Service  
 Marketing Dept. 33190  
 P.O. Box 3012  
 Columbus, OH 43210 U.S.A.  
 or call: 800-848-6538, ext. 2956 or  
 614-447-3670  
 fax: 614-447-3648  
 STNmail: CASDDSC

Name \_\_\_\_\_ Phone \_\_\_\_\_

Job Title \_\_\_\_\_

Organization \_\_\_\_\_

Address \_\_\_\_\_

ples, a premeasured flush solution is used to perform a one-point calibration of all the sensors. Two-point calibrations using a second premeasured solution are performed hourly, and test values can be updated every 4–6 min. Although this cannot be considered a continuous or real-time measurement system, this finite lag time in obtaining accurate values for the key critical care analytes is not much longer than the true response times of the optical sensors employed in the continuous in-line measurement systems (2–5 min).

The potential clinical use of in-line and on-line bedside testing is limited by the critical issue of biocompatibility. Systems designed for performing measurements in extracorporeal loops, either by direct insertion into the loop or as on-line sampling devices, can be used because patients undergoing cardiac surgery are systemically heparinized (administered large doses of the anticoagulant heparin) during the procedure. This helps to prevent formation of life-threatening emboli in the external loop that can pass back into the patient.

More widespread use of extracorporeal in-line chemical sensing systems for other clinical procedures or at the

bedside of intensive care patients is unlikely because the potential benefits of bedside testing may not outweigh the risks associated with implementing an extracorporeal blood loop (e.g., decrease in blood platelet count, increase in complications from bleeding). Implementation of semicontinuous on-line blood analyzers for routine bedside testing requires the development of a biocompatible in-dwelling catheter sample probe that will enable the automatic sampling of undiluted whole blood directly from the patient, with subsequent downstream measurement of blood gases as well as other critical care analytes via sensors that can be recalibrated periodically for greater accuracy.

**Continuous in vivo sensors.** Although considerable research effort and funds have been expended to date, relatively few catheter-type sensors are currently available for continuous in vivo (intravascular) measurements of critical care analytes. Advances in this technology have been severely limited by the inability to develop small (i.e., 20-gauge or 0.5-mm o.d.), durable, and biocompatible sensors that maintain adequate long-term stability when implanted in vivo. Useful lifetimes of such

sensors ideally should be equivalent to the maximum recommended arterial implant time (72–96 h). To attain such lifetimes, in vivo sensors must retain calibration stability for longer time periods than most conventional macro-size sensors used in laboratory instruments or even some of the newer bedside testing systems.

There is no simple and convenient means to fully calibrate (two-point calibration) the sensors once implanted. In some instances, sensor stability is directly related to the design used to miniaturize the sensing technology. For example, when first developed, ion-selective field effect transistors (ISFETs) were touted as an attractive approach to the design of in vivo electrolyte sensors because they used the same polymeric membrane-based ion-sensing chemistries employed in macro-laboratory-type instruments (19). Modern microelectronic fabrication techniques allow multiple sensors to be placed on a single implantable transistor chip. However, problems of encapsulation and unstable membrane/gate interfacial potentials have thus far prevented such devices from achieving the level of signal stability required for reliable in vivo measurements.

## Pre-engineered and prepackaged instrument solutions for your control requirements . . .

*Temperature • Pressure • Speed  
Level • Flow • Weight • Logic*

- Process monitoring and control from a single instrument to engineered systems
- Software for automation, remote operation and data acquisition
- Broad variety of options and accessories
- Complete system integration with Autoclave equipment

For further information write factory or call toll free:

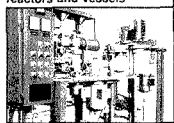
**1-800-458-0409**

Autoclave Engineers Group  
2930 W. 22nd St.  
Box 4007, Erie, PA 16512 USA

Complete  
Reaction  
Systems . . .



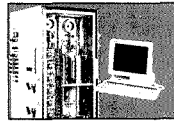
High and low pressure reactors and vessels



Reaction control and real time monitoring



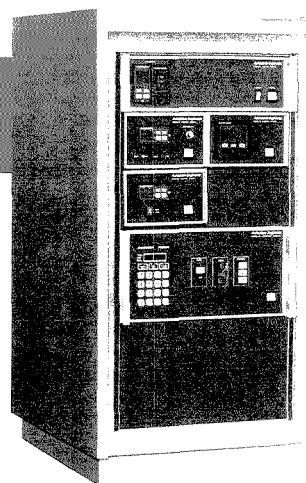
Instrumentation for measurement, control and automation



Micro-scale bench top reaction system - BTRS



TAP Reactor System



**Autoclave  
Engineers**



CIRCLE 1 ON READER SERVICE CARD

The second major obstacle in developing *in vivo* sensors is to make them fully biocompatible without compromising the performance of the sensing chemistries. Thrombus formation on an implanted sensor in a patient who is not systemically heparinized poses a major health risk to that patient. In addition, the clotting of cells at the surface of the implanted device can create a local environment adjacent to the sensor that is different in chemical composition (pH,  $P_{O_2}$ , etc.), than the bulk blood. Certain biocompatible membrane-type coatings, as well as the adsorption or covalent attachment of anticoagulating agents directly to the sensing surfaces of the miniaturized devices, have been used to ensure biocompatibility.

The use of fiber-optic blood gas and pH sensors has enabled development of a prototype *in vivo* sensor with dimensions suitable for direct insertion through a 20-gauge arterial catheter line (20) (see Figure 5a). To enhance biocompatibility, the entire surface of the sensor is coated with a layer containing covalently bonded heparin. In *in vivo* tests of this sensor demonstrated impressive long-term stabilities with drift rates for pH measurements of  $< 0.005/24$  h. In *in vivo* evaluation over a 4-h period in the femoral artery of an anesthetized dog (with only local heparinization at the implant site) yielded good correlation with measurements of discrete samples of the animal that were made on laboratory instruments.

Longer term *in vivo* stability must be demonstrated if this design is to be considered a viable invasive approach for obtaining continuous blood gas values. Furthermore, response times (2–5 min to reach equilibrium values) must be improved so that more rapid changes in blood gas values can be monitored accurately.

Researchers have reported the use of electrochemical sensors for continuous *in vivo* measurements of blood gases and electrolytes. However, in basic research studies with animals, the problem of *in vivo* thrombus formation is often overcome by systemic heparinization of the subject. Because there are added risks associated with systemic anticoagulation, this is not an option for routine clinical use of such devices in humans.

Common methods of rendering the devices less thrombogenic will not necessarily be compatible with the sensing chemistries of the devices. For example, the dual ion/gas-sensing catheter shown in Figure 5b was recently devised to monitor both  $P_{CO_2}$  and potassium simultaneously *in vivo* (21). However, when the outer silicone rubber

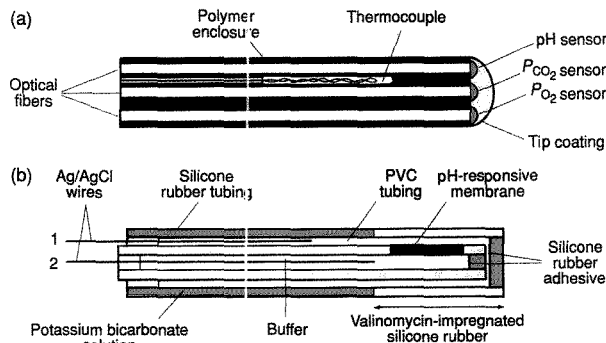


Figure 5. Continuous *in vivo* sensors.

(a) Optical combination blood gas catheter (0.61 mm o.d.). (Adapted with permission from Reference 20.) (b) Design of dual ion/gas sensing catheter (1.2 mm o.d.) configured to monitor  $K^+$  and  $P_{CO_2}$  simultaneously in whole blood. (Adapted from Reference 21.)

tubing containing the potassium-selective ionophore valinomycin was also doped with a lipophilic heparin salt (to allow slow leaching of heparin to the surrounding sample), the potassium sensitivity of the device was severely degraded. The  $P_{CO_2}$  sensing chemistry of the probe was unaffected by such treatment, because the outer silicone tubing served merely as a passive gas-permeable membrane for the internal  $CO_2$  sensing element of the device (polymer pH sensor). This clearly illustrates the challenge faced when trying to devise *in vivo* probes with multiple chemical sensors, particularly when actual chemical reactions must take place at the sensor-sample interface in order to obtain quantitative results.

#### Future directions

Advances in bedside testing and monitoring will depend on the quality of analytical results acceptable to clinicians managing critically ill patients. These clinicians expect consistent and highly accurate test values from instruments located in the controlled environment of the clinical laboratory. However, some discrepancies between laboratory and bedside test results will always exist because of changes in the blood sample composition that occur during transport to remote laboratories and because of the wide range of accuracy and precision obtainable with the new bedside measurement approaches. These differences may be acceptable to most clinicians who feel that obtaining test values more rapidly or continuously enhances the overall quality of health care.

A combination of measurement ap-

proaches will be used for future bedside monitoring. Some systems will serve merely as trend monitors or alarm-type systems (i.e., signals indicating that an analyte value is outside the normal range). Others will provide test values that correlate well with those that would be obtained if blood samples were drawn from the patient and sent to a main or satellite stat lab. The ideal technology would make it possible to obtain accurate values continuously for all critical care analytes using noninvasive methods, but this approach probably will not offer an analyte menu that includes pH, metabolites, and electrolytes.

In principle, invasive sensors or on-line techniques equipped with *in vivo* sampling probes offer more hope for future success in simultaneously monitoring all the key analytes. However, further research is required to solve the critical issues of sensor stability and sampling device-sensor biocompatibility. In the meantime, bedside-type discrete analyzer systems that can provide reasonably accurate values for all the analytes—used in conjunction with the best noninvasive trend monitors (e.g., pulse oximeters)—appear to offer the most cost-effective and reliable means of managing critical care and surgical patients.

#### References

- (1) Brock, A. J. *Greek Medicine*; AMS Press: New York, 1972.
- (2) Eichhorn, J. H.; Moran, R. F.; Cormier, A. D. *Blood Gas Preanalytical Considerations: Specimen Collection, Calibration and Controls*; National Committee for Clinical Laboratory Standards: Villanova, PA, 1989.

- (3) Turner, A. P.; Karube, I.; Wilson, G. S. *Biosensor Fundamentals and Applications*; Oxford University Press: New York, 1987.
- (4) Arnold, M. A.; Meyerhoff, M. E. *CRC Crit. Rev. Anal. Chem.* 1988, 20, 149-96.
- (5) Hahn, C.E.W. *J. Phys. E.* 1981, 14, 783-97.
- (6) Seitz, W. R. *CRC Crit. Rev. Anal. Chem.* 1988, 19, 135-73.
- (7) Wolfbeis, O. S. In *Molecular Luminescence Spectroscopy, Part 2*; Schulman, S. G., Ed.; John Wiley & Sons: New York, 1988; Chapter 3.
- (8) Oesch, U.; Ammann, D.; Simon, W. *Clin. Chem.* 1986, 32, 1448-59.
- (9) Wolfbeis, O. S. *Pure Appl. Chem.* 1987, 59, 663-72.
- (10) Janata, J. *Anal. Chem.* 1987, 59, 1351-56.
- (11) Takagi, M.; Ueno, K. In *Topics in Current Chemistry*; Vogtle, F.; Weber, E., Eds.; Springer-Verlag: Berlin, 1984; Vol. 121, pp. 39-65.
- (12) Charlton, S. C.; Fleming, R. L.; Zipp, A. *Clin. Chem.* 1982, 28, 1857-61.
- (13) Geddes, L. A.; Sadler, C. *Med. Biol. Eng.* 1973, 11, 336-39.
- (14) Abraham, E. *Emergency Medicine Clinics of North America* 1986, 4, 791-807.
- (15) Wiedemann, H. P.; McCarthy, K. *Clinical Chest Medicine* 1989, 10, 239-54.
- (16) Hicks, J. M. *Clin. Chem.* 1985, 31, 1931-35.
- (17) Severinghaus, J.; Naifeh, K. *Anesthesiology* 1987, 67, 551-58.
- (18) Siggaard-Andersen, O.; Gotghen, I. H.; Wimberley, P. D.; Rasmussen, J. P.; Fogh-Andersen, N. *Scand. J. Clin. Lab. Invest.* 1988, 48, Suppl. 189, 77-84.
- (19) McKinley, B. A.; Houtchens, B. A.; Janata, J. *Ion-Select. Electrode Rev.* 1984, 6, 173-208.
- (20) Miller, W. W.; Yafuso, M.; Yan, C. F.; Hui, H. K.; Arick, S. *Clin. Chem.* 1987, 33, 1538-42.
- (21) Collison, M. E.; Aebli, G. V.; Petty, J.; Meyerhoff, M. E. *Anal. Chem.* 1989, 61, 2365-72.



Mark E. Meyerhoff (left) received his B.A. degree in 1974 and his Ph.D. in analytical chemistry from the State University of New York at Buffalo in 1979. He joined the faculty at Michigan in the fall of 1979. His research interests include development of new ion-, gas-, and bio-selective membrane electrodes and the design of enzyme-linked competitive and noncompetitive binding assay methods.

Michael E. Collison received his B.S. degree in 1984 and his Ph.D. in analytical chemistry from the University of Michigan in 1989. His research interests include chemical and biological sensors, automated enzymatic chemical analysis, and chromatographic methods development.



The National Institute of Standards and Technology has developed a series of SRM's to serve as calibrants, test mixtures, and standardization materials for Quality Control of analytical instrumentation and methodology.

MEASUREMENTS and STANDARDS are important to everyone who needs quality. NIST has over 1,000 Standard Reference Materials that can help you calibrate instruments and check on measurement accuracy. For more information phone or write for a free catalog.

Telephone (301) 975-0SRM (6776)  
FAX (301) 948-3730

**STANDARD REFERENCE MATERIAL PROGRAM**

Building 202, Room 204  
National Institute of Standards and Technology  
Gaithersburg, MD. 20899



CIRCLE 94 ON READER SERVICE CARD

## ABBOTT LABORATORIES

Abbott Laboratories' Pharmaceutical Products Division is a leader in the development and manufacture of anti-infective, cardiovascular and anti-convulsant/neurological products. Supported by a significant investment to R&D, twice the industry standard, we perform renowned clinical studies, and maintain a variety of specialized labs featuring state-of-the-art developmental technologies. Our extensive technical resources create a superior environment for those who would like to make a significant personal and professional commitment.

## ANALYTICAL CHEMISTS

Individuals will be responsible for the development of suitable analytical procedures to support the synthesis and characterization of new bulk drug substances, support formulation efforts, and participate in the preparation of IND and NDA filings. A working knowledge of separation techniques such as GC and HPLC and a solid background in organic chemistry are required. Excellent oral and written communication skills are mandatory. A Ph.D. in chemistry is required.

Abbott provides competitive compensation and benefits including a profit sharing and a stock retirement plan. We are located in an attractive suburban area approximately 30 miles north of Chicago. For consideration, please send your resume with salary history to: **Patricia Handy, Corporate Placement, Job #7650, Abbott Laboratories, 1 Abbott Park Rd., Abbott Park, IL 60064.** Abbott is an Affirmative Action Employer.

## ABBOTT LABORATORIES



Quality  
Health Care  
Worldwide  
1888-1990

Get one box  
**FREE**  
with the first box  
you buy.  
For terms of offer, ordering information, or  
the name of your local Whatman distributor,  
please call 800-631-7290. In New Jersey,  
call 201-773-5800. Offer expires July 1, 1990.

# THE EASIEST WAY TO USE THE WORLD'S FINEST FILTER PAPER

## A range of ready-to-use filters

Choose from 28 quality Whatman brand filters or filter combinations, including glass microfibre, membranes, and membranes with pre-filters. Filters come already in place and are 47 mm in diameter. Whatman Filter Funnels conserve valuable storage space, too. They come neatly stacked—one inside the other—five to a box.

## Completely disposable

The new Whatman Filter Funnel is the only disposable filter funnel to house Whatman brand filters. It eliminates cross-contamination, cleanup, and breakage. So there's less mess. And its medical-grade polypropylene reservoir is safe and compatible with most solvents, and holds up to 250 mL of solution.

## Unique "pull tab"

A special feature of the Whatman Filter Funnel. Permits easy access to your filter for further analysis or culturing. You get the same high-quality reliable results you've come to expect from Whatman. In less time. With greater ease.

INTRODUCING  
The Whatman

# FILTER FUNNEL

For instant access to the Whatman Technical Support Team, please call 800-922-0361. In New Jersey, call 201-773-5800.



Whatman Laboratory Division

Whatman Inc., 9 Bridewell Place, Clifton, New Jersey 07014, Telephone 201-773-5800 Telex 133426 FAX 201-472-6949

Whatman (word and device) and Whatman (word only) are trademarks of Whatman Paper Ltd. 746-14-105

CIRCLE 145 ON READER SERVICE CARD

"Analytical Mass Spectrometry" is the subject of the 1990 Summer Symposium of the ACS Division of Analytical Chemistry. The symposium, to be held July 24-27 in Oak Ridge, TN, will be hosted by the Analytical Chemistry Division of Oak Ridge National Laboratory (ORNL). The general chairman is David Donohue of ORNL, and the program chairman is R. Graham Cooks of Purdue University. The symposium is sponsored by the ACS Division of Analytical Chemistry and ANALYTICAL CHEMISTRY and is cosponsored by the American Society for Mass Spectrometry. Unique to this year's symposium is a Graduate Student Competition featuring a special session on the future of mass spectrometry and cash awards for winning oral and poster presentations.

### Oak Ridge National Laboratory

Nestled in the wooded ridges of eastern Tennessee, Oak Ridge National Laboratory was built during 1942-45 as part of the Manhattan project. It quickly grew into a multidisciplinary laboratory dealing with all aspects of nuclear research, including reactor design, isotope production, actinide chemistry, and biological effects of radiation. Today ORNL is an energy research and development laboratory with a staff of more than 5000 scientists, engineers, and support personnel.

### Housing

The symposium will be held in the Pollard Auditorium of the Oak Ridge Associated Universities. The official hotel for the symposium is the Garden Plaza (615-481-2468), which is a short walk from the auditorium. A special group rate of \$52 per night has been arranged. Conferees should indicate on the registration form if they would like reservations at the Garden Plaza and, if so, if they wish to share a double room with a colleague. The deadline for reservations at the group rate is May 18.

Other hotels in Oak Ridge include the Diplomat (615-483-5615), the Holiday Inn (615-483-4371), the Alexander

Inn (615-483-3555), and the Ridge Inn Plaza (615-482-9968).

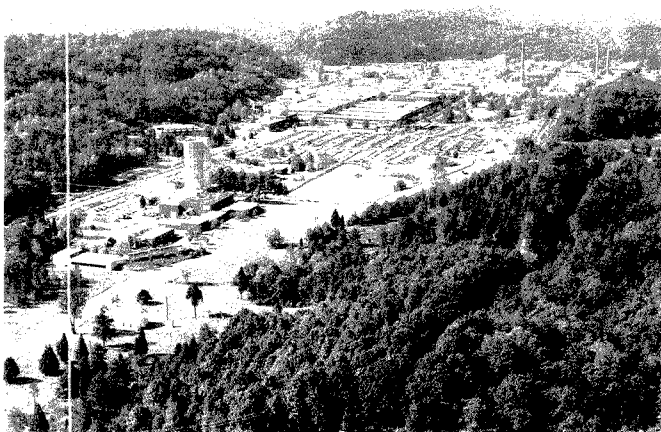
### Registration and special activities

Symposium registration will begin on Tuesday, July 24, at 7:00 P.M. in the lobby of the Garden Plaza Hotel. A welcoming reception will be held from 7:00 to 9:00 P.M., during which instrument manufacturers will exhibit poster displays of their products. Registration will continue in the lobby of the Pollard Auditorium from 8:00 A.M. to 4:00 P.M. on Wednesday, July 25, and Thursday,

July 26, and from 8:00 A.M. to noon on Friday, July 27.

A barbecue and outdoor activities are planned for Thursday beginning at 5:00 P.M. at Melton Hill Lake, a few miles outside of Oak Ridge. Transportation will be provided from the Garden Plaza and other hotels.

A free period on Thursday afternoon has been designated for sightseeing, shopping, or tours of the mass spectrometry facilities at ORNL. Conferees should indicate their interest in these tours on the registration form.



Oak Ridge National Laboratory



*David Donohue  
General Chairman*



*R. Graham Cooks  
Program Chairman*

The \$150 registration fee includes admission to all technical sessions, coffee breaks, the reception and poster session on Tuesday evening, and the Thursday barbecue. The \$50 student registration fee includes all of the above except the barbecue. Students and guests may order barbecue tickets on the registration form.

**Travel**

The nearest airport to Oak Ridge is Knoxville's McGhee-Tyson Airport, which is served by a number of national airlines. A 40% discount on domestic round-trip day or night coach fares is available on Delta Airlines. For information or reservations, contact Delta at 1-800-221-1212; be sure to give the meeting name, "Annual Summer Symposium," and the file number J18044.

Limousine service is available to the Garden Plaza and other hotels; cost is \$24.50 one-way and \$39.75 round trip. Several car rental companies are also located at the Knoxville airport.

**Family activities**

Within walking distance of the conference hotel are the American Museum of Energy and the Oak Ridge Civic Center, which houses a library, swimming pool, and gymnasium. Public tennis courts are less than one mile away.

Other points of interest in the Knoxville-Oak Ridge area include several TVA lakes with public picnic and swimming facilities, golf courses, shopping malls, and art galleries. Gatlinburg and the Great Smoky Mountains National Park are located 70 miles from Oak Ridge.

**Additional information**

For further information, contact David Donohue, Oak Ridge National Laboratory, P.O. Box 2008, Mail Stop 6142, Oak Ridge, TN 37831-6142 (615-574-8955). Questions concerning the technical program should be directed to R. Graham Cooks, Dept. of Chemistry, Purdue University, West Lafayette, IN 47907 (317-494-5263).

**Symposium format**

The symposium is divided into five sessions dealing with fundamentals, lasers and Fourier transform methods, mass spectrometry in the national laboratories, and new ionization and liquid chromatography/mass spectrometry methods. A special session on the future of mass spectrometry will involve the finalists in the Graduate Student Competition. Noninvited posters are welcome. Please enclose an abstract with the registration form. The complete program for the symposium follows.

*continued on p. 443 A*

Registration Form  
**43rd Annual Summer Symposium  
 on Analytical Chemistry**  
 July 24-27, 1990  
 Oak Ridge, TN

Name (Print) \_\_\_\_\_  
 Title \_\_\_\_\_  
 Institution \_\_\_\_\_  
 Address \_\_\_\_\_  
 City \_\_\_\_\_ State \_\_\_\_\_ Zip \_\_\_\_\_  
 Phone ( ) \_\_\_\_\_

**Registration Fees**

Registration, \$150 \$ \_\_\_\_\_  
 Student registration, \$50 \$ \_\_\_\_\_  
 Barbecue tickets, \$10 \$ \_\_\_\_\_  
 (Guests and students)  
 TOTAL ENCLOSED \$ \_\_\_\_\_

**Housing**

- I will arrange my own housing; send hotel list.
- Please reserve a room at the conference hotel from \_\_\_\_\_ to \_\_\_\_\_ (\$52/night; do not send payment with this form)
- I will share a room with \_\_\_\_\_
- Assign me a roommate.

**Laboratory Tours**

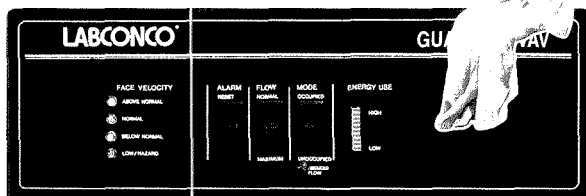
- Analytical Mass Spectrometry Laboratory
- FT-MS Laboratory

Return this form by May 18 with a check payable to "1990 Summer Symposium on Analytical Chemistry" to D. L. Donohue, Oak Ridge National Laboratory, P.O. Box 2008, Mail Stop 6142, Oak Ridge, TN 37831-6142.



# Always there

## The **NEW** Guardian VAV System watches over Protector® Hoods like a Guardian Angel



The NEW Guardian VAV System is the first self-contained variable air volume system designed and factory-installed by a fume hood manufacturer.

Guardian's exclusive safety and energy-saving features are always on the job protecting your lab and cutting your energy bills:

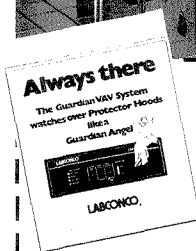
- Dual sensing systems, air flow/pressure and sash position sensors, insure safe conditions and guard against excessive energy use.
- Innovative integral design is factory mounted for easy installations. It's just like installing a traditional fume hood.
- Optional remote signal output permits tie in with building ventilation or alarm system.
- Easy-to-read lights monitor air flow through hood. You know the hood's safe to use at all times.
- Alarm immediately alerts user to the hazard of low air flow.
- "Unoccupied" setting lowers hood air volume requirements to increase energy efficiency even more when hood is not in use.

### Safety and Savings for New and Existing Labs

The all-new Guardian VAV System is a state-of-the-art variable air volume system with damper and safety control panel built right into the popular Labconco Protector Fiberglass Fume Hood. Eliminates the need for an auxiliary air system, and the costly additional blower and ductwork associated with them. Now you can protect your lab and your staff while you cut energy costs around the clock with NEW Guardian VAV.

**SEND TODAY FOR YOUR FREE GUARDIAN KIT. Complete and mail this coupon.**  
Or call toll-free 1-800-821-5525.

Available from:



**YES,**

I want to know more about how the Guardian VAV System can make my lab safer and more energy-efficient. Please send my FREE no-obligation Guardian VAV Kit to:

Name \_\_\_\_\_ Title \_\_\_\_\_

Company/Institution \_\_\_\_\_

Address \_\_\_\_\_

City \_\_\_\_\_ State \_\_\_\_\_ Zip \_\_\_\_\_

Telephone (\_\_\_\_\_) \_\_\_\_\_

Mail to: \_\_\_\_\_ ANC

**LABCONCO** Labconco Corporation 8811 Prospect, Kansas City, MO 64132

Or call TOLL-FREE 1-800-821-5525

In Missouri and Canada call 816/333-8811

# For Over Six Decades...

**ANALYTICAL  
CHEMISTRY**

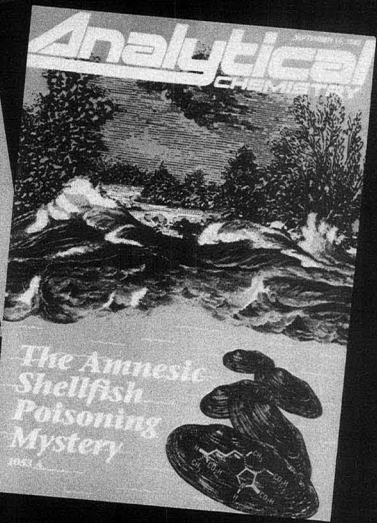
**analytical  
chemistry**



**ANALYTICAL CHEMISTRY**



**ANALYTICAL CHEMISTRY**



## The Leader in the Field.

*ANALYTICAL CHEMISTRY*, the world's foremost publication in the vital field of measurement science, comes to you semi-monthly packed with *more* research articles, special features and application papers.

Keeping pace with the changes has continued to make *ANALYTICAL CHEMISTRY* the pinnacle of publications in the field . . . for over 6 decades.

For your personal subscription:

**CALL TOLL FREE (800) 227-5558 (U.S. only)**  
**Outside U.S. (202) 872-4363**

**Telex: 440159 UI**  
**89 2582 ACSPUBS**



American Chemical Society  
1155 16th St., NW  
Washington, DC 20036

**Program**

**WEDNESDAY MORNING**

**Fundamentals of Analytical MS**

H. I. Kentamaa, *Chairperson*

- 8:15 **Welcoming Remarks.** D. L. Donohue, W. D. Shults, R. G. Cooks
- 8:30 **Determination of "Structure" in Gas-Phase Ionic Species.** D. Russell, Texas A&M U
- 9:00 **Ionization Methods Using Reaction Chemistry on Clusters.** S. Olesik, Ohio State U
- 9:30 **Fundamentals of Low-Energy vs. High-Energy Collisions for Analytical Applications.** V. Wysocki, Naval Research Laboratory
- 10:30 **Chemistry and Physics in a Mass Spectrometer: What Makes a Reaction Analytically Useful?** S. McLuckey, Oak Ridge National Laboratory
- 11:00 **Fundamental and Analytical Studies of Biomolecular Ions.** J. Adams, Emory U
- 11:30 **Ion Chemistry in the Trap and in Quadrupoles.** J. Brodbelt-Lustig, U of Texas

**WEDNESDAY AFTERNOON**

**MS in the National Laboratories**

M. Buchanan, *Chairperson*

- 1:00 **High-Precision Analyses of Nuclear**

- Materials by Thermal Ionization MS.**  
L. Callis, Los Alamos National Laboratory
- 1:30 **Time-of-Flight MS with Various Desorption Probes.** J. Hunt, Argonne National Laboratory
  - 2:00 **Neutral-Beam SIMS—Basic Principles and Practical Applications.** J. Delmore, Idaho Falls National Engineering Laboratory
  - 3:00 **Ion Trap MS as Applied to In-Field Analyses.** P. Hemberger, Los Alamos National Laboratory
  - 3:30 **Positron Ionization of Organic Molecules: Is It Worth the Trouble?** D. Donohue, Oak Ridge National Laboratory

**WEDNESDAY EVENING**

**Lasers and Fourier Transform Methods**

P. Savickas, *Chairperson*

- 7:00 **He:YAG Laser Desorption FT-ICR MS.** A. Marshall, Ohio State U
- 7:30 **Argon Ion, Nd:YAG, and CO<sub>2</sub> Laser Studies of Transition-Metal-Containing Ions Using FT-MS.** B. Freiser, Purdue U
- 8:00 **Laser-Induced Ionization Spectroscopy of Small Biological Molecules in Supersonic Jets.** D. Lubman, U of Michigan
- 9:00 **IR and UV Laser Desorption.** R. Cotter, Johns Hopkins U
- 9:30 **Laser Probes of Ion Chemistry.** M. Johnston, U of Colorado and U of Delaware
- 10:00 **Structural Characterization of Modified Nucleic Acid Constituents by Laser**

**Desorption FT-MS.** R. Hettich, Oak Ridge National Laboratory

**THURSDAY MORNING**

**Future of MS**

R. Freas, *Chairperson*

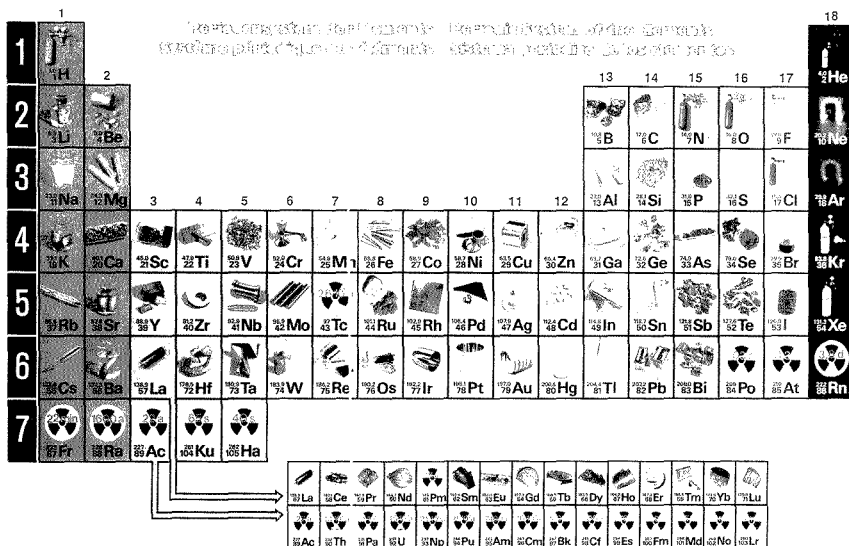
- 8:30 **Graduate Student Award Finalists—Oral and Poster**
- 12:00 **Presentation of Graduate Student Competition Awards.** W. D. Shults, Oak Ridge National Laboratory

**FRIDAY MORNING**

**New Ionization and LC/MS Methods**

R. Browner, *Chairperson*

- 8:30 **Electrospray Ionization MS.** R. Smith, Battelle Northwest Laboratory
- 9:00 **Electrochemistry and Enzymes On Line with MS.** R. Yost, U of Florida
- 9:30 **Electron Capture and Associated Secondary Processes in Trace Analysis by MS Methods.** E. Grimsrud, Montana State U
- 10:30 **Solution Chemistry: A Boon or a Bane?** K. Cook, U of Tennessee
- 11:00 **Operational Parameters and Their Effect on Liquid SIMS Spectra.** P. Todd, Oak Ridge National Laboratory
- 11:30 **Desorption Ionization: Recent Trends.** K. Busch, Georgia Institute of Technology
- 12:00 **Closing Remarks.** R. G. Cooks



Available in Poster size 25 x 38 in. K\_T 04 \$ 9.95  
 Binder size 11 x 16 in. K\_T 03 \$ 2.00  
 Wall size 67 x 90 in. K\_T 01 \$140.00  
 Shipping and handling \$ 2.50

VISA and Master Card accepted.  
 Please call for more information.

**E NATURALISTE**

Dept. Ac  
 1990 Charest ouest ste 117  
 Québec, Qc Canada G1N 4K8  
 Tél.: (418) 527-1414 Fax: (418) 527-1970

CIRCLE 96 ON READER SERVICE CARD

# 1990 Gordon Research Conferences

The aim of the Gordon Research Conferences is to extend the frontiers of science by fostering a free and informal exchange of ideas among those actively involved in research in particular fields. At each conference, meetings are held in the morning and evening, Monday through Friday, with the exception of Friday evening. The afternoons are available for recreation, reading, or participation in discussion groups.

To promote discussion and to protect individual rights, it is the established requirement of each conference that no information be used without specific authorization of the individual making the contribution. Recording of lectures and photographing of slides are also prohibited.

The unique concept of the conferences was established by Neil Gordon of Johns Hopkins University in 1931. Gordon foresaw the importance of establishing direct communication between scientists while removing the distractions at larger meetings.

This year, eight conferences are of particular interest to analytical chemists: analytical chemistry, electron spectroscopy, lasers in medicine and biology, physical electrochemistry, separation and purification, statistics in chemistry and chemical engineering, vibrational spectroscopy, and magnetic resonance in biology and medicine. Technical programs for these conferences follow. Other conferences of interest include synthetic membranes; organic geochemistry; diffraction methods in molecular biology; fuel science; fractals; environmental sciences—water; computational chemistry; zeolitic and layered materials; solid-state chemistry; origin of life; nuclear proteins, chromatin structure, and gene regulation; chemistry at interfaces; corrosion; solid-state studies in ceramics; catecholamines; biomolecular recognition and immobilization; bioelectrochemistry; biopolymers; and atomic and molecular interactions.

Conferences will be held both in New Hampshire and Rhode Island. For the



New Hampshire conferences, the fixed fee for resident participants is \$360, which covers registration, room (double occupancy), and meals. The \$320 fee for nonresident conferees covers registration and meals. The \$270 guest fee includes room and meals only. For conferences held in Rhode Island, fees are \$375 for resident participants, \$320 for nonresident conferees, and \$285 for guests. If registration cards with advance payment are postmarked at least three weeks prior to the conference, fees are \$50 less than those quoted above.

Additional information can be obtained from Alexander Cruickshank, Gordon Research Conferences, Gordon Research Center, University of Rhode Island, Kingston, RI 02881-0811 (401-783-4011 or 3372). From June 11 to August 24, Cruickshank can be reached at Colby-Sawyer College, New London, NH 03257 (603-526-2870).

## Analytical Chemistry

New Hampton School  
New Hampton, NH  
E. Yeung, *Chairperson*  
J. Glajch, *Vice Chairperson*

AUGUST 6-10

I. Warner, *discussion leader*  
**Role of Modern Array Detectors in  
Spectrochemical Analysis.** M. B. Denton

**Micro and Trace Analysis of Solids: Applications  
in Materials Science and Industry.** R. Gijbels

L. McGown, *discussion leader*  
**Electrokinetic Chromatography for the  
Thermodynamic Study of Molecular  
Complexation.** S. Terabe  
**Photophysics of Micellar Systems and  
Cyclodextrin Complexes.** L. J. Cline Love

R. Keller, *discussion leader*  
**Recent Advances in NMR.** A. Pines  
**Analytical Applications of Synchrotron  
Radiation.** J. Taylor

M. Arnold, *discussion leader*  
**Fiber-Optic Chemical Sensors and Enzyme-  
Based Biosensors.** O. Wolfbeis

D. Desiderio, *discussion leader*  
**Electrospray Ionization in MS.** J. Fenn

R. Smith, *discussion leader*  
**Analytical Chemistry in Biotechnology.**  
W. Hancock

**Automated DNA Sequencing and the Analysis of  
the Human Genome.** L. Smith

T. Cotton, *discussion leader*  
**Molecular Assemblies at Electrodes—Dynamics  
of Communication Channels in Organized  
Monolayer and Bilayer Systems.** M. Majda  
**Ultra Low Temperature Electrochemistry and  
Electrodes of High T<sub>c</sub> Superconducting  
Ceramics.** R. Murray

J. Robinson, *discussion leader*  
**Analytical Chemistry and the Stradivarius.**  
J. Nagyvary

S. Brown, *discussion leader*  
**Electrical and Chemical Dynamics in Learning,  
Recognition, and Memory of Self-Organizing  
Neural Networks.** S. Grossberg  
**Optical Processing of Analytical Data.**  
S. Bialkowski

# This is how the A&D Instant Rebate looks on paper.



## Now through April 30, 1990.

Right now, our analytical balances look better than ever.

Because right now, A&D is giving an instant rebate with each one sold.

Buy an ER Series analytical balance and your company gets an instant rebate of \$50. Buy one from our FR Series and the rebate jumps to \$100.

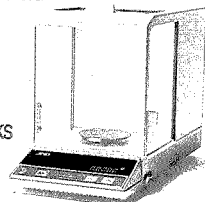
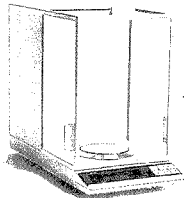
Just be sure to place your order by April 30, 1990.

Even without the rebate,

picking up an A&D analytical balance is a smart move. Not just because of our automatic calibration, ease-of-use, and wireless-remote options, but because of A&D's own technological breakthroughs. All of which can help you save money now. And down the road, too, thanks to our remarkable dependability.

Call 800-726-3364 today for the dealer nearest you.

Because while this offer looks good on paper, it looks even better in person.



Distributed in Canada by Johns Scientific Inc.  
800-268-4440

**A&D**  
A&D ENGINEERING, INC.

1555 McCandless Drive, Milpitas, CA 95035 (408) 263-5333

CIRCLE 7 ON READER SERVICE CARD

**Electron Spectroscopy**

Brewster Academy  
Wolfeboro, NH  
V. McKoy, *Chairperson*  
W. Eberhardt, *Vice Chairperson*

**JULY 16-20**

D. Menzel, *discussion leader*  
**Vibrational Lineshapes in Core Level Photoemission.** N. Martensson  
**High-Resolution Core Electron Spectroscopy.** C-T. Chen  
**Photoemission Studies of GaAs/CaF<sub>2</sub> Interface.** T. Tiedje  
**Some Recent Developments in Molecular Auger Spectroscopy.** F. P. Larkins

L. Sanche, *discussion leader*  
**Electron Impact Spectroscopy of Molecules at Low Energies: Experiment.** M. Allan  
**Electron Impact Spectroscopy of Molecules at Low Energies: Theory.** M.A.P. Lima

J. Dehmer, *discussion leader*  
**Laser-Based Methods for Novel Photoelectron Spectroscopy.** M. G. White  
**Memory Effects in Molecular Fragmentation upon Site-Specific 1s Excitation Observed by Coincidence Measurements.** K. Muller-Dethlefs  
**Multiphoton, Multielectron Ionization of Simple Molecules via Covariant Mapping Techniques.** K. Codring

H. C. Siegmann, *discussion leader*  
**Spin-Polarized Electron Scattering from Thin Magnetic Films.** D. Pescia  
**Spin-Polarized Inverse Photoemission.** M. Donath  
**Spin-Polarized Core Level Photoemission.** W. Gudat

**Coupling of Phonons and Low-Energy Electronic Excitations.** S. Kevan  
**Theory of Phonon Modes at Surfaces.** T. Rahman

**Theory of Nonlinear Processes at Surfaces.** A. Liebsch

**Normal Modes at the Surface of Metals.** E. W. Plummer

**Photoemission Studies of Semiconductor Surfaces.** R. Haight

**Time-Resolved Photoemission Using Lasers.** F. Meier

**Theory of Alkali Adsorption on Metals.** H. Ishida

D. Shirley, *discussion leader*  
**Photoelectron Holography.** J. Barton

A. M. Bradshaw, *discussion leader*  
**SEXAFS Studies of Chemisorbed Oxygen.** K. Baberschke

**Diffuse LEED Investigation of Oxygen on Ni and Other Systems.** K. Heinz

**Lasers in Medicine and Biology**

Kimball Union Academy  
Meriden, NH  
J. E. Boggan, *Chairperson*  
C. Puliafito, *Vice Chairperson*

**JULY 9-13****Effects of Tissue on Light**

B. Wilson, *discussion leader*  
**In Vivo Fluorescence.** S. Svanberg  
**In Vivo Optical Dosimetry.** W. Star  
**Laser Doppler.** R. Steiner

**Effects of Light on Tissue**

R. Birngruber, *discussion leader*  
**Photothermal Effects.** L. Svaasand  
**Nonlinear Photochemical Effects.** I. Koch'ev  
**Photoacoustic/Mechanical Effects.** R. Birngruber

J. Boggan, *discussion leader*  
**Tissue Optics.** S. Jacques  
**Laser-Based Spectral Diagnosis.** M. Feld

**Optical Trapping**

M. Berns, *discussion leader*  
**Optical Trapping: Principles and History.** A. Ashkin  
**Models and Biological Systems.** W. Wright  
**Biomechanics of Intracellular Activity.** S. Block  
**Cell Sorting by Optical Trapping.** T. Buican

**Time-Resolved Spectroscopy**

S. Jacques, *discussion leader*  
**Speakers:** B. Chance, J. Lakowitz, M. Paterson

**Photochemistry**

S. Bown, *discussion leader*  
**Photosensitizers in Medicine.** J. Van Lier  
**Potential Photophysical and Photochemical Reactions in Medical Therapy.** D. Phillips  
**What Are We To Achieve with PDT?** B. Henderson

**Tissue Ablation: Mechanism and Clinical Strategies**

C. Puliafito, *discussion leader*  
**High-Speed Imaging of UV Laser Ablation of Tissue.** R. Srinivasan  
**IR Laser Tissue Ablation.** J. Walsh  
**Control of Laser Ablation.** L. Deckelbaum

**Biomodulation with Lasers**

J. Basford, *discussion leader*  
**Speakers:** A. Meister, D. Harris

J. Boggan, *discussion leader*  
**Optical Mapping of Brain.** A. Grinvald  
**Photo-Ion Microscopy.** V. S. Letokhov

**Physical Electrochemistry**

Colby-Sawyer College (S)  
New London, NH  
J. O'M. Bockris, *Chairperson*  
H. C. Abruna, *Vice Chairperson*

**JULY 30-AUGUST 3****Structure of the Interfacial Region**

D. Schiffrin, *Chairman*  
**Speakers:** F. Silva, T. Kakiuchi, S.G.A. McLaughlin, A. A. Kornyshev

**Experimental Approach to Quantum Aspects of the Double Layer**

J. T. Hupp, *Chairman*  
**Speakers:** A. Nozak, K. Koval, J. T. Hynes, A. J. Heeger

**Nuclear Electrochemistry**

S. Pons, *Chairman*  
**Speakers:** R. A. Huggins, A. A. Wadsworth, R. Oriani, M. MacKubre

**New Experimental Methods in Electrochemistry**

W. O'Grady, *Chairman*  
**Speakers:** F. Wagner, E. Stuve, R. Corn, B. Schardt

**Bioelectrochemistry**

A. Heller, *Chairman*  
**Speakers:** H.A.O. Hill, I. Karube, J. J. Kuly

**Separation and Purification**

Colby-Sawyer College (N)  
New London, NH  
T. A. Hatton, *Chairperson*  
J. Sherman, *Vice Chairperson*

**AUGUST 13-17****New Developments in Affinity Separations.**

C. Lowe  
**Protein Separations Using Affinity Surfactants.** R. Carbonell  
**Organized Molecular Assemblies in Chemical Separation.** W. Hinze  
**Reverse Micelles and Microemulsions in Near-Critical and Supercritical Fluids.** J. Fulton

**Principles of Reactive Distillation.** M. Doherty  
**High-Purity Methyl Acetate via Reactive Distillation.** V. Agreda  
**Centrifugal Distillation.** G. Hubred

**High-Purity Gases for Electronics Applications.**

J. Solomon  
**Predictive Elution Strategies for HPLC.** V. McGuffin  
**Strategies for High-Speed GC.** R. Sachs

**Linear Solvation Energy Relationships: Solvatochromism and Chromatography.** P. Carr  
**Computational Analysis of Chiral Recognition in Chromatography.** K. Lipkowitz  
**Studies in Molecular Recognition.** J. Rebek

**Vortex Flow Filtration.** P. Rolceggio  
**How Fiber Contained Liquid Membranes for Environmental Pollution Control.** K. Sirkar

**Statistics in Chemistry and Chemical Engineering**

New Hampton School  
New Hampton, NH  
J. F. MacGregor, *Chairman*  
W. Q. Meeker, *Vice Chairman*

**JULY 30-AUGUST 3****Multivariate Design and Analysis.** S. Wold,

N. Kettaneh-Wold  
**Multivariable Process and Quality Control.** R. Swanson

**Recent Developments in Design: Constrained Designs and Robust Designs.** G.E.P. Box,

I. Hau, S. Jones  
**Neural Networks and Their Applications.** T. J. McAvoy

**Sensitivity Analysis in Modeling Chemical Plants for Design and Optimization.** G. Blau,

K. Kuenger  
**Planning Fractional Factorial Experiments To Accommodate Specific Interactions.** J. Wu

**Multivariate and Tensorial Calibration.**

B. Kowalski  
**Discrete Bayesian Method for Parameter Estimation.** P. M. Reilly

**Interactive Statistical Graphics.** D. Pregibon

## Vibrational Spectroscopy

Brewster Academy  
Wolfeboro, NH  
J. F. Rabolt, *Chairperson*  
T. A. Keiderling, *Vice Chairperson*

AUGUST 6-10

### Molecular Dynamics

Solvent/Solute Interactions Probed by  
Picosecond Transient Raman  
Spectroscopy. T. Gustafson

### Surfaces and Interfaces

Surface-Enhanced Raman Spectroscopy of Thin  
Molecular Assemblies. N. Ferris

### Biological Applications

Molecular Reorganizations in Biological  
Membranes: FT and Dispersive Raman and IR  
Spectroscopic Studies. I. W. Levin

### Novel Spectroscopic Techniques

Nitrogen Doping of Amorphous Carbon:  
Laboratory and Interstellar Observation of the  
Raman Active G and D Bands in the IR.  
D. Saperstein

Other topics to be included: vibrational  
intensities, high-resolution spectroscopy, and  
theoretical spectroscopic methods.

## Magnetic Resonance in Biology and Medicine

Tilton School  
Tilton, NH  
R. G. Bryant, *Chairperson*  
B. J. Gaffney, *Vice Chairperson*

JULY 16-20

### Magnetic Microscopy

G. Drobney, *chairperson*  
Microscopy by 3D Projection Reconstruction:  
Problems, Solutions, More Problems.  
P. Lauterbur

Stroboscopic Micro MRI: Arterial Stiffness and  
Blood Flow. L. Jelinski  
MR Microscopy/Histology. A. Johnson

### Spatial Localization

B. Gaffney, *chairperson*  
Chemical Shift Imaging. T. Brown

Oriented on Selectivity by Modern Time-Domain  
and High-Frequency ESR Methods. J. Freed

### Quantitation

G. Glover, *chairperson*  
Quantitation of Free Radical Formation through  
Spin Trapping. R. P. Mason  
Use of Natural Lineshapes in the Analysis of  
NMR Spectra. B. Balaban  
Quantitation and Relaxation. M. Henkelman

### Flow and Perfusion

J. Ackerman, *chairperson*  
Real-Time Perfusion Imaging. B. R. Rosen  
Perfusion and Flow. I. R. Young  
Molecular Diffusion and Microcirculation in  
Brain. D. LeBihan

### Relaxation

M. Tweedle, *chairperson*  
Proton Relaxation in Tissues. J. Gore  
Electron and Nuclear Relaxation. J. Kowalewski  
Relaxivity Enhancement of Protein-Bound  
Chelates. R. Lauffer

### Quadrupole Problems

T. Dixon, *chairperson*  
Physical State of Intracellular Sodium.  
C. Springer  
Sodium-23 NMR of Biological Systems:  
Applications to Striated Muscle. J. Ingwall  
Quadrupole Ion Relaxation in Crowded Protein  
Environments. T. Schleich

### New Twists

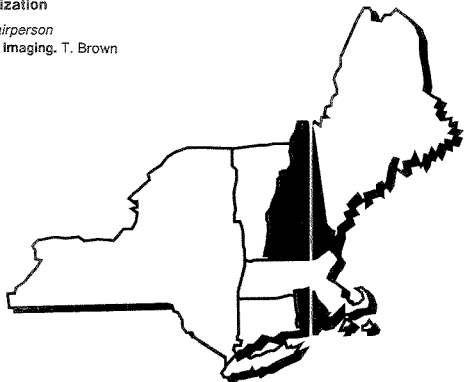
M. Klein, *chairperson*  
Solid-State NMR Distance Measurements and  
High-Field Dynamic Nuclear Polarization in  
Proteins. B. Griffen  
Pulsed Electron-Nuclear Resonance in  
Metalloproteins. H. Thomann  
Metabolite Uses of Tritium NMR Spectroscopy.  
M. Klein

### Spatial Localization

K. Ugurbil, *chairperson*  
Gradient Selection of Coherence Transfer: High-  
Resolution and In Vivo Applications. R. Hurd  
Advances in MRI Spatial Resolution in Humans.  
J. S. Hyde

### Spectroscopy

J. Gluckson, *chairperson*  
Carbon Spectroscopy of Tumors. L. Sillerud  
EPR Imaging Oximetry in Tissues. H. Halpern  
Proton Spectroscopy of Tumors. J. Saunders



# CHEMINERT THE ORIGINAL

LC Column  
Choices

Unpacked  
Glass  
Biocompatible

Microbore  
2 and 3mm bore,  
500psi

Standard  
6 to 50mm bore,  
up to 500psi

High Pressure  
1/8" bore, 1500psi  
1/4" bore, 2500psi

CHEMINERT® THE STANDARD

1-800-FOR-VICI

VICI  
VICI AG

Valco Instruments Co. Inc.  
P.O. Box 55603 Houston, Texas 77255  
Tel: (713) 688-9324 Fax: (713) 688-8106

Valco Europe  
Untertannberg 7 CH-6214  
Schenkon, Switzerland  
Tel: (045) 21 68 68 Fax: (045) 21 30 20

Discover new solutions

## New SFE system expands your sample preparation options

Say goodbye to tedious liquid-extraction sample prep for GC, HPLC, and UV-vis analyses. Supercritical fluid extraction (SFE) is faster and more efficient; uses inexpensive, nontoxic solvents like CO<sub>2</sub>; and allows easy control of selectivity via fluid pressure/density.

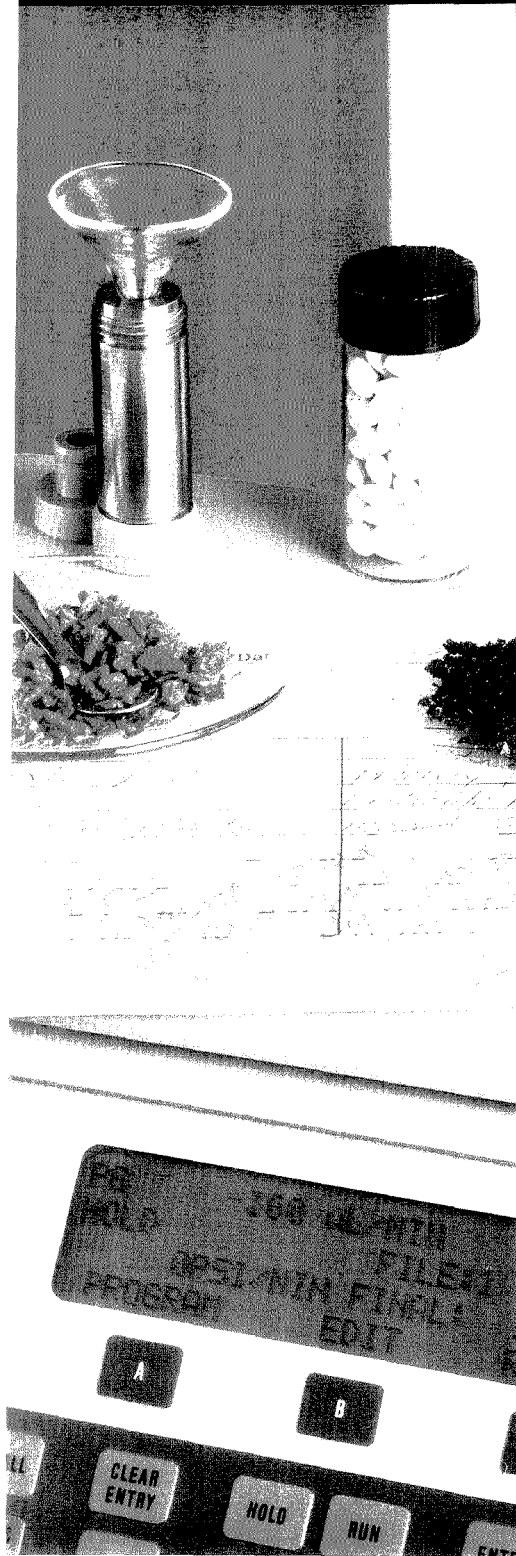
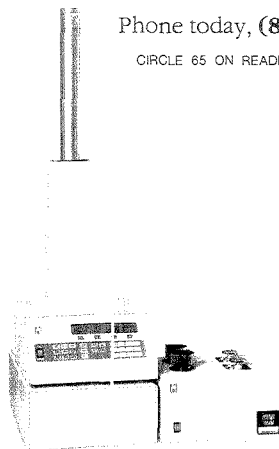
And with Isco's new extraction system, SFE just became even more powerful and accessible.

- The SFX™ 2-10 extractor uses quick-load sample cartridges up to 10 ml. Dual-chamber design gives you efficient, continuous operation.
- Capture extractants off-line in minimal solvent volume for immediate analysis.
- New Model 260D pump handles any SFE or SFC technique: flow range is 0.1 µl to 40 ml/min at up to 7500 psi.
- Digital pump controller lets you quickly set up and recall extraction conditions.

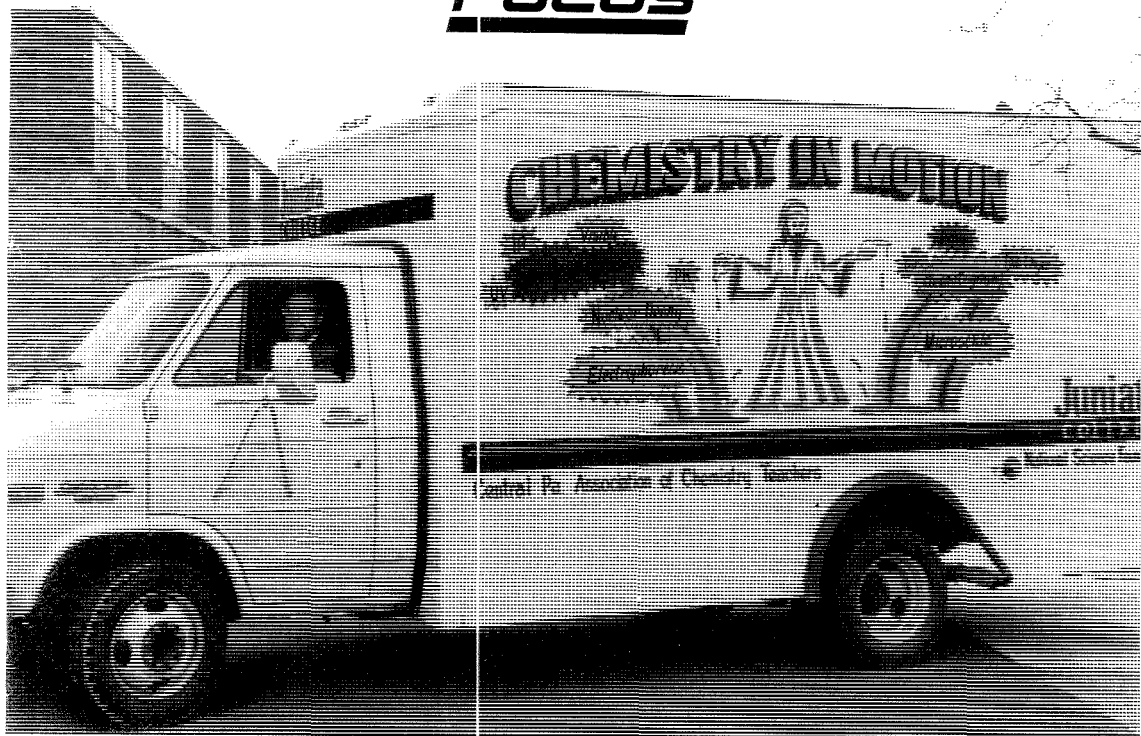
Phone today, **(800)228-4250**.

CIRCLE 65 ON READER SERVICE CARD

Isco, Inc.  
P.O. Box 5347  
Lincoln NE 68505  
Tel: (402)464-0231  
Fax: (402)464-4543







# CHEMISTRY ON WHEELS

As with other colleges and universities, the numbers of students entering Juniata College with an expressed interest in chemistry began steadily declining in the early 1980s. Concerned about the drop, Juniata chemists began talking with local high school chemistry teachers. What evolved from those discussions is a unique program that seeks to improve chemistry education by making high school teachers both better educators and better chemists.

The heart of the program, which started in the fall of 1988, is a van specially equipped with sophisticated instrumentation for use in high school laboratory experiments. Most of the equipment (see list on next page) is rarely available in high schools. The

van travels nearly every day to one or several of 25 participating high schools in six primarily rural central Pennsylvania counties. (Juniata College is located in Huntingdon, approximately 120 miles east of Pittsburgh.) According to project director and Juniata professor of chemistry Donald Mitchell, providing the equipment is a means to reignite interest in science among high school students. The program reaches more than 2000 students.

The van is equipped with padded shelves to protect delicate instruments, and everything is carefully tied down. The IR spectrometer, for instance, is fixed to a table that can be wheeled directly into a high school laboratory. Equipment and appropriate chemical supplies are delivered to the local

chemistry teacher. At the end of the day the equipment is retrieved, and any waste chemicals are collected for disposal.

The van's driver, Tom Spicher, is also a certified teacher knowledgeable in the use of the instruments, and he assists the teacher with operating and demonstrating the equipment. "Every high school gets at least six visits each year," says Spicher, "and some as many as 18." Each high school teacher decides when the equipment is needed.

Programs that deliver scientific equipment by van are not unique to the Juniata project. Genentech, for instance, has underwritten an instrument van that brings equipment for recombinant DNA experiments into California high school biology classes.

Lane Conn at San Francisco State University directs the California program.

The services provided by Juniata's van, however, represent only part of the college's program. Essential to the project are two-week summer workshops where teachers receive hands-on training and attend lectures on instrumental theory. Teachers develop and test the experiments they will present during the school year. Access to the analytical instruments offers teachers a variety of interesting and unique experiments to use. For instance, their students have measured the UV absorbance of commercial sunscreen lotions to determine whether they differ based on the sun protection factor ratings, used high-performance liquid chromatography to separate the pigments in the sweet drink grape Kool-Aid, and examined gasoline for traces of methanol by gas chromatography.

In addition to the summer workshop, all the teachers in the program are invited twice a year to seminars and lectures presented by well-known science educators. In the past two years teachers have heard Dorothy Gable from Indiana University discuss the teaching of problem solving and Henry Bent from the University of Pittsburgh describe the effective use of chemical demonstrations. The meetings also provide an opportunity for teachers to interact with their colleagues.

Besides sharpening teaching skills, the program encourages teachers to view themselves as chemists. Toward that end, teachers can spend the summer at the college to carry out basic research. "We envision this as a total support system for high school teachers," says Mitchell.

Students also receive special treatment. In the spring they and their teachers are invited to Juniata for what could be labeled a practice science fair. The science fair projects take full advantage of the instrumentation. For instance, last year a student prepared  $CCl_4$  using microscale equipment, identified it by IR spectroscopy, and demonstrated with GC that the synthesized product was purer than material in the school's stockroom. This year students will use electrophoresis to compare gene types of related fish species and determine glucose levels in blood serum by spectrophotometry. Besides exhibiting projects, the hope is that the practice science fair will prepare students for the more competitive regional fairs.

What does all this teacher support cost? Mitchell estimates that the five-year start-up period will cost around \$850,000. Most of that money will come from a five-year \$500,000 grant from

the National Science Foundation (NSF).

"The program brings science education to teachers and gives them the opportunity to enrich their background and practice hands-on science," says NSF's Ethel Schultz. "It is the scientists that really make the program credible." Additional funding comes from leading chemical manufacturers such as Dow and Du Pont or organizations such as the Merck Foundation.

Launching this program has also required a significant effort. The roots can be traced back to the spring of 1985 when local high school chemistry teachers were invited to meet at the college. It was then that the Central Pennsylvania Association of Chemistry

#### Van equipment list

- 8 spectrophotometers
- 1 IR spectrometer
- 3 gas chromatographs
- 2 electrophoresis apparatuses
- 1 high-performance liquid chromatograph with visible detector
- 12 pH meters
- 4 melting-point instruments
- 4 analytical balances
- 2 nuclear scalars
- 1 radon monitor
- 2 chart recorders
- 1 integrator
- 1 UV lamp
- 1 UV light box
- 1 compressor/pump
- 7 Eppendorf micropipets
- 1 digital thermometer
- 15 magnetic stirrers and hot plates
- 30 microscale glassware kits
- 1 superconductor demonstration kit
- 1 4-liter Dewar flask

Teachers (CPACT), a partnership between college and high school instructors, was formed.

At the same time, recalls Mitchell, Juniata chemists expressed a desire to work with talented high school students at the college. Unfortunately, for insurance and legal reasons it would have been necessary for teachers to accompany students on such outings, which made the idea impractical. The Juniata chemists instead vowed to bring the equipment to the schools.

It took until 1988 to acquire funding and stock the van. During the summer before the van began rolling, chemistry teachers from participating schools practiced using the equipment at the first workshop. "This is a teacher-driv-

en program," says Mitchell. "We don't tell teachers what they should be doing. We make resources available to them."

Eleanor Siegrist, a chemistry teacher at Hollidaysburg Area High School, was drawn to the program by an announcement in CPACT's newsletter. She has since participated in workshops, seminars, and the summer research program.

"It means a lot to have new equipment that really works," explains Siegrist. For instance, she finds that access to the program's digital top-loading balances leads to better experimental results for many of her students. Students are also performing more sophisticated experiments such as organic synthesis and characterization requiring microscale glassware kits, IR spectroscopy, and GC. According to Siegrist, students look forward to the approximately monthly visits of the van.

Prior to the van deliveries, Siegrist and many of her fellow high school teachers viewed laboratory instrumentation as a problem. "If the equipment breaks down you are stuck," she says. Funds to buy new equipment or fix old instruments were limited, and few teachers could make their own repairs. Not having equipment and lacking chemicals also hindered Siegrist from encouraging independent student projects.

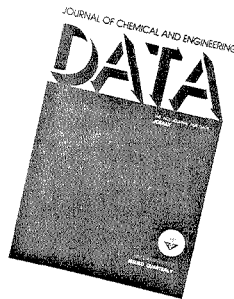
This year, Siegrist says she has 80 students involved in independent projects. Because the projects are worked on at home or after school, they add to the regular chemistry curriculum. Two of last year's independent projects were presented as student posters at a special science program at the Pennsylvania State University. In addition, Siegrist now organizes a local science fair.

The program has had an impact on other teachers. According to Mitchell, teachers are becoming more familiar with the instruments and thus less time is being spent on training. Instruments are being left at high schools and used without the van driver's assistance. This means that various instruments can be used simultaneously at different schools. According to Mitchell, during the second year of operation most equipment is in constant use. Recognizing the value of having this type of equipment available for their students, teachers are even persuading their school districts to buy some equipment for their school laboratories.

"Teachers had lost their identity as chemists," explains Mitchell. "Now they feel more like chemists; they have a good self-image." Adds Siegrist, "It's rekindled my interest in teaching."

*Alan R. Newman*

# JOURNAL OF CHEMICAL AND ENGINEERING DATA



## Get A World Of Precise, Accurate Data In This International, Quarterly Journal

Multidisciplinary in nature and international in scope, the *Journal of Chemical and Engineering Data (JCED)* features contributions by distinguished physicists, chemists, chemical engineers, mechanical engineers, biological scientists, and applied mathematicians from the world over. Their expert reports represent numerical data bases for private technical information systems, particularly in industry, that will broaden your scientific horizons and improve the quality of your work.

This unique journal offers you precise, accurate data on physical, thermodynamic and transport

properties of well-defined materials. It also keeps you informed about the latest international standards on symbols, terminology and units of measurement for reporting data properly.

You'll find numerical property data measurements on:

- pure substances of defined purity
- well-defined gaseous, liquid and solid mixtures
- semi-empirical and theoretical correlations useful in interpolating, extrapolating and predicting properties of scientific and technological importance

- new substances — the physical and spectral properties of inorganic, organic, and biochemical substances and other complex substances prepared by established synthetic procedures that may have major scientific and technological applications

### Editor

Bruno J. Zwolinski,  
*Texas A&M Univ.*

### Associate Editors

Henry V. Kehiaian,  
*Univ. of Paris, France*

Randolph C. Wilhoit,  
*Texas A&M Univ.*

### 1990 SUBSCRIPTION INFORMATION

Volume 35  
4 Issues Per Year



	U.S.	Canada and Mexico	Europe (Air Service Included)	All Other Countries (Air Service Included)
<b>ACS Members</b>				
1 year	\$ 30	\$ 35	\$ 37	\$ 40
2 years	\$ 54	\$ 64	\$ 68	\$ 74
<b>Nonmembers</b>				
1 year	\$207	\$212	\$214	\$217
<b>Supplementary Material on Microfiche</b>	\$ 12	\$ 16	\$ 16	\$ 16

Member subscription rates are for personal use only.  
For nonmember rates in Japan, contact Maruzen Co., Ltd.  
Journal subscriptions start January 1990 and are based on a calendar year.

### Address your orders or inquiries to:

American Chemical Society  
Sales and Distribution Department  
1155 Sixteenth Street, N.W.  
Washington, DC 20036

**Toll free** (800) 227-5558

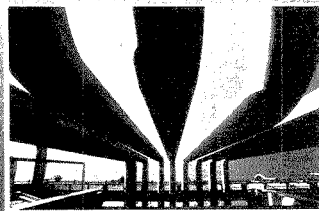
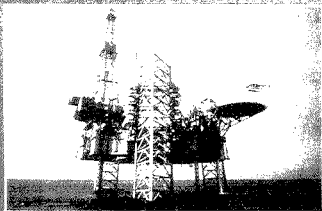
**Outside U.S.** (202) 872-4363

**Telex:** 440159 ACSPUI or  
892582 ACSPUBS

**Fax:** (202) 872-4615

This publication is available on microfilm,  
microfiche, and electronically through Chemical  
Journals Online on STN International.

# World Class Opportunities.



*True job challenge is a rarity today.* But Saudi Arabia has been challenging the experts for more than 50 years. As the free world's largest producer and exporter of oil and gas, the manager of a fourth of the globe's proven oil reserves, the Saudi Arabian Oil Company (SAUDI ARAMCO) has had to create its own technological feats.

*And it continues to.* Those technical achievements have been made in part with the international team of expatriates that are part of Saudi Aramco 44,000-member work force. Expatriates continue to play an important role at Saudi Aramco. By contributing their expertise, our professionals not only import new technology into Saudi Arabia, but also benefit from once-in-a-lifetime work experiences.

Saudi Aramco offers world-scale projects, remarkable people, a rich cultural experience. To accept the Saudi Aramco challenge is to accept personal growth, a new world perspective and professional enrichment.

You will have the opportunity to explore World Class Opportunities by meeting with Saudi Aramco representatives, Office #1, at the American Chemical Society Exposition, April 23-25, 1990 at the Hynes Convention Center in Boston.

Employment with Saudi Aramco will provide you with an interesting lifestyle in a multicultural environment, including comfortable family living arrangements, free medical care while in Saudi Arabia, fine schools and a broad spectrum of recreational opportunities, plus 36 calendar days of vacation annually, allowing for extensive travel. We provide an attractive compensation package which includes an expatriate premium.

## STABLE ISOTOPE CHEMIST

Will serve as the stable Isotope Scientist with the company and will be responsible for setting up/operating/training personnel on a new stable isotope ratio mass spectrometer. Will consult with exploration geologists and provide appropriate data interpretation. BS in Chemistry, advanced degrees preferred, with 15 years' experience and 5 years' in stable isotope technology essential.

## PROCESS CHEMIST

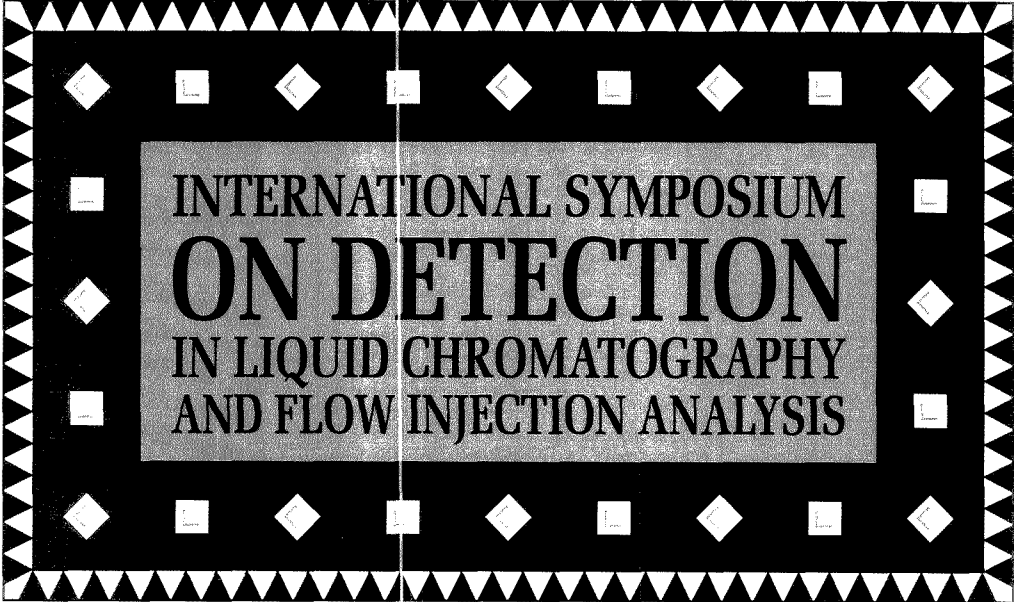
Will provide technical consulting services to refineries, gas/oil separation plants, and wet crude handling facilities in order to resolve field operational problems. BS in Chemistry, advanced degrees preferred, with 10 years' experience in petroleum industry and knowledge in process chemistry essential. Additional working experience with advanced analytical techniques is highly desirable; such techniques might include but are not limited to GC/FT-IR, fluorescence spectroscopy, GC/MS, X-ray techniques, scanning electron microscopy, and HPLC.

## SR. QA/QC ANALYTICAL CHEMIST

BS in Chemistry, advanced degree preferred, with 12 years professional experience, the last five of which should involve the candidate as a senior professional in an advanced quality assurance/quality control laboratory. Knowledge and experience with advanced analytical instrumentation required.

If unable to attend, please send your resume to: ASC, Employment Dept. 06X-M14-0, P.O. Box 4530, Houston, Texas 77210-4530.

# SAUDI ARAMCO



# INTERNATIONAL SYMPOSIUM ON DETECTION IN LIQUID CHROMATOGRAPHY AND FLOW INJECTION ANALYSIS

**Gary Christian**  
Department of Chemistry  
University of Washington  
Seattle, WA 98195

**Ira Krull**  
Northeastern University  
Barnett Institute  
341 MU, 360 Huntington Ave.  
Boston, MA 02115

**Julian Tyson**  
Department of Chemistry  
University of Massachusetts at Amherst  
Amherst, MA 01003

High-performance liquid chromatography (HPLC) and flow injection analysis (FIA) are the hydrodynamic techniques of greatest impact in contemporary analytical chemistry. They feature major technical differences (e.g., in the pressures and separator columns used and scope of application) as well as a gap of more than 15 years between development and commercialization. Nevertheless, HPLC and FIA are complementary techniques in terms of speed, capability, sensitivity, and certain modular elements.

The essential features of the continuous detection systems, in particular, are remarkably similar for both methods. This coincidence prompted the late Roland Frei to suggest a meeting on detection at which specialists in HPLC and FIA could discuss common problems and experiences.

Last year the International Symposium on Detection in HPLC and FIA was held September 20-22 in Cordoba, Spain. Final organization was handled by Miguel Valcarcel and Delores Luque de Castro of the University of Cordoba. The International Association of Environmental Analytical Chemistry, Hewlett-Packard, and the University of Cordoba (the symposium's host) sponsored the event. More than 400 scientists from 24 countries attended the meeting. Topics included luminescence, hyphenated techniques, electrochemistry, pre- and postcolumn derivatization, fast UV-vis detectors, and atomic spectroscopy.

## FOCUS

Whether the object is to determine many components in a complex mixture or to measure just one, detection system requirements are very similar, and many of the speakers took this as a framework for their lectures. Josef Huber of the University of Vienna pointed out that in FIA the chemical reactor design must primarily meet the requirements of the measuring system, whereas the requirements of the separation system have to be considered for HPLC reaction detection. The critical criterion is the reactor efficiency,  $N$ , which describes the longitudinal mixing per unit reactor volume. The aim is to design a flow reactor that minimizes

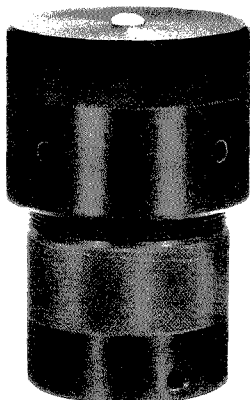
longitudinal mixing. Reactor volume, on the other hand, is dictated by reaction kinetics (i.e., the required reaction time).

From Huber's and subsequent lectures it soon became apparent that detection is more than just hardware. Whether chromatography or FIA, it is the judicious combination of on-line chemical derivatization with an appropriate detector that provides the basis for a versatile analytical methodology.

One area of common interest was multichannel detector systems. These systems have made a major impact on the information power of HPLC, and that capability is just now being explored in FIA. Anthony Fell of the University of Bradford in England described diode array detection in HPLC, emphasizing detection techniques, diode array advances, interfacing HPLC with diode array detectors, and methods for two- or three-dimensional data representations.

Several methods have been established for the qualitative and quantitative validation of chromatographic peak points: multiple absorbance-ratio correlation (MARC), second- and higher order derivative chromatograms, multiple-wavelength spectral suppression, principal component analysis, iterative target-testing reactor analysis, and multiple-component analysis. In addition, peak recognition techniques based on archive retrieval have been developed using spectral and time domain information.

## NEW MICROWAVE DIGESTION BOMBS



PAT. PENDING

**Now in two sizes,  
23 ml and 45 ml.**

The speed and convenience of microwave heating can now be applied to the digestion of inorganic, organic, or biological materials in a Teflon Lined Bomb. The new Parr Microwave Digestion Bombs have been designed to combine the advantages of closed high-pressure and high temperature digestion with the requirements of microwave heating. Many samples can be dissolved or digested with less than one minute heating times. As with all Parr Digestion Vessels, careful design and testing effort have gone into the safety and sealing aspects of this unique vessel and operating environment.

Call or write for Bulletin 4781 with complete technical details.



**PARR  
INSTRUMENT  
COMPANY**  
211 Fifty-third Street  
Moline, IL 61265  
Phone: (309) 762-7716  
Telex: 270226

## FOCUS

Nel Velthorst from the Free University of The Netherlands discussed recent advances in laser applications, especially for fluorescence in microcolumn chromatography and capillary electrophoresis (CE). According to Velthorst, low-temperature fluorescence line narrowing has very high selectivity for identification purposes. It can be used with thin-layer chromatography or as an off-line detection method in micro LC.

A different type of detection scheme was discussed by Douglas Westlund from Sweden's University of Uppsala. He reviewed methods for the indirect detection (photometric) of organic and inorganic analytes in reversed-phase HPLC. Indirect detection requires a probe compound with a large UV-absorbance or fluorescence, or strong electrochemical response as a mobile-phase component. An injected sample produces migrating zones where the local mobile phase deviates from the bulk. Analytes will thus co-elute where deficiencies or excesses of the probe—depending on charge and hydrophobicity—result in respectively negative or positive peaks (1, 2).

Velthorst also discussed indirect methods, describing results from Frei's laboratory on indirect UV-vis and fluorescence detection. Analyte ions affect the concentration of absorbing/emitting compounds in the mobile phase or in a postcolumn addition, resulting in a negative peak. Luminescence-quenching techniques were also presented, wherein an added detector species with a long luminescence lifetime is efficiently quenched by the analyte. In addition, work was presented from C. Gooijer's laboratory at the Free University of The Netherlands on novel luminescence detection approaches, especially luminescence quenching of a Tb-acetylacetonate complex to determine inorganic ions under ion-pair, reversed-phase HPLC conditions.

An overview of conventional, on-line HPLC electrochemical (EC) and fast-scanning EC detection for normal and microcolumn modes was given by L. J. Nagels from the Rijksuniversitair Centrum Antwerpen in Belgium. He emphasized using very slow flow rates for microcolumn LC-EC interfacing and characterized a disposable copolymer EC detector for analyses at flow rates of < 10  $\mu\text{g}/\text{min}$ .

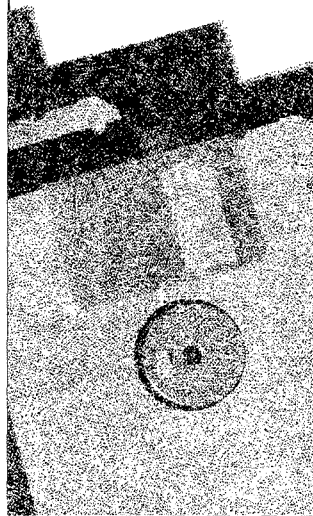
Several symposium speakers described EC detection schemes. L. Huber from Hewlett-Packard presented a flow-through solid electrode for EC detection in reversed-phase HPLC. This particular commercial unit combines a disposable, glassy carbon thin-layer electrode with optional pulsed

# ACS Software

High-quality software programs for the personal computer that meet the standards you expect from the ACS

For information about ACS SOFTWARE, call TOLL FREE (800) 227-5558 or write to:

American Chemical Society, Marketing Communications, 1155 Sixteenth Street, N.W. Washington D.C. 20036



CIRCLE 114 ON READER SERVICE CARD

amperometric detection methods. The electrode surface can be cleaned between actual current measurements.

Joseph Wang, from New Mexico State University, discussed biocatalyst-modified amperometric electrodes for detection in flowing streams. According to Wang, membranes for size or charge exclusion enhance the selectivity and stability of the electrodes. Cellulose acetate, polyaniline, and polyphenol coatings provide the desired size exclusion effect, whereas charged poly(4-vinylpyridine) or Nafion coatings are used for appropriate charge exclusion. Multifunctional operation (selectivity, catalysis, protection, etc.) is obtained with a multilayer or composite (mixed) electrode coating.

Some specialized applications of EC detectors were also described. Gyorgy Marko-Varga, from the University of Lund in Sweden, analyzed fermentation broth sugars using postcolumn, coimmobilized enzyme reactors and modified electrodes; and José Lima from the University of Oporto in Portugal discussed a tetraoctylammonium barbiturate-based PVC potentiometric detector for FIA that is sensitive to barbiturate ions.

Ultraminiaturized detection for microcolumn HPLC or CE methods was reviewed by Hans Poppe from the University of Amsterdam. A key consideration for these detectors is the smallest volume needed for detection, because that ultimately dictates the absolute detection limit and how far miniaturization can be taken. Poppe described a number of miniaturized systems for detection on the nanoliter scale, including liquid-liquid extraction, sheath flow reactor, enzyme-moderated reaction, and electrochemical systems.

Additional detection power, through on-line derivatization, was illustrated for heterogenous systems. Gary Christian and Jaromir Ruzicka, both from the University of Washington, reported on optosensing in FIA using the reversible sorption of hydrophobic reagents and analytes onto hydrophobic particles to selectively measure analytes. They described a porous, hydrophobic membrane detector that allows gases to diffuse (eg., NH<sub>3</sub>, HCl) but blocks passage or detection of nongaseous species such as NaOH. The gases are detected by the changing color of an indicator incorporated into the membrane. The implications of the complementary nature of FIA and HPLC (3) were presented.

New polymeric reagents for off- and on-line derivatization of nucleophiles were described by Ira Krull. Solid-phase, heterogenous derivatization leads to improved specificity and sensi-

tivity in HPLC, regardless of detection mode. Krull's group has designed a mixed-bed, solid-phase reactor containing three different tagging reagents, thereby leading to three derivatives with different chromatographic and detector properties. A novel approach was described for off- and on-line tagging of enantiomeric amines for Pirkle type chiral separations. In the future, according to Krull, all approaches to chiral recognition in HPLC should be possible via single or mixed-bed type polymeric reagents.

Several hyphenated techniques were also presented. Richard Browner from the Georgia Institute of Technology discussed the idea of using a particle beam (MAGIC) interface with HPLC/FT-IR. In his system a vapor aerosol of analyte particles is deposited on a salt disk/plate and rotated into the FT-IR beam. It appears that this new approach for LC/FT-IR interfacing may have some significant advantages over current practices.

Julien Tyson described detectors for atomic spectrometers. Because these spectrometers either operate intermittently (electrothermal atomizers) or produce a steady-state signal (nebulizers for flames or plasmas), some form of on-line chemistry will probably be needed to improve FIA and atomic spectrometry detection limits. Alternatively, nebulizers and spray chambers will have to be specifically designed for use with FIA introduction. According to Tyson, the single-well stirred tank model indicates that there should be some benefit from designs with reduced spray chamber volumes.

Some particularly relevant research by the symposium's organizers presented the dual use of an FIA manifold as a screening system and postcolumn reactor-detector in HPLC. Valcarcel and Luque de Castro exploited the rapid measurement frequency of FIA for screening large numbers of samples for total analyte content—in this case, toxic substances. Only elevated samples are then subjected to time-consuming chromatography, employing the same FIA configuration as a postcolumn reactor-detector.

Most of the participants acknowledged the high scientific level of the meeting and left Cordoba with the hope for future meetings on the same subject. The seed has been planted.

**References**

- (1) Denkert, M.; Hackzell, L.; Schill, G.; Sjögren, E. *J. Chromatogr.* 1981, 218, 31.
- (2) Arvilsson, E.; Commen, J.; Schill, G.; Westlund, D.; *J. Chromatogr.* 1989, 461, 429.
- (3) Ruzicka, J.; Christian, G. D. *Analyst*, in press.

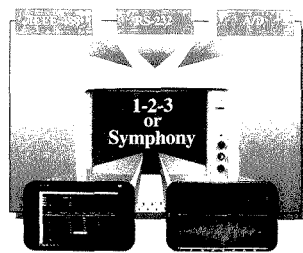
**Still using these tools**



**to enter your analytical/laboratory data into a spreadsheet?**

**If so, you need...**

**MEASURE**



Measure seamlessly integrates engineering and scientific data with either a Lotus 1-2-3 or Symphony spreadsheet where it is ready for immediate analysis, storage, or display. Measure accepts data from IEEE-488 and RS-232 instruments and plug-in data acquisition boards for IBM PC/XT/AT and PS/2 computers.

*Now supports new Lab-PC data acquisition board—high performance at a low cost.*

**Call for Free Catalog and a Demo Disk**

**(800) IEEE-488 • (512) 794-0100**



JAPAN (3) 788-1922 • FRANCE (1) 48 65 33 70  
WEST GERMANY (89) 80-7081  
ITALY (2) 4830-1892 • THE NETHERLANDS (7) 099-6360

CIRCLE 98 ON READER SERVICE CARD



Gary Christian earned his B.S. degree (1959) from the University of Oregon and a Ph.D. (1964) from the University of Maryland. In 1972 he joined the faculty at the University of Washington, where he is professor of chemistry. Christian's research interests include electroanalytical chemistry, atomic spectroscopy, process analysis, and flow injection analysis. He received the 1988 ACS Division of Analytical Chemistry Award for Excellence in Teaching. He has served on the Advisory Board of ANALYTICAL CHEMISTRY and is joint Editor-in-Chief of *Talanta* and presently chairs the ACS Division of Analytical Chemistry.



Ira Krull received his B.S. degree from the City College of New York (1962) and an M.S. degree (1966) and a Ph.D. (1968) from New York University. Krull is now associate professor of chemistry and a faculty fellow at Northeastern University's Barnett Institute. His research interests include trace metal analysis and speciation via chromatography with element-selective detection, solid-phase derivatization for detection in GC and HPLC, EC detection via photochemical reactions or photoelectrochemical detection in flowing streams, and biopolymer determinations with linear diode array and LALL spectroscopies in HPLC and FIA.



Julian Tyson obtained a B.Sc. degree (1971) from the University of Aberdeen in Scotland and his Ph.D. (1975) from London University (Imperial College). Last year he joined the faculty at the University of Massachusetts at Amherst after 13 years at the University of Technology, Loughborough, in the United Kingdom. His research focuses on flow injection and continuous flow techniques for enhancing analytical spectrometries (especially atomic spectrometry), solid sample introduction for atomic spectrometries, atomic fluorescence spectrometry, and spectroelectrochemistry.

New computer applications, shorter chapters and flexibility in derivation of equations make this text better than ever. New co-author brings greater student accessibility to this highly successful introductory analysis text.

# KNOWN QUANTITY

**ANALYTICAL CHEMISTRY: AN INTRODUCTION**  
Fifth Edition.  
Douglas A. Skoog, Stanford University;  
Donald M. West, San Jose State University;  
F. James Holler, University of Kentucky.

SAUNDERS COLLEGE PUBLISHING  
Catalysts for the Mind  
The Curtis Center, Independence Square West, Philadelphia, PA 19106

CIRCLE 128 ON READER SERVICE CARD

# RENT

Analytical Instruments  
lease or rent-to-own

- ✓ Free Instrument delivery & setup in selected areas.
- ✓ GC•MSD•FTIR•AA•ICP•LC•IR
- ✓ Choose from many major manufacturers
- ✓ Hewlett-Packard GC•MSD Systems in stock
- ✓ New Catalog of Chromatography Supplies.

—1-800-7-ON-SITE

**On-Site Instruments®**  
**ENVIRONMENTAL®**  
689 North James Road Columbus, Ohio 43219-1837  
(614) 237-3022  
USA—CANADA

CIRCLE 104 ON READER SERVICE CARD

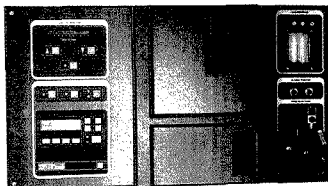


BAIRD  
ICP 2000

For high-performance, simultaneous plasma analysis, the 60-channel BAIRD ICP 2000 sets a new, sophisticated standard — not only in detection sensitivity, but in higher sample throughput and reliability of results. It's a spectrometer designed to be at the operator's complete command for comprehensive control of every analytical procedure. Obviously, it's a system with many innovations. For example:

### Solid-state generator

Plasma ignition is consistent, thanks to automated, reproducible microprocessor control. No torch meltdowns, blown-out circuits, or arc-overs, and never an anomalous, badly formed plasma. Since digital power control keeps operating conditions constant, calibration curves and interelement corrections stay applicable day to day. And there are no power tubes to replace.



### Integrated plasma controls

All in one place! Digital, so highly reproducible. Easy to use and logically organized — including RF, gas flows, and sample uptake. All necessary components (the peristaltic pump, for example) are included as standard. Gas flows are feedback-controlled for stability.

### Stand-down operation

Stand-up spectrometers suddenly seem old-fashioned. On the low-profile ICP 2000, the operators attend to analysis just as they attend to the work on their desks — while relaxed in the comfort of an armchair.

### ... plus Baird-quality optics for precision performance

The ICP 2000, a vacuum, one-meter polychromator, is built in the best tradition of Baird's famous, thermally stable optical system design — with rigid alignment and outstanding sensitivity. All that you've learned to expect from a company that's been the leader in atomic emission spectroscopy since 1936.

For more information on the new BAIRD ICP 2000, as well as its many software and accessory options, call or write Baird Analytical Instruments Division, 125 Middlesex Turnpike, Bedford, Massachusetts 01730. (617) 276-6163.

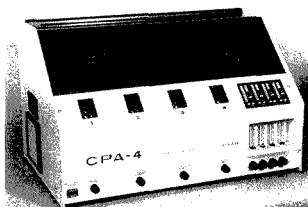
Imco Industries Inc.



# BAIRD ICP

CIRCLE 12 ON READER SERVICE CARD

# NEW PRODUCTS



**CPA-4 ashing system**, which can digest four samples simultaneously, includes vacuum pump and controls, sputtering power supply, metering and valves, and a stirrer to better expose surfaces to the sputtering plasma. Questron 401

**Spectrometer.** JY 50 E Spark SpectroAnalyzer, designed for solid metal analysis, allows simultaneous determination of more than 40 elements in < 1 min. The system features two independent, self-cleaning electrodes for sample conditioning and analysis. JY Division, Instruments SA 404

**Water.** RGW-5 reagent-grade water system provides 18-megohm, bacteria-free water at a rate of 2 L/min. The system features an ultrafiltration accessory for producing pyrogen-free water and an autoclavable 0.2- $\mu$ m final filtration cartridge. Vanguard International 405

**Detector.** Soma Model S-3400 chemiluminescence detector for HPLC, which features a cassette-type flow cell, displays luminescent energy intensity and photomultiplier voltage. The detector can accommodate both fast and slow reaction rates. JM Science 406

**Calorimeter.** Model 8244 heat conduction calorimeter features four differential sample cells; a temperature range of 10–70 °C; baseline noise of  $\pm 50 \mu$ W; and an optional data acquisition, graphics, and analysis software package. Hart Scientific 407

**Carbon dioxide.** Model 244 IR CO<sub>2</sub> analyzer features a measurement range of 0–3000 ppm. The sample gas is continuously drawn into the unit through a built-in vacuum pump. A self-draining water trap and dust filter are also provided. CEA Instruments 411

**Amplifier.** Model FG424 module adds computer control of the fine gain to spectroscopy amplifiers that have only manual gain control. Normally positioned between the amplifier and a multichannel analyzer, the postamplifier also provides computer control of dc offset. EG&G Ortec 408

**Rheometer.** Low shear 40 rheometer system features testing methods that include oscillation as a function of amplitude with constant frequency; single and series oscillatory measurements; shear jump, relaxation, and tension tests; and flow curves, equilibrium viscosity, and viscosity as a function of time and temperature. Contraves 409

**Electrophoresis.** Investigator 2D electrophoresis system is a high-resolution protein separation system that permits the use of large-format gels. A chiller maintains the slab gels at a constant temperature of 20 °C during two-dimensional electrophoresis. Millipore 410

**Spectrometer.** QuantoPort portable optical emission spectrometer operates in three modes for sorting, grading, and composition verification of bars, tubes, sheets, castings, ingots, and semifinished and finished metals. Up to 100 user-defined specification and identification programs can be stored. Applied Research Laboratories, Fisons Instruments 412

**Luminometer.** RML-10 rapid mixing luminometer allows the observation of reactions with half-lives as low as 15 ms. Features include anaerobic capability, variable ratio mixing, adjustable collection volume, and pneumatic drive. Hi-Tech Scientific 413

## Software

**Colorimetric analysis.** Color, designed for use with Spectra Calc or Lab Calc software, performs a variety of colorimetric analyses on data collected from commercial visible spectrophotometers. Calculations can be performed over standard or user-specified wavelength ranges. Galactic Industries 416

**Graphing.** SigmaPlot 4.0 is a scientific graphing software package that runs on IBM and compatible personal computers. Features include a pull-down menu interface, full nonlinear curve fitting, equation plotting, transform language, and specialized graph types. Jandel Scientific 415

## Manufacturers' Literature

**Solvents.** Brochure describes solvents for HPLC; trace analyte extraction; DNA synthesis; industrial hygiene monitoring; and analysis of hydrocarbons, oils and greases, and volatile organics. 12 pp. J.T. Baker 418

**FT-IR.** Application notes discuss contamination analysis by FT-IR microscopy and application of FT-IR spectroscopy to multicomponent analysis of carbohydrates in aqueous solution. Spectra-Tech 419

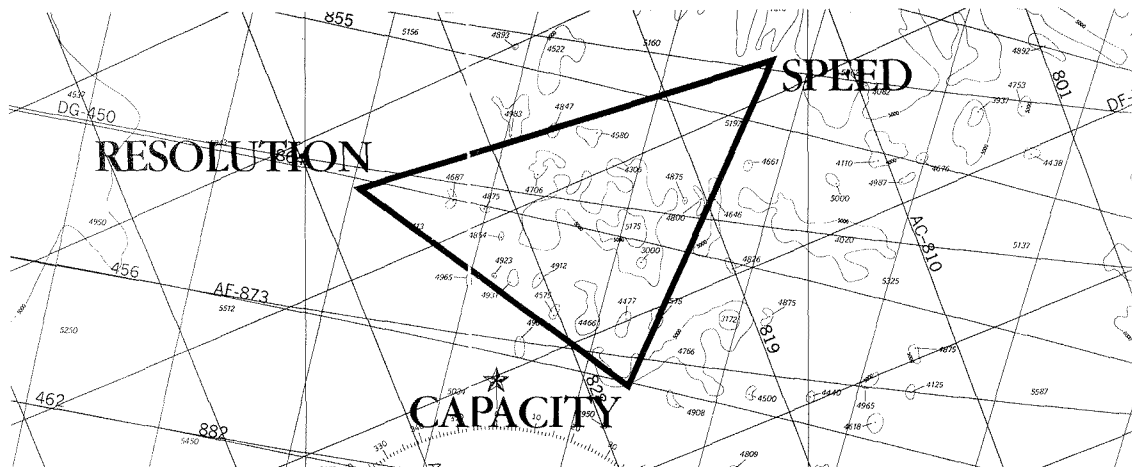
**Detector.** Brochure highlights the pulsed electrochemical detector, which features both conductometric and amperometric capabilities. A comparison with other detection methods is provided. Dionex 420

**LC.** *Mac-Mod Forum* includes information on poor column performance resulting from excess column volume and selection of stationary phases for reversed-phase HPLC. Mac-Mod Analytical 421

**Chromatography.** Brochure describes data systems and workstations for chromatography, including software for GC, IC, GPC, and HPLC applications. 19 pp. Waters Chromatography Division of Millipore 422

**Spectrophotometry.** Brochure highlights PC data management systems for DU series spectrophotometers. Data acquisition and manipulation capabilities are discussed. Beckman Instruments 423

For more information on listed items, circle the appropriate numbers on one of our Readers' Service Cards



# To biochromatographers, it's the Bermuda Triangle.

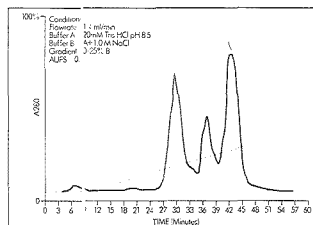
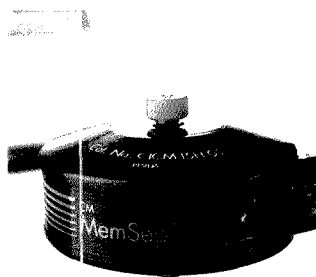
For anyone using traditional LC, it's an inescapable trap—increase your flow rate or capacity and your resolution will suffer.

But now there's a way to achieve high flow rates without sacrificing high resolution—with MemSep® Chromatography Cartridges.

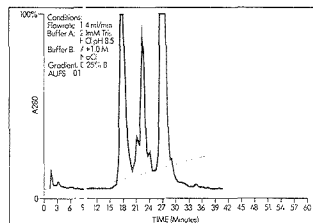
**Higher resolution without flow limitations.** Instead of gels, MemSep cartridges utilize a membrane matrix as the solid phase support.

By taking advantage of the better throughput and flow characteristics of membranes, MemSep cartridges provide resolution independent of flow. So anything you can do with gels you can do with MemSep cartridges. Only with MemSep cartridges, your sample comes off faster.

The MemSep membrane system provides better reproducibility and eliminates bed shift and collapse, channeling and fines.



Typical separation of Human Transferrin, Ovalbumin, and B-Lactoglobulin-A on Pharmacia DEAE Fast Flow.



MemSep iDEAE 1000 under same separation conditions as above.

**Compatible with your current protocols.** Equilibrating, loading, flushing and eluting are handled the same as with traditional columns, only faster.

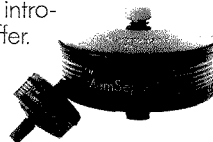
Purify and separate sugars, amino acids, peptides, proteins, enzymes, antibodies, DNA and RNA without establishing new procedures.

**Easy to scale up.** With MemSep cartridges you can keep the same conditions and the same time simply by going to a larger size.

Choose from four sizes in three makeups: ion exchange, Protein A and activated functional chemistries. All are reusable.

**Call for our special offer.**

Before your resolution vanishes into thin air, call 800-225-1380 (in MA: 617-275-9200) for details about our introductory offer.



## NEW PRODUCTS

### Catalogs

**Vacuum.** Catalog features vacuum components and systems, including mechanical rotary pumps, thin-film deposition systems and components, leak detection systems, and industrial and laboratory freeze dryers. 250 pp. Edwards High Vacuum International 425

**Instrumentation.** Catalog describes electrostatic energy analyzers, time-of-flight mass spectrometers, optical heat pipes, electron guns, boxcar integrators, and power supplies. Comstock 428

**Air analysis.** Catalog lists products for air sampling and analysis, including sorbent sample tubes, sample bags, calibrators, filters, impingers, and gas-monitoring badges. A guide to NIOSH, OSHA, and EPA air-sampling standards is provided. 84 pp. SKC 430

**Scientific equipment.** Catalog includes balances; centrifuges; chemicals; desiccators; furnaces; glassware; pH electrodes and meters; plasticware;

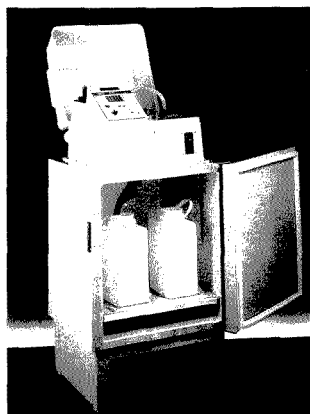
pumps; thermometers; and products for chromatography, spectroscopy, and water analysis. 196 pp. Markon Science 431

**Hoods.** Catalog describes conventional, air bypass, auxiliary air, perchloric acid, tissue culture, and demonstration fume hoods. A variety of laboratory equipment is also listed. 48 pp. Hemco 432

**Scientific equipment.** Catalog includes portable analysis systems and process and laboratory instrumentation. Spectrophotometers, colorimeters, turbidimeters, pH electrodes, and test kits are listed. 256 pp. Hach 426

**Chromatography.** Catalog features chromatography products and chemical standards for applications in industrial hygiene; environmental analysis; life sciences; and the petroleum, chemical, and food and beverage industries. 346 pp. Supelco 427

**Laboratory products.** Catalog contains reagents, solvents, instruments, and supplies for analytical, environ-



**Model 3760 Stinger refrigerated flow-through sampler** features a peristaltic pump that draws samples through a self-cleaning stainless steel or Teflon probe mounted directly in the flow stream. Isco 402

mental, and life sciences laboratories. A variety of reference tables are included. EM Science 429

### METERING VALVES for accurate, repeatable flow adjustment

Precise control of liquids and gases

Compact, low dead space designs

Ensured valve stability

Vacuum to 5000 PSI; temperatures to 400°F

Sizes 1/16" to 3/8" — orifices .020" to .125"

Brass, 316 stainless steel, or alloy 400

Choice of end connections — gageable SWAGELOK® Tube Fittings, CAJON® VCR® metal gasket face seal fittings, NPT 100% factory tested

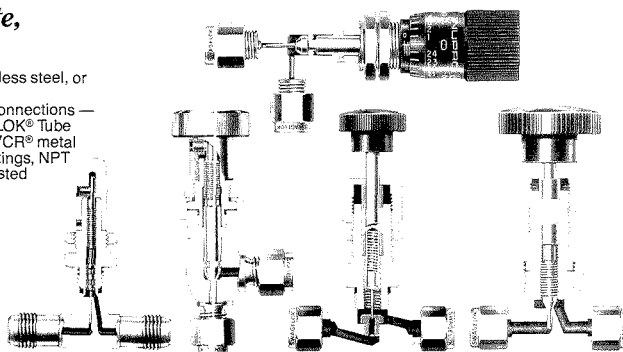


Immediately available from your local Authorized Sales & Service Representative.

CIRCLE 125

the **SWAGELOK** companies

SWAGELOK Co.  
Solon, Ohio 44139  
SWAGELOK Canada Ltd., Ontario  
© 1989 Swagelok Co. All rights reserved PG-3-012



### INLINE FILTERS for removal of system contaminants as small as 0.5 micron

Maintain system purity

Protect instruments and other components from particulate contamination

Sintered and strainer elements from 0.5 to 440 micron — replaceable or cleanable

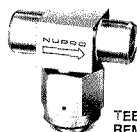
All-metal construction — brass or 316 stainless steel  
Corrosion-resistant

Compact designs — sizes 1/8" to 1/2"

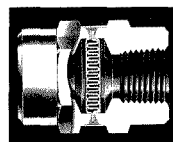
Pressures to 6000 PSI; temperatures to 900°F

Choice of end connections — gageable SWAGELOK® Tube Fittings, CAJON® VCR® metal gasket face seal fittings, NPT, weld

Immediately available from your local Authorized Sales & Service Representative.



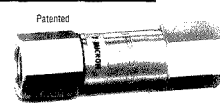
TEE TYPE REMOVEABLE



HIGH FLOW, ALL WELDED



COMPACT INLINE



A SWAGELOK COMPANY

NUPRO Company  
4800 East 345th St.  
Willoughby, OH 44094

SWAGELOK—TM Crawford Fitting Company  
CAJON—TM Cujan Company  
© 1989 Swagelok Co. All rights reserved PG-3-057

CIRCLE 126 ON READER SERVICE CARD

## INDEX TO ADVERTISERS IN THIS ISSUE

CIRCLE INQUIRY NO.	ADVERTISERS	PAGE NO.	CIRCLE INQUIRY NO.	ADVERTISERS	PAGE NO.
7.....	*A&D Engineering, Inc.....	445A	130, 131.....	*Spectra-Physics .....	416A
.....	Abbott Laboratories .....	437A	125.....	*Swagelok Company .....	462A
	Bentley, Barnes & Lynn, Inc.			Falls Advertising Company	
1.....	Autoclave Engineers Group .....	435A	135.....	*Tekmar Company .....	412A
	Altman-Hall Associates			Kenyon Hoag Associates	
12.....	Balrd Corporation .....	459A	142.....	*Valco Instruments Company, Inc.....	447A
	W.J. Hearn & Company, Inc.			Technical Advertising Associates	
16, 17.....	*Beckman Instruments, Inc.....	409A	140.....	*Varian .....	420A
	Esprit Communications			Lanig Associates	
14.....	*Bio-Rad Chemical Division .....	433A	145.....	Whalman .....	438A
	Pan & Associates			GrossTownsendFrankHoffman Inc.	
22.....	Corporation Scientifique Claisse, Inc. ....	418A			
30.....	*Dialog Information Services, Inc. ....	404A			
	HL&S Partners, Inc.				
45.....	Fisons Instruments .....	422A-423A			
	Kempsters, the Advertising Agency				
48.....	Gelman Sciences .....	411A			
52-56.....	*Gilson Medical Electronics, Inc. ....	406A-407A			
160-173.....	*Gilson Medical Electronics SA .....	406A-407A			
50.....	*Gow-Mac Instrument Company .....	414A			
	Scientific Marketing Services, Inc.				
60.....	Hamamatsu Corporation .....	428A			
	Ketchum/Mandabach & Simms				
62.....	*Hamilton Company .....	403A			
	Tallant, LaPointe & Partners, Inc.				
63.....	*Instruments SA, Inc./J-Y Division .....	419A			
	Kathy Wyatt & Associates				
65.....	*Isco, Inc. ....	448A			
	Farneaux Associates				
70.....	J&W Scientific .....	424A			
78.....	Labconco Corporation .....	441A			
	Prospect Avenue Associates				
80.....	*Leco Corporation .....	OBC			
92.....	*Metrohm, Ltd. ....	431A			
	Ecknauer + Schoch Werbeagentur ASW				
90.....	*Mettler Instrument Corporation .....	415A			
	Gilbert, Whitney & Johns, Inc.				
88.....	*Millipore Corporation .....	461A			
	Mintz & Hoke				
94.....	*National Institute of Standards & Technology	437A			
98.....	*National Instruments .....	457A			
96.....	Le Naturaliste .....	443A			
126.....	*Nupro Company/A Swagelok Company .....	462A			
	Falls Advertising Company				
106.....	O.I. Analytical .....	429A			
101, 102.....	*Omega Engineering, Inc.....	IFC			
	Media Business House				
104.....	*On-Site Instruments .....	458A			
114.....	*Parr Instrument Company .....	456A			
	FBA Marketing Communications				
120.....	Rheodyne, Inc. ....	427A			
	Bonfield Associates				
.....	Saudi Aramco .....	454A			
	Bernard Hodes Advertising				
128.....	Saunders College Publishing .....	458A			
	Dietrich Company, Inc.				
133.....	Siemens Analytical X-Ray Instruments, Inc. .	413A			

\* See ad in ACS Laboratory Guide.  
 \*\* Company so marked has advertisement in Foreign Regional edition only.  
 Advertising Management for the American Chemical Society Publications

### CENTCOM, LTD

*President*

**James A. Byrne**

*Executive Vice President*

**Benjamin W. Jones**

*Clay S. Holden, Vice President*

*Robert L. Voepel, Vice President*

**Joseph P. Stenza, Production Director**

500 Post Road East  
 P.O. Box 231  
 Westport, Connecticut 06880  
 (Area Code 203) 226-7131  
 Telex No.643310  
 FAX: 203-454-9939

### ADVERTISING SALES MANAGER

**Bruce E. Poorman**

### ADVERTISING PRODUCTION MANAGER

**Jane F. Gatenby**

### SALES REPRESENTATIVES

Philadelphia, PA ... CENTCOM, LTD., GSB Building, Suite 405, 1 Belmont Avenue, Bala Cynwyd, Pa. 19004. Telephone: 215-667-9666, FAX: 215-667-9353.

New York, NY ... John F. Rafferty, CENTCOM, LTD., 60 East 42nd St., New York, N.Y. 10165. Telephone: 212-972-9660

Westport, CT ... Edward M. Black, CENTCOM, LTD., 500 Post Road East, P.O. Box 231, Westport, Ct. 06880. Telephone: 203-226-7131, Telex 643310, FAX: 203-454-9939

Cleveland, OH ... Bruce E. Poorman, John C. Guyot, CENTCOM, LTD., 325 Front St., Suite 2, Berea, Ohio 44017. Telephone: 216-234-1333, FAX: 216-234-3425

Chicago, IL ... Michael J. Pak, CENTCOM, LTD., 540 Frontage Rd., Northfield, Ill. 60093. Telephone: 708-441-6383, FAX: 708-441-6382

Houston, TX ... Michael J. Pak, CENTCOM, LTD. Telephone: 708-441-6383

San Francisco, CA ... Paul M. Butts, CENTCOM, LTD., Suite 1070, 2672 Bayshore Frontage Road, Mountain View, CA 94043. Telephone: 415-969-4604

Los Angeles, CA ... Clay S. Holden, CENTCOM, LTD., Newton Pacific Center, 3142 Pacific Coast Highway, Suite 200, Torrance, CA 90505. Telephone: 213-325-1903

Boston, MA ... Edward M. Black, CENTCOM, LTD. Telephone: 203-226-7131

Atlanta, GA ... John C. Guyot, CENTCOM, LTD. Telephone: 212-972-9660

Denver, CO ... Paul M. Butts, CENTCOM, LTD. Telephone: 415-969-4604

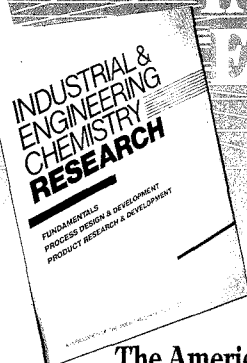
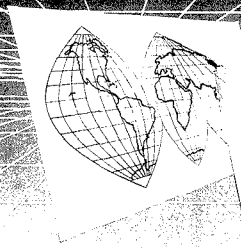
United Kingdom

Reading, England ... Malcolm Thiele, Technomedia Ltd., Wood Cottage, Shurlock Row, Reading RG10 0QE, Berkshire, England. Telephone: 073-434-3302, Telex #848800, FAX: 073-434-3848

Lancashire, England ... Technomedia Ltd., c/o Meconomics Ltd., Meconomics House, 31 Old Street, Ashton Under Lyne, Lancashire, England. Telephone: 061-308-3025

Continental Europe ... Andre Jamar, International Communications, Inc., Rue Mallar 1, 4800 Verviers, Belgium. Telephone: (087) 22-53-85, FAX: (087) 23-03-29

Tokyo, Japan ... Sumio Oka, International Media Representatives Ltd., 2-29 Toranomon, 1-Chome Minato-ku Tokyo 105 Japan. Telephone: 502-0656, Telex #22633, FAX: 591-2530



# INDUSTRIAL & ENGINEERING CHEMISTRY RESEARCH

The American Chemical Society offers you *the* interdisciplinary research journal in the broad field of chemical engineering and industrial chemistry.

INDUSTRIAL & ENGINEERING CHEMISTRY RESEARCH publishes original, state-of-the-art research findings from around the world.

## Quality Information That Gives You The Leading Edge

Each monthly issue of I&EC RESEARCH gives you access to new ideas . . . new techniques . . . new procedures—research that could prove crucial to you and your work.

In this one professional journal you will find reports on—

- fundamental and theoretical aspects of chemical engineering
- recent work on design methods and their applications
- current and future products involving chemical engineering processes
- process design and development
- new technologies
- special updates on timely symposia
- specially selected topics

I&EC RESEARCH helps you meet today's intense challenges in chemical technology with the most timely, innovative research. The editorial team and editorial advisory board are members of your profession—and reflect the broad spectrum of areas covered by the journal.

Start your subscription TODAY. Don't miss a single issue of I&EC RESEARCH!

I&EC RESEARCH covers all the areas previously addressed by the three I&EC quarterlies: *Fundamentals*, *Process Design & Development*, and *Product Research & Development*.

**Editor**  
Donald R. Paul  
Univ. of Texas, Austin

**Senior Editor**  
J.A. Seiner  
PPG Industries

**Editorial Advisory Board:**  
D.R. Bauer  
Ford Motor Co.

K.F. Jensen  
Univ. of Minnesota

C.J. King  
Univ. of California, Berkeley

H. Leidheiser, Jr.  
Lehigh Univ.

O. Levenspiel  
Oregon State Univ.

N.N. Li  
Allied-Signal Inc.

M. Morari  
California Institute of Tech.

J.P. O'Connell  
Univ. of Florida

J.F. Roth  
Air Products and Chemicals, Inc.

D.M. Ruthven  
Univ. of New Brunswick,  
Canada

J.J. Sirola  
Eastman Kodak Co.

C.M. Starks  
Cimarron Technical Assoc.

V.W. Weekman, Jr.  
Mobil R&D Corp.

Volume 29 (1990) ISSN 0888-5885 CODEN:IECRD	U.S.	Canada & Mexico	Europe Air Service Included	All Other Countries Air Service Incl.
ACS Members				
One Year	\$ 55	\$ 73	\$ 84	\$ 94
Two Years	\$ 99	\$135	\$157	\$177
Nonmembers	\$372	\$390	\$401	\$411

Member rates are for personal use only. Subscriptions are based on a calendar year. Foreign payment must be made in U.S. currency by international money order, UNESCO coupons, or U.S. bank draft, or order through your subscription agency. For non-member rates in Japan, contact Maruzen Co., Ltd. This publication is available in microfilm, microfiche, and the full text is available online on STN International.

In a hurry?  
CALL TOLL-FREE in the U.S. at **800-227-5558**, D.C. and outside the U.S. call 202-872-4363 for credit card orders, or write: **American Chemical Society**, Marketing Communications Department, 1155 16th Street, NW, Washington, D.C. 20036

EDITOR: **GEORGE H. MORRISON**ASSOCIATE EDITORS: **Catherine C. Fenselau, Georges Guiochon, Walter C. Herlihy, Robert A. Ostryoung, Edward S. Yeung****Editorial Headquarters**1155 Sixteenth St., N.W.  
Washington, DC 20036  
Phone: 202-872-4570  
Telefax: 202-872-4574Managing Editor: **Sharon G. Boots**Assistant Managing Editor: **Mary Warner**Associate Editor: **Louise Voreess**Assistant Editors: **Grace K. Lee, Alan R. Newman**Editorial Assistant: **Felicia Wach**Contributing Editor: **Marcia Vogel**Director, Operational Support: **C. Michael Phillippe**Head, Production Department: **Leroy L. Corcoran**Art Director: **Alan Kahan**Designers: **Amy Meyer Phifer, Robert Sargent**Production Editor: **Elizabeth E. Wood**Circulation: **Claud Robinson**Editorial Assistant, LabGuide: **Joanne Mullican****Journals Dept., Columbus, Ohio**Associate Head: **Marianne Brogan**Journals Editing Manager: **Joseph E. Yurvati**Senior Associate Editor: **Rodney L. Temos****Advisory Board:** **Bernard J. Bulkin, Michael S. Epstein, Renaat Gijbels, William S. Hancock, Thomas L. Isenhour, James W. Jorgenson, Peter C. Jurs, Alan G. Marshall, Lawrence A. Pachla, John F. Rabolt, Debra R. Rolison, Ralph E. Sturgeon, Shigeru Terabe, George S. Wilson, Mary J. Wirth, Richard N. Zare**  
Ex Officio: **Sam P. Perone****Instrumentation Advisory Panel:** **Daniel W. Armstrong, Bruce Chase, Thomas L. Chester, R. Graham Cooks, L. J. Cline Love, Sanford P. Markey, Brenda R. Shaw, Gary W. Small, R. Mark Wightman**Published by the  
**AMERICAN CHEMICAL SOCIETY**  
1155 16th Street, N.W.  
Washington, DC 20036**Publications Division**Director: **Robert H. Marks**Journals: **Charles R. Bertsch**Special Publications: **Randall E. Wedin**

Manuscript requirements are published in the January 1, 1990 issue, page 89. Manuscripts for publication (4 copies) should be submitted to ANALYTICAL CHEMISTRY at the ACS Washington address.

The American Chemical Society and its editors assume no responsibility for the statements and opinions advanced by contributors. Views expressed in the editorials are those of the editors and do not necessarily represent the official position of the American Chemical Society.

- Abruña, H. D., 782  
Angebrannt, M. J., 689  
Asouzu, M. U., 708
- Baker, B., 770  
Baldwin, R. P., 752
- Chen, T.-C., 774  
Cody, R. B., 698
- Davidson, E. R., 658  
Davis, J. A., 742  
Davis, J. M., 784  
Dewald, H. D., 779  
Doyle, M. J., 766
- Edmonds, C. G., 693
- Forcé, R. K., 678
- Grushka, E., 717  
Gunasingham, H., 755
- Harrington, P. de B., 729  
Ho, M. H., 708  
Honda, C., 680  
Hung, C.-C., 774
- Isaksson, T., 664  
Israeli, D., 717  
Izumi, J., 680
- Jorgensen, A. D., 683  
Joyce, R. J., 766
- Koch, L., 777  
Kowalski, B., 664  
Kuroda, Y., 712
- Laserna, J. J., 689  
Lipkowitz, K. B., 770  
Liu, Y., 766  
Loh, S. Y., 698  
Longmire, M. L., 747  
Loo, J. A., 693  
Luo, P., 752
- Maeda, M., 680  
Masman, D., 703  
McFadden, C. F., 742  
McLafferty, F. W., 698  
Melaragno, P. R., 742  
Mook, W. G., 703  
Morf, W. E., 738  
Morimoto, T., 680  
Murray, R. W., 747
- Naes, T., 664  
Nagao, M., 712  
Nagy, K. A., 703  
Nakagawa, T., 712  
Nakata, O., 674  
Namba, R., 674  
Neal, S. L., 658  
Nonidez, W. K., 708
- Okada, T., 734  
Oki, Y., 680
- Pai, S.-C., 774  
Pendley, B. D., 782  
Peterson, B. A., 779  
Picel, K. C., 683  
Poppitt, S. D., 703  
Pothier, N. J., 678  
Prabhu, S. V., 752
- Racey, P. A., 703  
Rocklin, R. D., 766  
Ruhe, A., 759  
Rusterholz, B., 738
- Sawada, T., 674  
Seiler, K., 738  
Seow, J. K. L., 755  
Shibukawa, A., 712  
Simon, W., 738  
Smith, R. D., 693  
Speakman, J. R., 703  
Stamoudis, V. C., 683  
Steiger, B., 759  
Strathearn, G. E., 703  
Sutherland, W. S., 689  
Swart, P. K., 722
- Takamoto, R., 674  
Tan, C.-H., 755  
Tanoura, M., 680
- Uda, H., 680  
Udseth, H. R., 693
- Voorhees, K. J., 729
- Walder, L., 759  
Warner, I. M., 658  
Watanabe, M., 747  
Williams, E. R., 698  
Winefordner, J. D., 689  
Wong, G. T. F., 774  
Wooster, T. T., 747
- Zhang, H., 747

# Resolution of Severely Overlapped Spectra from Matrix-Formatted Spectral Data Using Constrained Nonlinear Optimization

Sharon L. Neal,<sup>1</sup> Ernest R. Davidson,<sup>2</sup> and Isiah M. Warner\*<sup>3</sup>

Department of Chemistry, Emory University, Atlanta, Georgia 30322, and Department of Chemistry, Indiana University, Bloomington, Indiana 47405

A three-step scheme for resolving severely overlapped component spectra from bilinear matrix-formatted data is reported. After the number of sample components is determined, a positive basis is first formed consisting of the most dissimilar rows and columns of the matrix. The concentration factor matrix (CFM) corresponding to this nonnegative, minimally correlated basis will be diagonal if the basis vectors happen to be feasible estimates of the component spectra. When the CFM is not diagonal, a constrained nonlinear optimization routine is used in a second step to reduce the off-diagonal elements of the CFM to zero while maintaining the nonnegativity of the estimated spectra. In many cases, the nonnegativity and feasibility constraints are not sufficient to produce a unique set of component spectra estimates. Other criteria, such as the degree of overlap of the resolved spectra, may be used as the basis of a third step to generate an arbitrary, but unique, choice among the feasible estimates of the component spectra. The performance of this scheme is evaluated by analyzing synthetic and experimental fluorescence excitation-emission matrices (EEMs) exhibiting various levels of spectra overlap and random noise. Coincident spectra can be resolved from an EEM by using this approach in the case of some EEMs of rank greater than two. Evaluations using synthetic data indicate that this scheme can be applied to EEMs that have signal-to-noise ratios above 18. Successful resolution of experimental three- and four-component mixtures is illustrated.

## INTRODUCTION

The resolution of unknown component spectra from the two-dimensional spectra of mixtures is one of the most challenging mathematical problems in chemical analysis. The application of factor analysis (FA) (1, 2) to this problem has received quite a bit of attention in the recent literature due, no doubt, to the rather spectacular ability of these methods to extract predominant spectral features from raw data without a priori knowledge or assumptions specific to the component spectra. Having recognized that the singular vectors of the matrix, also known as principal components or abstract factors, are linear combinations of the component spectra, analysts have searched extensively for techniques to extract the component spectra from this orthonormal basis. The first FA curve resolution methods (3, 4) used nonnegativity and normalization constraints to resolve spectra from the orthogonal basis. Later efforts focused on finding reasonable estimates of the component spectra among the spectra forming the data matrix (5, 6) or on adjusting the estimated

spectra iteratively (7-9) to meet nonnegativity or dissimilarity criteria.

The performance of these methods varies widely, but all such methods have limited utility in the case of severe spectral overlap. In this report, we describe improved resolution of overlapped spectra, by using algebraic and spectroscopic properties of the data matrix to estimate the profiles of the component spectra. We illustrate the use of this method with second-order fluorescence data, but the approach is general for any bilinear (10), nonnegative matrix of digitized spectral data.

## THEORY

Analysis of a dilute solution of  $n$  fluorophores by video-fluorometry (11) produces a  $p \times q$  data matrix,  $\mathbf{E}$ . Each element,  $e_{ij}$ , represents the fluorescence intensity of the sample at wavelength  $\lambda_j$ , generated by excitation at wavelength  $\lambda_i$ . This matrix has been called the excitation-emission matrix (EEM) (12). The emission spectrum of a single fluorophore is independent of the excitation wavelength, so that  $\mathbf{E}$  has the form  $\gamma\mathbf{x}\mathbf{y}^T$  where  $\mathbf{x}$  is a normalized column vector of the digitized excitation spectrum,  $\mathbf{y}$  is a normalized column vector of the digitized emission spectrum, and the constant  $\gamma$  is a concentration-related intensity factor. For dilute multicomponent solutions, the matrix  $\mathbf{E}$  is simply the sum of the  $\mathbf{E}$  matrices of the individual components. In other words, the excitation and emission spectra of the sample components are basis vectors for the column and row spaces, respectively, of the EEM. Mathematically, the multicomponent EEM is represented by the expression

$$\mathbf{E} = \mathbf{X}\mathbf{Y}^T \quad (1)$$

where the columns of the  $p \times n$  matrix  $\mathbf{X}$  and the  $q \times n$  matrix  $\mathbf{Y}$  are the normalized excitation and emission spectra, respectively. The elements of the diagonal  $n \times n$  matrix  $\mathbf{\Gamma}$  are concentration-dependent scalars. A matrix of this form, which is the sum of the outer products of the component responses, has been called a bilinear matrix (10).

Unfortunately, the number and form of the component spectra are not generally apparent in experimental EEMs. Therefore, the component spectra must be estimated by using linear combinations of some more easily determined basis, e.g.

$$\mathbf{X} = \mathbf{A}\mathbf{I} \quad (2)$$

$$\mathbf{Y} = \mathbf{B}\mathbf{\Theta} \quad (3)$$

where the columns of  $\mathbf{A}$  and  $\mathbf{B}^T$  are basis vectors for the column and row spaces of  $\mathbf{E}$  and the columns of  $\mathbf{I}$  and  $\mathbf{\Theta}$  are the coordinates of the component spectra with respect to those basis vectors. Without constraints, any attempt to factor  $\mathbf{E}$  into the form of eq 1 usually yields an infinite number of solutions.

In this report, a scheme for choosing  $\mathbf{A}$  and  $\mathbf{B}$  and approximating the values of  $\mathbf{I}$  and  $\mathbf{\Theta}$  is described. This approach

<sup>1</sup> Present address: Department of Chemistry, Spelman College, Atlanta, GA 30314.

<sup>2</sup> Indiana University.

<sup>3</sup> Emory University.



imposes several fundamental properties of fluorescence spectra on the estimated spectra. The conditions under which this scheme is successful in extracting the true spectra are also discussed.

**Choosing a Nonnegative Basis.** The orthonormal basis vectors of the column and row spaces of the EEM provided by the singular value decomposition (SVD) (13) form an accessible basis that is frequently used in spectra estimation (3-9). In addition to the relative ease of computing this basis (14), the structure of the decomposition provides a mechanism for estimating the number of fluorescent components in the sample. In the orthonormal basis, the ideal EEM is given by the expression

$$\mathbf{E} = \mathbf{R}\Psi\mathbf{C}^T \quad (4)$$

where the  $n$  columns of  $\mathbf{R}$  and  $\mathbf{C}$  are the excitation and emission (column and row) singular vectors, respectively. The diagonal elements of  $\Psi$  are the singular values which reflect the fraction of the matrix variance associated with the corresponding pair of column and row basis vectors. Noise increases the rank of experimental EEMs to the smaller dimension of  $\mathbf{E}$  so that  $m$  ( $m = \min(p, q)$ ) rather than  $n$  basis vectors are required to describe the matrix. Determination of the number of sample components is trivial in samples that are sufficiently concentrated, because there are singular values associated with the spectra signal which are significantly larger than those that merely reflect noise in the data. Alternative indicators, such as the autocorrelation coefficients of the singular vectors (15) or cross-validation (16) can be used for more dilute samples. Once the number of sample components is determined, the  $n$  significant column and row singular vectors may be used to construct a least-squares approximation to the experimental EEM. These  $n$  primary singular vectors also provide a reduced basis in which the matrices  $\mathbf{X}$  and  $\mathbf{Y}$  can be expanded. Therefore, many matrix calculations can be performed more efficiently in the reduced basis, yet yield identical results to calculations utilizing the entire least-squares matrix.

However, the singular vectors are not usually good estimates of the component spectra. They are merely mathematical devices that generally lack significant properties of true fluorescence spectra, most notably nonnegativity. On the other hand, the  $n$  most dissimilar rows and columns of  $\mathbf{E}$  will also form bases for the row and column spaces of  $\mathbf{E}$ , with the additional advantage of being positive. Unfortunately, choosing these  $n$  vectors from the set of all  $p$  rows and  $q$  columns is a complicated combinatorial problem which requires examination of all  $n$ -element combinations of the  $p$  rows and  $q$  columns.

In this paper, a sequential (noncombinatorial) procedure for selecting  $n$  independent columns of  $\mathbf{E}$  is presented. The pair of columns with the smallest scalar product are selected as the first two members of the basis. The columns  $\{\mathbf{a}_1, \mathbf{a}_2\}$ , which meet this criterion are found by comparing the off-diagonal elements of the column correlation matrix,  $\mathbf{Z}$ , which are the scalar products of the normalized columns of  $\mathbf{E}$ , given by  $\mathbf{E} = \mathbf{E}\mathbf{N}$ , where  $\mathbf{N}$  is a diagonal matrix of the inverse square roots of the norms of the columns of  $\mathbf{E}$ . The column correlation matrix is efficiently computed from the singular vectors by using the expression

$$\mathbf{Z} = \bar{\mathbf{E}}^T \bar{\mathbf{E}} = \bar{\mathbf{Q}}^T \bar{\mathbf{Q}} \quad (5)$$

where  $\bar{\mathbf{Q}}$  is  $\Psi\mathbf{C}^T\mathbf{N}$ .

Once the first two columns have been chosen, an iterative procedure is used to choose the remaining columns of  $\mathbf{A}$ . The overlap matrix  $\mathbf{S}_t$  (where  $t$  is the number of columns chosen for  $\mathbf{A}$ ) is the product  $\mathbf{A}^T\mathbf{A}$  obtained by using the existing columns of  $\mathbf{A}$ . The matrix  $\mathbf{T}_t$  is the overlap matrix which would result if the  $i$ th column of  $\mathbf{E}$  were chosen as the  $t+1$

column of  $\mathbf{A}$ . The determinant of  $\mathbf{T}_t$  is

$$|\mathbf{T}_t| = |\mathbf{S}_t + \|\mathbf{e}_{\text{res}}\|^2| \quad (6)$$

where

$$\|\mathbf{e}_{\text{res}}\|^2 = \|\mathbf{e}_i - \mathbf{S}_t^{-1}\mathbf{e}_i\|^2 \quad (7)$$

and  $\mathbf{e}_{\text{res}}$  is the residual of expanding the  $i$ th column of  $\mathbf{E}$  in terms of the existing columns of  $\mathbf{A}$ . The column of  $\mathbf{E}$  which produces the largest  $|\mathbf{T}_t|$  had the largest residual when expanded in terms of the existing columns of  $\mathbf{A}$ . Therefore, adding this column to the basis will account for the largest portion of the variance not represented in the set  $\{\mathbf{a}_k; k = 1 \dots t\}$ . This column is added to the columns of  $\mathbf{A}$  and the procedure is repeated until  $n$  columns of  $\mathbf{E}$  have been chosen as basis vectors for the excitation spectra. This procedure, which we are calling best measured basis (BMB), can be applied similarly to the columns of  $\mathbf{E}^T$  to determine the nonnegative basis vectors for the row space of  $\mathbf{E}$ .

**Imposing Bilinearity.** In the columns of  $\mathbf{A}$  and  $\mathbf{B}$ , there are now basis vectors which span the spaces of  $\mathbf{X}$  and  $\mathbf{Y}$  and are nonnegative, as are fluorescence spectra. These properties make these vectors particularly well-suited for use as basis vectors in estimating the component spectra by eq 2 and 3. In fact, they may occasionally themselves, be the component spectra. However, these basis vectors are generated independently, i.e. without regard to the bilinear structure of  $\mathbf{E}$ . Matrices that span the column and row spaces of  $\mathbf{E}$ ,  $\mathbf{V}$ , and  $\mathbf{W}^T$ , for example, are consistent with bilinear structure, if  $\mathbf{E} = \mathbf{W}\Sigma\mathbf{V}^T$  where  $\Sigma$ , called the concentration factor matrix (CFM) in this report, is a positive diagonal matrix. Pairs of matrices that meet this condition are feasible estimates component spectra and will be referred to as compatible spectra.

There is no reason to expect that the columns of  $\mathbf{A}$  and  $\mathbf{B}$  are compatible with each other in this sense, though they span their respective spaces and are positive. Large off-diagonal elements of the CFM associated with the nonnegative basis indicate that the basis vectors are incompatible. The CFM is given by the expression

$$\Delta = (\mathbf{A}^T\mathbf{A})^{-1}\mathbf{A}^T\mathbf{E}\mathbf{B}(\mathbf{B}^T\mathbf{B})^{-1} \quad (8)$$

In some cases, the CFM generated by using eq 8 is not diagonal, even though the columns of  $\mathbf{A}$  and  $\mathbf{B}$  are feasible estimates of the component spectra. In this case, the matrix  $\Delta$  can be made diagonal by permutation of the columns of  $\mathbf{A}$  and  $\mathbf{B}$ . The columns of  $\mathbf{A}$  and  $\mathbf{B}$  are always permuted to place the largest elements of  $\Delta$  onto the diagonal at this point in the resolution scheme. Even when  $\mathbf{A}$  and  $\mathbf{B}$  are not compatible, this procedure orders the basis vectors so that they are more amenable to the rest of the scheme.

In the instance of incompatibility, a constrained nonlinear optimization method can be used to adjust the values of  $\mathbf{I}$  and  $\mathbf{\Theta}$  so that the estimated spectra are compatible as well as nonnegative. One of the disadvantages of constrained optimization is the capacity of these algorithms to collapse on the steep response surface grades formed by the constraints rather than converge on local optima. This problem is exacerbated as the number of constraints and variables increases; therefore, the program NLPQL (17), which is an implementation of the projected Lagrangian methodology (18, 19), was used, rather than the more commonly used simplex algorithm (20). One feature of these methods is that the performance of optimization methods is sensitive to the initial estimates of the variables. This is another reason that the nonnegative basis is more suitable than the singular vectors as basis vectors for the component spectra.

The CFM formed by  $\mathbf{A}$  and  $\mathbf{B}$  is diagonalized subject to the constraints that the estimated spectra remain nonnegative and normalized to unit length. This optimization is stated mathematically as

$$\text{minimize} \quad \sum_{k \neq 1} \hat{\gamma}_{kl}^2 \quad (9)$$

$$\text{where} \quad \hat{\Gamma} = \Pi^{-1} \Delta (\Theta^{-1})^T$$

subject to

$$\begin{aligned} \hat{\gamma}_{kk} &\geq 0, \\ \hat{\mathbf{X}} = \mathbf{A} \hat{\Pi} &\geq 0, \quad \langle \hat{\pi}_k, \hat{\pi}_k \rangle = 1 \\ \hat{\mathbf{Y}} = \mathbf{B} \hat{\Theta} &\geq 0, \quad \langle \hat{\theta}_k, \hat{\theta}_k \rangle = 1 \\ \Pi_{\text{init}} &= \Theta_{\text{init}} = \mathbf{I}_n \end{aligned}$$

For an input matrix  $\mathbf{E}$ , which can be written in the form of eq 1, the minimum of  $\sum_{k \neq 1} \hat{\gamma}_{kl}^2$  will always be zero. The resulting  $\Pi$  and  $\Theta$  will produce compatible sets of factors on the columns of  $\hat{\mathbf{X}}$  and  $\hat{\mathbf{Y}}$  when used in eq 2 and 3. This algorithm, referred to hereafter as the concentration factor matrix diagonalization (CFMD), is a generalization of Lawton and Sylvestre's self-modeling curve resolution (SMCR) (3) to  $n$  components. The constraints on the norms of the transforms were included to maintain the separation of the concentration and spectra information so that unique solutions can be generated. These constraints also reduce the number of degrees of freedom in  $\Pi$  and  $\Theta$  from  $2n^2$  to  $2n(n-1)$ .

Several authors (3, 4, 21, 22) have described the geometric significance of the nonnegativity constraints on the estimated spectra for two-, three-, and four-component systems. Accurate graphical representations of the constraints require elaborate iterative methods even for three-component systems (21). Therefore, a general algorithm for depicting the regions of feasible estimates of the component spectra has not been described. The generalization to  $n$  components is simpler to describe algebraically. The nonnegativity constraints on the excitation spectra are given by the equations

$$\hat{\mathbf{X}} = \mathbf{A} \hat{\Pi} \geq 0 \quad (10)$$

Those on the emission spectra are given by

$$\hat{\mathbf{Y}} = \mathbf{B} \hat{\Theta} \geq 0 \quad (11)$$

From  $\mathbf{E} = \mathbf{X} \Gamma \mathbf{Y}^T = \mathbf{A} \Delta \mathbf{B}^T$

$$\hat{\Theta} = \Delta^T (\hat{\Pi}^{-1})^T \hat{\Gamma}^{-1} \quad (12)$$

so that there are additional constraints on the coordinates of the excitation spectra

$$\hat{\mathbf{Y}} = \mathbf{B} \Delta^T (\hat{\Pi}^{-1})^T \hat{\Gamma}^{-1} \geq 0 \quad (13)$$

These constraints on both  $\hat{\Pi}$  and  $\hat{\Pi}^{-1}$  may lead to complete specification of some elements of  $\hat{\Pi}$  in favorable cases. Similarly, constraints on  $\hat{\Theta}$  and  $\hat{\Theta}^{-1}$  can specify elements of  $\hat{\Theta}$ .

**Choosing Solutions from the Feasible Regions.** The relationship between the compatible solutions generated by CFMD and the true component spectra is a function of the overlap of the component spectra. As the degree of overlap increases, the region between the row and column nonnegativity boundaries is widened. In these cases, there are an infinite number of feasible spectral estimates and simple diagonalization of  $\hat{\Gamma}$  will not generate a unique solution for eqs 2 and 3.

In the usual event that a range of compatible solutions exists, it is useful to have some criterion for choosing one solution from that range. The nonlinear optimization routine provides a flexible mechanism for incorporating a number of spectral features into a unique solution. Algorithms that minimize the dissimilarity (7, 8) or entropy (simplicity) (9) of the estimated spectra have been used for this purpose. By use of the constrained nonlinear optimization routine used in CFMD, these spectra features can be imposed on the resolved spectra by careful choice of the objective function used to generate the solution. Moreover, this approach will always

**Table I. Objective Functions That Impose Common Features on Resolved Spectra**

objective function	features imposed
$\max[\langle \hat{\mathbf{X}}^T \hat{\mathbf{X}} \rangle \times \det(\hat{\mathbf{Y}}^T \hat{\mathbf{Y}})]$	maximizes dissimilarity
$\max[\sum_k \hat{\pi}_{kk}^2 + \hat{\theta}_{kk}^2]$	maximizes similarity to $\mathbf{A}$ and $\mathbf{B}$
$\min[\sum_k (\sum_i \hat{\pi}_{ik}^2 + \sum_j \hat{\theta}_{jk}^2)]$	maximizes simplicity
$\min[\sum_k (\sum_i \hat{\pi}_{ik} \ln \hat{\pi}_{ik} + \sum_j \hat{\theta}_{jk} \ln \hat{\theta}_{jk})]$	maximizes simplicity (entropy minimization)

produce a compatible, nonnegative solution. The general form of the optimization is given by the expressions

$$\text{optimize} \quad f(\hat{\Pi}, \hat{\Theta}), \quad (14)$$

subject to

$$\begin{aligned} \hat{\mathbf{X}} &= \mathbf{A} \hat{\Pi} \geq 0, \\ \hat{\mathbf{Y}} &= \mathbf{B} \hat{\Theta} \geq 0, \\ \hat{\gamma}_{kk} &\geq 0 \\ \hat{\gamma}_{kl} &= 0 \text{ for } k \neq l, \\ \hat{\Pi}_{\text{init}} &= \hat{\Pi}_{\text{CFMD}}; \hat{\Theta}_{\text{init}} = \hat{\Theta}_{\text{CFMD}} \end{aligned}$$

where  $f(\hat{\Pi}, \hat{\Theta})$  is the objective function that imposes the desired spectra features. The entropy (or simply the sum of the spectra elements) measures the degree of dispersion of information across the spectral elements. Minimizing the entropy localizes the spectral bands. The correlation between vector similarity and distance is the basis of the objective function for the most dissimilar solution. The coordinates of the component spectra form  $n$  simplices inside which the coordinates of the rows and columns of the EEM must fall, because the rows and columns of  $\mathbf{E}$  form convex sets. The square of the volume of the simplex formed by the coordinates of the estimated spectra in the row and column spaces of  $\mathbf{E}$  is given by the determinants of the overlap matrices (eq 6) of the estimates. Maximizing those volumes produces the most dissimilar set of feasible component spectra. The objective function, which is maximized as the transforms  $\hat{\Pi}$  and  $\hat{\Theta}$  are diagonalized, implements the principles of target factor analysis methods such as key set analysis (6) or the best measured basis algorithm described above, by seeking the feasible solutions most like the columns of  $\mathbf{A}$  and  $\mathbf{B}$ . The justification for incorporating properties such as dissimilarity into the estimated spectra is primarily intuitive and heuristic, but the flexibility of the objective function approach, permits the analyst to adjust the degree of incorporation of spectral features to the information at his or her disposal. Table I lists four typical objective functions and the features they impose on the spectral estimates.

**Solution Simplex Minimization.** When the analyst has information concerning the data which warrants the choice of a particular unique solution, the use of specialized objective functions can produce a more useful solution than CFMD. For example, if the analyst is confident that the component spectra are not all severely overlapped, the least dissimilar solution, subject to compatibility and nonnegativity constraints, will frequently be more like the component spectra than the most dissimilar. This solution can be generated by aligning the coordinates of the spectral estimates with as many of the row and column coordinates as possible subject to the other constraints.

Several objective functions can be used to align the solution simplex with the row and column coordinates. Theoretically, the entropy function and the sum of the squares of the elements of the estimated spectra generate this solution. Minimizing the volume of the solution simplices is an alternative function which has several attraction features. First, minimizing the volume avoids the tendency of the sums, and to

a lesser extent the entropy, to weight the elements of the spectra unevenly, resulting in an estimated spectra with a larger average bandwidth than the optimal solution. Moreover, the function describing the volume is easier to differentiate than the entropy function, permitting the use of analytic gradients in the optimization routine which decreases the computation time significantly. In order to utilize the resolution information in both vector spaces, the product of the volumes of the excitation and emission solution simplices is used as the objective function in this third step. In this algorithm, which is referred to as solution simplex minimization (SSM), the objective function is given by the expression:  $\det(\hat{X}^T\hat{X}) \times \det(\hat{Y}^T\hat{Y})$ .

### EXPERIMENTAL SECTION

**Reagents.** The compounds 9,10-dimethylanthracene, 2,3-benzanthracene, anthracene, perylene, and fluoranthene (Aldrich Chemical Co., Milwaukee, WI) were acquired at 99%+ purity and used without further purification. Various combinations of these compounds were dissolved in glass-distilled cyclohexane (Burdick and Jackson, Muskegon, MI).

**Apparatus.** A Hewlett-Packard 9845B desktop minicomputer, equipped with a 7908 hard disk (Hewlett-Packard, Palo Alto, CA) was used to control the acquisition of second-order fluorescence spectra by the videofluorometer. The details of the spectrometer specifications and operation are described elsewhere (23). The data were transferred by HP terminal emulation software to a MicroVAX II (Digital Equipment Corp., Maynard, MA) for analysis and storage. The resolution programs are coded in FORTRAN 77.

### RESULTS AND DISCUSSION

The original description of SMCR (3) assumed that resolvable spectra lie on the nonnegativity boundary and have characteristic responses to the experimental parameters. Yet, it is clear from convex set theory (24, 25) that in mixtures of more than two components, characteristic bands place row and column coordinates on the vertices of the simplex formed by the component spectra and they need not lie on the nonnegativity boundary. On the other hand, characteristic base lines produce coordinates that lie on the nonnegativity boundary. It follows, then, that it is not the presence of characteristic bands that ensures the unique resolution of component spectra but the existence of base-line responses to wavelengths to which the remaining components are responsive. For two-component mixtures, these two conditions are identical because a characteristic base line for one component must occur at the wavelength of a characteristic band for the other component.

A synthetic three-component EEM was generated from hypothetical excitation and emission spectra that all exhibited characteristic base lines yet lacked characteristic bands. Figure 1 depicts the coefficients for expanding each row and column of  $E$  in terms of the singular vectors. For this graph, each row and column of  $E$  was normalized so that the sum of their elements was unity. The coefficients of these rows and columns are similarly normalized and consequently also sum to unity. With this convention, the coefficients are coordinates of a simplex that has the pure spectra as the extreme points (vertices) and the columns (and rows) of  $E$  as interior points. Only the coefficients of the rows and columns with respect to the second and third singular vectors are shown in Figure 1, but the first can be determined by using the fact that the coefficients sum to unity. The asterisks are the coordinates of the rows and columns of the matrix, the circles are the coordinates of the component spectra, and the crosses are the coordinates of the rows and columns selected by the CFMD procedure as the columns of  $A$  and  $B$ . Coordinates that coincide with the face of the component simplex indicate that those columns are weighted averages of just two-component emission spectra. This feature reflects the presence

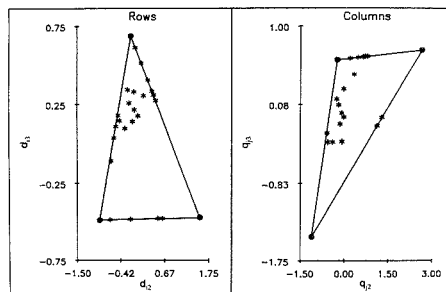


**Figure 1.** Coordinates of the columns and rows of a synthetic ternary EEM that has no characteristic bands. The coordinates of the columns,  $e_{ij}(\cdot)$ , are  $q_{ij}$  where  $e_{ij} = \sum_k d_k c_k q_{ij}$ . The coordinates of the rows,  $e_{ik}(\cdot)$ , are  $d_{ik}$  where  $e_{ik} = \sum_k d_k c_k q_{ik}$ . The CFMD solution lies at the vertices of the solid simplex (—). The coordinates of the component spectra (O) coincide with the CFMD solution.

of a characteristic base line in the excitation spectra of the third component. The simplex formed by the most dissimilar rows and columns would have excluded several of the matrix coordinates because  $A$  and  $B$  do not form a feasible solution. Not only does the simplex of the compatible solution found by CFMD, plotted with solid lines, include all the matrix coordinates but its vertices coincide with the coordinates of the component spectra despite the absence of row and column coordinates at these points. This example confirms the superfluity of characteristic bands; they are not necessary because the positions of the corresponding vertices are implied by coordinates on the opposite face of the component simplex.

Three criteria were used to evaluate the performance of solution simplex minimization (SSM). A series of ideal three-component EEMs that have systematic variations in the component spectra overlap were generated and analyzed. Then, the robustness of the algorithm was tested by analyzing ideal matrices that have unique, compatible factorizations to which various levels of random noise had been added. Finally, the results of these evaluations were compared to the resolution of experimental multicomponent EEMs acquired by using the videofluorometer.

The number of unique combinations of characteristic base lines in the spectra of  $n$  components is given by Pascal's triangle. In the case of three components, there are eight  $(1 + 3 + 3 + 1)$  hypothetical configurations of spectra overlap for three components. In the first all three-component spectra have characteristic base lines. There are three degenerate configurations consisting of two characteristic base lines. There are also three degenerate configurations exhibiting one characteristic base line. In the last configuration, the three-component spectra are completely overlapped.

Sixty-four synthetic EEMs were generated producing all possible combinations of overlap of excitation and emission spectra. The spectra were designed so that the number of characteristic bands equals the number of characteristic base lines. Synthetic spectra for each of the three components were simulated by using three adjacent Gaussian peaks of various heights. The various overlap conditions were simulated by varying the wavelength range of the simulated spectra. The EEMs were generated from the weighted outer products of the component spectra (eq 1). The same set of weights (concentration factor) were used for all 64 EEMs:  $\gamma_{11} = 5312$ ,  $\gamma_{22} = 3253$ ,  $\gamma_{33} = 1883$ .

The effectiveness of the resolution scheme consisting of BMB, CFMD, and SSM is excellent for the synthetic EEMs. The data matrices comprised of component spectra that each exhibits a characteristic band can be uniquely resolved by using the BMB algorithm. Fifteen EEMs comprised of com-

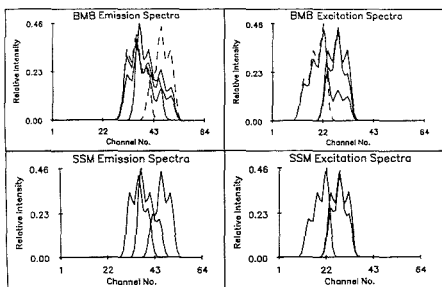


**Figure 2.** Spectra resolved from a synthetic ternary EEM that has  $n$  rather than  $2n$  characteristic base lines using BMB and SSM (—). The reference spectra (---) are included for comparison.

ponent spectra which have a total of  $[2n(n-1)]/n$  characteristic base lines are uniquely resolved using CFMD, despite the absence of characteristic bands.

The CFMD algorithm does not produce unique factorizations for the remaining 48 overlap combinations. In these cases, specialized objective functions can be used to take advantage of information imbedded in the data matrix. Figure 2 illustrates the successful resolution of all six-component spectra from one of the 64 typical EEMs that had just three characteristic base lines using SSM to produce the unique solution. The BMB solution, which is the initial estimate to the component spectra used by the optimization routine, and the component spectra are depicted in Figure 2 for reference. The existence of two characteristic base lines in the emission spectra and one in the excitation spectra provided sufficient information to compensate for the very severe overlap of the remaining excitation spectra. The BMB-CFMD-SSM sequence was able to successfully resolve, i.e. factor the EEM into the component spectra from which it was generated, 24 of the remaining 48 EEMs.

To compare the effect of noise on the performance of the optimization methods, various levels of random noise were added to three ideal matrices, which were successfully resolved by BMB alone, BMB with CFMD, and the BMB-CFMD-SSM sequence, respectively. The random noise was calculated by using the expression

$$n_{ij} = \text{RND}(e_{ij}^{1/2} + b) \quad (15)$$

where the random variable RND was equally distributed on the interval  $[-1,1]$ ,  $e_{ij}$  is the corresponding element of the ideal EEM, and  $b$  approximates the mean of the background. The first term of this expression approximates photon statistical noise and the second the dark current. The mean background value was subtracted from the degraded matrix before analysis. Each analysis was performed in triplicate unless otherwise indicated.

Table II lists the maximum signal-to-noise ratios (S/N) for the third component of the synthetic matrices used to evaluate the resolution algorithm and the average of the scalar products of the emission spectrum of the third component resolved from each noisy matrix by BMB and BMB-CFMD with the ideal spectrum. The third spectrum was used because it has the smallest S/N. An identifiable resolved spectrum is indicated by a scalar product equal to 0.95. This threshold was determined heuristically. The data in Table II indicate that BMB will extract recognizable spectra from matrices that it could resolve in the absence of noise as long as the S/N is above 5, and the BMB-CFMD is similarly useful for data that has S/N above 8. Table III lists the average scalar products of ideal spectra with the emission spectra of the third component resolved by SSM from EEMs generated by adding noise to the ideal data used to produce Figure 2. The data

**Table II.** Scalar Products of Emission Spectra Resolved from Third Component and Ideal Spectrum

S/N	BMB <sup>a</sup>	CFMD <sup>b</sup>
15		0.9894 ± 0.0131
10	0.9968 ± 0.0026	0.9714 ± 0.0300
9	0.9973 ± 0.0004	0.9508 ± 0.0557
8	0.9970 ± 0.0019	0.9697 ± 0.0051
7	0.9897 ± 0.0105	0.9344 ± 0.0194
6	0.9878 ± 0.0048	0.8340 ± 0.0499
5	0.9651 ± 0.0057	
4	0.6935 ± 0.1506	

<sup>a</sup>BMB, best measured basis. <sup>b</sup>CFMD, concentration factor matrix diagonalization.

**Table III.** Scalar Products of Emission Spectra Resolved from Third Component and Ideal Spectra

S/N	replicates	SSM <sup>a</sup>
50	5	0.9918 ± 0.0183
35	4	0.9963 ± 0.0023
25	4	0.9709 ± 0.0092
15	4	0.8855 ± 0.0550
10	5	0.9366 ± 0.0244

<sup>a</sup>SSM, solution simplex minimization.

indicate that the effects of noise on the SSM are more severe than on the CFMD. Not only is the S/N threshold higher for this algorithm, but the variability in the results is much higher at all noise levels. In fact, the optimization routine frequently converged on nonoptimal solutions. Eight replicate analyses were required to produce the data used to calculate the averages in Table III. The cause of this phenomenon has not been determined but may stem from limitations in the routines used to determine the best search vector. Another source of difficulty could be discontinuities that are introduced to the constraints with the addition of high-frequency noise.

To evaluate the validity of our models, the EEMs of several mixtures of polynuclear aromatic hydrocarbons (PNAs) were acquired by using the videofluorometer and analyzed by using both optimization-based algorithms. The average S/N of the experimental matrices was estimated by using the expression

$$S/N = \frac{\sum_{k=1}^m \psi_{kk}}{\sum_{i=n+1}^m \psi_{ii}} \quad (16)$$

where  $m = \min(q,p)$ .

The isometric projection of a mixture of anthracene, 9,10-dimethylanthracene, perylene, and 2,3-benzanthracene is shown in Figure 3. The resolution of the component spectra from this matrix using CFMD is illustrated by the vectors drawn with solid lines. The standard spectra of the components are included in Figure 3 for comparison and plotted with dashed lines. The estimated S/N for this matrix was 35 and the spectra of all four components are successfully resolved, illustrating that the diagonalization procedure is applicable to experimental data. Figure 4 illustrates the resolution of the component spectra from a mixture of 9,10-dimethylanthracene, perylene, fluoranthene, and 2,3-benzanthracene. The S/N of this matrix was approximately 25. In this case, the spectra of all four components are also successfully resolved, but a two-dimensional Savitsky-Golay filter was applied to the least-squares estimate of the matrix before the application of the resolution algorithm. The constraints also were relaxed by permitting small negative values (1%) in the resolved spectra.

## CONCLUSIONS

Several extensions or generalizations of Lawton and Sylvestre's self modeling curve resolution have been previously

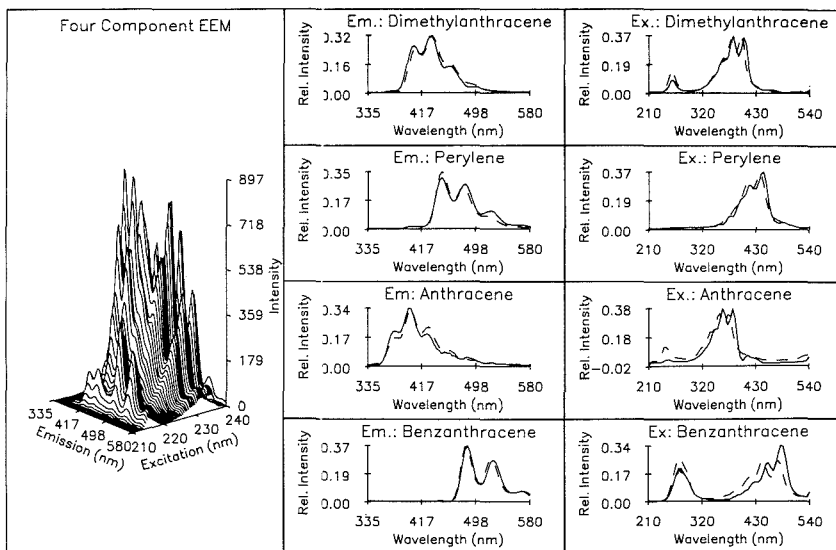


Figure 3. EEM and spectra resolved by CFMD (—) from a mixture of  $7.64 \times 10^{-6}$  M 2,3-benzanthracene,  $5.56 \times 10^{-7}$  M perylene,  $2.09 \times 10^{-6}$  M 9,10-dimethylantracene, and  $6.47 \times 10^{-6}$  M anthracene. Reference spectra are indicated by dashed lines (---).

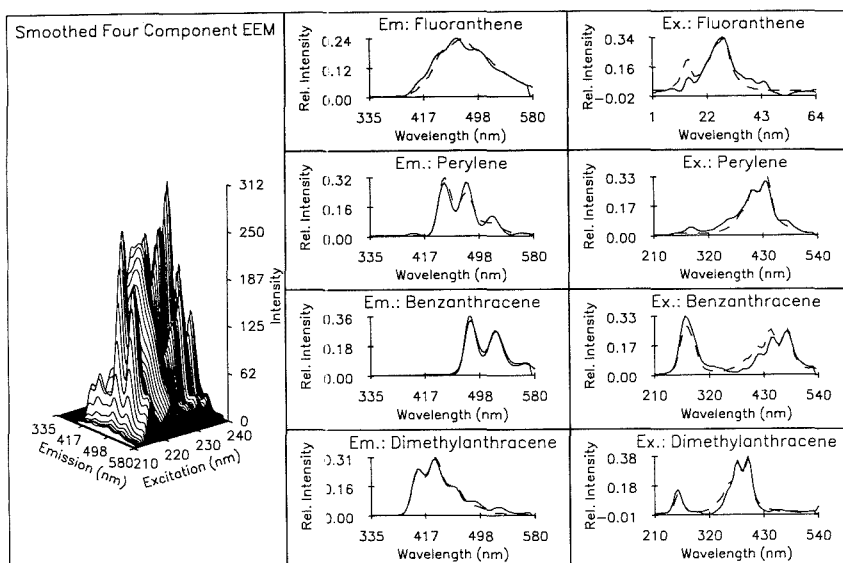


Figure 4. EEM and spectra resolved by CFMD (—) from a mixture of  $2.30 \times 10^{-6}$  M 2,3-benzanthracene,  $1.67 \times 10^{-8}$  M perylene,  $6.29 \times 10^{-7}$  M 9,10-dimethylantracene, and  $2.74 \times 10^{-6}$  M fluoranthene. Reference spectra are indicated by dashed lines (---).

described (4, 9, 21, 22, 26). The algorithm presented here differs in several respects. First, the CFMD uses the complementarity of the component spectra, as well as their nonnegativity and convexity, to estimate the component spectra. Most importantly, the flexibility of the nonlinear optimization approach permits the analyst to evaluate a wide variety of solutions as well as choose which features are incorporated into the solution. The scheme described in this report also allows the analyst to insert related data analysis tasks into the curve resolution scheme easily. For example, optimizing the volume function without the compatibility constraints is

theoretically a nongraphical alternative to evaluating the range of feasible solutions. The spectra that lie on the inner boundaries, i.e. those generated by the restrictions on the sign of the coefficients of the rows and columns expanded in terms of the component spectra, can be found by minimizing the volume, while those that lie on the nonnegativity boundaries can be found by maximizing the volume. Similarly, curve resolution can be coupled to calibration of known components by inserting the coordinates of standards into the CFMD and SSM routines (27).

This resolution scheme also differed from earlier algorithms

in the use of the SVD. The SVD was used in this scheme as an aid to rank estimation and calculation. All of the steps, can be performed, albeit more slowly, on **E** directly. The basis vectors chosen by the BMB method are used to estimate the spectra, so that matrices which are very large or intractable to the SVD may be analyzed by using this approach.

In the course of the development of this algorithm, it was determined that it is the existence of a characteristic base line rather than a characteristic response which governs spectral resolution. This observation is the crux of the solution simplex methodology. These evaluations also show that the optimization-based methods are more sensitive to noise than the target factor analysis method (BMB) presented here. Evaluations using synthetic data indicate that S/N thresholds of at least 8 are required for the resolution of recognizable spectra from nonideal EEMs using CFMD and those of at least 18 are needed for SSM. Additionally, the solution simplex minimization is more prone to nonconvergence than the CFMD.

Evaluations with experimental EEMs acquired by the videofluorometer confirm the conclusions drawn from the synthetic data for the diagonalization of the concentration factor matrix. The evaluations of synthetic data indicate that resolution of sets of spectra that do not have a  $2n$  characteristic base line may be possible but will require higher S/N.

Finally, it has been stated that this scheme is directly applicable to the results of bilinear multiparametric methods. It should also be noted that because concentration is nonnegative and convex, this method can be applied to matrices formed from collections of sample responses to one parameter.

#### ACKNOWLEDGMENT

We thank Dr. Henry Wolkowicz for providing us with a copy of NLPQL and the code for the nonlinear least-squares subproblem.

#### LITERATURE CITED

- (1) Harman, H. H. *Modern Factor Analysis*; University of Chicago Press: Chicago and London, 1976.

- (2) Malinowski, E. R.; Howery, D. G. *Factor Analysis in Chemistry*; John Wiley: New York, 1980.  
 (3) Lawton, W. H.; Sylvestre, E. A. *Technometrics* **1971**, *13*, 617.  
 (4) Ohta, N. *Anal. Chem.* **1973**, *45*, 533.  
 (5) Knorr, F. J.; Futrell, J. H. *Anal. Chem.* **1979**, *51*, 1236.  
 (6) Malinowski, E. R. *Anal. Chim. Acta* **1982**, *134*, 129.  
 (7) Gemperline, P. J. *Anal. Chem.* **1986**, *58*, 2656.  
 (8) Vandeginste, B. G. M.; Derks, W.; Kateman, G. *Anal. Chim. Acta* **1985**, *173*, 253.  
 (9) Sasaki, K.; Kawata, S.; Minami, S. *Appl. Opt.* **1984**, *23*, 1955.  
 (10) Wilson, B. E.; Lindberg, W.; Kowalski, B. R. *J. Am. Chem. Soc.* **1989**, *111*, 3797-3804.  
 (11) Johnson, D. W.; Callis, J. B.; Christian, G. D. *Anal. Chem.* **1977**, *49*, 747A.  
 (12) Weber, G. **1961**, *Nature* **190**, 27.  
 (13) Searle, S. R. *Matrix Algebra Useful for Statistics*; John Wiley: New York, 1983.  
 (14) Golub, G. H.; VanLoan, C. F. *Matrix Computations*; Johns Hopkins University Press: Baltimore, MD, 1983.  
 (15) Shrage, R. I.; Hendley, R. W. *Anal. Chem.* **1982**, *54*, 1147.  
 (16) Wold, S. *Technometrics* **1978**, *20*, 397.  
 (17) Schittowski, K. *Design, Implementation and Test of a Nonlinear Programming Algorithm*; Springer-Verlag: New York, in press.  
 (18) Scales, L. E. *An Introduction to Nonlinear Optimization*; Springer-Verlag: New York, 1985.  
 (19) Gill, P. E.; Murray, W.; Wright, M. H. *Practical Optimization*; Academic Press: London and New York, 1981.  
 (20) Nelder, J. A.; Mead, R. *Comput. J.* **1965**, *7*, 308.  
 (21) Borgen, O. S.; Kowalski, B. R. *Anal. Chim. Acta* **1985**, *174*, 1.  
 (22) Borgen, O. S.; Davidsen, N.; Mingyang, Z.; Oyen, O. *Mikrochim. Acta* **1986**, *2*, 63.  
 (23) Warner, I. M.; Fogarty, M. P.; Shelly, D. C. *Anal. Chim. Acta* **1979**, *109*, 351.  
 (24) Lay, S. R. *Convex Sets and Their Applications*; John Wiley: New York, 1982.  
 (25) Bronsted *An Introduction to Convex Polytopes*; Springer-Verlag: New York, 1983.  
 (26) Meister, A. *Anal. Chim. Acta* **1984**, *161*, 149.  
 (27) Nelson, G.; Neal, S. L.; Warner, I. M. *Spectroscopy* **1988**, *3*, 24.

RECEIVED for review July 14, 1989. Revised manuscript received December 19, 1989. Accepted December 29, 1989. This work was supported in part by grants from the National Science Foundation (CHE-8609372) and the Office of Naval Research. I. M. Warner acknowledges support from an NSF Presidential Young Investigator Award (CHE-8351675). S. L. Neal acknowledges the support of a graduate fellowship from the National Organization of Black Chemists and Chemical Engineers sponsored by the Procter and Gamble Company.

## Locally Weighted Regression and Scatter Correction for Near-Infrared Reflectance Data

Tormod Naes\* and Tomas Isaksson

MATFORSK, Osløvegen 1, 1430 Ås, Norway

Bruce Kowalski

Laboratory of Chemometrics, University of Washington, Seattle, Washington 98195

This paper investigates the effect of multiplicative scatter correction (MSC) and nonlinear regression based on the first two and three principal components for near-infrared reflectance (NIR) spectroscopy data. The focus will be on linearity/nonlinearity as well as treatment of outliers. The main contribution of the paper is the presentation of and testing of a calibration method based on classification and local least-squares regression. The theory is illustrated by three examples from NIR analysis. The local linear calibration outperformed traditional methods in two of the examples.

\* Author to whom correspondence should be sent.

#### INTRODUCTION

Most calibration techniques used in near-infrared reflectance (NIR) spectroscopy are linear in the sense that they produce models that are linear functions of the spectral reflectances or absorbances (1, 2), i.e. log (1/reflectance). Such methods, for instance principal component regression (PCR) (3), partial least-squares (PLS) regression (4), Fourier regression (5), and different versions of stepwise multiple linear regression (SMLR), have proved useful in practice.

In many studies, other functions or corrections of the spectral reflectances combined with linear calibrations are tested (5-7). The idea behind these approaches is to improve linearity, to optimize predictions, and to eliminate or reduce

"nuisance" effects such as light scatter variations. In many cases, such approaches have led to improvements over traditional methods. Some studies have also indicated the possibility of using nonlinear regressions of the spectral values or functions of them (9).

In the paper by Isaksson and Naes (9), the main emphasis was on multiplicative scatter correction (MSC) (6) of the spectra before linear calibration. The advantages of using the MSC as well as the reasons for the advantages were studied for a designed experiment based on water, starch, and fish protein. It was found that MSC led to a better linear fit and improved prediction results and offered better outlier treatment and even better interpretation possibilities compared to untransformed data. The results also indicated that the MSC made diffuse NIR analysis more similar to classical Beer's law spectroscopy. These results were then used as an argument for using the first few principal components in a polynomial regression equation. This approach was studied in more detail in Naes and Isaksson (11) and also gave promising results compared to the linear PCR.

The focus of the present paper is on the effect of MSC and nonlinear regression based on the principal components. A nonlinear regression is proposed for this purpose: a relatively new nonparametric regression method from the statistical literature (12) (locally weighted regression (LWR)), which is easy to use (it is only based on simple local regression models) and very flexible. The present study is based on three NIR data sets covering both designed and undesigned experiments employing "full-spectrum" and "fixed-filter" instruments.

In this paper, scalars are denoted by lowercase italic letters, vectors by lowercase boldface letters, and matrices by capital boldface letters. To help the reader we have collected symbols and abbreviations used in the paper in a nomenclature section.

### THEORY

**Linear Regression.** In most applications of NIR spectroscopy, the calibration method used is linear in the spectral reflectances,  $R$  (equal to the intensity of the reflected radiation from the sample divided by the intensity of the radiation beam directly from a standard), or in some nonlinear function of them, for instance  $\log(1/R)$ . This means that the model for each sample is

$$y = b_0 + \sum_{k=1}^K b_k x_k + e \quad (1)$$

where  $y$  represents chemical concentration,  $x_k$ ,  $k = 1, \dots, K$ , the spectral value for all wavelengths (or functions of them), the  $b$ 's are regression coefficients to be determined in the calibration, and  $e$  is the error term.

Near-infrared data as represented by  $\mathbf{x}$  are in practice usually highly collinear. To obtain good estimates of the regression coefficient vector  $\mathbf{b}$ , methods other than the ordinary multiple linear regression (MLR) therefore have to be applied (2). An important example of such a method is PCR (13), which compresses the information in the spectrum onto a principal component subspace before the regression. In other words, a lower-dimensional set of orthogonal principal component variables,  $t_a$ , is found and  $y$  is regressed on  $t_a$  instead of  $x_k$  using the model

$$y = q_0 + \sum_{a=1}^A q_a t_a + e \quad (2)$$

where the number of components,  $A$ , is usually taken to be much lower than the number of  $x$  variables,  $K$ . If desired, the estimates of the coefficients of this equation can finally be transformed back to the scale of the original spectral variables to obtain the regression coefficients  $\hat{\mathbf{b}}$ . Practice has shown that the main predictive information for PCR used on

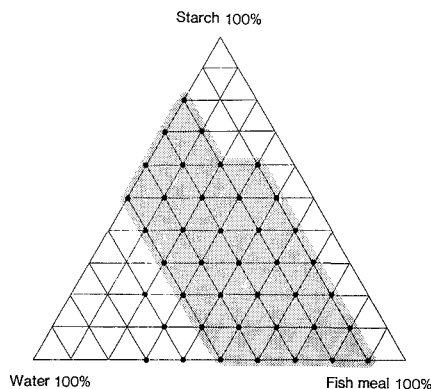


Figure 1. Design of the experiment based on water, fish meal, and starch considered in ref 9. The samples are denoted by dots. The shaded region is the one used for calibration in example 2.

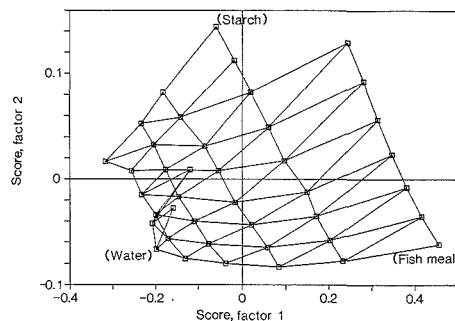
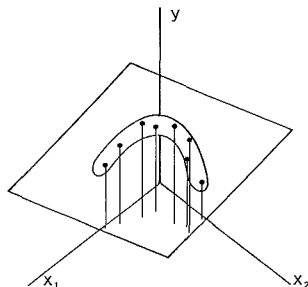


Figure 2. Principal component score plot for the samples in Figure 1 (based on 19 wavelengths).

NIR spectra is usually collected in the 2-10 principal components corresponding to the largest eigenvalues and beyond this point only minor improvements can be expected. Successful applications of the PCR method in NIR analysis are given in e.g. Cowe and McNicol (13) and Naes and Martens (14).

**Multiplicative Scatter Correction (MSC).** The multiplicative scatter correction (MSC) was first proposed by Martens et al. (15) and Geladi et al. (6) to eliminate (or reduce) the difference in light scatter between samples before the calibration. For each sample, this correction is based on regressing spectral values on the average spectrum (over samples) and correcting each spectrum by subtracting the intercept and dividing by the slope of the estimated regression equation. The corrected spectra  $\mathbf{x}$  with only a minor variability due to differences in light scatter are then used in eq 1 or 2. In Isaksson and Naes (9), the MSC was studied in some detail and improvements in prediction ability due to greater linearity between  $y$  and the  $x$  values and better outlier treatment and improvements in interpretation due to optimal prediction with fewer number of factors were obtained.

**PC Scores and Nonlinearity.** In Isaksson and Naes (9) a designed experiment based on a simplex lattice structure (Figure 1) was used to evaluate PCR and MSC. A principal component scores plot (Figure 2) revealed that the first two components (in a large region) contained the main information about chemical composition, although in a somewhat nonlinear (but still smooth) way. The nonlinear relation between the chemical composition and the principal component scores after



**Figure 3.** Illustration of a nonlinearity that can be modeled as a nonlinear function of the first principal component of  $x_1$  or  $x_2$  or as a linear function of two principal components. As we see, all points lie close to a plane in three-dimensional space.

scatter-correction was much simpler and smoother than for the uncorrected case.

**Nonlinear Regression.** On the basis of these results, Isaksson and Naes (9) considered nonlinear regression of  $y$  based on the first few principal components (on scatter-corrected data). By use of nonparametric fitting techniques (e.g. alternating conditional expectations (ACE) regression (16), projection pursuit regression (PPR) (17)), it was found that simple functions, for instance polynomial fitting equations in the first two principal components, gave reasonable fit with good prediction results. The same technique was studied in more detail by Naes and Isaksson (11), who obtained substantially better results with the nonlinear approach than with the linear one. It was argued that the improvements were due to both better functional fit to the data and a decrease in the number of significant outliers when considering only these very first dimensions.

This is also a strong empirical indication that in this case the principal components used to obtain optimal PCR predictions were necessary mainly to account for nonlinearities in the relationship between  $y$  and the first two principal components. This phenomenon is illustrated more clearly in Figure 3. As we see, the first principal component describes the main variability of the "banana", but two principal components are needed to get a good linear fit. On the other hand, there is only one phenomenon in the problem and a nonlinear function of the first principal component will have approximately the same effect as two principal components (10). In other words, the last principal component is necessary only to account for nonlinearities in the relation between the first one and  $y$ .

There are a number of nonlinear calibration methods to choose from. The nonparametric methods PPR and ACE regression were used by Isaksson and Naes (9) to indicate which type of function to use, while Naes and Isaksson (11) considered a full second-degree polynomial regression with interactions. The first approach is useful in pointing out function type, for instance degree and type of polynomial to use, and can therefore provide more parsimonious and well-fitted functions than the other. The direct polynomial is, however, much simpler to use, since ordinary linear regression can be used for the polynomial variables. To solve the overfitting problem, polynomial techniques can be accompanied with a stepwise deletion or addition of variables due to, e.g., statistical  $t$  tests on the regression coefficients.

In this paper we will, however, consider another nonlinear regression method that is quite easy to implement and has several attractive features. This method is called the locally weighted regression (LWR) and is proposed by Cleveland and Devlin (12). An implementation of a similar method was given

as early as in 1977 by Kowalski and co-workers in the Arthur program (18).

**Locally Weighted Regression (LWR).** This method was published as a proposal for estimating nonlinear regression surfaces when little information is available about the surface, here called  $g(\mathbf{x})$ . In this respect the method assumes no functional form of the surface except "smoothness" (continuity) and good local approximation to a simple function (as for instance a linear or a polynomial model).

For estimating the regression surface, the method is based on local regressions based on a linear (or for instance a quadratic) function. For each sample (no.  $i$ ) in the data set, the  $q$  closest points are selected and used in the regression. Each of these points are assigned a weight value dependent on its distance to  $\mathbf{x}_i$  (or  $t$ , since the method proposed here is based on a few principal components) and the regression is performed with respect to these weighted values (so-called weighted regression). The value of the fitted regression surface at  $\mathbf{x}_i$  is then called the fitted value or the estimated value for the regression surface at that point, i.e.  $\hat{g}(\mathbf{x}_i)$ .

No clear description is given by Cleveland and Devlin (12) of how to use the same idea in prediction of unknown samples. In this paper we propose that for each new sample, the  $q$  points in the calibration set which are closest to the prediction spectrum  $\mathbf{x}_p$  are selected, then the local regression surface based on these  $q$  samples are selected, and finally the predicted value  $y_p$  is obtained by applying the calibrated local equation for the prediction sample, i.e.  $\hat{g}(\mathbf{x}_p)$ . In other words, a new weighted regression calibration is done for each new prediction sample and each calibration is based on the  $q$  calibration points closest to it. Since the procedure in this application is supposed to be applied on very few principal components, the number of samples involved in each calibration can probably be held at a moderate level and therefore still keep the calibration/prediction quite easy to perform.

As can be seen, there are several parameters involved in this procedure. First of all,  $q$  (the number of samples in each regression), which is the parameter determining the degree of smoothness of the estimated surface, has to be determined (the higher the  $q$ , the smoother the surface). Secondly, selection of a weighting function  $w_j(\mathbf{x}_j)$ , for the  $q$  points  $j = 1, \dots, q$  in the regression may be required. This corresponds to determining the relative influence of the closest compared to the more distant points. Thirdly, the type of function to fit at each stage is a matter of choice and depends certainly on the surface under consideration. Finally, the distance concept must be determined in order to select the samples that are to be involved in each calibration.

In this paper we choose the Euclidean distance, here called  $\rho$ , based on the actual principal components weighted to variance equal to 1, i.e. the Mahalanobis distance based on the original principal components. Furthermore, we will use the same weighting function as described in the original paper by Cleveland and Devlin (12) which is equal to

$$w_j(\mathbf{x}_j) = W(\rho(\mathbf{x}_j, \mathbf{x}_i) / d(\mathbf{x}_i)) \quad (3)$$

where  $W(u) = (1 - u^2)^3$  for  $u$  less than 1 and  $W(u) = 0$  for  $u$  larger than 1. The function  $d(\mathbf{x}_i)$  is the maximum of  $\rho(\mathbf{x}_j, \mathbf{x}_i)$  over the  $q$  points involved in the regression. As a function of  $j$ , the weight is large for  $\mathbf{x}_j$  close to  $\mathbf{x}_i$  and small for  $\mathbf{x}_j$  far from  $\mathbf{x}_i$ .

We will consider different values of  $q$  (or  $f = q/I$ , the fraction of all points used in each regression) and investigate cross-validation (19) as a method to determine the optimal value. It should be mentioned that in the cross-validation performed in the examples, the scores or principal components are taken as fixed. In other words, determination of the principal components is not part of the cross-validation. Cleveland and Devlin (12) developed another procedure for



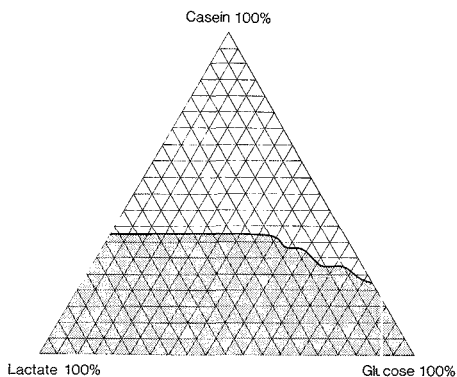


**Figure 4.** Illustration of the design of example 1 (one sample for each intersection of lines). The shaded region is the one used for the locally weighted regressions.

selecting  $q$  based on an idea similar to the idea behind  $C_p$  plots (20) in least-squares regression. Both linear and quadratic fits are used in this paper. By a quadratic function we will here mean a polynomial with first-order, second-order, and interactions terms. With two factors, this gives a function of the form

$$y = b_0 + b_1x_1 + b_2x_2 + b_3x_1x_2 + b_4x_1^2 + b_5x_2^2 + e \quad (4)$$

for each sample.

**The Number of Principal Components.** An important point in this type of regression is selection of the number of principal components to use in the nonlinear equation. As for linear methods, sufficient factors are required to ensure that the most information is present. On the other hand, too many factors leads to overfitting (10). With reasonably many factors, it is, however, probably better to use one factor too many than taking the risk of not incorporating enough useful variance. Cross-validation can be used as a guide for the selection.

For the data considered in Isaksson and Naes (9), it appeared that after MSC, the principal components scores plot was (in a large region and except from a smooth nonlinearity) similar to what would be expected if Beer's law applies. This means that in the case of closure ( $\sum y_i = 100\%$ ), the number of dominating chemical components minus one is a reasonable first approximation to the number of factors to use (if MSC is used).

### EXPERIMENTAL SECTION

The following three examples will be used to evaluate the usefulness of the MSC and the LWR approach on principal components of scatter-corrected data. The focus will be on prediction ability, outliers, and interpretation.

**Example 1.** This data set is based on a designed experiment using a monochromator instrument (Technicon InfraAlyzer 500) with a closed cup. The constituents are glucose (Art. 8342, E. Merck, Darmstadt), casein (Denmark Acid Casein, Milco Export, Viby J., Denmark), and lactate (Ca-Lactate, Prod 27604, BDH Chemicals, Ltd., Poole, England). There are 231 samples altogether of which 116 samples (every second sample) are used in the calibration set and 115 in the prediction step. Glucose weight percent is the constituent for which calibration is performed. The spectral data are from wavelengths in the range 1103–2500 nm. Averages of adjacent spectral points are taken ending up with 117 spectral ( $\log(1/R)$ ) values. The design is illustrated by the whole grid in Figure 4. The shaded region is discussed below.

**Example 2.** Water, potato starch, and fish meal (freeze-dried cod) were mixed in different proportions. The calibration set consists of the samples in the shaded part of the grid in Figure 1 (and Figure 5). The prediction set is designed as shown in

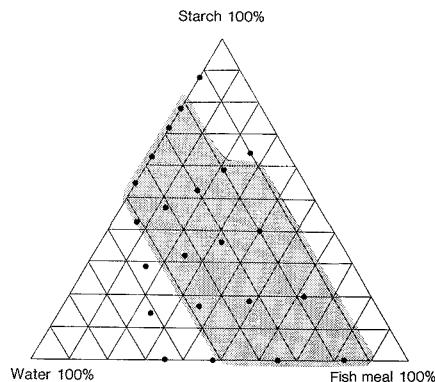


**Figure 5.** Illustration of the design of the prediction set used in example 2. The samples are denoted by dots. The shaded region is the one used as calibration set (see also Figure 1).

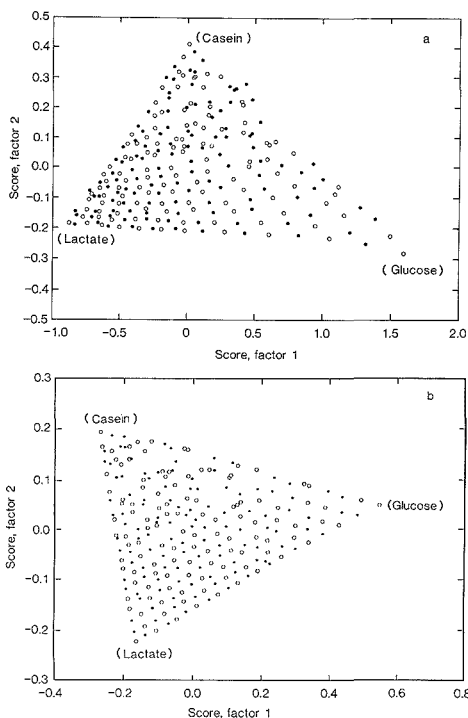


**Figure 6.** Principal component score plots of the full set (a) before and (b) after scatter correction (example 1). The open circles are calibration samples and the filled circles are prediction samples.

Figure 6. The spectra were measured on a fixed filter instrument. Technicon InfraAlyzer 400, and they consist of measurements at the 19 standard wavelengths ( $\log(1/R)$ ). Protein weight percent is the constituent for which calibration is performed. For further details see ref 9.

**Example 3.** In this example we use the fish data (rainbow trout) presented in ref 21. These consist of measurements of fat percent and absorbance at nine wavelengths (each second wavelength from Technicon InfraAlyzer 400,  $\log(1/R)$ ) for 45 samples. The 20 first samples are as given by Naes (21), used in the calibration and the last 25 are prediction samples to be

used for testing the performance of the predictors. In ref 21, seven of the prediction samples were determined to be "outliers" due to bad fit to the calibration model and the prediction results were only reported for the remaining samples (18 in total). In this paper we will, however, consider both prediction sets in order to show the effect of MSC and LWR for "difficult" samples.

Altogether, the three sets cover small, moderate, and large calibration sets, full-spectrum as well as fixed-filter instruments, and designed experiments as well as randomly selected natural samples.

### COMPUTATIONAL METHODS

For all the data sets, principal component analysis was performed both before and after scatter correction. For comparison with the nonlinear regression, a linear principal component regression analysis was employed in each case. For the scatter-corrected data in examples 2 and 3, the determinants of the  $K$ -dimensional ( $K$  is the number of wavelengths) and  $(K - 1)$ -dimensional centered covariance matrices were equal to 0 within the working precision of the computer program. Therefore, in these cases the PCR results are only presented for  $a = 1, \dots, K - 2$ .

Based on the first two and/or three principal components the LWR described above was employed with different parameter values  $f = q/I$  (i.e. the fraction of the calibration set which is used in each local calibration) and both linear and quadratic fitting functions. For examples 2 and 3 both the cross-validation and prediction results were computed.

For outlier discussions in example 3 the leverages defined by

$$h_{ia} = t_{ia}^2 / t_a' t_a \quad (5)$$

for each sample  $i$  and factor  $a$ , were computed. Here  $t_{ia}$  denotes the principal component value of factor  $a$  and sample  $i$  and  $t_a$  denotes the vector of principal component scores along factor  $a$ . A large value of  $h_{ia}$  indicates an abnormality along axis  $a$  for sample  $i$ .

Results on prediction error in this paper are reported in RMSEP (root mean square error of prediction) computed over the test or prediction samples. The definition of this is

$$\text{RMSEP} = (I^{-1} \sum_{i=1}^I (\hat{y}_i - y_i)^2)^{1/2} \quad (6)$$

where  $I$  is the number of samples. This is the square root of the average of the squared differences between predicted and measured concentrations. Essentially the same measure is used in the cross-validations, but in that case it is denoted by RMSECV (root mean square error of cross-validation; see e.g. ref 10).

MATLAB (Mathworks, Inc.) was used for all regression computations.

### RESULTS AND DISCUSSION

**Example 1.** Principal components were obtained from uncorrected and scatter-corrected data. The scores for the prediction samples (115 samples) were computed from the eigenvectors obtained from the calibration samples (116 samples). The scores of the first two factors are given in parts a and b of Figure 6 (calibration samples are denoted by an open circle and prediction samples are denoted by a dot). The scores of the scatter corrected data show a somewhat more regular pattern in the region closest to lactate and glucose than the uncorrected data and, in the same region, the scatter-corrected scores show a pattern very similar to the design. Since the samples are essentially mixtures of three constituents with closure, it seems that in a substantial subregion, the MSC gives spectral information with similar linearity as if Beer's law applies. The rest of the region and the uncorrected data show a more complicated relationship to the chemical concentrations. In essence, this is the same conclusion as obtained by Isaksson and Naes (9).

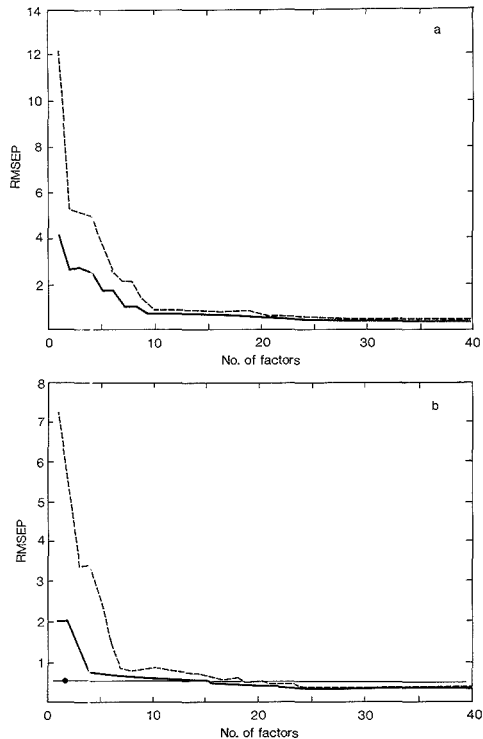


**Figure 7.** (a) The RMSEP's for PCR both before (---) and after (—) scatter-correction (example 1). (b) The RMSEP's for PCR both before (---) and after (—) scatter correction and LWR after scatter correction (horizontal line) computed on the reduced set (see Figure 5).

The RMSEP's of the PCR calibrations for the two cases are shown in Figure 7a. As can be seen they come down to approximately the same level of prediction ability (RMSEP = 0.36 after MSC and RMSEP = 0.40 before MSC) which is extremely good taking into account the big span of the constituents. These results also show the remarkable ability of linear methods to correct for nonlinear effects by incorporating enough factors. Notice, however, that the MSC curve comes down much faster to an acceptable level, showing the greater linearity between the percentage of glucose and the first few principal components of the spectral variables. However, the fact that both curves come down to approximately the same level shows that when all the  $x$  variables are used together, they give similar linearity with respect to  $y$  both before and after scatter correction. The conclusion from this is that the main advantage of MSC was to provide better linear fit for a smaller number of factors and to give better agreement to Beer's law properties in a subregion of the whole space.

The score plots in Figure 6 show that the pattern of the first few principal components (even after MSC) is too complicated to be well suited for nonlinear regression by a reasonably smooth function. We therefore decided to consider the nonlinear approach (LWR) only in the subregion where the score-plot is similar to the design (shaded in Figure 4). The principal component scores both before and after scatter correction are shown in Figure 8 and the results for the PCR are given in Figure 7b. The optimal value is now equal to 0.35 for both cases, a slight improvement compared to the full set.

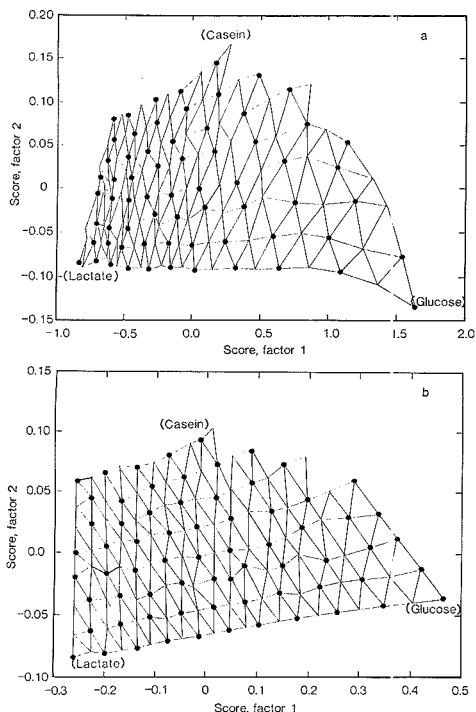


**Figure 8.** Principal component score plots of the samples in the shaded region of Figure 5, both (a) before and (b) after scatter-correction (example 1).

**Table I.** RMSEP for the Locally Weighted Regression in Example 1<sup>a</sup>

$f$	linear		quadratic PRED(2)
	PRED(1)	PRED(2)	
0.1	0.73	0.62	0.52
0.2	0.70	0.66	0.55
0.3	0.74	0.75	0.56

<sup>a</sup>The numbers in parentheses show the number of principal components used.

The nonlinear LWR results based on the first two principal components (the two with largest eigenvalue) of the MSC data are given in Table I. The best result in this case is RMSEP = 0.55. It is based on a quadratic model and a smoothing corresponding to  $f = 0.2$ . Notice that the results from only one factor and  $f = 0.2$  gave a result as good as 0.70 and also that 15 principal components in the linear PCR approach were needed to get the same results as the nonlinear approach based on the two first principal components.

This shows that in this case, even the principal components with very small eigenvalues contain predictive information which is not present in those with larger eigenvalues. In order to give such results, the estimate of the corresponding underlying principal component space generally has to be very stable and no significant outliers are allowed. The fact that all the constituents were well mixed powders providing quite homogeneous mixtures is probably an important reason for this result. (This is also probably the reason for the similarity between the scatter-corrected and uncorrected data as reported above.) The residuals from the best linear and non-

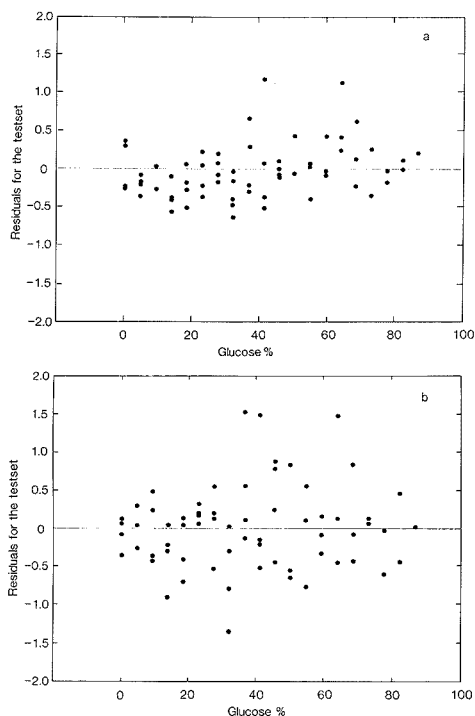


**Figure 9.** Prediction residuals versus  $y$  from the optimal (a) linear and (b) nonlinear approach (LWR) (example 1).

linear approach are shown in Figure 9. No clear nonlinearity is seen, but the residuals of the linear approach are generally closer to 0.

In summary, neither the MSC nor nonlinear LWR approach gave improvement in optimal RMSEP (A slight improvement was, however, observed when the MSC was used on the whole data set.) The scatter correction and LWR did, however, give better results with a substantially lower number of factors than for the uncorrected data. Especially so for the LWR after scatter correction where only 2 factors are needed to give satisfactory results (notice, however, that this result holds only in the shaded region in Figure 4). This fact can be important both from a robustness and from certain interpretation perspectives, which will be further discussed in example 3.

**Example 2.** The calibration data in this example (37 samples) is a subset of the original design performed by Isaksson and Naes (9) (see Figure 1) which contained 41 samples. The rest of the calibration set (four samples) were shown in the original paper to lie in a region with a more complicated relationship to the chemical concentrations (see also Figure 2). The prediction set is, however, different in this paper. We refer to the same paper for further calibration results based on the full set.

Notice that this difference in linearity for the different regions is exactly the same as observed for the first example, namely that the scores show nice structure in a subregion while outside this region the structure is more complicated. Notice also that the region with best linearity in both cases is quite extensive and contains a large span of the constituents (larger than used in many practical applications of NIR spectroscopy).

The PCR results are presented in Table II. Here, contrary to the former example, the MSC gave a substantial improvement compared to the uncorrected data. In ref 9 (where

**Table II. RMSEP and RMSECV for Scatter-Corrected and Uncorrected Data (Example 2)<sup>a</sup>**

A	before MSC		after MSC	
	CV	PRED	CV	PRED
1	22.52	23.96	15.12	16.78
2	5.96	11.48	2.64	3.11
3	4.73	6.67	2.52	3.42
4	5.65	4.58	2.22	2.38
5	4.58	3.44	2.29	2.13
6	5.43	3.43	1.83	1.84
7	5.66	6.34	1.86	1.84
8	3.88	3.53	1.95	1.83
9	3.03	6.88	1.80	1.58
10	2.58	7.43	1.46	1.00
11	2.48	7.85	0.99	1.20
12	2.27	8.06	1.12	1.14
13	2.22	8.32	1.10	1.47
14	2.46	8.39	1.12	1.39
15	2.53	6.65	1.42	1.41
16	3.04	6.78	1.48	1.41
17	2.25	7.62	1.39	1.33

<sup>a</sup> CV means cross-validation and PRED means prediction testing. A is the number of factors in the models.

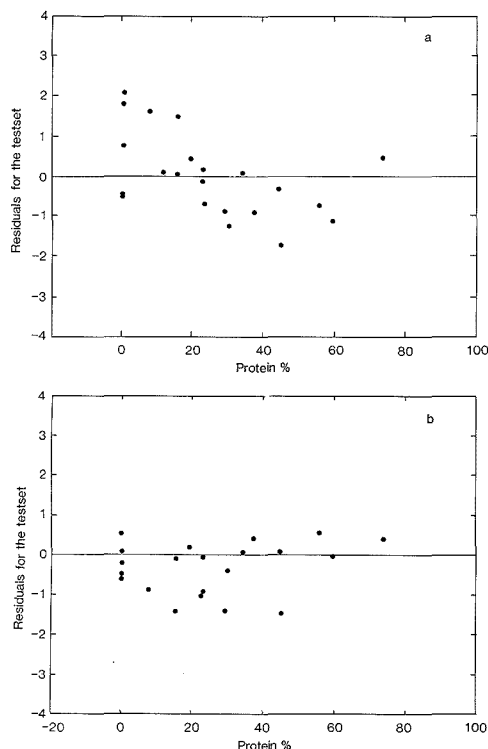


**Figure 10.** (a) Residuals for the test set versus  $y$  for the optimal PCR predictor. (b) Prediction residuals versus  $y$  for the optimal LWR predictor (example 2).

this smaller calibration set was considered as well as the full set) the reduction of certain unusual samples as measured by the leverage values was pointed out as a main reason for this. We refer to that paper and the treatment of the next example for further discussion of this aspect. The residuals from the best PCR prediction with 10 factors in X are given in Figure

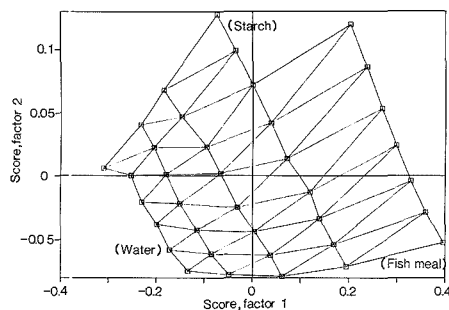


**Figure 11.** Principal component score plot of calibration set (example 2).

**Table III. RMSEP and RMSECV for the Linear and Quadratic Model Using the LWR Approach (Example 2)<sup>a</sup>**

f	linear		quadratic	
	CV(2)	PRED(2)	CV(2)	PRED(2)
0.1	1.19	0.77		
0.2	0.96	0.80	1.82	1.98
0.3	0.88	0.93	0.81	0.67
0.4	0.95	1.03	0.76	0.69
0.5	1.08	1.17	0.76	0.75
0.6	1.18	1.27	0.80	0.80
0.7	1.29	1.44	0.84	0.89

<sup>a</sup> The numbers in parentheses show the number of factors used.

**Table IV. RMSEP and RMSECV before and after Scatter Correction by the MSC (Example 3)<sup>a</sup>**

A	before MSC			after MSC		
	CV	PRED(25)	PRED(18)	CV	PRED(25)	PRED(18)
1	2.59	5.35	2.47	1.31	1.50	0.88
2	2.64	3.08	2.07	1.04	1.20	0.58
3	1.33	1.87	0.76	0.99	1.09	0.63
4	1.46	1.85	0.79	1.05	1.12	0.64
5	1.39	2.26	0.75	1.09	1.11	0.62
6	1.44	2.24	0.74	1.16	1.12	0.63
7	1.53	2.23	0.73	1.47	1.12	0.61

<sup>a</sup> CV means cross validation, PRED means prediction, and the numbers in parentheses show the number of samples used in the prediction set.

10a. The most striking feature is the strong negative slope in the plot.

The score plot of the first two factors after MSC (Figure 11) for the calibration set shows that the main information about chemical concentrations is in these two factors, although in a nonlinear way.

The results for the LWR after MSC are presented in Table III for prediction and cross-validation. The results are for both a linear and a quadratic function. The best results are obtained with a quadratic fit and compared to the PCR shows an improvement of 32%. The residuals for the best results are given in Figure 10b, showing much less nonlinearity than those in Figure 10a, but instead indicating that there is a tendency of negative bias in the predictions. The samples with largest bias are, however, identified as extrapolations outside the calibration population. Notice that cross-validation gives a reasonable estimate of the optimal  $f$  value for prediction.

It is important to emphasize that in addition to the obtained improvement in prediction ability by a nonlinear approach based on MSC data, the results again show that the important information is found in the first few (in this case, 2) principal components.

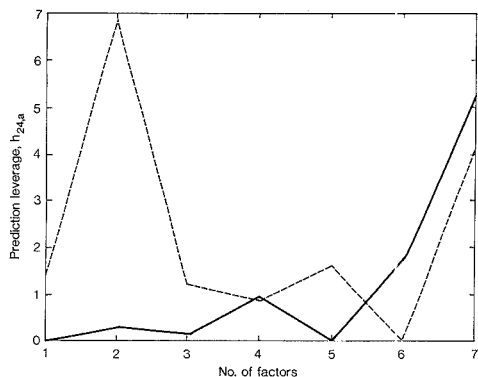


**Figure 12.** Leverages for each factor from 1 to 7 for sample 24 before and after scatter correction (example 3). The dotted line corresponds to leverages before scatter correction and the solid line shows the same after scatter correction.

**Table V. RMSEP and RMSECV for Linear and Quadratic Fit Based on 2 and 3 Principal Components (Example 3)<sup>a</sup>**

<i>f</i>	linear				quadratic PRED(2, 25)
	CV(3)	PRED-(2, 25)	PRED-(3, 25)	PRED-(3, 18)	
0.5	1.57	1.10	0.90	0.87	2.46
0.6	1.45	1.01	0.94	0.91	1.53
0.7	1.21	0.97	0.86	0.75	1.25
0.8	1.02	0.96	0.81	0.60	1.15
0.9	0.95	0.99	0.87	0.51	1.14

<sup>a</sup> CV means cross-validation and PRED means prediction. The first number in the parentheses show how many factors are used and the second shows the number of prediction samples used.

**Example 3.** The PCR results are given in Table IV for cross-validation and prediction both before and after scatter correction. The prediction results for the scatter-corrected data are substantially better than those obtained in the uncorrected case. For the smallest prediction set containing 18 prediction samples (i.e. the seven samples termed "outliers" by Naes (21) are omitted), the results are more similar than in the other case with 25 prediction samples, showing that the main difference is in the treatment of some of these seven "outliers" (see section 3, example 3). In other words, the MSC was able to substantially reduce the prediction error for some of these seven samples. On comparison of the (one-factor) leverages for the original and scatter-corrected data for the seven first factors and for one of the samples with large leverage values, as is done in Figure 12, it is seen that the leverages before MSC are substantially larger than after MSC. Prediction error formulas for regression show larger than expected errors for larger leverages, explaining the observed effect. In other words, as in Isaksson and Naes (9) we found that the MSC decreased the leverage values. The residuals are presented in Figure 13a,b, and as we see, the MSC has caused a substantial decrease of the most extreme values.

The results of the LWR (after MSC) are given in Table V for the local linear model using two and three principal components and for the quadratic model using two principal components. For 25 prediction samples the best results were obtained for  $f = 0.8$  and three principal components using linear regression. This RMSEP result is more than 20% better than the best result obtained with the PCR. This indicates that the nonlinearity in the relation is handled better using LWR based on principal components than with PCR. The prediction residuals for this case are presented in Figure 13c.

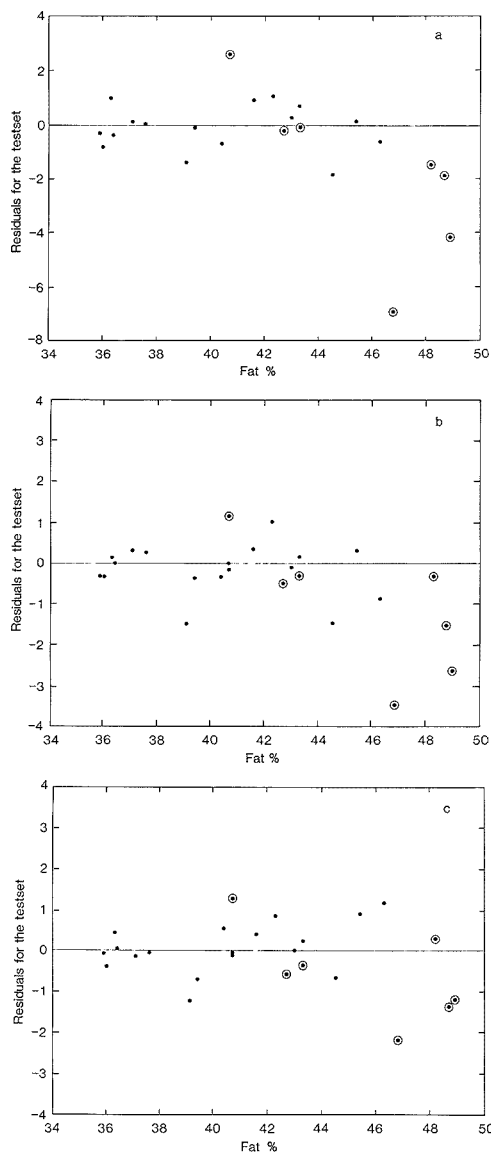


**Figure 13.** Prediction residuals for 25 prediction samples versus  $y$  for the PCR with 3 factors (a) before scatter correction, (b) after scatter correction, and (c) the LWR (after MSC) based on 3 factors and  $f = 0.8$ . The seven samples identified as "outliers" in Naes (21) are circled (example 3).

Compared to the residuals from the best PCR calibration (Figure 13a,b) the problem with the two most extreme samples to the right is substantially decreased. In particular, notice the very large improvement in going from PCR on raw data (RMSEP = 1.65) to LWR based on MSC data (RMSEP = 0.81).

A cross-validation and a prediction of the 18 prediction samples (Table V) were also performed. First, the cross-validation turned out to give a good estimate of the  $f$  with respect to prediction ability for the 18 prediction samples, but not

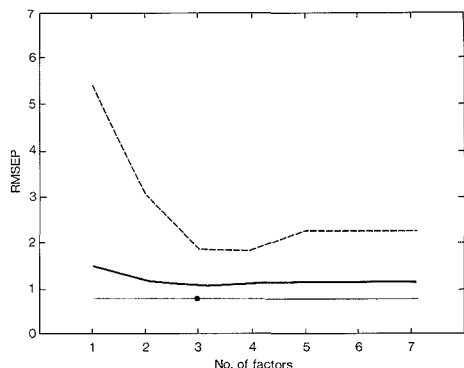


**Figure 14.** RMSEP's of the optimal PCR and LWR before and after scatter correction for 25 prediction samples (example 3). The horizontal line indicates the prediction ability for LWR and the dot indicates the number of factors used for this method (here 3). The upper curve corresponds to PCR before scatter correction and the lower curve to PCR after scatter correction.

as good for the full prediction set. However, even with  $f$  corresponding to the lowest RMSEP of cross-validation (sometimes called RMSECV), the corresponding prediction results even in this case are better than the best PCR results. Second, the results with and without the seven samples were now more similar compared to the PCR on the MSC data again showing that the nonlinearity is more serious for some of the seven samples than for the rest. It also indicates that when treated properly, all seven samples termed "outliers" by Naes (21) give reasonable prediction results. Some of them are still distant from the rest with respect to certain criteria, but with a proper calibration function, they can all be predicted with acceptable accuracy. This again shows that moderate extrapolation was easier with this method than with linear principal component regression.

To aid the comparison of the results, the RMSEP for PCR before and after MSC as well as for the LWR are shown in Figure 14 for 25 prediction samples.

### CONCLUSIONS

In this paper we have illustrated the use of multiplicative scatter correction and the nonlinear regression method called locally weighted regression based on the first few principal components using three different NIR data sets. In the examples both designed experiments and natural design were considered as well as both full-spectrum and fixed-filter instruments.

The main conclusion concerning MSC is that it provides spectral information which in a substantial (compared to the whole region) subregion seems to show a relatively linear relationship (Beer's law relationship) with the chemical concentrations. In addition to this, the MSC provided better prediction results in two out of the three cases when combined with PCR. In the third case only a slight improvement was obtained. It was also demonstrated how the MSC decreased the extremity of spectra as measured by the leverage values. This is important from a model-fit point of view as well as from a prediction (see prediction formula for PCR (14)) point of view. The conclusions were in complete accordance with those of Isaksson and Naes (9).

In all three examples the LWR based on the first two and/or three components gave good results over relatively large regions. In two of the examples it provided quite substantial improvements compared to PCR, while in the third example (which was the full-spectrum case) the PCR was better. All this indicates that the most important information

for prediction in large regions was found in the first few principal components and, when used properly, these can give good prediction results.

The results also show that neither the linear nor the nonlinear approach is universally preferable. Research should be done to investigate what types of data are suitable for the LWR. Preliminary investigations on two data sets based on mixtures of meat indicate that in these two cases, the linear approach was the best. Since these samples were collected from different animals, this points to heterogeneity or the complexity of the samples as an important factor in the comparison. It is possible that the LWR with more factors than two or three is the solution for such cases. The results for example 1 compared to those of examples two and three also indicate that the number of wavelengths used is a factor of interest in such a comparison.

Overall, the results in this paper clearly indicate that LWR is a good candidate to correct for nonlinearities in NIR relationships. It should, however, be mentioned that we only considered the weight function used by Cleveland and Devlin (12) for the weighting in the LWR method. Infinitely many possibilities exist and work should be done for optimization of the approach. Cross-validation was tested as a method for estimating the value of  $f$  (the degree of smoothing) and it gave reasonable estimates.

The fact that the main predictive information was found in two or three principal components in the examples studied also has implications for interpretation and search for structure in the sample set. The reason for this is the much better plotting possibilities in two and three dimensions than in, for example, eight dimensions.

For each prediction sample, the LWR method uses linear regression based on neighboring points. This implies that in the case of substantial nonlinearity it is very important to cover the space of principal components as well as possible to get good predictions. Designed experiments with even spread points have this property, pointing out the special importance of such designs for this type of method.

The regression method treated in this paper is only one of a number of good candidates for nonlinear regression. Some of these, for instance nonlinear PLS (22) and nonlinear principal components analysis (23) are more sophisticated than the approach used here and could of course give some improvement in certain cases. The present approach is, however, conceptually simpler and easy to use since it is based on the well established principal components analysis plus the simple concept of local linear regressions. (For the first author of this paper, the LWR algorithm was programmed in a couple of hours using MATLAB.) Another advantage with the method is that, as reported by Cleveland and Devlin (12), distribution theory for the approach based on LWR is developed for the case of normally distributed errors. This could be used for construction of, e.g., confidence bands for  $g(x_i)$  at  $x_i$ .

Since the proposed method is based on a smoothing type of regression based on principal components, it shares some basic ideas with the projection pursuit regression (PPR, mentioned above and used by Isaksson and Naes (9)). This type of regression is based on nonlinear smoothing functions of linear projections of the original variables. The difference is that PPR uses general projections rather than principal components and another type of smoother than the locally weighted regression. The similarity shows, however, that if the LWR approach based on the principal components gives a good fit, the same would be the case with PPR used on the whole spectrum. This last approach would, however, in such cases be more sensitive to overfitting than the one proposed.

The strong relation to the work of Robert et al. (24) should also be mentioned. The major difference between the two

approaches is the smoothing and the selection of variables to use in the local calibration. Robert et al. (24) used a type of local moving average, while we use a locally weighted regression. Robert et al. use the variables with highest correlation to  $y$ , while we use the components with largest variance after a scatter-correction. The present paper focuses more on the reason *why* a few principal components are sufficient and the calibration method proposed is closer to traditional calibration techniques. Which of the two strategies is the best remains to be answered.

Research has shown that transferring a calibration equation from one instrument to another or for instance changing the light source in the instrument often leads to problems. Since the method proposed here is only based on the first few principal components, it is therefore less sensitive to minor changes of the spectrum; our conjecture is that the proposed approach is a serious candidate for reasonable performance in such complicated cases. In other words, we expect the present approach to have certain robustness advantages compared to the traditional PCR or, for instance, PLS regression with many factors in the optimal solution.

#### ACKNOWLEDGMENT

Most of the work was done while the corresponding author was a visiting scientist at the Laboratory of Chemometrics, University of Washington, Seattle, WA. Don Dahlberg and Per Lea are thanked for helpful comments. Bjoerg Narum Nilsen is thanked for technical assistance.

#### SYMBOLS AND ABBREVIATIONS

$a, A$ :	number of factors (principal components)
ACE:	alternating conditional expectations
$b, b_k, b_0$ :	regression coefficients
$C_p$ :	method for determining the number of variables
CV:	cross validation
$e$ :	error term in the regression model
$f = q/I$ :	fraction of the total number of samples used in each calibration
$g(x)$ :	symbol for general regression surface
$h_{ia}$ :	leverage for sample $i$ and factor $a$
$I$ :	number of calibration samples
$I_0$ :	intensity of radiation directly on the detector
LWR:	locally weighted regression
MLR:	multiple linear regression
MSC:	multiplicative scatter correction
NIR:	near infrared reflectance
PCR:	principal component regression
PLS:	partial least squares
PPR:	projection pursuit regression
PRED:	prediction
$q$ :	number of samples in each local calibration
$q_a$ :	regression coefficients for the principal components
$R$ :	reflectance

RMS-ECV:	root mean square error of cross validation
RMS-EP:	root mean square error of prediction
SMLR:	stemwise multiple linear regression
$t_{ia}$ :	principal component score for sample $i$ and factor $a$
$u$ :	argument in weight function $W(u)$
$W$ :	weight function
$x_i$ :	spectral value at wavelength $k$
$y$ :	chemical concentration
$\rho$ :	Euclidean distance

#### LITERATURE CITED

- Hruschka, W. R. In *Near Infrared Technology in Agricultural and Food Industries*; (eds. Williams, P. C., Norris, K., Eds.; American Cereal Association: St. Paul, MN, 1987; pp 35-55.
- Martens, H.; Naes, T. In *Near-Infrared Technology in Agricultural and Food Industries*; Williams, P. C., Norris, K., Eds.; American Cereal Association: St. Paul, MN, 1987; pp 57-87.
- Cowe, I.; McNicol, J. W. *Appl. Spectrosc.* **1985**, *39*, 257-266.
- Martens, H.; Jensen, S. A. *Proceedings of the 7. th World Cereal and Bread Congress, Prague June 1982*; Holas and Kratochvíl, Eds.; Elsevier: Amsterdam, 1983; pp 607-647.
- McClure, F.; Hamid, A.; Giesbrecht, F. G.; Weeks, W. W. *Appl. Spectrosc.* **1984**, *38*, 322-329.
- Geladi, P.; McDougall, D.; Martens, H. *Appl. Spectrosc.* **1985**, *39*, 491-500.
- Hoerl, A. E.; Kennard, R. W.; Hoerl, R. W. *Appl. Stat.* **1985**, *34*, 114-120.
- Norris, K. H. (1983) *Proceedings of the IUFoST Symposium on Food Research and Data Analysis Sept. 1982, Oslo, Norway*; Martens, H., Russwurm, H., Eds.; Applied Science: Essex, UK, 1983; pp 95-113.
- Isaksson, T.; Naes, T. *Appl. Spectrosc.* **1988**, *42*, 1273-1284.
- Martens, H.; Naes, T. *Multivariate Calibration*; John Wiley and Sons; Chichester, 1989.
- Naes, T.; Isaksson, T. *Norwegian Food Research Institute*, unpublished results, 1988.
- Cleveland, W. S. J. *J. Am. Stat. Assoc.* **1988**, *83*, 596-610.
- Mandel, J. *Am. Stat.* **1982**, *36*, 15-24.
- Naes, T.; Martens, H. J. *Chemom.* **1988**, *2*, 155-167.
- Martens, H.; Jensen, S. A.; Geladi, P. *Proceedings of the Nordic Symposium on Applied Statistics* Christie, O. H. J., Ed.; Stokkand Forlag Publishers: Skagenkajen 12, N-4000 Stavanger, 1983; pp 205-233.
- Breiman, L.; Friedman, J. H. *J. Am. Stat. Assoc.* **1985**, *80*, 580-598.
- Friedman, J. H.; Stuetzle, W. *J. Am. Stat. Assoc.* **1981**, *76*, 817-823.
- Harper, A. M.; Dueser, D. L.; Kowalski, B. R.; Fasching, J. L. In *Chemometrics: Theory and Applications*; Kowalski B. R., Ed.; American Chemical Society: Washington, DC, 1977.
- Stone, M. *J. R. Stat. Soc., B.* **1974**, *111*, 111-133.
- Mallows, C. L. *Technometrics* **1973**, *15*, 661-675.
- Naes, T. *Technometrics* **1985**, *27*, 301-311.
- Wold S., Kettaneh-Wold, N.; Skagerberg, Bert *First Scandinavian Symposium on Chemometrics Oct. 6-8 1988, Lappenranta, Finland*; Minkinen, P., Ed., in press.
- Hastie, T. and Stuetzle, W. Technical report from Department of Statistics, University of Washington, Seattle, WA, 1988.
- Robert, P.; Bertrand, D.; Crochon, M.; Sabino, J. *Appl. Spectrosc.* **1989**, *43*, 1045-1049.

RECEIVED for review October 10, 1989. Accepted December 6, 1989.

# In Vitro Percutaneous Absorptiometry by Simultaneous Measurement Using the Photoacoustic Method and Absorbance

Ryuichi Takamoto, Ryujiro Namba, Okitsugu Nakata, and Tsuguo Sawada\*<sup>1</sup>

Shiseido Co., Ltd., Toxicological & Analytical Research Center, 1050 Nippa-cho, Kohoku-ku, Yokohama 223, Japan

A novel in vitro percutaneous absorptiometry utilizing a portable open-ended photoacoustic (PA) cell as the longitudinal diffusion cell was developed. With this system it was feasible to measure the reduction of drug applied to a membrane by the PA method and the amount of drug penetrating the membrane to the diffusion cell by absorbance, simultaneously in real time. A shikonin ointment prepared in a hydrocarbon vehicle was used as the model sample. The in vitro percutaneous absorptiometry was performed by means of a physiological saline solution and the skin of a hairless mouse. As a result, after the lag time the absorbance increased in proportion to time, whereas the PA signal reduced in proportion to the square root of time. As the signal obtained by the PA method corresponds to the amount of drug released from the ointment, a good correlation with Higuchi's theory is attained. Consequently, these results suggested the usefulness of this novel percutaneous absorptiometry technique which utilizes the PA method.

## INTRODUCTION

Establishment of an appropriate test method is indispensable for research and development in percutaneous absorptiometry. Various methods of percutaneous absorptiometry have been reported, although needless to say that most such methods employed by numerous researchers, as well as those used generally, are in vitro methods using a diffusion cell. In this method, the donor side and the receiver side of the diffusion cell must be filled with physiological saline solution or a certain solvent depending on the purpose of the test. This in vitro test is easily operable and the results are reproducible. Additionally, the results can be analyzed fairly easily by using Higuchi's theory (1). For example, the amount of drug released from such a suspension-type ointment can be calculated by this diffusion theory. If the release is less than 30%, the equation is given by

$$Q = (D(2C_0 - C_s)C_s t)^{1/2} \quad (1)$$

where  $Q$  is the amount of drug released per unit area of application,  $D$  is the diffusion coefficient of drug in the ointment,  $C_0$  is the initial concentration of drug in the ointment,  $C_s$  is the solubility of the drug in the ointment, and  $t$  is the time after application. This equation can also be described as

$$Q = kt^{1/2} \quad (k = \text{constant}) \quad (2)$$

According to these remarkably simple relationships, the amount of drug released from such a suspension-type ointment is shown to be proportional to the square root of time.

We came up with an idea that if by means of a longitudinal cell, which more closely reflects the clinical conditions as compared to the conventional parallel cell, we could both sensitively and simultaneously at real time measure the

reduction of drug on the donor and its increase on the receiver side, we could obtain all the information related to the vehicle, the drug, and its penetration in a single sample run. Thus, we developed a novel in vitro test method capable of simultaneously measuring the reduction of drug on the donor side by the PA method and the amount of drug penetrating through the skin by absorbance, in real time. A laser beam was employed as the light source. The portable open-ended PA cell that we developed was used for the PA method. Applications of percutaneous absorptiometry by the PA method using the open-ended PA cell have been reported by Kolmel et al. (2, 3) and its usefulness has been demonstrated.

We targeted the development of a hypersensitive in vitro test method using a laser beam as the light source. Furthermore, by applying the PA method and absorbance simultaneously to the longitudinal diffusion cell, we could expect that the cutaneous permeability of the drug and the releasing rate of the drug from the vehicle can be analyzed in closer relation to actual clinical conditions.

Thus, the newly developed in vitro test method for measuring PA signal and absorbance simultaneously was applied to the membrane transmission test by using an artificial membrane and in vitro percutaneous absorptiometry using the skin of a hairless mouse, to study its validity.

## EXPERIMENTAL SECTION

The in vitro percutaneous absorptiometer for simultaneously measuring the PA signal and absorbance was developed, as shown in Figures 1 and 2. The argon laser beam (wavelength, 488 nm; Spectra Physics, Model-164) used as the radiation source was intensely modulated with an A.O. modulator (Intra Action Corp., AOM-40) at 3.3 kHz (Function Synthesizer, NF, 1925) and was separated into two spectral directions, for both PA and absorbance measurements. The intensity of the radiation source was adjusted so as to give an output of 10 mW (below the maximum permissible exposure (MPE) on human skin) from the optical fiber (Mitsubishi Rayon, SK-40, 1 mm in diameter  $\times$  1 m) at the PA cell. The portable open-ended PA cell consisting mainly of brass was processed as a stick and chromium plated to enhance the scattering of light. Furthermore, it was equipped with an optical fiber to allow freedom of measurement, and the microphone could be moved to control the volume inside the cell. The capacity and the thickness of the air layer inside the cell were 0.1 cm<sup>3</sup> and 0.2 cm, respectively. The pipe connecting the sample chamber with the microphone chamber was 12 cm long. These values were chosen so that the cell would resonate at several kilohertz, a frequency which is hardly influenced by neither the surface potential of skin nor environmental noises. Before measurement, the microphone chamber of the cell was shifted around to control the capacity of the cell to maximize the amplification of PA signals by resonance. The obtained PA signals were analyzed by a lock-in amplifier (NF, 5610A) and thereafter recorded on a chart recorder (Rikadenki Kogyo, NP-0393). The laser beam for measuring the absorbance was further separated into two directions, one for the quartz longitudinal diffusion cell (Corp. Atock) capable of measuring absorbance and the other to the photocell (United Detector Technology, PIN-10DP) as the reference signal ( $I_0$ ). The measured signal ( $I$ ) and the reference signal ( $I_0$ ) were introduced into a differential amplifier (NF, P-61), and after calculation of the absorbance ( $-\log(I/I_0)$ ) with a computer (Nippon Denki, PC9801-VX), the relation between PA signal and absorbance as

<sup>1</sup> Present address: Department of Industrial Chemistry, Faculty of Engineering, The University of Tokyo, 7-3-1 Hongo, Bunkyo-ku Tokyo 113, Japan.



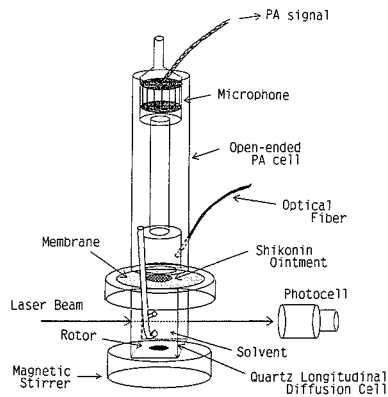


Figure 1. Illustration of diffusion cell applied in simultaneous measurement of the PA method and absorbance.

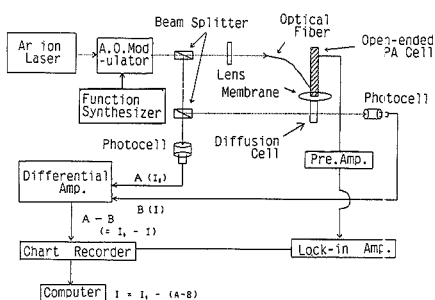


Figure 2. Diagram of the in vitro percutaneous absorptometry by simultaneous measurement of PA signal and absorbance.

a function of time was determined.

The major noise factors that affected the measurement of absorbance were scattered beams of laser and room light. By performing the experiments in a dark room and also by covering the photocell with an aluminum sheet to avoid light scattering, it became possible to transmit only the laser beam to the receiver side for optimum detection. The laser beam was emitted onto a point that was found not to be affected by stirring the solution. During measurement by the open-ended PA cell, a spike noise was found to generate when the rotor contacted the quartz cell. Therefore, the shape of the rotor was modified so as to give a stable rotation without touching the quartz cell. Consequently, a stable signal of less than 10% variation was achieved.

Shikonin ((S)-5,8-Dihydroxy-2-(1-hydroxy-4-methyl-3-pentenyl)-1,4-naphthalenedione;  $C_{16}H_{16}O_5$ , Wako Pure Chemical, Reagent class, >95%), a wound healing drug, which absorbs 488-nm light, was chosen as the model sample. Ointments containing 0.1–1%, 2%, and 3% of shikonin in a hydrocarbon base (Taisho Pharmaceutical, Plastibase) were prepared. Shikonin was dissolved in isopropyl alcohol (IPA) and mixed with the base, and the solvent was evaporated under vacuum. A porous silicone membrane (Fuji System) and the skin (defatted) of a hairless mouse (male mouse of SKH/HR-1 strain, 6 weeks old), were used. IPA and physiological saline solution were employed as solvents for the receiver side of the diffusion cell.

## RESULTS AND DISCUSSION

**Precision and Sensitivity of the Simultaneous PA/Absorbance Measuring System.** The precision of detection of PA/absorbance measurements for shikonin was investigated. Shikonin ointments (0.1–1.0%) were applied to a silicone membrane at an amount of 2 mg and a 5 mm diameter circle (0.2  $cm^2$ ), respectively, and were used as standard samples for the PA measurements. To measure the absor-

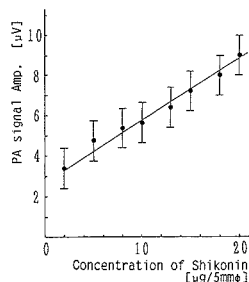


Figure 3. Calibration curve of shikonin ointment by open-ended PA cell ( $\pm 1$  SD shown in error bars).

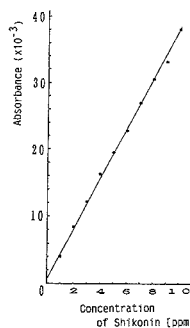


Figure 4. Calibration curve of shikonin by absorbance method.

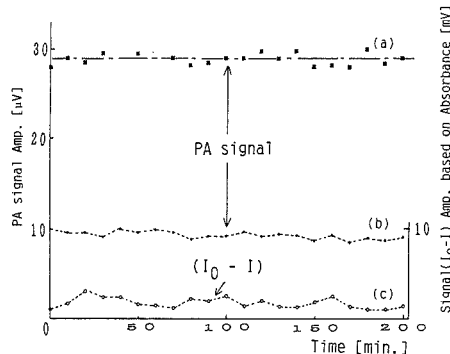


Figure 5. Stability of a novel in vitro percutaneous absorptometry: (a) sample, 3% Shikonin ointment; solvent, nil; (b,c) sample, vehicle; solvent, physiological saline solution.

bance, shikonin solutions (0.1–10 ppm in IPA) were applied to the receiver side of the diffusion cell. In Figures 3 and 4 are shown the results of the calibration curves for the PA/absorbance measurements. The PA signal obtained by an open-ended PA cell, gave a signal to noise (S/N) ratio of 46 and a correlation coefficient of 0.991 for shikonin (2–20  $\mu g/5$  mm diameter) with  $\pm 1$  standard deviation (SD). The correlation coefficient for the absorbance measurements was 0.998 for shikonin at 0.1–10 ppm. The next experiment was performed by applying only the base material to the silicone membrane, and the receiver side of the diffusion cell was filled with physiological saline solution. As shown in Figure 5, PA signal and the absorbance were found to be relatively constant. No bubbles were observed between the membrane and the receiver, until the end of measurement. Furthermore, the

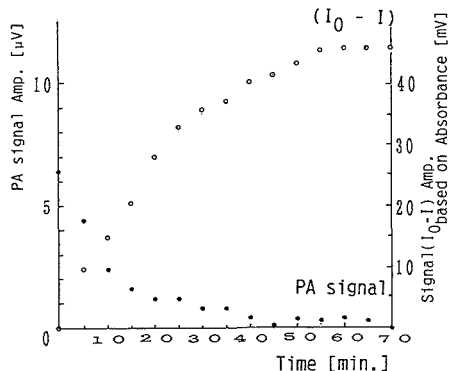


Figure 6. Permeability in vitro experiment with artificial membrane.

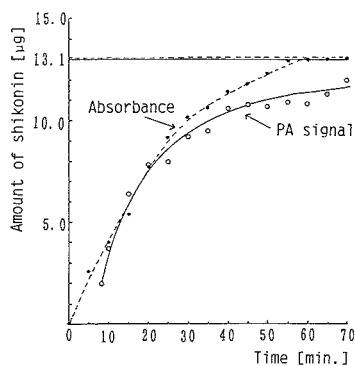


Figure 7. Comparison of absorbance (amount of shikonin passing through the membrane) and PA signal (amount of shikonin released from the ointment).

effect of shikonin upon laser beam emission was studied, the result of which is also shown in Figure 5. When PA signal was measured with an argon laser of 488 nm of the 3% shikonin ointment as the sample applied on a silicone membrane, the PA signal was found to be constant after repeated radiation of the beam for 200 min, implying that shikonin is not decomposed under this condition. Furthermore, the same result was obtained under radiation for up to 25 h.

#### Permeability Experiment with Artificial Membrane.

PA signal and absorbance were measured simultaneously on 1.3 mg of 1% shikonin ointment (equivalent to 13 µg of shikonin) applied (5 mm diameter) on a silicone membrane, using IPA as the diffusion cell solvent. As seen from Figure 6, the PA signal decreased as the absorbance increased. Since shikonin dissolves well in IPA in this system, the diffusion rate of shikonin in the membrane is very fast. It was observed that after a lag time of about 30 s, the absorbance increased, and 60 min later, only the vehicle remained on the membrane. The relationship between the amount of shikonin determined from the calibration graphs (Figures 3 and 4) and time is shown in Figure 7. The amount of shikonin at 60 min, as calculated from absorbance, was 13.1 µg, which was identical with the amount initially applied. Therefore, 100% of the initially applied shikonin can be considered to have transmitted the membrane. After about 30 min, the graph gradually loses linearity, which is possibly due to the reduction of concentration gradient at the donor and receiver sides of the cell. Time course of PA signal was assayed assuming that

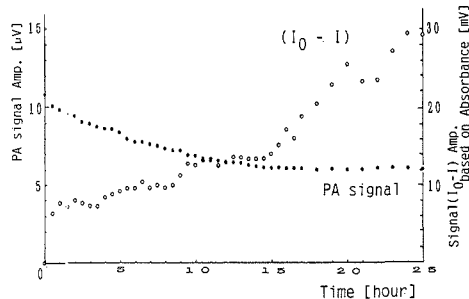


Figure 8. In vitro percutaneous absorptiometry using hairless mouse skin.

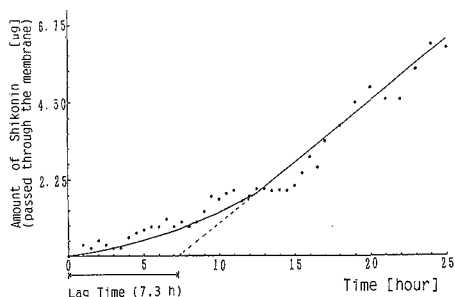


Figure 9. Time course of shikonin passing through the membrane determined from the absorbance.

the difference between the initial PA signal ( $Q_0$ ) and that  $t$  hours later ( $Q_t$ ), namely  $(Q_0 - Q_t)$ , corresponds to the amount of shikonin released from the ointment after  $t$  hours. Accordingly, it can be considered as the release of shikonin from the ointment, as a function of time. From these results, it seems that the time course of PA signal is interpretable to absorbance, or vice versa. It is considered that the difference between the PA curve and the absorbance curve is mainly due to the variation (20%,  $\pm 1$  SD) of PA calibration curve (Figure 3). Since the diffusion coefficient of shikonin is extremely high in this system, not much time difference is expected between the decrease of shikonin above the membrane and its increase below the membrane. Hence, the results obtained are considered fairly reasonable. Furthermore, the time course of PA signal was shown to indicate the reduction of shikonin above the membrane, and it was found that the transmission of drug through the membrane can be evaluated by the PA method.

#### In Vitro Percutaneous Absorptiometry Using Hairless Mouse Skin.

A series of in vitro percutaneous absorptiometries was performed on the skin of hairless mouse. Within a 5 mm diameter circle on the skin of a hairless mouse (defatted), 5 mg of 3% shikonin ointment (equivalent to 180 µg of shikonin) was applied. Employing physiological saline solution as the diffusion cell solvent, the absorbance and PA signal were measured simultaneously. The result is shown in Figure 8. An increase in absorbance and decrease in PA signal were also observed in the hairless mouse skin system, resembling a living body. Fluctuations in the absorbance are considered to be caused by floating matter and water-soluble matter deriving from the skin. Quantification of shikonin as calculated from absorbance is shown in Figure 9. The amount of shikonin passing through the skin started to increase proportionally to time after the 7 h lag time, and it was found that 3.4% of the initially applied shikonin had transmitted

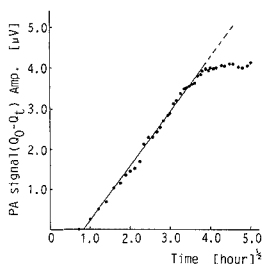


Figure 10. Correlation between PA signal ( $Q_0 - Q_t$ ) and square root of time.

the skin after 25 h. The rather longer lag time observed here is probably due to temperature (4), which in this experiment was ambient (20 °C), whereas the *in vitro* percutaneous absorptiometry experiments were undergone at 37 °C, with respect to body temperature. After 25 h, hardly any bubbles were observed between the skin and the receiver. Further, the PA signal ( $Q_0 - Q_t$ ), corresponding to the release of shikonin from the ointment, increased in proportion to the square root of time as shown in Figure 10. This result correlates favorably with Higuchi's theory. After about 15 h, the graph gradually loses linearity, which is possibly deriving from the reduction of partition coefficient (skin/vehicle) of shikonin due to the concentration of the receiver side approaching a saturated state.

Consequently, we can expect this *in vitro* percutaneous absorptiometry system, whereby the PA signal and the absorbance is measured simultaneously, to be capable of analyzing both the drug-releasing process and its transmission process through the skin, real time, in a system resembling actual clinical conditions.

### CONCLUSION

A novel *in vitro* percutaneous absorptiometry system, capable of measuring the reduction of the drug above the skin and the amount permeating through the skin simultaneously in real time, was developed upon application of the PA signal and absorbance measurement utilizing a longitudinal diffusion cell. Experiments performed on model shikonin ointments confirmed the following two points. First of all, in the system

using silicone membrane with high diffusion coefficient of drug, the time course of PA signal and absorbance showed a similar trend. In a practical *in vitro* percutaneous permeability experiment using the skin of a hairless mouse, the PA signal showed a favorable correlation with Higuchi's theory. These results suggested the usefulness of this newly developed *in vitro* percutaneous absorptiometry, enabling us to measure the PA signal and absorbance simultaneously. A practical problem, yet unsolved with regard to using a laser beam as the light source, is the limitation in wavelength despite its high sensitivity, which restricts the number of drugs amenable to this technique. However, by oscillating multiple Ar<sup>+</sup> laser beams and using a nonlinear optical crystal wavelength conversion unit (Ascal, UVA-4), CW-UV lights of several wavelengths are attainable. By oscillating UV light with this method, we have recently carried out a series of experiments on various drugs. This newly developed *in vitro* percutaneous absorptiometry system can be further modified by introducing a thermoregulating device with which to control the temperature of the diffusion cell solvent. By doing so, we should be able to perform various studies, such as the releasing process of drugs and vehicle, under conditions resembling those of actual clinical situations. From this study it became clear that the membrane transmission phenomenon of a drug is measurable by means of a portable open-ended PA cell. Applications of this PA cell to the measurement of human percutaneous absorption *in vivo* are under way.

### ACKNOWLEDGMENT

The authors thank Fujihiro Kanda (Toxicological & Analytical Research Center, Shiseido Co., Ltd.) for help in critical reading of this paper.

Registry No. Shikonin, 517-89-5.

### LITERATURE CITED

- (1) Higuchi, T. *J. Pharm. Sci.* **1961**, *50*, 874-875.
- (2) Kolmel, K.; Sennhenn, B.; Giese, K. *J. Soc. Cosmet. Chem.* **1986**, *37*, 375-385.
- (3) Giese, K.; Nicolaus, A.; Sennhenn, B.; Kolmel, K. *Can. J. Phys.* **1986**, *64*, 1139-1142.
- (4) Fritsch, W. C.; Stoughton, R. B. *J. Invest. Dermatol.* **1963**, *41*, 307-312.

RECEIVED for review August 22, 1989. Accepted December 18, 1989.

# Surface-Enhanced Raman Spectroscopy at a Silver Electrode as a Detection System in Flowing Streams

Neil J. Pothier and R. Ken Forcé\*

Department of Chemistry, University of Rhode Island, Kingston, Rhode Island 02881

**An analytical application for surface-enhanced Raman spectroscopy at a silver electrode is described. Raman spectra of several DNA bases have been recorded in a 30- $\mu$ L flow cell under flowing conditions. An optical multichannel analyzer allowed high-quality spectra to be recorded with integration times of less than 5 s. The Raman intensity vs concentration yields a monotonic relationship over 4 orders of magnitude. Limits of detection for adenine, thymine, and cytosine were 175, 233, and 211 pmol, respectively. The samples could be rapidly desorbed off the surface of the electrode in less than 10 s. The technique shows promise as a solute property detector for high-performance liquid chromatography and flow injection analysis.**

## INTRODUCTION

Surface-enhanced Raman spectroscopy (SERS) has received considerable interest since first reported in 1974 by Fleischmann and co-workers (1). Several articles appearing in the literature are directed toward a better theoretical understanding associated with the giant enhancement in the Raman spectra of molecules resulting from interactions at or near a SERS active surface (2-4). SERS has been studied most extensively in silver sols and films and at roughened silver and gold electrodes (5-10). Recent applications of SERS include Ag microspheres and Ag-coated filter paper (11, 12). Excellent reviews on the theory and application of SERS have recently appeared (13, 14). However, only a few articles have appeared detailing SERS as a useful analytical technique in flowing streams (15-18).

Our research is directed toward the development of SERS as a detector for high-performance liquid chromatography (HPLC) and flow injection analysis (FIA). From previous work we have demonstrated the ability to collect SERS spectra of 0.05 M pyridine in aqueous media under dynamic conditions in a 200- $\mu$ L Raman flow cell (17). In a three-electrode 30- $\mu$ L flow cell under flowing conditions we have demonstrated the ability to rapidly adsorb and desorb selected DNA bases by controlling the applied potential at a silver electrode. In addition we have successfully demonstrated with an optical multichannel analyzer (OMA) that high-quality spectra spanning a 800- $\text{cm}^{-1}$  window can be collected in less than 5 s, yielding the vibrational molecular fingerprint of solutes eluting through the cell.

## EXPERIMENTAL SECTION

**Instrumentation.** The SERS flow cell utilizes a three-electrode system consisting of a 4 mm o.d. silver working electrode, a platinum foil auxiliary electrode, and a saturated calomel electrode (SCE) mounted in a Plexiglas cell constructed in our laboratories. See Figure 1. The silver working electrode consists of 4 mm diameter Ag foil which has been epoxy cemented into a 4 mm glass tube and soldered to a copper lead. The electrode is easily removed for polishing or alignment from its threaded housing. Two standard HPLC fittings act as inlet and exit ports and a glass microscope slide provides a window for spectroscopic detection. The platinum (1 mil thick) foil auxiliary electrode

surrounds the working electrode to minimize variations in the potential field. A gasket provides a nominal cell volume of 30  $\mu$ L.

The cell was evaluated in two different spectrographic systems. System 1 utilized a Jarrell-Ash  $3/4$ -m Czerny-Turner single monochromator with a 1180 lines/mm grating blazed at 500 nm. Incident 514.5-nm radiation from a Spectra-Physics Model 2000 Ar<sup>+</sup> ion laser operated at 20 mW at the cell served as the source. A camera lens collected and focused the scattered light onto the entrance slit of the monochromator. A Shott OC 550 cutoff filter was used to attenuate the incident laser radiation and allowed for a window from 900 to 1700  $\text{cm}^{-1}$  to appear across the focal plane of the polychromator. Because of the spectral limits of the cutoff filter, Raman bands below about 900  $\text{cm}^{-1}$  could not be observed. Mounted at the exit focal plane is an OMA (Princeton Instruments Model IRY-700 Demo) regulated by a Model ST-120 controller. The OMA was operated at -20  $^{\circ}$ C. Data from the OMA was controlled and stored on a Dell Model 220 microcomputer using DMA software obtained from Princeton Instruments.

A potentiostat (PARC Model 364) was used to maintain potentiostatic control of the cell and to electrochemically roughen the silver electrode surface by oxidation-reduction cycles (ORC's). For SERS to occur the surface of the electrode must be roughened from an ORC. The silver electrode is first polished with 6-, then 3-, and finally 1- $\mu$ m diamond paste and rinsed with distilled water, methyl alcohol, and again with water and placed in the SERS cell. The ORC's consist of stepping the voltage to +0.2 V vs SCE in order to pass between 100 and 150  $\text{mC}/\text{cm}^2$  and then stepping the voltage to -0.6 V where the greatest enhancement for pyridine and other nitrogen-based compounds have been reported (18, 19). This procedure yielded a very reproducible surface. The solutes are injected into the flowing solvent, and when the solutes entered the cell another 1-2 s ORC is performed. Preliminary results showed that the greatest enhancement was obtained when an ORC was performed while the solute was present in the cell.

An Altex Model 110A HPLC pump was used to maintain a constant flow of solvent through the cell. The mobile phase consisted of 0.1 M KCl in 0.01 M  $\text{KH}_2\text{PO}_4$  buffer adjusted to pH 7.00 with KOH.

Because the most intense Raman bands for the DNA bases examined in this study all lie below 900  $\text{cm}^{-1}$ , the single spectrograph with cutoff filter prevented their study on that system. Therefore, a second instrument configuration utilizing a Spex 1401 double monochromator with the same collection optics as described above was employed. The OMA was mounted at the exit slit where the conventional photomultiplier tube is housed. With this configuration, we had adequate stray light rejection. However, only a 50-70- $\text{cm}^{-1}$  optical window could be viewed across the face of the OMA because the intermediate and exit slits of the Spex were not removed. Since the objective was to evaluate the time response under potentials leading to selective adsorption or desorption of the analyte to the Ag electrode, this was not a serious limitation. Limits of detection studies were evaluated with this arrangement.

All chemicals used were ACS reagent grade and used without further purification. Adenine, cytosine, and thymine were obtained from Sigma Chemical Co. (St. Louis, MO). The mobile phase consisted of 0.1 M KCl and 0.01 M  $\text{KH}_2\text{PO}_4$  (Fisher Scientific Co.) buffered at pH 7.00 and was used to dissolve the DNA bases. A solution of 0.05 M pyridine (Fisher) was also prepared in this mobile phase. Serial dilutions of adenine, thymine, and cytosine were prepared from 5.88, 7.77, and 7.02 mM stock solutions, respectively.

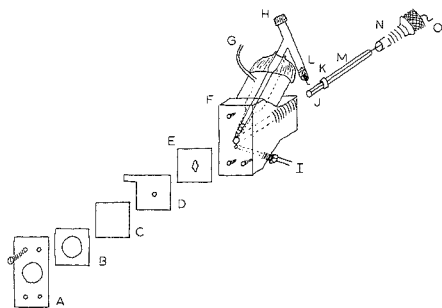


**Figure 1.** 30- $\mu$ L SERS flow cell: (A) metal window frame; (B) rubber gasket; (C) 2 cm  $\times$  2 cm  $\times$  1 mm glass window; (D) platinum foil auxiliary electrode; (E) 30- $\mu$ L gasket; (F) Plexiglas cell; (G) exit tubing; (H) calomel reference electrode; (I) inlet tubing; (J) silver working electrode; (K) rubber O-ring; (L) silver wire lead; (M) 4-mm glass tubing; (N) knurled nut; (O) copper lead.

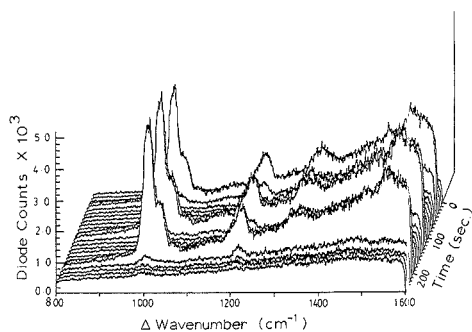


**Figure 2.** 200- $\mu$ L repeat injections of 0.05 M pyridine injected into phosphate buffered 0.1 M KCl flowing at 1.0 mL/min.

## RESULTS AND DISCUSSION

For SERS to be of practical use as a detector for high-performance liquid chromatography (HPLC) and flow injection analysis (FIA) it is necessary that the analyte be rapidly and selectively removable from the electrode surface. As can be seen in Figure 2 with 200  $\mu$ L repeat injections of 0.05 M pyridine into the phosphate-buffered KCl flowing at 1.0 mL/min, we can repetitively cycle and analyze on and off the electrode with very rapid time response. At the time of injection, the electrode was subjected to a rapid 1-s ORC; the potential was then manually adjusted to  $-0.6$  V vs SCE and held there for 20–30 s and was then manually adjusted to  $-1.2$  V to desorb the analyte. Raman spectra were obtained continuously during this time and either stored in memory or written to disk. As can be seen, the reproducibility from one injection to another is excellent. Also, it is clear that the analyte can be completely removed from the electrode in less than 10 s under flowing conditions. The signal was integrated on the face of the OMA for 5 s and every other frame was stored. To verify the efficiency of removal, on selected injections, after desorbing the analyte, the potential was manually adjusted back to  $-0.6$  V after about 30 s and no evidence of any pyridine could be detected.

Illustrated in Figure 3 are the time-dependent traces for 400- $\mu$ L injections of adenine, cytosine, and thymine into the phosphate buffered 0.1 M KCl flowing at 1.0 mL/min. At the time of injection, the electrode was subjected to a 1-s ORC, the potential was manually adjusted to  $-0.6$  V, two or three frames were integrated, and then the potential was manually

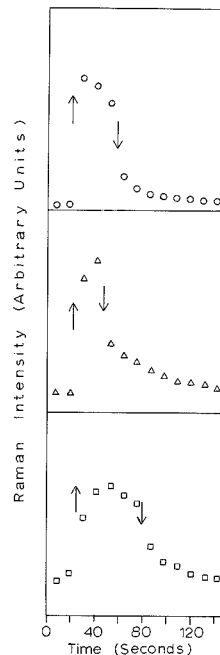


**Figure 3.** 400- $\mu$ L injections of 5.10 mM adenine (O) detected at 732  $\text{cm}^{-1}$ , 9.83 mM cytosine ( $\Delta$ ) detected at 796  $\text{cm}^{-1}$ , and 4.96 mM thymine ( $\square$ ) detected at 776  $\text{cm}^{-1}$ . The upward pointing arrows ( $\uparrow$ ) indicate the potential step to  $-0.6$  V, the enhancing potential. The downward pointing arrows ( $\downarrow$ ) indicate the potential step to  $-1.3$  V, the desorbing potential.

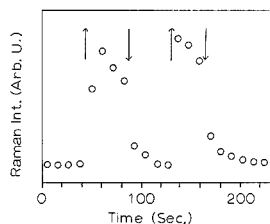


**Figure 4.** Duplicate 400- $\mu$ L injections of 5.10 mM adenine injected into phosphate buffered 0.1 M KCl flowing at 1.0 mL/min, detected at 732  $\text{cm}^{-1}$ . The upward pointing arrows ( $\uparrow$ ) indicate the potential step to  $-0.6$  V, the enhancing potential. The downward pointing arrows ( $\downarrow$ ) indicate the potential step to  $-1.3$  V, the desorbing potential.

adjusted to  $-1.3$  V to desorb the analyte. It proved necessary to step to a more cathodic potential to efficiently remove the DNA bases from the surface of the electrode. Adenine was found to give somewhat higher enhancement than either cytosine or thymine. If one closely examines Figure 3, it can be seen that the majority of the material can be eluted from the electrode in about 10 s. The downward pointing arrows indicate the point where the potential was stepped to  $-1.3$  V, the desorbing potential. The delay in analyte removal is in part attributed to a large (400  $\mu$ L) dead volume between injection and cell. With this taken into account, the majority of the analyte is removed from the electrode in a fraction of a second. For each run, the spectra were integrated for 5 s, and every other frame was stored in memory. As can be seen from Figure 4, repeat injections of adenine showed a reproducibility of 5%.

To determine the sensitivity of SERS at a Ag electrode for selected DNA bases, standard solutions of adenine were injected under stopped flow conditions and the intensity of the 732-cm<sup>-1</sup> band was integrated for 5 s. Stopped-flow conditions were utilized because of the difficulty in coordinating manual adjustment of the potentiostat and the applied potential as the analyte entered the cell. The intensity showed a monotonic relationship with concentration and a detection limit of 510 pmol. In addition, under stopped-flow conditions, adenine, thymine, and cytosine limits of detection were evaluated with a photomultiplier tube (RCA C31034-RF) and yielded 175, 233, and 211 pmol, respectively. Even though the cell volume reported here is at least a factor of 5-10 smaller than any other design reported in the literature, it is not optimum, and only a very small fraction of the total cell volume is being interrogated by the laser beam. Also, since SERS is a surface phenomenon, a very small fraction of the total analyte in the cell is being probed. With further improvements in cell volume and the ratio of cell volume to electrode area, it should be possible to considerably reduce the limits of detection below those reported here.

This research has clearly proven the rapid response to adsorption and desorption controlled by potential modulation at the silver electrode. The technique yields good reproducibility. The concentration and volume ranges are rapidly approaching those necessary for modern liquid chromatographic systems. The need for a solute property detector yielding qualitative and quantitative information is of extreme importance in complex biochemical separations, and we feel SERS at a Ag electrode may prove beneficial as a detector for HPLC and FIA.

Continuing research in this laboratory is directed toward the utilization of gold electrodes, which have proven a very stable SERS active substrate (20-22). In addition further

miniaturization of the cell and computer control of the potentiostat are presently under development.

#### ACKNOWLEDGMENT

We thank Charles Nittrouer and Princeton Instruments for the use of the optical multichannel analyzer and associated data acquisition hardware and software.

#### LITERATURE CITED

- (1) Fleischmann, M.; Hendra, P. J.; McQuillan, A. J. *Chem. Phys. Lett.* **1974**, *26*, 163.
- (2) *Surface Enhanced Raman Spectroscopy*; Chang, R. K., Furak, T. E., Eds.; Plenum Press, New York, 1982.
- (3) Fleischman, M.; Hill, I. R. *Compr. Treatise Electrochem.* **1984**, *8*, 373.
- (4) Jeanmire, D. L.; Van Duyne, R. P. *J. Electroanal. Chem. Interfacial Electrochem.* **1977**, *84*, 1.
- (5) Suh, J. S.; Moskovits, M. *J. Am. Chem. Soc.* **1986**, *108*, 4711.
- (6) Moskovits, M.; Suh, J. S. *J. Phys. Chem.* **1984**, *88*, 1293.
- (7) Joo, T. H.; Kim, M. S. *Chem. Phys. Lett.* **1984**, *112*, 65.
- (8) Chou, Y. C.; Liang, N. T.; Tse, W. S. *J. Raman Spectrosc.* **1986**, *17*, 481.
- (9) Gao, P.; Gosztola, D.; Leung, L.; Weaver, M. J. *Electroanal. Chem. Interfacial Electrochem.* **1987**, *233*, 211.
- (10) Weaver, M. J.; Hupp, J. T.; Barz, F.; Gordon, J. G., II; Philpott, M. R. *J. Electroanal. Chem. Interfacial Electrochem.* **1984**, *160*, 321.
- (11) Vo-Dinh, T.; Uzeil, M.; Morrison, A. L. *Appl. Spectrosc.* **1987**, *41*, 4.
- (12) Laserna, J. J.; Campiglia, A. D.; Winefordner, J. D. *Anal. Chem. Acta* **1981**, *208*, 21.
- (13) Garrell, R. L. *Anal. Chem.* **1989**, *61*, 401A.
- (14) Birko, R. L.; Lombardi, J. R. *Spectroelectrochemistry, Theory and Practice*; Gale, R. J., Ed.; Plenum Press: New York, 1988.
- (15) Ni, F.; Thomas, L.; Cotton, T. M. *Anal. Chem.* **1989**, *61*, 888.
- (16) Berthod, A.; Laserna, J. J.; Winefordner, J. D. *Appl. Spectrosc.* **1987**, *41*, 1137.
- (17) Forcé, R. K. *Anal. Chem.* **1989**, *60*, 1987.
- (18) Freeman, R. D.; Hammaker, R. M.; Meloan, C. E.; Fateley, W. G. *Appl. Spectrosc.* **1988**, *42*, 456.
- (19) Leung, L. W. H.; Weaver, M. J. *J. Am. Chem. Soc.* **1987**, *109*, 5113.
- (20) Garrell, R. L.; Beer, K. D. *Spectrochim. Acta* **1988**, *43*, 617.
- (21) Patterson, M. L.; Weaver, M. J. *J. Phys. Chem.* **1985**, *89*, 1331.

RECEIVED for review August 11, 1989. Revised manuscript received December 26, 1989. Accepted January 2, 1990.

## Laser-Induced-Fluorescence Detection of Sodium Atomized by a Microwave-Induced Plasma with Tungsten Filament Vaporization

Yuji Oki,\* Hisanori Uda, Chikahisa Honda, Mitsuo Maeda, Jun Izumi,<sup>1</sup> Takashi Morimoto,<sup>1</sup> and Masazumi Tanoura<sup>1</sup>

Department of Electrical Engineering, Kyushu University, Hakozaki, Fukuoka 812, Japan

The laser-induced-fluorescence (LIF) technique is applied to the detection of Na atoms in pure water for a concentration range down to pg/cm<sup>3</sup>. Na compounds are dissociated by a microwave-induced plasma of He with a tungsten filament vaporization system. Calibrating the absolute density at the observing region, the efficiency of this atomizer is estimated. It is shown that the atomizer can generate high atomic densities by filament heating. For example, the number density reaches 10<sup>7</sup> atoms/cm<sup>3</sup> for a 10-μL sample of 1 pg/cm<sup>3</sup>.

The sensitivity of laser-induced-fluorescence (LIF) spectroscopy with a tunable dye laser is excellent especially for

<sup>1</sup>Nagasaki R & D Center, Mitsubishi Heavy Industries, Ltd., 1-1 Akunoura-machi, Nagasaki 850-91, Japan

the detection of atomic species. In an extreme case, the detection of individual atoms is possible when using a vapor cell or an atomic beam (1-4). Applications of these techniques to the atomic analysis are expected to provide sensitivity much higher than traditional methods. The first application of LIF to the flame atomic fluorescence spectroscopy was reported Fraser and Winefordner in 1971 (5, 6). Detection limits of metals (Ca, Na, Sr, Mg, etc.) lower than 1 ng/cm<sup>3</sup> were reported by Weeks et al. (7); furthermore, lower detection limits were obtained with a graphite furnace. For example, Hohimer and Hargis obtained 20 pg/cm<sup>3</sup> in Cs (8) and 0.5 pg/cm<sup>3</sup> in Ti (9).

In LIF, it is not difficult to detect atoms with concentrations as low as 10<sup>6</sup>-10<sup>8</sup> atoms/cm<sup>3</sup> in an atomic vapor cell. The potentiality of the LIF method in the detection sensitivity is extremely large. However, the atomizer usually limits it.

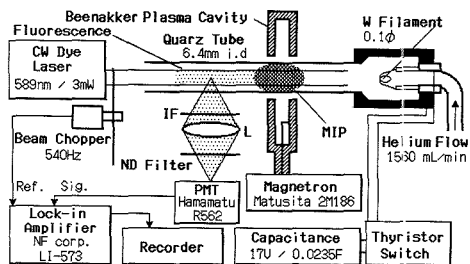


Figure 1. Instrument design.

Therefore, it is important to evaluate the performances of the atomizer, that is, the atomizing efficiency, the background radiation, the fluorescence quenching, and so on.

In this paper, we report the LIF detection of Na atoms atomized by a microwave-induced plasma (MIP) of He with a tungsten filament vaporization system (10) with a detection sensitivity on the order of  $\text{pg}/\text{cm}^3$ . We also have measured the absolute number of dissociated Na atoms by comparing the fluorescence intensity of three Na vapor cells buffered with He, have evaluated the atomizing efficiency, and have discussed the detection limit of this method.

### EXPERIMENTAL SECTION

Figure 1 shows the experimental setup. A continuous wave (CW) dye laser, pumped by an argon ion laser (Spectra Physics 164) and tuned by a tuning wedge and two solid etalons, was used for excitation of the  $D_2$  line of Na atoms. The laser spectral bandwidth was  $\sim 3.3$  pm. The fluorescence was detected with a photomultiplier tube (PMT) through an interference filter (IF) with a spectral bandwidth of 1 nm and a maximum transmission of 70%. The LIF signal was recorded by a pen recorder through a lock-in amplifier (NF Corp., LI-573) or directly recorded by a storage oscilloscope. If necessary, ND filters were used to prevent PMT saturation.

The atomizer was constructed from a Beekker-type microwave cavity (11), a quartz discharge tube, and a filament chamber. The filament was a looped tungsten wire of 0.1 mm diameter mounted in an acrylic chamber. He carrier gas flowed through the discharge tube which was open to the atmosphere. The discharge tube (6.4 mm i.d., 10 mm o.d.) was made of synthesized quartz having a Na concentration was less than 0.05 ppm in order to avoid fluorescence from atoms sputtered from the wall. The microwave plasma was generated by means of a cavity (83 mm diameter, 10 mm thickness) powered by a magnetron through a coaxial cable.

The analytical procedure is as follows. Water samples of 10  $\mu\text{L}$  were placed on the filament, and slowly evaporated by heating with a current of 1.7 A for 1 min while flowing He carrier gas. After the MIP was turned on with a magnetron current of 40 mA (80 W), the filament was flash heated by a 0.0235-F capacitor charged to 17 V. The discharge current had an exponential shape with a decay time of 100 ms. When the dye laser was tuned to the  $D_2$  line of Na, fluorescence at the same wavelength was observed over a range of about 10 mm downstream from the microwave cavity for about 100 ms after filament flashing. Since there was no severe background light from the MIP in this position, fluorescence could be observed with a good signal to noise (S/N) ratio.

To calibrate the absolute Na number density in the atomizer, we prepared three Na vapor cells made of Pyrex glass, whose internal He buffer gas pressures were 760, 350, and less than 1 Torr, respectively. The atomizer was replaced with these vapor cells set in an oven with a temperature controller, and the fluorescence intensity was measured with the same optical configuration of the detection system as in the previous experiment.

### RESULTS AND DISCUSSION

**Detection of Sodium Atoms.** Figure 2A shows an example of the oscilloscope waveform of the LIF signal. After 300 ms

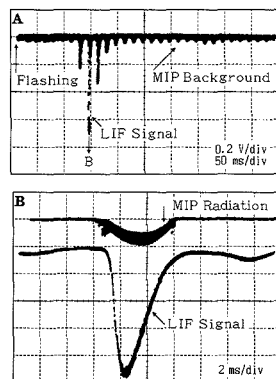


Figure 2. An example of oscilloscope traces of LIF signal and MIP background: sample concentration,  $10 \text{ ng}/\text{cm}^3$ .

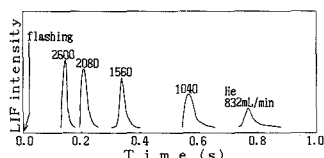


Figure 3. LIF envelope pulses for various He flow rate: sample concentration,  $1 \text{ ng}/\text{cm}^3$ .

of flash heating the filament, the LIF signal appeared. The plasma discharge was turned on and off with a frequency of 60 Hz, because the power supply of the magnetron had a half-wave rectifier at ac 60 Hz. Therefore, the LIF signal, as well as the background plasma radiation, showed a pulse shape with a repetition frequency of 60 Hz. In Figure 2B, the LIF and the MIP radiation pulses are shown. Na compounds are atomized only when the plasma is turned on. However, the LIF signal decreased at the tail of the MIP pulse. This may mean that the dissociated atoms in the ground state decreased, because of the increase in ionized and excited atoms.

With an increase in the plasma power, stationary fluorescence was observed without the sample. The fluorescence (called "residual fluorescence") was probably due to the Na atoms sputtered from the wall of the discharge tube. It could not be removed by washing the tube. In the present experiment, the plasma power was decreased to the level at which this fluorescence could be ignored.

Figure 3 shows the envelope of LIF signals at various He flow rates. With a decrease of the flow rate, the delay time between the heating pulse and the signal and the half-width of the signal pulse increased, which indicates that the sample is carried by He. The delay time agreed with the value calculated from the He flow rate. The product of the peak intensity and the half-width of the LIF signal was almost constant in the flow-rate range of 1500–2600 mL/min. The amplitude of the signal depended on the total length of the discharge tube  $L$  and the position of cavity. After the optimization process, we determined  $L = 300$  mm. The cavity was placed at the center of the tube.

The rate equation for excitation of a two-level system by the monochromatic flux  $I$  is given by

$$\frac{dn_2}{dt} = \frac{I}{c} g(\nu) (B_{12}n_1 - B_{21}n_2) - A_{21}n_2 \quad (1)$$

where  $n_1$  and  $n_2$  are the populations in the lower and the upper levels;  $A_{21}$ ,  $B_{12}$ , and  $B_{21}$  are Einstein coefficients for sponta-

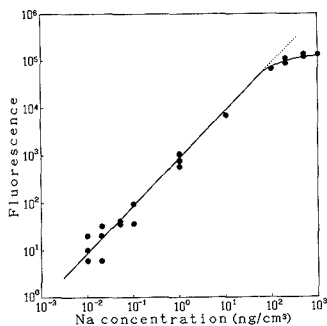


Figure 4. Analytical curve for Na measurement.

neous emission, absorption, and stimulated emission;  $g(\nu)$  is the line profile. The steady-state solution of eq 1 is

$$n_2 = \frac{g_2}{g_1 + g_2} n_1 \frac{I/I_s}{1 + I/I_s} \quad (2)$$

where the relationship

$$g_1 B_{12} = g_2 B_{21} = g_2 A_{21} c^3 / 8\pi h \nu^3 \quad (3)$$

was used.  $g_1$  and  $g_2$  are the statistical weights of the lower and the upper levels, and  $n$  is the atomic density.

In eq 2, the saturation power  $I_s$  is given by

$$\begin{aligned} I_s &= \frac{g_1}{g_1 + g_2} \frac{8\pi h \nu^3}{c^2 g(\nu_0)} \\ &= \frac{g_1}{g_1 + g_2} \frac{8\pi h c^2}{\lambda^5} \frac{\pi(\Delta\lambda)_N}{2} \end{aligned} \quad (4)$$

The LIF photon number observed per solid angle  $d\Omega$  and per second is

$$\begin{aligned} \psi &= V n_2 A_{21} \frac{d\Omega}{4\pi} \\ &= \frac{g_2}{g_1 + g_2} \frac{I/I_s}{1 + I/I_s} V A_{21} n \frac{d\Omega}{4\pi} \end{aligned} \quad (5)$$

In the case of  $I \ll I_s$ , the LIF signal is proportional to the laser power  $I$ . For  $g_2/g_1 = 2$  and  $(\Delta\lambda)_N = \lambda^2 A_{21} / 2\pi c = 1.15 \times 10^{-2}$  pm, the saturation power  $I_s$  is  $1.27 \times 10^{-2}$  W/cm<sup>2</sup> for mono-chromatic radiation.

Considering that 9 axial modes existed within the Doppler bandwidth and the cross section of our laser beam was 0.043 cm<sup>2</sup>, the saturation power was 4.9 mW. In fact, the fluorescence intensity was proportional to the laser power when it was less than 6.5 mW, and so we set the laser power at 3.0 mW in this experiment. In a two-level system, the detection limit is determined by the stray light, which is mainly the scattered laser light. As a result, excessive excitation power over the saturation level results in a decrease in the S/N ratio. The analytical measurement was performed by the use of a lock-in amplifier with a chopper. A feedback loop to synchronize the signal (60 Hz) and the chopping (540 Hz) frequency is required to avoid beating of the signal.

Figure 4 plots the analytical calibration curve of Na atoms in a wide range. The analytical curve is linear over 4 orders of magnitude up to 100 ng/cm<sup>3</sup>. The reproducibility of the signals was  $\pm 8.5\%$  in dispersion for ten succeeded measurements at a concentration of 1 ng/cm<sup>3</sup>.

**Detection Limit and Absolute Density.** For measurements near the detection limit, there were some problems that interfered with detection. The first one is the purity of water. We prepared pure water from water continuously circulating through two serial ion-exchange-resin filters to dilute the standard sample. The conductivity 0.06  $\mu$ S/cm is approxi-

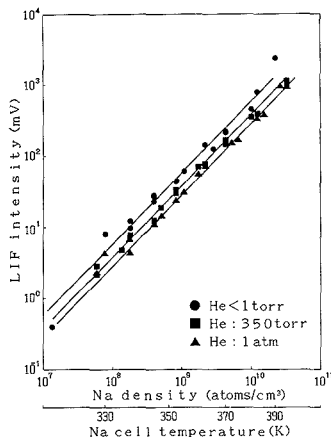


Figure 5. Calibration curves of Na densities using Na vapor cells.

mately the lower limit of our filter system. When this pure water was dropped on the filament, however, the LIF signal also appeared, corresponding to approximately 20 pg/cm<sup>3</sup> Na. No signal was observed, when the filament was flashed without dropping water.

The background radiation includes three components, that is, the plasma radiation, the scattered stray laser light, and the residual fluorescence from Na atoms sputtered off the wall. The S/N ratio is determined by fluctuations of these components, because the stationary component can be removed at the lock-in amplifier stage. Fluctuation of the residual fluorescence is observed after flashing; however, this can be discriminated from the signal, because of the delay time in the appearance of the fluorescence. The amplitude of the fluctuation was 2  $\mu$ V on the pen recorder traces, which corresponded to a Na concentration of 2 pg/cm<sup>3</sup>. Therefore, the detection limit calculated from  $S/N = 2$  is 4 pg/cm<sup>3</sup> in the present experiment.

The LIF signal voltage  $V_F$  for the two-level system is given by the formula

$$V_F = A_{21} \frac{g_2}{g_1 + g_2} \frac{I/I_s}{1 + I/I_s} n V \frac{d\Omega}{4\pi} \eta_1 \eta_2 e G R_L \quad (6)$$

where  $V$  and  $d\Omega$  are the observation volume and the solid angle,  $e$  is the charge of electron,  $\eta_1$  is the transmittance of the optical system, and  $\eta_2$ ,  $G$ , and  $R_L$  are the quantum efficiency, the current amplification factor, and the load resistance of the PMT, respectively.

In the LIF experiment, the laser intensity can be increased up to the saturation level ( $I \gg I_s$ ). Thus we can expect a high-intensity LIF signal even for the very low atomic density. For example, eq 6 predicts the number of the signal photoelectrons at the PMT at  $10^8$ /s for the Na density of  $10^5$  atoms/cm<sup>3</sup>,  $V = 0.1$  cm<sup>3</sup>,  $A_{21}^{-1} = 16$  ns,  $d\Omega = 0.1$  sr,  $\eta_1 = 0.30$ , and  $\eta_2 = 0.10$ . It should be noted, therefore, that the S/N ratio is not determined by the shot noise of the PMT detector. The LIF intensity was strong enough to be seen by the naked eye even at a concentration of 10 pg/cm<sup>3</sup>. The fluctuation of the background radiation directly depended on stability of the plasma and the laser, so that the S/N ratio can be improved by stabilization of the plasma and the laser.

It is difficult to know the absolute density  $n$  from  $V_F$  by using eq 6. We determined the  $n$  value in the atomizer by the aid of reference vapor cells. The absolute Na density in the vapor cell can be calculated from the cell temperature. The absolute density is calibrated by replacing the atomizer



with a vapor cell in an oven and comparing the LIF intensity  $I_F$  in the same system.

Figure 5 shows the PMT output voltage  $V_F$  as a function of the Na density  $n$  for three vapor cells with different buffer gas pressures. The Fairbank formula was used for the conversion from temperature to Na number density ( $n$ ).  $V_F$  is proportional to  $n$  over a number density range from  $10^7$  to  $10^{11}$   $\text{cm}^{-3}$ . The detection limit  $10^7$   $\text{cm}^{-3}$  is relatively high, because it is determined by stray light and no attempt to decrease it has been made. The  $V_F$  value for the vapor cell with a He gas pressure of 1 atm is 50% smaller than that of the evacuated cell because of collisional quenching by He. From Figure 5, the output PMT voltage of 1 mV corresponds to the atomic density  $n$  of  $1.68 \times 10^7$  atoms/ $\text{cm}^3$  at 1 atm.

We calculated the total number of dissociated atoms  $N$  passed through the observing region in the atomizer by the following formula:

$$N = nsvS \quad (7)$$

where  $s$  is the cross section of the discharge tube,  $v$  is the He velocity, and  $S$  is the integrated pulse form of the LIF signal in mV; consider the absolute density and the atomization efficiency for the LIF signal shown in Figure 2A obtained for a concentration of 10 ng/ $\text{cm}^3$ . The maximum number density is  $1.18 \times 10^{11}$  atoms/ $\text{cm}^3$ , because the peak voltage in Figure 2A is 700 mV and a 10% ND filter is used. Integration of the envelope of the LIF signal in Figure 2A provides  $S = 280$  mV s;  $s = 0.043$   $\text{cm}^2$ ,  $v = 108$   $\text{cm/s}$  and  $n = 1.68 \times 10^7$  atoms/ $\text{cm}^3$  (mV). Therefore,  $N = 2.62 \times 10^{11}$  atoms. We define the atomizing efficiency  $\beta_a$  as

$$\beta_a = \frac{\text{number of dissociated atoms } N}{\text{number of atoms (ions) in sample water}} \quad (8)$$

Since the number of atoms in a 10  $\mu\text{L}$  sample of water of 10 ng/ $\text{cm}^3$  is  $2.7 \times 10^{12}$ ,  $\beta_a$  is calculated to be 9.7%. However, shown in Figure 2A, since the plasma was turned on and off, the integration should not be done along the envelope but the pulse shape. In that case, the efficiency is given by  $\beta_a = 1.6\%$ .

The feature of this type of atomizer is that the instantaneous number density obtained in the observation region is large, because rapid injection of the sample is attained by flash heating. According to the results mentioned above, a peak density of  $1.18 \times 10^7$  atoms/ $\text{cm}^3$  is obtained for the sample of 1 pg/ $\text{cm}^3$ . Therefore, we can expect atomic detection of less than 1 pg/ $\text{cm}^3$  by decreasing the noise sources.

#### ACKNOWLEDGMENT

The authors thank Shin'ichi Ichitsubo and Tatsuya Izuha for their assistance.

#### LITERATURE CITED

- (1) Fairbank, W. M., Jr.; Hansch, T. W.; Schawlow, A. L. *J. Opt. Soc. Am.* **1975**, *65*, 199-204.
- (2) Gelbwachs, J. A.; Klein, C. F.; Wessel, J. E. *IEEE J. Quantum. Electron.* **1978**, *QE-14*, 121-125.
- (3) Balykin, V. I.; Letokhov, V. S.; Mishin, V. I.; Semchishen, V. A. *JETP Lett.* **1977**, *26*, 357-360.
- (4) She, S. Y.; Fairbank, W. M., Jr. *Opt. Lett.* **1978**, *2*, 30-32.
- (5) Fraser, L. M.; Winefordner, J. D. *Anal. Chem.* **1971**, *43*, 1693-1697.
- (6) Fraser, L. M.; Winefordner, J. D. *Anal. Chem.* **1972**, *44*, 1444-1451.
- (7) Weeks, S. J.; Haraguchi, H.; Winefordner, J. D. *Anal. Chem.* **1978**, *50*, 360-368.
- (8) Hohimer, J. P.; Hargis, P. J., Jr. *Appl. Phys. Lett.* **1977**, *30*, 344-346.
- (9) Hohimer, J. P.; Hargis, P. J., Jr. *Anal. Chim. Acta* **1978**, *97*, 43-49.
- (10) Kawaguchi, H.; Vallee, B. L. *Anal. Chem.* **1975**, *47*, 1029-1034.
- (11) Beenakker, C. I. M. *Spectrochim. Acta* **1976**, *31B*, 483-486.

RECEIVED for review September 22, 1989. Accepted December 21, 1989.

## Prediction of Gas Chromatography Flame Ionization Detector Response Factors from Molecular Structures

Andrew D. Jorgensen\*

Department of Chemistry, University of Toledo, Toledo, Ohio 43606

Kurt C. Picel<sup>1</sup> and Vassilis C. Stamoudis<sup>2</sup>

Argonne National Laboratory, Argonne, Illinois 60439

The prediction of flame ionization detector response factors as a function of molecular structure components is evaluated with modern capillary column gas chromatography equipment that included an on-column injector. The effect on the standard carbon content based response by electronegative atoms is analyzed for various functional groups. This study updates much earlier work that characterized the decrease in signal response by using average correction factors for each functional group. The effective carbon number concept based on naphthalene as the internal standard was used. For 56 compounds containing a single functional group, predictions based on these average responses reproduced the actual response to within 1.7% on average. This model was then extended to bifunctional groups with similar success for several molecules. The effects of changes in temperature programming and concentration were found to be minimal within the range studied.

<sup>1</sup>Environmental Research Division.

<sup>2</sup>Environment, Safety and Health, Support Services Division.

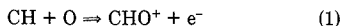
#### INTRODUCTION

High sensitivity, uniform response to hydrocarbons, and a broad linear range have made the flame ionization detector (FID) perhaps the most widely used detector in gas chromatography. The FID response of hydrocarbons is generally proportional to the mass of carbon present in the sample, but the degree of signal reduction due to partially oxidized carbon atoms in heteroatomic compounds varies markedly with heteroatom and bond types. Compounds that contain, for example, oxygen, nitrogen, or halogens give varied responses but can be quantified by the FID if corrections are made for the usual loss of sensitivity caused by the presence of these atoms in various functional groups. Correction factors can be determined either through the analysis of authentic standards or from accurate predictions of loss of response based on measurements made for compounds of related molecular structure.

Predictive methods would be quite useful if they could accurately indicate the change in response caused by the presence of one or more heteroatomic functional groups. Correction factors have long been used for various function-

alities. However, a comprehensive approach is needed for determining FID response precisely so that a broadly applicable system for predicting response can be developed. Modern analytical instrumentation allows highly precise response measurements to be made for the wide variety of substances that are needed for the development of such a system. Furthermore, systematic response predictions could be easily automated on computerized data systems to greatly facilitate analysis of complex organic mixtures and reduce the requirement for analyzing large numbers of authentic standards. To this end the present work has determined the response of a large number of compounds from many different chemical classes in order to critically reevaluate the conclusions of earlier reports and to begin to develop a systematic approach for predicting FID response in general on the basis of molecular structure. A system to accurately predict the response for a large number of compounds, many of them related to coal liquids, will be presented.

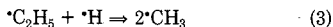
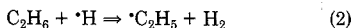
Although many questions about the specifics of flame chemistry in the FID remain unanswered, there is general agreement that the primary source of ions in the flame is the chemical ionization caused by the reaction of an oxygen atom with a radical containing a single carbon (1-5). The most commonly proposed reaction is



Schaefer (6) has presented data suggesting that reactions other than eq 1 are also significant contributors to ion production. He based his conclusion on the temperature dependence of the ion current.

Some work has been able to distinguish the relative contribution of the ground state of CH compared to that of some excited states of the radical (7, 8). Although the latter are much more effective at producing ions, it was demonstrated that the reaction of the former is primarily responsible for the ion current in the FID.

The origin of CH and related radicals has been the cause for considerable speculation, and divergent views have been defended. Blades (2, 9) has presented data to support the theory that in most cases radicals are produced by a series of hydrogen-stripping and hydrogen-cracking reactions that occur in the reducing section of the flame. For example



Sternberg (1) presented a table that summarized data from a variety of compounds and allowed prediction of the effective carbon number (ECN) of a compound from its structure. For example, he found that the presence of a carbonyl group reduced the effective number of carbons by one, while a primary alcohol caused a decrease of 0.6 carbon. Other researchers working at about the same time obtained similar results (10-12).

More recently two groups have reported on the FID response of various compounds. Tong and Karasek (13) determined a large number of absolute response factors for aliphatic and aromatic hydrocarbons and a few substituted species. They concluded that average response values were sufficiently accurate for the quantification of hydrocarbon compounds in many applications. A slight quantitative distinction between alkanes and aromatics was seen. However, their study included only a small number of nonhydrocarbons, and it was not possible to make a firm statement about most other classes.

Scanlon and Willis (14) used their own data and some results from the literature to maintain that the ECN concept is of value in checking the results from samples of known

composition. The evaluation of column performance was mentioned as an example. Their instrumentation was also of modern design, and they did employ an internal standard, but some of their results were achieved by using a split rather than an on-column injection.

Frequently we need to find the approximate concentration of a large number of species in a complex mixture, such as a coal-derived liquid. Typically a gas chromatograph/mass spectrometry analysis provides the molecular structure for the components. Because hundreds of compounds may be present and because a degree of accuracy equal to a few percent is sufficient, the preparation and analysis of accurately prepared standards are not practical or required. In many cases it would also be quite difficult to obtain a substance in sufficient purity for use as a standard. We therefore concluded that it was time to expand the review of ECNs to a wider range of compounds than has been reported in the recent literature and to develop a systematic approach for predicting FID response. We wanted to confirm that the presence of a particular functional group could be characterized by a single adjustment to the ECN and to determine whether these effects could be described in a simple additive fashion for polyfunctional compounds. Our eventual aim was to develop a computer program that would query the user for structural information about each peak in a chromatogram, calculate the ECN from information in a data base, and use the area and concentration of the internal standard to calculate the concentration of the component.

## EXPERIMENTAL SECTION

**Instrumentation.** All analyses were performed by using a Hewlett-Packard 5880A gas chromatograph equipped with an FID and a J&W Scientific on-column injector. The column was J&W Scientific's DB-5, 30 m  $\times$  0.32 mm i.d., with a 0.25- $\mu$ m film thickness, purchased from Alltech Associates. The carrier gas was helium at a linear flow velocity of 40 cm/s. The detector gas flows were 35 mL/min for hydrogen, 410 mL/min for air, and 30 mL/min for nitrogen as the make-up gas. The oven was programmed for an initial hold of 2 min at 30 °C, then 10 °C/min until all peaks were eluted or a temperature of 300 °C was reached. All mass measurements were performed on a Mettler AC100 analytical balance.

**Chemicals.** The solvent for all mixtures was methylene chloride (HPLC grade from Baker Chemicals and Fisher Scientific). The compounds were of 98% or greater stated purity, except for two with 97% and two unstated. They were obtained from Aldrich Chemical Co., Fluka Chemicals, and Chemical Procurement Laboratories (one compound only). Naphthalene was the internal standard; it had a stated purity of 99+%. The purity of each compound was checked by performing a separate GC analysis of the substance at high concentration in methylene chloride. The final relative response factors for each compound was corrected for the total amount of chromatographable impurities that were found. The average correction was 0.6%. Only three corrections were above 2%, and 2.6% was the largest.

**Procedure.** An accurately weighed sample of approximately 60 mg of each compound was dissolved in solvent in a 25-mL volumetric flask to make stock solutions. A mixture of 5-10 compounds was prepared by adding 0.90 mL of stock solution for each and a like amount of the internal standard stock, using a 1.0-mL gas-tight syringe, to a second 25-mL volumetric flask to give concentrations of about 50 ppm by mass. A few compounds were also studied at 200 and 10 ppm to look for a concentration effect. At least three sets of all stock solutions, including the internal standard and mixtures, were prepared, and each mixture was analyzed 3 or more times. Solutions were usually analyzed within 24 h of preparation. Injection volumes were between 1 and 2  $\mu$ L.

## RESULTS AND DISCUSSION

The precision of the relative response factors (RRF) measurements was uniformly good. For the set of three or more injections of the same solution, the average variation from the

Table I. FID Response for Nitrogen Heterocycles

name	formula	RRF	ECN	ECN minus no. of carbons	% error in pre- diction
pyrrole	C <sub>4</sub> H <sub>5</sub> N	0.646	3.38	-0.62	-0.2
pyridine	C <sub>5</sub> H <sub>5</sub> N	0.691	4.26	-0.74	2.6
2-picoline	C <sub>6</sub> H <sub>7</sub> N	0.727	5.28	-0.72	1.8
3-picoline	C <sub>6</sub> H <sub>7</sub> N	0.723	5.25	-0.75	2.4
2,3-lutidine	C <sub>7</sub> H <sub>9</sub> N	0.752	6.28	-0.72	1.4
3,4-lutidine	C <sub>7</sub> H <sub>9</sub> N	0.801	6.70	-0.30	-4.8
3,5-lutidine	C <sub>7</sub> H <sub>9</sub> N	0.772	6.45	-0.55	-1.1
3-ethylpyridine	C <sub>7</sub> H <sub>9</sub> N	0.747	6.26	-0.75	2.1
5-ethyl-2-methyl- pyridine	C <sub>8</sub> H <sub>11</sub> N	0.788	7.45	-0.55	-1.0
2-propylpyridine	C <sub>8</sub> H <sub>11</sub> N	0.760	7.18	-0.82	2.7
indole	C <sub>8</sub> H <sub>7</sub> N	0.811	7.41	-0.59	-0.5
5-methylindole	C <sub>9</sub> H <sub>9</sub> N	0.815	8.34	-0.66	0.4
quinoline	C <sub>9</sub> H <sub>7</sub> N	0.825	8.32	-0.68	0.7
4-methylquinoline	C <sub>10</sub> H <sub>9</sub> N	0.854	9.54	-0.46	-1.7
carbazole	C <sub>12</sub> H <sub>9</sub> N	0.897	11.70	-0.30	-2.8
acridine	C <sub>13</sub> H <sub>9</sub> N	0.973	12.21	-0.79	1.4
averages				-0.62	1.7

Table II. FID Response for Ketones

name	formula	RRF	ECN	ECN minus no. of carbons	% error in pre- diction
3-pentanone	C <sub>5</sub> H <sub>10</sub> O	0.614	4.12	-0.88	1.8
2-hexanone	C <sub>6</sub> H <sub>12</sub> O	0.659	5.15	-0.85	1.1
3-heptanone	C <sub>7</sub> H <sub>14</sub> O	0.686	6.11	-0.89	1.5
3-octanone	C <sub>8</sub> H <sub>16</sub> O	0.711	7.11	-0.89	1.3
3-nonanone	C <sub>9</sub> H <sub>18</sub> O	0.738	8.19	-0.81	0.2
cyclohexanone	C <sub>6</sub> H <sub>10</sub> O	0.672	5.14	-0.86	1.2
1-indanone	C <sub>9</sub> H <sub>8</sub> O	0.799	8.24	-0.76	-0.5
3-methylcyclo- pentanone	C <sub>6</sub> H <sub>10</sub> O	0.654	5.00	-1.00	3.9
acetophenone	C <sub>8</sub> H <sub>8</sub> O	0.761	7.13	-0.87	1.0
benzylacetone	C <sub>10</sub> H <sub>12</sub> O	0.790	9.14	-0.86	0.7
benzophenone	C <sub>13</sub> H <sub>10</sub> O	0.887	12.60	-0.40	-3.2
9-fluorenone	C <sub>13</sub> H <sub>8</sub> O	0.887	12.47	-0.53	-2.2
averages				-0.80	1.6

Table III. FID Response for Hydrocarbons

name	formula	RRF	ECN	ECN minus no. of carbons	% error in pre- diction
Alkanes					
<i>n</i> -octane	C <sub>8</sub> H <sub>18</sub>	0.854	7.61	-0.39	4.1
<i>n</i> -decane	C <sub>10</sub> H <sub>22</sub>	0.891	9.89	-0.11	0.3
<i>n</i> -dodecane	C <sub>12</sub> H <sub>26</sub>	0.928	12.34	+0.34	-3.4
<i>n</i> -tetradecane	C <sub>14</sub> H <sub>30</sub>	0.884	13.68	-0.32	1.8
Aromatics					
1,2,4-trimethylbenzene	C <sub>9</sub> H <sub>12</sub>	0.970	9.09	+0.09	-1.9
averages				-0.08	2.3

mean for the RRF was usually a few tenths of a percent. For the set of replicate solutions of the same compound, the average variation from the mean was 1.1% for the entire complement of 71 compounds. This number is quite consistent with an assumption that the primary sources of uncertainty are the determination of mass and the delivery of 0.90 mL of solution. The four normal hydrocarbons did exhibit an average variation for the replicate set of solutions equal to 2.6%, more than twice the value for the entire set. This may

Table IV. FID Response for Ethers and Furans

name	formula	RRF	ECN	ECN minus no. of carbons	% error in prediction
Ethers					
anisole	C <sub>7</sub> H <sub>8</sub> O	0.728	6.14	-0.86	1.4
diphenyl ether	C <sub>12</sub> H <sub>10</sub> O	0.859	11.41	-0.59	-1.6
xanthene	C <sub>13</sub> H <sub>10</sub> O	0.858	12.20	-0.80	0.2
Furans					
2,3-benzofuran	C <sub>8</sub> H <sub>6</sub> O	0.761	7.01	-0.99	3.0
dibenzofuran	C <sub>12</sub> H <sub>8</sub> O	0.865	11.35	-0.65	-1.1
averages				-0.78	1.5

Table V. FID Response for Alcohols and Phenols

name	formula	RRF	ECN	ECN minus no. of carbons	% error in prediction
Primary Alcohols					
1-pentanol	C <sub>5</sub> H <sub>12</sub> O	0.663	4.56	-0.44	-4.4
1-heptanol	C <sub>7</sub> H <sub>16</sub> O	0.728	6.60	-0.40	-3.6
Secondary Alcohols					
2-hexanol	C <sub>6</sub> H <sub>14</sub> O	0.667	5.32	-0.68	0.8
3-octanol	C <sub>8</sub> H <sub>18</sub> O	0.725	7.37	-0.63	-0.1
2-nonanol	C <sub>9</sub> H <sub>20</sub> O	0.743	8.36	-0.64	-0.0
1-indanol	C <sub>9</sub> H <sub>10</sub> O	0.824	8.62	-0.38	-3.1
2-indanol	C <sub>9</sub> H <sub>10</sub> O	0.842	8.42	-0.58	-0.7
Phenols					
phenol	C <sub>6</sub> H <sub>6</sub> O	0.709	5.21	-0.79	2.9
<i>p</i> -cresol	C <sub>7</sub> H <sub>8</sub> O	0.756	6.38	-0.62	-0.3
1-naphthol	C <sub>10</sub> H <sub>8</sub> O	0.806	9.06	-0.94	3.2
2-naphthol	C <sub>10</sub> H <sub>8</sub> O	0.804	9.05	-0.95	3.4
averages				-0.64	2.0

Table VI. FID Response for Amines and Esters

name	formula	RRF	ECN	ECN minus no. of carbons	% error in pre- diction
Amines					
aniline	C <sub>6</sub> H <sub>7</sub> N	0.748	5.43	-0.57	-0.3
4-aminobiphenyl	C <sub>12</sub> H <sub>11</sub> N	0.868	11.45	-0.55	-0.3
1-aminonaphthalene	C <sub>10</sub> H <sub>9</sub> N	0.873	9.75	-0.25	-3.4
2-aminofluorene	C <sub>13</sub> H <sub>11</sub> N	0.851	12.03	-0.97	3.2
averages				-0.58	1.8
Esters					
ethyl acetate	C <sub>7</sub> H <sub>8</sub> O <sub>2</sub>	0.400	2.75	-1.25	-0.8
propyl acetate	C <sub>9</sub> H <sub>10</sub> O <sub>2</sub>	0.462	3.68	-1.32	1.2
methyl benzoate	C <sub>9</sub> H <sub>8</sub> O <sub>2</sub>	0.635	6.75	-1.25	-0.3
averages				-1.27	0.8

have been due to the less than ideal solvent for such nonpolar compounds. Preliminary additional work with hexane as the solvent improved precision.

Tables I-VI give the results for a set of 56 compounds. Except for the hydrocarbons, each compound contained only one functional group. The fifth column in each table gives the difference between the ECN and the actual number of carbons in a given compound, i.e., the change in ECN due to the presence of the functional group. The average value for this change is given for each class of compounds. For example, nitrogen heterocycles with one nitrogen atom (Table I) have ECN values that are, on average, 0.62 less than their actual

Table VII. Summary of ECN Changes and Prediction Errors

class	no. of compounds	av % error in prediction	average ECN change	ref 1 ECN change
nitrogen heterocycles	16	1.7	-0.62	
ketones	12	1.6	-0.80	-1.0
amines primary	4	1.8	-0.58	-0.6
alcohols and phenols	11	2.0	-0.64	-0.6 (1°) -0.75 (2°)
ethers and furans	5	1.5	-0.78	-1.0
esters	3	0.8	-1.27	-1.25
hydrocarbons	5	2.3	-0.08	0
total	56	av 1.7		

carbon count. For this set of compounds the range is between 0.30 and 0.82 carbons.

For each class of compounds, the average ECN loss was used to calculate a predicted ECN value. The last column of each table gives the difference between this predicted ECN and the actual ECN is a percentage of the latter. A negative number indicates that the predicted ECN and therefore the RRF was lower than the observed RRF. Below this last column is the average of the absolute value of these percent errors in prediction. Note that some tables have distinctions within a group, e.g., primary and secondary alcohols and phenols. However, the statistics are calculated for the entire group. A case could be made for treating these subgroups separately. Sternberg (1) has done this for some classes, and we are pursuing this line of research in the case of alcohols and hydrocarbons.

Table VII summarizes the group data from Tables I-VI and gives the comparable numbers quoted by Sternberg (1). Note that the average difference between the predicted ECN and its experimental value was only 1.7%. Of the 56 compounds, 36 (64%) differed by less than 2% and 43 (77%) by less than 3%. These results clearly indicate that one can assume a single value for the change in ECN due to the presence of one functional group and achieve a quite reasonable degree of accuracy, at least under the conditions of these experiments. Even though the range of values for the shift in ECN seems at first glance to be rather large (e.g., -0.30 to -0.82 for the nitrogen heterocycles), one must remember that these are fractions of a single carbon out of the total number of carbons in a compound. Therefore, a difference of 0.30 between the experimental and predicted ECN is only 3% for a compound with 10 carbons.

Ironically, the poorest prediction record was found for hydrocarbons, but only a small number of these compounds were included because there are numerous reports in the literature for this class. This group's average prediction error of 2.3% is quite acceptable for the purposes of this work. The second highest percent error in prediction was found for the alcohols and phenols. This finding seems to support the need for discriminating among the three chemically different hydroxyl groups (primary, secondary, and phenol). However, the 2.0% average difference is not high enough to justify any distinction at this time.

The last column of Table VII gives the results of Sternberg as reported in 1962 (1). Excellent agreement is seen for primary amines, esters, and hydrocarbons. The average value for all of the alcohols and phenols is also quite reasonable, given the earlier data for primary and secondary alcohols. The observed effects of oxygen for ketones and ethers, including furans, are less than those obtained by Sternberg to a rather significant degree. This may very well reflect more efficient chromatography with modern columns and perhaps the use of higher purity standards in the present work. In fact, it is

## Nitrogen Heterocycles

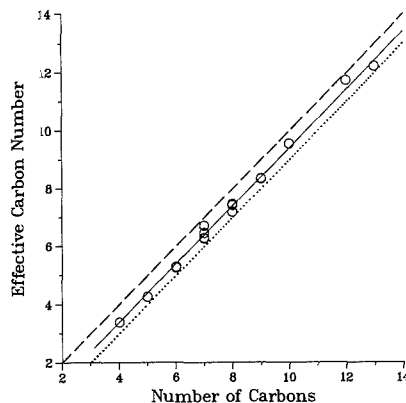


Figure 1. ECN versus carbon number of nitrogen heterocycles. Symbols indicate experimental points: (---) ECN equals number of carbons (no effect); (···) each heteroatom reduces ECN by 1.0 (full effect); (—) carbon number minus average change in ECN for group.

## Ethers and Furans

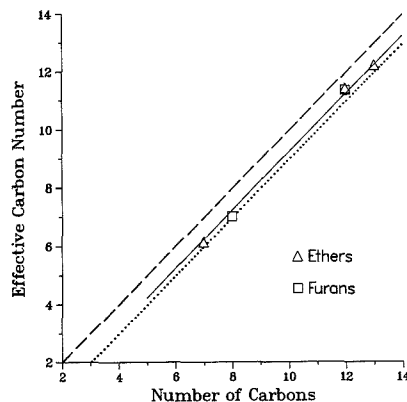


Figure 2. ECN versus carbon number for ethers and furans. Symbols and lines are as in Figure 1.

quite surprising that only these differences are found, given the significant changes that have occurred in instrumentation in the last 25 years.

Figures 1-5 present these results in graph form for five of the compound classes studied. The plots give ECN versus the actual number of carbons. Symbols indicate experimental points, the dashed line is for the case of ECN equaling the number of carbons (no effect), and the dotted line is for the case in which each heteroatom causes as reduction of exactly one carbon in the ECN (full effect). The solid line through the symbols is not the best line in a least-squares sense but is determined by subtracting the average change in ECN for the group from the number of carbons. That is, the intercept is shifted with the data, but the slope is fixed at one. In all cases it is apparent that the solid line gives a significantly better fit to the data than either the dashed line (no effect) or the dotted line (full effect).

Table VIII includes the results from three additional groups of compounds. Two of the three sulfides studied showed very slight increases in response from what would be expected from

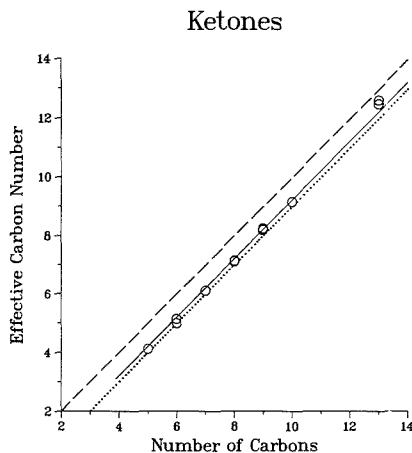


Figure 3. ECN versus carbon number for ketones. Symbols and lines are as in Figure 1.

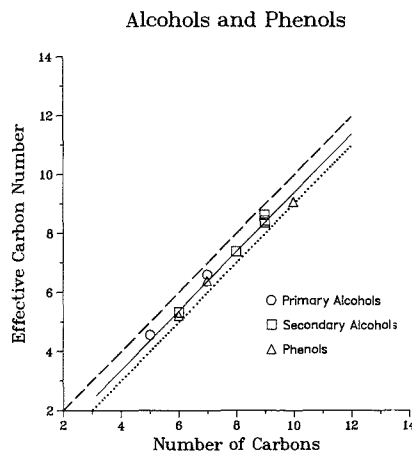


Figure 4. ECN versus carbon number for alcohols and phenols. Symbols and lines are as in Figure 1.

the analogous hydrocarbons. The third compound, thianaphthene, had a reduced response, but by only 0.21 effective carbon. These data are consistent with the commonly accepted notion that the presence of sulfur atoms does not affect the FID response in a significant way.

The second small data set in Table III contains two nitriles. They fortuitously yielded identical shifts of  $-0.42$  carbon. This differs rather significantly from the value of  $-0.70$  given in ref 1. We offer no suggestions for this difference, except those already noted above in the case of ketones and ethers. The agreement is striking, even if it is only for two compounds.

The additivity of functional group effects on the ECN was addressed in a study of six additional compounds. The details of this work are given in Table IX. Each compound contained two separate functional groups. Table IX gives a predicted ECN value expected from the simple sum of the average ECN shifts given in Table VII and also the experimental ECN. In four of the six cases the agreement is excellent, with a difference of 1.5% or less. The other two compounds have an error in prediction of 3.3% and 4.4%. The latter is for catechol, which contains two hydroxyl groups on adjacent carbons

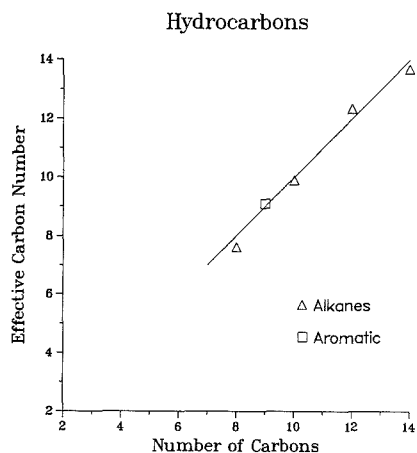


Figure 5. ECN versus carbon number for hydrocarbons. Symbols and lines are as in Figure 1.

Table VIII. FID Response

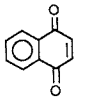
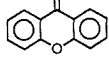
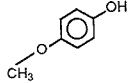
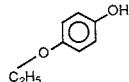
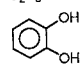
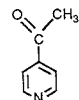
name	formula	RRF	ECN	ECN minus no. of carbons
Sulfides				
thianaphthene (thionaphthene)	$C_8H_6S$	0.744	7.79	-0.21
dibenzothiophene	$C_{12}H_8S$	0.837	12.04	+0.04
thianthrene	$C_{12}H_8S_2$	0.703	12.09	+0.09
Nitriles				
benzotrile	$C_7H_5N$	0.818	6.58	-0.42
1-cyanonaphthalene	$C_{11}H_7N$	0.885	10.58	-0.42
Aminopyridines				
4-aminopyridine	$C_5H_6N_2$	0.492	3.61	-1.39
2-(methylamino)pyridine	$C_6H_8N_2$	0.618	5.21	-0.79
2-(dimethylamino)pyridine	$C_7H_{10}N_2$	0.656	6.26	-0.74
4-(dimethylamino)pyridine	$C_7H_{10}N_2$	0.642	6.12	-0.88

of a benzene ring. The proximity of these functional groups may account for the only modest agreement in this case because the carbons involved may not be responding independently in the flame. Although only a small number of compounds have been studied in this evaluation of additivity, a favorable preliminary conclusion is justified.

The simplest way to view the effect of an electronegative atom on a carbon atom in the FID is to assume that the bond between them survives the reducing part of the flame in a certain percent of the molecules and that the pair therefore does not undergo oxidative ionization in the oxidizing region. Although only a small fraction of all of the carbon atoms will be ionized, the heteroatom seems to have a proportional effect on that fraction.

The esters present an interesting application of this simple picture. Since the ether bond in an ester includes one carbon already bonded to an oxygen in the carbonyl, a simple addition of effects would not be expected. Table VII indicates that a carbonyl in a ketone causes a reduction of 0.80 in effective carbons and a that simple ether causes a reduction of 0.78. The overall reduction for the ester might be predicted along the following lines: the carbonyl carbon will be removed from ionization 80% of the time, the ether oxygen will remain with one of the two carbons 78% of the time, with half of this frequency, 39%, for each of the carbons. However, for the

Table IX. Compounds with Multiple Functionalities

structure	name	group(s)	no. of carbons	reduction	ECN predicted	ECN experimental	% difference
	1,4-naphthoquinone	two ketones	10	$2 \times 0.80$	8.40	8.34	+0.8
	xanthone	ketone + ether	13	$0.80 + 0.78$	11.42	11.56	-1.2
	4-methoxyphenol	phenol + ether	7	$0.64 + 0.78$	5.58	5.50	+1.5
	4-ethoxyphenol	phenol + ether	8	$0.64 + 0.78$	6.58	6.37	+3.3
	catechol	two phenols	6	$2 \times 0.64$	4.72	4.94	-4.4
	4-acetylpyridine	N in ring + ketone	7	$0.62 + 0.80$	5.58	5.52	+1.1

carbonyl carbon, this ether oxygen has an effect only for the 20% of the time when the carbonyl oxygen does not remain. Therefore that total reduction of carbon will be

$$\begin{array}{l} \text{carbonyl carbon} \quad 0.80 + 0.20(0.78/2) = 0.88 \\ \text{second ether carbon} \quad 0.78/2 = 0.39 \\ \text{total} \quad = 1.27 \end{array}$$

Interestingly, this is exactly the value found in the small set of three esters studied in the present work, and it is virtually identical with Sternberg's result of 1.25 (1). One must be cautious about over-interpreting from this quite small sample of compounds, but the agreement is quite supportive of the suggested analysis. These facts lend further weight to our working model, which does include the additivity of effects.

Additive effects were further studied by using aminopyridines. The results are summarized in Table VIII. Although three of the four compounds have quite consistent shifts in ECN, one of them gave a value almost twice that of the other three. Somewhat more disturbing is the fact that the presence of an amino group and a nitrogen in a ring would be expected to cause a change in response equal to -0.58 and -0.62, respectively. This sum of -1.20 is not too far from the 4-aminopyridine result of -1.39, but it is quite far from the approximately -0.80 found for the other three compounds. Possible sorptive losses would produce effects in the opposite direction. We have no other suggestions for these discrepancies.

We have performed some experiments to see if the numbers reported here are valid for other experimental conditions. A set of ketone mixtures was analyzed in duplicate at a temperature program rate of 4 °C/min rather than the 10 °C/min used for all of the other studies. The mean RRF values from these runs were on average slightly greater than the results in Table II, with two-thirds higher and one-third lower. The average of the absolute values of the percent deviations was 2.1%.

The concentration dependence of the results was tested with

additional mixtures of these ketones at nominal concentrations of 200 and 10 ppm. At the higher concentration, five of the eight compounds differed by less than 3% from the results in Table II and seven of eight by less than 4%. At the lower concentration, the results for 3-pentanone and 1,4-naphthoquinone were above the numbers in Table II by about 6%, the 3-hexanone was low by the same amount, and 2-hexanone was low by almost 11%. The remaining four compounds differed by 2.5% or less. The analysis scheme presented in the present work must be used with caution at low concentrations. Some of the variations seen in all three of these tests of conditions must be ascribed to differences in chromatographic conditions and small data sets.

Variations in flame conditions might be expected to cause unacceptable deviations. We have begun a comprehensive study using a wide variety of hydrogen and air flow rates. Preliminary indications are that although absolute responses do vary measurably with hydrogen concentration, the relative responses as obtained by using an internal standard are sufficiently constant for the type of analysis that we propose.

If one wanted to use the RRF values reported in this work but did not want to use naphthalene as an internal standard, a simple determination of the RRF between the desired internal standard and the naphthalene would give a correction factor that could be applied to all of the needed numbers. If the new standard were one of the other compounds in this study, even that experiment would be unnecessary. Scanlon and Willis (14) used tridecane and tetradecane as their ECN standards and found the ECN of naphthalene to be 10.01. Therefore, our assumed value of 10 would make the present RRF values be appropriate also for the alkanes that they used.

Future work in this area is needed to more firmly establish the additivity of effects before the entire process can be accurately modeled. We would envision the automated use of RRF values from a computerized data base or from a calculation, either based on the individual contributions of all the structural groups.

One can, therefore, conclude that FID responses for a wide variety of compounds can be predicted to a good degree of accuracy, typically 2-3%. This obviates the need to obtain high-purity standards and to accurately prepare and analyze solutions of these compounds as long as one confirms that good chromatographic conditions are present. If one needs greater accuracy than this method provides, standards of actual purity greater than 98% would have to be obtained, and at least two sets of standard solutions would have to be prepared, because one can expect a single solution to differ from the mean of a set of standards by 1% or more (see text above). Although the primary use for this technique is expected to be the quantification of components in a complex organic mixture if a molecular or at least a general structural identification can be made, other uses for response prediction would be in evaluations of sample purity and column performance.

#### ACKNOWLEDGMENT

Victoria Vlastnik is acknowledged for assistance in data collection and Doug Hoffman for technical assistance. The preliminary work cited was performed by Maria Portellos.

#### LITERATURE CITED

- (1) Sternberg, James C.; Gallaway, William S.; Jones, David T. L. In *Gas Chromatography*; Brenner, N., Callen, J. E., Weiss, M. D., Eds.; Academic Press: New York, 1962; pp 231-267.

- (2) Blades, Arthur T. *J. Chromatogr. Sci.* **1973**, *11*, 251-255.  
 (3) Blades, Arthur T. *Can. J. Chem.* **1976**, *54*, 2919-2924.  
 (4) Nicholson, Anthony J. C.; Swingle, D. L. *Combust. Flame* **1980**, *39*, 43-52.  
 (5) Nicholson, Anthony J. C. *J. Chem. Soc., Faraday Trans. 1*, **1982**, *78*, 2183-2194.  
 (6) Schaefer, B. A. *Combust. Flame* **1984**, *56*, 43-49.  
 (7) Cool, Terrill A.; Tjossem, Paul J. H. *Chem. Phys. Lett.* **1984**, *111*, 82-88.  
 (8) Cool, Terrill A.; Goldsmith, John E. M. *Appl. Opt.* **1987**, *26*, 3542-3551.  
 (9) Blades, Arthur T. *J. Chromatogr. Sci.* **1984**, *22*, 120-121.  
 (10) Perkins, G., Jr.; Rouayheb, G. M.; Lively, L. D.; Hamilton, W. C. In *Gas Chromatography*; Brenner, N., Callen, J. E., Weiss, M. D., Eds.; Academic Press: New York, 1962; pp 269-285.  
 (11) Perkins, Gerald, Jr.; Laramy, R. E.; Lively, L. D. *Anal. Chem.* **1963**, *35*, 360-362.  
 (12) Ackman, R. G. *J. Gas Chromatogr.* **1964**, *2*, 173-179.  
 (13) Tong, H. Y.; Karasek, F. W. *Anal. Chem.* **1984**, *56*, 2124-2128.  
 (14) Scanlon, James T.; Willis, Donald E. *J. Chromatogr. Sci.* **1985**, *23*, 333-340.

RECEIVED for review September 18, 1989. Accepted December 22, 1989. A.D.J. gratefully acknowledges the support of the Argonne National Laboratory Education Division. This work was supported by the U.S. Department of Energy, Assistant Secretary for Fossil Energy, under Contract W-31-109-Eng-38.

## Surface-Enhanced Raman Analysis of Sulfa Drugs on Colloidal Silver Dispersion

W. S. Sutherland, J. J. Laserna,<sup>1</sup> M. J. Angebrannt, and J. D. Winefordner\*

Department of Chemistry, University of Florida, Gainesville, Florida 32611

**Surface-enhanced Raman spectrometry (SERS) of three sulfa drugs (sulfadiazine, sulfamerazine, and sulfamethazine) is reported. Silver colloidal dispersions prepared by simple borohydride reduction of silver nitrate are used as substrates. The capability of SERS for spectral fingerprinting of analytes with close structural properties using easily prepared substrates and relatively simple instrumentation is illustrated. By careful attention to the liming in the measurement, quantitative information can be obtained from silver colloids. Linearity was achieved up to 100 ng mL<sup>-1</sup>. Limits of detection range in the low nanograms per milliliter level.**

The discoveries of sulfonamides (sulfa drugs) and antibiotics constitute some of the most significant medical achievements of this century. They have therapeutic uses both in human and veterinary medicine and in disease prevention in livestock. In 1935, over  $100 \times 10^6$  kg of these drugs were used annually. Over 5000 sulfa drugs, which have a general structure of the type  $H_2NC_6H_4SO_2NHR$ , have been synthesized and tested. Fewer than 30 of these have proven worthy of sustained use (1). Their biological activity is based on the inhibition of the biosynthesis of folate cofactors in bacteria by blocking a step in the formation of dihydrofolic acid from *p*-aminobenzoic acid (2). The sulfapyrimidines, where the R group is a pyrimidine

ring, have been touted as the ultimate stage of development of sulfa drugs. Important members of this group are sulfadiazine, sulfamerazine, and sulfamethazine (3).

During the 1940s, these drugs enjoyed widespread use in combating bacterial infections in humans and in the treatment of diseases affecting pet and food-producing animals. Recently, the reduction of sulfa drug use in humans has been triggered by increased bacterial resistance to the drugs and the development of more effective antimicrobial agents. However, the use of sulfa drugs in veterinary medicine has persisted because the drugs are easily administered in feed and water, are economical, and have proven to be effective for the treatment of livestock diseases. The use of combinations of two or more sulfa drugs was also shown to be of therapeutic value. During treatment with sulfa drugs, the higher the concentration of drug that can be maintained in the body, the greater its effect. However, increasing the drug concentration also increases the side effects, the most common of which is crystalluria, a deposition of crystals in the renal tubules due to the limited solubility of the sulfa drugs in water. However, when used in combination, each drug acts independently. Since all of the sulfapyrimidines have been shown to have the same therapeutic effect, combination therapy allows a higher total drug concentration to be maintained in the blood while minimizing the effects of crystalluria.

The use of sulfa drugs to promote growth and treat diseases of livestock animals has been a major cause of sulfa drug tissue residue in swine marketed for human consumption. In 1973, the U.S. Food and Drug Administration set a tolerance of 100 ng of sulfonamide per gram of edible tissue. Random assays

\* Author to whom correspondence should be addressed.

<sup>1</sup> On leave: Department of Analytical Chemistry, Faculty of Sciences, University of Malaga, 29071 Malaga, Spain.

of tissues for drug and agricultural chemical residues in slaughter animals and fowl are made monthly in all packing plants butchering for commercial sale (1). At present, both the FDA and the Food Safety and Inspection Service (FSIS) rely on modifications of the Bratton-Marshall (B-M) procedure (4) for monitoring residues. The Bratton-Marshall reaction involves diazotization of the paraminobenzene group with nitrous acid and the subsequent coupling of the diazotized moiety with an amine to yield a stable, purple compound which absorbs strongly at 545 nm. One major disadvantage to this technique is that all sulfonamides form compounds with absorption maxima at 545 nm. The drug treatment history of slaughtered animals may not be well-known, and determination of which sulfa drug or drug combinations exist in the tissue could be important. A second disadvantage of the B-M technique is that interference is produced when primary aromatic amines other than sulfonamides are diazotized and yield highly colored products. Other methods that have been developed to overcome these problems include thin-layer chromatography (TLC) (2), resonance Raman spectroscopy (5), and high-performance liquid chromatography (HPLC) (6). A comprehensive review of all the analytical methods used for sulfonamides was presented by Horwitz (7, 8). A major defect inherent to all residue assay methods in current use is that the limit of reliable measurement is of the same order of magnitude as the tolerance they are intended to enforce (1).

Surface-enhanced Raman spectrometry (SERS) has been recently proposed as a novel analytical technique for trace analysis and characterization. From an analytical point of view, the most outstanding characteristic of SERS is that it provides spectral fingerprint capability at trace concentration level, an attribute of only a few analytical techniques. This property arises by the combination of the strong dependence of vibrational spectroscopy on structure and the enhancement of Raman cross section of molecules at rough metallic surfaces. In addition, fluorescence of the analyte or concomitants is not as serious a limiting factor in SERS as it is in regular Raman spectrometry. Analysis of mixtures (9-11) and quantitative analysis (10, 12-14) have been recently reported using SERS. A variety of analytes, including water contaminants (15), polycyclic aromatic compounds (11, 16, 17), drugs (12), pesticides (18), and nitrogen-containing heterocyclics (10, 19) have been examined.

In the present paper, the surface-enhanced Raman analysis of the three primary sulfapyrimidines (sulfadiazine, sulfamerazine, and sulfamethazine) is reported for the first time. Silver colloidal dispersions prepared by simple borohydride reduction of silver nitrate are used as substrates. The results illustrate the potential of SERS for trace analysis and characterization of analytes with close structural properties.

#### EXPERIMENTAL SECTION

**Apparatus.** The spectra reported here were obtained by use of the 514.5-nm line of an argon ion laser (Spectra Physics, series 2000). The nonlasing plasma lines were removed through the use of a predispersing grating. The power at the sample was typically 100 mW. Spectra were obtained with a 0.85-m double grating spectrometer (Spex Industries, Model 1403). The spectrometer resolution was set to 10  $\text{cm}^{-1}$ . The detector was a cooled RCA, Model C31034, gallium arsenide photomultiplier tube coupled to standard photon counting electronics. Data acquisition, storage, processing, and plotting were under control of an IBM PC compatible microcomputer. All spectra reported represent single scans and are provided without spectral smoothing. Right angle geometry was used for Raman sampling.

**Chemicals and Procedure.** All chemicals used were analytical reagent grade or equivalent. Demineralized water was used throughout. Sulfadiazine, sulfamerazine, and sulfamethazine were purchased from Sigma. They are used without further purification. Stock aqueous solutions (100  $\mu\text{g mL}^{-1}$ ) contained about

**Table I. Surface-Enhanced Raman Bands of Sulfa Drugs on Colloidal Silver (Raman Shift,<sup>a</sup>  $\text{cm}^{-1}$ )**

sulfadiazine	sulfamerazine	sulfamethazine
230 sh	230 sh	238, s
294 sh	290 sh	
364 vw	342 vw	
416 vw	410 vw	396 vw
458 vw	462 vw	458 vw
506 vw	508 vw	516 vw
	544 vw	554 w
574 m	582 m	590 m
634 w	626 vw	638 vw
684 w	674 w	674 w
	762 s	738 m
818 s	830 m	834 m
974 vw	976 vw	968 bb
	1002 vw	
1068 sh	1066 sh	1054 w
1114 vs	1114 vs	1112 vs
1186 vw	1174 vw	1186 vw
	1252 vw	1260 vw
	1312 m	1302 vw
1340 m		1356 sh
	1390 m	1394 m
1410 w		
	1454 w	
1502 w	1502 w	1506 w
1594 s	1594 s	1594 s
1630 sh	1630 sh	1622 sh
	2930 m	2922 m
3050 sh	3068 sh	3074 sh
3258 bb	3258 bb	3242 bb
3378 bb	3396 bb	3380 bb

<sup>a</sup> Key: v, very; w, weak; m, medium; s, strong; sh, shoulder; bb, broad band.

3% methanol to help dissolve the drugs. Silver hydrosols were prepared as follows: A silver nitrate solution was prepared by adding 65 mL of water to 35 mL of a  $5.0 \times 10^{-3}$  M  $\text{AgNO}_3$  solution. The solution was ice-cooled and then added dropwise with vigorous stirring to a sodium borohydride solution prepared by adding 120 mL of water to 180 mL of a  $2.0 \times 10^{-3}$  M  $\text{NaBH}_4$  solution. The  $\text{NaBH}_4$  solution was also ice-cooled. The resulting silver hydrosol presented an absorption maximum at 400 nm, characteristic of silver particles with diameters between 1 and 50 nm (20). This was experimentally verified by filtering a small amount of the silver colloidal solution onto a polycarbonate track-etched (PCTE) membrane and imaging the resulting surface with scanning electron microscopy. This was possible since the smooth surface of the PCTE membrane yields high contrast and is ideal for SEM imaging of small objects (21). Each sample was prepared by adding 0.1 mL of the sulfa drug solution to 0.9 mL of the Ag colloid at room temperature. After mixing, 0.5 mL of the resulting sample was transferred to the liquid cell and placed in the Spex Model 1459 illuminator.

#### RESULTS AND DISCUSSION

The surface-enhanced Raman spectra of sulfadiazine, sulfamerazine, and sulfamethazine are shown in Figure 1. The numerical values of the band positions in inverse centimeters are listed in Table I. The extreme structural similarity of the three drugs, which only differ in the presence of methyl group in the pyrimidine ring of the molecule, should be noted. The spectral fingerprinting capability of SERS at trace concentration levels can be illustrated by an analysis of the spectra.

The drugs have several common spectral features. They show a narrow, very strong band at  $1114 \text{ cm}^{-1}$  in the case of sulfadiazine and sulfamerazine and at  $1112 \text{ cm}^{-1}$  in the case of sulfamethazine. They show also a common strong band at  $1594 \text{ cm}^{-1}$ . Shoulders in the low-energy side of this band appear in the three drugs. The broad band peaking at around  $3390 \text{ cm}^{-1}$ , with shoulders at  $3070 \text{ cm}^{-1}$  and  $3258 \text{ cm}^{-1}$ , is also



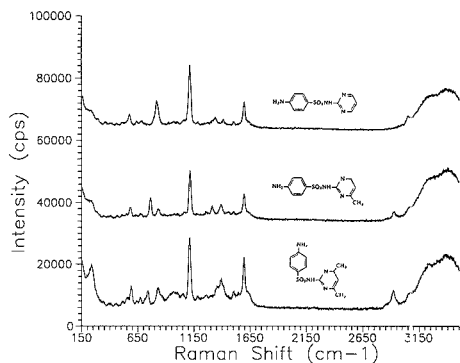


Figure 1. Surface-enhanced Raman spectra of sulfadiazine (top), sulfamerazine (middle), and sulfamethazine (bottom) on colloidal silver.

common to the three drugs. A common mode at around 580  $\text{cm}^{-1}$  is also present. Sulfadiazine and sulfamerazine show a shoulder at 230  $\text{cm}^{-1}$  in the decaying background of Rayleigh scattering. In the case of sulfamethazine, there is a well-defined band at 238  $\text{cm}^{-1}$ .

Sulfamerazine and sulfamethazine show several spectral singularities with respect to sulfadiazine. Both show a common mode at around 2930  $\text{cm}^{-1}$ , which is not shown by sulfadiazine. The peaks at 738 (sulfamethazine) and 762  $\text{cm}^{-1}$  (sulfamerazine) do not appear in the case of sulfadiazine. Sulfamerazine shows a weak mode at 1454  $\text{cm}^{-1}$ , which is not shown by the other two drugs. Sulfamethazine can be distinguished from the other two drugs by a number of spectral features. For instance, it shows a broad band at 968  $\text{cm}^{-1}$ , which in the other two drugs appear as very small peaks at around 975  $\text{cm}^{-1}$ . Also, the combination of a band at 1394  $\text{cm}^{-1}$  with a shoulder in the high energy side at 1356  $\text{cm}^{-1}$  is unique to sulfamethazine.

No attempts were made to provide a complete vibrational analysis of the compounds. However, on the basis of group frequencies, tentative assignments of the most prominent spectral features can be done. The very strong 1114–1112  $\text{cm}^{-1}$  band common to the three drugs can be due to the  $\text{SO}_2$  symmetric stretching in the sulfonamide group (22, 23). The 1594- $\text{cm}^{-1}$  mode in the three compounds can be due to a ring stretching mode. The shoulder at around 1630  $\text{cm}^{-1}$  can be due to  $\text{NH}_2$  bending. The vibrations at 3050–3074  $\text{cm}^{-1}$  could be due to aromatic C–H stretching modes, while those at 3258–3380  $\text{cm}^{-1}$  could be due to N–H stretching modes. The band at 2930  $\text{cm}^{-1}$  in sulfamerazine and that at 2922  $\text{cm}^{-1}$  in sulfamethazine are presumably due to the methyl C–H stretching vibration. No band in this region appears in the spectrum of sulfadiazine.

The conventional Raman spectra (CRS) of the pure drugs (solid state) were also recorded. Figure 2 shows the spectra, while the peak positions are listed in Table II. In general, the vibrational modes in the SERS spectra are shifted with respect to the CRS. The most prominent peaks in the CRS were at 1150  $\text{cm}^{-1}$  for sulfadiazine, at 1153  $\text{cm}^{-1}$  for sulfamerazine, and at 1144  $\text{cm}^{-1}$  for sulfamethazine, while the corresponding peaks in the SERS spectra appear at 1114, 1114, and 1112  $\text{cm}^{-1}$ , respectively. There were smaller shifts for the second most intense mode: 1598  $\text{cm}^{-1}$  (sulfadiazine) and 1596  $\text{cm}^{-1}$  (sulfamerazine and sulfamethazine) in the CRS, and 1596  $\text{cm}^{-1}$  for the three drugs in the SERS spectrum. As expected, the bandwidths (full widths at half maximum, fwhm) of the solid-state spectra are smaller than those in SERS. For instance, the fwhm for the CRS band of sulfadiazine at 1598  $\text{cm}^{-1}$  was 12  $\text{cm}^{-1}$ , while the same vibrational mode in the

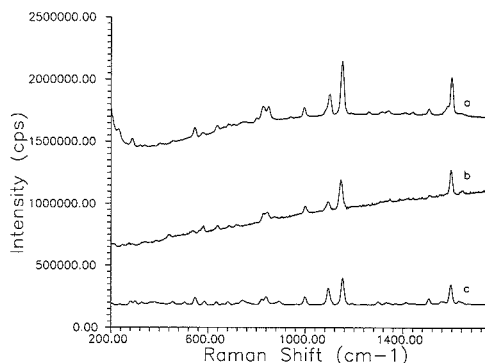


Figure 2. Unenhanced, conventional Raman spectra of the sulfa drugs (crystalline, pure compounds): (a) sulfadiazine, (b) sulfamerazine, (c) sulfamerazine.

Table II. Conventional Raman Bands of Sulfa Drugs (Solid Phase) (Raman Shift,<sup>a</sup>  $\text{cm}^{-1}$ )

sulfadiazine	sulfamerazine	sulfamethazine
229 sh	237 w	206 vw
286 w	282 dbl, w	213 vw
319 vw	300 dbl, w	248 vw
339 vw	328 w	273 vw
373 vw	365 w	290 vw
402 vw	380 w	330 vw
455 vw	456 w	342 vw
544 w	504 w	386 vw
578 vw	547 m	439 w
636 w	585 w	529 vw
661 vw	634 w	538 w
706 vw	659 vw	567 vw
750 vw	681 w	579 w
800 w	715 vw	637 w
827 dbl, m	743 m	685 w
848 dbl, m	769 sh	716 vw
939 vw	822 dbl, m	829 dbl, m
995 m	840 dbl, m	842 dbl, m
1098 s	892 w	873 vw
1150 vs	963 vw	999 w
1259 w	999 m	1092 w
1312 v	1094 s	1144 vs
1338 w	1153 vs	1306 vw
1407 vw	1191 w	1345 vw
1438 w	1241 vw	1385 vw
1505 w	1298 w	1416 vw
1581 sh	1333 w	1440 vw
1598 vs	1371 vw	1466 vw
	1413 w	1478 vw
	1506 m	1509 w
	1560 w	1559 vw
	1596 vs	1596 vs
	1629 w	1640 w

<sup>a</sup> Key: v, very; w, weak; m, medium; S, strong; sh, shoulder; dbl, doublet.

SERS spectrum, held at 1594  $\text{cm}^{-1}$ , shows a fwhm of 22  $\text{cm}^{-1}$ . It should be noted, however, that the CRS are superimposed on a strong background, presumably due to fluorescence of the drug or of some impurity.

**Quantitative Study.** Experiments were conducted to study the dependence of SERS intensity with the adsorbate concentration added to the silver colloid. First it was noticed that for the drugs studied there was a dynamic component in the measured SERS intensity. Addition of the drug to the hydrosol did not result in an immediate development of the intensity. Figure 3 shows the time dependence of SERS intensity for sulfadiazine. As shown, there was a rapid increase

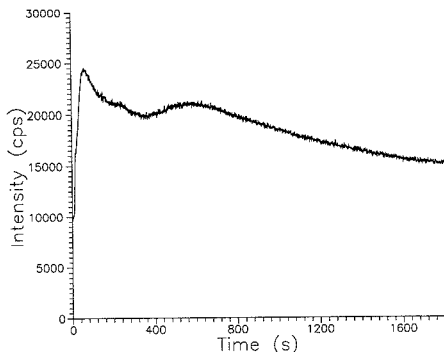


Figure 3. Time dependence of SERS intensity of sulfadiazine, monitored at a Raman shift of  $1112\text{ cm}^{-1}$ ; sulfadiazine concentration,  $1\text{ }\mu\text{g mL}^{-1}$ ; colloidal silver.

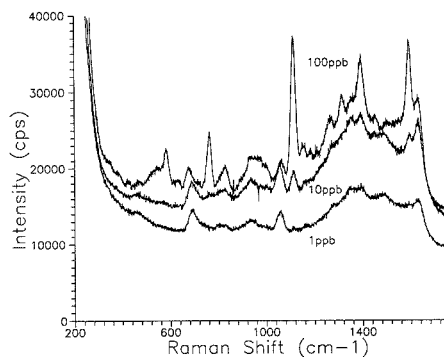


Figure 4. Surface-enhanced Raman spectra of sulfamerazine obtained at different drug concentrations. The relative intensities of the spectra represent true values.

in intensity during the first minute after mixing hydrosol and drug (hydrosol activation), which decrease slowly afterward. Activation of silver hydrosols has been reported previously (24–27). All subsequent experiments were made with careful attention to the timing of the measurement, the spectral scans starting 30 s after mixing hydrosol and drug.

Secondly, it was found that the SERS spectra of the drugs varied as the adsorbate concentration changed. Figure 4 shows the SERS spectra of sulfamerazine at three different concentrations. As shown, at lower concentrations, the SERS spectral features are poorly defined. Several bands can be seen in the spectrum corresponding to  $1\text{ ng mL}^{-1}$  of sulfamerazine, including two apparent peaks between  $600$  and  $1100\text{ cm}^{-1}$  and a broad band between  $1200$  and  $1700\text{ cm}^{-1}$ . These features remain constant for all concentrations of the sulfa drugs used and are also present in the blank. Possible sources are contaminants, luminescence background of the metal substrate (28), or graphitic carbon (29). These bands, if they cannot be removed, may affect limit of detection of sulfa drugs by colloidal SERS, although the  $1112\text{-cm}^{-1}$  peak, which is used for trace detection of these drugs, does not overlap any of these background features. It is also noticed that some modes grow at a different rate with concentration than other modes do. For instance, the mode at  $1630\text{ cm}^{-1}$  of sulfamerazine is more intense than the mode at  $1594\text{ cm}^{-1}$  at low concentrations ( $<10\text{ ng mL}^{-1}$ ). Similar changes were observed for the other two drugs studied. Those spectral changes may be an indication of different orientations of the adsorbate at the metal surface

Table III. SERS Calibration Curves for Sulfa Drugs on Silver Colloids

	calibration equation <sup>a</sup>	$r^b$
sulfadiazine	$y = 66.74x + 679.8$	0.997
sulfamerazine	$y = 143.82x + 771.2$	0.999
sulfamethazine	$y = 16.62x + 751.3$	0.999

<sup>a</sup> Linear least-squares fit.  $y$  represents SERS intensity in counts per second at  $1114\text{ cm}^{-1}$  (sulfadiazine and sulfamerazine) or at  $1112\text{ cm}^{-1}$  (sulfamethazine).  $x$  represents drug concentration in  $\mu\text{g mL}^{-1}$ . The concentration range used for all three least-squares calculations was  $1$  to  $100\text{ ng mL}^{-1}$ . <sup>b</sup> Correlation coefficient.

as the analyte concentration changes.

Table III summarizes the linear least-squares fit of the calibration curves for the sulfa drugs. The SERS intensities were measured at the most prominent peak of each drug, i.e.,  $1114\text{ cm}^{-1}$  for sulfadiazine and sulfamerazine and  $1112\text{ cm}^{-1}$  for sulfamethazine. Although other peaks could be chosen to monitor the intensity changes with concentration, observation of Figure 4 indicates the peak selected in each case presented the following advantages: (a) it provides the largest dynamic range, 2 orders of magnitude for each drug; selection of the vibrational mode at  $1390\text{ cm}^{-1}$  would provide a shorter linear dynamic range; (b) it allows the maximum sensitivity (slope), since the concentration dependence of the intensity is the largest; and (c) the limit of detection is improved since the selected peak is superimposed on a much lower background than that for the other peaks. For instance, Figure 4 shows that the peak at  $1114\text{ cm}^{-1}$  in sulfamerazine is over a lower background than the second most intense peak, at  $1594\text{ cm}^{-1}$ . Virtually the same arguments can be used for the choice of the monitoring Raman shifts for the other two drugs. Table III shows that the sensitivity changed with the drug considered. The sensitivity was maximum for sulfamerazine and minimum for sulfamethazine. The correlation coefficients were adequate in the three cases. Limits of detection calculated for a signal-to-noise ratio of 3:1 were found to be  $1\text{ ng mL}^{-1}$  for sulfadiazine and sulfamerazine and about  $10\text{ ng mL}^{-1}$  for sulfamethazine.

In conclusion, the results demonstrate that silver hydrosols can be developed as a practical substrate for the SERS detection of sulfonamides. They are an attractive approach because of the ease of production and manipulation. However, SERS intensities in this substrate are determined by an activation period which must be studied and optimized in each practical situation. Compounds of very similar structure can be fingerprinted in this substrate easily. In addition, extremely high sensitivity as well as quantitative information can be obtained with careful attention to the timing of the measurement process. This study constitutes a laboratory test on pure sulfa drugs. Although limits of detection for the colloidal SERS technique are found to be below  $10\text{ ng mL}^{-1}$ , the limit of reliable measurement, used by the FDA and FSIS, may be somewhat larger. A method for obtaining the sulfa drugs from real tissue samples that is compatible with the SERS experiment needs to be developed. Several of these methods are described by Horwitz (7, 8). Also, as is the case with TLC, HPLC, and all methods besides the Bratton-Marshall technique, collaborative studies among different laboratories need to be performed in order to ascertain the ultimate usefulness of colloidal SERS detection in the monitoring of sulfa drugs in edible animal tissue.

**Registry No.** Sulfadiazine, 68-35-9; sulfamerazine, 127-79-7; sulfamethazine, 57-68-1; silver, 7440-22-4; silver nitrate, 7761-88-8.

#### LITERATURE CITED

- (1) Bevil, R. F. In *CRC Handbook Series in Zoonoses; Volume 1, Section D: Antibiotics, Sulfonamides, and Public Health*; CRC Press, Inc.:

- Boca Raton, FL, 1984; pp 3, 30-31, 355-365.
- (2) Sigel, C. W.; Woolley, J. L. In *Densitometry in Thin Layer Chromatography*; Touchstone, J. C., Sherma, J., Eds.; Wiley: New York, 1979.
  - (3) Sophian, L. H.; Piper, D. L.; Schneller, G. H. *The Sulfapyrimidines*; Press of A. Colish: New York, 1952; p 10.
  - (4) Bratton, A. C.; Marshall, E. I. *J. Biol. Chem.* **1939**, *128*, 537.
  - (5) Sato, S.; Higuchi, S.; Tanaka, S. *Anal. Chim. Acta* **1980**, *120*, 209.
  - (6) Johnson, K. L.; Jeter, D. T.; Claiborne, R. C. *J. Pharm. Sci.* **1975**, *64*, 1657.
  - (7) Horwitz, J. J. *Assoc. Off. Anal. Chem.* **1981**, *64*, 104.
  - (8) Horwitz, J. J. *Assoc. Off. Anal. Chem.* **1981**, *64*, 814.
  - (9) Vo-Dinh, T.; Meier, M.; Wokaun, A. *Anal. Chim. Acta* **1986**, *181*, 139.
  - (10) Laserna, J. J.; Campiglia, A. D.; Winefordner, J. D. *Anal. Chem.* **1989**, *61*, 1697.
  - (11) Vo-Dinh, T. In *Chemical Analysis of Polycyclic Aromatic Compounds*, Vo-Dinh, T., Ed.; Wiley: New York, 1989; p 451.
  - (12) Torres, E. L.; Winefordner, J. D. *Anal. Chem.* **1987**, *59*, 1626.
  - (13) Laserna, J. J.; Berthod, A.; Winefordner, J. D. *Talanta* **1987**, *41*, 605.
  - (14) Laserna, J. J.; Berthod, A.; Winefordner, J. D. *Microchem. J.* **1988**, *38*, 125.
  - (15) Carrabba, M. M.; Edmonds, R. B.; Rauh, R. D. *Anal. Chem.* **1987**, *59*, 2559.
  - (16) Moody, R. L.; Vo-Dinh, T.; Fletcher, W. H. *Appl. Spectrosc.* **1987**, *41*, 966.
  - (17) Enlow, P. D.; Buncick, M. C.; Warmack, R. J.; Vo-Dinh, T. *Anal. Chem.* **1986**, *58*, 1119.
  - (18) Alak, A. M.; Vo-Dinh, T. *Anal. Chem.* **1987**, *59*, 2149.
  - (19) Laserna, J. J.; Campiglia, A. D.; Winefordner, J. D. *Anal. Chim. Acta* **1988**, *208*, 21.
  - (20) Creighton, J. A.; Blatchford, C. G.; Albrecht, M. G. *J. Chem. Soc., Faraday Trans.* **1979**, *75*, 790.
  - (21) Brock, T. D. *Membrane Filtration: A User's Guide and Reference Manual*; Science Tech. Inc.: Madison, WI, 1983; p 185.
  - (22) Dollish, F. R.; Fateley, W. G.; Bentley, F. F. *Characteristic Raman Frequencies of Organic Compounds*; Wiley: New York, 1974; p 53.
  - (23) Baranska, H.; Labudzinska, A.; Terpiński, J. *Laser Raman Spectrometry. Analytical Applications*; Ellis Horwood: Chichester, 1987; p 136.
  - (24) Laserna, J. J.; Torres, E. L.; Winefordner, J. D. *Anal. Chim. Acta* **1987**, *200*, 469.
  - (25) Berthod, A.; Laserna, J. J.; Winefordner, J. D. *Appl. Spectrosc.* **1988**, *41*, 1137.
  - (26) Blatchford, C. G.; Campbell, J. R.; Creighton, J. A. *Surf. Sci.* **1983**, *120*, 435.
  - (27) Kerker, M.; Siiman, O.; Wang, D.-S. *J. Phys. Chem.* **1984**, *88*, 3168.
  - (28) Heritage, J. P.; Bergman, J. G.; Pinczuk, A.; Worlock, J. M. *Chem. Phys. Lett.* **1979**, *67*, 229.
  - (29) Cooney, R. P.; Mernagh, T. P.; Mahoney, M. R.; Spink, J. A. *J. Phys. Chem.* **1983**, *87*, 5314.

RECEIVED for review August 22, 1989. Accepted December 26, 1989. J. J. Laserna gratefully acknowledges the Direccion General de Investigacion Cientifica y Tecnica (DGICYT), Ministerio de Educacion y Ciencia, Spain, for financial support. This research was supported by NIH Grant NIH-R01-GM11373-26.

## Effect of Reducing Disulfide-Containing Proteins on Electropray Ionization Mass Spectra

Joseph A. Loo, Charles G. Edmonds, Harold R. Udseth, and Richard D. Smith\*

Chemical Methods and Separations Group, Chemical Sciences Department, Pacific Northwest Laboratory, Richland, Washington 99352

**Electropray ionization produces multiply charged molecular ions for biomolecules with molecular weights in excess of 100 000. This allows mass spectrometers with limited mass-to-charge range to extend their molecular weight range by a factor equal to the number of charges. The maximum number of observed charges for peptides and smaller proteins correlates well with the number of basic amino acid residues (Arg, Lys, His), except for disulfide-containing molecules, such as lysozyme and bovine albumin. However, reduction of disulfide linkages with 1,4-dithiothreitol (Cleland's reagent) may allow the protein to be in an extended conformation and make "buried" basic residues available for protonation to yield higher charged molecular ions by the electropray ionization process. For larger proteins reduction of disulfide bridges greatly increases the maximum charge state, but charging of basic amino acid residues remains less efficient than for smaller proteins.**

### INTRODUCTION

Electropray ionization coupled with mass spectrometry (ESI-MS) began with the seminal experiments of Dole (1, 2), and after a 20-year gestation, reemerged in the laboratory of Fenn (3-5), who first published results of electropray ionization mass spectra of large molecules with molecular weights of up to 40 000 and demonstrated the propensity for multiple charging produced by this soft ionization technique (6, 7). The ability to produce multiply charged molecular ions for biomolecules allows mass spectrometers to analyze compounds with molecular weights exceeding the mass-to-charge ( $m/z$ ) range

of the instrument by a factor equal to the molecule's charge state. In fact, proteins with molecular weights in excess of 130 000 have been successfully analyzed in our laboratory by ESI-MS with a quadrupole mass spectrometer of limited  $m/z$  range (1700) (8). Initial tandem mass spectrometry (MS/MS) results of  $m/z$  selected multiply charged molecular ions of relatively large biomolecules appear promising (9-11).

The mechanism for desorption of multiply charged molecular ions from highly charged liquid droplets remains uncertain. The ion evaporation model of Iribarne and Thomson (12, 13), in which Coulombic explosion of rapidly evaporating liquid droplets of high charge density results in smaller charged droplets and continues this sequence until solute field-assisted desorption occurs, is widely accepted. However, slightly different mechanisms involving expulsion of very small charged droplets, or perhaps multiply charged molecular clusters as the Rayleigh limit is approached, may also operate. In this model, these very small droplets would then form the analyte ions of interest by evaporation of neutral solvent molecules. Regardless of the detailed mechanism(s) for the small submicrometer diameter droplets, the efficient transfer to the gas phase of highly charged macromolecules from the surface of the shrinking droplets is now well established. The maximum number of charges a molecule can retain by the ESI process for poly(ethylene glycol) oligomers has been estimated by Wong et al. (5) based upon an electrostatic repulsion argument. In their model the maximum charge state consistent with molecular stability was determined. Unsurprisingly, their ESI-MS data indicated multiple charging somewhat less than predicted by this approach. One explanation advanced for this observation was that ion evaporation is determined by

the kinetics for transport to the surface and the charge-state-dependent rate of ion evaporation from the droplet surface (7).

For peptides and proteins, we had previously observed (14) [as later supported by Covey et al. (15)] an approximate correlation between the maximum positive (multiply protonated) charge state observed in our positive ion electrospray ionization mass spectra and the total number of basic amino acid residues (i.e., arginine, lysine, and histidine) in the primary sequence plus the N-terminal amino group. For example, glucagon (average molecular weight,  $M_r = 3483$ ) possesses two arginines, one lysine, one histidine, and the N-terminal amino group; its ESI mass spectrum shows  $(M + 5H)^{5+}$  as the highest multiply charged species. However, the correlation for hen egg white lysozyme, a protein with 18 basic amino acids, is poor;  $(M + 14H)^{14+}$  is the most highly charged molecular ion observed. While the solution pH strongly affects protein charge state in solution, the effect upon ESI mass spectra is often quite small. A general assumption is that quaternary structure is lost for electrosprayed proteins, and for multimeric proteins the noncovalently bonded subunits are observed separately in the electrospray ionization mass spectra (8). For example, an ESI mass spectrum of lactate dehydrogenase from rabbit muscle ( $M_r = 140\,000$ ) yields multiply charged ions indicative of the four identical subunits ( $M_r = 35\,000$ ) (8). Clearly, the electrostatic forces leading to gas-phase ion formation are more than sufficient to separate the weakly bonded and similarly charged subunits in the absence of the stabilizing role of the solvent. Little is yet known regarding the effect of higher order structure on the extent of multiple charging. Thus, the factors governing both maximum charge state and the distribution of states remain largely undetermined.

In this study we have investigated aspects of the effect of protein structure upon ESI mass spectra by comparison of proteins with and without reduction of native disulfide bridges. By cleavage of cysteine-cysteine bonds, and thus by affecting the higher order structure of the protein, a dramatic effect on the number of positive charges is observed. The analytical utility of disulfide reduction reactions with ESI-MS and its relevance to collisionally activated dissociation (CAD) studies are addressed.

#### EXPERIMENTAL SECTION

The instrumentation used in this study and typical operating conditions have been previously described (8, 9, 16, 17). Samples in an aqueous acidic buffer solution, consisting of 1–5% (v/v) glacial acetic acid, are introduced through a 100  $\mu\text{m}$  i.d. fused silica capillary at a rate of 1  $\mu\text{L}/\text{min}$  and mixed with a liquid sheath electrode, typically methanol, flowing at 3  $\mu\text{L}/\text{min}$ , at the tip of the electrospray ionization source. Analyte and sheath flow are independently controlled by separate syringe pumps. A potential of +5 kV is applied to the sheath electrode, producing highly charged liquid droplets of  $\sim 1\ \mu\text{m}$  diameter (18) at atmospheric pressure in a flow of dry nitrogen to aid the desolvation process. The ESI source is mounted 1.5 cm from the entrance of the quadrupole MS. Highly charged ions are sampled through a 1-mm nozzle orifice and 2-mm skimmer and are efficiently transported through a cryopumped region by the radio frequency (rf) quadrupole lens to a quadrupole mass spectrometer for detection. For positive ions, the typical focusing lens voltage is +1 kV, with the nozzle at +200 V and the skimmer at ground potential. The mass spectrometer (Extrel Co., Pittsburgh, PA) used for these studies has an effective  $m/z$  range of 1700. Scan rates varied between 30 and 2 min over the entire  $m/z$  range. With the current data system (Teknivent, St. Louis, MO), peak abundances are collected at integer  $m/z$  values. Routine calibration of the  $m/z$  scale for ESI-MS was performed with low molecular weight polymers, such as poly(ethylene glycol) (average molecular weight 1000), monitoring both the singly charged (singly sodiated) and doubly charged (doubly sodiated) molecular ion distributions. Calibration was periodically checked by ESI-MS with well-characterized

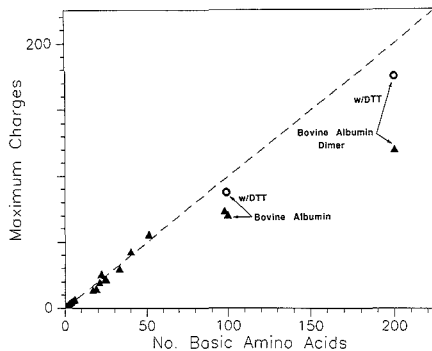


Figure 1. Correlation between basic amino acid residues (arginine, lysine, and histidine) and maximum positive charge observed in ESI mass spectra for a number of peptides and proteins examined in our laboratory. The dashed reference line has a slope of 1. (See Table I for a more complete listing.)

protein samples, such as horse heart cytochrome *c* ( $M_r = 12\,360$ ). While 50–100 pmol of material was consumed for each spectrum, we have demonstrated the ability to analyze low femtomole quantities with our present instrumentation (19).

The protein samples were commercially obtained from Sigma Chemical Co. (St. Louis, MO) with the exception of lactate dehydrogenase (CALBIOCHEM Corp., San Diego, CA) and methionine-human growth hormone (kindly provided by Dr. Ian Jardine, Finnigan MAT) and used without further purification. ESI mass spectra were obtained for the native proteins immediately after glacial acetic acid was added to the aqueous solution. Reduction of disulfide bonds was carried out with Cleland's reagent, 1,4-dithiothreitol (DTT) (20). A small amount of an aqueous DTT solution was added to an aliquot of the undenatured protein solution ( $\sim 0.1\ \text{mM}$ ) in distilled water, such that the final DTT concentration was approximately 5–10 mM. After a period of over 12 h at room temperature, glacial acetic acid was added (1–5%) to the protein sample containing DTT and its mass spectrum obtained. A commercial sample of an *S*-carboxymethyl derivatized bovine  $\alpha$ -lactalbumin was prepared in similar fashion.

#### RESULTS AND DISCUSSION

As first demonstrated by Fenn and co-workers (6, 7), electrospray ionization produces multiply charged (typically protonated) molecular ions for high molecular weight peptides and proteins. For compounds with molecular weights greater than  $\sim 10\,000$ , a typical ESI mass spectrum shows a bell-shaped distribution of charge states, composed of multiply protonated molecular ions, effectively extending the molecular weight range addressable by a factor equal to the number of charges. For a pure compound, any two peaks in the ESI mass spectrum provide sufficient information to determine both the charge state and the ion mass since adjacent peaks differ by only one charge (6–11, 14–16). Additional peaks can be utilized for improved molecular weight precision and accuracy. The ability to shift the multiple charge distribution to higher  $m/z$  (a decrease of charge state) by changing the liquid sheath composition (14) or by increasing the collision energy in the high-pressure region of the atmospheric pressure inlet (such that the more highly charged species undergo CAD) has been previously demonstrated (16).

For most peptides and proteins, with molecular weights ranging from a few hundred to  $\sim 40\,000$ , a relatively good linear correlation is observed between the number of basic amino acid residues (plus one for the N-terminus) and the maximum positive charge state observed in the ESI mass spectrum, as demonstrated in Figure 1 and Table I. Additionally, tandem mass spectrometry (9) of the various multiply protonated species for melittin ( $M_r = 2845$ ) (up to the  $(M +$

**Table I. Peptides and Proteins Analyzed by Electrospray Ionization-Mass Spectrometry**

peptide/protein	$M_r$	amino acid residues		disulfide linkages	maximum ESI charge
		total	basic (+N-term)		
Leu-enkephalin	555	5	1	0	1
bradykinin	1060	9	3	0	3
gramicidin S	1141	10	2	0	2
angiotensin I	1296	10	4	0	4
melittin	2846	26	6	0	6
glucagon	3483	29	5	0	5
cytochrome c (horse)	12360	104	25	0	21
$\alpha$ -lactalbumin (bovine)	14175	123	17	4	13
lysozyme (hen egg)	14306	129	19	4	14
myoglobin (horse)	16950	153	33	0	29
$\beta$ -lactoglobulin B	18277	162	21	2	19
trypsin inhibitor (soybean)	20091	181	22	2	23
Met-human growth hormone	22255	192	24	2	21
carbonic anhydrase (bovine)	29024	259	39	0	42
lactate dehydrogenase (rabbit muscle)	35500	333	51	3	55
bovine albumin	66266	582	100	17	71
ovotransferrin	77500	684	98	15	73
bovine albumin dimer	133000	1164	200	34	120

6H)<sup>6+</sup> species) produced by electrospray ionization support this assumption (i.e., that the positive charges reside on the three lysine residues, the two arginine sites, or the N-terminal amino group). Biemann and co-workers (21) have also speculated that protonation for peptides occurs at basic amino acid sites (when present). This suggestion is also supported by gas-phase proton affinity data for amino acids; arginine, histidine, and lysine were found to have the highest proton affinities (22).

However, ESI mass spectra of *selected* proteins with molecular weights exceeding 10 000 (e.g., lysozyme) do not yield the expected high positive charge states that would be indicated by their amino acid sequence. A common feature of such proteins is the presence of more than one disulfide bridge. For example, hen egg lysozyme and bovine  $\alpha$ -lactalbumin each have four disulfide bonds. Bovine albumin has as many as 17 cysteine-cysteine bridges in its primary sequence (23), and the maximum number of charges observed in its ESI mass spectrum (8) (slightly greater than 60 positive charges) is much less than the 100 basic residues seemingly available for protonation.

A number of studies dealing with the mass spectrometric analysis of disulfide-containing peptides with fast atom bombardment (FAB-MS) (24-27) and plasma desorption (PD-MS) (28, 29) have been published. Monitoring the reduction reaction of disulfide bonds with reducing agents (such as DTT) by mass spectrometry allows one to assess the rate and extent of reaction and obtain important information regarding the number of disulfide bonds (by measuring the small mass increase associated with the reaction to form sulfhydryl groups) and the nature of the linkages (e.g., whether the peptide is composed of several peptide chains linked by interchain disulfide bonds). For example, it is possible to follow the reduction reaction of insulin, by FAB-MS and PD-MS,

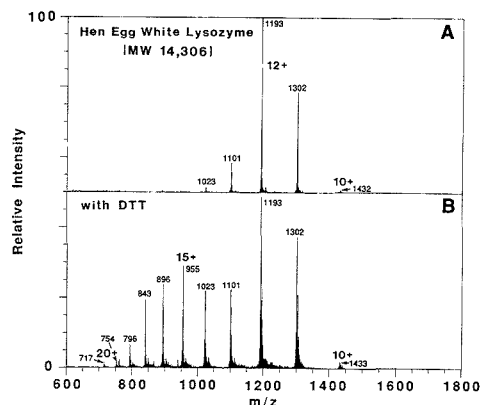


**Figure 2.** (A) ESI mass spectra of hen egg white lysozyme in 5% glacial acetic acid and (B) upon the addition of DTT.

and monitor the disappearance of the intact molecular ion as the ions indicative of the A-chain and the B-chain, bound by two disulfide bridges in the native state, appear (25, 26, 28, 29). ESI-MS has been used (11) to distinguish the oxidized form of somatostatin ( $M_r = 1637.9$ ), a cyclic peptide due to an intramolecular cysteine-cysteine linkage, from its reduced state ( $M_r = 1639.9$ ) in much the same manner as reported by PD-MS (28) and FAB-MS (25, 30). A 1 and 0.67  $m/z$  unit difference between the doubly and triply charged molecular ions, respectively, of the oxidized and reduced state was measured by ESI-MS instead of measuring a molecular weight difference of 2 for the singly charged molecular ion. Tandem mass spectrometry (11) of the doubly and triply charged reduced state yields much more fragmentation versus the corresponding oxidized state since two bonds must be broken to generate a typical product ion from the cyclic portion of the molecule. Martin and Biemann (30) have previously published similar results for the singly charged molecular ion generated by FAB. A recently published study (31) demonstrated the capability to monitor the reduction reaction of the cyclic peptide, oxytocin, by  $\beta$ -mercaptoethanol with ion spray MS and MS/MS. Alternatively, oxidation of disulfide-containing peptides by performic acid (oxidizing half-cystinyl groups to cysteic acid) followed by mass spectrometric analysis of peptides can determine the number of disulfide linkages present (27). Since disulfide bond reduction in proteins ( $M_r > 10\ 000$ ) using DTT has been noted (32), the same type of information should be obtainable with electrospray ionization mass spectrometry for substantially larger proteins.

Because it is well established that protein conformation in solution depends in a complex fashion upon the intramolecular forces dictated by its amino acid sequence, the direct reductive cleavage of disulfide bonds should greatly affect the higher order structure of the protein. A protein with disulfide bonds in its native conformation may have several basic amino acid sites that are effectively "buried" in the globular structure, resulting in more hydrophobic environments that are not as readily protonated. Disulfide-cleavage reactions should allow the protein to "relax" into more extended conformations, allowing such buried sites to be more readily protonated.

Evidence for this is demonstrated by the following comparisons of mass spectra of ESI generated gas-phase ions from highly charged liquid droplets for disulfide-containing proteins, and its DTT reduced form. The typical electrospray ionization mass spectrum for lysozyme is shown in Figure 2A with multiple charging clearly evident up to the  $(M + 14H)^{14+}$  species. However, as previously discussed, egg white lysozyme

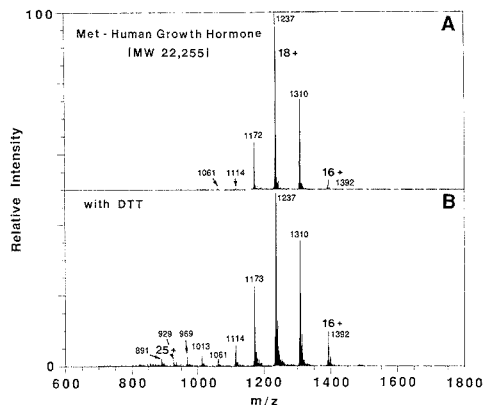


Figure 3. (A) Electrospray ionization mass spectra of Met-human growth hormone in 5% acetic acid and (B) upon reduction with DTT.

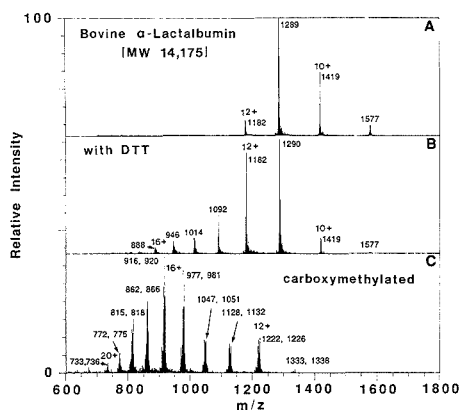


Figure 4. (A) ESI mass spectra of bovine  $\alpha$ -lactalbumin, (B) after reduction with DTT, and (C) a mass spectrum from a commercial sample of the reduced and carboxymethylated form.

has a total sum of 18 basic amino acids. Breaking cysteine-cysteine linkages with the addition of DTT allows greater multiple protonation to occur, as demonstrated in Figure 2B. The same effect has been observed for a number of other proteins. Met-human growth hormone ( $M_r = 22\,255$ ) has a total sum of 23 basic amino acids and an N-terminal group, yet its ESI mass spectrum (Figure 3A) shows only a trace of the  $(M + 21H)^{21+}$  molecular ion, with the  $(M + 18H)^{18+}$  species dominant. The addition of DTT to reduce its two disulfide bonds (Figure 3B) increases the relative abundance of the more highly charged molecular ions, allowing a maximum charge state where all basic sites can be protonated. Similar results are shown in Figure 4 for bovine  $\alpha$ -lactalbumin, a protein with a covalent structure quite similar to chicken lysozyme that also possesses four disulfide linkages. Its typical ESI mass spectrum (Figure 4A) shows the  $12+$  species as the highest charged ion, compared to the total of 16 basic amino acids. Reduction of the disulfide bonds with DTT allows the molecule to obtain up to 16 positive charges (Figure 4B). Reduction of disulfide bonds with subsequent carboxymethylation (with iodoacetate) yields similar results, but with even greater protonation than anticipated, as shown in Figure 4C. From Bojesen's proton affinity (PA) data (22), glutamine has a similar gas-phase PA as lysine. It may be possible that

Table II.  $M_r$  Determination for Three Proteins by ESI-MS

protein	$M_r$ (measured)	$M_r$ (expected) <sup>a</sup>
lysozyme (hen egg) <sup>b</sup>		
native	$14\,306.5 \pm 4.1$	14 306.2
reduced	$14\,311.5 \pm 6.4$	14 314.1
$\alpha$ -lactalbumin (bovine) <sup>c</sup>		
native	$14\,174.7 \pm 6.1$	14 175.0
reduced	$14\,180.8 \pm 5.7$	14 183.0
carboxymethylated	$14\,645.6 \pm 5.8$	14 647.4
	$(14\,703.0 \pm 2.7)^c$	$(14\,705.4)^c$
Met-human growth hormone <sup>d</sup>		
native	$22\,254.2 \pm 4.8$	22 255.2
reduced	$22\,259.3 \pm 7.4$	22 259.2

<sup>a</sup>From amino acid sequence. <sup>b</sup>Figure 2. <sup>c</sup>Figure 4. <sup>d</sup>Figure 3. <sup>e</sup>See text for explanation.

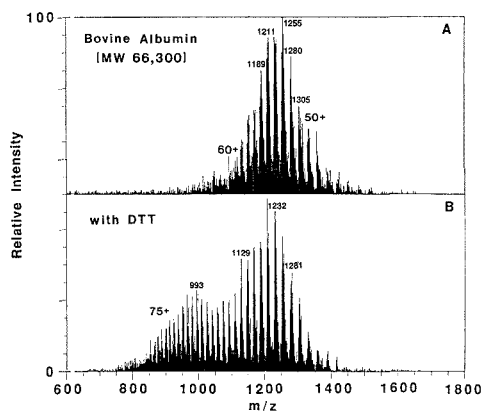


Figure 5. (A) ESI mass spectra of bovine albumin before and (B) after reduction of its disulfide linkages.

three of the five glutamine residues of  $\alpha$ -lactalbumin can be protonated under our ESI conditions. Similarly, the data from lysozyme (Figure 2) and Met-human growth hormone (Figure 3) indicate additional charging beyond predicted values. Both proteins contain Gln residues (3 and 14, respectively) as possible protonation sites. More experiments are needed to verify these results. In addition to an increase in multiple charging (up to  $+20$ ) for  $\alpha$ -lactalbumin, an increase in molecular weight due to eight carboxymethyl groups (an approximate molecular weight increase of 472 from the disulfide-bearing molecule), is deduced from the  $m/z$  shift observed (Table II). This shift allows one to readily determine the number of disulfide linkages in large proteins by ESI-MS. A closer inspection of the mass spectrum of  $S$ -carboxymethyl- $\alpha$ -lactalbumin also reveals that each multiply charged peak is actually a doublet with a peak separation consistent with an extra carboxymethylated moiety (Table II). Alkylation of similar-sized proteins with iodoacetate have found contributions due to reaction of the histidine and methionine side chains to form the carboxymethyl modification (33, 34). Lactalbumin has one methionine and three histidine residues which may undergo this type of reaction. An examination of the rate of reaction of bovine  $\alpha$ -lactalbumin with iodoacetate indicated that the single methionine residue was the most reactive site (34). Although the measured peak positions listed allowed an  $M_r$  accuracy and precision of generally better than  $\pm 0.03\%$ , improvements in the data system to allow recording of peak positions in less than one  $m/z$  unit intervals should

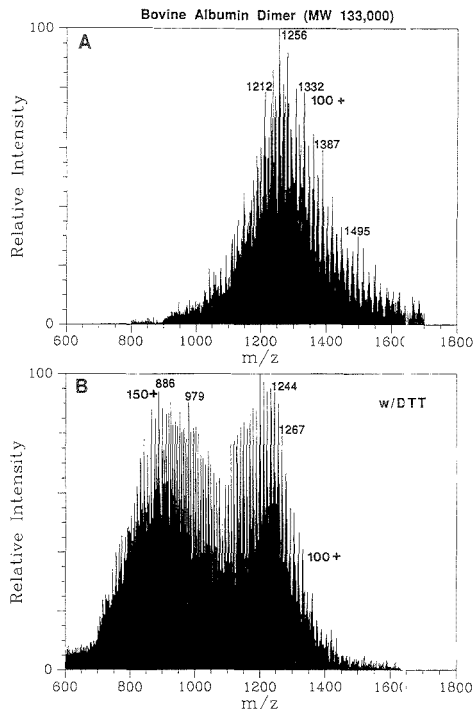


Figure 6. (A) ESI mass spectra of bovine albumin dimer before and (B) after the addition of DTT.

markedly enhance  $M_r$  measurements and should allow for unambiguous determination of the number of disulfide bonds (8).

Figures 5 and 6 depict similar results obtained for bovine albumin ( $M_r \sim 66\,600$ ) and the native bovine albumin dimer species ( $M_r \sim 133\,000$ ). Again, the dramatic increase in relative abundance of the higher charged species is evident. Over 175 positive charges can be resolved in the mass spectrum for the albumin dimer molecule treated with DTT, an increase of over 50 charges relative to the unreduced form.

The bimodal multiple charge distribution obtained after reaction with dithiothreitol is probably due to incomplete reduction or re-formation of the disulfide bonds. Separation of the reaction products by LC/MS (31) or capillary electrophoresis-MS (8, 35) should clarify the situation. Reactions are typically performed in buffered solutions with a pH of approximately 8–9 (20, 32). No attempt was made in this report to study the pH dependence of the effect of protein denaturing agents such as urea or guanidinium chloride upon the reduction reaction. However, the reaction in an unbuffered distilled water solution proceeded much slower than that reported for the buffered system (32). For example, Figure 5 compares mass spectra of unreduced bovine albumin (top figure) and the reaction product of albumin with DTT sampled after 12 h. A spectrum obtained after only 4 h shows only a slight increase in abundance of the higher charged molecular ions. Nearly complete reduction of bovine albumin with dithiothreitol is reported to occur in approximately 1 h at pH 8.2 (32). It is conceivable that even after 12 h with our system, reduction of disulfide bonds remains incomplete. Its globular structure may be partially retained, preventing protonation to the extent expected from the number of basic amino acid residues. Also, such large molecules may begin

to tax the electrospray ionization process by demanding too high a charge concentration on a small region of the droplet surface.

## CONCLUSIONS

The ability to produce and observe by ESI-MS a dramatic increase in the number of positive charges for disulfide-containing proteins as large as  $M_r > 130\,000$  upon the reduction of disulfide linkages with 1,4-dithiothreitol has been demonstrated. The enhanced protonation is presumably a result of allowing the protein molecule to attain a more extended tertiary structure, thus allowing otherwise inaccessible sites to be protonated. A good linear correlation between the maximum positive charge state observed in the ESI mass spectrum and the number of basic residues has been observed in the absence of disulfide bonds. The appearance of more highly charged molecular ions due to the reduction of disulfide bonds of peptides and proteins can be readily monitored by ESI-MS. The potential for quantitative determination of the number of disulfide bonds, particularly for larger proteins remains to be determined.

The production of more multiply charged molecular ions extends the mass spectrometer's molecular weight limit for MS and MS/MS experiments of large peptides and proteins. The efficient protonation is especially important for instruments of limited  $m/z$  range and the analysis of disulfide-containing proteins with limited number of basic amino acid residues. Highly charged parent ions allows more highly charged daughter ions to be produced and detected (9, 11, 36). For example, with a triple quadrupole instrument (1400  $m/z$  limit), doubly charged sequence ions were detected in the MS/MS spectrum of the  $(M + 3H)^{3+}$  ion from the B-chain of bovine insulin (oxidized,  $M_r = 3496$ ) (36). Abundant 4+ product ions were formed from CAD of the  $(M + 6H)^{6+}$  ion of melittin; however, the highest charged fragment ions from dissociation of the  $(M + 5H)^{5+}$  species were 3+ (9). Greater CAD efficiencies have been obtained for more highly charged species from large peptides (9, 37, 39) and proteins (10, 11, 37–39), facilitated by the higher energy collisions possible and perhaps by the strained (extended) conformation due to charge repulsion. Reduction of disulfide bridges, in addition of "opening" up the molecule and allowing product ions to be generated from regions formerly enclosed by disulfide linkages, allows ESI-MS/MS to directly access and probe more highly charged protein species.

## LITERATURE CITED

- (1) Dole, M.; Mack, L. L.; Hines, R. L.; Mobley, R. C.; Ferguson, L. D.; Alice, M. B. *J. Chem. Phys.* **1968**, *49*, 2240–2249.
- (2) Mack, L. L.; Kralik, P.; Rheude, A.; Dole, M. *J. Chem. Phys.* **1970**, *52*, 4977–4986.
- (3) Yamashita, M.; Fenn, J. B. *J. Phys. Chem.* **1984**, *88*, 4451–4459.
- (4) Whitehouse, C. M.; Dreyer, R. N.; Yamashita, M.; Fenn, J. B. *Anal. Chem.* **1985**, *57*, 675–679.
- (5) Wong, S. F.; Meng, C. K.; Fenn, J. B. *J. Phys. Chem.* **1988**, *92*, 546–550.
- (6) Mann, M.; Meng, C. K.; Fenn, J. B. *Anal. Chem.* **1989**, *61*, 1702–1708.
- (7) Meng, C. K.; Mann, M.; Fenn, J. B. *Z. Phys. D: At., Mol., Clusters* **1988**, *10*, 361–368.
- (8) Loo, J. A.; Udseth, H. R.; Smith, R. D. *Anal. Biochem.* **1989**, *179*, 404–412.
- (9) Barinaga, C. J.; Edmonds, C. G.; Udseth, H. R.; Smith, R. D. *Rapid Commun. Mass Spectrom.* **1989**, *3*, 160–164.
- (10) Smith, R. D.; Barinaga, C. J.; Udseth, H. R. *J. Phys. Chem.* **1989**, *93*, 5019–5022.
- (11) Loo, J. A.; Edmonds, C. G.; Barinaga, C. J.; Udseth, H. R.; Smith, R. D., unpublished results.
- (12) Iribarne, J. V.; Thomson, B. A. *J. Chem. Phys.* **1976**, *64*, 2287–2294.
- (13) Thomson, B. A.; Iribarne, J. V. *J. Chem. Phys.* **1979**, *71*, 4451–4463.
- (14) Loo, J. A.; Udseth, H. R.; Smith, R. D. *Biomed. Environ. Mass Spectrom.* **1988**, *17*, 411–414.
- (15) Covey, T. R.; Bonner, R. F.; Shushan, B. I.; Henion, J. *Rapid Commun. Mass Spectrom.* **1988**, *2*, 249–256.
- (16) Loo, J. A.; Udseth, H. R.; Smith, R. D. *Rapid Commun. Mass Spectrom.* **1988**, *2*, 207–210.

- (17) Smith, R. D.; Barinaga, C. J.; Udseth, H. R. *Anal. Chem.* **1988**, *60*, 1948-1952.
- (18) Fein, J. B.; Mann, M.; Meng, C. K.; Wong, S. F.; Whitehouse, C. M. *Mass Spectrom. Rev.* **1990**, *9*, 37-70.
- (19) Edmonds, C. G.; Loo, J. A.; Fields, S. M.; Barinaga, C. J.; Udseth, H. R.; Smith, R. D. In *Proceedings of the Second International Symposium on Mass Spectrometry in the Health and Life Sciences* (San Francisco, CA, August 1989); Burlingame, A. L., McCloskey, J. A., Eds.; Elsevier: Amsterdam, in press.
- (20) Cleland, W. W. *Biochemistry* **1964**, *3*, 480-482.
- (21) Johnson, R. S.; Martin, S. A.; Biemann, K. *Int. J. Spectrom. Ion Process* **1988**, *86*, 137-154.
- (22) Bojesen, G. J. *Am. Chem. Soc.* **1987**, *109*, 5557-5558.
- (23) Peters, T., Jr. In *Advances in Protein Chemistry*; Anfinsen, C. B., Edsall, J. T., Richards, F. M., Eds.; Academic Press: Orlando FL, **1985**, Vol. 37, pp 161-245.
- (24) Larsen, B. S.; Yergey, J. A.; Cotter, R. J. *Biomed. Mass Spectrom.* **1985**, *10*, 586-587.
- (25) Buko, A. M.; Fraser, B. A. *Biomed. Mass Spectrom.* **1985**, *12*, 577-585.
- (26) Morris, H. R.; Pucci, P. *Biochem. Biophys. Res. Commun.* **1985**, *126*, 1122-1128.
- (27) Sun, Y.; Smith, D. L. *Anal. Biochem.* **1988**, *172*, 130-138.
- (28) Chait, B. T.; Field, F. H. *Biochem. Biophys. Res. Commun.* **1986**, *134*, 420-426.
- (29) Roepstorf, P.; Nielsen, P. F.; Klarskov, K.; Højrup, P. *Biomed. Environ. Mass Spectrom.* **1988**, *16*, 9-18.
- (30) Martin, S. A.; Biemann, K. *Int. J. Mass Spectrom. Ion Processes* **1987**, *78*, 213-228.
- (31) Lee, E. D.; Mück, W.; Henion, J. D.; Covey, T. R. *J. Am. Chem. Soc.* **1989**, *111*, 4600-4604.
- (32) Bewley, T. A.; Li, C. H. *Int. J. Protein Res.* **1969**, *1*, 117-124.
- (33) Fruchter, R. G.; Crestfield, A. M. *J. Biol. Chem.* **1967**, *242*, 5807-5812.
- (34) Castellino, F. J.; Hill, R. L. *J. Biol. Chem.* **1970**, *245*, 417-424.
- (35) Loo, J. A.; Jones, H. K.; Udseth, H. R.; Smith, R. D. *J. Microcolumn Sep.* **1989**, *5*, 223-229.
- (36) Loo, J. A.; Barinaga, C. J.; Edmonds, C. G.; Udseth, H. R.; Smith, R. D. *Collected Abstracts: Proceedings of the 37th ASMS Conference on Mass Spectrometry and Allied Topics*, May 21-26, 1989, Miami Beach, FL; American Society for Mass Spectrometry: East Lansing, MI, pp 586-587.
- (37) Smith, R. D.; Loo, J. A.; Barinaga, C. J.; Edmonds, C. G.; Udseth, H. R. *J. Am. Soc. Mass Spectrom.*, in press.
- (38) Smith, R. D.; Barinaga, C. J. *Rapid Commun. Mass Spectrom.*, in press.
- (39) Smith, R. D.; Loo, J. A.; Edmonds, C. G.; Barinaga, C. J.; Udseth, H. R. *Anal. Chem.*, in press.

RECEIVED for review July 18, 1989. Accepted January 2, 1990. We thank the National Science Foundation (DIR 8903096) and the U.S. Department of Energy, through PNL Internal Exploratory Research, for support of this research under Contract DE-AC06-76RLO 1830. Pacific Northwest Laboratory is operated by Battelle Memorial Institute.

## Hadarnard Transform Measurement of Tandem Fourier-Transform Mass Spectra

Evan R. Williams, Stanton Y. Loh, and Fred W. McLafferty\*

Chemistry Department, Baker Laboratory, Cornell University, Ithaca, New York 14853-1301

Robert B. Cody

Nicolet Analytical Instruments, 6416 Schroeder Road, Madison, Wisconsin 53711

The simultaneous collection of multiple spectra using tandem (MS/MS) and multidimensional (MS/MS/MS) mass spectrometry from multiple precursors is demonstrated to yield correspondingly enhanced sensitivity. This approach utilizes Hadarnard transform deconvolution and takes advantage of the multichannel dissociation capability of Fourier-transform mass spectrometry. By application of this to an 11-component mixture, the 11 spectra of the products of dissociating 11 different combinations of six of the component molecular ions are measured; Hadarnard transformation yields individual spectra of the precursor ions exhibiting a signal-to-noise improvement of 1.8X over spectra measured separately, as predicted by theory. Precursor ion selection with high specificity and product formation with high abundance reproducibility are critical; spurious peaks resulting from imperfect reproducibility can be minimized by using simultaneous equation coefficients reflecting the degree of precursor dissociation. Extension of this technique to MS<sup>n</sup> spectra is demonstrated with simultaneous MS/MS/MS monitoring of three precursors and three daughters yielding nine spectra representing the nine possible dissociation pathways. For MS<sup>n</sup> spectra, coding the product relationships for each additional step (e.g., precursor → daughter, daughter → granddaughter) requires elimination of half of the remaining ions. No ions are lost for coding in an improved Hadarnard approach in which the combined daughter spectrum of the selected half of the precursors is subtracted from that of the other half.

Identification of scores of compounds in complex mixtures and structural elucidation of large molecules presents a dif-

icult challenge in chemical analysis. Tandem mass spectrometry (MS/MS, MS<sup>n</sup>) (1, 2) greatly increases the information obtainable from these samples and is widely used for solving "needle-in-the-haystack" type problems of trace components in complex mixtures. However, applying MS/MS to many components is hampered by the great sensitivity loss encountered if the MS-II spectrum of each precursor must be measured individually, discarding the precursor ions of all other components. When analysis time or sample quantity is limited, e.g., on-line trace analysis for toxic substances in incinerator exhaust, peptide sequencing, etc., the use of this technique is limited to just a few precursors. MS<sup>n</sup> spectra, in which mass-selected products are dissociated to produce further spectra, present an even greater measurement problem, since the number of possible dissociation or reaction pathways increases exponentially with *n*.

Recently two methods have been developed for simultaneous collection of MS/MS spectra in which only half, instead of all other, of the precursor ions must be discarded. Both methods utilize Fourier-transform (FT) ion cyclotron resonance (ICR) mass spectrometry (3-15). One uses a second FT step (14, 15) analogous to 2D-NMR; after initial radio frequency (rf) excitation of the precursor ions into cyclotron orbits, a deexcitation rf pulse after a specific delay time *t*<sub>1</sub> changes the effective abundance of specific precursor ions as a function of the phase difference, which is dependent on the precursor *m/z* value. The secondary mass spectra are then recorded as a function of *t*<sub>1</sub>; the Fourier transform of this function for a specific mass peak then shows the abundance originating from each precursor. In our Hadarnard transform (HT) method (3), half of the *p* precursor ions are selected and dissociated simultaneously, and the spectrum of the combined



products is measured; the process is repeated for a total of  $p$  times, selecting a different half of the precursors each time. The abundance of a specific mass peak in a spectrum represents the sum of contributions from each precursor used; thus each individual contribution can be calculated by using the corresponding abundance values from the  $p$  combined spectra, solving the  $p$  simultaneous equations for  $p$  unknowns, with the process repeated for each specific mass peak. Analytical applications of the Hadamard transform have been reviewed recently (16).

We present here more detailed applications of the HT method, demonstrating that the improvement in signal/noise (S/N) for both MS/MS and MS/MS/MS spectra is as expected, and propose a Hadamard differences method in which no precursor ions must be discarded. The Hadamard method requires the instrumental ability to select and simultaneously dissociate any combination of precursor ions, advantages of ion trap and Fourier-transform mass spectrometry (FTMS) that have received little attention. FTMS (4-13) has the further advantage of multiple precursor selection at high resolution over a wide mass range using Marshall's stored-waveform inverse Fourier-transform (SWIFT) excitation (12, 13). Such on/off selection of precursors for this multichannel dissociation provides the information relating precursors to their corresponding daughters in each of the series of combined MS-II spectra for the HT method (3, 17); precursor modulation for this encoding utilizes a sine function for the FT method (14, 15). In both the HT and FT methods, this signal modulation results in the loss of approximately half the signal (although a method proposed below makes this loss unnecessary). These methods differ in the number of MS-II combination spectra that must be measured. The minimum number of HT spectra is determined by the number of precursors that will be dissociated, while the FT method is independent of this number. On the other hand, for FT the number of spectra required depends directly on the precursor mass range and resolution, while these have no effect on the number of spectra required for HT. In addition, for the most common form of MS-II spectra, collisionally activated dissociation (CAD), reproducible product abundances require reproducible collision conditions, for which SWIFT (12, 13) used in the HT method is ideally suited. With the FT method, however, ion kinetic energy (and therefore collision energy) is a function of time, resulting in nonsinusoidal fragment abundance. Such FT deviations should also be encountered with photodissociation and other dissociation methods in which the extent of the interaction is regionally dependent.

Of the instruments commonly used for MS/MS, FTMS (4) has the further advantage of multichannel high-resolution detection (as well as selection) over a wide mass range, so that a complete MS-II spectrum of a precursor can be collected with the same efficiency as detection of a single daughter ion (5-7). The ability to store ions gives FTMS extensive capabilities for MS/MS including CAD (8-10, 18), dissociation with electrons (11), surfaces (19-21), and photons (18, 22-25), as well as ion-molecule reactions (26, 27). Finally, electrospray methods can now ionize molecules of 100 000 daltons producing multiply charged ions of only  $m/z \sim 1000$  (28-30); at this value FTMS resolving power is  $>10^6$ , promising unit resolution MS<sup>n</sup> measurements for characterization of important large molecules (30).

#### EXPERIMENTAL SECTION

A Nicolet FTMS-2000 with a 3-T magnet (3, 18, 20, 21) was used in the dual cell configuration (31). For the simultaneous collection of the MS-II spectra of 11 molecular ions (those representing the most abundant isotopic compositions), a synthetic 11-component mixture (Table I, all compounds were obtained commercially and used without further purification) was introduced in the source side at a pressure of  $10^{-6}$  Torr and ionized

Table I. Eleven-Component Mixture

no.	compound	M <sup>+</sup> , $m/z$	most abundant CAD ions, $m/z$
1	thiophene	84	58, 45
2	cyclohexanone	98	55, 79, 41, 69, 43
3	1,2-dimethylbenzene	106	91, 65
4	3-methylanisole	122	91, 92, 77, 107, 79, 121
5	2-methoxyphenol	124	109, 81, 53, 77
6	<i>n</i> -butylbenzene	134	91, 92
7	1-fluoro-4-nitrobenzene	141	83, 30, 111, 95, 57, 75
8	2-fluorobenzotrifluoride	164	114, 145, 163, 83
9	1-bromo-4-fluorobenzene	174	95, 75
10	1,2,4-trichlorobenzene	180	145, 109
11	4-bromoanisole	186	171, 143, 79, 77, 107, 156

with 20-eV electrons. For the spectra representing 11 different Hadamard combinations of six molecular ions, the ions were transferred to the analyzer side ( $10^{-9}$  Torr) and a Hadamard "mask" (32-34) was applied by ejecting five molecular ions using SWIFT excitation (12, 13). Fragment ions were ejected by using three additional SWIFT waveforms, leaving six isolated precursors in the cell. These ions were simultaneously excited to  $\sim 25$  eV kinetic energy with a single SWIFT waveform of frequencies for all 11 precursors and dissociated by using N<sub>2</sub> collision gas introduced via a set of pulsed valves (9). After a 500-ms reaction time, the resulting ions were brought into coherence with broad-band SWIFT excitation and detected (32K data points, 50 signal averaged scans). From these spectra were subtracted blank spectra, collected by eliminating the parent ion CAD pulse, to produce the 11 combination CAD spectra. The abundance at each  $m/z$  value for the individual MS-II spectra was calculated from the 11 combination spectra by simultaneously solving the resulting 11 equations (32-34) in which all coefficients are zeros or  $n$ 's, where  $n$  is the abundance (negative in sign) of each parent ion, normalized over all 11 spectra, determined from each subtracted spectrum. For example, for  $m/z$  171 the six combination spectra obtained by using 4-bromoanisole, 11, as the precursor show equal abundances, while no other combination spectra exhibit this peak; thus solving these simultaneous equations must show that  $m/z$  171 in the indicated abundance comes only from precursor 11.

For the simultaneous collection of the nine MS<sup>3</sup> spectra for three daughter ions of three precursors, molecular ions of 1-propen-3-ol ( $m/z$  58), 1-butanol ( $m/z$  72), and *n*-hexane ( $m/z$  86) were similarly isolated and dissociated. Daughter ions at  $m/z$  29 (C<sub>2</sub>H<sub>5</sub><sup>+</sup>, CHO<sup>+</sup>),  $m/z$  43 (C<sub>3</sub>H<sub>7</sub><sup>+</sup>, C<sub>2</sub>H<sub>5</sub>O<sup>+</sup>), and  $m/z$  57 (C<sub>4</sub>H<sub>9</sub><sup>+</sup>, C<sub>3</sub>H<sub>7</sub>O<sup>+</sup>) were isolated at unit mass resolution and again dissociated to produce complete granddaughter (MS-III) spectra. Hadamard masks were applied in both MS-I and MS-II stages by ejecting one molecular and one daughter ion prior to ion isolation. The remaining ions were dissociated simultaneously in each MS stage by CAD using pulsed N<sub>2</sub> collision gas. This was repeated for the nine possible ejection combinations representing the nine dissociation pathways (e.g. *n*-hexane  $\rightarrow$  C<sub>4</sub>H<sub>9</sub><sup>+</sup>  $\rightarrow$  granddaughters). The abundances at each  $m/z$  value for the individual MS-III spectra from each of these pathways were calculated from the resulting nine simultaneous equations.

#### RESULTS AND DISCUSSION

**Background Interference.** In this multistage FTMS experiment, the presence of any ions other than the chosen precursors for the CAD step was found to interfere seriously with daughter ion measurements. The procedures of the initial experiments (3, 17) were improved to minimize this problem. The cell pressure was kept low to avoid ion-molecule reactions, and the electron ionization energy was decreased to 20 eV to increase the relative abundances of molecular ions. To maximize the elimination of nonprecursor ions, their excitation by SWIFT (12, 13) appears ideal; the designated precursors should still have a low kinetic energy and remain in the FTMS

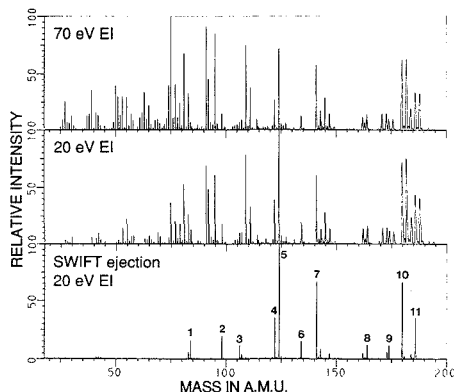


Figure 1. Mass spectra of 11-component mixture: 70-eV EI (top), 20-eV EI (middle), 20-eV EI after SWIFT ejection (bottom).

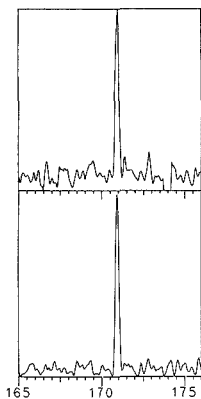


Figure 2. Daughter ion at  $m/z$  171 (loss of  $\text{CH}_3^+$ ) from 11 measured once (top) and after Hadamard transform with S/N improvement of 2.0 $\times$  (bottom).

cell. Figure 1 illustrates this for the molecular ions from the 11-component mixture. With the prototype SWIFT unit used, note that some ions other than the chosen precursors remain; these apparently represent ionic products of precursor CAD resulting from residual excitation. These did not appear to be due to incomplete ejection (27), as they were not decreased by increased excitation power. To remove these signals a "blank" spectrum is also measured for each precursor set under the same conditions, but without precursor excitation. Subtraction of its blank from each spectrum effectively eliminates this background problem; obviously, refinements to the selection technique making the blank measurement unnecessary are desirable.

**Signal-to-Noise Enhancement.** Hadamard transformation of the 11 combination spectra gave individual CAD spectra for each of the 11 precursors; all showed improved S/N. For example,  $m/z$  45 and 58 from precursor 1, and 143 and 171 (Figure 2) from 11 show an actual S/N improvement of 1.7, 1.8, 2.0, and 2.0 versus the same peaks in a single combination spectrum. Because the products from each precursor are measured six times in the 11 spectra, while for these spectra the random noise is averaged, a predicted enhancement of  $6/(11)^{0.5} = 1.8$  is expected (34), an agreement within experimental error (an enhancement of 2.4 $\times$  was obtained in the preliminary experiments without blank sub-

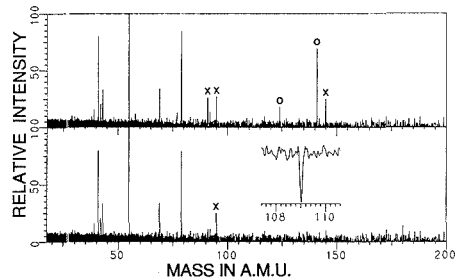


Figure 3. Hadamard transformed CAD spectra of 2 (~63% dissociation efficiency) using equation coefficients of zeros and ones (top), and modified equation coefficients (bottom; inset is negative peak, abundance 38% of that of base peak): O, other precursor ions; X, fragment peaks from other precursors.

traction) (17). This corresponds to a time savings of 3.3 $\times$  versus obtaining spectra of comparable S/N by individual measurement. For  $p$  precursors, the S/N enhancement should be  $p^{0.5}/2$  (for large  $p$ ; division by 2 because half the precursors are discarded), or a time savings of  $4/p$  (34).

**Anomalous Peaks in HT Spectra.** The individual spectra initially obtained by Hadamard transformation (3, 17), despite the careful selection of precursor ions, still contained peaks not from the precursor. These represent incomplete elimination ("cross-talk") of both fragment and precursor ions from other mixture components. A different SWIFT waveform was used to excite each set of six precursors; a substantial reduction in cross-talk was achieved by using the same CAD excitation waveform for each combination spectrum (frequencies for all 11 precursors applied with only six present). This minimizes the variation in degree of excitation; such variations in product abundances that are proportional to the precursor intensity should be expected (32-34) to result in cross-talk. Successful application of the HT method requires that the variations in measured peak abundances be random noise limited, a condition met by EI ionization as well as FTMS detection (35).

**Modified Equation Coefficients.** Even with these improvements, the Hadamard transformed MS-II spectrum of cyclohexanone (Figure 3, top) shows cross-talk ions at  $m/z$  124 and 141 from precursors 5 and 7, respectively, as well as fragment ions at  $m/z$  91 and 92 from 4 and/or 6,  $m/z$  95 from 7 and/or 9, and  $m/z$  145 from 10. As another possible source of product abundance variation dependent on precursor ion intensity, the pressure and concentration of mixture components in the inlet system were observed to vary by as much as 18% over the course of the measurements. To correct for these changes, the actual abundance values for each precursor in each MS-II spectrum, as shown in the blank spectrum, were used as coefficients ( $i$ ) in each of the 11 simultaneous equations ( $0.82 \leq i \leq 1$ ). This substantially reduced, but did not remove, the appearance of cross-talk ions in the Hadamard transformed spectra.

Yet another possible source of product yield fluctuations proportional to precursor intensity is variation in dissociation efficiency due to irreproducibility in gas introduction from the pulsed valves (static gas CAD gives much lower sensitivity) (18). The magnitude of the collisional dissociation (amount of precursor dissociated) is actually indicated by the resulting reduction in precursor ion abundance, i.e., the difference between its value in the blank and in the MS-II CAD spectrum. Using this difference as the equation coefficient  $i$  and recalculating give HT spectra of which seven (e.g., Figure 4) show virtually no significant (>10% base peak) anomalous peaks, and these are greatly reduced in the other four spectra (Figure 3, bottom). Note that this method does not correct

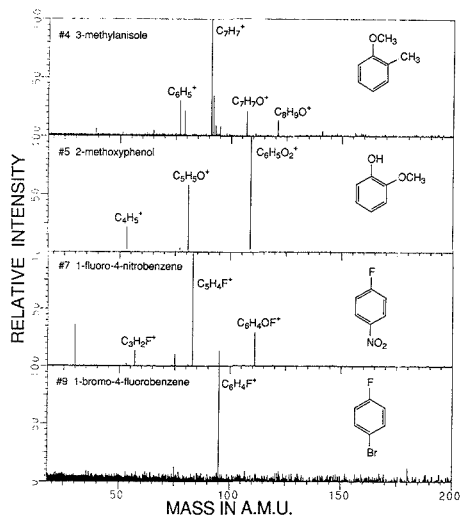


Figure 4. Typical Hadamard transformed CAD spectra, precursors 4, 5, 7, and 9 (top to bottom), with dissociation efficiencies of 60%, 48%, 59%, and 29%, respectively.

for changes in the relative abundance of fragments that can occur with variations in collision gas pressure and may be a source of the remaining anomalous peaks.

Using these difference  $i$  values can introduce artifacts, however. This artificially removes peaks corresponding to the precursor masses from all spectra; fragment ions corresponding to these masses, which are not significant in these 11 spectra, would improperly weight the combination spectrum and would not be detected. On the other hand, the remaining cross-talk peaks each appear to be accompanied by a complementary cross-talk peak of negative abundance in other HT spectra. The largest such negative peak observed, a fragment peak of 5 and 10 at  $m/z$  109 which is an anomalous positive peak in the HT spectrum of 1, is shown in Figure 3 (inset). Similarly, the  $m/z$  95 fragment peak from both 7 and 9 appears as positive and negative cross-talk peaks in HT spectra 1, 2, 6, and 10 and 3, 5, 8, and 11, respectively. It is conceivable that  $i$  value adjustments to eliminate negative peaks would minimize the positive cross-talk peaks.

Obviously, it would be better to eliminate the need for this difference  $i$  value through improvements in the reproducibility of the sample size and dissociation conditions. Other methods such as laser- or surface-induced dissociation could be more reproducible, and would have the further advantage of eliminating the collision gas. No delay for pumping away this gas and further computer automation should reduce the measurement time and, thus, reduce experimental drift. Derivation of the difference  $i$  value from abundances of primary product ions will also be investigated.

**MS<sup>n</sup> Spectra.** For MS/MS/MS, the above approach should apply also for measuring the combined MS-III spectra of multiple daughters formed from a single precursor ion. If such spectra are desired for multiple daughters of several precursors, two independent Hadamard masks can be applied to the  $p$  precursors and  $d$  daughters to obtain  $(p-d)$  combination MS-III spectra. This was tested with three precursors and three daughters, whose nine possible dissociation pathways will produce nine MS-III spectra; that for hexane<sup>+</sup> →  $m/z$  57<sup>+</sup> → products is shown in Figure 5. Because half of the daughter ions as well as half of the precursors are discarded to encode the MS/MS/MS pathway information, and because

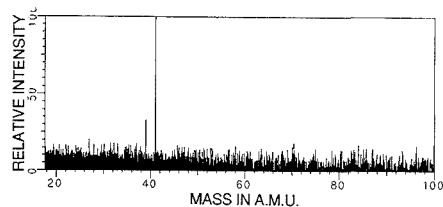


Figure 5. Two-dimensional Hadamard transform MS/MS/MS spectrum of *n*-hexane ( $C_6H_{14}^{+}$ ) →  $m/z$  57 ( $C_4H_9^{+}$ ) →  $m/z$  41 ( $C_3H_5^{+}$ ) and  $m/z$  39 ( $C_3H_3^{+}$ ).

the value of  $n$  is so small, the expected S/N enhancement,  $(2/3^{0.5})^2 = 1.3\times$  (observed 1.1 $\times$ ), is only marginally useful; basic signal levels were also poor in this preliminary MS<sup>3</sup> experiment. However, the expected  $m/z$  39 and 41 peaks, although not the weaker 27 and 29 peaks, are observed. Such a two-dimensional Hadamard transform apparently has not been previously reported for any type of spectra.

With the experimental improvements proposed above, such as computer automation, it should be possible to extend this approach to larger numbers of precursors and daughters, and even to  $n$  dimensions by applying a Hadamard mask in each stage of MS. Each stage increases exponentially the number of possible pathways in MS<sup>n</sup> experiments, which should make the Hadamard method even more valuable, although each additional stage also halves the precursor abundance yielding the MS<sup>n</sup> data. In general, for large values of  $p$  precursors and  $d_{(n-2)}$  intermediate daughters, a S/N enhancement of  $(p-d_1 \dots d_{(n-2)})^{0.5} / 2^{(n-1)}$  will be obtained, which corresponds to a time savings of  $2^{2(n-1)} / (p-d_1 \dots d_{(n-2)})$ . For example, complete MS-III information from 20 parents and 40 daughters can be obtained in  $\sim 1/50$  the time required for measuring them individually.

**Hadamard of Differences.** For optical instruments, Hadamard multiplexing uses a mask to modulate the source intensity for each wavelength channel, either transmitting or blocking its contribution to the total light signal (16). Thus, the signal from each channel is multiplied by either a +1 or a 0, respectively, and is so represented in the Hadamard array. Because each channel is blocked approximately half the time, half the total signal to the detector is lost to achieve the encoding. However, if the mask instead reflects the light to a second detector, multiplying each channel by +1 or -1, no signal is discarded (33). The individual signals from each of the  $p$  channels can be calculated by solving  $p$  simultaneous equations with coefficients of +1 and -1. Thus the time saving versus measuring each channel individually is  $p$  and the S/N gain is  $p^{0.5}$ .

For MS/MS this Hadamard of differences method would require separate dissociation of the two precursor sets and mass analysis of their products. This could be implemented in a dual cell FTMS by forming and partitioning the precursor ions between the two cells, dissociating the ions, and using a quadrature (34) spectrum measurement (to encode phase information necessary to produce negative as well as positive signals) that subtracts the signals of one cell from that of the other. A possible procedure would use a ring electrode around the conductance limit opening between the cells; half the precursor ions would be selectively excited to orbits large enough to keep these ions trapped by the cell end plate outside the ring electrode while the remaining precursors are selectively transferred to the other cell by momentarily grounding this electrode. The precursors in the first cell would be collisionally relaxed back to the cell center (especially effective for large ions) (36); this might also be effected electrostatically by applying a voltage pulse to all excite and receive ( $x,y$ ) plates (36), followed by collisional relaxation of the resulting  $z$ -axis excitation (37). Precursor ions in both cells would then be

dissociated, but daughter ion measurement in the two cells would use excitation waveforms shifted in phase by 180° (such as by reversing the electrical connections to the excitation plates of one cell). Daughter ions on both sides would be detected simultaneously, but the resulting signal for a particular  $m/z$  value would represent the difference (+ or -) between the abundances of each cell. As a result of encoding the precursor data, none of the ions need be discarded; however, the noise should not increase appreciably, as it is relatively independent of receiver plate area (38).

An even simpler approach could be feasible for precursor and daughter ions of similar  $m/z$  values, as encountered with electrospray ionization (28-30); if a linear precursor has 100 evenly spaced charges, a random fragmentation will produce two daughter ions of nearly the  $m/z$  value of the precursor (30). The two selected sets of precursors would be simultaneously excited, but with opposite phase, and dissociated (e.g., photodissociation) immediately, so that daughters of the two sets will be formed on opposite sides of the cell. The product ions would then continue in orbit with their characteristic frequencies, but in quadrature detection those of a particular frequency (and  $m/z$ ) value from the two sets would make amplitude contributions of opposite sign. Using this after the above dual cell method could similarly give MS/MS/MS information without discarding ions, which could also be done with a four-cell arrangement; both would require 90° phase offsets. Thus, in theory, MS-II spectra of 100 precursors could be collected in 1/100 the time (and, thus, with 1/100 the sample) required for those measured individually, as could the 100 MS<sup>3</sup> spectra from dissociating 10 daughters of 10 precursors. Implementation of the Hadamard of differences approach with FTMS is in progress.

### CONCLUSIONS

These preliminary experiments show that the Hadamard method can enhance the sensitivity for the measurement of MS<sup>n</sup> spectra, achieving the S/N improvement expected theoretically. Special attention to experimental detail is necessary to minimize the background of precursor ions other than those selected and the variation in the extent of precursor ion dissociation or reaction. This Hadamard method should be generally applicable to any mass spectrometer capable of selecting and dissociating multiple precursors and analyzing their products, such as the ion trap (39) or reflectron time of flight (RTOF) (40). In the ion trap, multiple parent ions can be selectively retained and dissociated by using appropriate rf frequencies, analogous to the FTMS experiment. In TOF, different combinations of parents can be selected by removing all others using a pulsed retarding grid, with these ions made to undergo photodissociation (41) or surface-induced dissociation in the reflectron lens assembly.

For MS<sup>n</sup> experiments, the possible gain in S/N is reduced with increasing  $n$ , as in each additional step half of the ions available for dissociation must be discarded to encode the corresponding pathway information. To avoid these losses a Hadamard differences method is proposed in which the product spectrum from the formerly discarded ions is subtracted from that of those usually measured. With this, in theory, all possible MS<sup>n</sup> spectra can then be collected with S/N for each equivalent to that obtained by this number of repeated measurements of the individual spectrum. More efficient collection of MS<sup>n</sup> spectra will surely increase their potential for analytical applications such as the analysis for many targeted compounds in highly complex mixtures. In addition, the HT method should greatly enhance the utility of MS<sup>n</sup> for structural elucidation of large molecules such as peptides (42, 43), especially those in mixtures (44, 45). For example, molecular ions from a mixture of two peptides, each with 1000 amino acids, could be dissociated, each peptide

producing ~75 fragment ions consisting of 10-20 amino acids. The corresponding 150 MS-III spectra, determined simultaneously, should then provide extensive sequence information on the peptides' fragments; their sequences would indicate those of the original two peptides to the extent to which the fragments represent the total structure and the information on their overlaps is unique. Although experimental and computer control of such measurements would have to be highly sophisticated, at least in theory the Hadamard differences method would provide the same S/N for any one of these MS-III spectra measured simultaneously with all 150 as measurement of that one individually with the same amount of sample. To the extent that the above experimental problems can be overcome, it is conceivable that such MS<sup>n</sup> measurements of even larger  $n$  can provide unique sequence information from the even larger molecules that can now be ionized by electrospray (28, 29) using unit resolution FTMS measurements (30).

### ACKNOWLEDGMENT

The authors are grateful to Alan G. Marshall and Chryso-stomos Wesdemiotis for valuable discussions.

### LITERATURE CITED

- (1) *Tandem Mass Spectrometry*; McLafferty, F. W., Ed.; Wiley: New York, 1983.
- (2) Busch, K. L.; Gilsh, G. L.; McLuckey, S. A. *Mass Spectrometry/Mass Spectrometry*; VCH Publishers: Deerfield Beach, FL, 1988.
- (3) McLafferty, F. W.; Stauffer, D. B.; Loh, S. Y.; Williams, E. R. *Anal. Chem.* **1987**, *59*, 2213-2216.
- (4) Conisarov, M. B.; Marshall, A. G. *Chem. Phys. Lett.* **1974**, *25*, 282-283.
- (5) Cody, R. B.; Kinsinger, J. A.; Ghaderi, S.; Amster, I. J.; McLafferty, F. W.; Brown, C. E. *Anal. Chim. Acta* **1985**, *178*, 43-66.
- (6) Allemann, M.; Kellerhals, H.; Wanczek, K. P. *Int. J. Mass Spectrom. Ion Processes* **1983**, *46*, 139-142.
- (7) James, C. F.; Wilkins, C. L. *J. Am. Chem. Soc.* **1988**, *110*, 2687-2688.
- (8) Cody, R. B.; Freiser, B. S. *Anal. Chem.* **1982**, *54*, 1431-1433.
- (9) Cody, R. B. *Anal. Chem.* **1988**, *60*, 917-923.
- (10) McLafferty, F. W.; Amster, I. J. *Int. J. Mass Spectrom. Ion Processes* **1986**, *72*, 85-91.
- (11) Cody, R. B.; Freiser, B. S. *Anal. Chem.* **1987**, *59*, 1054-1056.
- (12) Chen, L.; Wang, T. C.; Ricca, T. L.; Marshall, A. G. *Anal. Chem.* **1987**, *59*, 449-454.
- (13) Marshall, A. G.; Wang, T.-C. L.; Chen, L.; Ricca, T. L. In *Fourier Transform Mass Spectrometry*; Buchanan, M. V., Ed.; ACS Symposium Series, No. 359; American Chemical Society: Washington, DC, 1987; pp 21-33.
- (14) Pfandler, P.; Bodenhausen, G.; Rapin, J.; Houriet, R.; Gaumann, T. *Chem. Phys. Lett.* **1987**, *138*, 195-200.
- (15) Pfandler, P.; Bodenhausen, G.; Rapin, J.; Walser, M.-E.; Gaumann, T. *J. Am. Chem. Soc.* **1988**, *110*, 5625-5628.
- (16) Treado, P. J.; Morris, M. D. *Anal. Chem.* **1989**, *61*, 723A-734A.
- (17) Williams, E. R.; Loh, S. Y.; McLafferty, F. W.; Cody, R. B. *Adv. Mass Spectrom.* **1989**, *11*, 1878-1879.
- (18) Williams, E. R.; Furlong, J. J. P.; McLafferty, F. W., submitted for publication in *J. Am. Soc. Mass Spectrom.*
- (19) Matud, M. A.; Dekrey, M. J.; Cooks, R. G. *Int. J. Mass Spectrom. Ion Processes* **1985**, *67*, 285-294.
- (20) McLafferty, F. W.; Williams, E. R. Proceedings of the 1986 Conference on Chemical Defense Research; Aberdeen Proving Ground, MD, 1987.
- (21) Williams, E. R.; Henry, K. D.; McLafferty, F. W.; Shabanowitz, J.; Hunt, D. F., submitted for publication in *J. Am. Soc. Mass Spectrom.*
- (22) Durbar, R. C. In *Gas Phase Ion Chemistry*; Bowers, M. T., Ed.; Academic Press: Orlando, FL, 1984; p 129.
- (23) Hunt, D. F.; Shabanowitz, J.; Yates, J. R., III. *J. Chem. Soc., Chem. Commun.* **1987**, 548-550.
- (24) Lebrilla, C. B.; Wang, D. T.-S.; Mizoguchi, T. J.; McIver, R. T., Jr. *J. Am. Chem. Soc.* **1989**, *111*, 8593-8598.
- (25) Williams, E. R.; McLafferty, F. W., submitted for publication in *J. Am. Soc. Mass Spectrom.*
- (26) Nibbering, N. M. M. *Mass Spectrom.* **1985**, *8*, 141-160.
- (27) Mullen, S. L.; Marshall, A. G. *J. Am. Chem. Soc.* **1988**, *110*, 1766-1774.
- (28) Fern, J. B.; Mann, M.; Meng, C. K.; Wong, S. F.; Whitehouse, C. M. *Science* **1989**, *246*, 64-71.
- (29) Loo, J. A.; Udseth, H. R.; Smith, R. D. *Anal. Biochem.* **1989**, *176*, 404-412.
- (30) Herry, K. D.; Williams, E. R.; Wang, B.-H.; McLafferty, F. W.; Shabanowitz, J.; Hunt, D. F. *Proc. Natl. Acad. Sci. U.S.A.* **1989**, *86*, 9075-9078.
- (31) Ghaderi, S.; Littlejohn, D. P. *Adv. Mass Spectrom.* **1986**, *10*, 875.
- (32) Harwit, M.; Sloane, N. J. A. *Hadamard Transform Optics*; Academic: New York, 1979; pp 100-105.
- (33) Harwit, M. In *Transform Techniques in Chemistry*; Griffiths, P. R., Ed.; Plenum: New York, 1978; pp 173-197.

- (34) Marshall, A. G.; Verdun, F. R. *Fourier Transforms in NMR, Optical, and Mass Spectrometry: A User's Handbook*; Elsevier: Amsterdam, 1989.
- (35) Marshall, A. G. *Anal. Chem.* 1979, 51, 1710-1714.
- (36) Williams, E. R.; Henry, K. D.; McLafferty, F. W., submitted for publication in *J. Am. Chem. Soc.*
- (37) Rempel, D. L.; Huang, S. K.; Gross, M. L. *Int. J. Mass Spectrom. Ion Processes* 1986, 70, 163-184.
- (38) Hanson, C. D.; Kerley, E. L.; Castro, M. E.; Russell, D. H. *Anal. Chem.* 1989, 61, 2040-2046.
- (39) Kelley, P. E.; Stafford, G. C., Jr.; Syka, J. E. P.; Reynolds, W. E.; Louris, J. N.; Todd, J. F. *J. Adv. Mass Spectrom.* 1985, 10, 869-870.
- (40) Tang, X.; Ens, W.; Standing, K. G.; Westmore, J. B. *Anal. Chem.* 1988, 60, 1791-1799.
- (41) Laitting, K.; Cheng, P. Y.; Taylor, T. G.; Willey, K. F.; Peschke, M.; Duncan, M. A. *Anal. Chem.* 1989, 61, 1458-1460.
- (42) Wipf, H.-K.; Irving, P.; McCamish, M.; Venkataraghavan, R.; McLafferty, F. W. *J. Am. Chem. Soc.* 1973, 95, 3369.
- (43) Levsen, K. In *Tandem Mass Spectrometry*; McLafferty, F. W., Ed.; Wiley: New York, 1983; pp 41-66.
- (44) Cody, R. B., Jr.; Amster, I. J.; McLafferty, F. W. *Proc. Natl. Acad. Sci. U.S.A.* 1985, 82, 6367-6370.
- (45) Hunt, D. F.; Shabanowitz, J.; Yates, F. R.; Griffin, P. R.; She, N.-Z. In *Analysis of Peptides and Proteins*; McNeal, C., Ed.; Wiley: New York, 1986.

RECEIVED for review October 9, 1989. Accepted January 4, 1990. Generous financial support for this research was provided by the National Science Foundation (Grants CHE-8616907 and CHE-8620293), by the National Institutes of Health (Grant GM-16609), and by Perkin-Elmer through sponsorship of an ACS Analytical Chemistry Fellowship (for E.R.W.). This was presented in part at the 11th International Mass Spectrometry Conference, Bordeaux, France, August 1988.

## Interlaboratory Comparison of Different Analytical Techniques for the Determination of Oxygen-18 Abundance

J. R. Speakman,<sup>\*1</sup> K. A. Nagy,<sup>2</sup> D. Masman,<sup>3</sup> W. G. Mook,<sup>3</sup> S. D. Poppitt,<sup>1</sup> G. E. Strathearn,<sup>2</sup> and P. A. Racey<sup>1</sup>

*Department of Zoology, University of Aberdeen, Aberdeen, Scotland, U.K. AB9 2TN, Laboratory of Biomedical and Environmental Sciences, University of California, Los Angeles, 900 Veteran Avenue, Los Angeles, California 90024, and Rijksuniversiteit Groningen, Centrum voor Isotopen Onderzoek, Westersingel 34, 9718 CM Groningen, The Netherlands*

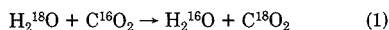
A series of six artificially enriched waters, containing between 2500 and 6500 ppm oxygen-18, was prepared by adding weighed portions of distilled water and highly enriched H<sub>2</sub><sup>18</sup>O. These waters were analyzed by radio activation analysis (proton activation, PAA) and by gas isotope ratio mass spectrometry (gIRMS) with CO<sub>2</sub> as the analysis gas. Carbon dioxide was prepared from water samples either by using the guanidine reaction, with 3-, 5-, and 10- $\mu$ L samples, or by isotopic equilibration, using small (10  $\mu$ L) and large (1.5 mL) samples. The large samples were diluted to the natural abundance range prior to analysis as were the 3- $\mu$ L guanidine samples. Precision was greatest with large sample CO<sub>2</sub> equilibration (mean relative standard deviation (RSD) = 0.108%). The other gIRMS gas preparation techniques had lower precision (3  $\mu$ L guanidine, RSD = 0.529%, 5  $\mu$ L guanidine, RSD = 0.364%, 10  $\mu$ L guanidine, RSD = 0.48%; 10  $\mu$ L equilibration, RSD = 0.43%) and the lowest precision occurred with PAA (RSD = 0.58%). For all the techniques except small sample equilibration, accuracy (percent deviation of mean evaluation from expected gravimetric mean) was worse than precision (RSD). Average deviations, including sign, were as follows: 3  $\mu$ L guanidine, -0.97%, 5  $\mu$ L guanidine, -1.43%, 10  $\mu$ L guanidine, -1.30%; 10  $\mu$ L equilibration, -0.33%; 1.5 mL equilibration, -1.55%; and proton activation, +0.68%. Gas IRMS, independent of the preparation technique, tended to undervalue abundance, and PAA tended to overevaluate abundance. Both precision and accuracy were very much worse at the high levels of enrichment studied than have previously been reported for estimates at the natural abundance levels of 1800-2050 ppm <sup>18</sup>O.

Two distinct analytical techniques are available for the evaluation of the enrichment of <sup>18</sup>O in samples of water, radio

activation analysis and gas isotope ratio mass spectrometry (gIRMS). In the former method samples are bombarded with particles of various types to effect nuclear reactions in the <sup>18</sup>O, the decay products of which can then be measured. The most useful technique involves proton bombardment (proton activation analysis, PAA) to form <sup>18</sup>F, which decays with a half-life of 110 min (1). This has the advantage that the product nuclide has a long half-life and does not therefore require very rapid product transfer systems which are necessary for analysis of other RAA products, for example <sup>17</sup>N (2) with a 4.14-s half-life or <sup>19</sup>O (3) with a 29-s half-life.

With gIRMS the water is converted to a gas and ionized at very low pressure. A mass spectrum is then measured for the major and minor beams which correspond to the appropriate masses for molecular ions containing either <sup>16</sup>O or <sup>18</sup>O. There are two problems with the direct analysis of gaseous water, firstly it is corrosive, and secondly it is difficult to remove from the inlet system of the analyser once analysis is complete (4). These problems lead to memory effects unless a long evacuation is performed between samples. Nevertheless a commercial machine is available (VG Isogas, Aquasira) which analyzes water directly (5) and is in widespread use (e.g. refs 6 and 7). The memory effects of this machine however, and the fact it is a single inlet device, restrict its usage to samples of relatively low <sup>18</sup>O enrichment (<1000‰ relative to V-SMOW) and to samples where the approximate range of the sample is known beforehand, so that appropriate standards may be run adjacent to the unknown.

The preferred gas for analysis by gIRMS is CO<sub>2</sub>. Several different procedures are available for the preparation of CO<sub>2</sub> from water for gIRMS analysis (reviewed in ref 8). The most popular technique is that of equilibration (9), in which water and CO<sub>2</sub> are mixed at a controlled temperature and react as follows:



After an equilibration period, which is dependent upon the system (7 h for large volume, well-agitated systems to 48-72 h for small volume equilibration), the CO<sub>2</sub> is removed and

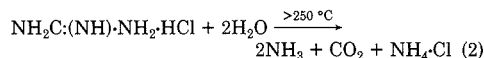
<sup>1</sup> University of Aberdeen.

<sup>2</sup> University of California.

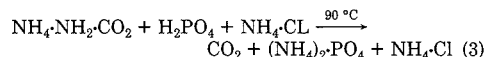
<sup>3</sup> Rijksuniversiteit Groningen.

purified cryogenically and admitted to the mass spectrometer. The enrichment of  $^{18}\text{O}$  in the original water is calculated (10), from the measured isotopic ratio in the carbon dioxide, the relative moles of each species originally present, and the equilibrium fractionation factor between  $\text{CO}_2$  and  $\text{H}_2\text{O}$  (which equals 1.0412 at 25 °C, refs 11 and 12). Commonly, large samples and automated agitation units are used (e.g., ref 13), however, systems are in use for routine analysis of much smaller samples of 2–100  $\mu\text{L}$  (14, 15).

An alternative technique is chemical conversion, utilizing guanidine hydrochloride to convert water to  $\text{CO}_2$  (12, 15, 16). This reaction involves a two-stage process. In the first stage 2–10  $\mu\text{L}$  of water and 100 mg of anhydrous guanidine hydrochloride are reacted together in a sealed vessel at 250 °C for 3 h. The reagents react as follows:



On cooling the ammonia and  $\text{CO}_2$  produced combine to form ammonium carbamate ( $\text{NH}_4\text{NH}_2\text{CO}_2$ ). Then, the vessel containing the products is broken under vacuum inside a second evacuated and sealed container having in it 1 mL of 6 M (100%) phosphoric acid. Heating at 90 °C for 90 min yields  $\text{CO}_2$  by the reaction



The carbon dioxide released is then purified cryogenically and introduced into the mass spectrometer.

The accuracy and precision of all these procedures have been previously investigated (see ref 8 for review), generally at levels of natural abundance of  $^{18}\text{O}$ , but more rarely at artificially high levels of enrichment. Even more infrequently comparison is made between two techniques for analysis of a given water (e.g., refs 1 and 17). To date however, no study has made a comparison of accuracy and precision of all three of the most widely used procedures (proton activation, equilibration, and guanidine conversion) across a series of water standards at high enrichment levels. This study presents such a comparison, across a nominal enrichment range of 2300–6500 ppm  $^{18}\text{O}$  (equal to 150 to 2280‰ vs V-SMOW).

Enrichments in this range are of interest principally because they are used routinely in tracer studies of animal metabolism, in particular the doubly labeled water technique, in which artificially high enrichments of both  $^{18}\text{O}$  and an isotope of hydrogen in the body water are produced by introducing the isotopes as water into the subjects body. The difference in the elimination rates of the isotopes is used to measure  $\text{CO}_2$  production (18–21).

## EXPERIMENTAL SECTION

**Preparation and Distribution of Water Standards.** A series of six solutions was prepared by dilution of a very high enrichment cocktail (VHEC) which contained both enriched levels of  $^2\text{H}$  and  $^{18}\text{O}$  at approximately 9 atom % excess (APE) and 19 APE, respectively (manufacturers values, Amersham International PLC, Yeda Isotopes). The dilutant consisted of double distilled tap water, henceforth called standard reference water (SRW).

The standards were prepared into glass vessels. Vessels and all other glassware involved in preparation were cleaned prior to use first by washing in trichloroethylene to remove grease, followed by complete immersion in a solution of Decon (Decon Labs Ltd.) in water, and ultrasound washed for 15 min. The vessels were finally sequentially rinsed in distilled water, a mix of 50:50 water and acetone, and lastly 100% acetone before air drying in an oven at 80 °C. During preparation all vessels were handled only with plastic gloves.

For all standards preparation involved mixing between 0.1 and 0.5 g of VHEC and 19 and 26 g of SRW. The detailed procedure

was as follows: weigh vessel (mass A); add 19–26 g of SRW to vessel; weigh vessel with SRW (mass B); calculate mass of VHEC to add, and add estimated quantity of VHEC using graduated syringe; weigh vessel containing SRW and VHEC (mass C); seal vessel. The vessels were sealed with rubber caps, and there was no evidence of fractionation of the standards over time after sealing.

All weighings were performed with a five-significant figure balance (Sartorius MP 2904, accuracy  $\pm 0.01$  mg) at 25 °C. Weighing was continued until stability was reached in the least significant digit, which was generally 45–60 s.

Samples of the standards from the stock in the vessels were flame sealed into 5-, 10-, or 100- $\mu\text{L}$  pipets (Vitrex) or in the case of large sample equilibration transferred into small glass bottles sealed with rubber gromets in metal caps. Five- and ten-microliter samples were used directly in gIRMS analyses and 100- $\mu\text{L}$  samples were subdivided and analyzed by PAA after distribution to the participant laboratories. Standards were accompanied only by an indication of the rank enrichments and an indication of the anticipated upper and lower limits of the entire series. All samples were therefore analyzed blind.

**Gravimetric Evaluation of Enrichments and Sensitivity Analysis.** The masses of VHEC and SRW in each vessel were calculated as mass C-B, and mass B-A, respectively. Given the mass of VHEC and SRW in each vessel the nominal enrichment of a given standard was calculated as follows:

$$E_S = \frac{(M_{\text{VHEC}}/MM_{\text{VHEC}})E_{\text{VHEC}} + (M_{\text{SRW}}/MM_{\text{SRW}})E_{\text{SRW}}}{(M_{\text{VHEC}} + M_{\text{SRW}})/MM_{\text{MIX}}} \quad (4)$$

where  $E_S$ ,  $E_{\text{VHEC}}$ , and  $E_{\text{SRW}}$  are the enrichments of  $^{18}\text{O}$  in the standard, the very high enrichment cocktail, and the standard reference water, respectively.  $M_{\text{VHEC}}$  and  $M_{\text{SRW}}$  are the masses of very high enrichment cocktail and standard reference water, respectively.  $MM_{\text{VHEC}}$ ,  $MM_{\text{SRW}}$ , and  $MM_{\text{MIX}}$  are the molecular masses of the very high enrichment cocktail, standard reference water, and the final mix, respectively.

The unknown molecular masses were evaluated from the estimated isotopic abundances of  $^1\text{H}/^2\text{H}$  and  $^{16}\text{O}/^{18}\text{O}$  as follows:

$$MM_{\text{SRW}} = 2(1.000147) + 16.0039 = 18.00428$$

$$MM_{\text{VHEC}} = 2(1.08) + 16.38 = 18.54$$

$$MM_{\text{MIX}} = \frac{(MM_{\text{VHEC}}M_{\text{VHEC}}) + (MM_{\text{SRW}}M_{\text{SRW}})}{(M_{\text{VHEC}} + M_{\text{SRW}})}$$

The enrichment of standard reference water ( $E_{\text{SRW}}$ ) was evaluated by using gIRMS (guanidine). While this appears to be an incestuous characterization, mass spectrometric abundance evaluations at natural abundance levels have been validated on many previous occasions (reviewed in ref 8) and therefore we do not feel this represents a serious source of bias. The mean enrichment of SRW ( $E_{\text{SRW}}$ ) evaluated in this way equaled 1999.9 ppm  $^{18}\text{O}$  ( $n = 8$ ). The enrichment of  $^{18}\text{O}$  in the VHEC was unknown and was unfortunately beyond the range of accurate evaluation by either gIRMS or PAA. The enrichment of the VHEC was therefore evaluated by solving eq 4 for  $E_{\text{VHEC}}$  and substituting the mean evaluated enrichment across all techniques (except 3  $\mu\text{L}$  guanidine, which was analyzed at a later date) for the most dilute of the standard series (standard 1) for  $E_S$ . With this method the calculated value for  $E_{\text{VHEC}}$  equaled 187140 ppm  $^{18}\text{O}$ . Substituting this enrichment estimate into eq 4 with the appropriate masses of the SRW and VHEC in all the standard series except the most dilute yielded the nominal gravimetric evaluations for the series (Table I).

All the component parameters in eq 4 are measured with error. The sensitivity of the nominal enrichments to these errors was assessed by using a sensitivity analysis, by allowing the component variables to vary in the following ranges. The masses of SRW and VHEC were allowed to vary by  $\pm 0.0001$  g, which is 10 times worse than the reported accuracy of the balance. Variation in the enrichment of the most dilute standard (I) equaled 4.04 ppm across all the techniques (s.e.,  $n = 6$  methods, see below). This variation results in a range for the estimate of  $E_{\text{VHEC}}$  of 185380–188930 ppm  $^{18}\text{O}$  and this range was used in the sensitivity analysis. Empirically observed maxima and minima in the evaluations of  $E_{\text{SRW}}$  were also used in the analysis (minimum = 1995.8 ppm, maximum = 2009.0 ppm  $^{18}\text{O}$ ). The effects of these

**Table I. Nominal Enrichments of  $^{18}\text{O}$  in a Series of Six Standard Solutions<sup>a</sup>**

std	nominal enrichment (ppm $^{18}\text{O}$ )	range (ppm $^{18}\text{O}$ )	
		min	max
I	2312.1	2303.0	2329.2
II	2730.6	2720.6	2740.6
III	3385.2	3367.3	3403.5
IV	4751.8	4716.3	4787.3
V	5449.6	5405.5	5493.8
VI	6504.1	6446.6	6561.7

<sup>a</sup> Enrichment for standard I was the mean enrichment evaluated across seven preparation techniques. The range for standard I was the range across these techniques. Nominal enrichments for standards II–VI were evaluated gravimetrically from the weighed quantities of a standard reference water, at natural abundance (1999.9 ppm  $^{18}\text{O}$ ), mixed with a very high enrichment cocktail (187140 ppm  $^{18}\text{O}$ ). The ranges for standards II–VI were estimated by using a sensitivity analysis (refer to text and Table I).

**Table II. Effects of Error in the Component Parameters of an Equation for Calculation of the Nominal Enrichment of  $^{18}\text{O}$  in Standard VI, by Gravimetric Procedures**

	manipulation	ppm $^{18}\text{O}$		error, %
		original	recalcd	
1. mass of std ref water	+0.0001 g	6504.12	6504.10	-0.00035
	-0.0001 g	6504.12	6504.14	+0.00034
2. mass of VHEC <sup>a</sup>	+0.0001 g	6504.12	6504.96	+0.013
	-0.0001 g	6504.12	6503.24	-0.0134
3. enrichment of std ref water	set to 1995.8 ppm	6504.12	6500.47	-0.056
	set to 2009.0 ppm	6504.12	6512.96	+0.136
4. enrichment of VHEC <sup>a</sup>	set to 185380 ppm	6504.12	6451.30	-0.812
	set to 188930 ppm	6504.12	6560.83	+0.872

<sup>a</sup> Very high enrichment cocktail.

variations in the estimate of the nominal enrichment of the most enriched standard (VI) are shown in Table II. Clearly the most influential factor was variation in  $E_{\text{VHEC}}$ . Since  $E_{\text{VHEC}}$  was evaluated as a mean across all the methods, the calculated nominal enrichments will not be biased in favor of, or against, any one technique. Maximum and minimum limits to the gravimetric evaluations for the series were defined by setting the worst possible combinations of errors, and these limits are shown with the mean nominal enrichments in Table I.

**Analyses.** Analyses of the samples were made by proton activation analysis (1) (KAN) and by gIRMS using the guanidine preparation technique (12, 15, 16) for 5- and 10- $\mu\text{L}$  samples (JRS/SDP/PAR) and 3- $\mu\text{L}$  samples (GS/KAN) and the equilibration technique (9, 15) for 10- $\mu\text{L}$  (DM/WGM) and 1.5-mL samples (GS/KAN). In addition the most dilute solution was also analyzed by direct mass spectrometry of gaseous water (22) using an Aquasira machine (W. Scott, Scottish Universities Research and Reactor Centre, East Kilbride). Due to a laboratory accident standard II was analyzed only by PAA and by the small volume equilibrium technique. For large volume equilibrium and 3  $\mu\text{L}$  guanidine, standard waters were further diluted (by a factor of 1:50 or 1:100) with a characterized water at background abundance (1989 ppm  $^{18}\text{O}$ ) prior to analysis. In the case of gIRMS all enrichments were calculated on the basis of the major to minor beam ratios (44:46 for  $\text{CO}_2$ ) in comparison to known working standards using dual inlet machines (Finnigan-MAT and VG Isogas) and then normalized to the V-SMOW/SLAP scale (23). Absolute enrichments (ppm) were then calculated (4) by using 2005.2 ppm as the best estimate of the enrichment of V-SMOW (24).

## RESULTS

Estimated mean isotope enrichments, standard deviation of replicate analyses, precision (relative standard deviation,

standard deviation  $\times 100/\text{mean}$ ), and number of replicates for all techniques and all standards are summarized in Table III. In addition, accuracy, calculated as the percentage deviation of the technique's mean evaluation from the mean nominal enrichment (Table I) for standards II–VI, and for standard I as percent deviation from the average enrichment across all techniques, is also shown in Table III.

Precision (relative standard deviation) remained almost constant throughout the range of evaluations for any given technique. Mean and standard deviation precision across all six standards were as follows: guanidine 3  $\mu\text{L}$  (0.528% standard deviation = 0.08%,  $n = 5$ ); guanidine 5  $\mu\text{L}$  (0.364%, standard deviation = 0.13%,  $n = 5$ ); guanidine 10  $\mu\text{L}$  (0.492%, standard deviation = 0.13%,  $n = 5$ ); equilibrium 10  $\mu\text{L}$  (0.435%, standard deviation = 0.33%,  $n = 6$ ); equilibrium 1.5 mL (0.108%, standard deviation = 0.009%,  $n = 5$ ); PAA (0.58%, standard deviation = 0.12%;  $n = 6$ ). Large sample equilibration had by far the best precision and was almost 4 times better than the other gIRMS sample preparation techniques which had a precision of approximately 0.4%. Precision for PAA was significantly lower than for gIRMS with all preparation techniques combined ( $t = 2.87$ ,  $p = 0.040$ , one-tailed) but not significantly lower than gIRMS excluding large sample equilibration ( $t = 1.94$ ,  $p = 0.077$ , one-tailed).

Significant differences in mean isotopic enrichment evaluations both between techniques and in comparison of the techniques to the nominal gravimetric evaluation were apparent for all the standards. Mean evaluations using guanidine were significantly lower than the gravimetric evaluations ( $t = 2.15$ ,  $p = 0.026$ ,  $n = 10$ , one-tailed). However, the degree of difference was progressively greater as standard enrichment increased and was most marked in the standard of greatest  $^{18}\text{O}$  enrichment (standard VI, Table III). In 11 out of 15 evaluations using guanidine, inaccuracy (percent deviation) was greater than precision (relative standard deviation). Small sample equilibration also significantly underestimated the nominal gravimetric enrichment ( $t = 2.25$ ,  $p = 0.037$ ,  $n = 6$ , one-tailed), however, the average deviation (-0.33%, standard deviation = 0.35%), was considerably smaller than the average deviation when using guanidine (-1.22%, standard deviation = 1.89%,  $n = 15$ ). In addition when small sample equilibration was used, the inaccuracy (percent deviation from nominal) was always exceeded by the precision (relative standard deviation). Although precision was greatest with large sample equilibration, it was also the least accurate technique (average deviation = -1.54%, standard deviation = 1.00%,  $n = 5$ ), and inaccuracy always exceeded precision. In addition the pattern of error was unusual in that for standards above the most dilute (III–VI) the accuracy progressively improved with increasing  $^{18}\text{O}$  enrichment. With PAA, abundances were significantly overestimated ( $t = 5.09$ ,  $p = 0.0017$ ,  $n = 6$ , one-tailed). This contrasted gIRMS, where the pattern, independent of preparation technique, was to underestimate abundance, relative to the nominal enrichments. In four of six evaluations with PAA inaccuracy (percent deviation) exceeded precision (relative standard deviation). The average deviation was +0.68%, standard deviation = 0.30%,  $n = 6$ .

## DISCUSSION

There are few validation comparisons in the literature in which accuracy and precision of these techniques have been examined at the levels of enrichment reported here, and none in which the three techniques are all compared across a standard series and analyzed blind.

**Precision.** The use of guanidine to prepare  $\text{CO}_2$  was originally described by Boyer et al. (16), who reported a precision of 108% (standard deviation) at natural abundance (2000 ppm), which is equivalent to a relative standard deviation of 1%. This is 2 to 3 times worse than the precision reported

Table III. Evaluations of  $^{18}\text{O}$  Enrichment of Six Standard Waters, Analyzed by Proton Activation Analysis (PAA) and by Gas Isotope Ratio Mass Spectrometry of  $\text{CO}_2$  Prepared from the Water by Guanidine Conversion of 3-, 5-, and 10- $\mu\text{L}$  Samples, and Equilibration of Gaseous  $\text{CO}_2$  with 10- $\mu\text{L}$  and 1.5-mL Water Samples<sup>a</sup>

std		guanidine			$\text{CO}_2$ equilibrium		PAA
		3 $\mu\text{L}$	5 $\mu\text{L}$	10 $\mu\text{L}$	10 $\mu\text{L}$	1.5 mL	
I	mean	2315.1	2313.7	2329.2	2307.6	2303.0	2316.0
	std dev	10.9	7.91	6.2	4.7	1.25	10.6
	RSD, %	0.47	0.34	0.26	0.20	0.05	0.46
	n	5	4	7	3	3	6
	error, %	+0.17	+0.06	+0.73	-0.19	-0.39	+0.16
II	mean				2723.6		2747.3
	std dev				8.4		17.3
	RSD, %				0.31		0.63
	n				3		6
	error, %				-0.31		+0.55
III	mean	3336.2	3329.9	3353.5	3392.1	3282.0	3413.5
	std dev	15.6	16.2	19.6	15.9	9.03	23.5
	RSD, %	0.46	0.48	0.58	0.47	0.27	0.69
	n	5	4	6	3	3	6
	error, %	-1.44	-1.69	-0.99	+0.14	-3.1	+0.77
IV	mean	4711.4	4705.8	4704.8	4719.6	4673.0	4807.6
	std dev	22.9	13.4	24.6	5.76	2.5	33.3
	RSD, %	0.48	0.20	0.52	0.12	0.05	0.69
	n	3	4	6	3	3	6
	error, %	-0.85	-1.02	-1.04	-0.73	-1.71	+1.11
V	mean	5475.7	5440.4	5490.11	5410.4	5382.0	5499.3
	std dev	32.8	28.6	27.7	57.4	6.0	36.5
	RSD, %	0.59	0.52	0.50	1.06	0.11	0.66
	n	4	3	4	3	3	6
	error, %	+0.47	-0.23	+0.68	-0.77	-1.30	+0.85
VI	mean	6295.9	6234.7	6124.2	6497.5	6426.0	6549.0
	std dev	40.6	17.9	36.9	29.2	3.9	25.6
	RSD, %	0.64	0.28	0.6	0.45	0.06	0.39
	n	4	3	4	3	2	6
	error, %	-3.2	-4.19	-5.89	-0.15	-1.25	+0.63

<sup>a</sup>Direct gIRMS of water using an aquasira machine for standard I gave a mean of 2303.2 ppm, std dev = 2.2 ppm, RSD = 0.46%,  $n = 6$ . In all cases mean enrichment, standard deviation of replicate analyses, precision (relative standard deviation), number of replicates, and accuracy, expressed as the percentage deviation from the nominal gravimetric abundance (standards two to six) or percentage deviation from the mean estimate across all techniques (standard one), are shown.

here. However, mass spectrometry instrumentation has improved significantly over the past 30 years and the difference in precision reflects this improvement in instrumentation rather than any differences in preparation. More recently precision of the technique at natural abundance (V-SMOW) was estimated at 0.198‰ (standard deviation) or 0.02% (relative standard deviation,  $n = 10$ ) (12), which is very much better than with any technique reported here. A similar precision at natural abundance to that found by Dugan et al. (12), when analyzing biological samples (0.08–0.28‰, standard deviation,  $n = 4$ ) was found by Wong et al. (15) but precision declined at higher enrichment (0.88–1.07‰, standard deviation,  $n = 4$ , at 250‰, equivalent to approximately 2.1 ppm at 2506.5 ppm  $^{18}\text{O}$  or 0.08% relative standard deviation). This latter precision is better than that reported in this study. However this greater precision may depend upon the ability to utilize working standards closer to the unknown, which was not run blind. A precision of 60 ppm (standard deviation,  $n = 10$ ) at 15700 ppm was found by Hoefs (4), which is equivalent to a relative standard deviation of 0.38%, which is almost equal to the precision reported for guanidine here. Over a range of solutions from 1980 to 12010 ppm  $^{18}\text{O}$  using 1.5- $\mu\text{L}$  water samples and the guanidine method for gas preparation (1), precision was highly variable between samples, and over the same enrichment range as used in the present study varied between 0 and 10% (relative standard deviation). To some extent this variation reflects the use of older mass spectrometric instrumentation but may also reflect the very small sample volume. This may indicate there is a minimum

volume necessary for precise evaluation when using the guanidine technique. We did not however find any significant improvement in precision as sample size increased from 3 to 10  $\mu\text{L}$ , and therefore if there is a critical minimum volume, it is certainly less than 3  $\mu\text{L}$ .

The precisions of analyses with gIRMS, for gases prepared by the guanidine procedure and by small sample  $\text{CO}_2$  equilibration, were lower than previous evaluations at natural abundance. One factor influencing this decline in precision is the inability to run appropriate comparison standards of similar abundance to unknowns. Machine parameters, for example the HT potential and beam focusing currents, must all be optimized therefore to measure enrichments at the natural abundance level of the comparison standard, and these may not necessarily also be the best settings for precise measurement at high abundance. This interpretation of the poor precision of gIRMS at high abundance is supported by the observation that the precision with large volume equilibration, in which the sample were diluted to near to natural abundance levels prior to analysis had significantly improved precision over the other preparation techniques, and in some range as previous measurements, also at natural abundance (7, 13, 25–28). An average precision of  $\pm 400$  ppm for large volume sample equilibration for samples ranging up to 100000 ppm, analyzed without dilution, was found by Dostrovsky and Klein (29), which in the mid-range is equivalent to 0.8% (relative standard deviation), but again precision would be expected to be worse on old instrumentation, consequently the effect on analyzing large volume equilibration samples at



high enrichment levels without dilution cannot be judged from that study. However, the 3- $\mu$ L guanidine samples were also prepared from diluted samples and these samples do not show improved precision. The reason for the low precision with these samples is obscure, but may reflect inexperience with the guanidine procedure in the laboratory which ran these samples (GS/KAN).

PAA was used by Wood et al. (1) to evaluate a range of solutions from 1980 to 12010 ppm  $^{18}\text{O}$ . Precision over the range used in that study averaged 2.62% (relative standard deviation, standard deviation = 0.66%,  $n = 11$ ), which is more than 4 times worse than in the current study. The reasons for this improvement include better  $\gamma$ -counting techniques, improved data analysis software, increased control of the cyclotron beam focus and intensity, and practice.

**Accuracy.** For all techniques, except small sample equilibration, inaccuracy exceeded precision, and many evaluations fell outside the calculated range for the gravimetric nominal enrichments (Tables I and III). The accuracy reported here for guanidine preparation is much worse than that reported previously for evaluations at background levels (12). The tendency for guanidine preparation to underestimate at high enrichments, relative to gravimetric estimates, has been previously noted (1); however in that study no large reduction in accuracy above 6000 ppm was found. The dramatic fall off in accuracy above 6000 ppm found in the present study is unlikely to be a consequence of isotopic fractionation during the reaction at high enrichments, since it was also evident in the 3- $\mu$ L samples which were diluted prior to analysis. Neither can it be attributed to a bias in a particular mass spectrometer. Indeed the consistency of the estimates between the 3- and 5/10- $\mu$ L guanidine preparations is remarkable, considering the 3- $\mu$ L samples were prepared from diluted samples and measured on a different mass spectrometer. The causes of the consistency remain unknown.

The consistent underevaluation of on average 1% with all the gIRMS techniques indicates some fractionation is occurring, possibly during cryogenic capture of the evolved products, since this is the only common point across the different techniques performed in different laboratories and analyzed on different machines.

The relatively poor accuracy when employing large volume equilibration was unexpected, especially since small sample equilibration showed the best precision. Two factors may have influenced this error. Firstly the large sample equilibrium samples were sealed in small bottles rather than flame-sealed in capillaries, and fractionation may have occurred during storage and transit (UK to USA) due to exchange with atmospheric water. Secondly errors may have been introduced at dilution. The sensitivity analysis in this study (Table II), for a similar dilution process however indicates this is unlikely to contribute much to the error unless gross weighing errors were made. Both of these factors can be eliminated however since the same inaccuracy was not apparent with 3- $\mu$ L guanidine preparation which was performed on the same waters. The most probable cause of this accuracy error was contamination in the automatic manifold, whereby water from one sample was not fully purged from the system and could then exchange with the subsequent sample.

Consistent overestimation of the theoretical abundance of samples by PAA was also reported by Wood et al. (1). In that case inaccuracies in the method may have reflected inaccuracies in the natural abundance comparison samples. In the current study that source of error seems unlikely to be of importance since the natural abundance comparator was checked prior to calculations by gIRMS. Over evaluation of abundance at high enrichments by on average 0.68% (standard deviation = 0.3%,  $n = 6$ ) would appear therefore to be a

feature of the PAA technique. One possible cause of this error was fractionation during distillation of the water into microcapillaries, as described by Nagy (30), although Wood et al. (1) found no evidence of fractionation at this stage of the process in their study.

## CONCLUSIONS

Current techniques for the evaluation of isotopic abundance of  $^{18}\text{O}$  in artificially enriched water varied in both precision and accuracy over the range 2500–6500 ppm  $^{18}\text{O}$ . All gIRMS techniques studied underestimated the abundance, while PAA overestimated abundance. However, the least significant differences were found when using small sample  $\text{CO}_2$  equilibration. Where absolute enrichment estimates are required, as opposed to relative abundance estimates, which are used in, for example, the doubly labeled water technique (18–21), small sample equilibration would appear to be the best technique. Precision was greater with large volume equilibration on samples which had been diluted to close to the natural abundance range prior to analysis. However these samples also had a decreased accuracy, which offset the greater precision. Undiluted gIRMS analyses involved lower precision and PAA the lowest precision. Generally however precision was better than accuracy, suggesting that evaluations of analysis techniques based upon precision estimates of replicate samples alone are insufficient.

## ACKNOWLEDGMENT

We thank A. E. Fallick, T. Donnelly, and W. Scott, of the Scottish Universities Research and Reactor Centre, East Kilbride, Scotland; J. Parinayakosol, at the University of California, Los Angeles; and B. Dumoulin, at the Centrum voor Isotopen Onderzoek, Groningen, The Netherlands for their assistance. We also thank W. W. Wong of the Childrens Nutrition Research Center, Houston, TX and B. McGaw of the Rowett Research Institute, Aberdeen, Scotland, for their comments on an earlier draft of this paper.

Registry No.  $^{18}\text{O}$ , 14797-71-8; water, 7732-18-5.

## LITERATURE CITED

- Wood, R. A.; Nagy, K. A.; MacDonald, N. S.; Wakakuwa, S. T.; Beckman, R. J.; Kaaz, H. *Anal. Chem.* **1975**, *47*, 646–650.
- Amiel, S.; Peisach, M. *Anal. Chem.* **1963**, *35*, 323–327.
- Kamemoto, T. *Nature* **1964**, *203*, 513–514.
- Hoefs, J. *Stable Isotope Geochemistry*; Springer-Verlag: New York, 1973.
- Wong, W. W.; Cabrera, M. P.; Klein, P. D. *Anal. Chem.* **1984**, *56*, 1852–1858.
- Prentice, A. M.; Black, A. E.; Coward, W. A.; Davies, H. L.; Goldberg, G. R.; Murgatroyd, P. R.; Ashford, J.; Sawyer, M.; Whitehead, R. G. *Br. Med. J.* **1986**, *292*, 983–987.
- Schoeller, D. A.; Leitch, C. A.; Brown, C. *Am. J. Physiol.* **1986**, *251*, R1137–R1153.
- Wong, W. W.; Klein, P. D. *Mass Spectrom. Rev.* **1987**, *5*, 313–342.
- Cohn, M.; Urey, H. C. *J. Am. Chem. Soc.* **1938**, *60*, 679.
- Craig, H. *Geochim. Cosmochim. Acta* **1957**, *12*, 133.
- Brenninkmeijer, C. A. N.; Kraft, P.; Mook, W. G. *Isot. Geosci.* **1983**, *1*, 181–190.
- Dugan, J. P.; Borthwick, J.; Harmon, R. S.; Gagnier, M. A.; Glahn, J. E.; Kinsel, E. P.; MacLeod, S.; Viglino, J. A.; Hess, J. W. *Anal. Chem.* **1986**, *57*, 1734–1736.
- Roether, W. *Int. J. Appl. Radiat. Isot.* **1970**, *21*, 379–387.
- Kishima, N.; Sakai, H. *Anal. Chem.* **1980**, *52*, 356–358.
- Wong, W. W.; Lee, L. S.; Klein, P. D. *Anal. Chem.* **1987**, *59*, 690–693.
- Boyer, P. D.; Graves, D. J.; Suelter, C. H.; Dempsey, M. E. *Anal. Chem.* **1961**, *33*, 1906–1909.
- Wong, W. W.; Lee, L. S.; Klein, P. D. *Am. J. Clin. Nutr.* **1987**.
- Litson, N.; McClintock, R. *J. Theor. Biol.* **1966**, *12*, 46–74.
- Nagy, K. A. *Am. J. Physiol.* **1980**, *238*, 466–473.
- Nagy, K. A. *Ecol. Monogr.* **1987**, *57*, 111–128.
- Speakman, J. R.; Racey, P. A. *Sci. Prog.* **1988**, *72*, 227–237.
- Majzoub, M.; Nief, G. *Adv. Mass Spectrom.* **1968**, *4*, 511–520.
- de Wit, J. C.; van Straaten, C. M.; Mook, W. G. *Geostand. Newsl.* **1980**, *4*, 33–36.
- Baertschi, P. *Earth Planet. Sci. Lett.* **1976**, *31*, 341–344.
- Whyte, R. K.; Bayley, H. S.; Schwarcz, H. P. *Am. J. Clin. Nutr.* **1985**, *41*, 801–809.
- Epstein, S.; Mayeda, T. *Geochim. Cosmochim. Acta* **1953**, *4*, 213–224.
- Bottinga, Y.; Craig, H. *Earth Planet. Sci. Lett.* **1969**, *5*, 285–295.

- (28) Fairbanks, R. G. *J. Geophys. Res.* **1982**, *87*, 5796-5808.  
(29) Dostrovsky, I.; Klein, F. S. *Anal. Chem.* **1952**, *24*, 414-415.  
(30) Nagy, K. A. *The Doubly Labelled Water Method: A Guide to Its Use*; UCLA Publication No. 12-1417; UCLA: Los Angeles, CA, 1983.

RECEIVED for review November 27, 1989. Accepted December 12, 1989. The idea for this study originated during a British

Council sponsored visit by J.R.S. to D.M. for which we are grateful. J.R.S. was supported by NERC Grant GR3/5155 to P.A.R. and S.D.P. by a SERC studentship. Research done at the University of California, Los Angeles, was funded by US DOE Contract DE-ACO3-76-SF00012 and by US NSF Grant AMB 8600112.

## Flow Injection Analysis of L-Lactate with Enzyme Amplification and Amperometric Detection

Moore U. Asouzu,<sup>1</sup> William K. Nonidez,\* and Mat H. Ho

Department of Chemistry, University of Alabama at Birmingham, Birmingham, Alabama 35294

A flow injection analysis method for the determination of the lactate anion with enzyme amplification and amperometric detection is described. The system utilizes an oxygen electrode for measurement of changes in the oxygen concentration in the flow stream. Two enzymes, lactate oxidase and lactate dehydrogenase, were randomly coimmobilized on aminopropyl controlled-pore glass (AMP-CPG) and packed into a reactor.  $\beta$ -NADH was used as a coenzyme for the regeneration of lactate from pyruvate. The experimental conditions for the determination of the lactate anion were studied for this system by the simplex and the univariate methods. The results obtained under these two conditions were compared. The simplex experimental condition yielded a calibration curve whose linear portion had a slope that was 1.2 times greater than that of the linear portion of the curve obtained under univariate conditions. The limit of detection under simplex condition was  $1.19 \times 10^{-7}$  M vs  $3.29 \times 10^{-7}$  M lactate under univariate conditions. The relative standard deviation obtained for this system at  $6 \times 10^{-6}$  M lactate ( $n = 10$ ) was about 2.5% under simplex conditions and 3.6% under univariate maximization conditions.

### INTRODUCTION

Cyclic reactions involving amplification are often the method of choice for the enzymatic determination of small amounts of biologically important compounds whose quantitation would be otherwise difficult (1-8). Although its use in analytical chemistry has been limited, there is a resurgence of interest in enzyme amplification as a result of the need for better and more sensitive biological sensors (9).

Enzyme-mediated amplification has been used to analyze for a variety of substrates (1-8). The lactate oxidase/lactate dehydrogenase amplification cycle using  $\beta$ -NADH/ $\beta$ -NAD<sup>+</sup> couple is by far the most reported scheme in the literature. This scheme is shown in Figure 1. Many analytical procedures utilizing these enzymes are based on either spectrophotometric or spectrofluorometric detection of  $\beta$ -NADH (4, 7). While the former is not very sensitive, the latter suffers from the relatively weak fluorescence of  $\beta$ -NADH and interference from the components of biological matrices such as serum (4). Other methods are based on the electrochemical oxidation of  $\beta$ -

NADH to  $\beta$ -NAD<sup>+</sup>, which is usually complicated by a required large overpotential (11), or on the electrochemical oxidation of hydrogen peroxide which suffers from interference from ascorbic acid and  $\beta$ -NADH (2), or on the measurement of the decrease in oxygen concentration in bulk solution (10).

Scheller et al. have published a study involving the use of lactate/pyruvate cycling in enzyme amplification in a flow injection system (8) using a thermistor as a detector. However, no optimization procedures of the technique were carried out and a linear calibration curve was not demonstrated.

This paper describes an apparatus for flow injection analysis of lactate anion that uses a packed-bed enzyme column upon which lactate oxidase/lactate dehydrogenase are randomly coimmobilized. The depletion of oxygen, which takes place in the mobile phase when lactate ion reacts in this column in the presence of  $\beta$ -NADH, is measured with a Clark oxygen electrode. Optimum operating parameters are determined by both the univariate and the simplex approach. The chemical and the physical variables of interest in this system include the concentration of  $\beta$ -NADH, electrode potential, flow rate, and sample volume. Detection limits and linear range are additionally determined.

### EXPERIMENTAL SECTION

**Reagents and Solutions.** Lithium lactate, lactate oxidase (from *pediococcus* species, 10-30 units/mg of protein), L-lactate dehydrogenase (type XI from rabbit muscle, 700-1400 units/mg of protein), and glutaraldehyde were purchased from Sigma Chemical Co., St. Louis, MO.  $\beta$ -NADH (grade 1, 100% disodium salt) was purchased from Boehringer Mannheim Biochemicals, Indianapolis, IN. Aminopropyl controlled-pore glass (AMP-CPG; mean pore diameter, 569 Å; pore volume, 1.15 cm<sup>3</sup>/g; surface area, 43 m<sup>2</sup>/g; 120/200 mesh) was obtained from Electronucleonics, Fairfield, NJ. Distilled and triple deionized water was used for solution preparations. Phosphate buffer was prepared and titrated to pH 7.4 with sodium hydroxide.  $\beta$ -NADH solutions were prepared daily in phosphate buffer and protected from light. A 3 mM L-lactate stock solution was also prepared in the phosphate buffer. Working standards of lactate were prepared by diluting aliquots of this stock solution with phosphate buffer.

**Lactate Oxidase/Lactate Dehydrogenase Reactor.** Thirty units of lactate oxidase and 700 units of lactate dehydrogenase were coimmobilized randomly on AMP-CPG by using the glutaraldehyde method (12). Forty milligrams of AMP-CPG was washed several times with deionized water, rinsed with phosphate buffer, and dried. It was then reacted with 0.500 mL of glutaraldehyde (1.0% in phosphate buffer, pH 7.4) for 30 min in reduced oxygen atmosphere at room temperature. The derivatization was continued for another 30 min in the open with constant shaking. Excess glutaraldehyde was washed off thoroughly first with deionized water (100 mL) and then with buffer (50 mL). The

\* Author to whom correspondence should be addressed.

<sup>1</sup> Present address: Department of Chemistry Troy State University, Troy, AL 36082.

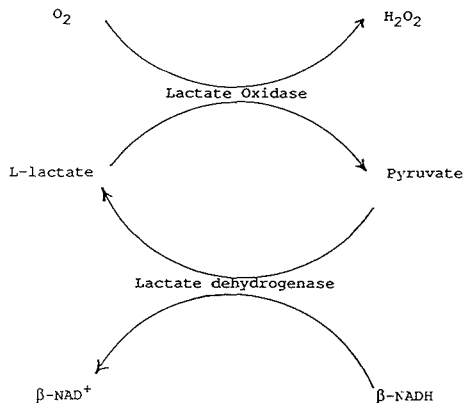


Figure 1. Enzyme amplification scheme for lactate.

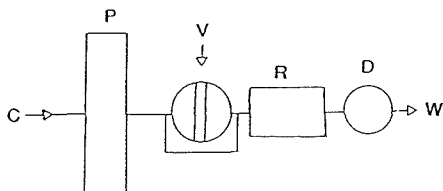


Figure 2. Schematic diagram of flow injection system: C (carrier line); P (pump); V (injection valve with bypass); R (enzyme reactor); D (detector); W (waste).

derivatized AMP-CPG was incubated with the enzymes in 0.400 mL of buffer overnight at 4 °C followed by extensive washing with cold phosphate buffer. The enzyme beads were then packed into the reactor cartridge. The reactor was a precision microbore Pyrex glass capillary column 50 mm long and 3 mm in internal diameter obtained from Rainin Instrument Co. Inc., Woburn, MA. When not in use, the reactor was filled with phosphate buffer and stored at 4 °C.

**Apparatus.** The flow injection system, Figure 2, consists of a pump (rabbit peristaltic, Rainin), an injection valve (Rheodyne Model 7010; Rheodyne, Inc., Cotati, CA) modified with a bypass, an oxygen electrode (Beckman Model 670552; Beckman Instrument Co., Fullerton, CA), and a BAS Model LC-4B amperometric detector (Bioanalytical Systems, Inc., West Lafayette, IN). Teflon tubing (0.8 mm i.d.) was used throughout the FIA system. The flow cell for the oxygen electrode, Figure 3, was designed and built in our laboratory and was constructed in three parts. The bottom portion is a Teflon cylinder into whose upper surface a circular depression was drilled to a depth of 0.7 cm. On the floor of this depression a further depression was drilled to a depth of 0.2 cm. The center of this second depression contains an inlet port for liquid, and an outlet port in its side. The inlet-outlet system was designed so that carrier flow is against gravity to help reduce any incidence of air bubbles. The threaded steel electrode mount to the cell allows the threaded steel electrode mount to be tightened without risk of stripping threads which would have normally been placed in the Teflon portion. A strip chart recorder was used to record response peaks. The system was kept at  $25 \pm 1$  °C with a thermostated water bath. The electrode's electrolytic gel and retaining Teflon membrane were replaced when the background current became unacceptable, or the electrode became unstable.

**Procedures for the Univariate Maximization Study.** The probe was stabilized daily by pumping carrier (phosphate buffer) through the flow cell for 2 h while a constant potential of -550 mV (vs Ag/AgCl) was applied. The variables maximized were pH of the phosphate buffer solution, applied electrode potential, flow rate, sample volume, and  $\beta$ -NADH concentration. The maximized function was signal-to-noise ratio. Signal values were obtained by measuring the height of a response peak from the

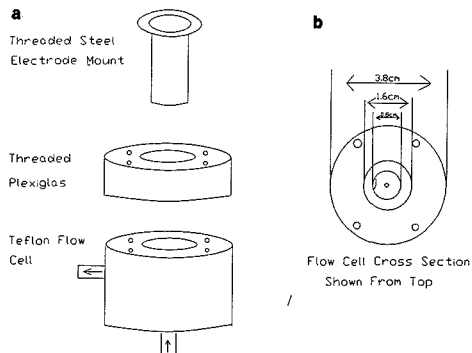


Figure 3. (a) Schematic diagram of flow cell. (b) Cross-section of lower portion.

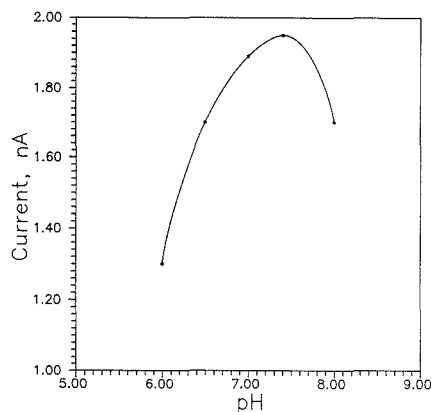


Figure 4. Effect of pH on amplification for maximization studies: sample volume, 75  $\mu$ L (1.5  $\mu$ M lactate); applied potential, -560 mV (vs Ag/AgCl);  $\beta$ -NADH concentration, 0.30 mM; flow rate, 0.80 mL/min.

base line. Noise values were obtained by measuring the mean value of the peak-to-peak noise at high amplification levels. These parameters were maximized in turn by holding the value of all but the parameter of interest constant. This process was terminated when the maximum for each variable was determined. The calibration curve (at maximized conditions) for L-lactate was prepared by carrying out four replicate injections of working standard containing  $\beta$ -NADH. The responses (current) for these injections were averaged to calculate the average response for each point. For all determinations, the value of the maximized parameters was used.

**Procedure for Simplex Optimization.** Optimization was carried out in terms of the actual experimental parameters ( $\beta$ -NADH concentration, sample volume, flow rate, and applied potential). The optimized function was signal-to-noise ratio. The initial simplex was chosen arbitrarily. The applied potential was constrained to values greater than -600 mV, which is the minimum recommended by the manufacturer of the oxygen electrode.

The calibration curve was prepared by carrying out four replicate injections of working standard, containing  $\beta$ -NADH, whose response currents were averaged to determine the current for each point. For all measurements, the values of the optimized parameters were used.

## RESULTS AND DISCUSSION

**Univariate Maximization.** Figures 4-9 show the results of the univariate maximization studies. Figure 4 is a plot of response current vs pH for the system described above. The literature values for maximum pH range for lactate oxidase

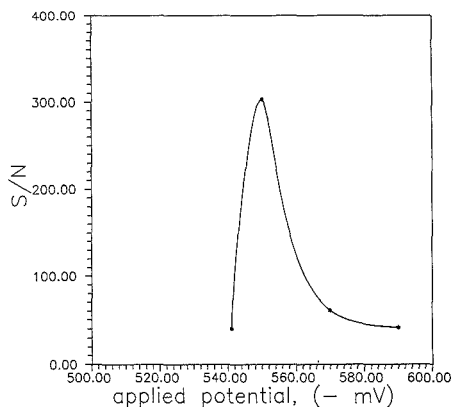


**Figure 5.** Effect of applied potential on signal-to-noise ratio for the maximization studies: sample volume, 0.201 mL (6  $\mu$ M lactate);  $\beta$ -NADH concentration, 0.10 mM; flow rate, 1.03 mL/min; pH = 7.4.

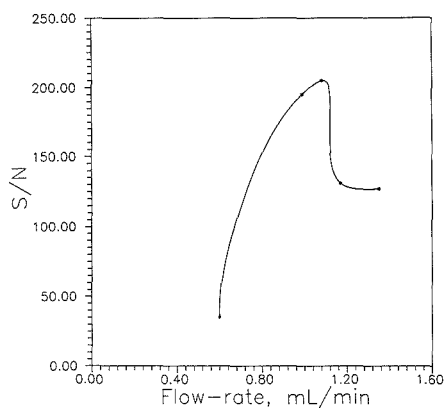


**Figure 6.** Effect of flow rate on signal-to-noise ratio for the maximization studies: sample volume, 0.201 mL (6  $\mu$ M lactate); applied potential, -550 mV (vs Ag/AgCl);  $\beta$ -NADH concentration, 0.10 mM; pH = 7.4.

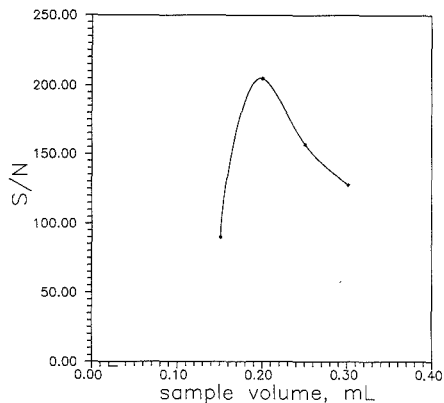


**Figure 7.** Effect of injected sample volume on signal-to-noise ratio for the maximization studies: lactate concentration, 6  $\mu$ M; applied potential, -550 mV (vs Ag/AgCl);  $\beta$ -NADH concentration, 0.10 mM; flow rate, 1.08 mL/min; pH = 7.4.

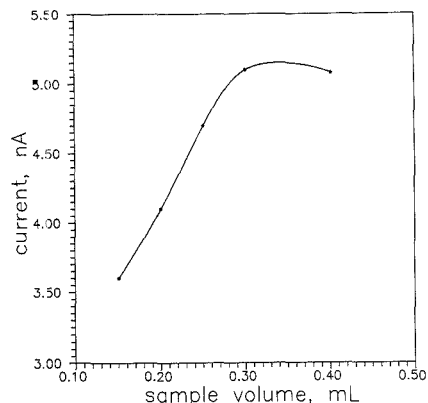


**Figure 8.** Effect of injected sample volume on signal for the system: lactate concentration, 6  $\mu$ M; applied potential, -550 mV (vs Ag/AgCl);  $\beta$ -NADH concentration, 0.10 mM; flow rate, 1.08 mL/min; pH = 7.4.

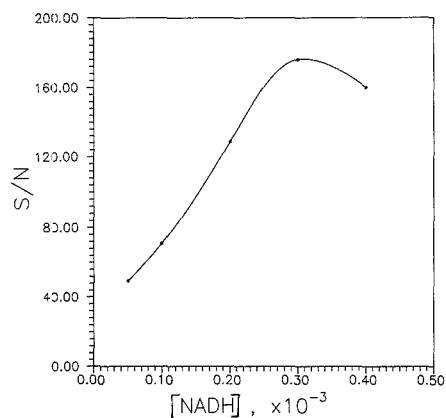


**Figure 9.** Effect of  $\beta$ -NADH concentration on signal-to-noise ratio for the maximization studies: sample volume, 0.201 mL (6  $\mu$ M lactate); applied potential, -550 mV (vs Ag/AgCl); flow rate, 1.08 mL/min; pH = 7.4.

and lactate dehydrogenase are 6.5–7.0, and 7.0–7.8, respectively (13, 14). An additional influence is the presence of  $\beta$ -NADH whose oxidation to  $\beta$ -NAD<sup>+</sup> is favored at pH 7.35 (14). The experimentally determined maximum pH of 7.4 therefore represents a compromise and was adopted for further experiments.

The plot of signal-to-noise ratio vs applied potential shown in Figure 5 exhibits a maximum at -550 mV. At potentials less negative than this, the signal-to-noise ratio is degraded because the decrease in signal is greater than the decrease in the observed noise. At potentials more negative than -550 mV, the signal-to-noise ratio is degraded because the signal increases only gradually with a larger increase in the observed noise. The manufacturer recommends an applied potential of -560 mV, which is 10 mV more negative than the optimum observed.

A plot of signal-to-noise ratio vs flow rate shown in Figure 6 exhibits a maximum. At flow rates before this maximum, the signal increases substantially as flow rate increases with little increase in noise observed. At flow rates after the maximum, the noise increases, leading to a degradation of signal-to-noise ratio.

The maximum sample volume was found to be 0.200 mL. Above this volume the signal-to-noise ratio decreased due mainly to an increase in noise, Figure 7. The fact that a 0.200-mL sample loop caused the system to produce less noise is believed to be an eccentricity of this system alone. A plot of signal value alone vs sample volume (Figure 8) reveals that the signal reaches a plateau at approximately 0.300 mL. Volumes larger than this do not cause larger signals. This is probably due to the saturation of the enzyme with the large amount of analyte and coenzyme and the dispersion characteristics of the system.

The system response was found to increase between  $\beta$ -NADH values of 0.05 and 0.3 mM. System response decreased at  $\beta$ -NADH concentrations greater than 0.3 mM, Figure 9. This decrease is attributed to the fact that impurities in  $\beta$ -NADH exhibit enzyme inhibition characteristics at high concentration. This phenomenon has been observed previously (15).  $\beta$ -NADH concentration was fixed at 0.3 mM.

**Simplex Optimization.** The signal-to-noise ratio of the amplification scheme for lactate determination based on the lactate oxidase/lactate dehydrogenase cycle was optimized by determining the necessary experimental conditions by means of a modified simplex optimization method originally introduced by Spendley (16) and later modified by Nelder and Mead (17). In this method the experimental variables are represented as the axes of a graph in  $n + 1$  dimensions where  $n$  is the number of variables. Each point in  $n + 1$  dimensional hyperspace corresponds to a set of experimental conditions and a given response to those experimental conditions.

If an  $n$  variable system is being explored, the experiment is initially performed  $n + 1$  times to produce a geometric figure which is the initial simplex. Each point in the simplex is then ranked by response from best to worst. The worst point is then reflected through a point on the opposite face of the simplex, which is found on the center of the hyperface formed by all the simplex points except the worst, to generate a new simplex. By repeating this procedure, along with appropriate expansions and contractions suggested by Nelder and Mead, the simplex is made to climb the response hypersurface until the top is reached. The experimental conditions defined by the last reflected point are then accepted as the optimum conditions.

A computer program based on the above algorithm was written in this laboratory in Pascal and tested on mathematical functions. It is available for use on an Apple II\* or an MS-DOS microcomputer and a listing of the source code is available from the author. Table I is a compendium of simplex optimization data for this system. All parameters were unrestricted in magnitude except the potential applied to the oxygen electrode. This value was not allowed to drop below -600 mV vs a Ag/AgCl electrode in order to prevent damage to the Clark-type electrode.

The initial simplex was defined in steps 1-5. These values were chosen semiarbitrarily heeding the experience gained in the maximization experiments in order to choose values which gave reasonable current and noise measurements. The simplex converged upon the optimum values of response at step 15 as shown in Table I.

On comparison of these values with the values obtained in the univariant maximization studies it should be noted that all the maximization parameters except the sample volume are well verified by the simplex. The sample volume predicted by the simplex optimization program was 0.235 mL compared to 0.201 mL by the univariant maximization procedure. This discrepancy has been speculated about earlier.

**Calibration Curves.** Calibration curves were constructed by use of both the maximized and optimized system parameters. The simplex method yielded a curve with a linear

Table I. A Compendium of Simplex Optimization Data for the System<sup>a</sup>

step	FR, mL/min	$\beta$ -NADH, mM	sample vol, mL	-E, mV	S/N
1	1.13	0.280	0.302	600	55
2	1.17	0.290	0.352	580	65
3	0.99	0.250	0.251	540	100
4	1.08	0.270	0.226	560	133
5	1.04	0.260	0.276	550	138
6 R	1.01	0.255	0.251	515	89
7 CR	1.04	0.261	0.261	536	84
8 R	0.90	0.231	0.157	513	70
9 CR	0.97	0.245	0.206	530	106
10 R	1.00	0.251	0.216	554	130
11 CR	1.01	0.253	0.228	549	130
12 R	1.06	0.265	0.217	554	108
13 CR	1.04	0.261	0.226	551	116
14 R	1.11	0.277	0.272	575	48
15 CW	1.01	0.253	0.222	541	130
16 R	1.03	0.258	0.251	549	130
17 CR	1.03	0.258	0.245	550	130
18 R	1.04	0.260	0.232	551	130
19 CR	1.04	0.259	0.235	550	130
20 R	1.03	0.259	0.241	550	130
21 CR	1.03	0.259	0.241	550	130
22 R	1.03	0.260	0.236	550	130
23 CR	1.03	0.259	0.237	550	130

<sup>a</sup>Lactate concentration = 6  $\mu$ M. pH = 7.4. Key: flow rate; R, reflection; CR and CW, contractions.

portion whose slope was 1.2 times greater than that of the linear portion of the calibration curve produced by the univariant method. The limit of detection (18) determined for the simplex method was  $1.19 \times 10^{-7}$  M vs  $3.29 \times 10^{-7}$  M for the univariant method. The relative standard deviation obtained for this system at  $6 \times 10^{-6}$  M lactate ( $n = 10$ ) was about 2.5%, using the simplex condition, and 3.6%, using the univariant maximization condition.

An amplification factor was determined for the simplex optimized coupled-enzyme system by comparing the slope of the linear portion of the calibration curves of the amplified and unamplified systems. An amplification of about 70 times was obtained for the system ( $\beta$ -NADH present) relative to the unamplified case ( $\beta$ -NADH absent). The amplified system was found to be nonlinear at L-lactate concentrations greater than 4  $\mu$ M (as was the calibration curve obtained under conditions prescribed by the univariant maximization method). The calibration curve for lactate is described by the equation  $Y = (2.27 \times 10^6)X - 0.0099$ . The lactate concentration used for the optimization and the univariant maximization studies is a bit higher than that of the highest concentration in the linear range of the calibration curve. Its sensitivity, however, is about half of that of the linear portion ( $1.11 \times 10^6$ ), and we consider this adequate.

**Stability of Immobilized Enzyme Reactor.** The stability of the enzyme column was evaluated by performing repetitive analyses over a period of 90 days. The results in Table II indicate that after the construction of the column the electrode's response increased from days 1 through 3. On days 13, 17, and 21, the responses of the electrode were the same. After this, the responses drop markedly and eventually to less than half of its original value (days 28, 34, 85, and 90, respectively). The initial increase in response has been observed previously (19) and attributed to a repacking phenomenon. The eventual loss of response is due to the denaturation of the enzymes and their loss through leaching.

## CONCLUSION

The ability to analyze for lactate ion by flow injection analysis using a packed-bed enzyme column was assessed and

Table II. Stability of the Enzyme Column<sup>a</sup>

day no.	response, nA	% change from day 1
1	5.28	—
2	5.44	3.0
3	5.60	6.0
13	5.92	12.1
17	5.92	12.1
21	5.92	12.1
28	5.76	9.1
34	5.44	3.0
85	2.68	-49.2
90	2.34	-55.7

<sup>a</sup> Lactate concentration = 3  $\mu$ M; pH = 7.4;  $\beta$ -NADH = 0.1 nM; sample volume = 0.302 mL; flow rate = 1.0 mL/min; applied potential = -560 mV.

optimum operating conditions were determined. This assessment indicates that systems of this sort have potential for the analysis of lactate in biological systems. The added prerequisites of low detection limits, simplicity, and fast sampling times (60 samples per hour) increase this competitiveness.

The negative aspects of the analysis center around the limited linear range of the analysis and the need to periodically reevaluate the response of the system due to enzyme degeneration.

**Registry No.** L-Lactic acid, 79-33-4; lactate oxidase, 9028-72-2; lactate dehydrogenase, 9001-60-9.

## LITERATURE CITED

- (1) Schubert, F.; Kirstein, D.; Scheller, F.; Applequist, R.; Gorton, L.; Johansson, G. *Anal. Chem. Lett.* **1986**, *19*, 1273.
- (2) Scheller, F.; Schubert, F.; Olsson, B.; Gorton, L.; Johansson, G. *Anal. Chem. Lett.* **1986**, *19*(15 & 16), 1691.
- (3) Schubert, F.; Kirstein, D.; Schroder, K. L.; Scheller, F. W. *Anal. Chim. Acta* **1985**, *169*, 391.
- (4) Imasaka, T.; Zare, R. N. *Anal. Chem.* **1979**, *51*, 2082.
- (5) Johansson, A.; Stanley, C. J.; Self, C. H. *Clin. Chim. Acta* **1985**, *148*, 119.
- (6) Johansson, A.; Stanley, C. J.; Self, C. H. *J. Immunol. Methods* **1985**, *83*, 89.
- (7) Roehrig, P.; Wolff, C. M.; Schwing, J. P. *Anal. Chim. Acta* **1983**, *153*, 181.
- (8) Scheller, F.; Siegbahn, N.; Danielsson, B.; Mosbach, K. *Anal. Chem.* **1985**, *57*, 1740.
- (9) Frew, J. E.; Hill, H. A. O. *Anal. Chem.* **1987**, *59*, 933A.
- (10) Mizutani, F.; Shimura, Y.; Tsuda, K. *Chem. Lett.* **1984**, 199.
- (11) Kulys, J. *J. Biosensors* **1986**, *2*, 3.
- (12) Motola, H. A.; Asfaha, I. *Anal. Chem.* **1980**, *52*, 2332.
- (13) Sigma Technical Bulletin, 1986.
- (14) McComb, R. B.; Bond, L. W.; Burnett, R. W.; Keech, R. C.; Bowers, G. N. *Clin. Chem.* **1976**, *22*(2), 141.
- (15) Bergmeyer, H. *Method of Enzymatic Analysis Vol. 1*; Chemie-Academic Press: New York and London, 1987.
- (16) Spendley, W.; Hext, G. R.; Himsworth, F. R. *Technometrics* **1962**, *4*, 441.
- (17) Nektier, J. A.; Mead, R. *Computer J.* **1965**, *7*, 308.
- (18) Miller, J. C.; Miller, J. N. *Statistics for Analytical Chemistry*; John Wiley and Sons: New York, 1986.
- (19) Dixon, J. D.; Stolzenbach, F. E.; Berenson, J. A.; Kaplan, N. O. *Biophys. Res. Commun.* **1973**, *52*, 905.

RECEIVED for review August 17, 1989. Accepted January 2, 1990. The authors gratefully acknowledge funding for this project by the Graduate School of the University of Alabama at Birmingham through the Graduate School Faculty Research Grant.

## Stereoselective Determination of Free Warfarin Concentration in Protein Binding Equilibrium Using Direct Sample Injection and an On-Line Liquid Chromatographic System

Akimasa Shibukawa,\* Miwa Nagao, Yoshihiro Kuroda, and Terumichi Nakagawa  
Faculty of Pharmaceutical Sciences, Kyoto University, Sakyo-ku, Kyoto-shi 606, Japan

A new on-line high-performance liquid chromatography system was developed for the stereoselective determination of free drug concentration in drug-protein binding equilibrium. When a 40–300- $\mu$ L portion of a sample solution containing 50–200  $\mu$ M racemic warfarin (Wf) and 100–550  $\mu$ M human serum albumin was directly injected into the internal-surface reversed-phase silica column, Wf gave a trapezoidal peak exhibiting a plateau region. The concentration in the plateau region was equal to the free Wf concentration in the initial sample solution. By the delivery of a portion (90  $\mu$ L) of the eluent in the plateau region into the chiral separation column (Chiral AGP column) by column switching, the free concentrations of respective enantiomers of Wf were determined. The results agreed well with those obtained by the conventional ultrafiltration method. The precision was also confirmed by the within-run and day-to-day reproducibilities (coefficient of variation  $\leq 3.05\%$ ,  $n = 5$ ). The present method is simple and rapid and four sample solutions can be analyzed within 1 h without pretreatment.

### INTRODUCTION

Because of difficulty in stereoselective synthesis and enantiomeric purification, many enantiomeric drugs are used

clinically as racemates. However, the pharmacological activity and side-effects between enantiomers are usually significantly different (1, 2). In addition, protein binding, the reversible binding of drugs with plasma proteins such as albumin and  $\alpha_1$ -acid glycoprotein, is often different between enantiomers (3). Protein binding causes significant effects on the pharmacological and pharmacokinetic properties of drugs (4–6), because only a free drug can pass through a capillary vessel and cell membrane to reach the action site and be subjected to glomerular filtration. Hepatic metabolism of most drugs is also limited by the free fraction of drug in blood. Therefore, it becomes inevitable in clinical chemotherapy to study the stereoselective protein binding of optically isomeric drugs. Thus, the development of a simple and rapid method to determine the free concentration of a drug enantiomer is of practical demand.

Recently we developed a high-performance frontal analysis (HPFA) method to determine free drug concentration in plasma or protein-containing solution by direct sample injection (7). In HPFA the high-performance liquid chromatography (HPLC) column is packed with specially designed stationary phase which excludes macromolecules such as albumin but retains small compounds on the hydrophobic ligands in the pores. When enough volume of sample solution in a state of drug-protein binding equilibrium is injected

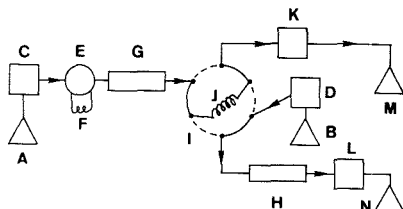


**Figure 1.** Schematic diagrams of the present on-line HPLC system: (A) mobile phase for HPFA; (B) mobile phase for chiral separation; (C, D) pump; (E) sample injector; (F) injector loop; (G) column for HPFA; (H) column for chiral separation; (I) six-way switching valve; (J) loop; (K, L) detector; (M, N) waste.

directly into the column, a zone appears at the top of the column where the drug concentration in the mobile phase reaches steady state and the same protein binding equilibrium as in the sample solution is reproduced in the interspace of the stationary particles. As a result, the drug is eluted as a trapezoidal peak with a plateau, and the drug concentration in this region is the same as that of the free drug in the sample solution. Consequently, the free drug concentration can be determined from the plateau height. The chromatographic processes of HPFA are explained in detail in a previous paper (8). The authors applied the HPFA method to the determination of free concentrations of indomethacin in albumin solutions and of carbamazepine in human plasma (7, 8). The results were in good agreement with those obtained by the ultrafiltration method.

Clinically, warfarin (Wf) is administered to patients as a racemic mixture. It has been known that hypoprothrombinemic activity of the *S* isomer is 2–5 times more potent than that of the *R* isomer (9–11) and that *S* isomer binds to human serum albumin (HSA) more strongly than the *R* isomer (12–14). Consequently, the free fraction of the *R* isomer in human serum (1.18% of the total Wf concentration 40–50  $\mu\text{g/mL}$ ) became higher than that of the *S* isomer (0.903%) (15).

One of the attractive trends in HPLC is the development of a coupled-column system which facilitates simple, rapid, and specific separation. In the present paper, we developed a new on-line HPLC system that enables the determinations of free concentrations of drug enantiomers following direct injection of sample solutions in a state of drug–protein binding equilibrium. The system was set up by the on-line combination of HPFA with direct chiral separation using a protein-immobilized silica column. Warfarin–human serum albumin (HSA) mixed solution was used as a model sample, and the results were compared with those obtained by the ultrafiltration method.

#### EXPERIMENTAL SECTION

**Reagents and Materials.** HSA (fatty acid free) was purchased from Sigma (St. Louis, Mo). Warfarin potassium was manufactured by Eisai Co., Ltd. (Japan). Weighed amounts of these materials were dissolved in potassium phosphate buffer (pH 7.4, ionic strength ( $I$ ) = 0.17). The concentration of HSA was determined spectrophotometrically by using extinction coefficient  $E_{1\text{cm}}^{1\%} = 5.31$  at 279 nm. The Wf–HSA mixed solutions were kept at 37 °C before use.

**Determination of Free Wf Enantiomers by the On-Line HPLC System.** The schematic diagram of the on-line HPLC system used in this study is shown in Figure 1. The HPLC column for HPFA (ISRP silica column) and that for the chiral separation (Chiral AGP column) were connected in series via a six-way valve. The Wf–HSA mixed solutions were injected into the ISRP silica column (G) without any pretreatment. When a plateau region of Wf peak was eluted, a part of the eluent for this region passing through the loop (J) (ca. 90  $\mu\text{L}$ ) was delivered to the Chiral AGP column (H) by switching the valve (I) from the

solid line to the dashed line to determine the concentrations of Wf enantiomers. For all samples, the valve was switched at 10.0 min after sample injection, so that HSA was not delivered into the Chiral AGP column since it was completely size-excluded from the ISRP silica column. After the line switching, Wf remaining in the ISRP silica column was quickly eluted out by elevating the flow rate of mobile phase to 1.0 mL/min, and the next sample solution was injected while the chiral separation of the previous sample was proceeding in the Chiral AGP column. Four samples could be analyzed within 1 h.

The apparatus and HPLC conditions are as follows.

**Apparatus:** pump, TriRotar III (Jasco, Japan) and LC-3A (Shimadzu, Japan); UV detector, SPD-2A (Shimadzu, Japan); integrated data analyzer, Chromatopac C-R3A (Shimadzu); injector, Rheodyne type 7125 injector with a 5-mL loop.

**HPFA conditions:** stationary phase, ISRP silica support of 5  $\mu\text{m}$  mean particle diameter packed in a 15 cm  $\times$  4.6 mm i.d. stainless-steel column (Regis Chemical Co.); mobile phase, potassium phosphate buffer (pH 7.4,  $I = 0.17$ ); flow rate, 0.5 mL/min; detection, UV 308 nm; column temperature, 37 °C, controlled in a water bath.

**Chiral separation conditions:** stationary phase, Chiral AGP column (10 cm  $\times$  4.0 mm i.d., ChromTech AB, Sweden); mobile phase, potassium phosphate buffer (pH 7.0,  $I = 0.02$ )/acetonitrile = 89/11 (v/v); flow rate, 1.0 mL/min; detection, UV 210 nm; column temperature, 37 °C, controlled in a water bath.

To obtain the calibration line, the ISRP silica column was removed from the line (the injector was connected directly with six-way valve) and 1 mL of the seven standard solutions containing 0.292–14.4  $\mu\text{M}$  of racemic Wf was injected. After the loop (J) was filled with the standard solution, the valve (I) was switched to deliver the standard solution in the loop into the chiral separation column. The calibration equations for the *R* and *S* isomers were concentration ( $\mu\text{M}$ ) = 0.241  $\times$  area + 0.0563,  $R > 0.9998$ , and concentration ( $\mu\text{M}$ ) = 0.240  $\times$  area + 0.0469,  $R > 0.9998$ , respectively.

**Determination of Free Drug Concentration by Ultrafiltration.** A disposable ultrafiltration kit, Molcut II (UFPI LGC, Millipore Co.), was used as a reference standard method to determine free drug concentration. Each 200- $\mu\text{L}$  portion of the filtrate containing free Wf was obtained by pressurizing 1 mL of the sample solution with 2 mL of air. All filtration procedures were performed at 37 °C. A 90- $\mu\text{L}$  portion of the filtrate was subjected to the Chiral AGP column to determine the free form concentration of each enantiomer. The HPLC conditions were the same as those described above.

The peak areas of Wf enantiomers obtained by injecting a 90- $\mu\text{L}$  portion of the buffer solution of 0.5  $\mu\text{M}$  Wf were the same with those obtained by injecting the same portion of the filtrate through the membrane. This indicated that Wf was not adsorbed onto the ultrafiltration membrane.

#### RESULTS AND DISCUSSION

**HPFA of Wf in HSA Solution.** The internal-surface reversed-phase (ISRP) silica support developed by Pinkerton and co-workers (16, 17) was used as a stationary phase of the HPFA method in the present system. This support consists of two different surfaces: the moderately hydrophobic internal surface of the pores covalently binding tripeptide partitioning phase (glycyl-L-phenylalanyl-L-phenylalanine) and the hydrophilic external surface of the particles covalently binding diol-glycine groups. This support retains Wf in the pores but size-excludes HSA. Although the tripeptide ligand is optically active, this support shows no stereoselectivity for Wf, and the peaks of the enantiomers were completely overlapped with each other.

The appearance of the plateau region of a drug peak is essential in HPFA (8). To decide the suitable injection volume of HPFA, the relation between Wf elution curve and the sample volume was investigated. Figure 2A–E shows the influence of sample volume upon the chromatograms of a 200  $\mu\text{M}$  Wf–550  $\mu\text{M}$  HSA mixed solution. The mobile phase was the phosphate buffer which was also used to prepare the sample solution. Organic solvent, which may influence the

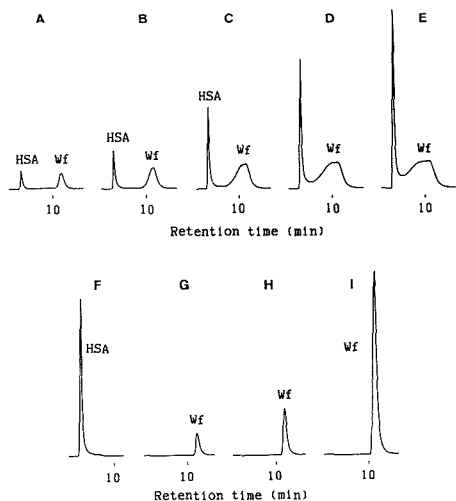


**Figure 2.** Chromatograms of 200  $\mu\text{M}$  warfarin (Wf)-550  $\mu\text{M}$  HSA mixed solution (A-E), 550  $\mu\text{M}$  HSA solution (F), and 200  $\mu\text{M}$  Wf solution (G-I) injected into the ISRP silica column: (injection volume) (A) 5  $\mu\text{L}$ , (B) 10  $\mu\text{L}$ , (C) 20  $\mu\text{L}$ , (D) 30  $\mu\text{L}$ , (E) 40  $\mu\text{L}$ , (F) 40  $\mu\text{L}$ , (G) 5  $\mu\text{L}$ , (H) 10  $\mu\text{L}$ , (I) 40  $\mu\text{L}$ ; (HPLC conditions) stationary phase, ISRP silica column (15 cm  $\times$  4.6 mm i.d.); mobile phase, potassium phosphate buffer (pH 7.4,  $I = 0.17$ ); flow rate, 0.5 mL/min; detection, UV 308 nm; column temperature, 37  $^{\circ}\text{C}$ .

nature of the protein binding equilibria, was not contained in the mobile phase. As injection volume increased, the Wf peak became spread toward the HSA peak. The broadening of Wf elution curve was caused by the binding to HSA in the mobile phase. This was apparent from the comparison with the chromatograms of Wf solution without containing HSA (Figure 2G-I). The Wf peak did not split into two peaks due to bound and free species, because, as shown previously (18, 19), the reversible Wf-HSA interaction occurs much faster than the chromatographic partition. The effect of protein binding was more clearly shown by injecting larger sample volume. When 40  $\mu\text{L}$  of this solution was injected, Wf gave a trapezoidal peak exhibiting a plateau region. Further increase in the sample volume did not produce elevation of plateau height, but widened the plateau region. The injection volume of this sample was, consequently, decided as 40  $\mu\text{L}$ . Similar results were obtained in the case of indometacin-albumin solution and carbamazepine in human plasma (7, 8).

In a similar manner, suitable injection volumes were determined to be 40  $\mu\text{L}$  for the sample solution containing 550  $\mu\text{M}$  HSA (the free Wf fractions were 0.798-1.06%), 60  $\mu\text{L}$  for that containing 300  $\mu\text{M}$  HSA (1.57%, 1.84%), and 300  $\mu\text{L}$  for that containing 100  $\mu\text{M}$  HSA (6.16%, 9.64%). As shown in Figure 3, the plateau region appeared after injecting these volumes of the sample solutions. As reported in the previous paper (8), the sample solution with lower HSA concentration, that is, higher free Wf fraction, necessitated larger injection volumes to obtain this region.

**Determination of Free Wf Enantiomers by an On-Line HPLC System.** The free concentrations of Wf enantiomers were determined by delivering a given portion (ca. 90  $\mu\text{L}$ ) of the plateau region passing through the loop (J in Figure 1) into the Chiral AGP column. This support, prepared by binding  $\alpha_1$ -acid glycoprotein to the porous silica of 5- $\mu\text{m}$  particle diameter (20), can separate Wf enantiomers without any derivatization under aqueous mobile phase condition. It was reported that a different type of the protein-immobilized

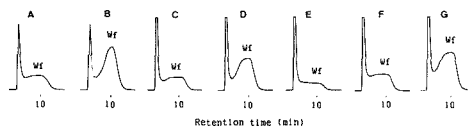


**Figure 3.** High-performance frontal analysis of warfarin (Wf)-HSA mixed solution: (sample) (A) 50  $\mu\text{M}$  Wf-100  $\mu\text{M}$  HSA, (B) 100  $\mu\text{M}$  Wf-100  $\mu\text{M}$  HSA, (C) 50  $\mu\text{M}$  Wf-300  $\mu\text{M}$  HSA, (D) 100  $\mu\text{M}$  Wf-300  $\mu\text{M}$  HSA, (E) 50  $\mu\text{M}$  Wf-550  $\mu\text{M}$  HSA, (F) 100  $\mu\text{M}$  Wf-550  $\mu\text{M}$  HSA, (G) 200  $\mu\text{M}$  Wf-550  $\mu\text{M}$  HSA; (injection volume) (A, B) 300  $\mu\text{L}$ , (C, D) 60  $\mu\text{L}$ , (E-G) 40  $\mu\text{L}$ . The absorbance units full scale of chromatograms A and B was 4 times larger than that of chromatograms C-G. Other HPLC conditions were the same as in Figure 2.

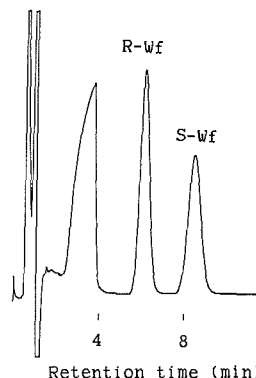


**Figure 4.** Chiral separation of warfarin (Wf). For HPLC conditions, see text.

silica column (bovine serum albumin immobilized silica column; Resolvosil) could also be used for the stereoselective determination of total Wf concentrations (not free concentrations) in human plasma after deproteinization of the samples (21).

Figure 4 shows the chromatogram of the chiral separation obtained after injection of 200  $\mu\text{M}$  Wf-550  $\mu\text{M}$  HSA mixed solution. The *R*(+) and *S*(-) isomers were well separated from each other with retention times 6.1 and 8.5 min, respectively. The optical assignments were performed by use of an optical rotation HPLC detector (ChiraMonitor, Model 750/25, Applied Chromatography Systems, Ltd., England). The peaks eluted within 4 min are the system peaks, which also appeared when the eluent of the HPFA was injected. The concentrations of *R* and *S* isomers in Figure 4 were determined as 1.16 and 1.00  $\mu\text{M}$ , respectively. Chiral inversion between the isomers was not observed during the chromatographic process. This was confirmed by the rechromatography of the fractionated Wf enantiomers.

Table I lists the free concentrations of Wf isomers determined by the present system and by the ultrafiltration method. Figure 5 shows the Scatchard plots of racemic Wf-HSA interaction constructed from these data. The free concentration of racemic Wf was the sum of both enantiomers. The binding parameters of the high affinity site were calculated from the plots, where the data obtained from 100  $\mu\text{M}$  Wf-100  $\mu\text{M}$  HSA mixed solution were excluded because they deviated from linearity caused by the influence of the low affinity binding. As found in Table II, the association constant ( $K = 1.96 \times 10^5 \text{ M}^{-1}$ ) and the number of sites on one HSA molecule ( $n = 1.24$ ) obtained by means of the HPFA method were in reasonable agreement with those obtained by means of the ultrafiltration method ( $K = 1.70 \times 10^5 \text{ M}^{-1}$ ,  $n = 1.30$ ) and with the literature values (14, 22-24). These results



**Table I. Free Concentrations ( $\mu\text{M}$ ) of Warfarin (Wf) Enantiomers in Human Serum Albumin (HSA) Solution Determined by Ultrafiltration Method and High-Performance Frontal Analysis (HPFA) Method<sup>a</sup>**

sample Wf ( $\mu\text{M}$ )-HSA ( $\mu\text{M}$ )	HPFA					
	ultrafiltration ( $n = 3-5$ )		within-run ( $n = 5$ )		day-to-day ( $n = 5$ )	
	(R)-Wf	(S)-Wf	(R)-Wf	(S)-Wf	(R)-Wf	(S)-Wf
50-100	1.75 (2.16%)	1.51 (2.17%)	1.63 (0.914%)	1.45 (0.577%)	1.67 (2.83%)	1.48 (2.19%)
100-100	4.98 (2.45%)	4.65 (1.70%)	4.88 (0.848%)	4.76 (0.576%)	5.00 (2.76%)	4.85 (3.05%)
50-300	0.452 (2.83%)	0.345 (7.74%)	0.431 (1.16%)	0.353 (2.03%)	0.433 (2.25%)	0.350 (2.34%)
100-300	1.08 (0.925%)	0.860 (0.760%)	0.993 (0.525%)	0.843 (1.12%)	0.987 (2.31%)	0.849 (0.569%)
50-550	0.243 (3.10%)	0.191 (4.25%)	0.220 (0.827%)	0.179 (1.21%)	0.218 (0.752%)	0.178 (3.04%)
100-550	0.580 (2.09%)	0.469 (4.75%)	0.471 (0.435%)	0.393 (0.557%)	0.472 (0.930%)	0.391 (1.78%)
200-550	1.29 (0.891%)	1.04 (2.55%)	1.13 (1.08%)	0.976 (1.02%)	1.15 (0.991%)	0.986 (1.04%)

<sup>a</sup> Values in parentheses are percent coefficient of variation.

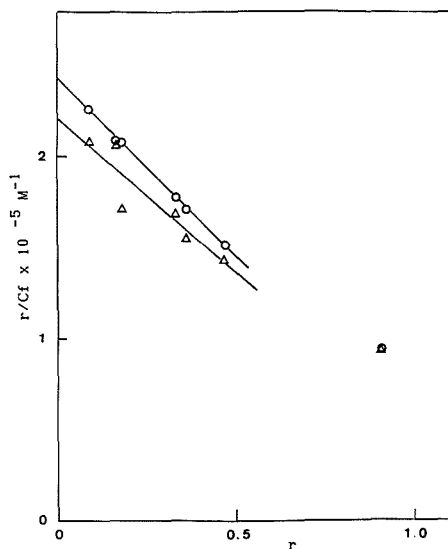


**Figure 5.** Scatchard plots of racemic warfarin-HSA interaction obtained by means of HPFA (O) and ultrafiltration method ( $\Delta$ ).  $r$  represents the moles of the bound Wf per mole of HSA. The binding parameters ( $n = 1.24$ ,  $K = 1.96 \times 10^5 \text{ M}^{-1}$  for HPFA, and  $n = 1.30$ ,  $K = 1.70 \times 10^5$  for the ultrafiltration method) were estimated by curve fitting using the equation  $r/Cf = -Kr + Kn$ . The solid lines were the best fitted ones.

support the reliability of the HPFA method.

As for the free concentrations of Wf isomers listed in Table I, good agreement is found between the results obtained by these two methods: the linear regression line was  $C_{FA} = 0.989 C_{UF} - 0.0730$ ,  $R = 0.9996$ , for the R isomer and  $C_{FA} = 1.03 C_{UF} - 0.0563$ ,  $R = 0.9997$ , for the S isomer, where  $C_{FA}$  and  $C_{UF}$  are the free concentrations determined by the present method (the data of within-run analyses) and by the ultrafiltration method, respectively. The within-run and day-to-day reproducibilities of the present method were percent coefficient of variation  $\leq 1.12$  and 3.05, respectively. These results indicate the feasibility of the present HPLC method for a simple and rapid determination of free concentration of Wf enantiomers. In all sample solutions, the free concentration of R isomer is significantly larger than that of the S isomer by

**Table II. Estimated Parameters for High Affinity Binding of Warfarin-HSA at pH 7.4**

$n^a$	$K^b$ ( $\text{M}^{-1}$ )	temp, $^{\circ}\text{C}$	concn of phosphate buffer, M	method	ref
1.24	$1.96 \times 10^5$	37	0.067 M	HPFA	c
1.30	$1.70 \times 10^5$	37	0.067 M	ultrafiltration	c
1	$5.4 \times 10^5$	22	0.1 M	fluorescence	14
0.95	$2.31 \times 10^5$	37	0.2 M	equilibrium dialysis and ultrafiltration	22
1.38	$2.03 \times 10^5$	37	0.067 M	frontal analysis	23
1.16	$2.1 \times 10^5$	37	0.067 M	frontal analysis	24
1.31	$2.18 \times 10^5$	37	0.067 M	Hummel-Dreyer	24

<sup>a</sup> Number of sites on one HSA molecule. <sup>b</sup> Association constant.  
<sup>c</sup> This paper.

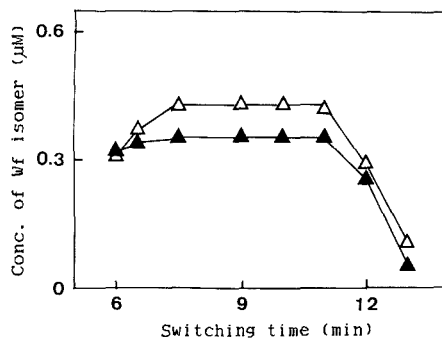


**Figure 6.** Relation between column switching time and the concentrations of R ( $\Delta$ ) and S ( $\blacktriangle$ ) Wf isomers in the heart-cut portion.

1.03-1.24-fold ( $T$  test at the 5% level comparing the variance in the  $R/S$  ratio of the free concentrations with that in the seven data of the  $R/S$  peak area ratio obtained to prepare the calibration lines). This result coincides with the previous finding that the S isomer binds with HSA more strongly than the R isomer (12-14), and the  $R/S$  ratio of the free concentration in human plasma was  $1.32 \pm 0.256$  (15).

Figure 6 shows the relation between the switching time after injection of a 60- $\mu\text{L}$  portion of 50  $\mu\text{M}$  Wf-300  $\mu\text{M}$  HSA mixed solution and the assay values of Wf isomer concentrations. The plateau region appeared in 7.2-11.5 min (see Figure 3C), where the concentrations determined after the column switching at 7.5, 9.0, 10.0, and 11.0 min were almost unchanged

( $0.426 \pm 0.0066 \mu\text{M}$  for *R* isomer and  $0.352 \pm 0.0013 \mu\text{M}$  for *S* isomer). These values agreed well with the free concentrations obtained by the ultrafiltration method (see Table I). This indicates that the free Wf concentration can be determined stereoselectively by the heart-cut of any part of the plateau region.

To apply the present HPLC system to other drugs, the following points should be noted.

The mobile phase condition of HPFA should be selected not to disturb drug-protein binding equilibrium. The addition of organic modifiers or ion-pair reagents and use of pH value and ion strength much different from those of the sample solutions should be avoided, because they may cause peak splitting (18, 19).

In the HPFA method, the retention time of drugs can be manipulated by the selection of column length or the nature of the stationary phase. In addition to the ISRP silica, other HPLC supports which exclude macromolecules but retain small molecules, such as the porous poly(vinyl alcohol) gel (Asahipak GS-320, Asahi Chemical, Japan) (25) and the shielded hydrophobic phase silica column (Supelco, Bellefonte, PA) (26), can also be applicable to HPFA.

The injection volume should be decided with attention that the sample with higher free drug fraction requires larger injection volume in HPFA.

A chiral separation column which does not allow injection of aqueous sample solution is unsuitable, because the aqueous mobile phase of HPFA is directly delivered to the chiral separation column.

A column-switching technique is also effective for HPFA of optically inactive drug. Even when the zonal drug peak overlaps with interfering peaks and a clear plateau cannot be obtained, the free drug concentration can be determined by delivering a part of the plateau region to a second column which enables good separation. Since the ISRP silica column shows not only the reversed-phase but also the weak cation-exchange retention mode (27), a conventional reversed-phase column such as ODS silica may be useful as a second column.

#### LITERATURE CITED

- (1) Powell, J. Robert; Ambre, John J.; Ruo, Tsuen I. *Drug Stereochemistry*; Wainer, Irving W., Drayer, Dennis E., Eds., Marcel Dekker, Inc.:

- New York and Basel, 1988; Chapter 10.
- (2) Ariens, E. J. *Chiral Separations by HPLC, Applications to Pharmaceutical Compounds*; Krstulovic, A. M., Ed.; Ellis Horwood Limited: Chichester, 1989; Chapter 3.
- (3) Lam, Y. W. Francis. *Pharmacotherapy* **1988**, *8*, 147-157.
- (4) Kwong, Tai C. *Clin. Chim. Acta* **1985**, *151*, 193-216.
- (5) Svensson, Craig K.; Woodruff, Marlene N.; Baxter, James G.; Laika, David. *Clin. Pharmacokinet.* **1986**, *11*, 450-469.
- (6) Taylor, E. Howard; Ackerman, Bruce H. *J. Liq. Chromatogr.* **1987**, *10*, 323-343.
- (7) Shibukawa, Akimasa; Nakagawa, Terumichi; Nishimura, Naohiro; Miyake, Mamoru; Tanaka Hisashi. *Chem. Pharm. Bull.* **1989**, *37*, 702-706.
- (8) Shibukawa, Akimasa; Nishimura, Naohiro; Nomura, Kayoko; Kuroda Yoshihiro; Nakagawa Terumichi. *Chem. Pharm. Bull.* **1990**, *38*, 443-447.
- (9) Ebel, John. M.; West, Bruce D.; Link, Karl P.; *Biochem. Pharmacol.* **1966**, *15*, 1003-1006.
- (10) Breckenridge, A.; Rus, M. O.; Wesseling, H.; Lewis, R. J.; Gibbons, R. *Clin. Pharmacol. Ther.*, **1974**, *15*, 424-430.
- (11) O'Reilly, Robert A. *Clin. Pharmacol. Ther.* **1974**, *16*, 348-354.
- (12) Sellers, Edward M.; Koch-Weser, Jan. *Pharmacol. Res. Commun.* **1975**, *7*, 331-336.
- (13) Miller, J. H. M.; Small G. A.; *J. Pharm. Pharmacol.* **1977**, *29*, 33P.
- (14) Otagiri, M.; Otagiri, Y.; Perrin, J. H.; *Int. J. Pharm.* **1979**, *2*, 283-294.
- (15) Yacobi, Avraham; Levy Gerhard. *J. Pharmacokinet. Biopharmacol.* **1977**, *5*, 123-131.
- (16) Hagastam, I. Helene; Pinkerton, Thomas C. *Anal. Chem.* **1985**, *57*, 1757-1763.
- (17) Pinkerton, T. C.; Miller, T. D.; Cook, S. E.; Perry, J. A.; Räteike, J. D.; Szczerba, T. J. *BioChromatography* **1986**, *1*, 96-105.
- (18) Shibukawa, Akimasa; Nakagawa, Terumichi; Miyake, Mamoru; Nishimura, Naohiro; Tanaka, Hisashi. *Chem. Pharm. Bull.* **1989**, *37*, 1311-1315.
- (19) Pinkerton, Thomas C.; Miller, Terry D.; Janis, Linda J. *Anal. Chem.* **1989**, *61*, 1171-1174.
- (20) Hermansson, Jörgen; Schill, Göran. *Chromatographic Chiral Separation*; Zief, Morris, Crane, Laura J., Eds.; Marcel Dekker, Inc.: New York and Basel, 1987; Vol. 40, Chapter 10.
- (21) Ch. Ya-Qin; Wainer, Irving W. *Pharm. Res.* **1988**, *10*, 680-683.
- (22) Tillement, J.-P.; Zini, R.; d'Athis, P.; Vassent, G. *Eur. J. Clin. Pharmacol.* **1974**, *7*, 307-313.
- (23) Oester, Y. T.; Keresztes-Nagy, Steven; Mais, Roland F.; Becktel, Jack; Zaroslinski, John F. *J. Pharm. Sci.* **1976**, *65*, 1673-1677.
- (24) Sebille, Bernard; Thuaud, Nicole; Tillement, Jean-Paul. *J. Chromatogr.* **1978**, *167*, 159-170.
- (25) Yoshiura, Masahiko; Iriyama, Keiji. *J. Liq. Chromatogr.* **1986**, *9*, 177-188.
- (26) Gisch, Daryl J.; Hunter, Briant T.; Feibush Binyamin. *J. Chromatogr.* **1988**, *433*, 264-268.
- (27) Nakagawa, Terumichi; Shibukawa, Akimasa; Shimono, Norihito; Kawashima, Tomoko; Tanaka, Hisashi; Haginaka, Jun. *J. Chromatogr.* **1987**, *420*, 297-311.

RECEIVED for review September 14, 1989. Accepted December 18, 1989.

# Characterization of Overlapped Chromatographic Peaks by Their Second Derivative. The Limit of the Method

Eli Grushka\* and Dror Israeli

Department of Inorganic and Analytical Chemistry, The Hebrew University, Jerusalem, Israel

The second derivative of a chromatographic signal can aid in the recognition of composite peaks. In the case of a two-component composite, the second derivative has three maxima and two minima. The time position of the second of the three maxima is indicative of the point where the peak envelope of each component cross each other. This second maximum can be used to trigger the end of integration of the first component and the beginning of the integration of the second component. In theory, the second derivative approach works well. The present paper investigates the limits of the method. It was found that, depending on the separation between the two components in the composite, there is a peak height ratio below which the method fails to recognize the existence of a composite system. The greater the separation, the smaller the height ratio. At  $4\sigma$  separation, the minimum height ratio that the method can still recognize as a composite is around  $10^{-5}$ . However, the useful range of the approach may extend to a lower range of height ratios due to the small changes in the area with relatively large changes in the peak height ratio. Noise also affects the useful range of the method. In general, as the noise increases, the method fails at higher peak height ratios. A surface describing the useful range of the method is given as a function of the signal-to-noise ratio, the separation, and the height ratio.

## INTRODUCTION

The differentiation of the chromatographic detector signal, either in the time domain or in the wavelength axis, can be used to gain some important information on the purity of the eluting peak. Among the first to describe the differentiation of the chromatographic signal were Ashley and Reilly (1). They used time-based derivatives to electronically sharpen and deconvolute the peaks. Grushka (2, 3) used derivatives in the time domain to characterize severely overlapped chromatographic peaks. Zelt and his group (4) and Traveset and his co-workers (5) used spectrometers capable of taking derivatives of spectra as detectors in high-performance liquid chromatography (HPLC) and in thin-layer chromatography (TLC). Berridge (6) used time-based derivatives of the chromatogram as an aid to optimize the mobile phase selection in HPLC. Fell and his co-workers (7-10) have used derivatives to obtain qualitative and quantitative information from the chromatogram. Gerow and Rutan (11) used derivatives with Kalman filters in order to smooth TLC chromatograms. Grant and Bhattacharyya (12) used derivatives to determine the purity of chromatographic peaks. Ebel (13) discussed briefly the use of derivatives in deconvolution techniques. Recently, Grushka and Atamna (14) have shown that the time-based second derivative can be used as a criterion to terminate and initiate the area integration of strongly overlapped peaks ( $0.5 < R_s < 0.75$ ).

Although overlapped peaks with resolutions between 0.5 and 0.75 can be recognized by the eye as a composite, an integrator may have difficulties in recognizing the existence

of multiple components. A composite made up of two peaks with resolution between 0.5 and 1 is characterized by a second derivative having three maxima and two minima. The time position of the second maximum of the second derivative is a good indication of the crossover point of the concentration profiles of the two components. Therefore, the time position of the second maximum of the second derivative can be used as a criterion to stop the integration of the first peak in the composite and start the integration of the second peak. Grushka and Atamna have shown that for noiseless Gaussian peaks this approach works well (14). The areas thus measured were a linear function of the amounts of the components in the composite. More importantly, the areas were independent of the separation between the peaks (14).

Since the preliminary results were promising (14), the limitation of the method must be examined to check the useful range of the approach. The second derivative method is valid as long as it has three maxima and two minima. The method fails once the system of five extrema collapses into three extrema as is the case with severely overlapped peaks. Failure of the method is due to four main reasons: (a) the resolution is below a critical value so that the two components severely overlap, (b) the height of one of the components is below a critical value so that it disappears under the envelope of the major component, (c) the noise in the detector signal is large enough to interfere with the differentiation process, and (d) the chromatographic peaks are not Gaussians but of other asymmetric shapes which grossly distort the second derivative curves. The present paper will examine theoretically the first three limitations, and it will establish some guidelines showing the useful range of the method.

## THEORETICAL CONSIDERATIONS

Before going into the theoretical analysis, several parameters need to be defined. In this study, composite peaks are assumed to be made up of two Gaussians. Since the two components elute very closely, we assume that the peak widths are the same. In the following treatment we will assume that the concentration of the second component in the composite is equal to, or smaller than, the first component. Since Gaussian peaks are symmetrical, the conclusions reached by using the above assumption can be extended to cases where the first component is the smaller of the two. The height ratio is defined here as the height of the second peak divided by the height of the first peak,  $H_2/H_1$ . Thus, very low height ratios mean very small amounts of the second component in the composite. The separation is given in terms of the standard deviation of the peaks.

**Separation and Height Limitation.** The limits placed on the method by the separation between the components and by the peak height are related. The height of one peak at which it will disappear under the second peak in the composite is a function of the separation between the peaks. To find the limit imposed by the height ratio of the peaks and the separation between them, we need to calculate the point at which the five extrema in the second derivative collapse into three: two maxima and one minimum. Due to the transcendental nature of the equation describing the second de-

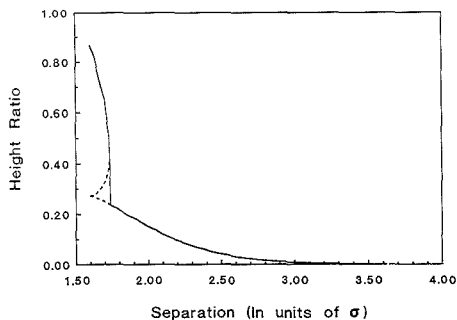


**Figure 1.** Peak height ratio at which the second derivative fails. The dashed lines enclose a region of ambiguity (see text).

derivative of a composite made up from two Gaussians, numerical techniques must be employed to find this point of collapse.

Figure 1 shows the height ratio, at which the second derivative method fails as a function of the separation between the components in the case of *noiseless Gaussian peaks*. For cases where the height ratio of the components is above the solid line, the method is successful in recognizing and quantifying composites. Of course, the greater the separation, the smaller the height ratio at which the method fails. At a  $4\sigma$  separation the theoretical height ratio limit is about  $1 \times 10^{-5}$ . Under normal conditions,  $4\sigma$  separations do not present difficulties for integrators. However, when one of the peaks in the composite is very small, the perturbation that it causes on the composite envelope is very minute and conventional integrators will frequently miss it. Unexpectedly, Figure 1 indicates that, for noiseless Gaussians, the second derivative method can characterize composites even at the 10000:1 height ratio.

In the separation range of about  $4-1.75\sigma$ , the height ratio at which the method fails increases monotonically although not linearly. At  $1.75\sigma$  separation there is a sudden and marked increase in the height ratio at which the method fails. The fact that the method works at separations less than  $2\sigma$  is quite surprising. At such separations, the two components in the composite are completely merged and conventional integrators lose their effectiveness. Yet, the second derivative can discern the two components provided that the height ratio of the peaks is above the critical value. At a separation of  $1.75\sigma$ , that critical value is about 0.24.

Below the separation of  $1.74\sigma$  the second derivative can still be used, but its behavior is more complicated. Above the solid line of the curve in Figure 1, the second derivative behaves in the "normal" manner in so far as the time position of its second maximum occurs before the actual maximum of the second component. However, below the solid line, there is a range of height ratios and separations where the second derivative shows again three maxima and two minima. That range is bounded by the broken lines in Figure 1. In this region, the second maximum in the second derivative occurs *after* the actual maximum position of the second component. Figure 2 compares four composites with four height ratios at a separation of  $1.7\sigma$ . The first component in the composite was assumed to have a retention time of 120 (in arbitrary units) and a standard deviation of 20. Therefore, the retention time of the second component is 154. The height ratio of 0.8 (Figure 2A) represents a case above the solid line of Figure 1. The second maximum in the second derivative curve occurs at time 143. At height ratio of 0.5 (Figure 2B), which is below the solid line in Figure 1 but above the broken line, the second derivative has only two maxima. While the derivative indi-

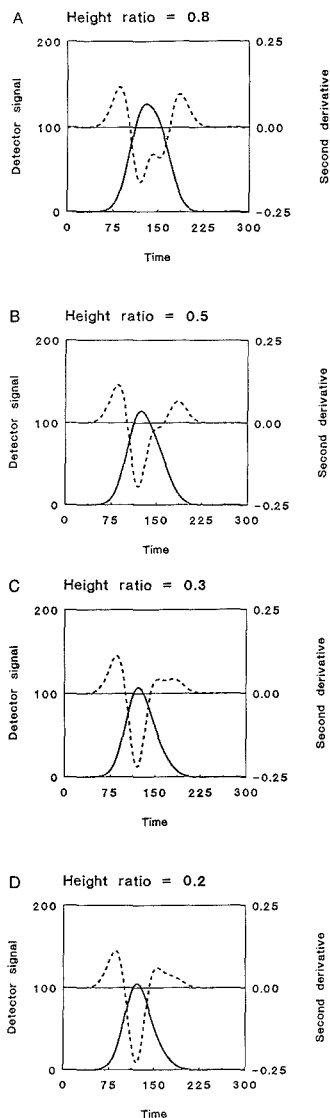


**Figure 2.** Four composites and their second derivatives. In all cases the separation is  $1.7\sigma$ . The detector signal scale is in arbitrary units. The solid curve is the composite; the dashed curve is the second derivative. Four different height ratios are given: (A) height ratio above the solid line in Figure 1, (B) height ratio below the solid line but above the broken lines, (C) height ratio within the broken lines, and (D) height ratio below the broken lines.

cates, in this case, that the peak is a composite, it does not allow the recognition of peak-start and peak-end. The height ratio of 0.3 (Figure 2C) is inside the area bounded by the broken lines. Here, the second derivative curve has again three maxima. However, the second maximum occurs at time 157, which is past the peak maximum. Thus, while the method can be used to initiate and/or terminate the integrator, the areas recovered will be erroneous. The height ratio of 0.2 (Figure 2D) represents a case below the broken lines. The

second derivative still indicates the existence of a composite peak, but it cannot be used for quantitative purposes since it has only two maxima.

The region bounded by the broken lines in Figure 1 is small. On the separation axis it extends from  $1.74\sigma$  to  $1.6\sigma$ . The region is widest at  $1.74\sigma$  separation; it covers height ratios from about 0.41 to 0.24. The existence of this region is troublesome since it may lead to erroneous qualitative results. However, the region may be recognized by the fact that the second maximum occurs on the bottom part of the tail of the composite and by the positive second minimum of the second derivative curve.

To be useful, the method should be able not only to indicate the end and start of peaks but also to give areas which are proportional to the concentration injected, even at very low height ratios. Figure 3 shows graphs of second peak area as a function of height ratio for four separations:  $4\sigma$ ,  $3\sigma$ ,  $2\sigma$ , and  $1.7\sigma$ . At each separation, the figure gives three lines: (a) the solid line is the area measured under the composite starting at the time position of the second maximum of the second derivative, (b) the short-dashed line represents the theoretical area of the complete second peak, and (c) the long-dashed line is the area of the second component only, from the time position of the second maximum in the second derivative. The lines were least-squares fitted to areas generated with the computer. In all cases the fits were very good with correlation coefficients better than 0.997. Table I gives the data obtained from the least-squares procedure for the composite and for the second component when the first peak height is 10 (arbitrary units) and  $\sigma$  is 20. The line obtained from the area of the complete ( $-\infty$  to  $+\infty$ ) second peak is identical at all separations: the slope is 501.198, the intercept is around  $10^{-6}$ , and the correlation coefficient is unity.

Figure 3 and Table I show some important points. At  $4\sigma$  separation the method is linear down to height ratios of  $1 \times 10^{-4}$ . However, because of the nonzero intercept, and the relatively gentle slope, changes in the areas with changes in the height ratios are small at height ratios below 0.01. In the height ratio range of 0.01–0.001 the method should be used with care; the area changes between 27.237 and 22.773. Below a height ratio of 0.001, the method is not usable at all: the area changes between 22.773 at  $H_2/H_1$  of 0.001 and 22.351 at  $H_2/H_1$  of 0.0001. The situation is much the same for  $3\sigma$  separation, although the method fails at a higher height ratio due to the smaller separation. The linear range extends to a height ratio of 0.008. However, below  $H_2/H_1$  of 0.01 the qualitative information obtained from the method is not reliable. At  $2\sigma$  separation the method is, again, linear all the way to the failure point at  $H_2/H_1$  of 0.15. At this separation, the whole linear range yields valid qualitative information. At  $1.7\sigma$  separation, the method is linear and valid down to the height ratio of 0.6. While this range of linearity is rather small, it permits the analyst to recognize and to quantitate composites that conventional integrators could not handle.

At  $4\sigma$  and  $3\sigma$  separations the composite area, as measured from the time position of the second maximum in the second derivative, is larger than that of the area of either the complete Gaussian or the area, from the point of integration initiation, of the second component only. The reason that the area of the composite is greater than that of the complete Gaussian is as follows. The peak recognition scheme by the second derivative causes a truncation of some of the area from the second component and the inclusion of some area due to the first component. The contribution of the area of the first solute in the composite is greater than the area loss due to the truncation of the second solute. The only case where the area lost equals the area gained should occur when the two components are of equal height. Indeed, Figure 3 shows that

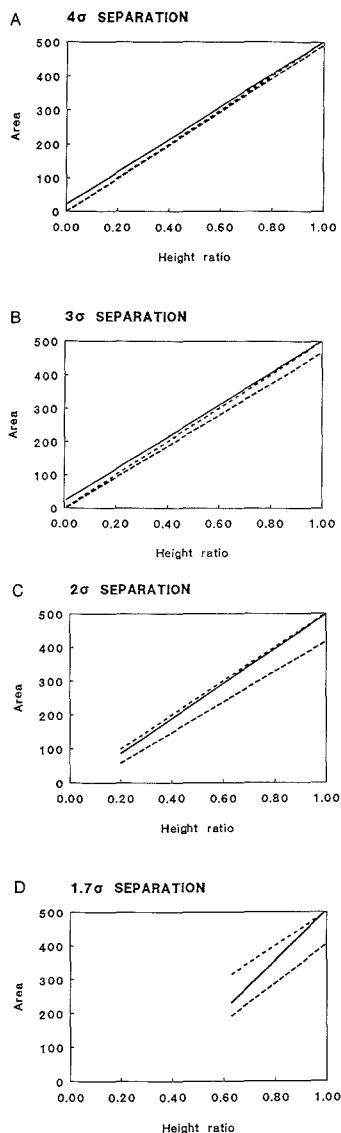


Figure 3. Linearity of the measured areas as a function of the height ratio. The solid line describes the area of the composite from the time position of the second maximum of the second derivative, the long-dashed line describes the area only of the second component from the above time and the short-dashed line describes the area of the complete Gaussian. Four separations are shown: (A)  $4\sigma$ , (B)  $3\sigma$ , (C)  $2\sigma$ , and (D)  $1.7\sigma$ .

at the height ratio of 1 the area of the composite (from the time position of the second maximum in the second derivative) equals the area of the complete Gaussian.

As the separation decreases, see Figure 3 at  $2\sigma$  and  $1.7\sigma$  separations, the composite area becomes smaller than that of the complete Gaussian. As the separation decreases, the second maximum in the second derivative tends to shift closer to the position of the peak maximum. Therefore, the area of the second component that is lost in the recognition process

**Table I. Slopes, Intercepts, and Correlation Coefficients Obtained from Least-Square Fits of the Integrated Area to the Height Ratio of the Peaks<sup>a</sup>**

		$4\sigma$	$3\sigma$	$2\sigma$	$1.7\sigma$
slope	composite	479.876	481.344	515.186	745.206
	2nd comp	491.379	468.124	449.084	575.151
int	composite	22.199	21.551	-16.266	-239.008
	2nd comp	0.164	-0.940	-31.260	-170.184
corr coef	composite	0.999985	0.999972	0.99931	0.9985
	2nd comp	0.999996	0.999985	0.99942	0.9992

<sup>a</sup>The entries for "composite" refer to area under the composite envelope; "2nd comp" refers to areas belonging only to the second component. All areas are calculated from the time position of the second maximum in the second derivative curve.

far exceeds the area of first component that is included in the area of the composite. The result is that the area of the composite is smaller than that of the complete Gaussian. Only when the height ratio is unity does the area lost equal that gained and the composite area will, as before, equal that of the complete Gaussian. That behavior is observed in Figure 3.

The slope of the line due to the composite area becomes larger as the separation decreases. The intercept becomes smaller and, then, more negative. Between  $4\sigma$  and about  $2.5\sigma$ , the changes in the slope and the intercept are not too great. Therefore, in that separation range, calibration curves are independent to a large extent from the separation. More on this point was discussed by us previously (14). As the separation decreases below  $2.5\sigma$ , the changes in the slope and intercept become larger and larger. From a practical point of view the increasing dependence of the slope and intercept on the separation means that the chromatography has to be controlled tightly if the quantitative results are to be meaningful. The short linear range of the method at small separations and the need for tight chromatographic control stress again the fact that there are no substitutes for good chromatography: if the resolution is too small, one is better off trying to improve the chromatographic system rather than manipulating, numerically or electronically, the detector signal.

**Limitation due to Noise.** The preceding discussion assumed that the peaks were noiseless. The presence of noise, however, should have deleterious effects on the second derivative method. To check the effect of noise, we generated composite peaks with noise. The noise levels given are in terms of peak-to-peak levels and not in terms of root mean square. In the preceding treatment, it will be assumed that a time region in the chromatogram was isolated to contain only a suspected composite peak. Thus, we assume that there is a prior recognition of the peak beginning and end. The following procedure checks to see if the peak is a true single peak or a composite.

Derivatives magnify the noise and the second derivative trace is noisier than the original detector trace. Therefore, the second derivative approach may either converge to the wrong system of maxima and minima thus identifying wrongly a composite peak or miss entirely the presence of a composite. To utilize the derivative method, a smoothing process must be employed. There are several ways to smooth data. We chose the following procedure to smooth the derivative data and to identify the correct combination of maxima and minima: (a) Noisy chromatograms were generated and stored in a digitized manner in the computer. (b) By use of the Savitzky-Golay method (15), the second derivative was computed by using a filter window whose width is a function of an estimated peak width. The filter used a second order polynomial. The examples that will be shown shortly use a 17-point window. (c) Next, the highest point in the second derivative trace is located and height thresholds are established at  $\pm 0.5$  of the highest point. (d) All maxima and minima that exceed the thresholds are found. (e) The extrema

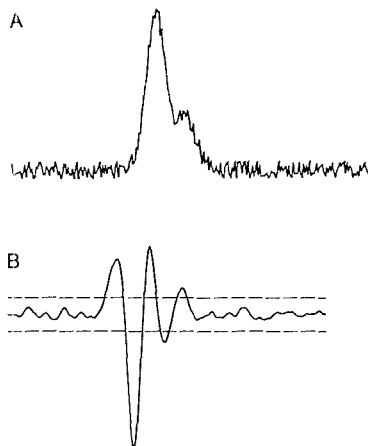


**Figure 4.** A noisy composite and its smoothed second derivative. The dashed lines give the threshold limits for searching minima and maxima. The separation between the two components is  $3\sigma$ ; the height ratio is 0.33; S/N ratio is 10. The existence of three maxima alternating with two minima ensures the identification of the composite.

are searched for a pattern of successive three maxima alternating with two minima. This last step leads to one of several possible courses of action. (f1) If alternating three maxima and two minima are found, then a composite is declared and the time position of the second maximum in the second derivative curve is used to stop the integration of the first peak and start the integration of the second peak. (f2) If more than five extrema are located, then the method fails due to noise. Further attempts to locate the composite are pursued, if desired, outside the procedure described here. (f3) If five extrema are found but the two minima do not alternate with the three maxima, the method fails due to noise. (g) If there are less than five extrema, the threshold is halved and steps d-f are repeated. This iteration process continues until one of the conditions in steps f1-f3 is met.

Figure 4 gives an example of the procedure. Figure 4a shows the composite that is made up of two Gaussian peaks at a separation level of  $3\sigma$ , height ratio of 0.33, and signal-to-noise (S/N) ratio of 10. Figure 4b gives the smoothed second derivative of the composite. The dashed lines indicate the height thresholds. The figure gives the results of the second iteration. In the first iteration, the thresholds were higher and the algorithm found only two maxima and two minima. In the second iteration, alternating three maxima and two minima were found outside the height thresholds. At this stage the algorithm recognized the composite, the iteration process was stopped, and the integration can proceed. The small maxima and minima inside the height thresholds are due to noise and they were rejected from the count of maxima and minima.

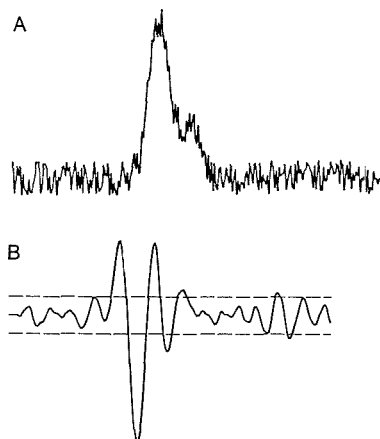


**Figure 5.** A noisy composite and its smoothed second derivative. The dashed lines give the threshold limits for searching minima and maxima. The separation between the two components is  $3\sigma$ ; the height ratio is 0.33; S/N ratio is 5. The existence of four maxima above the threshold causes the method to fail.

Figure 5 gives a case where the approach fails. The composite is similar to that shown in Figure 4, except that the S/N ratio here is 5. The composite is shown in Figure 5a and the derivative in Figure 5b. Figure 5b shows the second iteration, and in the present case there are four maxima above the threshold and two minima below. The method fails since there are more than three maxima.

The previous example demonstrates clearly the difficulties associated with noise. In the case of noiseless peaks, the second derivative approach will have no problems in recognizing a composite at  $3\sigma$  separation and height ratio of 0.33. Severe noise makes this recognition very difficult. Therefore, it would be of interest to obtain the lower limit of the second derivative method to recognize composites of noisy peaks. Using the algorithm described above to locate the extrema of the second derivative curve, we examined the limits at which the method fails. Figure 6 describes a surface in the coordinate system of S/N ratio, separation, and height ratio. On the surface, the procedure described here recognizes composites in 90% of the attempts made. Above the surface, the method is very reliable. Below the surface the method fails too frequently to be of practical value.

The features of the surface are as expected. In general, as the separation decreases, the limiting S/N ratio becomes higher and the method is less sensitive to the presence of double peaks. For example, at the height ratio of 1 and a separation of  $4\sigma$ , the limiting S/N ratio is about 3, while at a separation of  $2\sigma$  the limiting S/N ratio is about 8. Similarly, as the height ratio decreases, the limiting S/N ratio increases. For example, at a separation of  $2\sigma$  and a height ratio of 1, the limiting S/N ratio is 8 while at the height ratio of 0.2, the

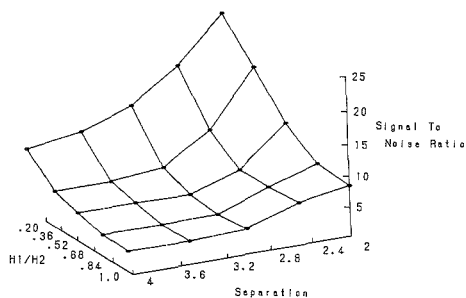


**Figure 6.** A surface describing the noise-related limit of the second derivative method. The surface is plotted as a function of S/N ratio, separation, and height ratio.

limiting S/N ratio is about 20.

### CONCLUSIONS

The second derivative can be used to recognize and to quantify composite peaks that are made up of two Gaussian peaks. In cases where the S/N ratio is very high and the separation is moderate (between  $3\sigma$  and  $4\sigma$ ), the method can be used to obtain quantitative information about the components in the composite even at height ratios of 100 to 1. However, noise in the signal will decrease the effective range of the method. At very noisy signals and small separations, the limit of the method seems to occur at a height ratio of 0.3.

The method described here to overcome noise effects is a first attempt to deal with the problem. The approach uses a rather simplistic algorithm to locate the maxima and minima of the second derivative. More ambitious search routines might be more efficient in identifying the extrema profile of the second derivative. With such search routines, the useful range of the second derivative method can be enlarged and composites of smaller height ratios can be quantified.

### LITERATURE CITED

- (1) Ashley, J. W., Jr.; Reilley, C. N. *Anal. Chem.* **1965**, *35*, 626, 627.
- (2) Grushka, E.; Monacelli, G. C. *Anal. Chem.* **1972**, *44*, 484-489.
- (3) Grushka, E. *Anal. Chem.* **1972**, *44*, 1733-1738.
- (4) Zelt, D. T.; Owen, J. A.; Marks, G. S. *J. Chromatogr.* **1980**, *189*, 209-216.
- (5) Traveset, J.; Such, V.; Goizalo, R.; Gelpi, E. *J. Chromatogr.* **1981**, *203*, 51-58.
- (6) Berridge, J. C. *Chromatographia* **1982**, *16*, 172-174.
- (7) Fell, A. F.; Scott, H. P.; Gill, R.; Moffat, A. C. *Chromatographia* **1982**, *16*, 69-78.
- (8) Fell, A. F.; Scott, H. P.; Gill, R.; Moffat, A. C. *J. Chromatogr.* **1983**, *273*, 3-17.
- (9) Fell, A. F.; Scott, H. P.; Gill, R.; Moffat, A. C. *J. Chromatogr.* **1983**, *282*, 123-140.
- (10) Clark, B. J.; Fell, A. F.; Scott, H. P.; Westerlund, D. J. *Chromatogr.* **1984**, *286*, 261-273.
- (11) Gerow, D. D.; Rutan, S. C. *Anal. Chim. Acta* **1986**, *184*, 53-64.
- (12) Grant, A.; Bhattacharyya, P. K. *J. Chromatogr.* **1985**, *347*, 219-235.
- (13) Ebel, S. *Chromatographia* **1986**, *22*, 373-378.
- (14) Grushka, E.; Atamna, I. *Chromatographia* **1987**, *24*, 226-232.
- (15) Savitzky, A.; Golay, M. J. E. *Anal. Chem.* **1964**, *36*, 1627-1639.

RECEIVED for review September 5, 1989. Accepted December 18, 1989.

# Calibration of the Ion Microprobe for the Quantitative Determination of Strontium, Iron, Manganese, and Magnesium in Carbonate Minerals

Peter K. Swart

Rosenstiel School of Marine and Atmospheric Science, Marine Geology and Geophysics, University of Miami, Miami, Florida 33149

The necessary operating conditions have been determined for the measurement of trace concentrations of Mg, Mn, Fe, and Sr in calcite and dolomite using a Cameca 3f ion microprobe with the energy filtering method. With this technique, the presence of interferences can be ascertained by examining the deviation of the measured isotopic ratios of an element from their natural values as a function of the kinetic energy acquired during the sputtering process. With the energy filtering method it is possible, using an energy offset of  $-50$  V, to reduce interferences from other species at masses 24, 54, and 88 for Mg, Fe, and Sr. Although Mn has only one stable isotope, it is believed that a similar voltage offset may be suitable for this element. By use of these conditions, calibration lines have been established for Mg, Fe, Mn, and Sr employing 11 calcite and dolomite standards. It is estimated that for carbonate materials, concentrations of Mn, Mg, and Sr can be quantitatively measured as low as 1 ppm and Fe as low as 10 ppm. No significant differences in calibration were observed between calcite and dolomite. The slopes and intercepts of the relationships were found to remain constant within error over periods of 3 years.

## INTRODUCTION

Although the ion microprobe has been used for geological and metallurgical problems for a considerable period of time, its application to sedimentary rocks has been limited. In particular the analysis of carbonate minerals has been, until recent studies by Mason (1) and Veizer et al. (2), virtually nonexistent. This investigation reports the analytical conditions necessary to achieve the high resolution and sensitivity necessary for trace element analyses of dolomites and calcites using an energy filtering method previously applied to silicates and sulfides (3, 4).

The secondary ion spectrum of any mineral is extremely complex as a result of the presence of a multitude of molecular ion species produced by interaction between the ion beam, the sample, and gases in the background of the mass spectrometer. This process produces dimers, oxides, and hydrides which overlap the various ionic species of interest. For example, the mass spectra shown in Figure 1 are produced through the interaction of an oxygen ion beam with calcite and dolomite samples. Species occurring at major masses have been tentatively identified (Table I). In calcite, the main contribution to mass 40 can be considered to be derived from  $^{40}\text{Ca}^+$ , but in dolomite as a result of a large concentration of Mg, the species  $^{24}\text{MgO}^+$ , is also present. In order to correct or remove these interferences and thereby obtain meaningful concentration data, three different approaches, spectral stripping, increased mass resolution, and energy filtering have been used by various workers. The validity of these methods has been discussed by Shimizu and Hart (4).

**Spectral Stripping.** This technique, used by Mason (1) and Veizer et al. (2), involves the estimation of the contribution of an ionic or molecular species to one particular mass of

Table I. Possible Interferences Occurring at Masses of Interest in This Study

mass	species
24	$^{24}\text{Mg}^+$ , $^{48}\text{Ca}^{2+}$ , $^{23}\text{NaH}^+$ , $^{12}\text{C}_2^+$
25	$^{25}\text{Mg}^+$ , $^{24}\text{MgH}^+$ , $^{12}\text{C}_2\text{H}^+$
26	$^{26}\text{Mg}^+$ , $^{24}\text{MgH}_2^+$ , $^{25}\text{MgH}^+$
40	$^{40}\text{Ca}^+$ , $^{24}\text{Mg}^{16}\text{O}^+$
41	$^{40}\text{CaH}^+$ , $^{24}\text{Mg}^{16}\text{OH}^+$ , $^{25}\text{Mg}^{16}\text{O}^+$
42	$^{42}\text{Ca}^+$ , $^{24}\text{Mg}^{18}\text{O}^+$ , $^{26}\text{Mg}^{16}\text{O}^+$ , $^{40}\text{CaHH}^+$ , $^{25}\text{Mg}^{16}\text{OH}^+$
43	$^{43}\text{Ca}^+$ , $^{42}\text{CaH}^+$ , $^{24}\text{Mg}^{18}\text{OH}^+$ , $^{26}\text{Mg}^{16}\text{OH}^+$ , $^{86}\text{Sr}^{2+}$
44	$^{44}\text{Ca}^+$ , $^{25}\text{Mg}^{18}\text{O}^+$ , $^{86}\text{Sr}^{2+}$
46	$^{46}\text{Ca}^+$
54	$^{54}\text{Fe}^+$ , $^{42}\text{Ca}^{12}\text{C}^+$ , $^{40}\text{Ca}^{14}\text{N}^+$ , $^{26}\text{Mg}^{16}\text{O}^{12}\text{C}^+$
55	$^{55}\text{Mn}^+$ , $^{54}\text{FeH}^+$ , $^{43}\text{Ca}^{12}\text{C}^+$ , $^{42}\text{Ca}^{12}\text{CH}^+$ , $^{40}\text{Ca}^{14}\text{NH}^+$ , $^{26}\text{Mg}^{16}\text{O}^{12}\text{CH}^+$ , $^{42}\text{Ca}^{12}\text{CH}^+$
56	$^{56}\text{Fe}^+$ , $^{55}\text{MnH}^+$ , $^{40}\text{Ca}^{16}\text{O}^+$ , $^{44}\text{Ca}^{12}\text{C}^+$ , $^{42}\text{Ca}^{14}\text{N}^+$
57	$^{57}\text{Fe}^+$ , $^{56}\text{FeH}^+$ , $^{40}\text{Ca}^{16}\text{OH}^+$ , $^{44}\text{Ca}^{12}\text{CH}^+$ , $^{42}\text{Ca}^{14}\text{NH}^+$
86	$^{86}\text{Sr}^{2+}$ , $^{43}\text{Ca}_2^+$
87	$^{87}\text{Sr}^{2+}$ , $^{86}\text{SrH}^+$ , $^{43}\text{Ca}_2\text{H}^+$
88	$^{88}\text{Sr}^{2+}$ , $^{87}\text{SrH}^+$ , $^{44}\text{Ca}_2^+$

interest by measuring related masses. This method was considered to be inadequate (3) because there was no unequivocal method of identifying the ions present or predicting the composition of the sample being analyzed. For example, in the case of  $^{88}\text{Sr}^+$ , abundances were corrected for the contribution of  $^{44}\text{Ca}_2^+$  by analyzing mass 80 (1, 2). Assuming that mass 80 is composed primarily of  $^{40}\text{Ca}_2^+$ , a contribution for  $^{44}\text{Ca}_2^+$  can be made by subtracting the appropriate isotopic ratio from mass 88. This type of correction will naturally vary according to the chemical composition of the carbonate being analyzed. In particular dolomites will have a large contribution to mass 80 from  $^{40}\text{Ca}^{24}\text{MgO}^+$ , and therefore separate calibration curves must be developed for carbonates with variable Mg concentrations. In addition to taking extra time, counting errors are compounded, as the final ion yield is calculated by subtracting a fraction of the mass 80 yield from that measured at 88. For other elements, this technique becomes more complicated and subject to more assumptions and uncertainties.

**Increased Mass Resolution.** Increasing the mass resolution of the ion probe allows isotopes to be separated by virtue of their small differences in mass. With this approach  $^{44}\text{Ca}_2^+$ , which has an atomic mass of 87.910962, can be separated from  $^{88}\text{Sr}^+$  (mass = 87.905619). In this particular example, a mass resolution of  $>16000$  would be required. The mass resolution necessary to separate other possible contaminating molecular species that might be encountered in carbonates can be calculated and is tabulated by Mason (1). Necessary resolutions generally exceed 1000. Although this approach has been successfully used with silicates and sulfides (5, 6), ion yields from carbonates are significantly lower, so that increasing the resolution of the ion probe decreases the sensitivity to such an extent that in order to obtain a sufficient number of counts, extended counting periods become necessary. This further leads to problems of machine instability over long time periods necessary for counting and, therefore, this approach cannot



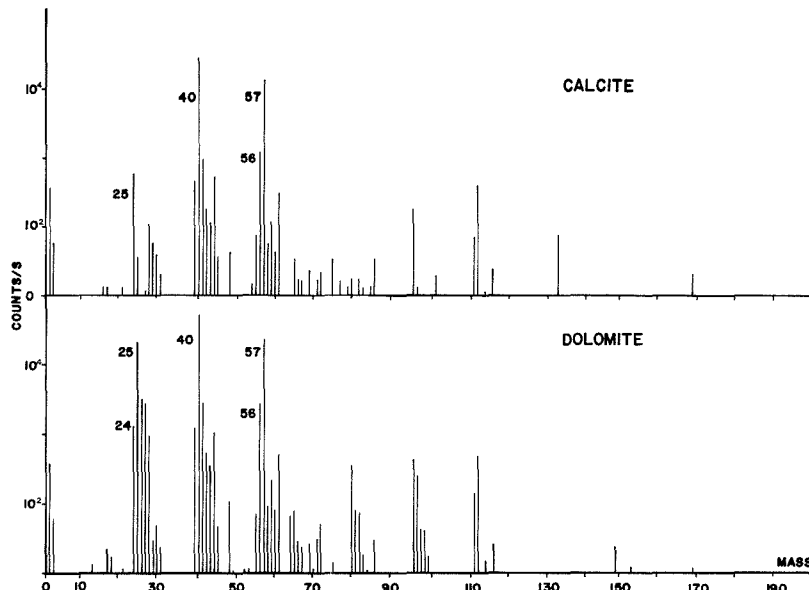


Figure 1. Mass spectra produced through the interaction of an oxygen beam with a calcite (A) and dolomite (B) sample. Major molecular and ionic species responsible for the major peaks have been tentatively identified. For identification of possible species at these masses, see Table I.

be considered practical for routine elemental analyses in carbonate materials at this time.

**Energy Filtering.** The final method, which has been utilized in this study, is that of energy filtering as used by Shimizu et al. (3), and first suggested by Herzog et al. (7). The energy-filtering technique can be employed on instruments in which the ion beams form a crossover of rays between the electrostatic and magnetic analyzers. Therefore, the Mattauch-Herzog design as used in the ARL and AEI probes operated by the University of Chicago and University of Cambridge and reported in the studies of Mason (1) and Veizer et al. (2) on carbonates cannot utilize this approach. This design is utilized in the Cameca IMS 3f used in this study. This method has been extensively used for the measurement of trace elements and isotopic ratios in silicates and sulfides (3, 4, 8, 9) but, as yet, not for carbonates.

The rationale behind this technique is that different interfering molecular species attain different ranges of kinetic energies during the sputtering process. Oxides ( $\text{CaO}^+$ ) and dimers ( $\text{Ca}_2^+$ ) tend to have a much narrower distribution of energies than free ions ( $\text{Ca}^+$ ), and therefore with an altered accelerating voltage (using a voltage offset), a segment of the energy spectrum can be examined, which contains proportionally less of these interfering species. The energy spectra of different free, molecular, and complex ions produced in a calcite matrix are shown in Figure 2. Notice in that in Figure 2b the intensity of the ion beam at mass 56 primarily resulting from  $^{40}\text{CaO}^+$  decreases much more rapidly than if the beam had been composed primarily of single ion such as  $^{56}\text{Fe}^+$ . Dimers such  $\text{Ca}_2^+$  show similar behavior, while hydrides  $^{40}\text{CaH}^+$  and doubly charged ions  $^{40}\text{Ca}^{2+}$  do not exhibit any significantly different behavior compared to metallic ions (Figure 2a). The energy-filtering approach can be tested by examining the isotopic composition of an element as measured with the ion microprobe and comparing it to its correct natural abundance. As interfering species are reduced, the correct natural abundance should be attained. Such measurements have been made on all elements of interest, and the results

are presented in the following section.

## EXPERIMENTAL SECTION

**Operating Conditions.** The appropriate instrumental conditions were determined by plotting the isotopic ratios of elements against voltage offset; the voltage offset enables ions with a range of kinetic energies to be examined. A voltage offset of  $-50$  V was able to virtually eliminate interferences for all elements with the exception of  $^{56}\text{Fe}$  (see later discussion). All analyses could therefore be completed at one location on the specimen within a relatively short period of time. For all samples, polished thin sections were prepared and coated with gold. Although only one sample could be mounted at a time, it was possible to prepare standards with several samples on one thin section. Comparisons could then be made between standards analyzed with and without letting the specimen chamber up to atmosphere. A primary ion beam of  $\text{O}^+$  ions was used with a net energy of 13.2 keV (sum of the primary and secondary ion beam potentials). The secondary ion beam was focused before each analysis to give a spot size of between 10 and 15  $\mu\text{m}$ , thereby giving a mass resolution of between 600 and 700 amu. If the beam was improperly focused, then it was possible to produce an ion beam with different energy characteristics. Consequently proper focusing of the beam was an essential prerequisite. After being focused, the beam was left for 15 min on the sample for count rates to stabilize. The stabilization time was determined by measuring intensities for masses 40 and 24 on the sample with respect to time. At the start of a sequence of analyses, each mass of interest was centered by the computer at  $-50$  V offset. Centering the peaks at 0 V frequently led to misidentification of the correct peak position. Counting times for each element varied according to its abundance, but did not exceed 30 s. After background correction, a sequence of five consecutive analyses were averaged and the standard deviations determined. The sample was then moved to a new position and the sequence started again.

Although several models have been proposed for obtaining concentration data from intensities of secondary ions (10-12), in this study an empirical approach has been used. In this technique intensities are taken relative to  $^{40}\text{Ca}^+$ , as variations in such ratios are relatively insensitive to surface conditions.

**Materials.** The carbonate materials used for standards were obtained from various sources. Three of the calcites (ISC, NCC,

Table II. Concentration of Trace Elements of Samples and Relative Intensities Measured in This Investigation

	Mg	Mn	Fe	Sr
LFC <sup>a</sup>	723 (128, 5)	434 (44, 6)	5062 (377, 6)	480 (59, 5)
ISC <sup>a</sup>	781 (90, 5)	724 (75, 6)	1006 (109, 6)	114 (24, 5)
NCC <sup>a</sup>	2617 (243, 6)	1404 (140, 7)	14659 (2016, 7)	909 (218, 6)
WC <sup>b</sup>	120429	432 (44, 4)	2865 (179, 4)	69 (25, 4)
WM <sup>b</sup>	118344	651 (15, 31)	3925 (378, 3)	76 (27, 3)
GMC <sup>c</sup>	920	524	336	201
TCC <sup>c</sup>	746	516	2478	897
HPD <sup>c</sup>	2059	12451	90	1983
M85 <sup>c</sup>	120104	2029	12476	297
D100057 <sup>c</sup>	119480 <sup>d</sup>	111	721	211
C36321 <sup>c</sup>	nm	777	105	188

<sup>a</sup> Analyses provided by A. E. Dickson (University of Cambridge), AMOCO (ICP, Dr. Fisher), and University of Miami (AA). <sup>b</sup> Analyses from this paper and AMOCO. <sup>c</sup> Analyses from this paper. Figures in parentheses refer to standard deviation and number of analyses. <sup>d</sup> Data for Mg from Jarosewich and Macintyre (13).

Table III. Relative Intensities of Ion Measured on Samples Listed in Table II, Measured in 1988

	24	std dev	55	std dev	54	std dev	88	std dev
LFC	8.2E-04	2.6E-04	2.3E-04	5.9E-05	7.9E-05	2.5E-05	4.2E-04	5.5E-05
ISC	8.4E-04	1.2E-04	2.8E-04	3.2E-05	1.7E-05	1.2E-05	1.3E-04	2.3E-05
NCC	3.5E-03	4.4E-04	7.3E-04	6.9E-05	2.7E-04	2.9E-05	8.4E-04	1.7E-04
WC	1.6E-01	7.6E-02	2.5E-04	3.1E-05	6.6E-05	8.9E-06	1.6E-04	3.7E-04
WM	2.7E-01	5.0E-03	4.2E-04	4.8E-05	6.5E-05	1.4E-05	1.0E-04	4.2E-05
GMC	1.0E-03	6.4E-04	2.6E-04	6.7E-05	1.0E-05	6.5E-06	2.0E-04	1.5E-04
TCC	7.8E-04	2.0E-04	2.3E-04	6.3E-05	5.5E-05	1.3E-05	8.7E-04	1.7E-04
HPD	1.6E-03	7.8E-04	5.6E-03	3.1E-03	7.9E-06	2.4E-06	2.3E-03	2.0E-03
M85	2.0E-01	5.9E-02	3.6E-03	3.6E-04	6.4E-04	5.0E-05	3.5E-04	1.3E-04
D 10057	3.3E-01	2.2E-02	4.5E-05	9.3E-05	2.8E-05	3.5E-06	4.4E-04	3.5E-05
C 36321	1.3E-04	5.8E-05	4.4E-04	7.3E-05	7.8E-06	2.2E-06	2.9E-04	1.6E-06

Table IV

## Variation in the Relative Intensity of Seven of the Standards Measured in January 1987

	24	std dev	55	std dev	54	std dev	88	std dev
LFC	1.0E-03	1.6E-04	1.7E-04	3.2E-05	8.8E-05	1.5E-05	3.8E-04	1.5E-04
ISC	9.1E-04	1.3E-04	2.7E-04	8.0E-05	2.2E-05	3.1E-06	1.3E-04	7.0E-05
NCC	3.0E-03	6.4E-04	6.2E-04	1.2E-04	2.1E-04	4.0E-04	8.2E-04	3.2E-04
WC	3.2E-01	2.3E-02	2.1E-04	7.6E-04	8.6E-05	4.3E-05	1.3E-04	1.5E-05
WM	3.7E-01	5.3E-02	3.3E-04	8.3E-05	7.6E-05	2.6E-05	9.1E-05	3.1E-05
D 10057	3.4E-01	1.39E-02	1.1E-04	3.1E-06	2.3E-05	9.0E-06	3.9E-04	1.2E-04
C 36321	2.2E-04	5.7E-05	4.9E-04	1.7E-05	2.4E-05	1.1E-05	2.4E-04	1.5E-05

## Variation in the Relative Intensity of Three Standards Measured in January 1986

	24	std dev	55	std dev	54	std dev	88	std dev
LFC	1.1E-03	3.3E-04	1.5E-04	2.5E-05	5.1E-05	1.4E-05	4.5E-04	2.1E-04
ISC	1.39E-03	5.4E-04	3.8E-04	8.0E-05	2.9E-05	9.8E-07	2.5E-04	1.2E-05
NCC	3.5E-03	3.8E-04	5.0E-04	1.0E-04	4.6E-04	6.4E-04	9.9E-04	1.8E-04

and LFC), provided by A. E. Dickson (University of Cambridge, U.K.), are identical with those reported by Mason (1). We have also included two other analyses on these samples, one measured by using atomic absorption (AA) techniques at the Rosenstiel School of Marine and Atmospheric Sciences, University of Miami, and the other by inductively coupled plasma (ICP) at AMOCO Research (Table II). In addition, six new samples, three calcites, HPD, LCC, and FCC, and three dolomites, WC, WM, and M85, as well as the Smithsonian calcite and dolomite standards, C136321 and D 10087, were analyzed (13). Wet chemical analyses on these eight samples were obtained from AMOCO and from our own analyses presented here (Table II).

Data presented in the following section consist of an average of 20 spots on each standard. Error bars represent  $\pm 1$  standard deviation. During the collection of data the standard deviation of an individual analysis can be estimated by the approximation  $1/\sqrt{n}$  \* mean ( $n$  = number of counts) (Table III). A best fit line was then calculated for each element and the standard error of the slope and constant determined. The equations are shown in Figures 5, 6, 9, and 11. In addition, data for five of the standards, NCC, ISC, LFC, WC, WM, C36321, and D10057, were obtained

over a period of two years and data for three standards, NCC, ISC, and LFC, were obtained over three years. These values are included in order to ascertain the reproducibility of the standards (Table IV).

In order to utilize our measurements to calculate concentrations of trace elements, an empirical approach was used in which the ratio of the mass of interest relative to calcium was correlated with the concentration of the trace element in the carbonate. Mass 40 was used as a reference mass, rather than mass 42, as in previous studies of carbonates (1, 2). These workers used mass 42 because the intensity of mass 40 under the instrumental conditions they used was too great and could possibly damage the collector. Although similar problems were found in this study at 0 voltage offset, intensities were sufficiently reduced at the offsets eventually used that no problems were encountered. Veizer et al. (2) also reported significant problems from interferences of  $^{28}\text{SiO}^+$  at mass 42 as result of silicate inclusions in their carbonates. No such problems were encountered in this study, both as a result of the apparent absence of such inclusions in our samples and also because the energy filtering method was able to reduce such interferences to an acceptable level (Figure 3).

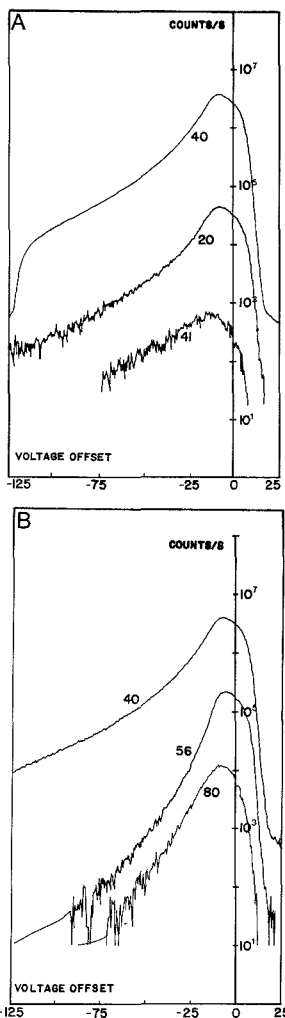


**Figure 2.** Energy spectra for various ionic and molecular species produced by the reaction of an  $O^-$  beam and a calcite sample. In part A masses 40 ( $^{40}\text{Ca}^{2+}$ ) and 41 ( $^{40}\text{CaH}^+$ ) are shown relative to mass  $^{40}\text{Ca}^+$ . These species show no differences in their energy spectra compared to  $^{40}\text{Ca}^+$ . In part B  $^{40}\text{Ca}_2^+$  and  $^{40}\text{Ca}^{16}\text{O}^+$  are shown relative to  $^{40}\text{Ca}^+$ . Note that at increased offset voltages the ratio of simple ionic species to more complex molecular species increases.

## RESULTS

**Calcium.** Although calcium is the most abundant element in all the samples analyzed, significant contributions from  $^{28}\text{Mg}^{16}\text{O}^+$  and  $^{24}\text{Mg}^{18}\text{O}^+$  to mass 42 are possible in Mg-rich samples such as dolomite. Additional interferences may result from  $^{12}\text{C}^{16}\text{O}_2^+$ ,  $^{40}\text{CaHH}^+$ , and  $^{42}\text{CaHH}^+$ . The presence of these interferences can be clearly seen in Figure 3. With an offset of  $-20$  V, the  $44/(40 + 42 + 44)$  and  $42/(40 + 42 + 44)$  ratios can be reduced to within one standard deviation of the natural abundance of these isotopes.

**Magnesium.** Magnesium has three stable isotopes, 24, 25, and 26, which have natural abundances of 78.99, 10.00, and 11.01%. The percentages of mass 25 and 26 are plotted in Figure 4 for a dolomite standard (M85) and a calcite (NCC)

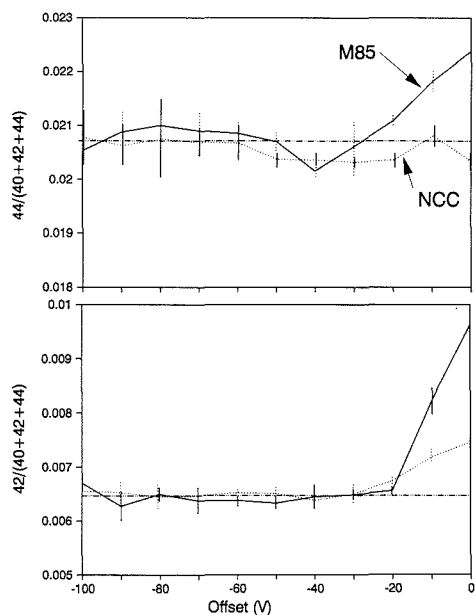


**Figure 3.** Change in mass  $44/(40 + 42 + 44)$  and  $42/(40 + 42 + 44)$  ratio with respect to increasing energy offset for a dolomite (M85) and a calcite (NCC). The horizontal line represents the natural abundance. Vertical bars are equal to 1 standard deviation.

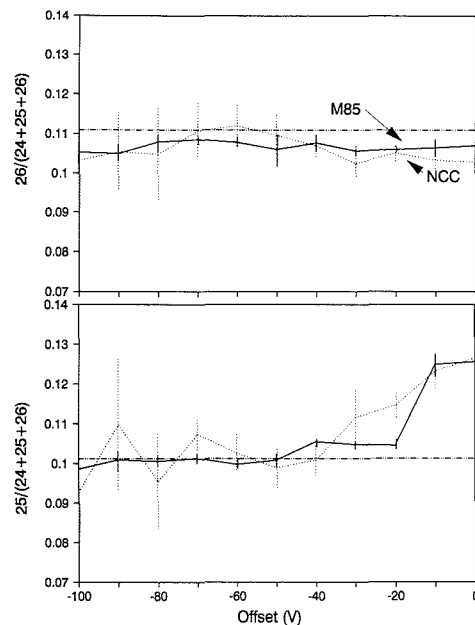


**Figure 4.** Change in the mass  $25/(24 + 25 + 26)$  and mass  $26/(24 + 25 + 26)$  ratio with respect to increasing energy offset for a dolomite and calcite sample as in Figure 4. The horizontal line represents natural abundance. Vertical bars are equal to 1 standard deviation.

as a function of voltage offset of the accelerating voltage. From these data it can be seen that at 0 voltage offset there is

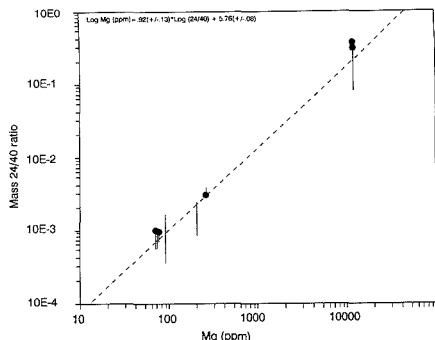


**Figure 5.** Calibration line between mass 24/40 ratio and concentration of magnesium in the bulk sample. The error bars represent  $\pm 1$  standard deviation. The values shown in brackets are one standard error. The solid circle markers represent analyses of standards during 1987. Data for these are shown in Table IIIa.

significant deviation from the correct isotope ratio. Such deviation takes the form of an excess of mass 25 and disappears with an offset of  $-50$  V. Although energy filtering is generally not effective at removing hydride interferences, in this case the most probable interference at mass 25 is  $^{24}\text{MgH}^+$ . Other possible interferences at these masses are listed in Table I.

The concentration of Mg ranged from 12.04% in the dolomites to 723 ppm in LFC. As a result of the large differences in Mg concentration between dolomite and calcite, the correlation line in the calcite samples has been extrapolated to the dolomites. Although these dolomites lie within error on this line (Figure 5), the dolomites generally gave inconsistent mass 24/40 ratios. At the present time results on Mg-rich samples such as dolomites do not appear to be consistent enough to allow small differences in Mg content to be determined.

**Manganese.** Manganese is monoisotopic and therefore it is impossible using this approach to determine the presence of interferences. Possible interferences are shown in Table I. In the study of Veizer et al. (2),  $^{43}\text{Ca}^{12}\text{C}^+$  was considered to be the most probable interfering ion, while Mason (1) suggested,  $^{28}\text{Mg}^{18}\text{O}^{12}\text{C}^+$  and  $^{26}\text{Mg}^{16}\text{O}^{13}\text{C}^+$ . Veizer et al. (2) suggested that  $^{43}\text{Ca}^{12}\text{C}^+$  would contribute approximately 1 ppm Mn. Mason (1) concluded that the effect for  $\text{MgOC}^+$  species was approximately 2 ppm per 1000 ppm Mg and therefore only important in dolomites. Considering that both of these studies (1, 2) were conducted at lower mass resolutions than this investigation and the finding in this study that significant interferences can be present even for the major elements, it is unlikely that quantitative concentration data can be obtained by using the approach of Veizer et al. (2) and Mason (1). Furthermore it is probable that major interferences not identified by these workers are also present. These include hydrides such as  $^{28}\text{Mg}^{16}\text{O}^{12}\text{CH}^+$  and  $^{42}\text{Ca}^{12}\text{CH}^+$ .

The concentrations of the standards used in this study range from 111 to 12476 ppm (Table II). With the exception of two samples of dolomite (M85 and HPD), all fall within one standard deviation of the best fit line (Figure 6). The line is approximately linear over 2 orders of magnitude and therefore can be extrapolated to concentrations of 10 ppm Mn, corresponding to a 55/40 ratio of  $1 \times 10^{-5}$ . The percent error estimated from counting statistics for the standard with the lowest concentration of Mn (111 ppm in D10057) is approximately 4%.

**Iron.** The spectrum of iron is dominated by  $^{40}\text{CaO}^+$  and  $^{40}\text{CaOH}^+$ . Even with a voltage offset of  $-90$  V, the isotopic

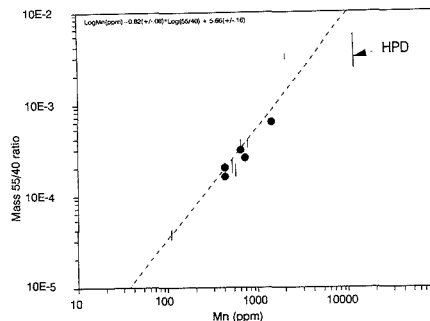


**Figure 6.** Calibration line for mass 55/40 and the concentration of Mn. The error bars represent  $\pm 1$  standard deviation. The values shown in parentheses are one standard error. The solid circular markers represent analyses of standards during 1987. Data for these are shown in Table IIIa.

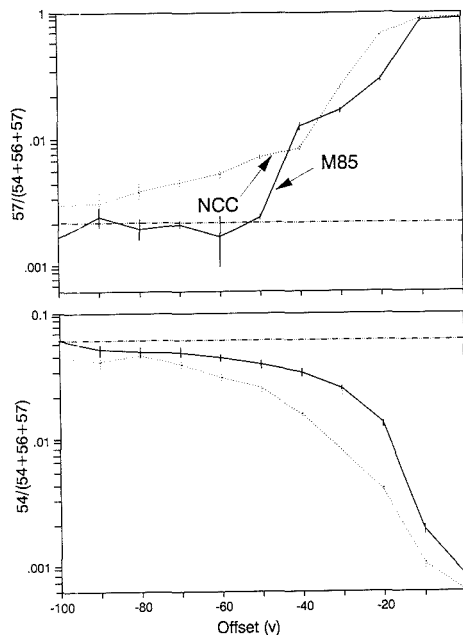


**Figure 7.** Mass 54/(54 + 56 + 57) and 57/(54 + 56 + 57) ratio with respect to energy offset; horizontal line represents the natural abundance. Vertical bars are equal to 1 standard deviation. Note that at  $-50$  V offset there is still a large difference between measured values and natural abundances.

ratios of Fe are outside one standard deviation of their natural value (Figure 7). However, even at these energy offsets, the intensity of the mass 56 peak exhibits a strong correlation with that of the mass 40 peak suggesting that unresolvable differences were still present. As a result of problems with these interferences in previous studies (1, 2), it was necessary to measure intensities at mass 54. This places a severe limitation of the detection of iron compared to other elements as  $^{54}\text{Fe}$  represents only 5.8% of the total abundance of Fe. Sensitivity is therefore reduced by between 10 and 20 times compared to Mn. In addition, the presence of high carbon backgrounds in some instruments may result in the production of species such as  $^{40}\text{Ca}^{12}\text{CH}_2^+$  interfering at mass 54, thereby further

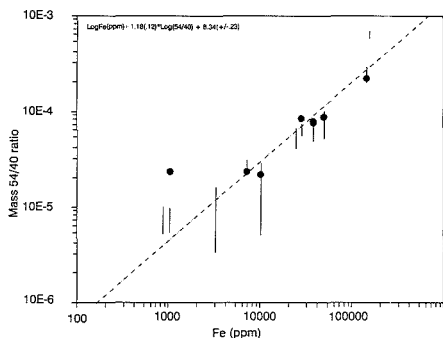


**Figure 8.** Calibration line between mass 54/40 ratio and the concentration of Fe in ppm measured in bulk samples. The error bars represent  $\pm 1$  standard deviation. The values shown in brackets are one standard error. The solid circular markers represent analyses of standards during 1987. Data for these are shown in Table IIIa.

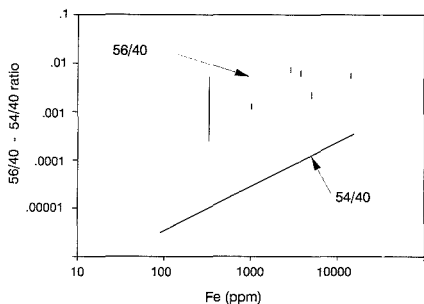


**Figure 9.** Relationship between mass 56/40 ratio and Fe concentration for six samples at  $-90$  V offset. The relationship between 54/40 and Fe concentration (Figure 8) is shown for comparison. Note the absence of significant correlation between the 56/40 ratio and Fe content.

reducing sensitivity for this element.

The concentrations of iron in the standards used in this study range from 90 to 14 500 ppm. The log of the 54/40 ratio plotted against the log of the iron concentration for all samples, with the exception of M85, falls close to one standard deviation from the best-fit line (Figure 8). However, the 56/40 ratio shows little relationship to the concentration of iron and is directly correlatable to the intensity of mass 40 (Figure 9). It is possible that with the use of greater voltage offsets correct 56/(54 + 56 + 57) isotopic ratio could be obtained; however, the use of large offsets reduces the intensity of the ion beam appreciably and therefore reduces the sensitivity and detection limits of other trace elements. The results therefore support the conclusions of Mason (1) and Veizer et al. (2) that since interferences at mass 56 cannot be easily resolved, mass 54 is the most suitable isotope for measuring concentrations of Fe. However, the standard deviation estimated from total counts is high in samples with low Fe concentrations. For example, in HPD the total number of counts used to calculate the mass 54/40 ratio is approximately 100, corresponding to an error of 10%.

**Sr**ontium. The principal interference at mass 83,  $^{44}\text{Ca}_2^+$ , can be removed with an energy offset of  $-20$  V (Figure 10). At offsets lower than this value, the 87/(86 + 87 + 88) and 88/(86 + 87 + 88) ratios of the two standards investigated remained constant within analytical error.

The strontium concentration of the samples investigated in this study ranged from 10 000 to approximately 100 ppm. The log of the mass 88/40 ratio plotted against the log of the

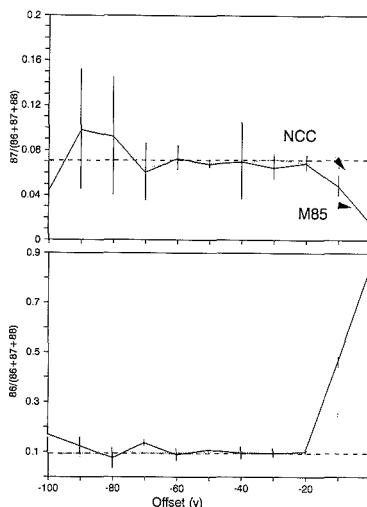


**Figure 10.** Change in mass 86/(86 + 87 + 88) and 87/(86 + 87 + 88) ratio with respect to increasing energy offset; horizontal line represents the natural abundance. Vertical bars are equal to 1 standard deviation.

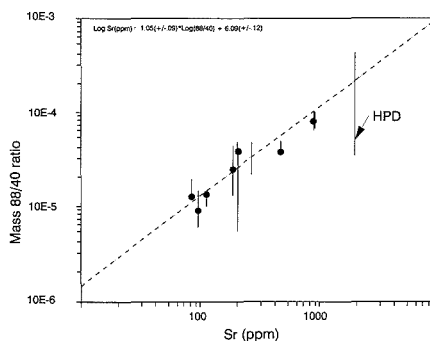


**Figure 11.** Calibration line between mass 88/40 ratio and the concentration of Sr in ppm measured in bulk samples. The error bars represent  $\pm 1$  standard deviation. The values shown in parentheses are one standard error. The solid circular markers represent analyses of standards during 1987. Data for these are shown in Table IV.

strontium concentration for all samples, including dolomites, plotted on a line with a slope of 1.05 ( $\pm 0.09$ ) and a correlation coefficient of +0.98 (Figure 11). This is in contrast to the results of Veizer et al. (2) who needed to establish separate calibration lines for Sr in calcite and dolomite. Although the lowest Sr standard used was 95 ppm, the linearity of the relationship from 10 000 to 100 ppm, enables the extrapolation to 88/40 ratios as low as  $10^{-6}$ , equivalent to a concentration of 1 ppm. The percent counting error on the sample with lowest Sr concentration (90 ppm, WC) is approximately 2%.

**Long-Term Reproducibility.** The majority of the data presented in this paper was collected during one session in January 1988. However, over the previous two years, data were collected under similar conditions for five of the standards finally analyzed. These data, shown in Table IV and in Figures 5, 6, 8, and 11, indicate that with the exception of Mg, similar analyses fall within one standard deviation of each other, suggesting that the slope of the relationships established can be utilized even if all standards were not

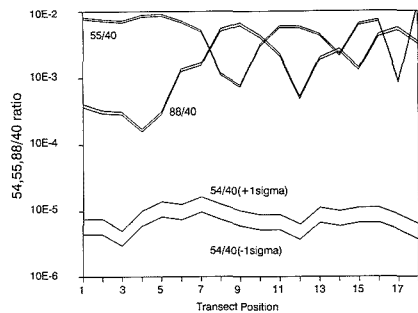


**Figure 12.** Results of 18 consecutive spot analyses across sample HPD. Each spot is approximately 20  $\mu\text{m}$  apart. The lines for each mass indicate the mean ratio plus and minus one standard deviation. The standard deviation has been estimated by using the expression  $1/\sqrt{n}$  mean. Hence for a total number of counts of 100, the standard deviation ( $\sigma$ ) is 10% of the mean. Note that for both masses 88 and 55, variations are significantly greater than can be explained by counting statistics. In the case of mass 54, a 10% variation is able to account for most of the observed variability.

analyzed at the same time as the samples.

### DISCUSSION

The data reported here represent the first attempt to apply the energy filtering approach to the quantification of the measurement of trace elements in carbonates, although there are many reports of using this technique in silicates (3, 4, 8, 9). Previous studies, which have attempted to use the ion microprobe for the analysis of trace elements (1, 2) in carbonates, used a spectral stripping method. Although these authors reported the analysis of trace elements at the parts-per-million level, the spectral stripping approach is still subject to a number of uncertainties. In particular at the mass resolutions of 500–600 amu (this study used higher mass resolutions) used previously (1, 2), this investigation has identified the existence of substantial interferences at all masses. Our approach has shown that using the energy filtering method, isotopic abundances can be measured that are statistically the same as natural occurrences. Important interferences can therefore be considered to have been eliminated and relative intensity ratios accurately measured. In addition, our studies on some of the samples indicate that even over periods as long as three years, similar ratios can be obtained on standards. Therefore, if instrumental conditions are similar, the relative ion beam intensities can be related directly to the relative intensities obtained in this investigation. The long-term reproducibility studies are in contrast to those reported by Veizer et al. (2) who showed significant differences between 88/42 ratios measured on separate occasions, differences that were greater than the standard deviation of the measurement.

The error involved in the calculation of any calibration between intensity ratios and concentration is dependent upon the compositional homogeneity of the standards analyzed. While there is no definitive way of ascertaining homogeneity before analysis, if sufficient analyses are made on a sample, a true mean intensity for the standard can be measured. Some of the standards analyzed in this investigation proved to be

heterogeneous for certain elements, ISC and GMC for Fe, HPD for Mn, and GMC and HPD for Sr. That the variation in trace element content is in fact true heterogeneity, and not a result of analytical uncertainty, can be verified by comparing the range of ratios with the standard deviation for each analysis estimated from counting statistics. For one of the standards that proved to be particularly heterogeneous (HPD), the ratios of 54/40, 55/40, and 88/40 have been plotted plus or minus one standard deviation. These data indicate that the change in ratios of 55/40 and 88/40 are all in excess of what might be expected from counting statistics (Figure 12). In contrast the 54/40 ratio exhibits a greater range of uncertainty as a result of the low count rate and its high standard deviation.

Certain of the other standards such as M85 deviated significantly from the best fit line for several elements. Such deviation is best explained in terms of analytical inaccuracy of the wet chemical data, even though repeated analyses produced similar results. An alternative explanation is that this sample was extremely heterogeneous for these elements. Contamination appears unlikely as according to the best fit line, the concentration of iron and manganese measured by wet chemical means was lower than that calculated by using the ion microprobe data. Typically bulk analyses produce higher concentrations as a consequence of the inability to remove small amounts oxides, clays, and other contaminants trapped between grains.

### ACKNOWLEDGMENT

Thanks are extended to S. Hart and N. Shimizu for use of the ion microprobe at MIT. Technical assistance was provided by V. Vahrenkamp and M. Guzikowski. Calcite standards (ISC, NCC, and LFC) were kindly provided by A. Dickson. J. Jarosevich of the Smithsonian Institute provided sufficient quantities of C36321 and D10057 to allow wet chemical determination of their Sr, Mn, and Fe concentrations. Additional analyses were provided by B. Fisher of AMOCO. S. Burns is thanked for making wet chemical analyses at RSMAS.

### LITERATURE CITED

- (1) Mason, R. A. *Chem. Geol.* **1987**, *64*, 209–224.
- (2) Veizer, J.; Hinten, R. W.; Clayton, R. N.; Lerman, A. *Chem. Geol.* **1987**, *64*, 225–237.
- (3) Shimizu, N.; Sarnet, M. P.; Allegre, C. J. *Geochim. Cosmochim. Acta* **1976**, *42*, 1312–1334.
- (4) Shimizu, N.; Hart, S. R. *Annu. Rev. Earth Planet. Sci.* **1982**, *10*, 483–526.
- (5) Steele, I. M.; Hutcheon, I. D.; Smith, S. V. *Geol. Soc. Am. Abstr. Programs* **1976**, *8*, 1119.
- (6) Hinten, R. W.; Long, J. V. P. *Earth Planet. Sci. Lett.* **1979**, *45*, 309–325.
- (7) Herzog, R. F. K.; Poschenrieder, W. P.; Satiwicz, F. G. *Radiat. Eff.* **1973**, *18*, 199–205.
- (8) Shimizu, N. *Phys. Chem Earth* **1975**, *9*, 655–669.
- (9) Shimizu, N. *Earth Planet. Sci. Lett.* **1978**, *39*, 398–406.
- (10) Anderson, C. A.; Hinthorne, J. R. *Anal. Chem.* **1973**, *45*, 1421–1438.
- (11) Anderson, C. A. *NBS Spec. Publ.* **1975**, No. 427, 79–119.
- (12) Simonds, D. S.; Baker, J. E.; Evans, C. A. *Anal. Chem.* **1976**, *48*, 134–1348.
- (13) Jarosevich, E.; Macintyre, I. G. *J. Sediment. Petrol.* **1983**, *53*, 677–678.

RECEIVED for review August 18, 1989. Revised manuscript received January 3, 1990. Accepted January 3, 1990. This research was supported by NSF Grants EAR 84-19359 and 86-07688 to P.K.S. Additional funding was supplied by Shell Research B.V.

# Multivariate Rule Building Expert System

Peter de B. Harrington\*<sup>1</sup> and Kent J. Voorhees

Department of Chemistry & Geochemistry, Colorado School of Mines, Golden, Colorado 80401

**A multivariate rule building expert system (MuRES) has been devised that acquires knowledge in the form of rules from training sets of multivariate analytical data. MuRES differs from conventional expert systems in that it generates rules that consist of a linear combination of all variables. MuRES advantageously combines the robust character of univariate expert systems and the feature transformation properties of linear classifiers. MuRES develops its own certainty factors and provides qualitative information regarding the classification. When evaluated with exemplary data, MuRES performed better than linear discriminant analysis, soft independent modeling of class analogy, and a univariate expert system.**

## INTRODUCTION

Expert systems are computer programs that use knowledge (expertise) regarding specific problem domains for inference. In the early 1980s, it was thought by many scientists that expert systems would have a profound influence in a broad range of applications. The unforeseen obstacle with expert systems was the difficulty of extracting knowledge from human experts and representing it in a logical and consistent format. This problem is often referred to as the knowledge acquisition bottleneck.

Expert systems usually structure knowledge in the form of a rule. Rule building expert systems avoid the knowledge acquisition bottleneck by acquiring their knowledge from training sets of data. At this moment, rule-building expert systems are more akin to pattern recognition methods than artificial intelligence methods. They differ from conventional expert systems in that they acquire empirical knowledge and they use algorithmic inference. Several chemical applications of these systems have been published (1-3). All of these expert systems are univariate in their approach.

Univariate expert systems derive rules that use only a single variable. These systems handle multivariate data by linking the rules which may use different variables together in the form of a tree. The problem with this approach is the variables are weakly associated.

Chemical data may contain a large degree of redundancy. The multivariate approach uses linear combinations of the variables. Linear transformation of the variables may reduce noise contained in the data under certain conditions. In addition, if the variables are redundant, optimizing one variable at a time will in most cases not produce the best result.

Other branching pattern recognition methods that use linear discriminants have been developed such as linear learning machines (LLM) and neural networks (NN) (4-7). Branching, multiple sequences of linear discriminants may accommodate nonlinearly separable data in the training set, as long as each branch performs a nonlinear operation on the data space. Typically, NNs operate on the variable space of the training data and LLM operate on the observation space.

A multivariate rule building expert system named MuRES has been devised for classifying mass spectra, but it may be

applied to any data consisting of more than one variable (8). From the context of rule building expert systems, MuRES is unique in that it uses feature transformation. From the broader perspective of pattern recognition, the novelty of MuRES is the use of information theory to build minimal spanning classification trees composed of LLMs.

MuRES calculate its own certainty factors and provides qualitative information regarding the decision processes. This system was evaluated by comparison to linear discriminant analysis (LDA) (9), soft independent modeling of class analogy (SIMCA) (10), and a previously developed univariate expert system (ES-1) (3) using a standard textbook problem set composed of chemical measurements of crude oil. MuRES was also compared with ES-1 and LDA for classifying polymer thin films by using their respective laser ionization mass spectra (LIMS).

## THEORY

Expert systems usually represent their knowledge in the form of rules. Rules are simple constructs that consist of an antecedent (the if clause of a rule) and a consequent (the then clause of a rule). Antecedents determine if a condition exists and consequents describe a course of action for a given condition. Most rule building systems develop rules whose antecedents only evaluate one variable at a time. Although rules that evaluate different variables may be linked together in a tree, these systems are univariate in their approach. From a geometrical perspective, univariate rules use decision planes that must be perpendicular to one of the axes of the coordinate system. A multivariate expert system's rules can have decision planes in any orientation.

Most rule building expert systems use the iterative dichotomizer three (ID3) algorithm which requires symbolic data (11, 12). A rule building expert system (ES-1) that transforms numerical data into symbolic data while maximizing the information content is described in ref 3. This previous system was univariate in its approach and was found to be a weak classifier, i.e., small perturbations in the training sets of data had deleteriously affected the classifier. For some cases, linear discriminant analysis had performed better than this expert system.

Multivariate analytical data often contains redundant information. Methods such as linear discriminant analysis that use feature transformation advantageously utilize redundancies in the data. MuRES was designed to combine the advantages of linear discriminant analysis with those of the univariate expert system. This system is included in the RESOLVE software; a mass spectral data analysis package developed at the Colorado School of Mines.

Because mass spectra often contain more than 100 variables, it is desirable to compress the spectra to produce an over-determined training set (13-15). The RESOLVE software compresses spectra by projection onto a set of principal components. This method of compression is utilitarian, because it reduces the number of variables while maximizing the information content. MuRES uses the mass spectral scores that are calculated by projecting the mass spectra onto a set of eigenvectors. However, MuRES may be applied without the compression step to data that already are over-determined.

<sup>1</sup>Present address: Clippinger Laboratories, Department of Chemistry, Ohio University, Athens, OH 45701-2979.

The knowledge base created by MuRES is in the form of simple binary rules whose antecedents are only true or false. A complex solution to a problem may be decomposed into a tree, often referred to as a classification tree, which consists of simple binary rules.

The conversion from numeric to symbolic representation is the essence of classification. Instead of representing a data object by one or more numbers, it may be represented by a symbol that designates the object's class association. Multivariate numeric data may be converted into symbolic data by projecting each observation onto a transformation vector  $T$ . This method is commonly used in pattern recognition and has been reviewed (16, 17). If a decision plane, which is defined by an orthogonal vector  $T$ , separates two classes in variable space, then each projection onto  $T$  will indicate a class by its value. If the decision plane contains the origin, the signs of the projections can be used instead of the values. Binary logic can be obtained by using the signs of the projections. Henceforth, all references to decision planes will assume that they contain the origin.

It may not be possible for a decision plane to pass between a class separation in  $v$ -dimensional space ( $v$  is the number of variables). Adding an extra variable of constant value to each observation, and thereby increasing the dimensionality of the space by one, will allow a decision plane to separate classes. This mathematical procedure is also used by least-squares regression methods to calculate the intercept of the regression line. Adding the additional variable introduces a degree of freedom which is realized as the translation (in  $v$ -dimensional space) of the origin with respect to the data set. MuRES uses this technique to obtain its transformation vectors. Other methods, such as discriminant analysis, require the origin to be fixed at the mean of the training set.

The attribute,  $a$ , is obtained by projecting the  $(v + 1)$ -dimensional observation onto the transformation vector  $T$ . The projection is accomplished by

$$a = \sum_{i=1}^{v+1} \mathbf{x}_i \times t_i \quad (1)$$

where  $\mathbf{x}_i$  is a vector component of observation  $X$ , which consists of  $v + 1$  variables, and  $t_i$  is a component of the transformation vector  $T$ .

Rule building expert systems typically use the ID3 algorithm, which requires symbolic data for construction of efficient classification trees (trees composed of a minimum number of rules). The ID3 algorithm incorporates Shannon's entropy and gives the optimal rule structure as defined by information theory. The above transformation converts the multivariate numeric data into symbolic data that is amenable to the ID3 algorithm. The algorithm finds rules that minimize the entropy of classification,  $H(C|A)$ .  $H(C|A)$  measures the uncertainty regarding a classification that exists after a rule is used and is given by

$$H(C|a_k) = - \sum_{j=1}^n p(c_j|a_k) \ln p(c_j|a_k) \quad (2)$$

$$H(C|A) = \sum_{k=1}^m p(a_k) H(C|a_k) \quad (3)$$

where  $H(C|a_k)$  is the entropy for a given attribute,  $a_k$ , that is obtained by summing the conditional probability of a class,  $c_j$ , occurring for  $a_k$ , over the number of classes  $n$ . The probability is obtained by counting the number of observations of class  $j$  and dividing that number by the total number of observations with attribute  $k$ .

Equation 3 is the sum of the entropies for each attribute weighted by the prior probability that the attribute occurs. The number of attributes,  $m$ , is equal to 2 (the attributes are

either positive or negative) and  $p(a_k)$  is the number of observations with a given attribute divided by the total number of observations.

A function optimization approach is used to find the transformation vector,  $T$ , that minimizes the entropy of classification  $H(C|A)$ . Optimization has been used to generate linear discriminants in previous studies which have been reported to be superior in performance to those obtained from the LLM method (18–20). A modified simplex was used for the classification results reported and is described in detail in ref 20. The simplex differs from the one cited in that it operates on the original  $v$ -dimensional data space and the  $v + 1$  component is determined from the algorithm to be given later.

Once a minimum  $H(C|A)$  is obtained, the distance is maximized between the two opposing closest projections on  $T$  (greatest negative point,  $a_L$ , and least positive point,  $a_G$ ). These projections are calculated by using the  $v$  components of  $T$ , so that the rules will not be biased by the value of the  $v + 1$  component and the distances of the data from the origin. Increasing the separation between  $a_L$  and  $a_G$  maximizes the selectivity of the rule and helps to define a unique decision plane. The effects of maximizing separation on classification performance have been described in detail for LLMs (21).

MuRES optimizes two parameters for the generation of each rule. The separation between closest points of opposite sign is maximized and the entropy of classification is minimized. The entropy parameter takes precedence over the separation parameter. In addition, only the  $v$  components are optimized by the simplex and the  $v + 1$  component of the transformation vector is obtained by the procedure described in the following two paragraphs.

The transformation vector of each rule is centered so that the zero point bisects the distance between  $a_G$  and  $a_L$ . This step further defines a unique decision plane and ensures that the rule is unbiased. The centering of the rule rotates the decision plane in the  $v + 1$  space and does not affect the qualitative information in the  $v$ -dimensional subspace. The centering procedure is given by

$$\bar{X} = (X_{aG} + X_{aL})/2 \quad (4)$$

$$k = \bar{X}^T T|_v \quad (5)$$

$$t_{v+1} = -k \quad (6)$$

where  $\bar{X}$  is the average calculated from the observations corresponding to the points  $a_L$  and  $a_G$ ,  $k$  is the inner product of  $\bar{X}$  and the transformation vector  $T$  over the  $v$  variables, and  $t_{v+1}$ , which is the component of the extra dimension, is equated to  $-k$  ( $k$  is the average value of  $a_G$  and  $a_L$ ). This procedure causes a zero value to be obtained when  $\bar{X}$  is projected onto  $T$ .

The optimization converges rapidly to a global optimum when all possible  $k$  values are examined for each simplex step. The projections are ordered by magnitude and the algorithm examines the  $k$  values that exist between each class change and selects the one that minimizes the entropy of classification and maximizes the rule separation.

Each rule partitions the data. The data are separated based on the sign of the projections on  $T$ . The algorithm is applied recursively to each partition until a zero entropy of classification is obtained. The recursive nature of the algorithm allows it to solve a nonlinearly separable problem by dividing it into several smaller linearly separable problems.

There exists an inherent problem with branching algorithms which partition data by observation. The number of observations that remain after partitioning may decrease so that the subsequent linear discriminants are no longer obtained from overdetermined data. This case occurs frequently when groups are overlapped.



Besides classification, an expert system should provide an indicator of the quality of its conclusion. Certainty factors are one such indicator and it is important for rule building expert systems to develop their own. For each rule, MuRES generates its certainty factors by eqs 7 and 8

$$\text{if } |a| > a_C \text{ then } \mu(a) = 1 \quad (7)$$

$$\text{if } |a| < a_C \text{ then } \mu(a) = |a|/a_C \quad (8)$$

where  $\mu(a)$  is a certainty factor,  $a$  is the projector of a data point onto a transformation vector, and  $a_C$  is the smallest positive projection of the training set onto a rule. These certainty factors are similar to those used by other expert systems.

The certainty factors linearly decrease from a value of unity when the absolute value of  $a$  is less than  $a_C$ . Values of unity indicate that the object being classified is consistent with the data used in the training set, while smaller values indicate that a projection has landed between  $a_L$  and  $a_C$  (i.e., in a region that was not spanned by the training set). If more than one rule is required for a classification, the minimum certainty factor is used. Values of unity do not mean the classification is correct, but indicate the unknown is consistent with the data used for training. The certainty factors may appear somewhat unselective. However, normalized data that are unique with respect to the training set will often project into the critical region (area between  $a_L$  and  $a_C$ ), as a result of maximized separation between classes.

In summary, MuRES selects the numeric feature transformation that produces symbolic attributes which give a minimum entropy of classification and maximum separation. The feature transformation used by MuRES attempts to remove ambiguity by finding the one decision plane that bisects the maximum separation between closest opposing points.

## EXPERIMENTAL SECTION

All calculations were performed on an IBM PS/2 Model 70 computer operating under MS-DOS 4.0 with the RESOLVE software package, a general purpose mass spectral data analysis system. The computer was equipped with a 25-MHz 80386 processor and a 25-MHz 80387 math coprocessor. Hardcopies of the graphs were obtained from screen dumps of the RESOLVE software to a Hewlett-Packard Laser Jet II printer.

The crude oil data were obtained from ref 9. The samples originated from sandstone in the Elk Hills, CA, petroleum reserve. These oils can be assigned to one of three stratigraphic units, Wilhelm sandstone (1), Sub-Mulina sandstone (2) and Upper sandstone (3). Each data observation contains five variables, vanadium (in percentage ash), iron (in percentage ash), beryllium (in percentage ash), saturated hydrocarbons (in percentage area), and aromatic hydrocarbons (in percentage area). The hydrocarbon values were obtained by gas chromatography. The computation time for MuRES rule development was approximately 10 min for the crude oil data.

The SIMCA results were obtained from single-component models for all three classes. Selecting the number of components to be used in the class models by cross validation, produced models that yielded inferior classification results to those of the single-component models.

The LIMS analyses were performed on the LIMA-2A laser microprobe instrument manufactured by Cambridge Mass Spectrometry, Ltd. (Cambridge, England). This instrument has been described in detail elsewhere (22) and is comprised of a focused, high-irradiance, quadrupled Nd:YAG laser system coupled to a time-of-flight mass spectrometer. The irradiance of the pulsed laser output can be varied from  $\sim 10^8$  to  $10^{12}$  W/cm<sup>2</sup> and the laser beam typically irradiates a 2–5  $\mu$ m diameter area on the sample surface. A complete mass spectrum is obtained for each irradiated volume by employing a transient waveform digitizer in the detection circuitry. The Sony-Tektronix 390 AD transient digitizer employed in these analyses was operated at a sampling frequency of 60 MHz. Its record length was 4096 channels which

permitted acquisition of mass spectra over a mass range from 1 to  $\sim 300$  amu.

Nylon 6 (1), nylon 12 (2), poly(1,4-butylene)terephthalate (3), polycarbonate (4) and polystyrene (5) samples were prepared by embedding beads of commercially available polymers in Spurr's epoxy resin (medium hardness) (6) and microforming 1  $\mu$ m thick sections. Three thin section samples were mounted onto high-purity silicon substrates. The poly(ethylene)terephthalate (Mylar 500D) (7) sample was provided in thin film form ( $\sim 0.5$  mm thick) and was analyzed without any sample preparation.

The LIMS irradiance corresponded to the threshold for ion detection and was typically 10 and 100 times this threshold value. The spectra presented in this paper were produced from high irradiance ( $\sim 10^{11}$  W/cm<sup>2</sup>) and positive ion analysis of the various polymers. The analytical craters produced at this irradiance were approximately 5  $\mu$ m in diameter, corresponding to a sampling volume of  $\sim 2.5$   $\mu$ m<sup>3</sup>.

Replicate spectra from 15 different sample locations were obtained for each polymeric thin film. The 105 spectra in the data set were normalized to unit vector length and then autoscaled. The spectra were compressed by eigenvector projection to produce abstract spectra composed of 30 scores, which accounted for 90% of the variance.

The terephthalate study used the first two principal components of the polymer data to identify the two terephthalate polymers. The first two factors accounted for 39% of the cumulative variance.

The epoxy investigated in this study consists of a few parts per hundred amine function of 4,4'-diaminodiphenyl sulfone (DDS), 80–90% by weight of tetraglycidyl 4,4'-diaminodiphenylmethane (TGDD) and 10–20% by weight of poly(glycidyl ether) of biphenol A Novolac epoxy. The epoxy spectra were collected under the same conditions as the polymer thin data, except the laser irradiance was lower ( $\sim 10^9$  W/cm<sup>2</sup>). The training set was composed of four groups each with 30 replicates of different resin (DDS) to hardener (TGDDM) ratios. The ratios and labels are (A) 0.2, B (0.75), C (1.0), and D (1.5). These data were normalized to unit vector length and then scaled by the average of the group mean deviations. The spectra transformed to abstract spectra consisting of 17 principal component scores which accounted for 75% of the cumulative variance. The evaluation epoxy had a resin to hardener ratio of 0.8 and was preprocessed and transformed under the identical conditions as the training set. Evaluation spectra were not used in the calculation of the scaling vector, the principal components, or any of the classification models.

All the classification techniques were applied to the principal component scores of the data. The training times for MuRES with the polymer and epoxy data sets were each less than 3 h.

## DISCUSSION OF RESULTS

The first set of experiments compares the ability of linear discriminant analysis (LDA), soft independent modeling of class analogies (SIMCA), a univariate expert system (ES-1), and MuRES for the classification of crude oil data. This data set was chosen because it is accessible, it is small, and of a chemical nature. The data were preprocessed by normalizing to unit length and scaling each variable by the average of the group standard deviations. Classifying these data is difficult, because the groups of crude oil are overlapped and contain outliers. See Figure 1 for a plot of the crude oil samples on the two discriminant functions obtained from LDA. This method of scaling is advantageous in comparison to autoscaling (23).

Internal validation is often referred to as the "leave one out procedure" or the jackknife method, which indicates the stability of a classification procedure with respect to each observation contained in the training set. Low internal validation values occur when a classifier fails to find generalities among the observations.

By use of internal validation the following classification accuracies were obtained: LDA, 66.1% (37/56); SIMCA, 83.9% (47/56); ES-1, 80.4% (45/46); MuRES, 89.3% (50/56). MuRES performed better than the other classification

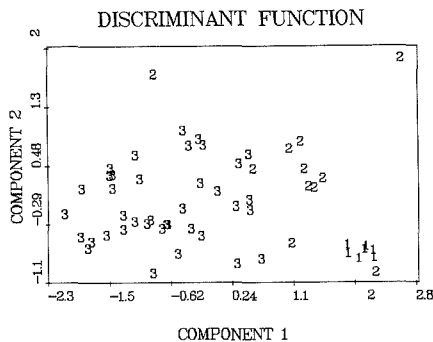


Figure 1. Plots the crude oil data on the two linear discriminant functions from LDA. See text for legend.

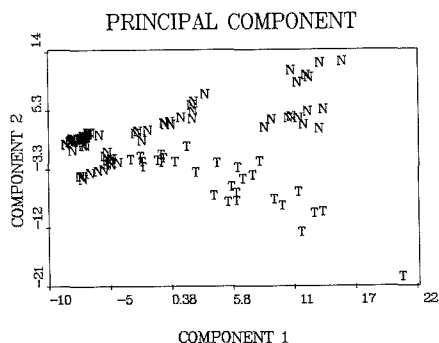


Figure 2. Plots the scores of the LIMS spectra on the first two principal components. The spectra was classified into terephthalate (T) or non-terephthalate (N) by these two scores.

methods. MuRES classification trees obtained from this data set often contained three or more rules. If the data set were linearly separable, classification trees would be obtained that contain two rules.

Classification trees obtained from randomly scattered data will contain an abundance of rules. Conversely, if class separations exist among the data, then the classification tree will contain a minimum number of rules. Extraneous rules will be obtained when the data are not linearly separable.

MuRES was also used for identifying laser ionization mass spectra (LIMS) from a set of polymer thin films. For the LIMS data, the SIMCA results were inferior and were not reported. It should be noted that SIMCA is a modeling method and does not perform well when discriminating among data with a small ratio of between group variance to within group variance. This study classified the polymer LIMS spectra on the basis of the presence of a terephthalate functional group. Only the scores on the first two principal components were used (Figure 2). This data set is two-dimensional and nonlinearly separable. The expert systems accommodate nonlinearly separable data. MuRES correctly classified the entire data set (105/105), ES-1 missed one observation (101/105), and discriminant analysis correctly classified 87/105.

MuRES was also used to identify the seven polymers in the LIMS data. The MuRES classification tree generated one less rule than ES-1 as shown in Figure 3. The MuRES tree contains the minimum number of rules that can be obtained for seven classes. The data are linearly separable by the rule transformations. However, MuRES transformations have one

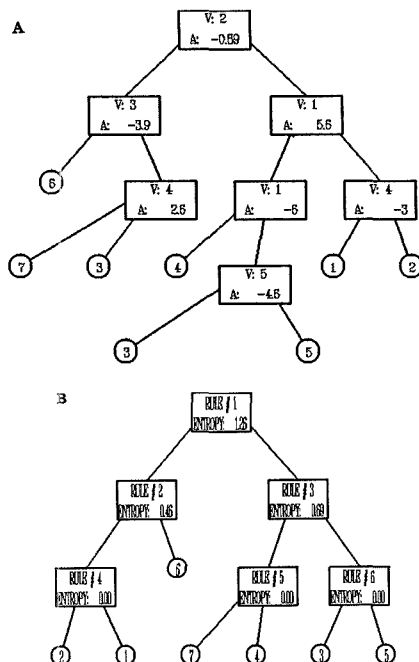


Figure 3. (A) ES-1 classification tree containing an additional rule (rectangles). A identifies the attribute used in the rule. The classification results are enclosed by circles. See text for legend. (B) MuRES classification tree containing six rules, which is the minimum number of rules possible for seven classes. See text for legend.

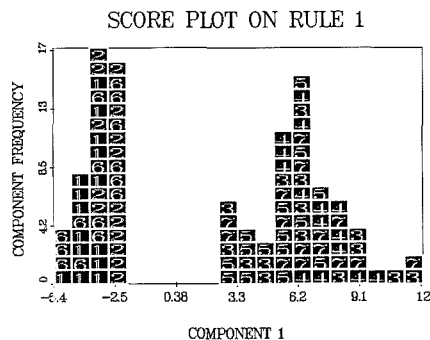


Figure 4. Histogram showing the separation produced by rule 1. Negative values move left down the tree and positive values move right.

more degree of freedom than other classifiers (e.g., discriminant functions), which do not allow the origin to be translated. The MuRES hierarchy of rules in the classification tree furnishes some chemical information (Figure 3B). Chemical information contained in spectral space is confounded by the efficient structuring of the classification tree. Other softer (less efficient) inductive algorithms have produced more meaningful tree structures (24).

MuRES was compared to ES-1 by using the cross validation procedure. ES-1 correctly classified 101/105 of the polymer spectra while MuRES correctly classified all of the spectra. Figure 4 is a histogram of the projections obtained from rule 1. Note that different classes are located on either side of the zero point and not both. Figure 5 shows the transformation

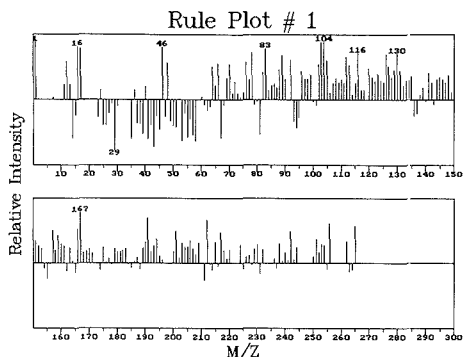


Figure 5. Rule structure containing positive and negative values.

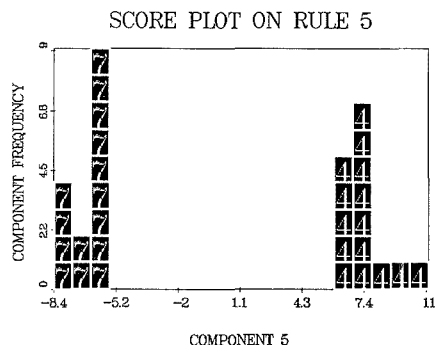


Figure 6. Histogram showing the separation produced by rule 4 between polycarbonate (4) and poly(ethylene)terephthalate (7).

vector of rule number 1. The rules contain qualitative information regarding the data separations. Negative intensities correspond to mass fragments that are discriminatory and common to LIMS spectra of nylon 6 (1), nylon 12 (2), and Spurr's epoxy (6). Similarly, the positive intensities are discriminatory for poly(1,4 butylene)terephthalate (3), polycarbonate (4), polystyrene (5) and poly(ethylene)terephthalate. Many of the positive peaks are characteristic of spectra from aromatic compounds, while many of the negative peaks are common to spectra of nitrogen-containing compounds.

Rule 5 separates polycarbonate spectra (4) from the poly(ethylene)terephthalate spectra (7). Figure 6 is a histogram of the projections on the transformation vector used by rule number 5. Figure 7B is the transformation vector of rule 5. The positive intensities of the transformation vector correspond to the discriminatory and common peaks of the set of polycarbonate (Figure 7A) and the negative features correspond to those of poly(ethylene)terephthalate (Figure 7C). Note both polycarbonate and poly(ethylene)terephthalate have peaks at mass 44, which is not surprising because both polymers contain oxygen. The transformation vector has a minuscule weight at this mass which is nondiscriminatory. Intensities at mass 42 are unique to poly(ethylene)terephthalate and given a large weight.

The final study compared MuRES with LDA to classify data not represented on the training set. Models were developed from a training set composed of 120 spectra obtained from four samples of epoxies with varying ratios of hardener to resin. A test set of 29 spectra were collected from an epoxy (P) whose physical properties (tensile strength and peak strain) differed but were most similar to those of epoxy (B). Therefore, assignment of the (P) epoxy formulation to group

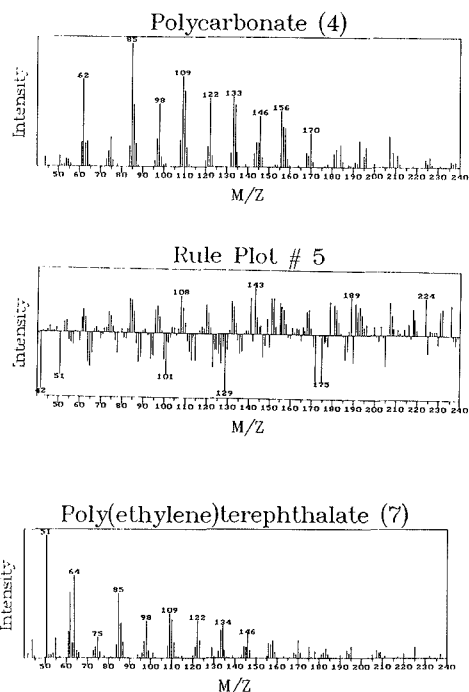


Figure 7. Positive peaks in rule 5 (B) corresponding to the discriminatory peaks of polycarbonate (A) and the negative peaks corresponding to those of poly(ethylene)terephthalate (C).

(B) was considered a correct assignment in this study. LDA correctly classified 28/29 and MuRES correctly classified 27/29 of the test spectra. Both classification methods missed the same spectrum, and the other spectrum that MuRES misclassified had the lowest certainty factor of all its class predictions. The groups of spectra did overlap and as a consequence the MuRES decision tree consisted of five rules instead of the minimum number of 3.

## CONCLUSION

MuRES provides an alternative to conventional rule building expert systems which rely on feature selection. By incorporating a multivariate approach, MuRES may develop more efficient and effective classification trees. Furthermore, the transformation vectors provide useful qualitative information. MuRES synergistically combines linear discriminants with the ID3 algorithm. Rule building expert systems are important, because they do not have a knowledge acquisition bottleneck. Provided with representative training sets, they may be able to develop customized expertise.

MuRES provides qualitative information regarding the problem domain, by both the hierarchy of rules in the classification tree and the relationship of the rule variables. MuRES is comparable to other methods of classification. Future research goals are the design of heuristic learning algorithms and the development of large adaptive knowledge bases (generalized expertise) from many diverse training sets of spectra.

The optimization process required by MuRES in rule development is the time-consuming step. Neural networks and parallel processing are two potential technologies that can be employed in decreasing the optimization time. Neural networks are similar to MuRES in that they use transformation

vectors and interconnections of rules (neurons). An expert system that develops a network of rules, instead of a tree, would resemble a neural network.

The knowledge acquired from present day expert systems applies to very specific problem domains and admittedly fits a very weak definition of knowledge. If rule-building expert systems develop rules mutually from several domains of data (e.g., spectra and structure), someday these systems may be considered intelligent. These algorithms may lay the foundation for future expert systems which could perform deep reasoning and acquire general knowledge.

#### LITERATURE CITED

- Schlieper, W. A.; Marshall, J. C.; Isenhour, T. L. *J. Chem. Inf. Comput. Sci.* **1988**, *28*, 159.
- Derde, M. P.; Buydens, L.; Gans, C.; Massart, D. L.; Hopke, P. K. *Anal. Chem.* **1987**, *59*, 1868.
- Harrington, P. B.; Voorhees, K. J.; Street, T. E.; di Brozolo, F. R.; Odom, R. W. *Anal. Chem.* **1989**, *61*, 715.
- Wasserman, Philip D. *Neural Computing Theory and Practice*; Van Nostrand Reinhold: New York, 1989.
- Jurs, P. C.; Kowalski, B. R.; Isenhour, T. L. *Anal. Chem.* **1969**, *41*, 21.
- Jurs, P. C.; Kowalski, B. R.; Isenhour, T. L.; Reilley, C. N. *Anal. Chem.* **1969**, *41*, 695.
- Jurs, P. C.; Isenhour, T. L. *Chemical Applications of Pattern Recognition*; Wiley: New York, 1975.
- Harrington, P. B.; Voorhees, K. J. Presented at the 1989 Pittsburgh Conference, Atlanta, GA, March 1988, 1528.
- Johnson, R. A.; Wichern, D. W. *Applied Multivariate Statistical Analysis*; Prentice-Hall, Inc: Englewood Cliffs, NJ, 1982; Chapter 10.
- Wold, S.; Sjostrom, M. In *Chemometrics: Theory and Application*; Kowalski, B. R., Ed.; American Chemical Society: Washington, DC, 1977; pp 242-282.
- Quilian, J. R. *Machine Learning: An Artificial Intelligence Approach*; Michalski, R. S., Carbonell, J. G., Mitchell, T. M., Eds.; Tioga Publishing Co.: Palo Alto, CA, 1983; p 463.
- Thompson, B.; Thompson, W. *Byte* **1986**, *11*, 149.
- Gray, N. A. B. *Anal. Chem.* **1976**, *48*, 2265.
- Jurs, P. C.; Stuper, A. J. *J. Chem. Inf. Comput. Sci.* **1976**, *16*, 238.
- Ritter, G. L.; Woodruff, H. B. *Anal. Chem.* **1977**, *49*, 2116.
- Gray, N. A. B. *Computer Assisted Structure Elucidation*; Wiley: New York, 1986; Chapter 5.
- Varmuza K. *Pattern Recognition in Chemistry*; Springer-Verlag: Berlin, 1980.
- Ritter, G. L.; Lowry, S. L.; Wilkins, C. L.; Isenhour, T. L. *Anal. Chem.* **1975**, *47*, 1951.
- Brunner, T. R.; Wilkins, C. L.; Lam, T. F.; Soltzberg, L. J.; Kaberline, S. L. *Anal. Chem.* **1976**, *48*, 1146.
- Katerline, S. L.; Wilkins, C. L. *Anal. Chim. Acta* **1978**, *103*, 417.
- Wangen, L. E.; Frew, N. M.; Isenhour, T. L. *Anal. Chem.* **1971**, *43*, 845.
- Dingle, T.; Griffiths, B. W.; Ruckman, J. C.; Evans, C. A., Jr. *Microbeam Analysis-1982*; Heinrich, K. F. J., Ed.; San Francisco Press: San Francisco, CA, 1982; p 365.
- Kvalheim, O. M. *Anal. Chim. Acta* **1985**, *177*, 71.
- Harrington, P. B. Presented at FACSS XVI, Chicago, IL, Oct 1989, 664.

RECEIVED for review June 27, 1989. Accepted December 12, 1989. Charles Evans and Associates acknowledge the support of NSF SBIR Grant No. ISI-8760431 for the LIMS analysis. Filippo Radicati di Brozolo and Robert W. Odom are thanked for collecting and supplying the LIMS polymer data.

## Indirect Conductometric Detection of Poly(oxyethylenes) after Chromatographic Separation

Tetsuo Okada

Faculty of Liberal Arts, Shizuoka University, Shizuoka 422, Japan

**Compounds with poly(oxyethylenes) (POE) separated on a K<sup>+</sup>-loaded cation-exchange resin are detected with indirect conductometry. The detection is based on a difference in mobility between bare K<sup>+</sup> and a POE-K<sup>+</sup> complex. The effects of K<sup>+</sup> concentration in mobile phases and the complexation ability of POE on peak size are quantitatively evaluated. On the basis of theoretical considerations, the quantification scheme, where one monodisperse POE is used as a standard material for determination of all oligomers detected, is also presented. This scheme is applied to POEs without chromophores, such as poly(ethylene glycols) and poly(oxyethylene) dodecyl ethers.**

#### INTRODUCTION

Conductometric detection has become more important and useful for high-performance liquid chromatography (HPLC) since the introduction of ion chromatography by Small et al. (1). This detection mode has been basically used for the analysis of ionizable compounds separated by ion-exchange (1), ion-exclusion (2), or ion-interaction mode (3), where a conductance change due to the elution of an analyte is related to ion equivalent conductance of the analyte and/or ions in a mobile phase. Conductometric detection is, thus, usually thought to be applicable only to ionic analyses. However,

utilizing the reaction of analytes and/or selecting appropriate mobile phases has made it possible to conductometrically detect some nonionic compounds.

Conductometric detection was first applied to the determination of nonionic compounds along with precolumn or postcolumn derivatization, where nonionic analytes were detected as the corresponding ionic counterparts. Aldehydes were, for example, conductometrically detected by oxidation to detectable forms, such as carboxylic acids (4) or sulfonate derivatives (5). Other conductometric detection schemes were based on changes in physical properties, such as dielectric constant or viscosity. The elution of a sample band was usually accompanied by changes in these physical properties and can be monitored as a conductometric change. Stevens et al. (6) showed indirect conductometric detection of water in organic solvents by using a methanolic mobile phase containing an acid. Tanaka and Fritz (7) also reported detection of nonionic compounds separated by ion-exclusion chromatography. Both studies were conducted along the same scenario. We reported different conductometric detection schemes, where complexation of carbohydrates with borate was utilized. Nonionic carbohydrates forming the ionic borate complexes (or enhancing the dissociation of boric acid by forming complexes) gave positive conductometric responses (8). Those forming neutral borate complexes (or not enhancing acidity of boric acid) were indirectly detected by use of an ionic carbohydrate-borate complex as a mobile phase additive (9).

Compounds containing poly(oxyethylenes) (POEs) as a part of the structure form metal complexes with some types of alkali, alkaline-earth, and transition metals (10). This complex formation is similar to that of a crown ether. The conductance of a salt solution decreases in the presence of PCEs, since POE-metal complexes have smaller mobility than the bare metal ion because of their larger sizes and higher microviscosity (11, 12). This nature of POE-metal complexes is applicable to the indirect conductometric detection of POEs if the appropriate separation mode can be employed. POEs have been usually separated on normal-phase columns with a nonpolar mobile phase such as hexane (13-15). Since most of salts are not dissociated in such a medium, the normal-phase separation is not apparently a suitable choice of the indirect conductometry. The author exploited the separation method of POEs on  $K^+$ -form cation-exchange resin with methanolic mobile phases and presented a retention model, which permitted to determine the formation constants of  $K^+$  complexes, to explain an effect of  $K^+$  concentration in mobile phases on the retention (16). In the present contribution, indirect conductometric detection of POEs and the quantification scheme are described with this separation technique.

### EXPERIMENTAL SECTION

The chromatographic system was composed of a Tosoh computer-controlled (Model pump CCPD), a column oven (Model CO-8000, Tosoh), a conductometric detector (Model CM-8000, Tosoh), a JASCO refractive index detector (Model 830-RI), and a Rheodyne injection valve equipped with a 100- $\mu$ L sample loop. A separation column was a TSK-gel IC-Cation-SW (4.6  $\times$  50 mm, packed with a silica-base cation-exchange resin with a particle size of 5  $\mu$ m, the ion-exchange capacity of which was 0.3 mequiv/g). Temperature was kept at 25  $^{\circ}$ C. The data acquisition system was composed of a Sanei dc amplifier, a Hioki digital voltmeter, which worked as an analog-digital converter, and an NEC personal computer, Model PC-9801 VX. The flow rate was maintained at 1 mL/min.

Poly(ethylene glycol) 400 (PEG 400) and poly(ethylene glycol) 1000 (PEG 1000) were purchased from Wako Chemicals. Poly-oxyethylated dodecyl alcohols (POE(*n*)D where *n* refers to the average number of oxyethylene units) were gifts from Nikko Chemicals. These POEs were used as received. Methanol of analytical reagent was distilled and stored with molecular sieves. Stored methanol was daily distilled again before the experiment. Acetone and dioxane were also of analytical grade. Water was deionized and distilled. Potassium iodide, which was selected because it was soluble in methanol relatively well and the ion-pair formation iodide with  $K^+$  or POE- $K^+$  was regarded as negligible in methanol (11), was dried under vacuum at 110  $^{\circ}$ C and stored in a desiccator.

### RESULTS AND DISCUSSION

**Detection of POEs.** HPLC separation of POEs without chromophores has been usually followed by refractometric detection (17). To improve the sensitivity and selectivity, some detection methods such as field desorption mass spectrometry (18), evaporative light scattering (13), moving wire-flame ionization (14), rotating disk-flame ionization (15), etc., have been developed. Although methods that allow us to use common detectors such as a UV or a conductometric detector should be introduced, such investigation has been few except for the use of precolumn derivatization (19). The author showed that POEs could be separated on a  $K^+$ -form cation-exchanger with methanolic mobile phases on the basis of the complexation of POEs with  $K^+$  bound on a cation-exchange resin (16). In this separation mode,  $K^+$  in mobile phases modified the retention of POEs and simultaneously permitted the indirect conductometric detection of POEs.

Figures 1 and 2 show examples of the indirect conductometric detection of oligomers contained in PEG 400 and POE(9)D, which were separated with 0.4 mM KI in methanol as a mobile phase. Peaks were detected as negative changes

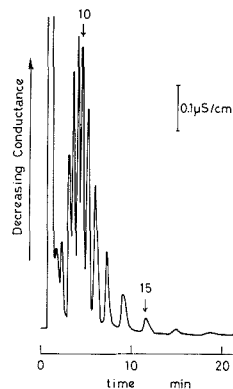


**Figure 1.** Separation of PEG 400 with indirect conductometric detection: mobile phase, 0.4 mM KI in methanol; sample concentration, 0.5 mg/mL. Other conditions are given in the text.

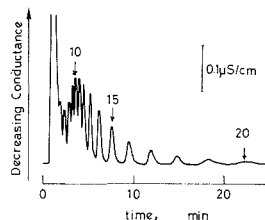


**Figure 2.** Separation of POE(9)D with indirect conductometric detection: mobile phase, 0.4 mM KI in methanol; sample concentration, 0.5 mg/mL. Other conditions are given in the text.

in conductance. As previously indicated (16, 20), five or six repeating oxyethylene (OE) units were needed for complexation with  $K^+$  bound on a cation-exchanger and thus POEs with four or less OE units were not retained on the stationary phase because of their low complexation ability. The elution order correlates with increasing the number of repeating OE units and the complexation ability.

**Effect of Complexation Ability on Peak Sizes.**  $K^+$  in a mobile phase reduced the retention of POEs by stabilizing  $K^+$ -POE complexes in the mobile phase. The effect of  $K^+$  in the mobile phase on retention can be evaluated by the following equation as reported previously, when multiple complexation (e.g. POE: $K^+$  = 1:2 or 2:1) can be ignored (16)

$$1/k' = 1/k_0'(1 + K_f C_{KI}) \quad (1)$$

where  $k_0'$  is the capacity factor obtained with a mobile phase not containing  $K^+$ ,  $K_f$  is the formation constant of a POE- $K^+$  complex, and  $C_{KI}$  is the concentration of KI in a mobile phase. This equation shows that a formation constant can be calculated from a linear plot of  $1/k'$  vs  $C_{KI}$ .

Intensity of the indirect conductometric responses is also related to the complexation ability of a POE. The following reaction occurs in a mobile phase



where P and  $PK^+$  represent a POE and its  $K^+$  complex. In most indirect detection methods, system peaks, which originate in the elution of a deficiency zone of detectable eluent components, are often observed (21). In the present case, no system peaks were observed as can be seen in Figures 1 and 2. This indicates that  $PK^+$  and  $K^+$  deficiency zones resulting from  $PK^+$  complex formation flow down the column at an identical rate. This can be explained by the fast reaction rate

of complexation reaction (eq 2) in mobile phases in comparison with that of the retention reaction. In this case, PK<sup>+</sup> and K<sup>+</sup> deficiency zones are not separated and eluted at the same time. Thus, K<sup>+</sup> concentration in effluents is kept constant. When a sample band of a monodisperse POE isolated on the column comes to a conductance cell, a change in conductance ( $\Delta_s$ , in millisiemens) can be given by

$$\Delta_s = \lambda_{PK}[PK^+] - \lambda_K[PK^+] \quad (3)$$

where  $\lambda_{PK}$  and  $\lambda_K$  represent limiting ion equivalent conductance of PK<sup>+</sup> and K<sup>+</sup>, respectively, and it was assumed that  $\lambda_{PK}$  and  $\lambda_K$  are independent of the K<sup>+</sup> and PK<sup>+</sup> concentrations. Substitution of  $[PK^+] = [P][K^+]K_f$ , where [P] and [K<sup>+</sup>] are the concentrations of POE and K<sup>+</sup> in the sample band, yields

$$\Delta_s = (\lambda_{PK} - \lambda_K)[P][K^+]K_f \quad (4)$$

If  $[K^+] \gg [P]$ ,  $[K^+]$  can be substituted by  $C_{KI}$

$$\Delta_s = (\lambda_{PK} - \lambda_K)[P]C_{KI}K_f \quad (5)$$

This equation shows that responses, which are negative because of the smaller ion limiting equivalent conductance of complexes than that of bare K<sup>+</sup>, will linearly increase with the POE concentration and  $C_{KI}$ . Actually, a linear relation was found between peak areas and  $C_{KI}$ . Equation 6 shows the relation between the peak area (A, in arbitrary units) of PEG(13) and  $C_{KI}$  (in millimoles per liter)

$$A = 120C_{KI} + 4.57(r = 1.00, \text{ for } C_{KI} = 0.2\text{--}0.6 \text{ mM}) \quad (6)$$

Although, according to eq 5 the intercept of eq 6 should be zero, eq 6 has a nonzero intercept. This is due to the fact that the effect of the concentration or ionic atmosphere on the ion equivalent conductance was ignored for simplicity for derivation of eq 5. Generally, this effect more strongly influences the conductance change in lower permittivity media. The relation between peak areas and  $C_{KI}$  is linear within a narrow range of  $C_{KI}$ , but may be described by a convex curve for wider  $C_{KI}$  range.

Another fact of importance is that we cannot optimize the condition for the detection independently of that for the separation. Large peaks, which do not necessarily mean good sensitivity because base-line noise also increases, can be easily obtained with the high concentration of a K<sup>+</sup> salt. However, this procedure must be accompanied by reduction of retention. The best sensitivity was obtained with 0.4–0.5 mM KI.

Detection limits of this method were 3–4 times as low as that of RI detection. Main components of PEG 400 were detectable at a 5  $\mu\text{g}/\text{mL}$  sample concentration.

**Reduction of Analytical Time.** Increasing complexation ability with the number of OE units suggests that very long analytical time is necessary to analyze samples containing POEs with a large number of OE units under isocratic conditions. From the practical point of view, an effort should be done to reduce the analytical time. The retention was strongly affected by various properties of a mobile phase, i.e., the dielectric constant, the donor strength of solvents toward K<sup>+</sup>, the concentration of K<sup>+</sup>, etc. Mobile phase additives brought about changes in these properties and influenced the complexation occurring both at the surface of the stationary phase and in a mobile phase. As mentioned above, it is obvious that the addition of K<sup>+</sup> brings about high background conductance, and thus the concentration that can be used to reduce the analytical time is limited.

Binary mixtures of solvents effectively modified the retention of POEs. In the previous study, the author investigated the effect of solvent on the retention of POEs and found the retention to be decreased in the order of ethanol > methanol > acetonitrile > acetone = dioxane = water (16). It was indicated that water interrupted the complexation both

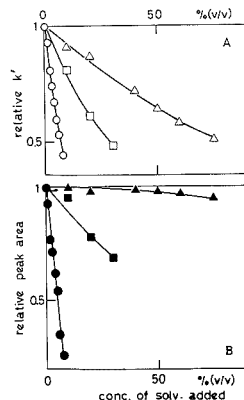


Figure 3. Decreases in the relative retention (A) and the relative peak area (B) of PEG(13) with concentration of a solvent added in the 0.4 mM KI methanolic mobile phase: circle, water; square, dioxane; triangle, acetone.

Table I. Formation Constants of PEG-K<sup>+</sup> Complexes in Methanol and 1/1 Acetone-Methanol

$n^a$	$K_f$ ( $\sigma^b$ ), M <sup>-1</sup>	
	methanol	acetone-methanol
6	219 (10)	227 (15)
7	487 (29)	433 (25)
8	579 (12)	527 (30)
9	884 (17)	639 (36)
10	1050 (33)	790 (43)
11	1200 (37)	928 (51)
12	1590 (65)	1130 (64)
13	1960 (98)	1370 (82)
14	2230 (170)	1550 (105)
15	2530 (198)	1680 (96)

<sup>a</sup> Number of repeating oxyethylens. <sup>b</sup> Standard deviation.

in solutions and on the surface of stationary phase because of the high solvation strength, but ion-pair formation between K<sup>+</sup> and sulfonic groups in the cation-exchanger principally interfered with the complexation on the surface of the stationary phase in low-permittivity media such as acetone and dioxane.

Figure 3 shows effects of the addition of water, acetone, and dioxane on both the retention and the peak area of PEG(13). Water most effectively reduced the retention (8% water content was needed to reduce the retention to half the value obtained with pure methanol, whereas 75% acetone or 25% dioxane was required to similarly reduce the retention), but simultaneously induced a marked decrease in sensitivity. On the other hand, acetone did not diminish the sensitivity. This indicates that, as inferred above, the complexation on the resin surface is more strongly interrupted in the presence of acetone than that in the mobile phase. To quantitatively evaluate these results, the complex formation constants in 1/1 acetone-methanol were determined according to eq 1 and compared with values in pure methanol. Formation constants for PEG in both media are listed in Table I together with standard deviations. Generally, a  $K_f$  value in pure methanol is 1.4 times as large as that in acetone-methanol solution. Thus, acetone is thought to be an unfavorable solvent for POE-K<sup>+</sup> complexation in comparison with methanol. However, indirect conductometric sensitivity is determined by the product of  $(\lambda_K - \lambda_{PK})$  and  $K_f$  values as shown in eq 5. In the acetone-methanol media, the large former value compensates for a

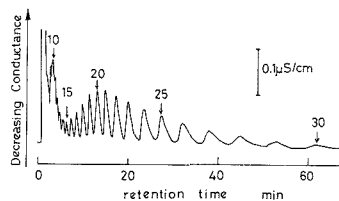


Figure 4. Separation of PEG 1000: mobile phase, 0.4 mM KI in 25/75 methanol-acetone; sample concentration, 0.5 mg/mL.

decrease in peak area due to low  $K_f$  value.

Among these three solvents tested, acetone was apparently the best choice to reduce retention without causing poor sensitivity. The only disadvantage of acetone-mixed methanolic mobile phases was to cause slightly higher background conductance (conductance of 0.4 mM KI solution increased from 42  $\mu\text{S}/\text{cm}$  for the purely methanolic solution to 50  $\mu\text{S}/\text{cm}$  for the 60% acetone-methanol solution). This is explained by a larger equivalent conductance of KI in acetone than in methanol. We did not determine the equivalent conductance in an acetone-methanol mixture but can infer the larger equivalent conductance than in pure methanol from the lower viscosity of acetone and constancy of Walden product. Figure 4 shows the oligomer separation of PEG 1000 with 0.4 mM KI in 25/75 methanol-acetone as a mobile phase. We can, thus, effectively control the retention by adding acetone in a mobile phase.

Gradient elution schemes are usually efficient for polymer analysis. However, gradient was not applicable to the present detection because changes in the solution properties necessarily cause a change in conductance. Therefore, to successfully employ the present detection, we must determine first the concentration of  $\text{K}^+$  in the mobile phase by considering the sensitivity and then select the acetone content to tailor the elution range to that for POEs of interest.

A  $\text{Ca}^{2+}$ -loaded column did not, for example, retain POEs at all (16). The retention time of POEs could be reduced by replacing a part of  $\text{K}^+$  in the stationary phase with  $\text{Ca}^{2+}$ . However, a decrease in the  $\text{K}^+$  concentration in the stationary phase caused a significant decrease in the capacity; overload easily occurred. Hence, the usefulness of a partly  $\text{Ca}^{2+}$ -loaded column was limited.

**Quantification of POE.** Standard materials of monodisperse PEG or POE( $n$ )D are not commercially available except for some short oligomers with less than eight OE units. Selective syntheses of POEs with more OE units are also difficult. However, in the present case, making an assumption and utilizing eq 5 permitted the calculation of the concentration of each oligomer. For quantification, it should be assumed that the mobility (or ion equivalent conductance) of a POE- $\text{K}^+$  complex is not different from that of another complex with a different POE length. This assumption will be invalid for a pair of POEs with much different POE length, but will be reasonable for POEs with the narrow distribution range. Burger-Guerrisi and Tondre (12) reported a conductometric study on the interaction of salts with POE and calculated equivalent conductance of KI-POE complexes ( $\Lambda_c$ ). They found  $\Lambda_c$  of PEG 10000-KI, POE[4]D-KI, POE[6]D-KI, and POE[8]D-KI to be 62.1, 66.2, 73.5, and 73.2  $\text{S cm}^2 \text{mol}^{-1}$ , respectively, where numbers in brackets refer to repeating OE units of monodisperse POEs. It is strange that POE[4]D-KI showed smaller  $\Lambda_c$  than POE[6]D-KI and POE[8]D-KI in spite of its smaller size. We cannot know the accuracy of their values, but can conclude that the difference in  $\Lambda_c$  is not large. If this assumption can be applicable to the present case,  $\lambda_{\text{PK}} - \lambda_{\text{K}}$  can be canceled by dividing the peak area of an oligomer

Table II. Data for the Quantification of Oligomers in PEG 400<sup>a</sup>

$n^b$	rel peak area	concn ratio	concn, mM
6 <sup>c</sup>	1	1	0.53
7	3.16	1.42	0.76
8	5.65	2.14	1.13
9	6.90	1.71	0.91
10	7.40	1.54	0.82
11	6.24	1.14	0.60
12	4.36	0.60	0.32
13	2.69	0.30	0.16
14	1.51	0.15	0.08
15	0.67	0.06	0.03

<sup>a</sup>Sample concentration was 0.5 mg/mL. <sup>b</sup>Number of repeating oxyethylens. <sup>c</sup>Standard compound.

Table III. Data for the Quantification of Oligomers in POE(9)D<sup>a</sup>

$n^b$	$K_f, \text{M}^{-1}$	$\sigma^c$	rel peak area	concn ratio	concn, $10^{-5} \text{M}$
7	381	9	0.75	1.30	9.9
8 <sup>d</sup>	660	8	1.4	1	7.6
9	848	36	1.34	1.04	7.9
10	1050	23	1.62	1.02	7.8
11	1280	36	1.81	0.93	7.1
12	1490	44	1.79	0.79	6.0
13	1860	86	1.5	0.62	4.7
1j	2080	139	1.70	0.54	4.1
15	2160	53	1.55	0.47	3.6
16	2270	94	1.26	0.37	2.8

<sup>a</sup>Sample concentration was 0.5 mg/mL. <sup>b</sup>Number of repeating oxyethylens. <sup>c</sup>Standard deviation. <sup>d</sup>Standard compound.

(A) by that of another oligomer (B). A ratio of peaks can be represented by the following equation

$$\Lambda_A/\Lambda_B = [P]_A K_{fA}/[P]_B K_{fB} \quad (7)$$

Formation constants ( $K_{fA}$  and  $K_{fB}$ ) can be calculated on the basis of eq 1, and the ratio of the concentration of oligomers can thus be calculated. Since at least one monodisperse oligomer is available for both PEG and POE( $n$ )D series, the concentration of each oligomer can be determined by using an available standard material. Tables II and III show results of the determination of oligomers contained in 0.5 mg/mL sample solutions of PEG 400 and POE(9)D, respectively. Both analyses were carried out in purely methanolic mobile phases. PEG[6] and POE[8]D were selected as standards for corresponding oligomer mixtures.  $K_f$  values for the PEG series are listed in Table I and those for the POE( $n$ )D series are listed in Table III together with analytical results. Since  $K_f$  values generally included ca. 5% relative errors, the concentrations listed in tables involve more ambiguity.

#### ACKNOWLEDGMENT

I thank Tosoh Co. for the courteous gift of separation columns.

Registry No. POE, 25322-68-3; POEnD, 9002-92-0.

#### LITERATURE CITED

- (1) Small, H.; Stevens, T. S.; Bauman, W. C. *Anal. Chem.* **1975**, *47*, 1801-1809.
- (2) Okada, T. *Anal. Chem.* **1988**, *60*, 2116-2119.
- (3) Iskandarani, Z.; Pietrzyk, D. J. *Anal. Chem.* **1982**, *54*, 2427-2431.
- (4) Lorrain, J.; Fortune, C. R.; Dellinger, B. *Anal. Chem.* **1981**, *53*, 1302-1305.
- (5) Val, D. L. D.; Rogers, M.; Fritz, J. S. *Anal. Chem.* **1985**, *57*, 1583-1586.
- (6) Stevens, T. S.; Chritz, K. M.; Small, H. *Anal. Chem.* **1987**, *59*, 1716-1720.
- (7) Tanaka, K.; Fritz, J. S. *J. Chromatogr.* **1987**, *409*, 271-279.
- (8) Okada, T.; Kuwamoto, T. *Anal. Chem.* **1986**, *58*, 1375-1379.

- (9) Okada, T. *Anal. Chem.* **1988**, *60*, 1336-1340.  
 (10) Cross, J. *Nonionic Surfactants*, Dekker: New York, 1987.  
 (11) Ono, K.; Konami, H.; Murakami, K. J. *Phys. Chem.* **1979**, *83*, 2665-2669.  
 (12) Burger-Guerrisi, C.; Tondre, C. J. *Colloid Interface Sci.* **1987**, *116*, 100-108.  
 (13) Bear, G. R. J. *Chromatogr.* **1988**, *459*, 91-107.  
 (14) Nakamura, J.; Matsumoto, I. *Nippon Kagaku Kaishi* **1975**, 1342-1347.  
 (15) McClure, J. D. J. *Am. Oil Chem. Soc.* **1982**, *59*, 364-373.  
 (16) Okada, T. *Anal. Chem.* **1990**, *62*, 327-331.  
 (17) Kudoh, M. J. *Chromatogr.* **1984**, *291*, 327-330.  
 (18) Otsuki, A.; Shiraiishi, H. *Anal. Chem.* **1979**, *51*, 2329-2332.  
 (19) Kudch, M.; Ozawa, H.; Fudano, S.; Tsuji, K. J. *Chromatogr.* **1984**, *287*, 337-344.  
 (20) Yansigida, S.; Takahashi, K.; Okahara, M. *Bull. Chem. Soc. Jpn.* **1977**, *50*, 1386-1390.  
 (21) Rigas, P. G.; Peitzyk, D. J. *Anal. Chem.* **1987**, *59*, 1388-1393.

RECEIVED for review September 1, 1989. Accepted December 18, 1989. This work was partly supported by Grant-in-Aid for Scientific Research (Grant No. 01740333) from the Ministry of Education Science and Culture, Japan.

## Design of a Calcium-Selective Optode Membrane Based on Neutral Ionophores

Werner E. Morf, Kurt Seiler, Bruno Rusterholz, and Wilhelm Simon\*

Swiss Federal Institute of Technology (ETH), Department of Organic Chemistry, Universitätstrasse 16, CH-8092 Zürich, Switzerland

A large variety of new optical ion-sensor constructions (optodes) can now be realized by using a poly(vinyl chloride) (PVC) membrane that incorporates a cation-selective neutral ionophore, a specially tailored  $H^+$ -selective neutral chromoionophore, and lipophilic anionic sites in the same plasticized PVC membrane. Such membranes generally combine the advantages of a highly selective and reversible recognition of given ionic substrates and of a straightforward optical transduction of the recognition process. The present membrane exhibits the theoretically expected absorbance response to  $Ca^{2+}$  activities in different pH-buffered samples. Dynamic range, reproducibility, response time, long-time stability, and selectivity of the new optode membrane are discussed.

### INTRODUCTION

The development of sensors with an optical transduction of the chemical recognition process (optical sensors; optodes (1)) has become a highly relevant and rapidly expanding area in analytical chemistry (1-26). These optical sensing devices are based on absorption, reflection, fluorescence, or chemiluminescence measurements, and they commonly make use of chemical compounds that drastically change their optical properties as the result of the actual recognition process. With only few exceptions, immobilized indicator dyes, especially fluorogenic substances, have so far been applied as the active materials. Very often, optical fibers are employed for focusing the incident light onto the corresponding sensing area of the probe and for guiding it back to the detector, but this is not required for fundamental studies of the presented type of membranes (26).

Recently, we reported on the design features (15), the morphological aspects (16), and the theoretical description (17) of a new class of optodes which are based on conventional, electrically neutral ionophores. These highly selective compounds have been widely applied in membranes of a large variety of ion-selective electrodes (for a review, see refs 27-34). For the preparation of optical sensing layers, such neutral carriers for cations or anions can be combined in the same bulk membrane phase with a second sort of highly selective neutral ionophores, so-called chromoionophores (18, 35) which

dramatically change their absorption spectrum in the UV-vis region upon complexation of the corresponding ionic species. The well-proved poly(vinyl chloride) (PVC) membrane technology can basically be adopted for these new optode systems, which is in clear contrast to some earlier approaches (10, 22-24).

Formally, two functional principles are possible for the present optical sensing devices (15-17): (I) a carrier-induced coextraction of cations and anions from the sample into the membrane phase, or (II) a carrier-induced exchange of cations or of anions between sample and membrane. In the first case the absorbance response depends under ideal conditions on the product of the respective ion activities in the sample solution, while in the second case the response is controlled by the corresponding ratio of ion activities.

Here, we report on the development of a novel optode membrane belonging to the group of neutral-ionophore-based cation exchangers. The present system was realized by combining a conventional  $Ca^{2+}$ -selective carrier (ETH 1001 (27)) and a newly prepared  $H^+$ -selective chromoionophore (ETH 5294; this work) together with lipophilic anionic sites in the same plasticized PVC membrane phase. A similar optical sensor utilizing the  $NH_4^+$ -selective carrier antibiotics nonactin/monactin was described previously (18). Membrane-coated glass plates instead of optical fibers were used for the present fundamental studies.

### EXPERIMENTAL SECTION

**Reagents.** Aqueous solutions were prepared with doubly quartz-distilled water and salts of the highest purity available.

For membrane preparation, ETH 1001 ( $Ca^{2+}$  ionophore), poly(vinyl chloride) (PVC; high molecular), potassium tetrakis(4-chlorophenyl)borate (KTPClPB), sodium tetrakis[3,5-bis(trifluoromethyl)phenyl]borate ( $NaTm(CF_3)_2PB$ ), bis(2-ethylhexyl)sebacate (DOS), and tetrahydrofuran (THF) were obtained from Fluka AG (Buchs, Switzerland).

For the synthesis of ETH 5294 ( $H^+$  chromoionophore), Nile Blue A chloride was obtained from Sigma Chemie GmbH (Deisenhofen, FRG) and stearoyl chloride (pract.) and ethyl acetate from Fluka AG (Buchs, Switzerland).

**Synthesis of 1,2-Benzo-7-(diethylamino)-3-(octadecanoylimino)phenoxazine (ETH 5294).** A suspension of 1 g (2.8 mmol) of Nile Blue A chloride in 100 mL of water was stirred at 65 °C for 30 min. After the addition of 100 mL of 0.5 M NaOH, the resulting red precipitate was extracted three times with 100



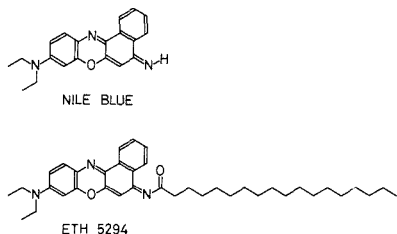


**Figure 1.** Constitutions of the basic (deprotonated) form of Nile Blue and of the new lipophilic isologue, the chromoionophore ETH 5294.

mL of  $\text{CH}_2\text{Cl}_2$ . The organic phase was filtered and the solvent evaporated to yield 510 mg (1.6 mmol) of the basic form of Nile Blue (see Figure 1).

To a solution of 317 mg (1 mmol) of basic Nile Blue in 13 mL of  $\text{CH}_2\text{Cl}_2$ , 242 mg (0.8 mmol) of freshly distilled stearoyl chloride dissolved in 2 mL of  $\text{CH}_2\text{Cl}_2$  was added. After being stirred at room temperature for 15 min, the reaction mixture was diluted with 50 mL of  $\text{CH}_2\text{Cl}_2$  and then washed with 50 mL of 0.1 M NaOH. The organic phase was filtered, the solvent evaporated, and the residue purified by flash chromatography (silica gel, ethyl acetate) and by recrystallization from ethyl acetate to yield 370 mg (0.63 mmol, 79.2%) of ETH 5294 (Figure 1).

The constitution of ETH 5294 was confirmed by  $^1\text{H}$  NMR (300 MHz,  $\text{CDCl}_3$ ), IR ( $\text{CHCl}_3$ ), fast atom bombardment mass spectrometry (FAB-MS), and UV-vis spectra (see below). Elemental analysis: Calcd for  $\text{C}_{36}\text{H}_{53}\text{N}_3\text{O}_2$  (583.9): C, 78.17; H, 9.15; N, 7.20. Found: C, 77.92; H, 9.35; N, 7.05.

**Membrane Preparation.** The optode membranes were prepared from a batch of 20 mg of ETH 1001, 5.5 mg of ETH 5294, 11.2 mg of the additive  $\text{NaTm}(\text{CF}_3)_2\text{PB}$  (to create lipophilic anionic sites), 143 mg of the plasticizer DOS, and 70 mg of PVC.

The membrane components were dissolved in 2 mL of freshly distilled THF. A 0.2-mL portion of this solution was injected onto a rotating, dust-free glass plate of 35-mm diameter (Herasil quartz glass, W. Möller AG, Zürich, Switzerland), which was located in a THF-saturated atmosphere. A hand-made spinning device (19) with a closed aluminium/Plexiglas cell was used (rotating frequency, 600 rpm). This allows the preparation of glass-supported membranes having controlled and highly reproducible thicknesses in the range between 0.5 and 7  $\mu\text{m}$  (19). After a spinning time of only about 4 s, the glass support with the optical sensing membrane was removed and stored at air for some minutes for further drying.

**Apparatus.** UV-vis absorbance measurements and spectra of the PVC membranes were taken with a flow-through cell (see Figure 2) (19) in a UVIKON Model 810 double-beam spectrophotometer (Kontron AG, Zürich).

The ion-selective electrodes were connected to FET operational amplifiers OPA 128 KM (Burr-Brown, Tucson, AZ). The analog signals were converted into digital ones with a Digital Multimeter Type 7150 (Solartron Schlumberger Instruments, Farnborough, UK). For the remote control, data storage, and handling, a personal computer, Apple IIe, was used with a GPIB IEEE 488 interface and an extended RAM memory (Apple Computer, Inc., Cupertino, CA), a real-time clock (Thunderware, Inc., Oakland, CA), a Model RX 80 matrix printer (Epson Corp., Nagano, Japan), and a graphic plotter, Color Pro 7440 (Hewlett-Packard, San Diego, CA), managed by a high-level language program (UCSD Pascal 1.3) written for this use. The pH values were determined with a pH glass electrode (Orion Ross Model 8103) and a Model SA 720 Orion pH meter (Orion Research AG, Küssnacht, Switzerland).

**Experimental Procedure. Absorption Experiments.** Two glass plates with identical membranes of about 2.5  $\mu\text{m}$  thickness were mounted into the measuring cell of the flow-through system. The reference cell of the spectrophotometer contained two glass plates without membranes. The solutions of the measuring and the reference cell were changed from outside of the spectrophotometer. All measurements were made in the transmittance mode (see Figure 2).

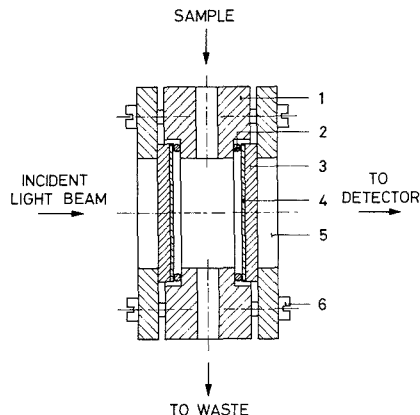


**Figure 2.** Schematic representation of the flow-through cell used for the present studies on optode membranes: (1) polypropylene support with sample inlet and outlet; (2) O-seal ring; (3) quartz glass support; (4) ion-sensing optode membrane; (5) Plexiglas cell wall; (6) screw for fixation.

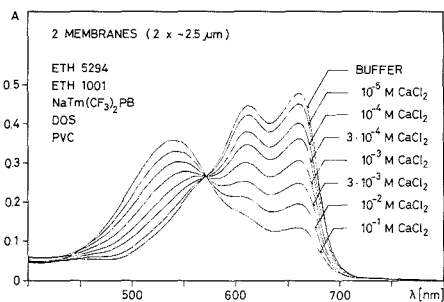


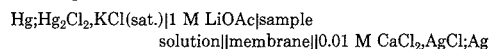
**Figure 3.** Absorption spectra of two 2.5  $\mu\text{m}$  thick optode membranes after equilibration with pH-buffered solutions (acetate buffer, pH 5.3) containing different concentrations of  $\text{CaCl}_2$ . The deprotonated form of ETH 5294 shows an absorbance maximum at a wavelength of 545 nm and the protonated forms at 614 and 660 nm, respectively.

The buffer solutions used for the characterization of the optode membrane were (a) a citrate buffer ( $10^{-3}$  M citric acid, adjusted with 0.1 M NaOH to a pH of 6.5), (b) an acetate buffer of pH 5.3 (0.163 M sodium acetate adjusted with 1 M acetic acid), (c) an acetate buffer of pH 5.9 (0.190 M sodium acetate adjusted with 1 M acetic acid), and (d) a Tris buffer of pH 7.1 (0.005 M tris(hydroxymethyl)aminomethane adjusted with 0.5 M  $\text{H}_2\text{SO}_4$ ).

Selectivity factors according to the separate solution method were determined by using 0.5 and 0.05 M solutions of the corresponding chloride salts in a citrate buffer (pH 6.5). For the determination of the  $\text{Mg}^{2+}$  selectivity factor a 0.1 M  $\text{MgCl}_2$ /Tris buffer solution (pH 7.1) was used as an additional sample. The selectivity coefficients were evaluated by comparing the response functions at  $\alpha = 0.5$  (see eqs 6 and 7).

Except for the recordings of the full absorption spectra given in Figure 3, the absorbance measurements were made at a fixed wavelength of 660 nm. Absorbance readings for reproducibility studies were taken 1 min after sample change.

**emf Measurements.** The membrane preparation and measuring technique of the emf measurements are described in detail elsewhere (33). All measurements were carried out on cells of the following type:



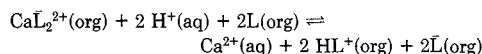
The membrane composition of the calcium ion selective electrode used consisted of 3.4 wt % ETH 1001, 2.0 wt %  $\text{KTPClPB}$ , 31.2

wt % poly(vinyl chloride), and 63.4 wt % DOS.

## RESULTS AND DISCUSSION

It was the primary aim to realize analytically useful optical sensors that are based on plasticized PVC membranes containing electrically neutral ion carriers of high selectivity. To this end, the H<sup>+</sup>-selective chromoionophore ETH 5294 shown in Figure 1 was synthesized. This proton carrier is a lipophilic isologue of the highly basic oxazine-dye molecule Nile Blue (see Figure 1). The native compound usually exists in the protonated, singly charged form in aqueous solutions at pH values below about 10 (36). The high basicity of the corresponding neutral chromoionophore ETH 5294 (L) is required in view of an adequate competition between the mediated H<sup>+</sup>-ion uptake and the complexation of the other primary ion M<sup>z+</sup> (here Ca<sup>2+</sup>) by the second neutral carrier (here ETH 1001 ( $\bar{L}$ )) of the optode membrane system.

Such a membrane is expected to favor the following ion-exchange reaction between the aqueous sample solution (aq) and the organic membrane phase (org), assuming a 1:2 ion/ligand complex for Ca<sup>2+</sup> and ETH 1001 (27)



The corresponding equilibrium constant  $K_{\text{exch}}$  depends on the stability constants  $\beta$  of the ionophore complexes and on the ionic distribution coefficients  $k$  (17)

$$K_{\text{exch}} = \frac{(a_{\text{Ca}^{2+}})[\text{HL}^+]^2[\bar{L}]^2}{[\text{Ca}\bar{L}_2^{2+}](a_{\text{H}^+})^2[\bar{L}]^2} = \frac{(\beta_{\text{HL}^+}k_{\text{H}^+})^2}{(\beta_{\text{Ca}\bar{L}_2^{2+}}k_{\text{Ca}^{2+}})} \quad (1)$$

where the activities  $a_i$  of species  $i$  refer to the aqueous solution and the concentrations  $[i]$  to the membrane which is assumed to behave as an ideal phase.

With  $[R^-]$  as the net concentration of negative sites in the membrane, the electroneutrality condition leads to the following concentration relationship:

$$[\text{HL}^+] + 2[\text{Ca}\bar{L}_2^{2+}] = [R^-] \quad (2)$$

If the concentration ratios of uncomplexed relative to total ionophore present in the membrane phase are denoted by  $\alpha$  and  $\alpha'$ , respectively, one can substitute

$$[\text{L}] = \alpha L_T; [\text{HL}^+] = (1 - \alpha)L_T \quad (3a, b)$$

$$[\bar{L}] = \alpha' \bar{L}_T; 2[\text{Ca}\bar{L}_2^{2+}] = (1 - \alpha')\bar{L}_T \quad (4a, b)$$

where  $L_T$  and  $\bar{L}_T$  are the respective total concentrations in the optode membrane.

The absorbance  $A$  of this system obviously is related to the fraction  $\alpha$  of the uncomplexed species  $L$

$$A = A_1\alpha + A_0(1 - \alpha) \quad (5)$$

$$\alpha = (A - A_0)/(A_1 - A_0) \quad (5a)$$

where  $A_1$  and  $A_0$  are the limiting absorbance values for  $\alpha = 1$  and  $\alpha = 0$ , respectively.

Equations 1-3 and  $R_T$  as the total net concentration of negative sites are used for deriving the final response function

$$\frac{(\alpha/2)\{R_T - (1 - \alpha)L_T\}}{[1 - \alpha]^2[\bar{L}_T - \{R_T - (1 - \alpha)L_T\}]^2} = \frac{1}{K_{\text{exch}}} \frac{(a_{\text{Ca}^{2+}})}{(a_{\text{H}^+})^2} \quad (6)$$

As was shown previously (15-18, 26) in a more general description this highly selective optical membrane exhibits an absorbance response that depends on the ratio of sample activities for the two ionic species involved.

It is evident from eq 6 that, even when ideally selective ionophores could be applied in the present optode membranes, an optical determination of Ca<sup>2+</sup> activities becomes possible

**Table I. Selectivity Coefficients  $K_{\text{Ca}^{2+}, \text{N}^{z+}}^{\text{opt}}$  of the Ca<sup>2+</sup>-Selective Optode Membrane for Interfering Ions N<sup>z+</sup> in Comparison with Corresponding Potentiometric Selectivities  $K_{\text{Ca}^{2+}, \text{N}^{z+}}^{\text{pot}}$  Using the Separate Solution Method (SSM) Approach**

ion N <sup>z+</sup>	log $K_{\text{Ca}^{2+}, \text{N}^{z+}}^{\text{opt}}$ (optode, this work)	log $K_{\text{Ca}^{2+}, \text{N}^{z+}}^{\text{pot}}$ (electrode, ref 27)
K <sup>+</sup>	-3.8	-3.9
Na <sup>+</sup>	-3.6	-3.5
Li <sup>+</sup>	-3.1	
Mg <sup>2+</sup>	-4.1	-5.5

only if the pH value of the sample is either measured simultaneously (e.g. by means of a pH-sensitive optode) or adjusted by an appropriate buffer solution. Correspondingly, as in the case of ion-selective electrode measurements, the determined activities depend on nonthermodynamic assumptions, conventions, or standardization procedures involved in the establishment of ion activity values for calibration and buffer solutions.

When interfering cations (N<sup>z+</sup> and J<sup>z+</sup>) compete with the primary ions for the complexation of the corresponding ionophores, the activities in eq 6 have to be replaced by sums of selectivity weighted activities (17, 18)

$$\text{LHS [eq 6]} = \frac{1}{K_{\text{exch}}} \frac{[a_{\text{Ca}^{2+}} + \sum_{\text{N}} K_{\text{Ca}^{2+}, \text{N}^{z+}}^{\text{opt}} a_{\text{N}^{z+}}^2/k_{\text{N}^{z+}}]}{[a_{\text{H}^+} + \sum_{\text{J}} K_{\text{H}^+, \text{J}^{z+}}^{\text{opt}} a_{\text{J}^{z+}}]^{1/z^+}} \quad (7)$$

This semiempirical extension of eq 6 is in analogy to the terms arising in the Nicolsky-Eisenman equation for ion-selective electrode potentials (27-34). The selectivity factors of the present optode membrane ( $K_{\text{Ca}^{2+}, \text{N}^{z+}}^{\text{opt}}$ ), separate solution method (SSM) are presented in Table I in comparison with the corresponding selectivities of a Ca<sup>2+</sup>-selective electrode ( $K_{\text{Ca}^{2+}, \text{N}^{z+}}^{\text{pot}}$ ) based on the same ionophore. The agreement is convincing, except for the optical Mg<sup>2+</sup> measurement, which is apparently affected by a Tris buffer interference. In contrast to a previously described optode membrane (18) which formally exhibited a response to ammonia, the present system is not expected to be sensitive to electrically neutral, ionogenic species.

Figure 3 shows the absorption spectra in the visible range, as obtained for the present Ca<sup>2+</sup>-selective optode membrane after equilibration with pH-buffering solutions containing different concentrations of CaCl<sub>2</sub>. Evidently, the maximum change in absorbance with varying sample concentration is observed at a wavelength of 660 nm.

In Figure 4 the absorbance values measured at 660 nm are given as a function of log ( $a_{\text{Ca}^{2+}}/a_{\text{H}^+}$ ). The hydrogen ion activities were measured with a pH glass electrode. The Ca<sup>2+</sup> ion activities in Figure 4a were determined with a Ca<sup>2+</sup>-selective electrode based on the ionophore ETH 1001. The calibration curves of the optode membrane show no significant differences between two buffer systems of different pH values and different ionic strengths  $I$  (citrate buffer pH = 6.5,  $I = 0.0087$ ; acetate buffer pH = 5.3,  $I = 0.163$ ). In Figure 4b, which exhibits the absorbance values measured in the presence of a constant sodium acetate background, the Ca<sup>2+</sup> activities were calculated by using a Debye-Hückel formalism (37). Curve II was calculated according to eq 6 using 7.1 for log  $K_{\text{exch}}$ , whereas the calculation of curve I is based on eq 7, taking the Na<sup>+</sup> interference (log  $K_{\text{Ca}^{2+}, \text{Na}^+}^{\text{opt}} = -3.6$ ; fixed interference method (FIM)) into account.

Apparently, the new chromoionophore ETH 5294 does not fulfil the basicity requirements for a sufficiently strong competition with the highly selective Ca<sup>2+</sup> ionophore at a physiological pH. This is in contrast to the previously described

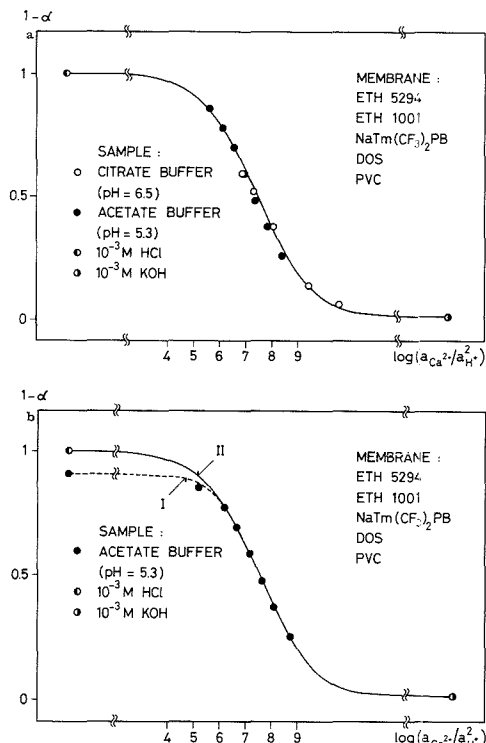


**Figure 4.** (a) Absorbance values at 660 nm of the optode membrane as a function of  $\log(a_{Ca^{2+}}/a_{H^+}^2)$  in two different buffer systems (citrate buffer, pH 6.5; acetate buffer, pH 5.3). The ion activities were derived from measurements with a  $Ca^{2+}$ -selective electrode and a pH glass electrode, respectively. The curve fitting the experimental points was calculated from eqs 5 and 6 by using  $\log K_{exch} = 7.1$ . (b) Absorbance values at 660 nm of the optode membrane as a function of  $\log(a_{Ca^{2+}}/a_{H^+}^2)$  in a sodium acetate buffer solution of pH 5.3. The  $Ca^{2+}$  activities were calculated according to a Debye-Hückel formalism. The hydrogen-ion activity was estimated with a pH glass electrode. Curve I was calculated from eqs 5 and 7 by using  $\log K_{exch} = 7.1$  and  $\log K_{Ca^{2+}NH_4^+} = -3.6$ ; curve II was calculated as in part a from eqs 5 and 6 with  $\log K_{exch} = 7.1$ .

optode membranes based on the macroretroilides nonactin/monactin in combination with the same chromoionophore (18). For that sensor system a linear response range was achieved for  $NH_4^+$  activities between about  $10^{-5}$  and  $10^{-3}$  M (at pH 7.35). Obviously, the extent of complexation of the ionophores involved should as far as possible be matched for an improvement of the response characteristics.

Figure 5 illustrates the absorbance response vs time recordings for the  $Ca^{2+}$ -selective optode membrane when it was exposed to repeated concentration step changes between  $10^{-3}$  and  $3 \times 10^{-4}$  M  $CaCl_2$  solutions (acetate buffer of pH 5.9). The results document a remarkably high reproducibility of the optical signals. The mean absorbance values with standard deviations, as obtained from the measured signals after 1 min, are  $0.2013 \pm 0.0005$  for the four upper traces, and  $0.1604 \pm 0.0003$  for the five lower traces. The precision of these absorbance determinations would correspond to a standard deviation of the derived activity values  $a_{Ca^{2+}}$  of  $<1.5\%$ .

On the other hand, Figure 5 also shows that the equilibration times for the  $Ca^{2+}$ -selective membranes are in the second-range and therefore comparable to those found for a previously described  $NH_4^+$ -selective optode membrane of the

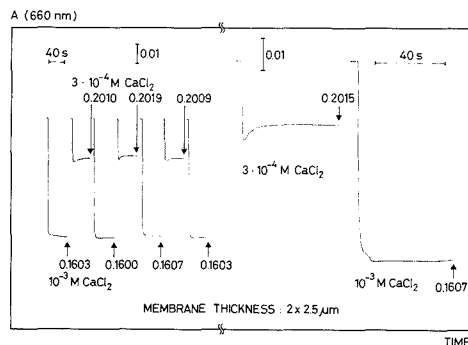


**Figure 5.** Short-time reproducibilities of the absorbance response of two  $2.5 \mu m$  thick membranes for sample changes between  $10^{-3}$  and  $3 \times 10^{-4}$  M  $CaCl_2$  (acetate buffer, pH 5.9).

same type (18). The response time compares favorably with the theoretically expected value (17) which is related to the typical diffusion time within a  $2.5 \mu m$  thick plasticized PVC membrane.

The absorbance signal at a wavelength of 660 nm for the optode membrane in contact with a  $3 \times 10^{-4}$  M  $CaCl_2$  acetate buffer solution (pH 5.3) was recorded during a time period of 15 h. The absorbance values for the calculation of the average value 0.3367 and the standard deviation 0.0005 (which correlates with the instrument stability) were taken every 30 min ( $n = 31$ ). Before and after this long-time measurement the absorbance spectra taken were nearly identical; a slight decrease in intensity of only about 1% was observed at 660 and at 614 nm.

Further fundamental studies as well as research work aiming at the development of similar optical membranes with selectivity for other ions and their application in different sensor systems are in full progress.

#### LITERATURE CITED

- Lübbers, D. W.; Opitz, N. *Z. Naturforsch.* **1975**, *30c*, 532.
- Opitz, N.; Lübbers, D. W. *Int. Anesthesiol. Clin.* **1987**, *25* (3), 77.
- Seitz, W. R. *Anal. Chem.* **1984**, *56*, 16A-34A.
- Peterson, J. I.; Goldstein, S. R.; Fitzgerald, R. V.; Buckhold, D. K. *Anal. Chem.* **1980**, *52*, 864.
- Wolfbeis, O. S. *Fresenius' Z. Anal. Chem.* **1986**, *325*, 387.
- Janata, J. *Anal. Chem.* **1987**, *59*, 1351.
- Borman, S. *Anal. Chem.* **1987**, *59*, 1161A.
- Miller, W. W.; Yafuso, M.; Yan, C. F.; Hui, H. K.; Arick, S. *Clin. Chem.* **1987**, *33*, 1538.
- Kulp, T. J.; Caminis, I.; Angel, St. M.; Munkholm, Ch.; Walt, D. R. *Anal. Chem.* **1987**, *59*, 2849.
- Wolfbeis, O. S.; Schaffar, B. P. H. *Anal. Chim. Acta* **1987**, *198*, 1.
- Badley, R. A.; Drake, R. A. L.; Shanks, I. A.; Smith, A. M.; Stephenson, P. R. *Philos. Trans. R. Soc. London* **1987**, *B 316*, 143.
- Fuh, M.-R. S.; Burgess, L. W.; Hirschfeld, T.; Christian, G. D.; Wang, F. *Analyst*, **1987**, *112*, 1159-1163.
- Alder, J. F.; Ashworth, D. C.; Narayanaswamy, R.; Moss, R. E.; Sutherland, I. O. *Analyst* **1987**, *112*, 1191.
- Gehrich, J. L., et al. *IEEE Trans. Biomed. Eng.* **1988**, *BME-35*, 117.
- Morf, W. E.; Seiler, K.; Lehmann, B.; Behringer, Ch.; Hartman, K.; Simon, W. *Pure Appl. Chem.* **1989**, *61* (9), 1613.
- Morf, W. E.; Seiler, K.; Lehmann, B.; Behringer, Ch.; Tan, S.; Hartman, K.; Sörensen, P.; Simon, W. In *Ion-Selective Electrodes*; Pungor, E., Ed.; Akadémiai Kiado: Budapest, 1989; Vol. 5, pp 115-131.
- Morf, W. E.; Seiler, K.; Sörensen, P.; Simon, W. In *Ion-Selective Electrodes*; Pungor, E., Ed.; Akadémiai Kiado: Budapest, 1989; Vol. 5, pp 141-152.
- Seiler, K.; Morf, W. E.; Rusterholz, B.; Simon, W. *Anal. Sci.* **1989**, *5*, 557-561.
- Seiler, K. *Diss. ETH Zürich*, in preparation.
- Janata, J.; Bezegh, A. *Anal. Chem.* **1988**, *60*, 62R-74R.
- Wolfbeis, O. S.; Weis, L. J.; Leiner, M. J. P.; Ziegler, W. E. *Anal. Chem.* **1988**, *60*, 2028-2030.
- Schaffar, B. H.; Wolfbeis, O. S. *Anal. Chim. Acta* **1989**, *217*, 1-9.
- Zhujiun, Z.; Mullin, J. L.; Seitz, W. R. *Anal. Chim. Acta* **1986**, *184*, 251.
- Werner, T. C.; Cummings, J. G.; Seitz, W. R. *Anal. Chem.* **1989**, *61*, 211-215.
- Suzuki, K.; Tohda, K.; Tanda, Y.; Ohzora, H.; Nishihama, S.; Inoue, H.; Shirai, T. *Anal. Chem.* **1989**, *61*, 382-384.

- (26) Périsset, P. M. J.; Hauser, P. C.; Tan, S. S. S.; Seiler, K.; Morf, W. E.; Simon, W. *Chimia (Switzerland)* **1989**, *43*, 10-11.
- (27) Ammann, D.; Morf, W. E.; Anker, P.; Meier, P. C.; Pretsch, E.; Simon, W. *Ion-Select. Electrode Rev.* **1983**, *5*, 3-92.
- (28) Morf, W. E.; Simon, W. In *Ion-Selective Electrodes in Analytical Chemistry*; Freiser, H., Ed.; Plenum Press: New York, London, Washington, Boston, 1978; Vol. 1, pp 211-286.
- (29) Pungor, E., Ed. *Ion-Selective Electrodes*; Akadémiai Kiadó: Budapest, 1985; Vol. 4.
- (30) Kimura, K.; Shono, T. In ref 3, pp 155-174.
- (31) Solsky, R. L. *Anal. Chem.* **1988**, *60*, 106R-113R.
- (32) Wuthier, U.; Pham, H. V.; Zünd, R.; Welti, D.; Funck, R. J. J.; Bezegh, A.; Ammann, D.; Pretsch, E.; Simon, W. *Anal. Chem.* **1984**, *56*, 535.
- (33) Meyerhoff, M. E.; Pretsch, E.; Welti, D. H.; Simon, W. *Anal. Chem.* **1987**, *59*, 144.
- (34) Bühner, T.; Gehrig, P.; Simon, W. *Anal. Sci.* **1988**, *4*, 547.
- (35) Dix, J. P.; Vögtle, F. *Chem. Ber.* **1981**, *114*, 638.
- (36) Woislowski, S. J. *Am. Chem. Soc.* **1953**, *75*, 5201-5203.
- (37) Meier, P. C. *Anal. Chim. Acta* **1982**, *136*, 363-368.

RECEIVED for review September 12, 1989. Accepted December 6, 1989. This work was partly supported by the Swiss National Science Foundation, by Ciba-Corning Diagnostics Corp., and by Eppendorf Gerätebau, Hamburg.

## Fabrication of Pyrolytic Carbon Film Electrodes by Pyrolysis of Methane on a Machinable Glass Ceramic

Christopher F. McFadden and Paula Rossi Melaragno\*

Department of Chemistry, Ebaugh Laboratories, Denison University, Granville, Ohio 43023

James A. Davis

Owens/Corning Fiberglas, Technical Center, Granville, Ohio 43023

Pyrolytic carbon film electrodes were fabricated by low-temperature (850 °C) pyrolysis of methane onto a machinable glass ceramic material called Macor. As determined by cyclic voltammetry, good charge transfer characteristics were displayed by the electrodes without pretreatment. For the ferro/ferricyanide redox couple, heterogeneous rate constants on the order of  $2 \times 10^{-3}$  cm/s were obtained. Slight rate enhancements were observed after electrochemical pretreatment. Results obtained for the oxidation of dopamine and the reduction of methyl viologen were comparable to those obtained with a commercially available glassy carbon electrode. Electrodes were also fabricated at ca. 1000 °C with a simple Fisher burner arrangement, but electrochemical pretreatment was required before reliable performance was obtained. Electrode surfaces were renewable, since films could be burned off at temperatures greater than 650 °C and a fresh film could then be deposited on the substrate. Scanning electron microscopy indicated similar surface morphologies for films fabricated at 850 and 1000 °C. A pronounced change in surface morphology of the substrate was apparent after heating to 1000 °C.

### INTRODUCTION

Carbon films, useful as electrode surfaces, can be produced by pyrolysis of a carbonaceous gas onto a suitable substrate. A variety of materials have been employed as the substrate, including glassy carbon (1), graphite (2-5), porcelain ceramics (6), and quartz (7, 8). Deposition parameters believed to be important to the properties of the pyrolytic carbon film are time allowed for pyrolysis, temperature, partial pressure, and flow rate of the carbonaceous gas (3). Pyrolysis times as brief as a few minutes have been employed (7), although periods of several hours are more routine. The temperature of pyrolysis is typically between 1000 and 1200 °C. Pyrolysis is ordinarily performed in a tube furnace although a methane/oxygen torch (7) and a Bunsen burner (8) can also be used for quartz substrates. Recently, the low-temperature pyrolysis

of ethylene on nickel has been reported (9). Apparently, nickel acts as a catalyst, allowing carbon film formation at temperatures as low as 550 °C. Frequently, pure methane or ethylene has been used as the source gas, although successful pyrolysis has been reported for 10% methane in argon (3). The flow rate of the source gas over the heated substrate, when noted in the literature reports, has been relatively fast, i.e. 200-500 mL/min.

The charge transfer characteristics of pyrolytic carbon film (PCF) electrodes have been found to be similar but slightly inferior to those of glassy carbon (GC) electrodes. Differences between PCF and GC electrodes may be due to structural differences at the atomic level, such as differences in orientation of the graphite crystallites and/or the identity and extent of formation of surface functional groups. It is widely believed that these factors affect the charge transfer characteristics of all types of carbon electrodes (10-20). Like other carbon electrodes, the activity of PCF electrodes is sensitive to electrochemical pretreatment.

We report the fabrication of PCF electrodes by pyrolysis of methane onto a glass ceramic substrate called Macor. Macor is a unique ceramic material, in that it can be machined to tight tolerances by ordinary high-speed tools. Macor can be used immediately after machining, since no subsequent firing is required, unlike other ceramics, which are machinable only in the "green" or unfired state. Macor is nonporous and has a very low helium permeation rate in a vacuum. It is a good insulator material and is chemically inert (21).

Two slightly different pyrolysis methods were employed. One method involved deposition in a tube furnace at 850 °C (the maximum which was provided by the available furnace). This temperature is significantly lower than pyrolysis temperatures reported in the literature for noncatalytic surfaces. Pyrolysis times were relatively long, on the order of 10-20 h. Alternatively, a simple Fisher burner arrangement was employed. In this case, the temperature of pyrolysis was fixed at ca. 1000 °C by the flame temperature. Shorter pyrolysis times of 1-5 h were employed. In both methods, natural gas from the common laboratory line was employed as the source gas.

Good charge transfer characteristics were displayed by carbon films fabricated in the tube furnace without mechanical or electrochemical pretreatment. Heterogeneous rate constants on the order of  $2 \times 10^{-3}$  cm/s were obtained for the ferro/ferricyanide redox couple. This value is well within the range of values ( $1.5 \times 10^{-4}$  to 0.20 cm/s) that have been obtained at pretreated GC electrodes (20). Results obtained for the oxidation of dopamine and the reduction of methyl viologen were comparable to those obtained on GC. Results were quite reproducible from electrode to electrode and day to day for the same electrode. Electrode surfaces were essentially renewable since carbon films were easily burned off in air at temperatures greater than 650 °C and a fresh film could then be deposited on the surface.

Optimal performance was obtained for films fabricated with a Fisher burner only AFTER electrochemical pretreatment. Scanning electron microscopy (SEM) was employed in an attempt to determine if differences in surface microstructure were responsible for the difference in electrode performance. Both bare and PCF coated Macor surfaces were examined. No significant difference in the carbon films could be seen with SEM, but a pronounced change in surface morphology of the substrate was apparent after heating to 1000 °C.

The machinability of the substrate, the favorable charge transfer characteristics of the carbon film, and the renewability of the surface should make this type of electrode ideal for situations where an electrode of unique size and shape is required.

## EXPERIMENTAL SECTION

**Reagents.** Potassium ferrocyanide (Matheson, Coleman and Bell), dopamine (Sigma Chemical Co.) and methyl viologen dichlorohydrate (Aldrich Chemical Co.) were used as received. Solvents were 1.0 M KCl for ferrocyanide, 2 M H<sub>2</sub>SO<sub>4</sub> for dopamine, and 0.5 M phosphate buffer for methyl viologen. Phosphate buffer was adjusted to pH 7 by dropwise addition of NaOH (50% (w/w)). Natural gas (which consists primarily of methane, but also contains larger hydrocarbons like ethane, propane, etc.) was taken from the common laboratory line and was used without purification or dilution. Macor (product of Corning Glass Works) was purchased from Astro Met Associates, Inc. (Cincinnati, OH), and was machined to the desired size and shape with ordinary high-speed tools and a water-soluble coolant.

**Pyrolysis.** Macor was boiled in detergent after machining and rinsed first with distilled water and then methanol. A cylinder of clean Macor, of 1/8 in. diameter and 1 cm length was placed into a section of quartz tubing (Quartz Scientific, Inc., 5 mm i.d.) which was then placed into a tube furnace (Lindberg). The furnace was flushed with N<sub>2</sub> while heated at 850 °C. After this temperature was reached, methane was passed through a drying tube of activated charcoal and then through the oven at a flow rate of ca. 20.0 mL/min (measured with a bubble flow meter). After pyrolyzation (12–20 h) the system was allowed to cool to room temperature under N<sub>2</sub>.

Alternatively, the Fisher burner was substituted for the oven and was placed directly under the piece of Macor in the quartz tube. Nitrogen was passed over the substrate until the quartz was heated to red heat. Methane was then passed over the substrate at a flow rate of ca. 10.0 mL/min. The temperature inside the quartz tubing was determined to be between 962 and 1064 °C. A dark coating on the Macor was distinguishable after approximately 30 minutes and total pyrolysis times were from 1 to 5 h. The system was allowed to cool under N<sub>2</sub>.

Film thicknesses could be determined by measuring the difference in diameter of the cylinder before and after pyrolysis. A micrometer was used to measure diameter and the precision of the measurement was determined to be  $\pm 0.2$   $\mu$ m.

Carbon films could be removed by heating to 650 °C in the presence of air.

**Electrochemistry.** Carbon film electrodes were fabricated in the following manner. A cylinder of Macor with carbon film was placed inside a section of heat-shrinkable Teflon tubing (Alltech) so that the end of the cylinder was flush with the end

**Table I. Heterogeneous Rate Constants for Ferrocyanide on PCFM Electrodes**

scan rate, V/s	$\Delta E_p$ , V	$k^0$ , cm/s
0.020	95	$2.62 \times 10^{-3}$
0.075	130	$2.33 \times 10^{-3}$
0.100	145	$2.18 \times 10^{-3}$

of the tubing. A hot-air gun was used to shrink the tubing. Mercury was placed on top of the cylinder and a copper wire completed the electrical connection. Resistance across the electrode was determined to be in the range of 10–30  $\Omega$  for all electrodes, regardless of pyrolysis time or temperature. Electrochemical pretreatment consisted of potential cycling between limits of  $\pm 1.0$  V at scan rates of 0.500 V/s for 1/2-h increments. Electrochemical pretreatment was performed in 1.0 M KCl, in the presence of ferrocyanide.

GC indicator electrodes (BAS) were hand polished with 0.5- $\mu$ m alumina powder (Baikowski International Co.) and sonicated in deionized water. This procedure was then repeated a second time before use. All electrochemical experiments were performed with a platinum wire auxiliary and Ag/AgCl (BAS) reference electrode. All potentials quoted herein are relative to the Ag/AgCl reference potential. A BAS CV-27 potentiostat was used for cyclic voltammetry and chronoamperometry.

**Scanning Electron Microscopy (SEM).** The surface morphologies of virgin Macor pieces as well as individual electrodes were examined with a JEOL T-300 SEM. This instrument was operated in a secondary electron imaging mode with a 10–20 keV beam energy. Magnifications ranging from 50 $\times$  to 10,000 $\times$  were utilized for this study. Each sample was mounted onto a suitable sample stub with conductive carbon paint (SPI Supplies) and then coated with ca. 200 Å of gold in a sputter coater (Seevac, Inc.).

## RESULTS AND DISCUSSION

**Surface Characterization/Furnace Electrodes.** Pyrolytic carbon films deposited on Macor (PCFM) at 850 °C were dark metallic gray and completely covered the surface of the substrate. Coatings were reproducible from batch to batch, as far as could be detected with an optical microscope. PCFM was stable in all common organic solvents as well as in concentrated nitric and sulfuric acids. Films could not be rubbed or peeled off the Macor surface. Hardness of the film was judged to be between that of stainless steel and quartz since the film could not be scratched with an ordinary pocket knife but was scratched by a quartz edge.

Scanning electron microscopy (SEM) was employed to further characterize the surface. Representative photomicrographs of bare Macor (after exposure to 850 °C) and the carbon film formed in the furnace are given in Figure 1. The bare ceramic (Figure 1A) may be seen to have the high surface texture and angular features that are typical (at this magnification) of Macor after it has been machined. From Figure 1B, it can be seen that the carbon film completely covers the Macor substrate and consists of numerous particles that are less than 0.1  $\mu$ m in size. These species are agglomerated together to form rounded features that can be in excess of 10  $\mu$ m across.

**Charge Transfer/Furnace Electrodes.** Cyclic voltammetry was used to evaluate rates of charge transfer at PCFM electrodes for the ferro/ferricyanide redox couple. Representative voltammograms are shown in Figure 2. Reversible behavior was obtained at 5 mV/s, with  $\Delta E_p$  equal to 0.057 V,  $E^0$  equal to 0.226 V, and  $i_{pa}/i_{pc}$  equal to 0.949 (Figure 2A). At faster scan rates, the redox couple was only quasi-reversible, which can be seen from the voltammograms in Figure 2B. As scan rate increased, both anodic and cathodic peak potentials shifted, producing a corresponding increase in  $\Delta E_p$ .

The heterogeneous rate constant ( $k^0$ ) was estimated from  $\Delta E_p$  after the method of Nicholson (22). Values obtained are presented in Table I. (The decrease in  $k^0$  with increasing

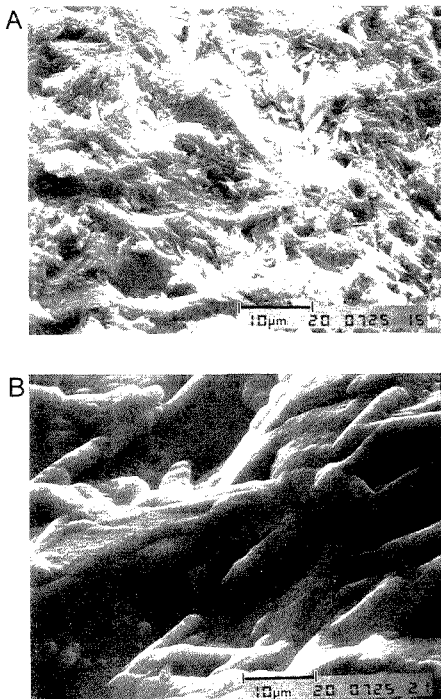


**Figure 1.** SEM photomicrographs (2000 $\times$ ) of the surface of (A) bare Macor which had been exposed to 850  $^{\circ}$ C and (B) PCFM produced at 850  $^{\circ}$ C.

scan rate was presumably due to uncompensated solution resistance.) The rate of charge transfer was quite respectable, especially considering the fact that the surface was not pretreated. Comparable rates have been obtained at polished GC (20) although rate constants nearly 100 times larger have been obtained with laser ablation (23).

Rate constants were fairly reproducible from electrode to electrode. Values obtained for  $k^{\circ}$  ranged from  $9.73 \times 10^{-4}$  to  $3.97 \times 10^{-3}$  cm/s. This variation is surprisingly small given the fact that pyrolysis times were not maintained strictly constant from electrode to electrode and ranged from 10 to 20 h. At least within this time frame the rate of electron transfer does not seem to be a sensitive function of pyrolysis time.

Residual current is shown in Figure 3 and illustrates a useful working range of from 1.1 to  $-1.2$  V. Less than  $1 \mu$ A residual current is obtained for potentials from 1.1 to  $-0.5$  V. (The small peak at  $-0.35$  is due to a trace of dissolved oxygen.) Residual current was quite consistent from electrode to electrode.

PCFM electrodes were found to be remarkably stable. Individual electrodes gave nearly identical results over periods of several months, even with constant use. Again, electrodes were not pretreated in any way between runs or even from day to day. After use, electrodes were simply washed, dried, and stored in air.

Electrode surfaces were essentially renewable. Carbon films were easily burned off in air at temperatures greater than 650  $^{\circ}$ C and fresh films could then be deposited on the substrate. Rate constants obtained by using "repyrolyzed" surfaces were within the range noted above. In fact, the voltammograms

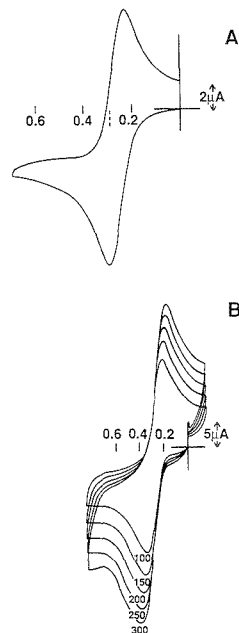


**Figure 2.** (A) Cyclic voltammogram of 1.0 mM ferrocyanide at PCFM electrode. The solvent was 1 M KCl and the scan rate was 5 mV/s. (B) Same as in A, but for the scan rates indicated in the figure.

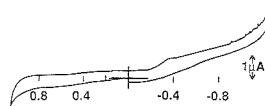


**Figure 3.** Residual current at PCFM electrode. The solvent was 1 M KCl, and the scan rate was 5 mV/s.

shown in Figure 2 were obtained with a "repyrolyzed" electrode. It should be noted, however, that the renewal procedure is more time-consuming and not as experimentally convenient as that provided by the dropping mercury or carbon paste electrode.

Preliminary experiments indicated that the rate of electron transfer was slightly enhanced by electrochemical pretreatment. The largest increase in  $k^{\circ}$  observed for a single electrode was a factor of 4.5 (from  $2.46 \times 10^{-3}$  to  $1.10 \times 10^{-2}$  cm/s), which was observed after potential cycling for  $1/2$  h. Pretreatment did increase the level of residual current although the amount varied from electrode to electrode. This could have been due to an increase in surface roughness. This interpretation was supported by chronoamperometric measurements of the electrode area before and after pretreatment. Electrode area increased by as much as 30% upon extensive pretreatment (i.e. several hours of potential cycling). We are at present systematically investigating the effect of electrochemical pretreatment on both  $k^{\circ}$  and residual current.

The one-electron reduction of methyl viologen dication ( $MV^{2+}$ ) to the cation radical ( $MV^{+\bullet}$ ) and the two-electron oxidation of dopamine (DA) to the quinone species were investigated. Our goal was simply to determine if results obtained at PCFM electrodes were similar to those obtained by using conventional electrodes. Heterogeneous rate constants were not calculated but  $E^{\circ}$ ,  $\Delta E_p$ , and  $i_{pa}/i_{pc}$  data are given

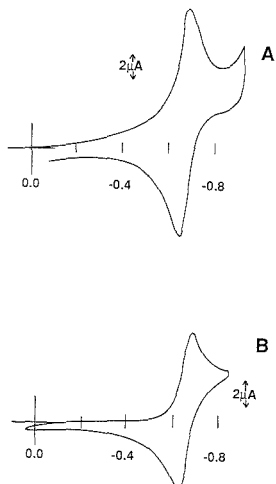


**Figure 4.** (A) Cyclic voltammogram of 1.0 mM  $MV^{2+}$  at PCFM electrode. The solvent was 0.5 M phosphate buffer (pH 7) and the scan rate was 20 mV/s. (B) Cyclic voltammogram of  $MV^{2+}$  at GC electrode. All other experimental conditions were the same as in part A.

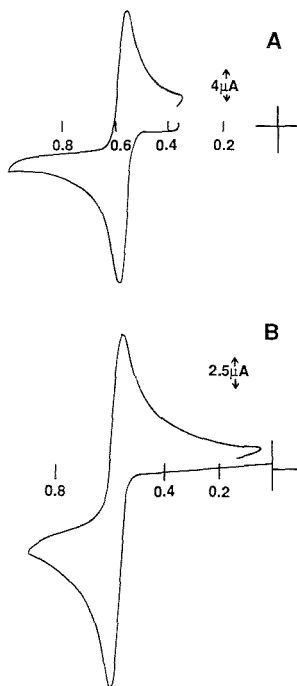


**Figure 5.** (A) Cyclic voltammogram of 1.0 mM DA at PCFM electrode. The solvent was 2 M  $H_2SO_4$  and the scan rate was 20 mV/s. (b) Cyclic voltammogram of DA at GC electrode. All other experimental conditions were the same as in part A.

in Table II. For comparison, results obtained in our laboratory at GC are also given.

From the voltammogram shown in Figure 4, it can be seen that the reduction of  $MV^{2+}$  is easily observed at PCFM, even

**Table II.**<sup>a</sup> Cyclic Voltammetric Data for Methyl Viologen and Dopamine on PCFM and GC

	$MV^{2+}$ <sup>b</sup>		DA <sup>c</sup>	
	PCFM	GC	PCFM	GC
$E^{\circ}$ , V	0.670	0.655	0.574	0.628
$\Delta E_p/n$ , V	0.041	0.050	0.038	0.028
$i_{pa}/i_{pc}$	1.12	0.905	1.11	1.00

<sup>a</sup> Scan rate, 20 mV/s. <sup>b</sup> 1.0 mM in 0.3 M phosphate buffer, pH 7. <sup>c</sup> 1.0 mM in 2 M  $H_2SO_4$ .

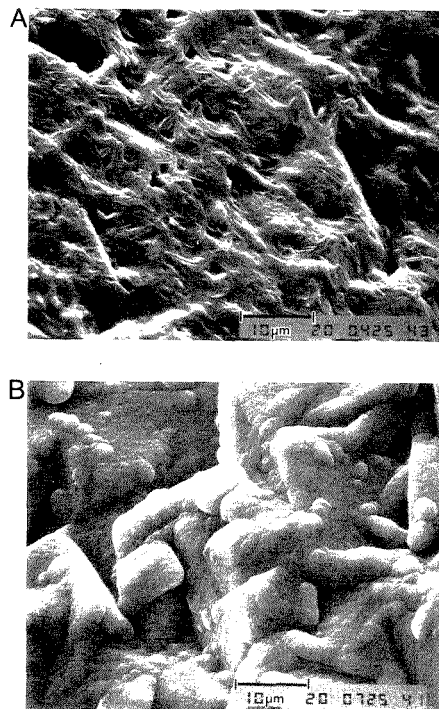


**Figure 6.** SEM photomicrograph (2000 $\times$ ) of the surface of (A) bare Macor after heating to 1000  $^{\circ}C$  and (B) PCFM fabricated at 1000  $^{\circ}C$ .

though it occurs in a potential region of relatively high residual current. Adsorption is clearly indicated by the shape of the voltammogram and small  $\Delta E_p$  (Table II). This is not surprising, since the cation radical also adsorbs on GC as indicated by  $\Delta E_p$  and the shape of the voltammogram shown in Figure 4B.

Voltammograms obtained upon the oxidation of DA are shown for both PCFM and GC electrodes in Figure 5. Again, the results are roughly comparable, which can be seen from both the voltammograms and parameters listed in Table II. Adsorption does not appear to be a significant problem at either electrode.

**Flame vs Furnace Electrodes.** Electrodes were fabricated at ca. 1000  $^{\circ}C$ , using a Fisher burner as the heat source. The visual appearance of films produced at this temperature was the same as that of films produced at 850  $^{\circ}C$ . Resistance was comparable to that obtained for films produced at 850  $^{\circ}C$ .

SEM photomicrographs of bare Macor and PCFM fabricated in the flame are shown in Figure 6. At this temperature, the apparent crystallinity of the bare ceramic has increased (i.e. a number of angular surface and near-surface features

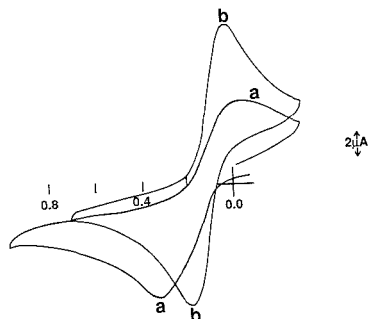


**Figure 7.** Cyclic voltammograms of 1.0 mM ferrocyanide at PCFM electrode fabricated at 1000 °C. The solvent was 1 M KCl and the scan rate was 20 mV/s. Trace a was before pretreatment. Trace b was after 75 min of potential cycling (as described in the Experimental Section).

have been formed). This observation is consistent with the published performance specifications for this material (21), which state 1000 °C as the maximum use temperature. The overall surface texture of the flame-induced PCFM, on the other hand, may be seen to be similar to that observed for the furnace-generated films.

Initial electrochemical performance of PCFM produced at 1000 °C was significantly different from that produced at 850 °C. In general, electron transfer characteristics were slower and less reproducible from electrode to electrode. From Figure 7, trace a, it can be seen that the ferro/ferricyanide redox couple was practically irreversible with  $\Delta E_p$  equal to 0.335 V. The rate of electron transfer was significantly enhanced after electrochemical pretreatment (potential cycling for 75 min), which can be seen from Figure 7, trace b. A significant improvement in peak shape was observed and  $\Delta E_p$  decreased to 0.150 V, which corresponds to  $k^0$  of  $1.54 \times 10^{-3}$ . It should be noted that this rate is comparable to that obtained at furnace-generated electrodes without pretreatment.

Electrodes fabricated in the furnace at 850 °C were clearly superior, at least before electrochemical pretreatment. Given the current interest in carbon surfaces and particularly those features that enhance the rate of electron transfer (10–20, 24, 25), it is of interest to consider differences between furnace and flame electrodes.

We have thus far identified two important differences in the two types of electrodes. First, films obtained in the furnace were thicker than those obtained in the flame. This was determined by comparing film thicknesses for two electrodes: one fabricated in the furnace at 850 °C for 20 h, yielding a thickness of 11.5  $\mu\text{m}$ , and the second fabricated with the Fisher burner for 2 h, yielding a thickness of 6.5  $\mu\text{m}$ . Film thickness appears to increase with pyrolysis time although temperature may also play a role, i.e., for pyrolysis times of equal length, films obtained at higher temperatures may be thicker. The relationship between pyrolysis time and temperature and film thickness is presently under investigation. It is possible that thicker films facilitate electron transfer, but for a definitive answer it will be necessary to systematically evaluate films of various thicknesses fabricated at the same temperature.

The second important difference was that the substrate surface was significantly changed after heating to 1000 °C as indicated by SEM. However, no change was observed upon heating to 850 °C. This suggests that the structure of the substrate itself might influence the rate of electron transfer, perhaps by modifying the orientation of graphite crystallites deposited during pyrolysis. Changes in the microstructure

of the carbon film were not detectable by using SEM, but may be discernible via other techniques such as Raman spectroscopy (24, 25).

## CONCLUSIONS

It should be possible to fabricate carbon film electrodes of various shapes and sizes using Macor as the substrate. Charge transfer characteristics displayed by PCFM electrodes are good enough to make these electrodes quite useful, although rate constants for ferro/ferricyanide are ca. 100 times smaller than those that can be obtained after intensive polishing (20) or heat (18–20) or laser (23) treatment of GC. Rate constants may be enhanced considerably after more extensive electrochemical pretreatment than that employed thus far; specifically larger voltage excursions should be employed, since pretreatment at potentials positive of 1.95 V has been correlated with enhanced rates at other carbon electrodes (24, 25). The fact that the carbon surface can be easily renewed is a significant advantage, particularly in applications requiring a unique electrode.

Macor appears to be superior to other substrates for forming active carbon films. Good electrochemical behavior was obtained for films fabricated at 850 °C, a temperature significantly lower than that conventionally employed for fabrication of pyrolytic carbon films (1–8). Surprisingly, electrodes fabricated at the more conventional temperature of 1000 °C did not perform as well without electrochemical pretreatment. These results indicate that the microstructure of the substrate (which is quite different at 850 and 1000 °C) may play an important role in determining charge transfer characteristics of the carbon film.

## ACKNOWLEDGMENT

The authors gratefully acknowledge the assistance of Jon Nebo for some initial pyrolysis experiments and Bhukumuzi M. Khumalo for cyclic voltammetry on glassy carbon.

## LITERATURE CITED

- Urbaniczky, C.; Lundstrom, K. *J. Electroanal. Chem. Interfacial Electrochem.* **1983**, *157*, 221–231.
- Bauer, H. H.; Spritzer, M. S.; Ewing, P. J. *J. Electroanal. Chem. Interfacial Electrochem.* **1968**, *17*, 299.
- Lundstrom, K. *Anal. Chim. Acta* **1983**, *146*, 97–108.
- Lundstrom, K. *Anal. Chim. Acta* **1983**, *146*, 109–115.
- Gustavsson, I.; Lundstrom, K. *Talanta* **1983**, *30*, 959–962.
- Bailey, A. L.; Brooks, W., R.; Lawrence, G. L. *Anal. Chem.* **1964**, *36*, 22–26.
- Blaedel, W. J.; Mabbott, G. A. *Anal. Chem.* **1978**, *50*, 933–936.
- Kim, Y. T.; Scarnulis, D. M.; Wing, A. G. *Anal. Chem.* **1986**, *58*, 1782–1786.
- Saraceno, R. A.; Engstrom, C. E.; Rose, M.; Ewing, A. G. *Anal. Chem.* **1989**, *61*, 560–565.
- Knoshita, K. *Carbon: Electrochemical and Physicochemical Properties*; Wiley: New York, 1988.
- Randin, J. P. *Encyclopedia of Electrochemistry of the Elements*; Bard, A. J., Ed.; Dekker: New York, 1976; Vol. 7, pp 1–291.
- Morcos, I.; Yeager, E. *Electrochim. Acta* **1970**, *15*, 953.
- Cabanis, G. E.; Diamantis, A. A.; Murphy, W. R. Jr.; Linton, R. W.; Meyer, T. J. *J. Am. Chem. Soc.* **1985**, *107*, 1845.
- Evans, J. F.; Kuwana, T. *Anal. Chem.* **1977**, *49*, 1632.
- Tse, D. C. S.; Kuwana, T. *Anal. Chem.* **1978**, *50*, 1315.
- Moiroux, J.; Ewing, P. J. *Anal. Chem.* **1978**, *50*, 1056.
- Kaman, G. N.; Willis, W. S.; Rusling, J. F. *Anal. Chem.* **1985**, *57*, 545.
- Fagan, D. T.; Hu, I. F.; Kuwana, T. *Anal. Chem.* **1985**, *57*, 2759.
- Hu, I. F.; Kuwana, T. *Anal. Chem.* **1986**, *58*, 3235.
- Hu, I. F.; Karweik, D. H.; Kuwana, T. *J. Electroanal. Chem. Interfacial Electrochem.* **1985**, *182*, 59.
- Grossman, D. G. *Am. Mach.* **1978**, (May).
- Nicholson, R. S. *Anal. Chem.* **1965**, *37*, 1531.
- Poon, M.; McCreery, R. L. *Anal. Chem.* **1986**, *58*, 2745–2750.
- Bowling, R. J.; Packard, R. T.; McCreery, R. L. *J. Am. Chem. Soc.* **1989**, *111*, 1217–1223.
- Bowling, R.; Packard, R. T.; McCreery, R. L. *Langmuir* **1989**, *5*, 683.

RECEIVED for review September 25, 1989. Accepted December 26, 1989. This research was supported by the Denison University Research Fund and the Anderson Endowment Program.



# Voltammetric Measurement of Ultraslow Diffusion Rates in Polymeric Media with Microdisk Electrodes

M. L. Longmire, M. Watanabe, H. Zhang, T. T. Wooster, and Royce W. Murray\*

Kenan Laboratories of Chemistry, University of North Carolina, Chapel Hill, North Carolina 27514-3290

Cyclic voltammetry and chronoamperometry were used in conjunction with microdisk electrodes in polymeric solvents to measure diffusion coefficients of ferrocene redox solutes down to  $10^{-12}$  cm<sup>2</sup>/s. Experimental manipulation of the parameter  $\tau$  ( $\tau = 4Dt/r^2$ ) results in diffusion profiles dominated by radial diffusion, linear diffusion, or a combination of the two. In the former two cases, adherence to the steady-state current equation for a microdisk and the Cottrell equation, respectively, was observed. Under conditions of mixed contribution, evaluation of diffusion coefficients was based on comparison of experimental and simulated current-time curves. Generally, diffusion coefficients  $>10^{-7}$  cm<sup>2</sup>/s were evaluated from steady-state potential sweeps. Diffusion coefficients  $<10^{-11}$  cm<sup>2</sup>/s could be evaluated by a standard Cottrell analysis. Values in the "transition region" were evaluated from the slope of nonzero intercept Cottrell plots. A numerical guideline, based on  $\tau$ , is presented.

Microdimensioned electrodes (1-7) have enjoyed considerable recent popularity owing to the advantages they offer in electrochemical measurements. The small electrode size and favorable background current characteristics facilitate *in vivo* measurements in mammalian rat brain (8) and even in single nerve cells (9). Because the small electrode areas mean small currents, they can be employed for ultrafast potential scan cyclic voltammetry to study fast homogeneous and heterogeneous electron transfer kinetics (10-13) and electrode reaction mechanisms (14), and in highly resistive solvents where macroelectrodes encounter debilitating uncompensated *iR* effects. Our laboratory has been particularly interested in the latter attribute of microelectrodes and have used them to explore electrochemical and transport phenomena in previously inaccessible, resistive solvents like low dielectric fluids (heptane and toluene) (15), ultralow temperature fluids (16), and rigid and semirigid polymers (17-20).

Our solid-state voltammetric investigations of transport phenomena in polymer solvents led to the present work. The polymers employed are primarily poly(ether)s, which readily dissolve alkali-metal salts such as LiClO<sub>4</sub> (21). These "polymer electrolytes" also dissolve redox molecules. Although their ionic conductivities (22) are modest compared to those of high dielectric fluid electrolyte solutions, electrochemical reactions of redox solutes in polymers can be observed (17-20) at microelectrodes placed into contact with the polymeric medium. The observed currents depend, among other factors, on the diffusion coefficient of the redox molecule in the rigid polymer solvent. This paper concerns the measurement of such solid-state polymer diffusion coefficients, *D*, which are characteristically small and variable.

Diffusional transport of small molecules (or ions) dissolved in polymeric solvents differs in several respects from diffusion in small molecule fluid solvents. Diffusion in a polymer depends on segmental motions of polymer chains (23-28), and accordingly any perturbation of polymer segmental mobility may induce a change in a solute's diffusion rate (i.e. its diffusion coefficient). The dissolution of any small molecule in a polymer, through its interaction (dipolar, coordinating,

hydrogen bonding, etc.) with the polymer chain, can alter chain segmental mobility, with the consequence that a solute's diffusion coefficient can depend on its own concentration or on that of other small molecules dissolved in the polymer. We have observed that dissolved small molecules or ions can either depress or speed up diffusion coefficients of redox molecules dissolved in poly(ether) solvents (17, 18). The accelerated diffusion in polymers results from diffusion-plasticization by added solutes. Diffusion coefficients of redox molecules are also strongly influenced by temperature (17, 20) and by the presence of ordered regions (i.e., crystallinity) (18) in the polymer. Finally, when physical diffusion rates are slow, and the electron self-exchange dynamics of the redox diffusant couple are fast, electron hopping can also contribute to transport of electrochemical charge. We have discussed this issue in other publications on diffusion in polymer solvents (17, 19), and diffusion coefficients reported in this work are uncorrected for electron hopping.

In polymer solvents, a solute diffusion coefficient is, thus, a dynamic variable. This behavior is different from typical diffusion phenomena in fluid media where solutes, particularly neutral ones, ordinarily diffuse at rates that are not strongly dependent on other solutes present. We have accordingly attached some importance to developing electrochemical techniques for measuring redox molecule diffusion coefficients in polymeric media over a range of concentration, temperature, plasticization, and crystallinity values. Understanding diffusion phenomena is also important in eventual solid-state voltammetric electroanalysis of polymeric materials. The diffusion coefficients we have encountered are both much smaller than those in fluid solutions and highly variable (spanning a 10<sup>6</sup>-fold range). The largest diffusion coefficients are found in polymers that are plasticized or are at elevated temperature while the smallest are those for polymeric diffusants in dry, partly crystalline polymers at room temperature.

The methodology for diffusion measurements in polymer solvents is not as straightforward as well-known procedures useful in fluid electrolytes (29). Two significant difficulties are as follows: (i) The small diffusion coefficients in polymer solvents are reflected directly in small measured currents. Small diffusion currents combine with the microelectrode tactic to help avoid resistance effects, but ultimately their small magnitude provokes measurement complications associated with signal amplification and noise filtering. Enhancing the currents by making the microelectrode larger is of limited utility, since polymer solvents that exhibit very slow redox molecule diffusion rates also generally exhibit small ionic diffusion rates, i.e., are particularly resistive media. (ii) The variability of the diffusion rates encountered causes uncertainty about the diffusion geometry of the measurement. Consider the dimensionless time parameter  $\tau = 4Dt/r^2$ , where *t* is the electrolysis time and *r* the electrode radius. When  $\tau = 1$ , the diffusion distance of solute is equal to the radius of the electrode. When  $\tau \gg 1$ , the diffusion geometry is radial, because the diffusion layer thickness is greater than *r*, whereas diffusion is linear when  $\tau \ll 1$  because the diffusion layer is thin relative to *r*. Ideally, a preliminary measurement of this parameter is used to guide the refinement of subsequent

experiments in which alterations in  $t$  or  $r$  place the measurement in one of the two limiting diffusion regimes. In practice, such choices of  $t$  or  $r$  are not always easy, and we have also frequently found that in a series of diffusion measurements on a given system (especially when varying temperature), the diffusion geometry drifts from one of the simple extremes to a mixed diffusion geometry. We describe here some tactics for dealing with these matters.

It is worth noting that the presently available repertoire of methods capable of measuring very slow diffusion rates includes NMR relaxation time measurements which measure down to  $10^{-15}$  cm<sup>2</sup>/s, radiotracer techniques capable of measuring values down to  $10^{-10}$  cm<sup>2</sup>/s, pulsed field gradient NMR capable of measuring values down to  $10^{-7}$  cm<sup>2</sup>/s (30), and photobleaching relaxation which has determined diffusion rates down to  $10^{-10}$  cm<sup>2</sup>/s (31). Low-frequency ac impedance, voltage relaxation, and dc polarization have also been used to measure values  $< 10^{-10}$  cm<sup>2</sup>/s (32, 33), relying on electrostatically induced migration of charged species in various matrices. The present measurements add microelectrode solid-state voltammetry to this useful list. The voltammetric approach to be reported, in which the diffusional driving force is a concentration gradient, has produced a diffusion rate measurement of  $10^{-12}$  cm<sup>2</sup>/s. This is the slowest voltammetrically measured diffusion coefficient of which we are aware. The capability to measure such small diffusion coefficients raises interesting questions concerning the redox ion concentration profile very close to the electrode surface, the effect of topological imperfections in the electrode surface, and the effect of redox probes whose physical dimensions are comparable to that of the diffusion layer.

### EXPERIMENTAL SECTION

**Chemicals.** Network poly(ethylene oxide) (network PEO) was synthesized according to a published procedure (34). Triol poly(ethylene glycol) (PEG) (Daiichi Kogyo Seiyaku) was dried at 50 °C under vacuum for 24 h; toluene 2,4-diisocyanate (Polysciences) was distilled under vacuum; methyl ethyl ketone (Fisher) was distilled at ambient pressure; and dibutyltin dilaurate (Aldrich) was used as received. Monomethoxy poly(ethylene glycol) (MPEG, nominal MW = 2000) was labeled with ferrocenecarboxylic acid (35) using a modification of a published procedure (36). Gel permeation chromatography established the molecular weight of the ferrocene-labeled polymer (designated CpFeCpC(O)NH-MPEG) as 2590. Ferrocenecarboxylic acid (Aldrich) was used as received. *N,N,N*-Trimethyl(ferrocenylmethyl)ammonium hexafluorophosphate (CpFeCpCH<sub>2</sub>N(CH<sub>3</sub>)<sub>3</sub><sup>+</sup>PF<sub>6</sub><sup>-</sup>) was metathesized from the iodide salt (K&K Laboratories) and purity determined by cyclic voltammetry.

**Electrochemical Experiments.** The electrode design, previously described (17–19), consisted of a 10- or 25- $\mu$ m Pt working microelectrode sealed in a glass capillary, coplanar in an epoxy tube with 26 gauge Pt and Ag wires, serving as auxiliary and reference electrodes, respectively. The present electrode assembly uses an epoxy (Epon 828, Miller-Stephens Chemicals) lattice rather than heat shrinkable tubing (18). The end of the tube was polished to expose the tips of the three metal wires, coplanar on a flat insulating surface, upon which a film of the polymer solution was placed. In the case of CpFeCpC(O)NH-MPEG, a drop of melted polymer in which LiClO<sub>4</sub> (Aldrich) was dissolved (O:Li molar ratio of 16:1) was placed on the electrode assembly which was then sealed in an air-tight container. For network PEO measurements, the polymer cross-linking reaction mixture was prepared by mixing appropriate quantities of triol PEO, toluene 2,4-diisocyanate, dibutyltin dilaurate, and LiClO<sub>4</sub> (34) in methyl ethyl ketone (O:Li = 50:1). A  $\sim 20$ - $\mu$ L drop of this mixture was placed on the electrode assembly where the cross-linking reaction proceeded, in an inert atmosphere, to form a resilient plastic film with good adherence to the electrode surface.

Cyclic voltammetric measurements were made with a locally constructed potentiostat (37). Chronoamperometry with this potentiostat was done with potential excitation supplied from a PAR Model 175 universal programmer. Current-time curves were

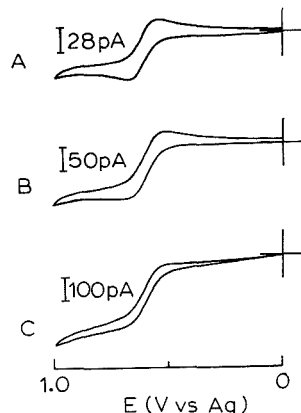


**Figure 1.** Microelectrode (25  $\mu$ m disk) cyclic voltammetry of 5 mM CpFeCpCH<sub>2</sub>N(CH<sub>3</sub>)<sub>3</sub><sup>+</sup> dissolved in network PEO/LiClO<sub>4</sub> (O/Li = 50) recorded at 5 mV/s and at (A) 35 °C, (B) 56 °C, and (C) 74 °C.

recorded on a Hewlett-Packard 7015b X-Y recorder. The hard copy curves were digitized with a Summagraphics Bit Pad Two data tablet and transferred to a PC where data analysis was done with locally written Pascal software. The data transfer procedure was necessary because of signal/noise problems encountered in direct analog to digital (A/D) conversion. All electrochemical experiments were performed in a Faraday cage.

Diffusion coefficients were generally determined by seeking the two limiting conditions ( $\tau \gg 1$  and  $\tau \ll 1$ , vide supra) of experimental behavior. When slow potential sweep rate cyclic voltammetry produced a steady limiting current, and a preliminary evaluation of  $D$  gave  $\tau > 50$ , confirming radially dominated diffusion,  $D$  was evaluated from the limiting current according to microelectrode theory. When, by choice of experimental time scale or electrode radius,  $\tau < 0.01$  so as to confirm linear diffusion,  $D$  was obtained from linear segments of Cottrell plots ( $i$  vs  $t^{-1/2}$ ) of chronoamperometric data. In some cases  $\tau$  was closer to unity as described in the text below, in which cases mixed diffusion geometry theory was applied.

### RESULTS

Examples of cyclic voltammetry of CpFeCp-CH<sub>2</sub>N(CH<sub>3</sub>)<sub>3</sub><sup>+</sup> in network PEO at 35, 56, and 74 °C in dry N<sub>2</sub> are shown in parts A–C of Figure 1, respectively. There are substantial changes in the voltammetric currents over this modest temperature span. Network PEO polymer does not exhibit any phase transitions in this temperature interval, but the effectively large activation barrier for diffusion in the polymer makes the ferrocene diffusion coefficient exhibit a strong temperature dependence.

The changes in diffusion rates in Figure 1 are accompanied by alterations in the voltammetric wave shapes as well. The shapes indicate a transition from (approximately) linear diffusion behavior at 35 °C to a more steady-state behavior at 74 °C. Clearly, an analysis based solely on steady-state microelectrode theory would yield a good estimate of  $D$  at the elevated temperature but would overestimate the value of  $D$  at 25 °C.

Diffusion rates in the linear diffusion regime can, in principle, be evaluated by using cyclic voltammetry at a succession of potential sweep rates ( $v$ ), plotting  $i_p$  vs  $v^{1/2}$ , or by potential step chronoamperometry, plotting  $i$  vs  $t^{-1/2}$  (Cottrell plot) (29). We prefer the second approach because by stepping the applied potential to values well beyond  $E^\circ$ , the uncompensated resistance effects of the large ionic resistance often encountered in the slowest diffusing cases are lessened. Examples of Cottrell plots are given in Figure 2 for a series of ferrocene

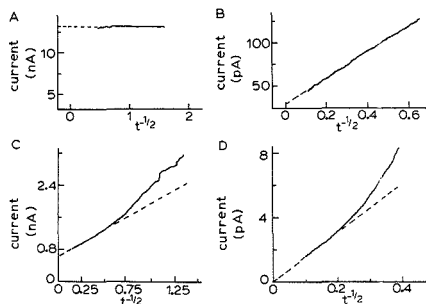


**Figure 2.** Cottrell plot at  $r = 12.5 \mu\text{m}$  disk of (A) 1 mM ferrocene in 0.1 M  $\text{Et}_4\text{NClO}_4/\text{acetonitrile}$  and at 25 °C, potential step time = 4 s, 0–0.8 V vs Ag; (B) 5 mM  $\text{CpFeCpCH}_2\text{N}(\text{CH}_3)_3^+$  dissolved in network  $\text{PEO}/\text{LiClO}_4$  (O/Li = 50), at 35 °C with potential step time of 100 s, 0–1.0 V vs Ag; Cottrell plot at  $r = 5 \mu\text{m}$  disk of (C) undiluted 429 mM  $\text{CpFeCp}(\text{O})\text{NH-MPEG}$  polymer with  $\text{LiClO}_4$  electrolyte salt (O/Li = 16) at 55 °C, with a potential step time of 45 s, 0–1.0 V vs Ag; and (D) 429 mM undiluted,  $\text{CpFeCp}(\text{O})\text{NH-MPEG}$  polymer with  $\text{LiClO}_4$  electrolyte salt (O/Li = 16) at 25 °C with a potential step time of 100 s, 0–0.1 V vs Ag. Time ( $t$ ) is in seconds.

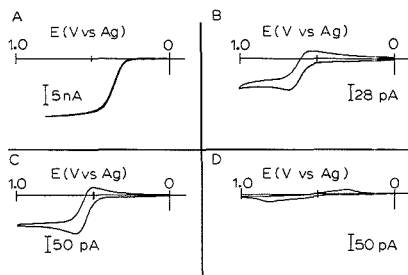


**Figure 3.** Microelectrode cyclic voltammetry at a sweep rate of 5 mV/s for (A) 1 mM ferrocene in 0.1 M  $\text{Et}_4\text{NClO}_4/\text{acetonitrile}$ ,  $r = 12.5 \mu\text{m}$ , temperature = 25 °C, (B) 5 mM  $\text{CpFeCpCH}_2\text{N}(\text{CH}_3)_3^+$  dissolved in network  $\text{PEO}/\text{LiClO}_4$  (O/Li = 50),  $r = 12.5 \mu\text{m}$ , temperature = 35 °C, (C) undiluted, 429 mM  $\text{CpFeCp}(\text{O})\text{NH-MPEG}$  polymer with  $\text{LiClO}_4$  electrolyte salt (O/Li = 16),  $r = 5 \mu\text{m}$ , temperature = 55 °C, and (D) undiluted, 429 mM  $\text{CpFeCp}(\text{O})\text{NH-MPEG}$  polymer with  $\text{LiClO}_4$  electrolyte salt (O/Li = 16),  $r = 5 \mu\text{m}$ , temperature = 25 °C.

solutions whose voltammetry is displayed in Figure 3. Of particular interest are the shapes of the Cottrell plots with reference to the corresponding voltammograms. Ferrocene diffuses in a fluid (acetonitrile) solution (Figure 3A) with  $D = 2.8 \times 10^{-5} \text{ cm}^2/\text{s}$  and gives a classical steady state current microelectrode voltammogram. Diffusion is fast enough that, on the relatively slow time scale of the potential step experiment (Figure 2A), the same steady state limiting current has already been attained.

The 5 mV/s voltammetry of  $\text{CpFeCp-CH}_2\text{N}(\text{CH}_3)_3^+$  in network PEO at 35 °C, as noted above, does not achieve a steady state current response, but (Figure 3B) exhibits moderate current peaking and hysteresis typical of partial linear diffusion control. When this polymer solution is observed on a somewhat faster chronoamperometric time scale, the Cottrell plot (Figure 2B) exhibits a linear segment but also a nonzero intercept indicating a long-time contribution from radial diffusion. This polymer exhibits a  $D = 1.4 \times 10^{-6} \text{ cm}^2/\text{s}$ .

Figure 3C,D and Figure 2C,D are cyclic voltammograms and Cottrell plots, respectively, of the ferrocene-labeled polymer,  $\text{CpFeCp}(\text{O})\text{NH-MPEG}$ , at temperatures above and below its melting temperature, respectively. In this case the ferrocene-labeled polymer chain serves as both electroactive moiety and electrolyte-dissolving solvent, and the diffusion

process is linear polymer self-diffusion. The polymer exhibits a melting transition at 53 °C; self-diffusion is thus much faster at 55 °C than at 25 °C. Ionic mobility in the polymer electrolyte also changes with temperature, so that large uncompensated resistance effects are encountered at the lower temperature, even at slow potential sweep rates, as is evident from the cyclic voltammogram (Figure 3D). The  $R_{\text{uncomp}}C$  time constant for establishing the potential step control at the microdisk electrode also seems to be quite long in the room temperature Figure 2D experiment, where the currents settle to the Cottrell line only after ca. 15 s. The excess, short-time charge in the Figure 2D response is a very small quantity, ca.  $10^{-10} \text{ equiv}/\text{cm}^2$ , which is consistent with a double layer capacitive charge, or possibly a monolayer of adsorbed charge. The time constant to attain Cottrell behavior is smaller (ca. 1 s) at 55 °C (Figure 2C), since the polymer electrolyte is more conductive there, but the excess short-time charge is too large to be solely capacitive and presumably represents Faradaic reaction of solvent impurities. We did not attempt to correct these effects with "blank" (no ferrocene) experiments, since the ferrocene is attached to the polymer solvent molecule. At 55 °C, there is a nonzero intercept associated with a radial contribution at the longest times, whereas the Cottrell plot passes through the origin (as ideally expected) at 25 °C where the diffusion is much slower and more exactly linear.

## DISCUSSION

We next consider extraction of diffusion coefficient values from data like the above. The chronoamperometric response at a microdisk is mathematically expressed (38) as

$$i = nFAD^{1/2}C/(\pi t)^{1/2} + arnFDC \quad (1)$$

where  $A$  and  $r$  are electrode area and radius, and the other terms have their usual meaning.  $a$  is a coefficient that depends on both electrode geometry and experimental time scale. For  $\tau > 50$ ,  $a = 4$  for a microdisk; however, for  $\tau \leq 50$ , a more complex expression is required. Shoup and Szabo (39) have presented a more detailed analytical expression describing the total current at a microdisk

$$i = 4nFDrC\{0.7854 + 0.8862\tau^{-1/2} + 0.2146 \exp(-0.7823\tau^{-1/2})\} \quad (2)$$

where  $\tau$  is as noted earlier

$$\tau = 4Dt/r^2 \quad (3)$$

When  $\tau < 0.01$  (i.e., slow diffusion or short time), eq 2 reduces to the Cottrell equation for linear diffusion

$$i = nFAD^{1/2}C/(\pi t)^{1/2} \quad (4)$$

When  $\tau > 50$ , eq 2 simplifies to the time-independent expression for currents at microdisk electrodes under radial diffusion control

$$i = 4nFrDC \quad (5)$$

Analogous, detailed computational theory for the mixed diffusion problem in the context of potential sweeps has been recently presented by Bond and Oldham et al (4).

Equations 4 and 5 represent extremes of diffusion behavior which have the virtues of great simplicity for data analysis. In a given circumstance, experimental conditions representing these extremes can, in principle, be sought by manipulation of the electrode radius and experimental time-scale variables represented in the parameter  $\tau$ . When microelectrodes are used, linear diffusion requires keeping the electrolysis time as short and the electrode radius as large as practical, within the constraint of avoiding debilitating uncompensated resistance effects. (The chosen redox solute concentration is an additional variable in the latter regard.) Radial diffusion can be sought by increasing the electrolysis time or by decreasing the electrode radius, again within practical limits.

Table I. Diffusion Coefficients and Variables Necessary for Calculation of  $\tau$  for the Polymer Systems Studied

	solvent	$r$ , $\mu\text{m}$	concn, mM	temp, $^{\circ}\text{C}$	time, <sup>b</sup> s			diffusion coefficients, <sup>d</sup> $\text{cm}^2/\text{s}$		
					$t_{\text{linear}}$	$t_{\text{radial}}$	$t_{\text{meas}}^c$	$D_{\text{CV}}$	$D_{\text{CA}}$	$D_{\text{int}}$
CpFeCp	aceto <sup>a</sup>	12.5	1	25	$1.4 \times 10^{-4}$	0.7	40	$2.8 \times 10^{-5e}$		$(2.7 \times 10^{-5})$
CpFeCpCH <sub>2</sub> N(CH <sub>3</sub> ) <sub>3</sub> <sup>+</sup>	network PEO	12.5	5	35	0.26	$1.3 \times 10^3$	3-100	$(2.2 \times 10^{-8})$	$1.4 \times 10^{-8e}$	$(1.1 \times 10^{-8})$
CpFeCpCH <sub>2</sub> N(CH <sub>3</sub> ) <sub>3</sub> <sup>+</sup>	network PEO	12.5	5	56	0.12	590	10-80	$(4.6 \times 10^{-8})$	$4.4 \times 10^{-8e}$	$(9.9 \times 10^{-9})$
CpFeCpCH <sub>2</sub> N(CH <sub>3</sub> ) <sub>3</sub> <sup>+</sup>	network PEO	12.5	5	74	$4.2 \times 10^{-5}$	210	50	$(9.3 \times 10^{-8})$		
CpFeCpC(O)NH-MPEG	undiluted labeled MPEG	5	429	55	0.89	$4.4 \times 10^3$	5-40	$(1 \times 10^{-9})$	$7.4 \times 10^{-9e}$	$(6.0 \times 10^{-9})$
CpFeCpC(O)NH-MPEG	undiluted labeled MPEG	5	429	25	120	$5.9 \times 10^6$	30-100	$(1.0 \times 10^{-11})$	$4 \times 10^{-12e/f}$	

<sup>a</sup> Acetonitrile. <sup>b</sup>  $t_{\text{linear}}$  corresponds to the maximum time, after applying a potential, at which linear diffusion accounts for >90% of response.  $t_{\text{radial}}$  corresponds to the minimum time, after applying a potential, at which radical diffusion accounts for >90% of response.  $t_{\text{meas}}$  is the time (or range of times) at which  $D$  was measured. <sup>c</sup> The first and fourth times are cyclic voltammetric sweep times, and the remaining are chronoamperometric step times. <sup>d</sup>  $D_{\text{CV}}$  was determined by measuring the current 100 mV after  $E^{\circ}$  and applying eq 5.  $D_{\text{CA}}$  was determined from a comparison of experimental data with an iterative calculation based on eq 2 (method a), and  $D_{\text{int}}$  was determined from the y intercept of a Cottrell plot of the experimental data (method b). <sup>e</sup> Most reliable data; other values are shown in parentheses. <sup>f</sup>  $D_{\text{CA}}$  was determined from the slope of a Cottrell plot.

The experiments shown in Figure 2A and 3A, and 2D and 3D, represent examples of the extremes of large and small  $\tau$ , respectively, that occurred primarily by the use of small  $r$  in a fluid electrolyte, and by encountering very small  $D$  in a polymer solvent, respectively. The diffusion rate in the fluid electrolyte was obtained by using eq 5 and that in CpFeCpC(O)NH-MPEG with eq 4; these results are given by the top and bottom entries, respectively, in Table I. The Cottrell plot for the ferrocene-tagged polymer yields a linear segment only at longer time (due to the excess short-time currents noted above), but that linear segment extrapolates to the origin in the manner ideally expected for a linear diffusion regime. The cyclic voltammetry of this polymer (Figure 3D) also illustrates the connection between extremely slow redox molecule diffusion and low diffusivity of the electrolyte ions; the voltammetry is severely spread out due to uncompensated  $iR$ .

To represent, or detect, mixed radial/linear diffusion, which we call the "transition region", it is useful to plot eq 2 in a log-log fashion as in Figure 4. The current axis has been normalized by dividing by eq 5, so large values of  $\tau$  giving radial diffusion conditions give  $\tau$ -independent currents, whereas small values of  $\tau$  give a linear log-log plot with a slope of  $-0.5$  (i.e., eq 4). Figure 4 also represents the errors (in the measured  $D$ ) associated with using one or the other limiting eqs (4 or 5) when  $\tau$  equals some value within the transition region. The errors have been calculated by numerical comparisons of eq 2 vs eqs 4 and 5. Thus, when  $\tau = 0.01$ , there is a 5% error associated with using the linear diffusion eq 4 (rather than exact theory), and when  $\tau \approx 100$ , there is a 5% error associated with using the radial diffusion eq 5 rather than the exact eq 2. Figure 4 is thus a convenient guide in the treatment of experimental results that provides insight as to the calculational penalty for employing simple diffusion theory in mixed diffusion chronoamperometry. It is noted that a comparison of Figure 4 of this paper with the values in Table I of ref 4, indicates the same numerical error associated with assuming purely radial conditions, and that plots analogous to Fig. 4 can be found in the literature for potential sweeps (40, 41) and for microbands (42, 43).

Mixed diffusion situations prove to be common in polymer solution voltammetry with 10 and 25  $\mu\text{m}$  microdisks (which are convenient with respect to fabrication and longevity); the experiments of Figures 2B and 3B and 2C and 3C of CpFeCp-CH<sub>2</sub>N(CH<sub>3</sub>)<sub>3</sub><sup>+</sup> in network PEO at 25  $^{\circ}\text{C}$  and of CpFeCpC(O)NH-MPEG at 55  $^{\circ}\text{C}$  are examples. The cyclic voltammograms in these cases display slight current peaks and a non-steady-state current response, indicating that both linear and radial geometries contribute to the diffusion. The Cottrell plots for both solutions (Figures 2B and 2C) give linear segments; that for the ferrocene-labeled polymer, as in Figure

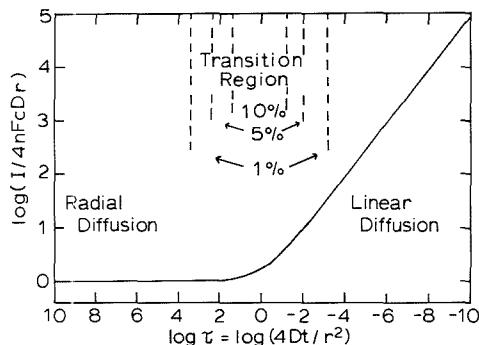


Figure 4. log-log plot of eq 2. The current axis has been normalized by dividing by eq 5 (see text), and the dotted lines represent the error association with using one or the other limiting equations 4 or 5 when  $\tau$  equals some value within the transition region.

2D, is brief owing to the time constant problem noted above. Both polymer solutions also give plots with positive intercepts as would be expected from eq 1 when there is a mixed contribution to diffusion.

We calculated the diffusion coefficient in polymer solutions exhibiting mixed diffusion like Figure 2B,C in three ways: (a) comparing the experimental current-time data to a curve calculated from eq 2 using  $D_{\text{CA}}$  as the iterated parameter, (b)  $D_{\text{int}}$  from the intercept of a linear extrapolation of the Cottrell plot using eq 1, and (c)  $D_{\text{CV}}$  from the pseudo-steady-state limiting current of the cyclic voltammograms in Figure 3B,C. In the first instance, an initial Cottrell line was drawn as shown in Figure 2B,C to give a preliminary estimate of  $D_{\text{CA}}$ . The results for the mixed diffusion cases are given by the second and fifth entries in the  $D_{\text{CA}}$  column in Table I and the corresponding measurement times are given in the column labeled  $t_{\text{meas}}$ . As anticipated, when the voltammetry has a pseudo-steady-state character (like Figure 3B,C), the  $D_{\text{CV}}$  evaluated from the pseudo-steady-state limiting current tends to be larger than that ( $D_{\text{CA}}$ ) obtained from the eq 2 iteration. The difference is greatest for a very slowly diffusing redox molecule (CpFeCpC(O)NH-MPEG at 25  $^{\circ}\text{C}$ ), because its diffusion profile is most remote from achieving steady state. Secondly, the values of  $D_{\text{int}}$  obtained from the intercept of the Cottrell plot are consistently the smallest and are lower than that from the eq 2 iteration (Table I). The difference between  $D_{\text{CA}}$  from the iteration (method a) and  $D_{\text{int}}$  from the intercept (method b) comes about because a linear extrapolation to the intercept was used to obtain  $D_{\text{int}}$  in Figure 2B,C, whereas the exact eq 2 predicts curvature in a Cottrell plot at small values of  $t^{-1/2}$

(large times) leading to an intercept with current represented by eq 5 at very long time. The linear extrapolation produces  $D_{\text{int}}$  values that are too small. Finally, the  $D_{\text{CA}}$  values from the (method a) comparison of experimental and calculated current-time curves lie between the extremes of ( $D_{\text{CV}}$ ) using eq 5 and ( $D_{\text{int}}$ ) the intercept of a linear Cottrell plot extrapolation. These results, and those derived from linear Cottrell, zero-intercept results, are thought to give the best measure of the diffusion rates.

The reliability of the above measurements can be inspected by calculating  $\tau$  for the estimated  $D$  and the given time scale and electrode radius, with reference to Figure 4. We represent such calculations by using the  $t_{\text{linear}}$ ,  $t_{\text{radial}}$ , and  $t_{\text{mess}}$  columns in Table I.  $t_{\text{linear}}$  corresponds to the maximum time, after the potential step, at which linear diffusion accounts for  $\geq 90\%$  of the response (i.e.,  $\leq 10\%$  error in using eq 4).  $t_{\text{radial}}$  corresponds to the minimum time at which radial diffusion accounts for  $\geq 90\%$  of the response (i.e.,  $\leq 10\%$  error in using eq 5).  $t_{\text{mess}}$  is the experimental time scale. For ferrocene in fluid acetonitrile and for CpFeCpC(O)NH-MPEG at 25 °C, as noted above, the measurement time scale clearly falls into the "pure" radial and linear regimes, respectively. The cases of CpFeCp-CH<sub>2</sub>N(CH<sub>3</sub>)<sub>3</sub><sup>+</sup> in network PEO and CpFeCpC(O)NH-MPEG at 55 °C fall into the "transition region" of Figure 4; that is,  $t_{\text{mess}}$  does not, for either, lie well outside the linear and  $t_{\text{radial}}$  boundaries.  $t_{\text{mess}}$  is for both however, closer to the linear limit (i.e.,  $\tau < 1$ ), and the behavior of the Cottrell plots is consistent with this observation.

It is worthwhile at this point to consider some practical features of the tactics mentioned above, and of some others, for removing a particular experiment from the Figure 4 transition region, or at least from its central portion. Seeking linear diffusion conditions means using larger electrode radii and shorter electrolysis time; these tactics produce, however, larger currents, and the practical utility of this approach depends on the polymer solvent resistivity. Lower concentrations of the redox molecule offer relief from resistance effects, but the level of background currents ultimately limits this avenue. (In practical terms we have seldom been able to employ submillimolar concentrations.) Of course, when diffusion is very slow, achieving linear diffusion is easier, even with small microelectrodes (Figure 2D), but the sizes of the measured currents then become uncomfortably small. In the other direction, seeking radial diffusion conditions means using smaller electrodes or longer electrolysis times; the former tactic again is limited by the requirement of measurable currents and the latter by the overall system stability.

It should be evident from the sizes of the currents measured here, that current sensitivity is an especially important consideration for the given polymer solvents and microdisk electrodes. It appears that a basic change in electrode geometry and/or current measurement capability will be required to overcome this limitation. For this reason we have begun exploration of microband electrodes and of ac voltammetry in the polymer solvents and will report on these in the future. We believe that electrochemical voltammetry may be capable of quantitative measurements in solid materials, including other materials beside polymers, of both neutral and charged redox moieties diffusing even more slowly than the  $10^{-12}$  cm<sup>2</sup>/s diffusion rate described here. Hopefully, studies in this direction will open up electroanalytical opportunities in solid-state chemistry.

It should be noted that the theory for mixed diffusion at microelectrodes is already in the literature and that our presentation of it has been in the context of dealing with a new and unfamiliar situation. The mixed diffusion theories have been previously considered in the context of fast time experiments in fluid media where  $D$  is consistently in the  $10^{-6}$

to  $10^{-8}$  cm<sup>2</sup>/s range. They have not been, heretofore, applied to the measurement of very small diffusion coefficients. It has only been recently that solid-state voltammetry has provided an environment in which diffusion of redox probes is very slow but measurable.

The magnitudes of self-diffusion coefficients reported here for ferrocene labeled PEO raise interesting questions of both experimental and fundamental importance. Of experimental concern is the thickness of the diffusion layer as compared to the topology of the electrode and the size of the electroactive molecule. Typically it is assumed that the topological imperfections of the electrode surface (surface roughness) are small as compared to the thickness of the diffusion layer, therefore, the surface can be approximated as a smooth surface with a measurable area (14). However, if (because of a small  $D$ ) the diffusion profile is thin with respect to the surface roughness of the electrode, the microscopic rather than the macroscopic area would be necessary to correctly calculate the diffusion coefficient.

Fundamentally, if the size of the electroactive molecule is comparable to the thickness of the diffusion layer, one must ask if (i) Fick's laws of diffusion still apply and (ii) the concentration at the electrode surface is homogeneous and representative of the bulk solution. These are just a few of the questions which become more accessible to study (35, 45) as we become capable of measuring very low diffusion coefficients.

#### LITERATURE CITED

- (1) Aoki, K.; Tokuda, K. *J. Electroanal. Chem.* **1987**, *273*, 163.
- (2) Szabo, A.; Cope, D. K.; Tallman, D. E.; Dovach, P. M.; Wightman, R. M. *J. Electroanal. Chem.* **1987**, *217*, 417.
- (3) Saraceno, R. A.; Ewing, A. G. *J. Electroanal. Chem.* **1988**, *257*, 83.
- (4) Zoski, C. G.; Bond, A. M.; Coyle, C. L.; Myland, J. C.; Oldham, K. B. *J. Electroanal. Chem.* **1989**, *263*, 1.
- (5) Cheek, G. T.; Monery, R. *Anal. Chem.* **1989**, *61*, 1467.
- (6) Tokuda, K.; Morita, K.; Shimizu, Y. *Anal. Chem.* **1989**, *61*, 1763.
- (7) Penner, R. M.; Heben, M. J.; Lewis, N. S. *Anal. Chem.* **1989**, *61*, 1630.
- (8) Wightman, R. M.; May, L. J.; Michael, A. C. *Anal. Chem.* **1988**, *60*, 769A.
- (9) Wallingford, R. A.; Ewing, A. G. *Anal. Chem.* **1988**, *60*, 1975.
- (10) Bond, A. M.; Henderson, T. L. E.; Mann, D. R.; Mann, R. F.; Thormann, W.; Zoski, C. G. *Anal. Chem.* **1980**, *60*, 1878.
- (11) Oldham, K. B.; Zoski, C. G.; Bond, A. M.; Sweigart, D. A. *J. Electroanal. Chem.* **1988**, *248*, 467.
- (12) Andrieux, C. P.; Garreau, D.; Hapiot, P.; Saveant, J. M. *J. Electroanal. Chem.* **1988**, *248*, 447.
- (13) Montenegro, M. I.; Pletcher, D. J. *Electroanal. Chem.* **1988**, *200*, 371.
- (14) Howell, J. O.; Wightman, R. M. *J. Phys. Chem.*, **1984**, *88*, 3915.
- (15) Geng, L.; Murray, R. W. *Inorg. Chem.* **1986**, *25*, 311.
- (16) McDevitt, J. T.; Ching, S.; Sullivan, M.; Murray, R. W. *J. Am. Chem. Soc.* **1989**, *111*, 4528.
- (17) Watanabe, M.; Longmire, M. L.; Murray, R. W. *J. Phys. Chem.*, in press.
- (18) Geng, L.; Longmire, M. L.; Reed, R. A.; Barbour, C. J.; Murray, R. W. *Chem. Mat.* **1989**, *1*, 58.
- (19) Longmire, M. L.; Watanabe, M.; Zhang, H.; Wooster, T. T.; Murray, R. W., unpublished material.
- (20) Reed, R. A.; Geng, L.; Murray, R. W. *J. Electroanal. Chem.* **1986**, *208*, 185.
- (21) Shriver, D. F.; Papke, B. L.; Ratner, M. A.; Dupon, R.; Wong, T.; Brodwin, M. *Solid State Ionics* **1981**, *5*, 83.
- (22) Gorecki, W.; Andreani, R.; Berthier, C.; Armand, M.; Mali, M.; Roos, J.; Brinkman, D. *Solid State Ionics* **1986**, *18* & *19*, 295.
- (23) Armand, M. B. *Annu. Rev. Mater. Sci.* **1986**, *16*, 245.
- (24) Vincent, C. A. *Prog. Solid State Chem.* **1987**, *17*, 145.
- (25) Ratner, M. A.; Shriver, D. F. *Chem. Rev.* **1988**, *88*, 109.
- (26) Armand, M. B.; Chabango, J. M.; Duclot, M. *J. Fast Ion Transport in Solids*; Mundy, J. N., Shenoy, G. K., Eds.; Pergamon: New York, 1979; p 131.
- (27) Watanabe, M.; Sanui, K.; Ogata, N. *Macromolecules* **1986**, *19*, 815.
- (28) Stainer, M.; Hardy, L. C.; Whitmore, D. H.; Shriver, D. F. *J. Electrochem. Soc.* **1984**, *131*, 784.
- (29) Bard, A. J.; Faulkner, L. *Electrochemical Methods: Fundamentals and Applications*; John Wiley & Sons, Inc.: New York, 1980.
- (30) Chadwick, A. V.; Worboys, M. R. *Polymer Electrolyte Reviews*; MacCallum, J. R., Vincent, C. A., Eds.; Elsevier Applied Science: London, 1987; pp 275-314.
- (31) Smith, B. A.; Mumby, S. J.; Samulski, E. T.; Yu, L. *Macromolecules* **1986**, *19*, 470.
- (32) Weppner, J.; Huggins, R. A. *Annu. Rev. Mater. Sci.* **1978**, *8*, 269.
- (33) Basu, S.; Worrall, W. L. In *Proceedings of the Symposium on Electrode Materials and Processes for Energy Conversion and Storage*;

- Srinivasan, S., Will, F. S., Eds.; The Electrochemical Society: Princeton, NJ, 1977; p 861.
- (34) Watanabe, M.; Nagano, S.; Sanui, K.; Ogata, N. *Polym. J.* **1986**, *18*, 809.
- (35) Pinkerton, M. J.; LeMest, Y.; Zhang, H.; Watanabe, M.; Murray, R. W. *J. Am. Chem. Soc.*, in press.
- (36) Zalipsky, S.; Glion, C.; Zilkha, H. *Eur. Polym. J.* **1983**, *19*, 1177.
- (37) Ewing, A. G.; Dayton, M. A.; Wightman, R. M. *Anal. Chem.* **1981**, *53*, 1842.
- (38) Dayton, M. A.; Brown, J. C.; Stutts, K. J.; Wightman, R. M. *Anal. Chem.* **1980**, *52*, 946.
- (39) Shoup, D.; Szabo, A. *J. Electroanal. Chem. Interfacial Electrochem.* **1982**, *140*, 237.
- (40) Aoki, K.; Akimoto, K.; Tokuda, K.; Matsuda, H.; Osteryoung, J. J. *Electroanal. Chem. Interfacial Electrochem.* **1984**, *171*, 219.
- (41) Aoki, K.; Honda, K.; Tokuda, K.; Matsuda, H. *J. Electroanal. Chem. Interfacial Electrochem.* **1985**, *182*, 267.
- (42) Aoki, K.; Tokuda, K. *J. Phys. Chem.* **1987**, *237*, 163.
- (43) Morris, R. B.; Franta, D. J.; White, H. S. *J. Phys. Chem.* **1987**, *91*, 3556.
- (44) Petek, M.; Neal, T. E.; Murray, R. W. *Anal. Chem.* **1971**, *43*, 1069.
- (45) Seibold, J. D.; Scott, E. R.; White, H. S. *J. Electroanal. Chem. Interfacial Electrochem.* **1989**, *264*, 281.

RECEIVED for review September 12, 1989. Accepted December 21, 1989. This research was supported in part by grants from The Department of Energy and The National Science Foundation.

## Constant Potential Amperometric Detection at a Copper-Based Electrode: Electrode Formation and Operation

Peifang Luo, Sunil V. Prabhu,<sup>1</sup> and Richard P. Baldwin\*

Department of Chemistry, University of Louisville, Louisville, Kentucky 40292

**Copper-based chemically modified electrodes (CMEs) previously used for the amperometric detection of carbohydrate compounds can be prepared via several different chemical and electrochemical procedures including exposure of glassy carbon to a CuCl<sub>2</sub> solution galvanically with a Cu counter electrode and plating of metallic Cu by cathodic deposition. In the former case, the mechanism most likely involves the formation of a coating of slightly soluble CuCl by a spontaneous redox reaction between Cu<sup>2+</sup> and Cu metal. All of the Cu CMEs exhibit similar cyclic voltammetric and constant potential amperometric response toward carbohydrates and offer detection limits at the picomole level in chromatography applications.**

We have recently described the application of a Cu-based chemically modified electrode (CME) for the amperometric detection of carbohydrates and related compounds following separation by anion-exchange chromatography (1-3). This CME is of particular interest for two principal reasons. First, it offers detection capabilities in the nanomole-to-picomole range for simple mono- and oligosaccharides as well as related amino sugars, alditols, and aldonic, uronic, and aldaric acids. And second, it enables the detection to be carried out under constant potential conditions and thus is compatible with the simple constant-potential electrochemical detection units already in common use among chromatographers. Previous reports have focused on evaluating the analytical performance of the Cu CME and on applying it in specific chromatographic schemes for the separation and analysis of various carbohydrate compounds. To this point, however, comparatively little has been determined concerning the structure of the CME and its mechanism of operation. In this communication, we describe experiments that serve to provide more information concerning both of these questions.

\* Author to whom correspondence should be addressed.

<sup>1</sup> Current address: Merck & Co., P.O. Box 2000, Mail Code R80L-123, Rahway, NJ 07065.

### EXPERIMENTAL SECTION

**Reagents.** Carbohydrates and related compounds, purchased from Sigma or Fisher Chemical Cos., were used as received without further purification. Stock solutions (1.0 mM) were prepared in deionized water and were brought to the desired concentration and pH by dilution with mobile phase just prior to use. Mobile phases used for flow injection experiments were prepared from carbonate-free NaOH, and all solutions were degassed with N<sub>2</sub> before use.

**Electrodes.** CMEs were prepared from Models MF-2012 and MF-1000 glassy carbon electrodes obtained from Bioanalytical Systems (West Lafayette, IN). The various modification procedures employed are described in detail in the results section. The metallic copper electrode used for comparative experiments was made by sealing a 2-mm-diameter Cu wire in a glass tube; it was polished with alumina and held at -1.3 V vs Ag/AgCl for 3 min in 0.50 M NaOH before voltammetric scans were initiated. In most cases, the electrodes were cycled briefly from 0.0 to +0.6 V in 0.15 M NaOH before use in flow detection systems. This usually served to decrease background currents and the length of time required for the background to become stable.

**Apparatus.** Cyclic voltammetry (CV) was performed with a Pine Instrument Co. (Grove City, PA) Model RDE4 potentiostat with an Ag/AgCl (3.0 M NaCl) reference electrode and a platinum wire auxiliary electrode. Flow injection experiments were carried out with a Beckman Model 110B pump, an SSI (State College, PA) Model LP-21 pulse dampener, a Rheodyne (Berkeley, CA) Model 7125 injector with a 20- $\mu$ L sample loop, and a Bioanalytical Systems Model LC-4B amperometric detector. All experiments were performed at room temperature.

### RESULTS

In the initial report (1), the Cu CME was prepared simply by immersing a commercially available glassy carbon electrode assembly into an aqueous CuCl<sub>2</sub> solution. If, after several minutes of soaking, the electrode was removed from the copper solution and rinsed with water, a light-colored deposit that gradually changed to green could be seen to have formed spontaneously on the glassy carbon. Subsequent X-ray fluorescence measurements made on the modified electrode surface at this point indicated that the principal constituents of the deposit were Cu and Cl; scanning electron microscopy revealed that much of the film was in the form of hexagonally

Table I. Alternative Methods for Forming Cu CME

modification approach	medium	procedure	probable surface species	$E_0$ for glucose <sup>a</sup> (V vs Ag/AgCl)
A	0.050 M CuCl <sub>2</sub>	100 $\mu$ A reduction current was applied for 1–3 min	CuCl	+0.50
B	0.050 M Cu(NO <sub>3</sub> ) <sub>2</sub>	200 $\mu$ A reduction current was applied for 1–3 min	Cu metal	+0.48
C	0.050 M Cu(NO <sub>3</sub> ) <sub>2</sub>	a droplet of Cu(NO <sub>3</sub> ) <sub>2</sub> was placed onto GCE and allowed to air-dry; a drop of 0.15 M NaOH was placed onto the resulting film and allowed to air-dry	Cu(OH) <sub>2</sub> /CuO	+0.50

<sup>a</sup> CVs were obtained for 0.0050 M glucose in 0.15 M NaOH.

shaped crystalline structures, 1–2  $\mu$ m in diameter, seemingly embedded into and across the glassy carbon surface (2). When subsequently used in voltammetric and flow injection experiments, this electrode, referred to as a Cu CME, gave large currents between +0.4 and +0.6 V vs Ag/AgCl for the oxidation of numerous carbohydrates and related compounds. The principal requirement for the carbohydrate oxidation to be observed was that extremely basic conditions, with hydroxide concentrations of at least  $10^{-3}$  M, had to be maintained.

It was subsequently discovered that the procedure described above was successful in efficiently forming an active deposit on the glassy carbon surface only in those instances where the entire cell assembly, including the metallic electrical contacts, was submerged in the CuCl<sub>2</sub> solution. Furthermore, the rate of the deposition process could be greatly enhanced by deliberately attaching a short piece of freshly polished copper wire to the built-in electrical contact during exposure to the CuCl<sub>2</sub> solution. Under these conditions, the surfaces of both the glassy carbon electrode and the copper wire lost their initial shiny appearance and took on a dull white cast within 30 s. After the modification process was allowed to continue for 1 min and the electrode was removed from the solution and rinsed with deionized water, the glassy carbon gradually took on the same green color noted above. Most important, the performance of this electrode in CV and flow injection analysis of carbohydrate compounds was qualitatively the same as that of the Cu CME prepared by the original procedure.

Subsequently, several other variations in the CME preparation procedure, summarized in Table I, were investigated and found to produce electrodes possessing essentially the same activity toward carbohydrates. The variations studied included constant current reductive deposition from both CuCl<sub>2</sub> and Cu(NO<sub>3</sub>)<sub>2</sub> solutions and evaporative deposition of a Cu(NO<sub>3</sub>)<sub>2</sub> film. In addition, a metallic copper electrode, formed by sealing an ordinary Cu wire into a glass tube, was also considered. Each of these approaches produced electrodes that exhibited similar steady-state CVs in both blank and glucose-containing solutions. Shown, for example, in Figure 1 are voltammograms run in 0.50 M NaOH for both the plain copper wire electrode and a CME formed by electrodeposition from CuCl<sub>2</sub> (i.e., method A from Table I). In both cases, the CVs, which match those previously reported for metallic Cu electrodes in strongly alkaline solution (4–7), show evidence of all three Cu oxidation states. Specifically, the anodic waves labeled A, B, and C correspond to the formation of Cu(I), Cu(II), and Cu(III) species, respectively, while cathodic peaks D and E represent the re-formation of Cu(I) and Cu(0). (Note that here, as in the previous studies (4–7), wave C could be seen in CV only for NaOH concentrations of 0.2 M or higher.) The principal difference exhibited by electrodes prepared by the different procedures involved the current–voltage behavior seen on their very first CV scans. In particular, the principal anodic activity (i.e., B') for the CMEs prepared from CuCl<sub>2</sub> solution was shifted to more positive potentials on the initial scan. The precise appearance of these initial oxidation pro-

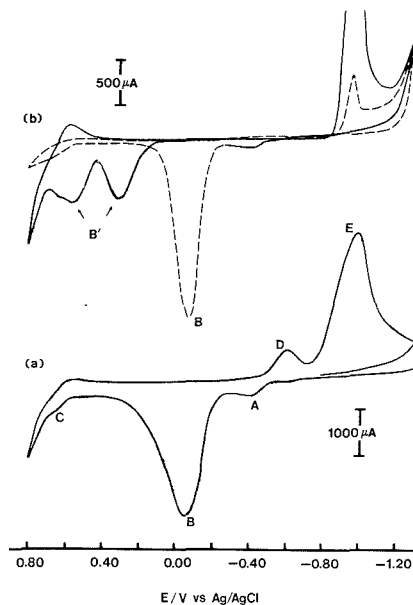
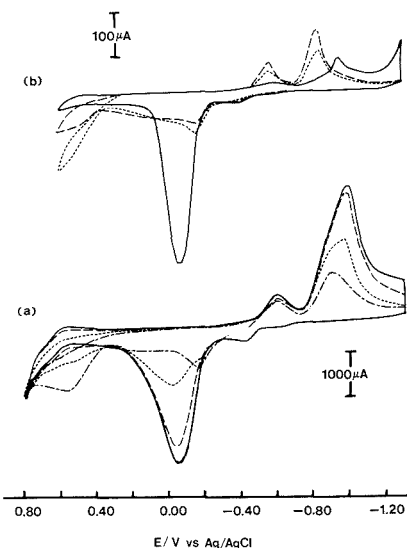


Figure 1. Cyclic voltammograms of (a) copper wire electrode and (b) Cu CME in blank solution: electrolyte, 0.50 M NaOH; scan rate, 20 mV/s; first cycle (—), second cycle (---).

cesses depended on the specific hydroxide concentration employed and the thickness of the film deposited onto the CME surface. For the 0.5 M NaOH conditions in Figure 1, at least two distinct oxidations were observed while, at lower basicity, the potentials of the waves shifted somewhat, occasionally to such an extent that nearly complete overlap occurred. But, in all cases, these waves disappeared on the second and all later scans; and the CV for the CME exactly matched that for the plain copper electrode. Interestingly, physical exposure of the Cu CME to strongly alkaline solutions changed the CME film to yellow. Subsequent scanning of the electrode potential to values more positive than the carbohydrate oxidation caused the electrode surface to take on a black or dark gray appearance. An additional effect of scanning to extremely positive potentials was a rapid deterioration of the CME surface that was reflected by decreased currents for all the waves in the succeeding CVs.

The primary effect of glucose addition on the CV behavior was also identical for both the Cu CME and the plain Cu electrode. As shown in Figure 2 for the CME, this consisted of a marked decrease in peaks B and E and the development of a new anodic wave at +0.50 V. It is worthwhile noting that this glucose-related wave, which was the one used for carbohydrate detection both here and in our earlier studies did not occur at a potential very close to either Cu(II) or Cu(III)



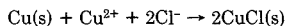
**Figure 2.** Cyclic voltammograms of (a) copper wire electrode and (b) CuCME in glucose-containing solution: electrolyte, 0.50 M NaOH; scan rate, 20 mV/s; glucose concentrations, 0.0 M (—), 0.0020 M (---), 0.010 M (-·-·-), and 0.030 M (- - -).

formation (waves B and C in Figure 1) but was very reminiscent of the wave seen for the initial CV scan in the blank (wave B'). The fact that electrodes formed via all the different procedures exhibited this same wave at +0.50 V and thereby gave useful carbohydrate detection capabilities demonstrates clearly that the presence of  $\text{Cl}^-$ , though helpful for CME formation according to our initial approach (1–3), was not essential to fabricate Cu-based electrodes capable of oxidizing carbohydrate compounds in an analytically useful fashion.

### DISCUSSION

While several aspects of carbohydrate oxidation at the Cu CME remain to be resolved, the experiments described above allow some of the important characteristics to be explained—in particular, the electrode itself and its likely mode of formation. Perhaps most important in this regard is the observation that formation of an active CME surface requires participation not only of  $\text{Cu}^{2+}$  but also of metallic Cu, either from the cell assembly's electrical contacts or from intentionally added Cu wire. This suggested to us the involvement of a galvanic  $\text{Cu}^+$ -forming redox reaction as a likely element in the formation of the CME. As the solubility of cuprous chloride is rather low (8), generation of a cuprous ion under the 0.1 M  $\text{Cl}^-$  conditions in effect might easily lead to the deposition of CuCl on the glassy carbon surface.

This possibility is supported indirectly by several additional factors. First, X-ray fluorescence analysis, described earlier (2), indicated that the freshly formed CME surface contains principally Cu and Cl. Second, experiments in which salts, such as  $\text{Cu}(\text{NO}_3)_2$ , were used in place of  $\text{CuCl}_2$  during open-circuit conditions failed to produce an active CME surface. Third, the initial deposition and subsequent reaction of CuCl accounts well for the appearance of the CME observed at various stages in its usage: light-colored initially and then green on exposure to air, CuCl; yellow, after exposure to NaOH,  $\text{Cu}_2\text{O}$ ; and black, after exposure to oxidizing potentials, CuO (8). Finally, measurement of the open-circuit potential during CME formation yielded a value consistent with that calculated for CuCl formation according to the reaction



The measured potential during CME formation was 260 ( $\pm 10$ ) mV, while the calculated value ( $[\text{Cu}^{2+}] = 0.050 \text{ M}$ ,  $[\text{Cl}^-] = 0.10 \text{ M}$ ,  $K_{sp}$  for CuCl =  $1.7 \times 10^{-7}$ ) was 243 mV.

Our conclusion, based on all these observations, is that the deposition of a CuCl film, according to the above reaction, represents the most likely explanation for the formation and initial state of the Cu CME as used previously for carbohydrate detection (1–3). It seems equally clear that, once formed and then subjected to other chemical and electrochemical conditions, the CuCl deposit is readily converted to a Cu/oxide or hydroxide system similar to that known to occur under highly basic conditions for metallic Cu (4–7). Thus, the freshly deposited CuCl film on its initial CV scan exhibited unique current-voltage properties that subsequently disappeared and were replaced by those characteristic of Cu metal electrodes. Most important, it is apparent that it is the latter, long-lived surface structure that is responsible for the CME's long-term activity toward carbohydrates.

The actual mechanism of the carbohydrate oxidation still remains difficult to specify with certainty. Previously, we have suggested an electrocatalytic mechanism for carbohydrate oxidation which might be initiated by a Cu(III) surface species (1, 2). An alternative possibility, suggested by the CV behavior in Figure 2, is that the active surface state might be a Cu(II) species whose formation is shifted from -0.05 V in blank NaOH solution to +0.5 V in the presence of the carbohydrate analyte. It is of interest that Van Effen and Evans reported that simple aldehydes undergo oxidation at both Cu(II) and Cu(III) oxide surfaces in 1.0 M NaOH (9). Furthermore, Cu(II) complexes have previously been used as postcolumn additives for the electrochemical detection of reducing sugars (10). In that approach, the Cu species reacts with the carbohydrate and becomes reduced to the cuprous state which can be monitored amperometrically by reoxidation to  $\text{Cu}^{2+}$ . However, in contrast to the current work, only reducing sugars gave such a response, and the response occurred at much lower potentials, in the vicinity of the solution-phase Cu(I)/Cu(II) redox couple at 0.0 V vs Ag/AgCl, than with the Cu CME. Thus, it appears that, even if the Cu(II) state is the important one for the CME, some factor such as adsorption or complexation of the carbohydrate analyte must be acting to shift the cuprous oxidation to the unusually positive potentials seen, for example, in Figure 2. A third possibility, suggested by the work of Frei et al. (11, 12), is that complexation of Cu(II) by the carbohydrates acts to solubilize the oxide/hydroxide layer present in basic solutions and thereby increase the current observed for copper oxidation. This phenomenon, however, was reported by Frei for amino acids as analytes—but only for much less basic conditions and at much lower potential than in the current work.

Finally, there is a particularly important question concerning the best form of Cu electrode to recommend for analytical applications—e.g., metallic copper or the Cu CME formed by any of the several procedures employed. Although any of the Cu electrodes studied here could be used in principle, we found that the Cu CME formed galvanically by attachment of a clean copper wire to the electrode assembly and immersion into 0.05 M  $\text{CuCl}_2$  seemed to exhibit marginally superior performance in terms of background noise levels, detection limits, and ease of operation. The Cu CME formed by this technique exhibited detection limits at the pmol level and provided sufficient stability and reproducibility that 100 glucose injections carried out over a 1.5-h period gave a relative standard deviation of less than 1%.

### LITERATURE CITED

- (1) Prabhu, S. V.; Baldwin, R. P. *Anal. Chem.* **1989**, *61*, 852–856.
- (2) Prabhu, S. V.; Baldwin, R. P. *Anal. Chem.* **1989**, *61*, 2258–2263.



- (3) Prabhu, S. V.; Baldwin, R. P. *J. Chromatogr.*, in press.  
(4) Miller, B. J. *Electrochem. Soc.* **1989**, *116*, 1675-1680.  
(5) Abd El Haleem, S. M.; Ateya, B. G. *J. Electroanal. Chem. Interfacial Electrochem.* **1981**, *117*, 309-319.  
(6) Pyun, C.-H.; Park, S.-M. *J. Electrochem. Soc.* **1986**, *133*, 2024-2030.  
(7) Drogowska, M.; Brossard, L.; Menard, H. *Corrosion (Houston)* **1987**, *43*, 549-552.  
(8) *The Merck Index*, 9th ed.; Merck & Co.: Rahway, NJ, 1976; pp 345-347.  
(9) Van Effen, R. M.; Evans, D. H. *J. Electroanal. Chem. Interfacial Electrochem.* **1979**, *103*, 383-399.  
(10) Watanabe, N.; Inoue, M. *Anal. Chem.* **1983**, *55*, 1016-1019.  
(11) Kok, W. Th.; Hanekamp, H. B.; Bos, P.; Frei, R. W. *Anal. Chim. Acta* **1982**, *142*, 31-45.  
(12) Kok, W. Th.; Brinkman, V. A. Th.; Frei, R. W. *J. Chromatogr.* **1983**, *266*, 17-26.

RECEIVED for review November 13, 1989. Accepted January 8, 1990. This work was supported by the National Science Foundation through EPSCoR Grant 86-10671-01 and by the University of Louisville College of Arts and Sciences.

## Fiber-Optic Glucose Sensor with Electrochemical Generation of Indicator Reagent

Hari Gunasingham,\* Chin-Huat Tan, and Jimmy K. L. Seow

Department of Chemistry, National University of Singapore, Kent Ridge, Singapore 0511

**An electrochemically generated tetrathiafulvalene redox mediator provides a convenient and reversible indicator reagent for a glucose fiber-optic sensor. The fabrication and characterization of this sensor based on a thin-layer cell configuration are described. The performance of the fiber-optic sensor is compared with that of an amperometric enzyme electrode in flow-injection and steady-state analyses. The upper limit of the linear range in the flow-injection mode is about 12 mM, whereas in the steady-state mode it is about 3 mM. The sensor is less prone to interfering species and dissolved oxygen. It can be used continuously for 2 days without significant loss of activity.**

### INTRODUCTION

Although the efficacy of fiber-optic sensors has been demonstrated in many analytical applications (1-3), they do suffer from a number of practical limitations that have prevented their more widespread use. One significant limitation is the difficulty of finding suitable, long-lasting, and reversible indicator reagents. Most colorimetric and fluorometric reagent systems are inherently irreversible because the analytical reaction invariably involves the formation of a tightly bound complex or an irreversible adduct.

The requirement of a suitable reversible reagent systems is a particular limitation when developing enzyme-based fiber-optic sensors. Consequently there have been only a few practical examples. There have been essentially three approaches to the development of such sensors:

- (i) The fiber-optic sensor directly measures enzymatic generation of a spectrophotometrically detectable product (4, 5).
- (ii) The product of the enzymatic reaction is detected through a secondary reaction resulting in a change in the optical properties of the indicator reagent. For example, a fiber-optic sensor for glucose has been developed where the principle of measurement is the change in the fluorescence of an oxygen-sensitive dye where fluorescence is quenched by oxygen (6). Another example is also a sensor for glucose determination based on chemiluminescence generated by reaction of peroxyoxalate with hydrogen peroxide formed in the enzymatic reaction (7).

(iii) A dehydrogenase enzyme is immobilized at the end of a fiber-optic probe with fluorometric detection of consumed or generated nicotinamide adenine dinucleotide for measurement of lactate or pyruvate (8). Here a fresh supply of nicotinamide adenine dinucleotide has to be provided in the external sample solution.

Another route to developing an enzyme-based fiber-optic sensor that has not been hitherto explored is to make use of a redox mediator dye as the indicator reagent. Such dyes have been well developed in conventional enzymatic analysis (9) and dry chemistry systems (10). The fundamental problem in regard to their application to fiber-optic sensors, however, is the fact that most redox dyes are irreversible. Consequently, it is necessary to provide a large reagent reservoir or provide a means of renewing the reagent.

The subject of this paper concerns the fabrication and characterization of a reversible enzyme-based fiber-optic sensor for glucose. Reversibility is afforded through the electrochemical regeneration of an optically active redox mediator. In this work, use is made of tetrathiafulvalene, which is a good redox mediator for glucose oxidase and also possesses desirable optical properties (11). The usefulness of the glucose fiber-optic sensor is demonstrated in steady-state and flow-injection analysis.

### EXPERIMENTAL SECTION

**Chemicals and Solutions.** Tetrathiafulvalene (TTF) (>99%) was obtained from Fluka Chemie AG, Buchs/Switzerland. Glucose oxidase (GOX) (EC 1.1.3.4 Type II from *Aspergillus niger*), bovine serum albumin (BSA) (fraction V 96-99% albumin), glutaraldehyde, (GLA) (25% aqueous), and D-(+)-glucose were from Sigma Chemical Co. (St. Louis, MO). All other reagents used were of AnalaR grade. All aqueous solutions were made up in 0.1 M pH 7.4 sodium phosphate buffer solution containing 0.01% (w/v) sodium azide prepared with Millipore Milli Q grade water. Glucose solutions were allowed to mutarotate overnight before use.

**Construction of Enzyme Electrode.** Working electrodes were made from disks cut from 3 mm diameter platinum (Johnson Matthey, England) or glassy carbon (Tokai, Japan) rods. Electrical contact was made with a copper wire connected to one side of the disk with silver-loaded epoxy resin. The disk was then press fit into a Teflon holder and sealed with epoxy resin so that only a circular plane was exposed. Electrodes were polished with abrasive paper and then mirror polished with 0.3- $\mu$ m diamond paste (K-5000, Kyoto, Japan). Prior to use, electrodes were

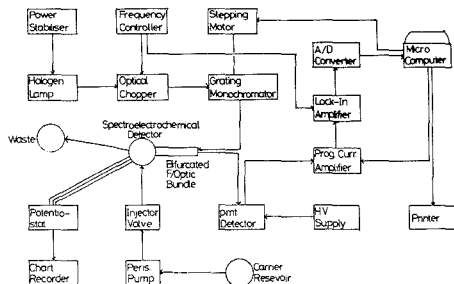


Figure 1. Schematic diagram of the optical-electrochemical system.

cleaned successively with ethanol and nitric acid and ultrasonically in distilled water. The electrodes were then oven-dried at 80 °C for 1 h.

Enzyme electrodes were prepared by evaporating droplets (2 × 5 μL) of TTF/acetone solution onto the electrode surface. Ten microliters of 4% glucose oxidase solution was deposited over the TTF layer and then dried at 4 °C overnight. Finally, 2.5 μL of freshly prepared 1:1 mixture of 5% BSA and 2.5% glutaraldehyde was deposited on top of the dried glucose oxidase and then covered with a polycarbonate membrane (0.03 μm pore size from Nuclepore, Pleasanton, CA). The membrane was held tightly in place with a Teflon cap. The enzyme electrode so made was allowed to set at 4 °C overnight.

**Optical System.** A schematic diagram of the experimental setup is given in Figure 1. The light source is a halogen lamp (12 V, 100 W, Halo Star, Watan, Germany) operated with a current stabilized power supply (Bentham, Model 505). The source light was modulated with an optical chopper (Bentham, Model 218) at a frequency of 200 Hz. The chopper frequency provided the reference input to the lock-in amplifier (LIA) (Princeton Applied Research, Model 5104).

A monochromator (Bentham, Model M300EA) utilizing a holographic grating (Bentham G324HOu24, 2400 lines/mm) coupled to a built-in stepping motor drive (Bentham, Model SMD38/IEEE) was used to obtain a wavelength range between 220 and 620 nm with a resolution of 0.5 nm. The light from the monochromator was passed through one arm of the bifurcated fiber-optic bundle (Quentron, Model 777-1, Australia).

The signal arising from specular reflection at the electrode is then passed through the other arm of the bifurcated fiber-optic bundle to the photomultiplier tube detector (Bentham, DH3 (UV)) powered by a high-voltage supply (Bentham, Model 215). The enhanced signal from the photomultiplier is delivered to the programmable current amplifier (Bentham, Model 265HF) and then to the LIA. The entire system was under the control of a computer (Model HP9826, Hewlett-Packard) via the HP-IB (IEEE/488) interface. The control software written in HPBASIC 3.0 enabled the measurement of intensity against time or wavelength.

Prior to each measurement, the reference and analytical signals were brought into phase at the input of the LIA's phase-sensitive detector. Optical measurements were then carried out at this fixed phase.

**Thin-Layer Cell.** Steady-state and flow-injection measurements were made with a modified thin-layer cell that enabled the fiber-optic probe and enzyme electrode to be mounted opposite each other. Figure 2 shows an exploded view of the thin-layer cell. The reference electrode was Ag/AgCl and the counter electrode was graphite. The working volume of the cell could be adjusted by varying the number of polyester film spacers (each of 125 μm thickness measured by a micrometer). The spacers had a central hold of 1 cm diameter. The entire cell was blackened to keep out ambient light. Sample solutions were injected by means of a four-way manual injector (Valve V-7, Pharmacia Fine Chemicals, Sweden). Sample solutions were delivered with a peristaltic pump (Eyela Model MP-3, Tokyo Rikakikai, Tokyo, Japan). The pump was calibrated prior to use. For the steady-state measurements, a large volume loop (1 mL) was used and the flow rate was kept at 0.4 mL/min. For the cyclic voltammetric studies, a continuous delivery of glucose solution was

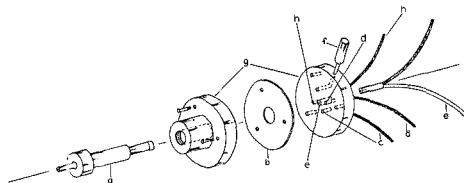


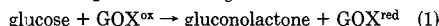
Figure 2. Exploded view of thin-layer cell: (a) enzyme electrode; (b) polyester spacer; (c) counter electrode; (d) solution inlet; (e) bifurcated fiber-optic bundle; (f) Perspex salt bridge for reference electrode; (g) Perspex body; and (h) solution outlet.

provided at 0.4 mL/min. In this way, a steady-state flux of glucose could be achieved over an extended period. For flow-injection analysis (FIA), a 50 μL volume loop was used which afforded the characteristic peak profiles.

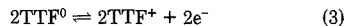
Cyclic voltammetry and amperometric studies were performed with a PAR potentiostat/galvanostat Model 273. Voltammograms and current-time curves recorded with an XY recorder (Gratpec, Model WX2400).

## RESULTS AND DISCUSSION

**Principle of Operation.** TTF has been shown to serve as a redox mediator for glucose oxidase (12). The redox mediation takes place via a homogeneous electron exchange between the first oxidation state, TTF<sup>+</sup>, and the enzyme active center. The glucose oxidase catalyzed reaction with glucose occurs according to the following scheme:



TTF<sup>+</sup> can be regenerated at the electrode surface



For practical purposes, we can define a reaction layer lying between the electrode surface and membrane wherein reactions 1 and 2 take place. TTF<sup>+</sup> is regenerated at the electrode surface and diffuses into the reaction layer. By monitoring the generation or consumption of TTF<sup>+</sup> in the reaction layer it is feasible to derive an analytical response that can be related to the glucose concentration. Higher glucose concentrations result in faster rates of TTF<sup>+</sup> reduction and lower TTF<sup>+</sup> levels. A steady-state flux of TTF<sup>+</sup> is established when the rate of its regeneration at the electrode is counterbalanced by the rate of its loss from the reaction layer.

The reaction scheme represented by eqs 1–3 indicates that the analytical signal is not dependent on the oxygen concentration. However, there is a possibility that there is competition between TTF<sup>+</sup> and oxygen for oxidation of GOX. Experiments were carried out in the air-saturated and deaerated solutions to verify this. It was found that the air-saturated solution resulted in a reduction in the steady-state amperometric signal by about 5%, whereas it had a negligible effect on the fiber-optic signal. The reduction in the amperometric signal is probably more due to the negative current arising from the reduction of H<sub>2</sub>O<sub>2</sub> than an effect on the TTF<sup>+</sup> concentration. This is confirmed by injecting a solution containing 2 mM H<sub>2</sub>O<sub>2</sub> which gave no significant fiber-optic signal but a reduction current for the amperometric signal.

In terms of its spectra characteristics, TTF<sup>+</sup> can be distinguished from the neutral TTF<sup>0</sup> by its ability to absorb in the visible region between 540 and 580 nm. This is shown in Figure 3, which records reflectance spectra at various applied potentials. As can be seen, the reflectance intensity around this wavelength range is greatly diminished with increasing potential due to the formation of TTF<sup>+</sup>.

Figure 4a further shows the decrease in the reflectance intensity (at 570 nm) with the formation of TTF<sup>+</sup> as the

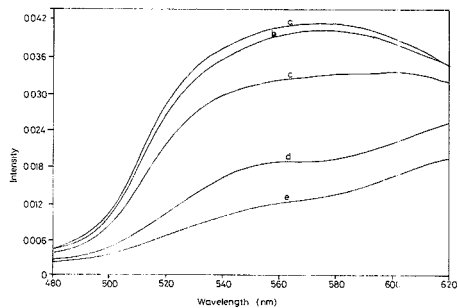


**Figure 3.** Specular reflectance spectra at Pt/TTF-GOX enzyme electrode for various applied potentials: (a) 0 mV, (b) 100 mV, (c) 200 mV, (d) 250 mV, (e) 300 mV; spacer thickness, 250  $\mu\text{m}$ ; flow rate, 0.4  $\text{mL min}^{-1}$ .

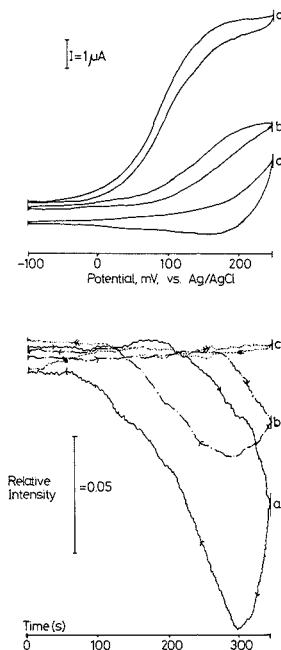


**Figure 4.** Cyclic voltammograms and corresponding reflectance intensity at Pt/TTF-GOX enzyme electrode in (a) phosphate buffer pH 7.4 (b) with 2 mM glucose solution or (c) with 10 mM glucose solution; cyclic voltammetry scan rate, 1 mV/s; reflectance wavelength, 570 nm; spacer thickness, 250  $\mu\text{m}$ ; flow rate, 0.4  $\text{mL min}^{-1}$ .

electrode potential is scanned to more positive values. The decreased reflectance intensity arises because of the increased absorption of light as the  $\text{TTF}^+$  concentration increases. In the reverse scan (to more negative potentials) the reflectance intensity increases due to the reduction of  $\text{TTF}^+$  back to the neutral state, indicating the reversible nature of the redox mediator.

In the presence of 2 mM glucose, the amount of  $\text{TTF}^+$  in the reaction layer is diminished via reactions 1 and 2. Figure 4b thus shows the reflectance intensity to be higher at more positive potentials compared to Figure 4a.

In the presence of excess glucose, however, the reflectance intensity of Figure 4c appears to be relatively unaffected as the potential is scanned to more positive potentials. This is

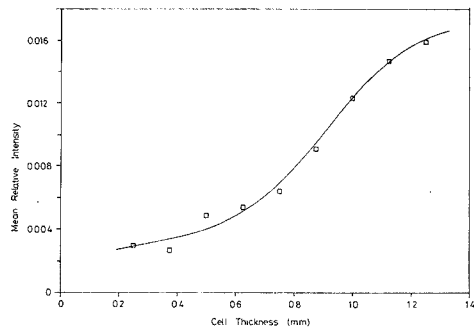


**Figure 5.** Effect of cell thickness on relative reflectance intensity: glucose concentration, 6 mM glucose; operating potential, 250 mV vs Ag/AgCl; sample volume, 50  $\mu\text{L}$ . Other conditions are the same as in Figure 4.

because all the  $\text{TTF}^+$  in the reaction layer is converted to  $\text{TTF}^0$  via the enzymatic reaction or lost by diffusion through the membrane. In this case  $\text{TTF}^+$  generated at the electrode surface is immediately reduced as it diffuses into the reaction layer.

In contrast with the response of the TTF coated enzyme electrode described above, it was found that a glucose oxidase immobilized electrode without TTF loading gave no significant response in the wavelength range between 400 and 620 nm. As might be expected, the reflectance signal from the glassy carbon electrode was generally found to be lower (by about a factor of 10) and noisier than the absolute reflectance signal from the platinum electrode. While this reduced the sensitivity of the detector, the response time and upper linear range were unaffected.

**Effect of Cell Thickness.** Increasing the cell thickness was found to enhance the reflected light intensity, although the response time was slightly increased. The effect of cell thickness on the relative intensity (with reference to the base line prior to the injection of glucose) on flow-injection peak is shown in Figure 5; the increase in intensity is due to two factors:

First, it is due to an increase in the effective area of the electrode (or reaction layer) exposed to the incident light from the fiber-optic probe. Also, when a bifurcated fiber-optic bundle is used, up to a point, the further the reflector is away, the greater the overlap between the "cone of light" emerging from the fiber (from the source) and the "cone of light" accepted by the fiber (to the detector). The enhancing effect of increasing the cell thickness, however, reaches a limit at around 1.2 mm, presumably where maximum overlap of the "cones of light" occurs.

Second, the enhancement of the reflected light intensity is due to the increase in residence time in the cell as the cell thickness increases. The longer the residence time, the larger the time scale and the more  $\text{TTF}^+$  that is consumed.

**FIA Response.** Figure 6a shows reflectance light intensity (with reference to the base line prior to injection of glucose) versus time plots for injections of increasing concentrations of glucose in the FIA mode. Before a sample injection, the concentration of  $\text{TTF}^+$  in the reaction layer is a maximum and, consequently, the base-line reflectance intensity-time response is a minimum. When the glucose sample is injected into the cell, the reflected light changes as the  $\text{TTF}^+$  concentration in the reaction layer changes in relation to the glucose concentration profile as the sample plug passes through the cell.

It is of interest that the corresponding current-time plots for amperometric detection are significantly sharper than the

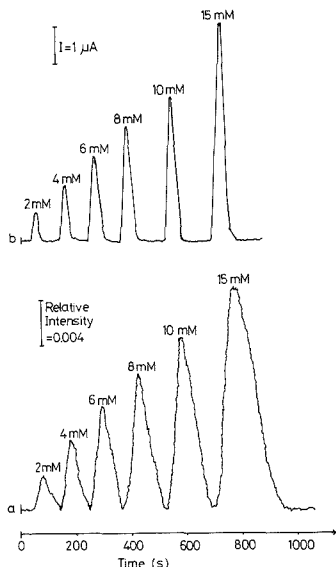


**Figure 6.** FIA peak profiles for (a) fiber-optic sensor and (b) amperometric sensor: operating potential, 250 mV; flow rate, 0.4 mL/min; sample volume, 50  $\mu$ L; spacer thickness, 500  $\mu$ m; TTF loading, 25  $\mu$ g.

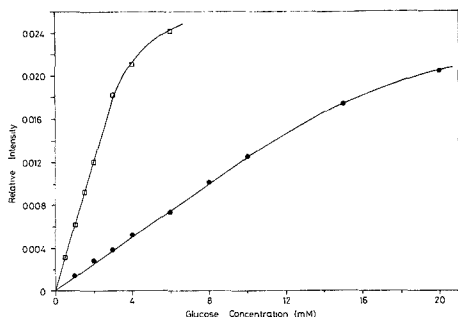


**Figure 7.** Calibration plots for glucose-based enzyme electrode: (□) steady-state mode, (●) FIA mode; operating potential, 250 mV; flow rate, 0.4 mL/min; spacer thickness, 500  $\mu$ m; TTF loading, 5  $\mu$ g.

reflectance-time plots of the fiber-optic sensor. Closer examination of these plots shows that the contribution to band broadening for the fiber-optic sensor response arises mainly in the trailing edge of the peak. By way of comparison, for the 15 mM glucose sample, the time taken to reach the peak apex was 50 and 65 s for amperometric and fiber-optic detection, respectively. In contrast, the time taken to reach the base line from the apex to the trailing edge was 80 and 180 s, respectively.

The particularly slow response in the trailing edge is due to the fact that regeneration of TTF<sup>+</sup> in the reaction layer (via electrochemical oxidation and diffusion) takes place relatively slowly. There is also a lag time due to the time taken for the TTF<sup>+</sup> to diffuse in the channel. The latter can be reduced by using smaller spacers.

**Linear Range.** Figure 7 compares the linear range for the fiber-optic sensor in the steady-state and FIA modes. As in Figures 5 and 6, the reflectance intensity is measured with reference to the base-line reflectance intensity prior to in-

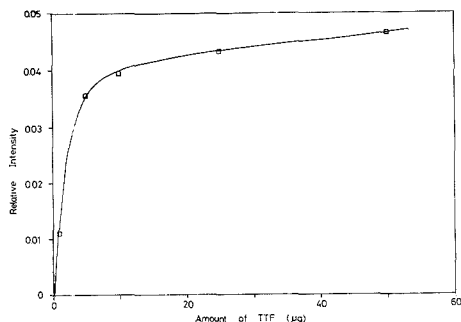


**Figure 8.** Effect of TTF loading on electrode surface on steady-state reflectance: electrode, platinum; steady-state reflectance measured with 2 mM glucose solution; working potential, 250 mV; cell thickness, 500  $\mu$ m.

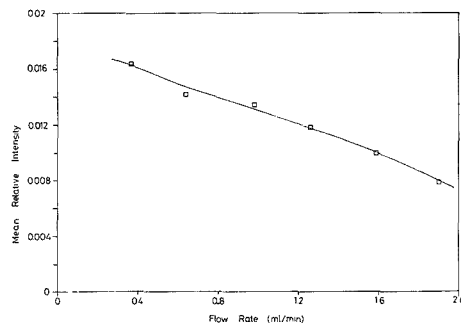


**Figure 9.** Effect of flow rate on relative reflectance intensity. Conditions are the same as in Figure 7. Glucose concentration was 6 mM.

jection of glucose. In general, the upper limit for the former is about 3 mM, whereas for the latter it is about 12 mM.

The generally lower linear range can be attributed to the fact that, under steady-state conditions, the glucose concentrations in the cell are higher. Consequently, most of the TTF<sup>+</sup> in the reaction layer is converted to TTF<sup>0</sup>.

The way of overcoming this is by increasing the concentration of TTF<sup>+</sup> in the reaction layer. This can be done to a limited extent by increasing the TTF loading on the electrode. A study of the effect of TTF loading was made by recording relative intensity with reference to the base line prior to the injection of 6 mM glucose at +250 mV against TTF loading as shown in Figure 8. Increasing the loading appears to initially improve the relative response reaching a limiting value after a loading of about 10  $\mu$ g. At this level of loading the linear range can be extended to about 15 mM.

**Effect of Flow Rate.** Figure 9 shows the effect of flow rate on the FIA response. The relative intensity with reference to the base-line intensity varies approximately as the inverse square root of flow rate, which is related to the reduced residence time of the glucose sample.

**Stability.** The stability of the electrode mostly depends on the availability of TTF. For this reason, the lifetime of the fiber-optic electrode will be substantially reduced if the applied potential on the electrode is continuously held at a positive value resulting in the loss of TTF as TTF<sup>+</sup>. In our work, we have used the fiber-optic electrode continuously for 2 days with only a slight reduction in the response.

**Comparison of Fiber-Optic Electrochemical Detection and Amperometric Detection.** Table I compares the performance of fiber-optic electrochemical detection and am-

Table I. Comparison of Fiber-Optic and Amperometric Detection<sup>a</sup>

	fiber-optic	amperometric
	Linear Range	
steady state	4 mM	20 mM
FIA	12 mM	40 mM
detection limit	0.2 mM	0.005 mM
	Interfering Species <sup>b</sup>	
ascorbic acid	1.6	2.4
paracetamol	N.D. <sup>b</sup>	0.1
uric acid	N.D.	0.3
lysine	N.D.	N.D.
leucine	N.D.	N.D.
N <sub>2</sub> O <sub>2</sub>	N.D.	-1.2 <sup>d</sup>
effect of oxygen <sup>e</sup>	N.D.	-5%

<sup>a</sup>Electrode = platinum. Operating potential = 250 mV. Cell thickness = 500  $\mu$ m. TTF loading = 5  $\mu$ g. Flow rate = 0.4 mL/min. Reflectance wavelength = 570 nm. <sup>b</sup>N.D., no signal detected for species. <sup>c</sup>Data for interferences presented are given in terms of the ratio of the signal for 2 mM interfering species to the signal of 2 mM glucose solution. <sup>d</sup>Negative sign arises because H<sub>2</sub>O<sub>2</sub> gives a reduction current at this potential. <sup>e</sup>Data presented are the relative signal of air-saturated solution to the deaerated solution 2 mM glucose.

perometric detection based on the TTF-mediated enzyme electrode. The linear range for fiber-optic electrochemical detection was lower than that for amperometric detection. The detection limit for amperometric detection was found to be about 0.005 mM, compared to fiber-optic electrochemical

detection, which has a detection limit of about 0.2 mM. Table I also compares the effect of various chemical species and oxygen on the response of the fiber-optic and amperometric detector. It is of interest that the fiber-optic sensor appears to be relatively less sensitive to these species. Also, no significant effect on oxygen of the fiber-optic response is observed.

## ACKNOWLEDGMENT

We acknowledge the assistance of Ishak bin Ismail in constructing the thin-layer cell.

## LITERATURE CITED

- (1) Seitz, W. R. *CRC Crit. Rev. Anal. Chem.* **1988**, *19*, 135.
- (2) Seitz, W. R. *Anal. Chem.* **1984**, *56*, 16A.
- (3) Peterson, J. I.; Vureck, G. G. *Science* **1984**, *224*, 123.
- (4) Arnold, M. A. *Anal. Chem.* **1985**, *57*, 565.
- (5) Wolfbeis, O. S. *Anal. Chem.* **1985**, *58*, 2876.
- (6) Tretnak, W.; Leiner, M. J. P.; Wolfbeis, O. S. *Analyst* **1988**, *113*, 1519.
- (7) Abdel-Latif, M. S.; Guilbault, G. G. *Anal. Chem.* **1988**, *60*, 2671.
- (8) Wangsa, J.; Arnold, M. A. *Anal. Chem.* **1988**, *60*, 1080.
- (9) Blick, K. E.; Liles, S. M. *Principles of Clinical Chemistry*; J. Wiley and Sons: New York, 1985; Chapter 10.
- (10) Walter, B. *Anal. Chem.* **1983**, *55*, 499A.
- (11) Kaufman, F. B.; Schroeder, A. H.; Engler, E. M.; Kramer, S. R.; Chambers, J. Q. *J. Am. Chem. Soc.* **1980**, *102*, 483.
- (12) Albery, W. J.; Bartlett, P. N.; Craston, D. H. *J. Electroanal. Chem.* **1985**, *194*, 223.

RECEIVED for review April 10, 1989. Accepted December 13, 1989. This work was supported by the award of grants from the National University of Singapore and the Singapore Science Council.

## Poly(vitamin B<sub>12</sub>)-Modified Carbon Electrodes Used as a Preconcentration-Type Sensor for Alkylating Agents

Beat Steiger, Annette Ruhe, and Lorenz Walder\*

*Institute of Organic Chemistry, University of Berne, Freiestrasse 3, CH-3012 Berne, Switzerland*

A multiple-use electrochemical sensor for alkylating agents based on a poly(vitamin B<sub>12</sub>) chemically modified electrode (B<sub>12</sub>-CME) is described. Preconcentration is switched on and off depending on the applied potential, i.e. the presence of Co(I). It is related to oxidative addition of RX from dilute solutions to the immobilized vitamin B<sub>12a</sub> (Co(II)-R) yielding surface-confined alkylcobalamins (Co(III)-R). With cyclic voltammetry the solution concentration of RX (primary alkyl iodides and bromides) can be correlated with the reduction current of the alkylcobalamins. The detection limit ([RX]<sub>DL</sub>) depends on preconcentration time ( $\tau$ ) and the homogeneous reactivity of vitamin B<sub>12a</sub> (Co(I)) toward RX ([CH<sub>3</sub>I]<sub>DL</sub> = 4.3  $\times 10^{-7}$  M for  $\tau$  = 5 min). Concomitant with a measurement the B<sub>12</sub>-CME is regenerated. Photocurrents are observed at the B<sub>12</sub>-CME in the presence of alkylating agents when it is illuminated with visible light. The potential-dependent formation and cleavage of an organometallic adduct between CME sites and the analyte are considered a new sensor principle suited for organic analytes.

In recent years chemically modified electrodes (CMEs) have found broad applications as sensors in electroanalysis (1, 2). The concepts used for increasing the current response of an

electroactive analyte on a CME are based on (i) the catalysis of the otherwise sluggish electron transfer, (ii) membrane barrier effects for interfering substrates, and (iii) preconcentration of the analyte in the modifying layer.

Most reports on the sensor abilities of CME's deal with the determination of inorganic metal ions, but only a few studies are directed toward organic analysis. Classified according to the three concepts these are (i) catalysis of sulfhydryl (3, 4), NADH (5, 6), carbohydrate (7, 8), and ascorbic acid oxidation (6), (ii) size selective membrane barriers for electroactive substrates in the kilodalton range (9), and (iii) preconcentration based on ion exchange phenomena and/or hydrophobic-hydrophilic interactions at polymer modified electrodes used for the detection of viologens (10), protonated aromatic amines (11, 12), and phenolic compounds (13), as well as phenolic analytes at a lipid-modified electrode (14). The closely related detection of vitamin K<sub>1</sub>, K<sub>2</sub>, and E on a monolayer derivatized electrode has been described in terms of molecular recognition (15). Preconcentration based on covalent bond formation between modifier and analyte has been reported in one case only (16).

The preconcentration method (iii) consists of a sequential procedure: accumulation  $\rightarrow$  detection  $\rightarrow$  regeneration. A certain time delay is used to achieve a detectable concentration of the analyte at the CME by any kind of attractive interaction

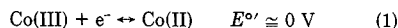
between CME sites and the analyte. The current response observed in the measuring step should then be representative for the analyte surface concentration that is itself related to the solution concentration and eventually to the preconcentration time. In the regeneration step, which may coincide with the measuring step, the analyte is finally expelled from the modifier and the CME is ready for another measurement. Ideally—from a practical point of view—all three steps are controlled by the electrode potential. One way to induce the required affinity change between preconcentration and regeneration electrochemically has been demonstrated earlier in another context and is based on CMEs coated with electroactive ion exchangers (17). Depending on the electrochemically tunable fixed charge in the CME, ionic analytes will either be accumulated or expelled.

Preconcentration and regeneration based on the electrochemically induced formation and cleavage of a covalent bond between electrode modifier and organic analyte have so far not been described but seem very attractive for two reasons: (i) The reactivity of organic compounds and their natural classification is based on the presence of functional groups. CME's with preconcentration properties related to functional group reactivities would show this "natural" chemoselectivity. (ii) Many covalent bond formations in organic chemistry proceed irreversibly with a large driving force. High sensitivity is expected if such reactions may be applied to the preconcentration step and complete expulsion of the analyte from the CME if applied to its regeneration. The electrochemical control of the formation and cleavage of a covalent bond between CME sites and functional groups of the analyte molecules is closely related to EC mechanisms in organic electrochemistry. Electron transfer to (from) the CME should be localized at the reaction centers which then become nucleophilic (electrophilic) in order to induce accumulation and should involve (at more negative (positive) potentials) CME-analyte-centered orbitals to ensure regeneration.

Preconcentration related to the imine formation between the carbonyl functionality of an analyte and primary electrode surface-confined amines has been reported (16). However, accumulation is not induced by an electron transfer and the imine function cannot be broken electrochemically. Moreover, Miller reported on the electrochemically induced cleavage of an amide linkage used for controlled drug release from CME's (5), a reaction that can be considered as the electrochemically induced regeneration of the free amine functions in the CME.

Transition-metal complexes exhibit rich redox chemistry combined with large changes in their reactivity toward organic substrates. The electrochemical formation of metal-carbon  $\sigma$  (or  $\pi$ ) bonds from a reactive metal oxidation state is well documented (18). Some M-C bonds display stabilities that ensure essentially irreversible bond formation but still allow M-C centered electroactivity at more reducing (oxidizing) potentials. M-C bond formation and cleavage or—in the case of a metal complex derivatized electrode—preconcentration, measurement, and regeneration may then be controlled by the electrode potential applied to the CME (Figure 1).

A naturally occurring candidate fulfilling these conditions is vitamin B<sub>12</sub>. The relevant homogeneous (redox-)chemistry is well-known and summarized in eq 1–10 (19). Three metal-centered oxidation states are accessible (eq 1, 2). Co(I)



exhibits high nucleophilic reactivity toward alkylating agents leading to relatively stable organocobalamins (eq 3) (20).

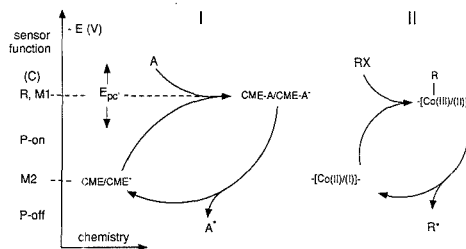
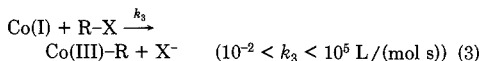
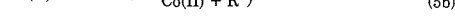
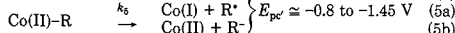
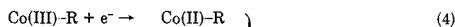
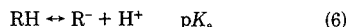


**Figure 1.** Sensor properties of a surface-confined adduct-forming electrocatalyst: A, RX, analyte; CME, chemically modified electrode; P-on, P-off, preconcentration-on, -off; M1, measurement based on irreversible adduct-reduction at  $E_{pc}^{\circ'}$  combined with regeneration (R) and eventually catalysis (C); M2, measurement based on CME oxidation; I, general case; II, B<sub>12</sub>-CME.

Reduction of these compounds to short-lived one-electron intermediates occurs for unactivated primary alkylcobalamins in the range -1.4 to -1.6 V (vs SCE) and leads in a fast chemical follow-up reaction to alkyl radicals or anions and again Co(I) (eq 4 + 5) (21). If one includes activated al-

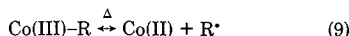
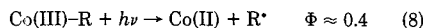


alkylcobalamins a correlation of the cathodic peak potentials of Co(III)-R ( $E_{pc}^{\circ'}$ ) and the  $pK_a$  of RH (eq 6, 7) is observed,

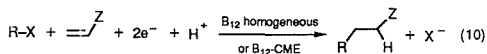


$$pK_a = a + b \cdot E_{pc}^{\circ'} \quad (7)$$

generally the more acidic RH, the more positive  $E_{pc}^{\circ'}$  (22, 23). Two further types of Co-C breaking modes are of importance, i.e. the photochemical (eq 8) and the thermal cleavage (eq 9).



Because of back reaction 9, both forward reactions are observed at maximum rate only if  $\text{R}^{\cdot}$  is irreversibly trapped by another scavenger than Co(II), e.g. an activated olefin as shown in eq 10. Vitamin B<sub>12</sub> catalyzes the electroreduction of alkyl



Z = electron-withdrawing group

halides according to the sequence of reaction 2  $\rightarrow$  3  $\rightarrow$  4  $\rightarrow$  5, 2  $\rightarrow$  3  $\rightarrow$  8, or 2  $\rightarrow$  3  $\rightarrow$  9 (24). Its use as an electrocatalyst in organic synthesis (22) or for the treatment of wastewater (25) is well documented. More direct related to electroanalysis is the current amplification effect that has been observed in the B<sub>12</sub>-catalyzed reduction of vicinal dibromides (25). However, this phenomenon is probably restricted to analytes exhibiting very large  $k_3$  values. We have recently reported on the derivatization of carbon electrodes with polymeric forms of vitamin B<sub>12</sub>. Surface modification was achieved by thermal curing a diamino derivative of vitamin B<sub>12</sub> (Co $\alpha$ ,Co $\beta$ -dicyano-7-des-carboxy-7 $\beta$ -(3',5'-diaminobenzoyloxy)methylcob(III)yrinic acid hexamethyl ester (1) and a diepoxide (e.g. Araldit B (2)) on the electrode surface (Figure 2) (26).

With carbon felt electrodes as the catalyst support, C-C bond formation according to eq 10 (26) and carbon-skeleton rearrangements (27) have been achieved on these CMEs. We also reported on some preliminary results on poly(vitamin B<sub>12</sub>)-modified basal plane pyrolytic graphite (BPG) electrodes

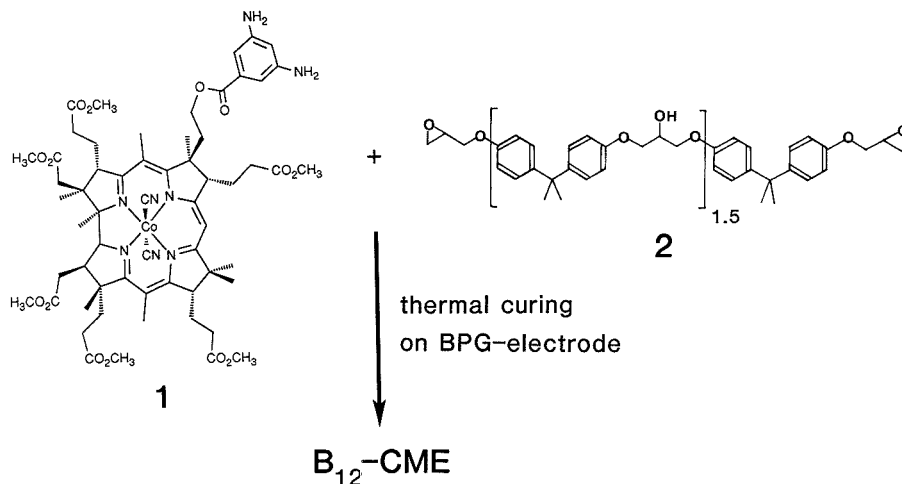


**Figure 2.** Synthesis of the B<sub>12</sub>-CME. Polymerization by thermal curing of the vitamin B<sub>12</sub> derivative (1) and the diepoxide (2) (Araldit B) on basal plane pyrolytic graphite electrodes.

and their use as preconcentration-type sensors toward alkylating agents (28). To the best of our knowledge this was the first example of preconcentration, measurement, and regeneration related to an electrochemically induced, irreversible covalent bond formation and cleavage between analyte and CME. In this work the B<sub>12</sub>-based sensor is described in detail. A simple model is presented that correlates its sensitivity toward alkylating agents in terms of the reactivity of monomeric vitamin B<sub>12</sub> toward RX.

Notably, a lipophilic derivative of vitamin B<sub>12</sub> incorporated into a liquid membrane has earlier been shown to be a selective anion carrier (29). In contrast to the B<sub>12</sub>-CME presented in our work, the membrane-potential-based sensor is related to reversible and fast axial coordination chemistry at Co(III).

### EXPERIMENTAL SECTION

**Reagents and Solvents.** All electrochemical measurements were performed with rigorous exclusion of oxygen. The argon was purified with BTS catalyst (BASF) in conjunction with molecular sieves. Acetonitrile (far-UV, Romil Chemicals) was used without further purification. Dimethylformamide (Fluka AG, Buchs, Switzerland, puriss.) was freshly distilled over P<sub>2</sub>O<sub>5</sub> under reduced pressure. Tetrabutylammonium perchlorate (Fluka, purum) was twice recrystallized from ethyl acetate. Phenethyl iodide was synthesized from phenethyl bromide (Fluka, purum), by a halide exchange reaction (30), the other reagents have been obtained from Fluka AG and are of purum or puriss. grade, except neopentyl iodide which is of pract. grade. All alkylating agents used as analytes were freshly distilled prior to use.

**Electrodes.** Pyrolytic graphite disk electrodes were made as described by Anson (31) and used for poly-B<sub>12</sub> derivatization (26, 27). The derivatized basal plane surface of the electrode was 0.173 cm<sup>2</sup>. A thin graphite slice was cut from the surface parallel to the graphite plane before each new derivatization step.

**BPG Electrode Modification.** To 0.1 mL of a solution of 1 (26) (6.3 mg, 5.28 × 10<sup>-6</sup> mol) in CH<sub>2</sub>Cl<sub>2</sub> (1 mL), 0.1 mL of a solution of Araldit B (2) (Ciba Geigy AG, Basel, Switzerland) (40.6 mg, corresponding to 1.06 × 10<sup>-4</sup> mol epoxide functionalities) and dimethylbenzylamine (3.6 mg) in 5 mL of CH<sub>2</sub>Cl<sub>2</sub> was added. A 1.5-μL portion from this solution of the monomers (molar ratio Co:Araldit = 1:2) was applied to the electrode surface (2.3 × 10<sup>-8</sup> mol of Co/cm<sup>2</sup>) with a syringe. After evaporation of the solvent, polymerization was induced by thermal curing of the electrode at 120 °C for 1 h.

**Electrochemistry.** Cyclic voltammetry at the B<sub>12</sub>-CME or on glassy carbon was performed with a PAR 173/179 potentiostat

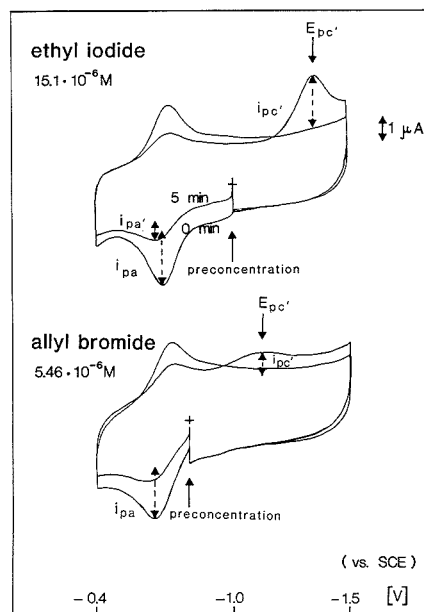


**Figure 3.** Detection of ethyl iodide ( $15 \times 10^{-6}$  M) and allyl bromide ( $5.46 \times 10^{-6}$  M) on the B<sub>12</sub>-CME in CH<sub>3</sub>CN/LiClO<sub>4</sub> (0.2 M) by cyclic voltammetry. Preconcentration 5 min at -1 V (-0.8 V) or 0 min after regeneration. Wave at E<sub>pc'</sub> corresponds to reduction of Co(III)-C<sub>2</sub>H<sub>5</sub> or Co(III)-C<sub>3</sub>H<sub>7</sub>, respectively. Scan rate was 0.1 V/s.

and a PAR 175 function generator. A Metrohm cell with V = 20 mL, a SCE reference separated by a salt bridge, and a Pt wire as auxiliary electrode were used.

**Determination of *i*<sub>pc'</sub> and *i*<sub>pa</sub> at the B<sub>12</sub>-CME.** Oxygen-free solutions of the alkyl halides (10<sup>-7</sup>–10<sup>-8</sup> M) in acetonitrile/0.2 M LiClO<sub>4</sub> were prepared. The CME was potentiostated at -1.0 V (vs SCE) for 5 min under dimmed light conditions. During the accumulation step the solution was not stirred. Then a cyclic voltammogram (CV) with potential scan -1.0 → -0.5 → -1.5 → -0.5 V (*v* = 0.1 V/s) was recorded yielding *i*<sub>pc'</sub>. In order to ensure

quantitative stripping, two potential steps  $-1.0 \rightarrow -1.5 \rightarrow -1.0$  V were then applied and a CV ( $-0.5 \rightarrow -1.5 \rightarrow -0.5 \rightarrow -1.0$ ) was immediately recorded yielding  $i_{pa}$  (Figure 3). The CME was then ready for a new measurement.

**Determination of the Homogeneous Rate of Oxidative Addition of the Alkyl Halides to Vitamin B<sub>12</sub>. A. Based on the Reversal Parameter  $i_{pa}/i_{pc}$  in CV (32).** CV's of solutions of hydroxocobalamin hydrochloride (Roussel Uclaf) (0.3–1 mM) in DMF/tetrabutylammonium perchlorate (0.1 M) were recorded at  $v = 0.02$ – $1$  V/s (potential range 0 to  $-1$  V vs SCE) at a glassy carbon electrode (Metrohm AG,  $A = 0.07$  cm<sup>2</sup>) in the presence of the alkyl halide ( $>3$ – $10$  mM). By use of the published working curve for a reversible charge transfer followed by an irreversible chemical reaction,  $k_{obs}$  was obtained from the Co(II)/(I) couple (32).  $k_{obs}$  was plotted against [RX]. The second-order rate constants ( $k_3$ ) were calculated from linear regression analysis of these plots.

**B. Based on the Catalytic Current in CV's of RX in Presence of Vitamin B<sub>12</sub> (33).** Linear scan voltammograms of solutions of hydroxocobalamin hydrochloride (Roussel Uclaf) (0.3–1 mM) in DMF/tetrabutylammonium perchlorate (0.1 M) were recorded in the presence of alkylating agents ([RX]  $>3$ – $10$  mM) at a glassy carbon electrode (Metrohm AG,  $A = 0.07$  cm<sup>2</sup>) with  $v = 0.02$ – $0.5$  V/s (potential range  $-0.5$  to  $-1.7$  V vs SCE). A catalytic current occurring at potentials typical for Co(III)–R reduction and depending on [RX] was observed. In the reaction scheme (eqs 2–5) it is assumed that reaction 3 is the rate-limiting step. The linear dependence of the catalytic plateau current ( $i_{cat}$ ) on [RX]<sup>0.5</sup> found for prim. alkyl halides meets this condition. According to ref 24 and with  $D = 1.5 \times 10^{-6}$  cm<sup>2</sup>/s,  $A = 0.07$  cm<sup>2</sup>, and  $n = 1$ ,  $k_3$  was available. Some RX show in coulometric experiments  $1.5 > n > 1$  because of carbanion formation. However, no correction has been introduced for this minor error.

**Measurement of the Light-Chopped Photocurrent at the B<sub>12</sub>-CME.** The focused light of a 45-W halogen lamp passed through a CuSO<sub>4</sub> filter and a Compur shutter. It entered the Metrohm polarographic cell at the bottom and reached the CME. During the potential scan the shutter was opened and closed alternatively with  $\nu = 1$  Hz.

## RESULTS AND DISCUSSION

**Cyclic Voltammetry at the B<sub>12</sub>-CME in Presence of Alkylating Agents.** Cyclic voltammetry of B<sub>12</sub>-derivatized basal plane pyrolytic graphite (BPG) electrodes in the absence of alkylating agents revealed a well-defined Co(II)/(I) wave with the typical features of a surface-confined electroactive species, i.e. small peak separation centered around  $-0.68$  V and coulometry corresponding to  $1 \times 10^{-11}$  to  $1 \times 10^{-9}$  mol/cm<sup>2</sup> (28). The submono to multilayer response corresponds to a fraction of the applied monomer only. A freshly prepared B<sub>12</sub>-CME developed this electroactivity after conditioning, i.e. after performing some potential scans in pure acetonitrile/LiClO<sub>4</sub>. Typical cyclic voltammograms (CV) recorded with a conditioned vitamin B<sub>12</sub>-CME in the presence of  $15 \times 10^{-6}$  M ethyl iodide are shown in Figure 3.

If the potential scan ( $-1 \rightarrow -0.4 \rightarrow -1.5 \rightarrow -1$  V) was started after short equilibration ( $<3$  s) at  $-1$  V in order to reduce all metal centers in the CME to Co(I), the same CV as in the absence of the analyte was observed. However, after the electrode was potentiostated for 5 min at  $-1$  V, the peak currents of the Co(II)/(I) couple were smaller and a new cathodic wave at  $-1.45$  V showed up. On an identical subsequent scan except for performing no equilibration at  $-1$  V, the Co(II)/(I) response was again fully developed and no cathodic wave at  $-1.45$  V was present. This behavior was reproducible on a single B<sub>12</sub>-CME up to 20 times. At this point the peak currents were reduced by ca. 50% as compared to their original values. Generally the same behavior was observed with other alkylating agents (see Table I). The occurrence of the reduction wave at more negative potentials and the parallel decrease of the Co(II)/(I) response after preconcentration at  $-1$  V was definitely related to the presence of an alkylating agent, its reactivity, concentration, and the

**Table I. Detection Limits ([RX]<sub>DL</sub>) for Different RX at the B<sub>12</sub>-CME and Their Homogeneous Rate Constants for Oxidative Addition to B<sub>12</sub>**

RX	no.	log [RX] <sub>DL</sub> <sup>a</sup> M	$k_3$ , <sup>b</sup> M <sup>-1</sup> s
methyl iodide	3	-6.37	33000 <sup>c</sup>
ethyl iodide <sup>d</sup>	4	-5.31	3300 <sup>c</sup>
<i>n</i> -butyl iodide	5	-4.63	680 <sup>c</sup>
<i>n</i> -octyl iodide	6	-4.37	580 <sup>c</sup>
phenethyl iodide	7	-4.79	440 <sup>c</sup>
neopentyl iodide	8	-2.95	10 <sup>c</sup>
ethyl bromide	9	-3.20	32 <sup>c,d</sup>
<i>n</i> -butyl bromide	10	-2.80	8.8 <sup>c,d</sup>

<sup>a</sup> [RX] in CH<sub>3</sub>CN/LiClO<sub>4</sub> yielding  $i_{pc}/i_{pa} = 0.5$  at 5-min pre-concentration time. <sup>b</sup> Homogeneous rate constant for oxidative addition of RX to vitamin B<sub>12</sub> in DMF/TBAP. <sup>c</sup> Measurement based on catalytic current (see Experimental Section). <sup>d</sup> Measurement based on reversal parameter (see Experimental Section).

exposure time of the CME in its Co(I) oxidation state. (If the equilibration of the electrode was performed for 5 min at  $-0.4$  V, no decrease of the Co(II)/(I) couple and no new wave at more cathodic potentials were observed.) On the basis of the well-known homogeneous (redox-)chemistry of vitamin B<sub>12</sub> (eq 1–5), it is clear that during the 5-min equilibration the alkylating agent undergoes oxidative addition with surface-confined Co(I) centers according to eq 3. In the CV following this preconcentration the remaining unalkylated B<sub>12</sub> moieties exhibit reduced peak currents. (Preconcentration is used here in a broader sense as it includes the irreversible transformation of the analyte.) At more negative potentials ( $E_{pc}$ ) the product alkylcobalamin is reduced (eq 4), an alkyl fragment is expelled, and Co(I) is regenerated all-through the CME (eq 5).

As mentioned previously, the reduction potential of alkylcobalamin depends strongly on the Co-bound alkyl residue (eqs 6 and 7). Consistently  $E_{pc}$  of the surface confined alkylcobalamin obtained after preconcentration of allyl bromide appeared at  $-1.15$  V. From an analytical point of view  $E_{pc}$  contains valuable information on the alkyl residue of the alkylating agent. The B<sub>12</sub>-CME acts as a new type of reusable chemical sensor for alkylating agents (Figure 1, II). All the steps of the sequential sensing procedure are controlled electrochemically. Preconcentration is switched on and off (P-on, P-off) depending on the presence of Co(I) or Co(II) in the CME. Sensitivity and selectivity are related to the oxidative addition of RX to surface-confined Co(I) centers. Detection of an alkylating agent is possible either by using the decrease of the Co(II)/(I) wave (M2) or the linearly related increase of the Co–R(III)/(II) wave (M1). However, M2 and M1 measurements differ fundamentally in the sense that regeneration of the CME occurs in a M1 measurements (potential scan  $-1 \rightarrow -1.4 \rightarrow -1$  V) but not in a M2 measurement (potential scan  $-1 \rightarrow -0.4 \rightarrow -1$  V). In repetitive preconcentrations and M2 measurements the response is therefore related to the sum of all intermediate preconcentration times, in repetitive preconcentrations and M1 measurements the peak current is governed only by the last preconcentration time.

**Influence of Accumulation Time, RX Concentration, and Reactivity.** The CV in Figure 3 contains twice the reciprocal information on the presence of an alkylating agent ( $i_{pc}$ ,  $i_{pc}$ ). Analysis of the CV waves (heights and surfaces) indicated that coulometry of the alkylcobalamin reduction ( $i_{pc}$ ) is generally larger by a factor of ca. 1.5 as compared to the reversible Co(II)/(I) waves ( $i_{pa} - i_{pc}$ ). This fact is related to partial cleavage according to eq 5a and/or reduction of the radical (or its follow-up products) at the CME. The peak current ratio  $i_{pc}/i_{pa}$  was reproducible within 10% for the same analyte solution and constant preconcentration time inde-



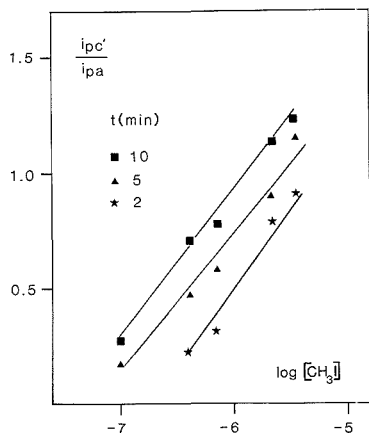


**Figure 4.** Detection of methyl iodide at submicromolar concentration levels in  $\text{CH}_3\text{CN}$ . Plot of  $i_{pc}'/i_{pa}$  vs  $\log [\text{CH}_3\text{I}]$  pre-concentrated for 10, 5, and 2 min. Other experimental conditions are given in Figure 3.

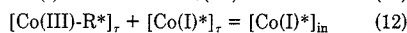
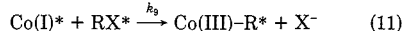
pendent of the activity of the CME. This ratio was obtained from two successive CV's: from the reduction of  $\text{Co(III)-R}$  after pre-concentration and from the  $\text{Co(I)}$  oxidation just after regeneration of the CME (Figure 3). It describes the portion of alkylated  $\text{B}_{12}$  units as compared to all electrochemically accessible  $\text{B}_{12}$  units and it uses the  $\text{Co(II)/(I)}$  response of the regenerated CME as an internal standard. On the basis of the coulometric results, peak current ratios  $0 < i_{pc}'/i_{pa} < 1.5$  correspond to 0–100% alkylated  $\text{B}_{12}$  units in the CME. Higher  $i_{pc}'/i_{pa}$  values are indicative for catalytic current contributions and may be expected at relatively large  $[\text{RX}]$  (26).

The influence of the analyte concentration on  $i_{pc}'/i_{pa}$  at fixed pre-concentration times is shown in Figures 4 and 5a. There exists an approximately linear dependence of  $i_{pc}'/i_{pa}$  on  $\log [\text{RX}]$  for  $0.3 < i_{pc}'/i_{pa} < 1.3$ . The dynamic range for the linear dependence amounts to approximately 1.2 logarithmic concentration units, except for methyl iodide, which exhibits a flatter slope. The dynamic concentration ranges reported for other CMEs are generally comparable to that observed here,

i.e. within a concentration factor of ca. 50 the current response can be related to the analyte concentration for organic (10, 16) or inorganic analytes (34–37). The dependence of  $i_{pc}'/i_{pa}$  on pre-concentration time at fixed analyte concentrations follows a logarithmic law again for ca.  $0.3 < i_{pc}'/i_{pa} < 1.3$  with a dynamic range of ca. 1.2 logarithmic time units (Figure 5b). Obviously pre-concentration does not reach an equilibrium within 20 min as naively expected from the irreversibility of eq 3. Other electrochemical sensors related to the pre-concentration technique show a time-independent response after some minutes (16, 37) or hours (10). Finally there exists a very large dependence of  $i_{pc}'/i_{pa}$  plots at constant pre-concentration time on the type of alkylating agent (Figure 6).

Alkyl iodides are displaced toward smaller concentrations as compared to alkyl bromides. Within one halide family the  $\text{RX}$  bearing the smaller  $\text{R}$  is also shifted toward smaller concentrations. These trends seem to correlate with the homogeneous reactivity of alkyl halides toward vitamin  $\text{B}_{12}$  (20). We defined arbitrarily the concentration  $[\text{RX}]_{\text{DL}}$  that corresponds to  $i_{pc}'/i_{pa} = 0.5$  at a pre-concentration time of 5 min as the detection limit ( $[\text{RX}]_{\text{DL}}$ ). The  $[\text{RX}]_{\text{DL}}$  values are obtained from best-fit straight lines in  $i_{pc}'/i_{pa}$  vs  $\log [\text{RX}]$  plots as shown in Figure 5.  $[\text{RX}]_{\text{DL}}$  values are listed in Table I for different  $\text{RX}$ . We should underline the very conservative definition of our detection limit.  $[\text{RX}]_{\text{DL}}$  is based on a 1:2 current relationship obtained from CV and corresponding to 33% of saturation. However, one would expect that 0.1–1% alkylcobalamins present in the CME after pre-concentration give a measurable current response in differential pulse polarography.

**Simple Model Correlating Homogeneous Reactivity with Sensor Sensibility.** It was assumed that the concentration of  $\text{RX}$  in the solution and in the CME ( $\text{RX}^*$ ) are identical and time independent even during pre-concentration ( $*$  = surface). Thus eq 11 describes the oxidative addition



$$i_{pc}'/1.5i_{pa} = [\text{Co(III)-R}^*]_{\tau}/[\text{Co(I)}^*]_{\text{in}} \quad (13)$$

$$\frac{i_{pc}'}{1.5i_{pa}} = \frac{[\text{Co(I)}^*]_{\text{in}} - [\text{Co(I)}^*]_{\tau}}{[\text{Co(I)}]_{\text{in}}} = 1 - \frac{[\text{Co(I)}^*]_{\tau}}{[\text{Co(I)}^*]_{\text{in}}} \quad (14)$$

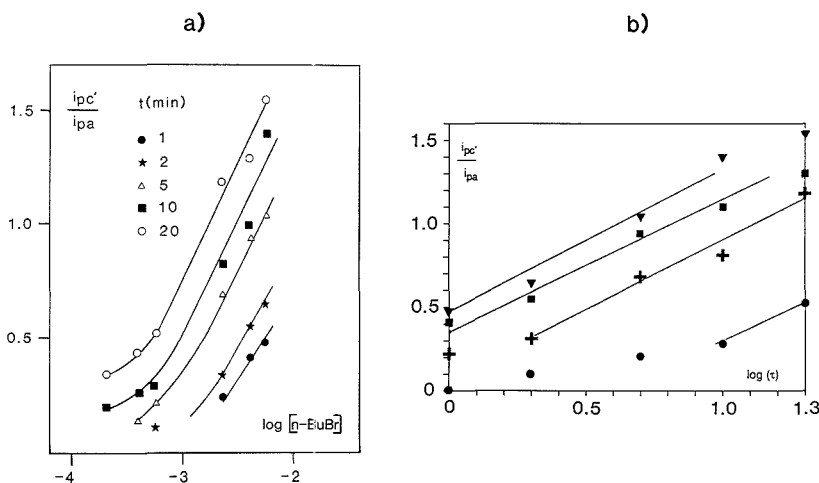


**Figure 5.** Concentration (a) and pre-concentration time (b) dependence of  $i_{pc}'/i_{pa}$  for  $n$ -butyl bromide: (a) pre-concentrated for 1, 2, 5, 10, and 20 min; (b)  $[\text{RX}] = 5.6 \times 10^{-3}$  ( $\nabla$ ),  $4.0 \times 10^{-3}$  ( $\blacksquare$ ),  $2.3 \times 10^{-3}$  ( $+$ ), and  $5.7 \times 10^{-4}$  ( $\bullet$ ). Best-fit straight lines are drawn in the range  $0.3 < i_{pc}'/i_{pa} < 1.3$ . Other experimental conditions as in Figure 3.

$$[\text{Co}(\text{I})^*]_t = [\text{Co}(\text{I})^*]_{\text{in}} e^{-k[\text{RX}]t} \quad (15)$$

$$i_{pc}/i_{pa} = 1.5 - 1.5e^{-k[\text{RX}]t} \quad (16)$$

of  $\text{RX}^*$  to surface-confined metal centers. The sum of surface concentrations of alkylated and unalkylated Co ions at any preconcentration time is equal to the initial  $[\text{Co}(\text{I})^*]$  (eq 12). The observed ratio  $i_{pc}/i_{pa}$  corrected for the different  $n$  values ( $n = 1.5$  and  $1$ , respectively) is then equal to the ratio of the corresponding surface concentrations after and before preconcentration (eq 13, 14). Equation 15 results from the assumed pseudo-first-order conditions with respect to  $[\text{RX}]$ . From eqs 14 and 15 an expression was obtained that correlates  $i_{pc}/i_{pa}$  with  $[\text{RX}]$ , preconcentration time ( $t$ ), and the reactivity of  $\text{RX}$  in the CME ( $k = k_3$ ) (eq 16). A plot of the theoretical  $i_{pc}/i_{pa}$  vs  $\log [\text{RX}]$  or vs  $\log t$  is shown in Figure 7.

The theoretical correlation exhibits a similar dynamic range as observed experimentally (Figures 4–6). If it is further assumed that the homogeneous rate of oxidative addition is not different from that in the CME ( $k = k_3 = k_2$ ), we may correlate the detection limit ( $[\text{RX}]_{\text{DL}}$ ) with the homogeneous rate ( $k_3$ ) and the preconcentration time ( $t$ ) (eqs 17 and 18).

$$0.5 = i_{pc}/i_{pa} = 1.5 - 1.5e^{-k[\text{RX}]_{\text{DL}}t} \quad (17)$$

$$[\text{RX}]_{\text{DL}} = 0.41/tk_3 \quad (18)$$

Equation 18 predicts that  $[\text{RX}]_{\text{DL}}$  is a function of the reciprocal rate of oxidative addition times the reciprocal preconcentration time. In order to test the model we determined  $k_3$  for all analytes (3–10) in one solvent (DMF) under pseudo-first-order conditions using electrochemical techniques (see Experimental Section).  $k_3$  values of 3 and 9 have earlier been reported by Schrauzer (20). They are identical with our results although another solvent was used. Experimental  $k_3$  and  $[\text{RX}]_{\text{DL}}$  values are shown in Table I and plotted in Figure 8 together with the theoretical  $[\text{RX}]_{\text{DL}}$  vs  $k_3$  dependence according to eq 18.

The experimental points lie approximately on a line with a slope very close to that predicted by eq 18. However, they are displaced by ca. 1 order of magnitude toward larger  $[\text{RX}]_{\text{DL}}$ . Several reasons may be invoked to explain this difference.

$k_3 < k_2$ : The homogeneous rates of oxidative addition of  $\text{RX}$  to vitamin  $\text{B}_{12}$  ( $k_2$ ) measured in DMF may be faster than those to the surface-confined polymeric  $\text{B}_{12}$  derivative 1 in acetonitrile.

$[\text{RX}]^* < [\text{RX}]$ : It was assumed that the active  $\text{RX}$  concentration in the CME is identical with that in solution and not affected by the preconcentration process. If diffusion of  $\text{RX}$  into the CME is slow, only a small steady-state concentration of  $\text{RX}^*$  would be present in the CME. The diffusion coefficients may then be governed by the relative size of  $\text{RX}$  and the meshes of the polymer. Inspection of the data in Figure 8 reveals that no such molecular size discrimination is observed, i.e. the bulkier analytes (6, 7, and 8) show no extra displacement to larger  $[\text{RX}]_{\text{DL}}$ . In the case of fast reacting analytes sensitivity (in terms of reciprocal  $[\text{RX}]_{\text{DL}}$ ) is increased by ca. 0.2 logarithmic concentration unit if preconcentration is carried out in a stirred solution. This indicates some impoverishment of  $[\text{RX}]$  during preconcentration for very dilute analyte solution and for large  $k_3$ . Consistently there exists some trend toward larger displacement from the theoretical line in Figure 8 for the faster reacting  $\text{RX}$ . Finally an unfavorable partitioning of  $\text{RX}$  between the CME and the solution may reduce the active  $[\text{RX}]$  in the CME.

**Preconcentration versus Catalysis.** So far all observations were consistent with preconcentration related to an irreversible reaction. No equilibrium was reached even after prolonged accumulation times and eq 18 predicts—naively

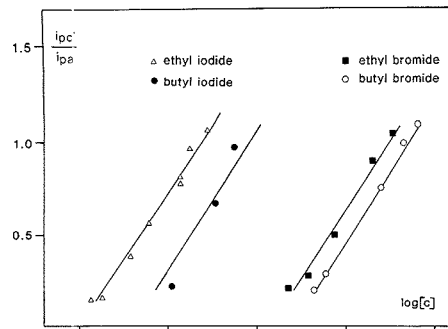


Figure 6.  $i_{pc}/i_{pa}$  vs  $\log [\text{RX}]$  plots for different  $\text{RX}$  obtained for 5 min preconcentration. The limit of detection  $[\text{RX}]_{\text{DL}}$  is defined as  $[\text{RX}]$  for  $i_{pc}/i_{pa} = 0.5$ . Other experimental conditions are given in Figure 3.

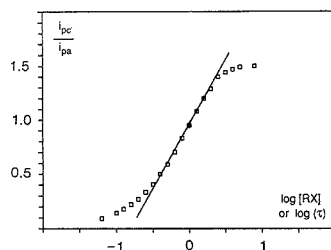


Figure 7. Theoretical  $i_{pc}/i_{pa}$  vs  $\log [\text{RX}]$  (or  $\log t$ ), plot calculated from eq 16.

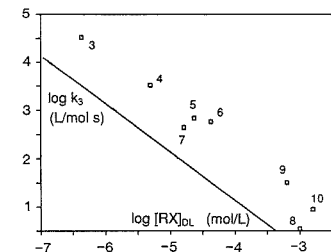
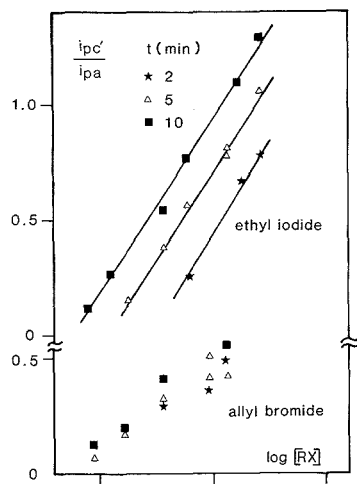


Figure 8. Detection limit ( $\log [\text{RX}]_{\text{DL}}$ ) as a function of homogeneous reactivity ( $\log k_3$ ). Values are from Table I. The straight line was calculated from eq 18 for 5-min preconcentration.

interpreted—quasi-infinitely small  $[\text{RX}]_{\text{DL}}$ . However, the stability of  $\text{Co}(\text{III})\text{-R}$  is limited. Photochemical, thermal, or reductive cleavage reactions of the  $\text{Co-C}$  bond according to eqs 4 + 5, 8, and 9 may proceed in parallel to oxidative addition. Thus a steady-state situation develops and  $[\text{Co}(\text{III})\text{-R}^*]$  becomes time-independent.

(a) *Reductive Cleavage Interfering with Preconcentration.* If allyl bromide was preconcentrated on a  $\text{B}_{12}$ -CME, the  $i_{pc}/i_{pa}$  ratios exhibited a smaller concentration dependence and no dependence on preconcentration time (Figure 9).

Probably reactions 4 and 5 were responsible for the steady-state behavior of allyl bromide. This hypothesis is strongly supported by the positive reduction potential of allylcobalamin as compared to ethylcobalamin (Figure 3). The potential difference between the  $\text{Co}(\text{II})/\text{I}$  couple and the reduction wave of allylcobalamin seems to be too small to prevent reduction of allylcobalamin during preconcentration even if it is carried out at  $-0.8$  V. However, the  $i_{pc}$  response of allyl bromide on the CME is still orders of magnitude larger



**Figure 9.** Catalysis prevents preconcentration.  $i_{pc}/i_{pa}$  vs  $\log [RX]$  plots for ethyl iodide and allyl bromide. Reductive cleavage of allyl-cobalamin in parallel with oxidative addition.

than the CV current observed in the direct reduction of allyl bromide.

(b) *Photolytic Analyte Stripping.* The Co-C bond of alkylcobalamins can be cleaved with visible light according to eq 8. The primary products are Co(II) and an alkyl radical. In the presence of an olefin their recombination (eq 9) is efficiently suppressed. Under the conditions of preconcentration and in the presence of an activated olefin we expected a light shot focused onto the surface of the CME to cause a cathodic current response that is related to the amount of photolyzed Co(III)-R units. This photochemical-induced measurement and regeneration of the CME would be of interest as it would not require any change in the applied potential. In practice only very small photocurrents were observed by using the preconcentration-photolysis technique and coulometry indicated that only a fraction of the Co(III)-R units underwent an irreversible cleavage. It was not possible to correlate the current with the relative amount of alkylated  $B_{12}$  units in the CME as in the case of the cathodic measurement-regeneration at  $E_{pc}$ . Possibly only the outermost layer(s) was (were) photolyzed and/or recombination (eq 9) was competitive with reduction.

The largest photocurrents were observed if the alkylating agents was present at relatively high concentration, i.e. under conditions where a catalytic current develops in the region of  $E_{pc}$ . CV's recorded at a  $B_{12}$ -CME under chopped light excitation are shown in Figure 10. A chopped catalytic current response is observed in the potential range -0.6 to -1.2 V. An analogous light-chopped photocurrent has been reported for the homogeneous  $B_{12}$ -catalyzed reduction of acetic acid anhydride in the presence of activated olefins (38). The rising portion of a single current tooth indicates that the kinetics in the case of the surface confined catalyst are in the range of 0.1 s, whereas in the homogeneous case typically some minutes are needed to achieve a steady state.

### CONCLUSION

In electrocatalysis two main mechanisms can be considered. Either an encounter between a substrate molecule and the active catalyst leads directly to the product and the inactive catalyst in one elementary step or a stable adduct is formed, which is cleaved in a subsequent electron-transfer step at a

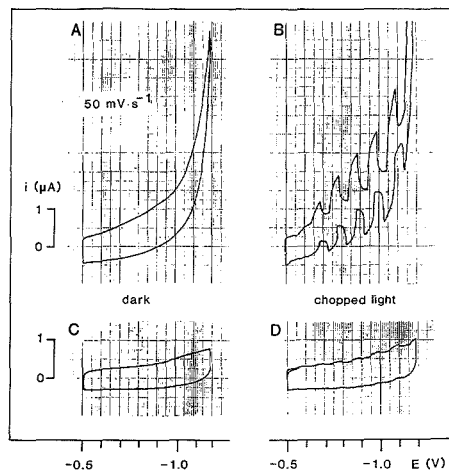


**Figure 10.** Cyclic voltammograms ( $\nu = 50$  mV/s) in presence of ethyl iodide (0.042 M) and acrylonitrile (0.05 M) in  $CH_3CN/LiClO_4$  (0.2 M) in the dark (A, C) and under chopped white light illumination ( $\nu \approx 1$  s $^{-1}$ ) (B, D) at a  $B_{12}$ -CME (A, B) and at an untreated BPG-electrode (C, D).

potential that is more reductive (oxidative) than that necessary to produce the active catalyst in absence of the substrate.

If such an adduct forming redox catalyst is bound to an electrode surface, the resulting CME will generally exhibit sensor-properties toward the substrate that is reduced (oxidized) in the homogeneous case. Principally two types of sensor working modes are available, one is related to catalysis and the other to preconcentration. In the first case the electrode potential is set to a value corresponding to the reductive (oxidative) cleavage of the adduct yielding a catalytic current that is related to the analyte solution concentration. In the second case the electrode potential applied is too mild for reductive (oxidative) cleavage of the adduct to occur but high enough to ensure the presence of the active catalyst. Only adduct formation (preconcentration) takes place. Upon an excursion of the electrode potential the adduct is reduced (oxidized) and the current may be used for analytical information. This relation became obvious in the present work: The adduct-forming electrocatalyst vitamin  $B_{12}$  becomes a preconcentration type sensor for alkylating agents when immobilized on an electrode surface. We expect that other immobilized macrocyclic Co complexes that mimic  $B_{12}$  reactivity can substitute for vitamin  $B_{12}$  in the CME (39). However, sensitivity correlates with the rate constant for oxidative addition ( $k_3$ ) and most  $B_{12}$  model compounds exhibit smaller  $k_3$  values than the parent compound (20). Preconcentration and measurement of organic analytes at CME's that is related to the electrochemically induced formation and cleavage of organometallic compounds are surely not restricted to the poly- $B_{12}$  modified electrode and alkylating agents. Other metal complexes are known for their redox-tunable affinity toward other functional groups involving organometallic intermediates. Once electrode surface confined, they may also act as sensors with specificities that reflect their homogeneous chemoselectivities.

### ACKNOWLEDGMENT

We thank Professor F. Lohse, Ciba-Geigy AG, Basel, for making the diepoxide 2 available to us.

### LITERATURE CITED

- (1) Janata, J.; Bezegh, A. *Anal. Chem.* **1988**, *60*, 62R-74R.
- (2) Murray, R. W.; Ewing, A. G.; Durst, R. A. *Anal. Chem.* **1987**, *59*, 379A-390A.

- (3) Halbert, M. K.; Baldwin, R. P. *Anal. Chem.* **1985**, *57*, 591-595.  
 (4) Linders, C. R.; Kauffmann, J.-M.; Patriarche, G. J. *J. Pharm. Belg.* **1986**, *6*, 373-379.  
 (5) Lau, A. N. K.; Miller, L. L. *J. Am. Chem. Soc.* **1983**, *105*, 5271-5277.  
 (6) Ueda, C.; Tse, D. C.; Kuwana, T. *Anal. Chem.* **1982**, *54*, 850-856.  
 (7) Santos, L. M.; Baldwin, R. P. *Anal. Chem.* **1987**, *59*, 1766-1770.  
 (8) Prabhu, S. V.; Baldwin, R. P. *Anal. Chem.* **1989**, *61*, 852-856.  
 (9) Kuhn, L. S.; Weber, S. G.; Ismail, K. Z. *Anal. Chem.* **1989**, *61*, 303-309.  
 (10) Szentirmay, M. N.; Martin, C. R. *Anal. Chem.* **1984**, *56*, 1898-1902.  
 (11) Guadalupay, A. R.; Abreuña, H. D. *Anal. Lett.* **1988**, *19*, 1619-1632.  
 (12) Nagy, G.; Gerhardt, G. A.; Oke, A. F.; Rice, M. E.; Adams, R. N.; Moore, R. B., III; Szentirmay, M. N.; Marlin, C. R. *J. Electroanal. Chem. Interfacial Electrochem.* **1985**, *188*, 85-94.  
 (13) Coury, L. A.; Birch, E. M.; Heineman, W. R. *Anal. Chem.* **1988**, *60*, 553-560.  
 (14) Chastel, O.; Kauffmann, J.-M.; Patriarch, G. J.; Christian, G. D. *Anal. Chem.* **1989**, *61*, 170-173.  
 (15) Tabushi, I.; Kurihara, K.; Naka, K.; Yamamura, K.; Hatakeyama, H. *Tetrahedron Lett.* **1987**, *28*, 4299-4302.  
 (16) Price, J. F.; Baldwin, R. P. *Anal. Chem.* **1980**, *52*, 1940-1944.  
 (17) Factor, A.; Rouse, T. O. *J. Electrochem. Soc.* **1980**, *127*, 1313-1317.  
 (18) Pickett, C. J. *Electrochemistry* **1983**, *8*, 81-125; **1984**, *9*, 162-221.  
 (19) *B<sub>12</sub>*, Dolphin, D., Ed.; J. Wiley: New York, 1982; Vol. 1, Chemistry.  
 (20) Schrauzer, G. N.; Deutsch, E. *J. Am. Chem. Soc.* **1969**, *91*, 3341-3350.  
 (21) Lexa, D.; Savéant, J.-M. *J. Am. Chem. Soc.* **1978**, *100*, 3220-3222.  
 (22) Scheffold, R.; Abrecht, S.; Orlinski, R.; Ruf, H.-R.; Stamouli, P.; Tinembart, O.; Walder, L.; Weymuth, C. *Pure Appl. Chem.* **1987**, *59*, 363-372.  
 (23) Tinembart, O.; Walder, L.; Scheffold, R. *Ber. Bunsen-Ges. Phys. Chem.* **1988**, *92*, 1225-1231.  
 (24) Lexa, D.; Savéant, J.-M.; Soufflet, J. P. *J. Electroanal. Chem. Interfacial Electrochem.* **1979**, *100*, 159-172.  
 (25) Rusing, J. F.; Connors, T. F.; Owlia, A. *Anal. Chem.* **1987**, *59*, 2123-2127.  
 (26) Ruhe, A.; Walder, L.; Scheffold, R. *Helv. Chim. Acta* **1985**, *68*, 1301-1311.  
 (27) Murakami, Y.; Hisaeda, Y.; Ozaki, T.; Matsuda, Y. *J. Chem. Soc., Chem. Commun.* **1989**, 1094-1096.  
 (28) Ruhe, A.; Walder, L.; Scheffold, R. *Makromol. Chem., Macromol. Symp.* **1987**, *8*, 225-233.  
 (29) Schulthess, P.; Ammann, D.; Kräutler, B.; Caderas, C.; Stepánek, R.; Simon, W. *Anal. Chem.* **1985**, *57*, 1397-1401.  
 (30) Lango, D. T. *J. Org. Chem.* **1963**, *28*, 1770-1773.  
 (31) Oyama, N.; Anson, F. C. *J. Am. Chem. Soc.* **1979**, *101*, 3450-3456.  
 (32) Nicholson, R. S.; Shain, I. *Anal. Chem.* **1964**, *36*, 706-723.  
 (33) Savéant, J.-M.; Vianello, E. *Electrochim Acta* **1965**, *10*, 905-920.  
 (34) Whiteley, L. D.; Martin, C. R. *Anal. Chem.* **1987**, *59*, 1746-1751.  
 (35) Bakwiin, R. P.; Christensen, J. K.; Kryger, L. *Anal. Chem.* **1986**, *58*, 1790-1798.  
 (36) Prabhu, S. V.; Baldwin, R. P. *Anal. Chem.* **1987**, *59*, 1074-1078.  
 (37) Gehron, M. J.; Brajer-Toth, A. *Anal. Chem.* **1986**, *58*, 1488-1492.  
 (38) Walder, L.; Orlinski, R. *Organometallics* **1987**, *6*, 1606-1613.  
 (39) Toscano, P. J.; Marzilli, L. G. *Prog. Inorg. Chem.* **1984**, *31*, 105-204.

RECEIVED for review September 7, 1989. Accepted January 2, 1990. We thank the Swiss National Science Foundation for financial support.

## Photodissociation/Gas Diffusion/Ion Chromatography System for Determination of Total and Labile Cyanide in Waters

Yan Liu,\* Roy D. Rocklin, Robert J. Joyce, and Michael J. Doyle

Dionex Corporation, 1228 Titan Way, Sunnyvale, California 94088-3603

An automated system for determination of total and labile cyanide in water samples has been developed. The stable metal-cyanide complexes such as  $\text{Fe}(\text{CN})_6^{3-}$  are photodissociated in an acidic medium with an on-line Pyrex glass reaction coil irradiated by an intense Hg lamp. The released cyanide (HCN) is separated from most interferences in the sample matrix and is collected in a dilute NaOH solution by gas diffusion using a hydrophobic porous membrane separator. The cyanide ion is then separated from remaining interferences such as sulfide by ion exchange chromatography and is detected by an amperometric detector. The characteristics of the automated system were studied with solutions of free cyanide and metal-cyanide complexes. The results of cyanide determination for a number of wastewater samples obtained with the new method were compared with those obtained with the standard method. The sample throughput of the system is eight samples per hour and the detection limit for total cyanide is 0.1  $\mu\text{g/L}$ .

The determination of concentrations of total and labile cyanide is very important for many environmental and industrial applications. The sample pretreatment to obtain free cyanide is perhaps the most important aspect in cyanide analysis. The standard methods for cyanide analysis use acid distillation procedures to decompose metal cyanide complexes (1, 2). The standard methods have several drawbacks. The

acid distillation procedure is very time-consuming and labor intensive. The methods also suffer seriously from a number of interferences such as sulfide and thiocyanate. A different approach of sample pretreatment based on the photodissociation reactions of metal-cyanide complexes under UV-visible irradiation has been studied for the determination of total cyanide (3-6). Those studies have shown that complete decomposition of stable complexes such as  $\text{Fe}(\text{CN})_6^{3-}$  can be obtained in a few minutes when the sample solution is exposed to intense irradiation from high-pressure Hg lamps of several hundreds watts. However, thiocyanate interferes since it is converted to cyanide under UV irradiation when quartz tubings or vessels are used as reactors. It has been shown recently that the Pyrex glass reactor avoids the photoconversion of thiocyanate to cyanide (7).

The separation of cyanide ion from interferences is required in the determination of cyanide because the measurement methods are usually prone to interferences such as sulfide and thiocyanate. The tedious procedures such as precipitation and extraction are used in standard methods (1, 2). Recently, gas diffusion methods using hydrophobic porous membranes have been studied (8-10). Cyanide is separated as HCN gas from the acidic solution and HCN gas is collected in the basic solution on the opposite side of the membrane. The gas diffusion method separates cyanide from most ionic species in the sample solution. The drawback of the method is that it does not separate cyanide from sulfide since  $\text{H}_2\text{S}$  gas also diffuses across the membrane. Ion chromatography (IC) methods have been shown to be advantageous in the separation of cyanide from sulfide (11-14). However, IC methods may be subject to interferences if used without any sample

\*Corresponding author.

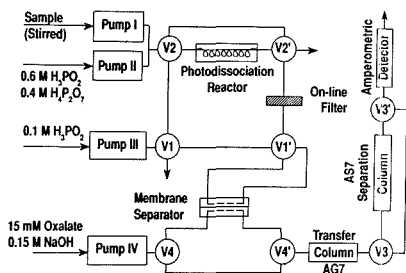


Figure 1. Block diagram of flow, separation, and detector components of the automated cyanide analyzer system.

pretreatments because of high concentrations of ions often present in wastewaters. The combination of the gas diffusion and IC methods would be a very attractive separation means for the determination of cyanide.

This paper reports an automated photodissociation/gas diffusion/IC system for determination of concentrations of total and labile cyanide in water samples. The new method uses an on-line photodissociation reactor to decompose the stable metal-cyanide complexes. The free cyanide is then separated from interferences in the sample matrix with a novel combined gas diffusion/IC separation scheme and is detected with an amperometric detector. The characteristics of the new method have been studied, and the method has been used to determine the concentrations of total cyanide and labile cyanide in a number of wastewater samples.

## EXPERIMENTAL SECTION

**Reagent and Solutions.** Standard solutions of free cyanide and complexed cyanide were 1000 mg/L cyanide expressed as CN in 0.05 M NaOH. Cyanide solutions of lower concentrations were prepared daily as needed by dilution in 0.05 M NaOH. A solution of 0.6 M H<sub>3</sub>PO<sub>4</sub>/0.4 M H<sub>4</sub>P<sub>2</sub>O<sub>7</sub> was prepared and used in the photodissociation step. The acidic carrier solution was a solution of 0.1 M H<sub>3</sub>PO<sub>4</sub>. A solution of 0.15 M NaOH and 0.015 M oxalate was used as the basic receiver solution in the gas diffusion separation and the eluant for the IC separation.

Wastewater samples from various industrial sources were collected and preserved according to the procedures in the EPA method (1) and were analyzed as soon as possible. Portions of some samples were spiked with either CN<sup>-</sup> or Fe(CN)<sub>6</sub><sup>3-</sup> ion to provide a concentration increase of 50 μg/L CN prior to analysis to determine the recovery of cyanide spikes. Portions of wastewater samples provided by a metropolitan water treatment plant were analyzed by the analytical laboratory of the plant using the EPA method for total cyanide analysis.

**Apparatus.** The arrangement of flow, separation, and detector components of the cyanide analyzer system is depicted in Figure 1. The photodissociation reactor consists of a Pyrex glass tubing (2 mm i.d.) coiled around a 90-W high-pressure Hg vapor lamp (Phillips Lighting). The glass tubing is coiled six turns in a coil diameter of 5 cm and has an inner volume of 2 mL. The glass coil is wrapped with reflecting aluminum foils for the maximum irradiation. The reactor is housed in an enclosed chamber and is cooled with an air fan. Hg lamps of 200, 400, and 550 W were also tested.

The gas diffusion membrane separator is constructed with two hydrophobic porous membrane strips of 1.7 cm by 15 cm sandwiched between three layers of supporting screen. The stack of membranes and screens are tightly clamped together with an external hardware housing similar to those of micromembrane suppressors used in the IC systems (15). The

stack of membranes and gasketed screens constitute two flow chambers, i.e. the acidic sample donor chamber (about 300 μL) and the basic receiver chamber (about 100 μL) on the different sides of the membranes. Several different hydrophobic porous membranes including 0.05- and 0.075-μm polypropylene (Celgard 2400 and 2500), 0.2- and 0.45-μm Gore-Tex Teflon, and 0.2-μm poly(vinylidene difluoride) (PVDF) membranes were tested.

The system operation sequences are designed so that the photodissociation step is carried out simultaneously along with the gas diffusion/IC separation step to increase the system sample throughput. At the beginning, the sample solution is pumped into the photodissociation reactor by pump I at 3.0 mL/min while being mixed with the H<sub>3</sub>PO<sub>4</sub>/H<sub>4</sub>P<sub>2</sub>O<sub>7</sub> acid solution from pump II at 1.0 mL/min for 2 min to fill the photodissociation reactor with the acidified sample solution. Pump I is a valveless pump (Fluid Metering, Inc.) and is found to be applicable to most wastewater samples containing particulates. The acidified sample solution is then left in the reactor for the decomposition of metal-cyanide complexes. At 0.1 min, the positions of V3, V3', V4, and V4' are switched simultaneously such that the separation column is off-line with the transfer column and the solution of cyanide ion from the previous run in the receiver chamber of the membrane separator is sent to the transfer column (IonPac-AG7) at 0.2 mL/min by the eluant from pump IV. The transfer column with operating pressure of 40 psi at 0.2 mL/min is used as the interface between the membrane separator with maximum operating pressure of 70 psi and the IC separation column (IonPac-AS7), which has an operating pressure of about 250 psi at a flow rate of 0.2 mL/min, due to the pressure constraint. At 2.0 min, the positions of V3, V3', V4, and V4' are switched back to their original positions such that the membrane separator is off-line with the transfer column but the transfer column is on-line with the separation column. The flow rate of pump IV is increased to 1.0 mL/min to carry out the IC separation of cyanide from other interferences such as sulfide. The cyanide ion is detected amperometrically by using a Ag electrode as previously described (12). Finally, after the sample solution has resided in the photodissociation reactor for 5 min, positions of V1, V1', V2, and V2' are switched according to a set of determined sequences such that 1.5 mL of photolyzed sample solution in the irradiated section of the photodissociation reactor is transferred to the membrane separator by the carrier acid solution from pump III at 1.5 mL/min. The on-line filter removes any particulates in the sample solution to avoid any problems they may cause to the membrane separator and IC columns. The released cyanide (i.e., HCN) in the acidic solution diffuses across the membrane to the receiver chamber of the membrane separator and is retained there as CN<sup>-</sup> ion until the next sample run. Each sample run usually takes 8 min.

All valves used in the flow system are four-way pneumatically actuated Teflon slider valves. The positions of the valves are controlled with automated solenoid air valves. All operations, data acquisition, and data processing of the cyanide analyzer system are automated by a Dionex instrument control and data analysis system.

## RESULTS AND DISCUSSION

**Photodissociation of Metal-Cyanide Complexes.** Most metal-cyanide complexes such as Fe(CN)<sub>6</sub><sup>3-</sup> undergo complex photochemical reactions to release cyanide ion in aqueous solution under UV-visible radiations (3). For the determination of total cyanide, it is critical to find the reaction conditions so that the dissociation of stable metal-cyanide complexes is rapid and complete, the released cyanide is preserved, and the interferences from other compounds in the sample

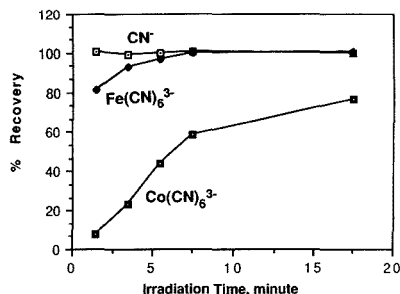


**Figure 2.** Effect of the irradiation time on the dissociation of  $\text{Fe}(\text{CN})_6^{3-}$  and  $\text{Co}(\text{CN})_6^{3-}$  and photochemical stability of  $\text{CN}^-$ . Sample solutions were  $100 \mu\text{g/L}$   $\text{CN}^-$ .

matrix are minimal. Parameters such as the wavelength and intensity of the radiation source, irradiation time, solution pH, sample matrix, etc. determine recovery of cyanide from metal-cyanide complexes and potential interferences. The other study has shown that the Pyrex glass reactor is more suitable compared to quartz reactors in photodissociation of metal-cyanide complexes for cyanide analysis because it avoids the conversion of thiocyanate to cyanide (7). Pyrex glass cuts off the transmission of UV radiation below 300 nm, the region that apparently causes the photoconversion of thiocyanate. High-pressure Hg lamps of 400–500 W were used in most other studies because those lamps provide very high intensity radiation. However, those high wattage lamps are not convenient to use due to the large amounts of heat produced. In this study, it was found that complete recovery of cyanide from  $\text{Fe}(\text{CN})_6^{3-}$  was obtained with high-pressure Hg lamps of 90, 200, 400, and 550 W. The sample solution was irradiated with each lamp for 5 min. The results indicate that all lamps provide sufficient intensity of irradiation to rapidly decompose stable complexes such as  $\text{Fe}(\text{CN})_6^{3-}$ . The 90-W lamp was chosen for further studies.

The photodissociation of metal-cyanide complexes was carried out in both acidic and basic solutions. The cyanide sample solutions prepared in 0.05 M NaOH were irradiated directly in the photodissociation reactor, or the same solutions were mixed on-line with the solution of 0.6 M  $\text{H}_3\text{PO}_2/0.4$  M  $\text{H}_3\text{P}_2\text{O}_7$  in 3:1 ratio before being irradiated in the photodissociation reactor. The hypophosphorous acid prevents the oxidation of released cyanide (HCN) to cyanate and the acids are photochemically stable (6). The effects of the irradiation time of the sample solution on the dissociation of  $\text{Fe}(\text{CN})_6^{3-}$  and  $\text{Co}(\text{CN})_6^{3-}$  and the photochemical stability of  $\text{CN}^-$  ion are shown in Figure 2. The results indicate that about 80% of  $\text{Fe}(\text{CN})_6^{3-}$  dissociate within 1.5 min of irradiation and complete dissociation of  $\text{Fe}(\text{CN})_6^{3-}$  is obtained in 5 min. The dissociation of  $\text{Co}(\text{CN})_6^{3-}$  is much slower and the degree of dissociation of  $\text{Co}(\text{CN})_6^{3-}$  increases from about 8% at 1.5 min to 77% at 17.5 min. This is likely due to the fact that  $\text{Co}(\text{CN})_6^{3-}$  is more kinetically inert and has a larger stability constant than  $\text{Fe}(\text{CN})_6^{3-}$ . The results also show that the  $\text{CN}^-$  ion is photochemically stable under the reaction condition since no decrease in the concentration of  $\text{CN}^-$  ion was observed with up to 17.5 min of irradiation. The irradiation time of 5 min was chosen for further studies since it is sufficient for complete dissociation of  $\text{Fe}(\text{CN})_6^{3-}$ , which is perhaps the most stable and abundant metal cyanide complex commonly found in wastewater samples.

The results of cyanide recovery from a number of metal cyanide complexes in both acidic and basic media are shown in Table I. Complete recoveries of cyanide were obtained from most metal cyanide complexes studied with the exception

**Table I. Results of Recovery Studies of Free Cyanide from Metal Cyanide Complexes**

species	acidic solution	basic solution
$\text{CN}^-$	$100 \pm 1^a$	$100 \pm 1$
$\text{Zn}(\text{CN})_4^{2-}$	$101 \pm 2$	$100 \pm 1$
$\text{Ag}(\text{CN})_2^-$	$99 \pm 2$	$102 \pm 2$
$\text{Cu}(\text{CN})_4^{2-}$	$99 \pm 1$	$101 \pm 1$
$\text{Hg}(\text{CN})_4^{2-}$	$100 \pm 1$	$99 \pm 1$
$\text{Pb}(\text{CN})_6^{2-}$	$101 \pm 1$	$95 \pm 2$
$\text{Fe}(\text{CN})_6^{3-}$	$98 \pm 2$	$99 \pm 1$
$\text{Co}(\text{CN})_6^{3-}$	$77 \pm 2^b$	$56 \pm 1^c$

<sup>a</sup> The results are given in the average percent recovery ( $\pm$  standard deviation of three runs) of cyanide relative to the solution of NaCN and all sample solutions  $100 \mu\text{g/L}$  in CN. Samples solutions were irradiated for 5 min except the solution of  $\text{Co}(\text{CN})_6^{3-}$ . <sup>b</sup> The irradiation time was 17.5 min. <sup>c</sup> The irradiation time was 15 min.

that the recovery from  $\text{Co}(\text{CN})_6^{3-}$  was somewhat lower, 77% in acidic solution and 56% in basic solution. For determination of total cyanide in most wastewater samples, it is preferred and often necessary to carry out the photodissociation of metal cyanide complexes in the acidic solution rather than in the basic solution. Wastewater samples often contain metal ions at high concentrations. The pH of sample solutions is usually adjusted to pH 12 to preserve cyanide upon sample collection. Most heavy metal ions form metal hydroxide precipitates at alkaline pH. The large amount of metal hydroxide precipitations can reduce the intensity of radiation imposing on the sample solution by reflecting and scattering the radiation and thus reduce the recovery of cyanide from the metal-cyanide complexes. Another study found that metal oxides like  $\text{TiO}_2$  can induce photocatalytic oxidation of cyanide to cyanate (16), which can also reduce the recovery of cyanide from sample solutions by the photodissociation method. In the new method presented here, the photodissociation reaction is carried out in acidic solution. The problems associated with metal hydroxides are mostly eliminated since metal hydroxide particles will be dissolved in acid. In addition, use of the reducing acid  $\text{H}_3\text{PO}_2$  is likely to minimize possible photocatalytic oxidation of cyanide ion by metal ions or metal oxides. Furthermore, the acidic solution environment promotes the dissociation of metal-cyanide complexes. For the system reported here, the formation of HCN in acidic solution also facilitates the separation of cyanide by the gas diffusion/IC separation scheme.

**Combined Gas Diffusion/IC Separation Scheme.** The combined gas diffusion/IC separation scheme was developed in this study as an improved separation method in the determination of cyanide since the two techniques complement each other. In this scheme, gas diffusion serves as the sample cleanup technique to separate cyanide from most ionic interferences since ionic species do not diffuse across the hydrophobic membrane. The gas diffusion membrane separators constructed with several different hydrophobic porous membranes of different pore sizes and materials were found to behave similarly in gas diffusion of HCN. The Celgard polypropylene membranes are physically stronger and easier to handle than other membranes during construction of the membrane separator. The polypropylene membranes also have higher water permeable pressures than other membranes because of their smaller pore sizes. The water permeable pressure determines the pressure limit over which the aqueous solution starts diffusing across the membranes. For the on-line interface of membrane separator and IC columns, it is necessary that the water permeable pressure of the membrane is higher than the operation pressure of the IC column at the given flow rate to ensure that no ionic species diffuse across the membrane during gas diffusion separation. The  $0.05\text{-}\mu\text{m}$

Table II. Results of the Determination of Total and Labile Cyanide Species in Wastewater Samples<sup>a</sup>

sample no.	total CN	labile CN	stable CN <sup>b</sup>	CN <sup>-c</sup>	Fe(CN) <sub>6</sub> <sup>3-c</sup>
1	154.5 ± 4.5	68.2 ± 2.0	86.3 ± 4.9	50.0 ± 1.3	49.5 ± 1.0
2	129.6 ± 2.0	33.0 ± 1.0	96.6 ± 2.2	49.5 ± 1.5	49.5 ± 1.6
3	87.5 ± 1.8	86.2 ± 1.1	1.3 ± 2.0	52.0 ± 1.0	49.6 ± 1.8
4	73.3 ± 2.1	0.7 ± 0.5	72.6 ± 2.2	47.7 ± 2.0	52.4 ± 1.3
5	28.9 ± 1.5	6.7 ± 1.0	22.2 ± 1.8	46.2 ± 1.5	50.4 ± 1.7

<sup>a</sup>Results are in  $\mu\text{g/L}$  CN (average  $\pm$  standard deviation of three runs). <sup>b</sup>The concentration of stable cyanide species is given as the differences between the concentrations of total cyanide and labile cyanide species, which were determined with and without the Hg lamp turned on, respectively. <sup>c</sup>The recoveries of cyanide from the additions of 50  $\mu\text{g/L}$  CN in forms of CN<sup>-</sup> and Fe(CN)<sub>6</sub><sup>3-</sup> to the wastewater samples, respectively.

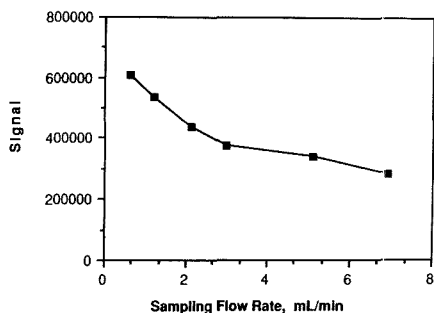


Figure 3. Effect of flow rate on the diffusion of HCN across the membrane.

Celgard membrane was chosen to construct the membrane separator.

In the gas diffusion/IC separation scheme, the basic solution in the receiver chamber of the membrane separator is static during gas diffusion separation. The flow rate of the acidified sample solution going through the donor chamber of the membrane separator is an important parameter in the separation scheme. Figure 3 shows the effect of flow rate on the amount of HCN diffusing across the membrane, which decreases as the flow rate increases. The results are expected since the contact time of the sample solution with the membrane is longer at lower flow rates and more HCN molecules can diffuse across the membrane. Therefore, it is important to keep the sample loading flow rate constant during gas diffusion separation. A flow rate of 1.0 mL/min was chosen as a compromise between speed of analysis and recovery of HCN.

The amount of cyanide ion concentrated in the receiver solution was found to be linear to the volume of sample solution passing through the membrane separator at the two constant flow rates studied, 0.6 and 3.0 mL/min. The concentration of cyanide ion by the membrane separator improves the detection limit of the method for determination of cyanide. It is found that the detector response of 1.5 mL of 100  $\mu\text{g/L}$  cyanide obtained with gas diffusion separation is about 7.5 times higher than that of direct injection with the collector chamber as the injection loop. The volume of the collector chamber is about 100  $\mu\text{L}$ . The efficiency of HCN diffusing across the membrane in the gas dialysis separation is estimated to be about 50% at 1 mL/min sample loading flow rate.

The gas diffusion technique separates cyanide from most ionic species. The separation of cyanide from sulfide and any other compounds that also diffuse through the membrane can be achieved by IC separation. Figure 4a shows the IC separation of cyanide from sulfide. The interference of sulfide is usually eliminated. However, if sulfide is present at high concentrations relative to the concentration of cyanide, tailing of the large sulfide peak may interfere with the determination of cyanide. A two-column heart-cutting technique was de-

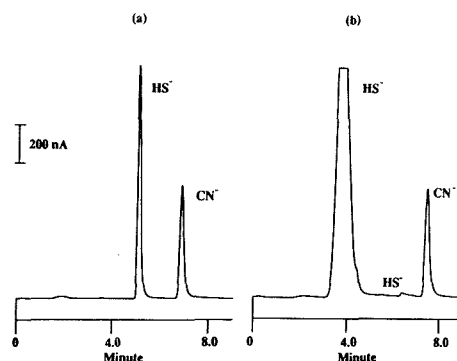


Figure 4. (a) Separation of cyanide and sulfide by ion chromatography: 100  $\mu\text{g/L}$  cyanide + 100  $\mu\text{g/L}$  sulfide. (b) Two-column IC separation of cyanide and sulfide: 100  $\mu\text{g/L}$  cyanide + 2000  $\mu\text{g/L}$  sulfide.

veloped to increase the tolerance to sulfide. In this method, the majority of sulfide is allowed to elute from the transfer column and to bypass the separation column and detector when the treated sample solution is transferred from the membrane separator to the transfer column, before the transfer column is switched on-line with the separation column. The remaining small fraction of sulfide in the sample is further separated from cyanide on the separator column. The results of the two-column separation are shown in Figure 4b (The first sulfide peak that usually bypasses the separator column and detector is shown to demonstrate that the majority of sulfide is eliminated.) By use of this method, the amount of sulfide going into the separation column and the detector is greatly reduced. Thus the system tolerance to sulfide is increased. The system can be used for samples containing 10 ppm sulfide and as low as 10 ppb cyanide without using any other sample pretreatments.

**Applications in Determination of Total and Labile Cyanide.** To demonstrate the capabilities of the automated cyanide analyzer system, the determination of total and labile cyanide was carried out for a number of water samples. In photodissociation mode, the system is configured to determine the concentration of total cyanide, and it yields the same response to the same concentration of total cyanide either in the form of free CN<sup>-</sup> ion or in forms of stable complexes such as Fe(CN)<sub>6</sub><sup>3-</sup>. The system is also used with the Hg lamp off to determine the concentration of labile cyanide species which include free cyanide and those relatively weak complexes like Ag(CN)<sub>2</sub><sup>-</sup> and Zn(CN)<sub>4</sub><sup>2-</sup> that are decomposed to free cyanide by acids such as the H<sub>3</sub>PO<sub>2</sub>/H<sub>4</sub>P<sub>2</sub>O<sub>7</sub> mixture used. The calibration curve for cyanide of the cyanide analyzer system was found to be linear over the range of 1 to 1000  $\mu\text{g/L}$  CN. The relative standard deviation of triplicate sample runs is usually 1–3% for concentrations above 20  $\mu\text{g/L}$  and 2–5% for concentrations in range of 1–20  $\mu\text{g/L}$ . The detection limit

**Table III. Results of the Determination of Total Cyanide in Wastewater Samples by the Cyanide Analyzer System and the EPA Method<sup>a</sup>**

sample no.	cyanide analyzer	EPA method
9	1410 ± 2.1	1680
10	1470 ± 5.2	1370
11	83.3 ± 2.0	91.6
12	37.8 ± 1.0	38.5
13	19.5 ± 0.8	17.5
14	4.9 ± 0.5	4.1

<sup>a</sup> Results are in  $\mu\text{g/L CN}$  (average  $\pm$  standard deviation of three runs).

for cyanide is 0.1  $\mu\text{g/L CN}$ . Lower detection limits could be obtained if a larger volume of the photolyzed sample solution was dialyzed with the membrane separator.

The results of total and labile cyanide determination in five industrial wastewater samples are summarized in Table II. The results show that significant fractions of cyanide species in most samples tested were stable metal cyanide complexes while the majority of cyanide species in sample 3 were labile cyanide species. Although the classification of labile cyanide species is operational, the cyanide analyzer system provides information about the speciation of cyanide in a water sample. The data on the speciation of cyanide in the water samples are potentially useful to understand the correlations between the speciation of cyanide in water samples and their biological effects. The five water samples were also spiked with known amounts of  $\text{CN}^-$  and  $\text{Fe}(\text{CN})_6^{3-}$ . The data in Table II show that recovery of added cyanide was satisfactory even though the sample matrices of most samples were very complex. Studies were also performed to compare the cyanide analyzer system and the EPA method for determination of total cyanide in water samples. The results given in Table III show that the concentrations of cyanide in water samples determined by the two methods are generally in agreement with each other. Although most samples tested did not cause much interferences, there are some potential interferences to the new method since the matrices of wastewaters can be very

complex. For example, organic surfactants in water samples may produce wetting problems with the membrane separator, which could cause the flow of aqueous solution across the membrane. A hydrophobic polymer column could be placed in front of the membrane separator to remove surfactants.

Compared to the current standard method, the cyanide analyzer system has several advantages. The photodissociation method provides rapid and complete recovery of cyanide from most stable complexes such as  $\text{Fe}(\text{CN})_6^{3-}$ . The combined gas diffusion/IC separation scheme eliminates most common interferences such as sulfide. The concentration of cyanide by the membrane separator makes it possible to determine cyanide at sub-microgram-per-liter levels. The system can be used to gain information about the speciation of cyanide in water samples. The automated system also provides relatively rapid sample throughput (8 samples/h) and is applicable to most wastewater samples.

#### LITERATURE CITED

- (1) EPA Methods for Chemical Analysis of Water and Wastes; Environmental Monitoring and Support Laboratory: Cincinnati, OH, 1983.
- (2) Standard Methods for the Examination of Water and Wastewater, 15th ed.; American Public Health Association: Washington, DC, 1980; p 312.
- (3) Moggi, L.; Bolletta, F.; Balzani, V.; Scandola, F. *J. Inorg. Nucl. Chem.* **1966**, *28*, 2589-2597.
- (4) Goulson, P. D.; Afghan, B. K.; Brooksbank, P. *Anal. Chem.* **1972**, *44*, 1845-1849.
- (5) Pihlar, B.; Kosta, L. *Anal. Chim. Acta* **1980**, *114*, 275-281.
- (6) Potlundi, C. The Determination of cyanide in hydrometallurgical process solutions and effluents by ion chromatography. Ranburg, Council for Mineral Technology, Report M128, 1984; p 37.
- (7) Kelaca, N. P. *J. Water Pollut. Control Fed.* **1989**, *61*, 350-356.
- (8) Hangos-Mahr, M.; Pungor, E.; Kuznecov, V. *Anal. Chim. Acta* **1985**, *178*, 289-298.
- (9) Nagashima, K.; Horie, H.; Suzuki, S. *Anal. Sci.* **1986**, *2*, 271-274.
- (10) Zhu, Z.; Fang, Z. *Anal. Chim. Acta* **1987**, *198*, 25-36.
- (11) Bond, A. M.; Heritage, I. D.; Wallace, G. G.; McCormick, M. *J. Anal. Chem.* **1982**, *54*, 582-585.
- (12) Rocklin, R. D.; Johnson, E. L. *Anal. Chem.* **1983**, *55*, 4-7.
- (13) Koch, W. F. *J. Res. Natl. Bur. Stand. (U.S.)* **1983**, *88*, 157-161.
- (14) Han, Kai; Koch, W. F. *Anal. Chem.* **1987**, *59*, 1016-1020.
- (15) Stillen, J. *J. LC* **1985**, *3*, 802-812.
- (16) Frank, S. N.; Bard, A. J. *J. Am. Chem. Soc.* **1977**, *99*, 303-304.

RECEIVED for review October 12, 1989. Accepted January 10, 1990.

## CORRESPONDENCE

### Computational Analysis of Chiral Recognition in Pirkle Phases

*Sir:* Understanding, at the molecular level, how enantio-recognition takes place is of fundamental significance in many areas of the chemical and biological sciences. Enantio-recognition is the ability to discriminate between enantiomers and in analytical chemistry it plays the central role in chiral chromatography (1-4). Although the forces between molecules are well understood and are fully documented, how these forces work *in concert* to selectively bind one of two mirror image isomers is not well understood.

There are two complementary paths one may follow to better understand enantioselection: experiment and theory. We select the latter because it has the potential of providing information not amenable to experimentation. In an earlier paper we developed the theory and presented the computational protocol needed to compute the relative free energies,  $\Delta\Delta G$ , of weakly bound diastereomeric complexes that form

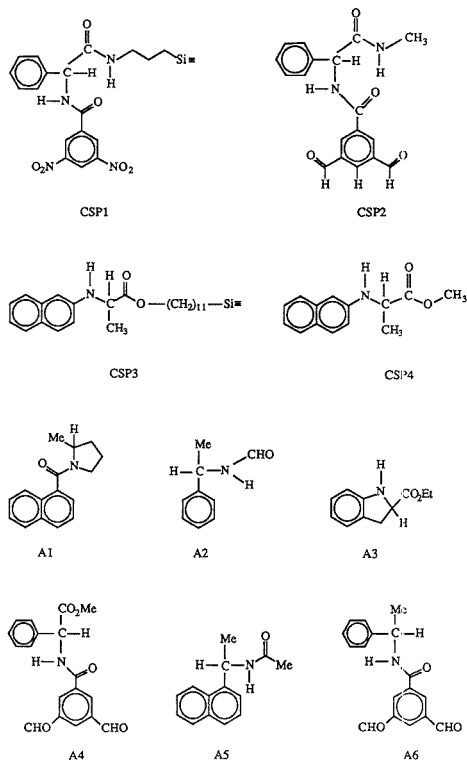
as transient species in chiral chromatography (5). Using that methodology, we were able to determine the relative retention order and the separability factor,  $\alpha$ , for four analytes on two commercially available Pirkle chiral stationary phases (CSP's) (6). We also developed a partitioning algorithm that gives us insight about what portion of the CSP is most responsible for analyte binding and which part of the CSP is most responsible for the enantioselectivity (6). Since then we have performed full scale simulations on two more analytes that are resolvable on Pirkle phases. Here we present these new data and provide an overview of what we have learned to date concerning enantioselective binding to Pirkle CSP's.

#### MOLECULAR MODELING

The systems we previously studied include the (*R*)-phenylglycine CSP1, modeled as CSP2, and the naphthyl-



alanine CSP3 modeled as CSP4 with analytes A1–A4. The



two new simulations we report here involve the selective binding of A5 to CSP2 and A6 to CSP4. The methodology and nomenclature we use are the same as in our previous paper (6) which should be referred to for details. Briefly, however, conformational analyses of CSP's and analytes are carried out to determine the distribution of conformational states accessible to each of those molecules at ambient temperature. We then select the conformational states of CSP and of analyte that account for at least 90% of the conformational population and used those rigid body structures to determine the inherent  $\Delta\Delta G$  between diastereomeric complexes. Although we use the term "rigid", we do allow several conformational states of analyte to mix with several conformational states of CSP giving some flexibility to the individual components making up the diastereomeric complex but we do not account for "induced fit" changes of structure once selector and selectand bind.

As before, atomic charges for the CSP and analyte were determined quantum mechanically and the microstates needed for statistical averaging were sampled by rolling the analyte over the van der Waals surface of the CSP. The position of analyte with respect to CSP is given in a polar coordinate system ( $r, \theta, \phi$ ) with  $r$  being the distance between origins on analyte and CSP and  $\theta$  and  $\phi$  being the latitude and longitude, respectively. The origins on the CSP and analyte in this and the previous study are the stereogenic carbons. More details concerning the quantum mechanical methods used along with the approximations and assumptions invoked in these simulations can be found in our earlier paper (6). Here we present our new results, what they mean, how they compare with our earlier work, and how the results from all six simulations fit

Table I. Results for the Calculation of  $\bar{E}$  for *R*-CSP2 with Analyte 5

complex designation	<i>R</i> - <i>R</i> diastereomer		<i>R</i> - <i>S</i> diastereomer		most retained
	$\bar{E}$ , kcal mol <sup>-1</sup>	% $\bar{E}$	$\bar{E}$ , kcal mol <sup>-1</sup>	% $\bar{E}$	
CSP2A-5A	-5.84	76.3	-6.26	78.0	<i>S</i>
CSP2A-5B	-1.21	15.8	-1.18	14.8	<i>R</i>
CSP2B-5A	-0.50	6.5	-0.48	6.0	<i>R</i>
CSP2B-5B	-0.11	1.4	-0.10	1.2	<i>R</i>
total	-7.66	100.0	-8.02	100.0	<i>S</i>
number of configurations sampled			$2.88 \times 10^6$	$2.88 \times 10^6$	
			$\alpha_{\text{expt}} = 1.86$	$\alpha_{\text{calc}} = 1.88$	

Table II. Results for the Calculation of  $\bar{E}$  for *S*-CSP4 with Analyte 6

complex designation	<i>S</i> - <i>R</i> diastereomer		<i>S</i> - <i>S</i> diastereomer		most retained
	$\bar{E}$ , kcal mol <sup>-1</sup>	% $\bar{E}$	$\bar{E}$ , kcal mol <sup>-1</sup>	% $\bar{E}$	
CSP4A-6A	-0.68	11.0	-0.73	11.6	<i>S</i>
CSP4B-6A	-0.70	11.3	-0.71	11.3	<i>S</i>
CSP4C-6A	-0.67	10.8	-0.70	11.1	<i>S</i>
CSP4D-6A	-0.58	9.3	-0.59	9.5	<i>S</i>
CSP4E-6A	-0.30	4.8	-0.36	5.7	<i>S</i>
CSP4F-6A	-0.31	5.0	-0.30	4.7	<i>R</i>
CSP4A-6B	-0.63	10.2	-0.66	10.4	<i>S</i>
CSP4B-6B	-0.63	10.1	-0.62	9.8	<i>R</i>
CSP4C-6B	-0.59	9.4	-0.57	9.1	<i>R</i>
CSP4D-6B	-0.58	9.2	-0.55	8.7	<i>R</i>
CSP4E-6B	-0.28	4.4	-0.25	4.1	<i>R</i>
CSP4F-6B	-0.28	4.4	-0.26	4.1	<i>R</i>
total	-6.23	100.0	-6.29	100.0	<i>S</i>
number of configurations sampled			$8.64 \times 10^6$	$8.64 \times 10^6$	
			$\alpha_{\text{expt}} = 1.40$	$\alpha_{\text{calc}} = 1.11$	

in with other researcher's conclusions about chiral recognition.

## RESULTS

Tables I and II list the computed free energies,  $\bar{E}$ , determined at 298 K for our two new simulations. The first column indicates the conformational state of CSP that is interacting, over all possible,  $r, \theta,$  and  $\phi,$  with a given conformational state of analyte. The free energies of binding for each rigid body contributor to both diastereomeric complexes along with the present contribution made by those rigid body structures is also provided. The right-hand column indicates which enantiomer would be longer retained on the column if the CSP and analyte were held fixed in those particular conformational states. The total free energies for the competing diastereomeric complexes are presented at the bottom of the tables along with the total number of microstates sampled for the simulation. Finally we present the experimental separability factor and that computed from our differential free energies of association by  $\Delta\bar{E} \approx \Delta\Delta G = -RT \ln \alpha$  for  $T = 298$  K.

Figure 1 illustrates the intermolecular potential energy surface for the RR and RS diastereomeric complexes formed when analyte 5 binds to CSP2. This surface, presented in contour form, depicts the averaged interaction energy between analyte as a function of latitude  $\theta$  and longitude  $\phi$  around CSP2. It statistically accounts, at each  $\theta$  and  $\phi,$  for all important conformations of analyte and of CSP as well as for all possible orientations of the two molecules with respect to one another.

Finally, Table III lists the enthalpy of binding attributable to the molecular fragments depicted in Figure 2. The partitioning algorithm used to assess which fragment of the CSP is most responsible for analyte binding is described in detail

in a previous paper (6). An important point to make, as pointed out by a referee, is that the way we partition the CSPs is completely arbitrary; other partitioning will give different results.

## DISCUSSION

The modeling we performed is at the atomic level and two requirements must be met. First, we must be able to reliably predict the absolute configuration of the analyte longest retained on the column, and second, we should be able to describe their relative separabilities,  $\alpha$ , which is related to the differential in free energy of analyte binding (7). Once these requirements are fulfilled, we assume the model we have is valid and we can begin extracting information from that model which is difficult or otherwise impossible to detect experimentally.

In Table I we predict the *S* enantiomer of analyte 5 to be longer retained on *R*-CSP1, and in Table II we predict the *S* enantiomer of analyte 6 to be longer retained on *S*-CSP3. These predictions are consonant with experiment. Furthermore we calculate a separability factor of  $\alpha = 1.88$  for analyte 5 on CSP2, which compares favorably with the experimental value of 1.86 (8), and an  $\alpha$  value of 1.11 for analyte 6 on CSP3, which is in qualitative agreement with the experimental value of 1.40 (9). A plot of calculated vs observed  $\alpha$  values (not shown) for all six analytes shows a linear relationship with a correlation coefficient of 0.76. The correlation improves somewhat when other examples (not related to this study) are included, suggesting the computational method we employ has some merit and can be used, in a qualitative way, to predict  $\alpha$  values. The results for the six analytes described here are nonetheless surprisingly good considering the assumptions made in the modeling (5). Overall, then, we can reliably predict which of two optical analytes is longer retained on a column and, a priori, with some degree of confidence, we can predict how well a racemic mixture will be resolved on a given column. On the basis of the agreement between theory and experiment, we feel confident that the information extracted from our simulations in the ensuing discussion is meaningful.

We address enantioselectivity by (i) determining where around the CSP the analyte is most likely to be found, i.e., the binding site, (ii) describing which part of the CSP is responsible for binding and which is responsible for enantiodifferentiation, and (iii) considering the validity of existing chiral recognition models.

(i) **Binding Sites.** Minima on the intermolecular potential energy of the complex indicate at which latitude,  $\theta$ , and longitude,  $\phi$ , the analyte is most likely to be found. As in our previous studies the intermolecular potential energy surfaces are generally flat with gently rolling hills separating minima, they have well-defined binding regions, and the surfaces for both diastereomeric complexes are very similar to one another suggesting both optical analytes bind in the same general region around the CSP. The potential energy surface of analyte 5 associating with CSP2 is presented in Figure 1 as an example.

The width and shallowness of these wells suggest wide amplitude sliding motions of analyte with phase will occur even at low temperatures. From the shapes of these low-energy wells along with "snapshots" of a large number of complexes within the well, we find the aromatic rings of CSP and analyte to remain in parallel but large amplitude sliding motions along the long and short axes of the DNB and the naphthylamine portions of the CSPs exit. These  $\pi$  stackings remain parallel to maximize  $\pi$ -acid- $\pi$ -base or charge transfer interactions. These wide amplitude sliding motions are evident for analytes associated on the front-side and the rear-side of the CSP. Generally speaking the preferred binding region is

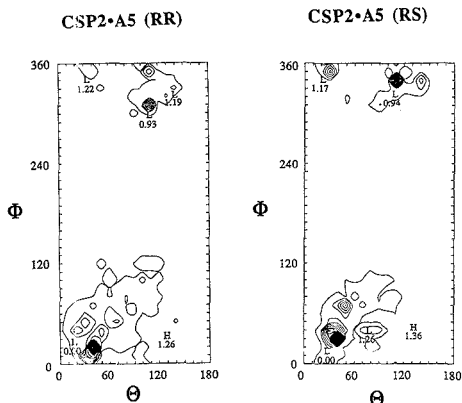


Figure 1. Statistically averaged intermolecular potential energy surfaces for CSP2-A5. Contours are in units of  $0.05 \text{ kcal mol}^{-1}$  with the global minimum arbitrarily set to zero. Actual data are an equally spaced rectangular array of data points  $10^\circ$  apart. High points are designated by H and low points by L.

Table III. Fragment Interaction Energies for Analyte 5 Binding to CSP2 and Analyte 6 Binding to CSP4

fragment	CSP2-A5		difference
	RR diastereomer %	RS diastereomer %	
1	45.4	56.8	11.4
2	45.4	34.5	10.9
3	9.2	8.7	0.5
CSP4-A6			
1	67.8	69.5	1.7
2	13.4	13.2	0.2
3	18.8	17.3	1.5

on the sterically less encumbered face of the CSP. Furthermore, this sliding motion is evident for both *R* and *S* analytes.

Overall, for all six analytes, we find flat intermolecular potential energy surfaces with broad energy wells indicative of transverse and longitudinal motions between stacked aromatic rings. Both *R* and *S* analytes can bind to the front and rear of the CSPs, but a preference is noted for binding on the less sterically congested face of the phase. Generally there are no distinguishing features or trends from the intermolecular potential energy surfaces that suggest one enantiomer docks in one region while its optical antipode docks in another. On the contrary, most of the potential energy surfaces suggest preferential docking of enantiomers to be in the same general region.

(ii) **Stereodifferentiation.** In a previous paper we described, in detail, how one can partition the enthalpy of binding into molecular fragments on the CSP (6). This partitioning is a structural one and, as mentioned earlier, is completely arbitrary. Table III lists the fragment interaction energies for CSP2 associating with analyte 5 and for CSP4 associating with 6 (Figure 2). These new findings taken together with our earlier ones indicate that fragments 1 and 3, the aromatic rings and spacer linkages, respectively, are usually, but not always, most responsible for analyte binding. Also presented in Table III is the difference each fragment feels between *R* vs *S* analyte, and, as such, is a chiral discrimination factor attributable to each fragment. Earlier we stated that the fragment bearing the stereogenic center on the CSP is the least stereodifferentiating, i.e. it is the part of the molecule least cognizant of differences between mirror image

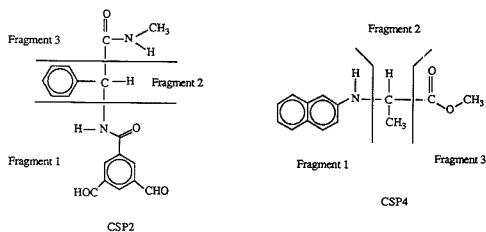


**Figure 2.** Partitioning of CSP2 and CSP4 into fragments. This partitioning is arbitrary.

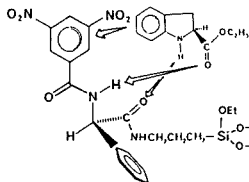


**Figure 3.** A representative example of one of Pirkle's chiral recognition models. The same intermolecular interactions he finds important in the recognition process are also found in our simulations.

isomers (6). The results from Table II taken together with our earlier data indicate this is not always the case. In fact, for the six systems modeled this is true only in three cases (in a fourth case the chiral discrimination is the same in fragments 1 and 2). Nonetheless while we can no longer claim that the fragment bearing the stereogenic center is the least stereodifferentiating fragment, we can say from our modeling that it is not the dominant fragment involved in chiral recognition.

(iii) **Chiral Recognition Models.** Chiral recognition models are usually displayed in the literature as pictures. These pictures are caricatures or cartoons of reality and are usually drawn in a way to provide the reader with the most important features of the state of the system. As we have pointed out, these diastereomeric complexes are dynamical and, by averaging over an infinite time period as done in our simulations, one can successfully reproduce experimental

results that are themselves the result of averaged measurements. Static pictures are, therefore, only partial representations of what is going on and should not be taken at face value. Nonetheless they impart to us most of the information the authors want to convey and, as a simplification of the very complex set of interactions that actually take place, they are especially valuable and useful in spite of their shortcomings.

Representations and explanations of how CSP1, CSP3, and related phases work are found in an insightful and wonderfully written review by Finn (2). For the sake of brevity we only point out here that the Pirkle models usually consist of aromatic  $\pi$  stacking and hydrogen bonding. Explicitly stated, and in agreement with our findings, is the dual role played by the phenyl group on CSP1 and the alkyl group on CSP3. These groups serve first as a conformational bias imparting to these phases their inherent templating ability and second as a steric impediment to keep the analyte from docking equally well on both sides of the CSP (10).

In all pictures generated by Pirkle and his group the major interactions are between the analyte and the CSP fragments we have denoted as fragment 1 and fragment 3. As an example consider the binding of analyte 3 to CSP2. The more retained *S* analyte has a well-defined minimum on the intermolecular potential energy surface (not shown) and the fragments most responsible for analyte binding are fragments 1 and 3 (see ref 6). The corresponding chiral recognition model previously published that portrays analyte association with CSP is shown in Figure 3 (11). Pirkle draws this as a classical three-point interaction model. We do not. Rather, two of the interactions depicted in Figure 3 (the  $\pi$  stacking and the analyte carbonyl association with the DNB amide) are accounted for as fragment 1 in Figure 3. In Finn's terminology (2) this is a "2-2" type model. This issue has been highlighted in studies on models for closely related systems (12, 13). Nonetheless, while Pirkle explicitly draws arrows from particular atoms on the analyte to those on the CSP and we do not, it is clear that fragments 1 and 3 are being portrayed by Pirkle as being responsible for binding.

Another issue with regard to Pirkle's chiral recognition models concerns the mode of interaction between analyte and CSP amide groups. Two types of stabilizing interactions are possible. One is called the hydrogen bond chiral recognition model that involves edge-on, bent hydrogen bonds (2). The second is called the dipole stacking chiral recognition model

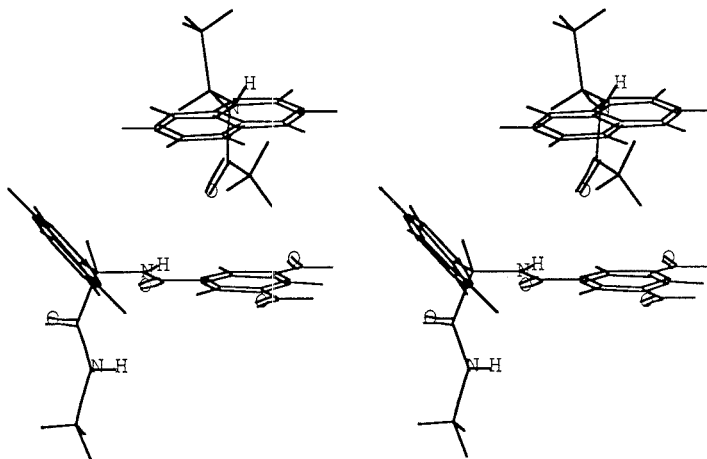


**Figure 4.** Stereoview of one of the microstates used to determine  $E$  for CSP2-A5. Most of the low-energy microstates have  $\pi$ -stacking and hydrogen bond chiral recognition rather than dipole stacking recognition.

where amide groups align face-to-face with their group moments antiparallel (2). Analytes A1 and A5 have amide groups that could interact either way with CSP1. Generally we do not find dipole stacking but we do observe hydrogen bonding. This conclusion is based upon examination of stereoviews of hundreds of "snapshots" near the global minima on the CSP2:A1 and CSP2:A5 surfaces. A typical stereoview is shown in Figure 4. Again keep in mind that this is only one snapshot of an infinite number of intermolecular arrangements that can take place and it does not adequately represent how the system exists over a long time period (as do our evaluations of  $\bar{E}$  and the fragmentation energies described above) but it clearly shows hydrogen bonding rather than dipole stacking.

### SUMMARY

The differential binding of two chiral analytes on two different Pirkle phases was simulated with atomistic modeling. These results were described and compared with earlier work. The results from this work taken together with our earlier results allow us to state the following: (1) The computational protocol we employ seems to be valid; we always predict the correct retention order and we can qualitatively determine separability factors. (2) The intermolecular potential energy surfaces describing the binding of analytes to these CSP's are very flat. Binding to the front and back sides of CSP1 and CSP3 is possible but a slight preference for binding to the sterically less encumbered face is evident. Generally speaking both *R* and *S* analyte bind to the same region. There is no evidence suggesting one analyte binds selectively to one portion of the CSP while the mirror image binds elsewhere. (3) The fragments on CSP1 most responsible for holding the diastereomeric complexes together usually are the DNB moiety and the amide spacer linkage while the naphthylamine is most responsible in CSP3. These fragments do the majority of the work holding the complexes together regardless of the chirality of the substrate. Again we conclude that one fragment does not selectively bind one enantiomer while another fragment binds its mirror image. (4) The fragment bearing the stereogenic center is not the dominant fragment in chiral recognition. This is consonant with Mislow's views (14) that the entire molecule is chiral, not just its asymmetric center.

(5) We conclude that simplification of the myriad of pairwise-additive interactions between molecules into a more manageable caricature or cartoon generally support the chiral recognition models developed by Pirkle.

### LITERATURE CITED

- (1) Souter, R. W. *Chromatographic Separations of Stereoisomers*; CRC Press: Boca Raton, FL, 1985.
- (2) *Chromatographic Chiral Separations*; Chromatographic Science Series Vol. 40, Zeif, M., Crane, L., Eds.; Marcel Dekker, Inc.: New York, 1987.
- (3) König, W. A. *The Practice of Enantiomer Separation by Capillary Gas Chromatography*; Huethig Publishing: Heidelberg, 1987.
- (4) Allenmark, S. G. *Chromatographic Enantioseparation. Methods and Application*; Ellis Horwood Series in Advanced Analytical Chemistry; Chalmers, R. A., Mason, M., Eds.; Ellis Horwood, Ltd.: Chichester, 1983.
- (5) Lipkowitz, K. B.; Demeter, D. A.; Zegarra, R.; Larter, R.; Darden, T. J. *Am. Chem. Soc.* **1988**, *110*, 3446.
- (6) Lipkowitz, K. B.; Baker, B.; Zegarra, R. *J. Comput. Chem.* **1989**, *10*(5), 718.
- (7) Koppenhoefer, B.; Bayer, E. *Chromatographia* **1985**, *19*, 123.
- (8) Pirkle, W. H.; Welch, C. J.; Hyun, M. H. *J. Org. Chem.* **1983**, *48*, 5022.
- (9) Pirkle, W. H.; Pochapsky, T. C.; Mahler, G. S.; Corey, D. E.; Reno, D. S.; Alessi, D. M. *J. Org. Chem.* **1986**, *51*, 4991.
- (10) Pirkle, W. H.; Pochapsky, T. C. In *Packings and Stationary Phases in Chromatographic Techniques*; Unger, K., Ed.; Marcel Dekker, Inc.: New York, 1989; Chapter 12.
- (11) Pirkle, W. H.; Pochapsky, T. C.; Mahler, G. S. and Field, R. E. *J. Chromatogr.* **1985**, *348*, 89.
- (12) Topiol, S.; Sabio, M.; Moroz, J.; Caldwell, W. B. *J. Am. Chem. Soc.* **1988**, *110*, 3367.
- (13) Topiol, S.; Sabio, M. *J. Chromatogr.* **1989**, *461*, 129.
- (14) Mislow, K.; Siegel, J. *J. Am. Chem. Soc.* **1984**, *106*, 3319.

Kenny B. Lipkowitz\*  
Brian Baker

Department of Chemistry  
Purdue University School of Science at Indianapolis  
(PUSSI)  
1125 East 38th Street  
Indianapolis, Indiana 46205

RECEIVED for review June 19, 1989. Accepted December 20, 1989. This work was funded by the donors of the Petroleum Research Fund, administered by the American Chemical Society, and by the National Science Foundation (CHE-8901828).

## TECHNICAL NOTES

### Maleic Acid/Ammonium Hydroxide Buffer System for Preconcentration of Trace Metals from Seawater

Su-Cheng Pai,\* Tsai-Chu Chen,<sup>1</sup> and George T. F. Wong<sup>2</sup>

*Institute of Oceanography, National Taiwan University, Taipei, Taiwan, R.O.C.*

Chin-Chang Hung

*Department of Oceanography, National Taiwan Ocean University, Keelung, Taiwan, R.O.C.*

#### INTRODUCTION

Preconcentration is often required in the determination of trace metals in seawater. Among the many proposed preconcentration schemes, the complexation/solvent extraction

(1-3) and the chelating ion-exchange methods (3, 4) are probably the most widely used. The efficiencies of these methods are critically pH-dependent and the optimal pH may vary from method to method and from metal to metal. Thus, the analytical protocols frequently require the addition of buffers to adjust the pH of the sample to the desired value. Furthermore, during the developmental stage of a new method, before the optimal pH has been identified, empirical tests often have to be carried out over a wide pH range at

<sup>1</sup> Present address: Department of Environmental Engineering, University of Cincinnati, Cincinnati, OH.

<sup>2</sup> Present address: Department of Oceanography, Old Dominion University, Norfolk, VA.

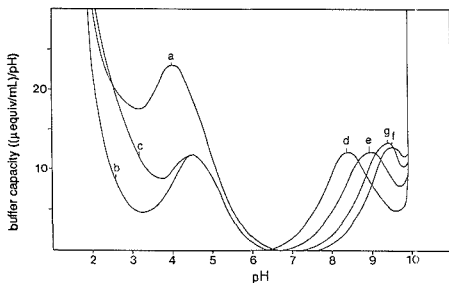


**Figure 1.** Buffering capacity curves of various buffer ligands in seawater at a concentration of 0.02 M. The position of each peak on the pH scale reflects the  $pK'$  value: a, citrate; b, acetate; c, phthalate; d, Tris; e, borate; f, ammonium; g, glycine.

regular intervals. In such a situation, different buffers or a combination of various buffer systems would have to be used.

An ideal buffer should provide an adequate buffering capacity over a wide range of pH, have minimal interaction with the metal of interest, not react with other constituents of seawater in a manner that will interfere in the subsequent analysis, and be made up of chemicals that can be easily purified from contaminating trace metals. Presently, the most commonly used buffer ligands are acetate (1, 2, 5), citrate (1, 5, 6), glycine (7), borate (8), and ammonium ions (1, 3, 5, 6). The buffering capacities of these ligands at 0.02 M in seawater are shown in Figure 1. Among these, acetate and ammonium ions are frequently used in combination (2-4, 9, 10). However, it can be seen that a conspicuous gap exists between pH 6 and 7 where none of them can provide an adequate buffering capacity. There are limitations in choosing other buffers. For example, citrate forms strong complexes with Cr and Fe at a certain pH range (7, 11) and phosphate precipitates with Ca and Mg at pH above 6 (1).

In this paper, we will describe a buffer system, the ammonium maleate system, which is made of a mixture of hydrochloric acid, maleic acid, and ammonium hydroxide, and its buffering capacity covers a wide pH between 2 and 9. The working buffers are simple to prepare, easy to use, and can be rendered free from trace metal contaminations readily. The buffer system has been applied successfully to the preconcentration of trace metals in seawater by both the APDC + DDTC/MIBK solvent extraction and the Chelex-100 chelating ion-exchange technique in our laboratories.

## EXPERIMENTAL SECTION

**Reagents. Ammonium Hydroxide Solutions.** Ammonium gas was distilled off a concentrated ammonium hydroxide solution (28%) and redissolved in double distilled water (DDW). The exact concentration of the purified ammonia solution was determined by titration with a standardized acid. A 2 N working solution was prepared by dilution with DDW.

**Hydrochloric and Nitric Acids.** Concentrated HCl and  $HNO_3$  were purified by sub-boiling distillation (12), then stored in Teflon bottles. The exact concentrations were determined by titrations with a standardized base. Working solutions (2 N) were prepared by dilution with DDW.

**Maleic Acid/Ammonium Hydroxide Stock Buffer Solution.** A 58.01-g portion of maleic acid was dissolved in ca. 600 mL of water. The pH of this solution was adjusted to ca. 6.5 with concentrated ammonium hydroxide. The solution was diluted to ca. 1 L and then passed through a Chelex-100 column (20 cm  $\times$  2 cm i.d.) packed with 10 g of 100-200 mesh resin in the ammonium form at a flow rate of not more than 2 mL/min. The effluent was collected directly into a Teflon bottle.

**Working Ammonium Maleate Buffers.** The working buffer solutions for prescribed pH values were prepared by diluting 400 mL of the stock buffer solution to 500 mL after various amounts

**Table I. Preparation of the Maleic Acid/Ammonium Hydroxide Working Buffers**

pre-scribed pH	vol (mL) of acid or base added to 400 mL of stock buffer then diluted to 500 mL				pH of working buffer <sup>a</sup>	resultant pH when added to seawater at 5% (v/v) ratio <sup>b</sup> (n = 4)
	2 N HCl	2 N HCl	2 N $NH_4OH$	2 N $NH_4OH$		
2.0	27.0				1.12	2.03 $\pm$ 0.01
2.5	21.0				1.87	2.49 $\pm$ 0.02
3.0	18.8				2.23	2.97 $\pm$ 0.03
3.5	17.6				2.51	3.47 $\pm$ 0.03
4.0	15.8				2.76	4.01 $\pm$ 0.01
4.5		90.0			4.17	4.50 $\pm$ 0.00
5.0		64.0			4.98	5.01 $\pm$ 0.01
5.5		30.0			5.50	5.51 $\pm$ 0.00
6.0		9.0			6.00	6.01 $\pm$ 0.01
6.5					6.47	6.50 $\pm$ 0.01
7.0				7.0	6.95	6.99 $\pm$ 0.03
7.5				15.0	7.59	7.53 $\pm$ 0.03
8.0				48.0	8.26	8.02 $\pm$ 0.02
8.5			20.0		8.80	8.52 $\pm$ 0.01
9.0			40.0		9.28	9.00 $\pm$ 0.01

<sup>a</sup> Small pH adjustment of the mixed working buffer is necessary because the HCl and ammonia might vary from batch to batch.

<sup>b</sup> Resultant pH values (25 mL of working buffer added to 500 mL of seawater) measured at 25 °C.

of hydrochloric acid or ammonium hydroxide were added as shown in Table I. The working buffer solutions are thus all ca. 0.4 F with respect to maleate.

**Trace Metal Standards.** The Merck Titrisol standards of Cd, Co, Cu, Fe, Mn, Ni, Pb, and Zn were diluted to desired concentrations.

**Seawater.** Coastal seawater was collected in a 25-L polyethylene carboy 10 km east of Keelung Harbor, Taiwan. The sample was filtered through a Whatman GF/C filter, preserved with 1 mL of chloroform, and then stored.

**Instrumentation.** A Hitachi Model Z-8000 atomic absorption spectrometer with Zeeman background correction was used throughout this work for the determination of metals.

**Determination of Buffering Capacity.** The quantitative measure of the buffering strength of a solution at a given pH is usually termed as "buffering capacity", which is defined as the number of millimoles of strong acid/base required per milliliter to cause a unit change in pH. The buffering capacity of a maleate ion added seawater was measured by the following procedure:

Twenty-five milliliters of stock buffer solution was added to 500 mL of seawater to yield a concentration of maleate of ca. 0.02 F. The mixture was titrated with 1 N HCl, NaOH, or  $NH_4OH$ . The pH of the solution after each addition of the titrant was noted. The buffering capacity at a given pH was estimated from the tangent of the titration curve at that pH.

## RESULTS AND DISCUSSION

**Capacity of the Maleic Acid/Ammonium Hydroxide System.** Maleic acid was chosen for detailed study for the following reasons: its  $pK_1$  and  $pK_2$  values are 1.92 and 6.23 (13), so that it may act as a buffer at pH around 6; it does not form strong complexes with most trace metals of interest (13); it has a high chemical stability, a relatively low toxicity, and a reasonably high solubility so that solutions and concentrations below 0.5 M may be prepared readily. The buffering capacity of a mixture of maleic acid, ammonium hydroxide, and seawater (20 mL of stock ammonium maleate buffer added to 500 mL of seawater) at various pH values is shown in Figure 2. Below pH 2.5 and above 7.5, the solution was strongly buffered by water (hydrogen ions) and ammonium ions, respectively. A maximum peak was found at 5.5 which should be equal to  $pK_2'$  of maleic acid in seawater. The shift of  $pK_2$  (6.23) at infinite dilution to  $pK_2'$  (5.5) in seawater reflects the effect on the high ionic strength of seawater of the dissociation constants of acids. Minimum buffering ca-

**Table II. Removal of Heavy Metal Impurities from Ammonium Maleate Stock Buffer (0.5 F with respect to maleate) by Passing through Chelex-100 Columns**

resin wt, g	flow rate, mL/min	pH	removal, %								
			Cd	Co	Cu	Fe	Mn	Ni	Pb	Zn	
0.5	5	3	2	8	95	90	0	54	41	18	
		4	22	73	97	78	5	92	55	88	
		5	53	97	99	76	14	95	64	98	
		6	86	>99	>99	79	42	95	80	>99	
		7	>99	>99	>99	60	85	97	93	>99	
		8	>99	>99	98	5	99	98	95	>99	
		10.0	2	6.5	>99	>99	>99	99	>99	>99	>99

<sup>a</sup>Initial spiking concentration: 10 µg/L for each metal.

pacities were observed at pH 3.5 and 7. Even at these minima, the value exceeded 3 (µequiv/mL)/pH and should be adequate for most analytical purposes. Thus, the maleic acid–ammonium hydroxide and/or hydrochloric acid buffering system alone can cover the entire pH range from pH 2 to 9 without the need of adding other ligands.

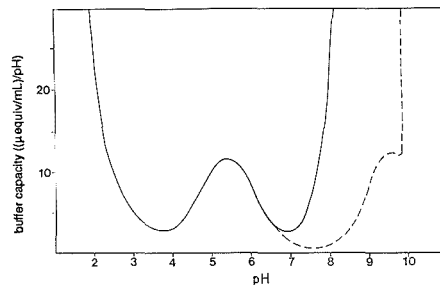
A series of working buffers was prepared from these three chemicals as described in Table I. When they were added to seawater at a ratio of 5% (v/v), the resulting pH of the seawater varied progressively from pH 2 to 9 at 0.5 pH intervals with a precision of better than 0.03 pH unit. Thus, the need for monitoring the resulting pH of the sample with a pH meter upon the addition of acid, base, or buffer in order to reach a desired pH may be eliminated. By simplification of the steps needed to bring a sample of seawater to a given pH, it makes the adjustment of a large number of samples to a variety of pH values in the search for an optimal pH during method development much easier. The procedure may be simple enough to allow for the preconcentration of trace metals from seawater to be performed onboard ship.

**Purification of Buffer.** Trace metal impurities in the stock buffer solution can be removed by passing it through a Chelex-100 column. A test was made to find out the optimal pH and removal efficiencies. Each of the eight trace metals, namely, Cd, Co, Cu, Fe, Mn, Ni, Pb, and Zn, was added to the stock buffer at a concentration of 10 µg/mL. The pH of the buffer solution was then adjusted to pH 3–8 at 1 pH unit intervals, and then passed through a Chelex-100 column containing 0.5 g of resin at a flow rate of ca. 5 mL/min. The trace metals retained by the column were recovered by elution with 2 N nitric acid and determined by atomic absorption spectrometry. The results are given in Table II. The removal efficiencies for most metals showed an increasing trend with increasing pH. Unlike other metals, Fe is poorly removed at higher pH. To compensate for this, an intermediate pH of 6.5 was chosen and the removal efficiencies of the column were further improved by using a larger dimension (containing 10 g resin) and operating at a slower flow rate of 2 mL/min.

**Table III. Analysis of Trace Metals in a Coastal Seawater Sample by Chelex-100 Preconcentration/GF-AAS Using the Ammonium Maleate Buffer at pH 6.5<sup>a</sup>**

element	analytical blank, µg/L	concn found, µg/L		recovery, %	% recovery using acetate buffer (pH 5.5)
		sample	sample + 1 µg/L		
Cd	0.005	0.06 ± 0.01	1.10 ± 0.03	104	99
Co	<0.01	n.d. ± 0.02	0.96 ± 0.07	96	98
Cu	0.02	0.77 ± 0.05	1.75 ± 0.11	98	98
Fe	<0.1	2.10 ± 0.20	3.05 ± 0.24	85	78
Mn	0.01	1.45 ± 0.05	2.42 ± 0.09	97	64
Ni	<0.1	0.23 ± 0.11	1.18 ± 0.08	95	95
Pb	<0.01	n.d. ± 0.01	0.98 ± 0.03	98	102
Zn	0.12	5.70 ± 0.06	6.66 ± 0.11	96	99

<sup>a</sup>All values are the mean of triplicated measurements. Concentrations were calculated from the calibration curves constructed by adding standards to the analytical blank, i.e. the eluate from the third column.

**Figure 2.** Buffering capacity curves of a seawater sample (500 mL) added with 25 mL of ammonium maleate stock buffer (ca. 0.02 F with respect to maleate): (solid line) HCl/ammonium hydroxide as the titrant; (dash line) HCl/NaOH as the titrant.

Under these conditions, more than 99% of all metals spiked were removed.

**Application to a Seawater Sample.** Filtered coastal seawater and trace metal added seawater (spiked with Cd, Co, Fe, Mn, Ni, Pb, and Zn) were analyzed by the Chelex-100/graphite furnace atomic absorption spectroscopy (GF-AAS) technique (14) using the nominated buffer and operating at pH 6.5.

A 500-mL aliquot of the sample, with an added 25 mL of the ammonium maleate buffer, was allowed to pass through three consecutively connected Chelex-100 columns (each contained 2 g of 100–200 mesh resin in ammonium form) at a flow rate of 5 mL/min. Each column was rinsed separately with four 5-mL portions of 1 M purified ammonium acetate (pH 5.5) to remove alkali and alkaline-earth elements (3, 4), followed with five 1-mL portions of DDW, and then eluted with four 2-mL portions of 2 N nitric acid. The final eluate (made up to 10.0 mL) from the first column was measured for the heavy metal contents in that seawater; the eluate from the second column was measured to check the residues; and the third column was accounted for the analytical blank. Portions (2.0 mL) of this blank was precisely withdrawn, to which were spiked 0.2 and 0.5 µg of each metals of interest in order to construct calibration curves. The recoveries of the spiked trace metals were calculated from the concentrations of trace metals in the sample and the spiked sample. For comparison, a separate sample was analyzed by the same procedure but using the conventional ammonium acetate buffer at pH 5.5. Both results are given in Table III.

In the experiment where maleate buffer was used, the recoveries of the spiked elements (except for Fe) were all in the range of 95–104%, which should be considered quantitative within experimental uncertainties. The recovery for Fe was comparatively low at 85%. In the experiment where acetate buffer was used at pH 5.5, the recoveries for Cd, Co, Cu, Ni,

Pb, and Zn were also found satisfactory, ranging between 98% and 102%, but recoveries for Fe and Mn were only 73% and 64%, respectively. These results suggested that the use of the proposed ammonium maleate buffer system has more advantages than that of ammonium acetate for the Chelex-100 operation, by obviously improving the recoveries of Fe and Mn and also providing higher buffering capacity at pH 6.5.

These two buffers were also applied to the APDC + DDTC/MIBK solvent extraction method at pH 4.5 for comparison, but the results did not show significant difference.

### CONCLUSION

The proposed hydrochloric acid/maleic acid/ammonium hydroxide buffer system can be used to bring the pH of seawater samples to predetermined values of pH between 2 and 9 with a high degree of precision. It covers the pH of 6-7 where none of the buffering system presently in use can work effectively. These advantages benefit the search of an optimal pH in developing a new method and make the routine pre-concentration procedure much quicker and easier so that it can be performed onboard ship readily. Since the need of using a pH meter to measure the pH of a seawater sample while adjusting its pH to the desired value is virtually eliminated, the risk of contamination can be largely reduced.

### ACKNOWLEDGMENT

The authors wish to thank Mr. Gwo-Ching Gong of the National Taiwan Ocean University, Keelung, for his helpful assistance in preparing the experiment.

**Registry No.** NH<sub>4</sub>OH, 1336-21-6; HCl, 7647-01-0; Cd, 7440-43-9; Co, 7440-48-4; Cu, 7440-50-8; Fe, 7439-89-6; Mn, 7439-96-5; Ni, 7440-02-0; Pb, 7439-92-1; Zn, 7440-66-6; maleic acid, 110-16-7; water, 7732-18-5; Chelex-100, 11139-85-8.

### LITERATURE CITED

- (1) Danielsson, L. G.; Magnusson, B.; Westerlund, S. *Anal. Chim. Acta* **1978**, *98*, 47-57.
- (2) Magnusson, B.; Westerlund, S. *Anal. Chim. Acta* **1981**, *131*, 63-72.
- (3) Sturgeon, R. E.; Berman, S. S.; Desaulniers, A.; Russell, D. S. *Talanta* **1980**, *27*, 85-94.
- (4) Kingston, H. M.; Barnes, I. L.; Brady, T. J.; Rains, T. C.; Champ, M. A. *Anal. Chem.* **1978**, *50*, 2064-2070.
- (5) Sugimae, A. *Anal. Chim. Acta* **1980**, *121*, 331-336.
- (6) Miyazaki, A.; Barnes, R. M. *Anal. Chem.* **1981**, *53*, 299-304.
- (7) Williams, M. C.; Cokal, E. J.; Niemczyk, T. M. *Anal. Chem.* **1986**, *58*, 1541-1547.
- (8) Statham, P. J. *Anal. Chim. Acta* **1985**, *169*, 149-159.
- (9) Danielsson, L. G.; Magnusson, B.; Zhang, K. *At. Spectrosc.* **1982**, *3*, 39-40.
- (10) Paulson, A. J. *Anal. Chem.* **1986**, *58*, 183-187.
- (11) Pai, S. C.; Whung, P. Y.; Lai, R. L. *Anal. Chim. Acta* **1988**, *211*, 257-270.
- (12) Mattinson, J. M. *Anal. Chem.* **1972**, *44*, 1715-1716.
- (13) Martell, A. E.; Smith, R. M. *Critical Stability Constants*; Plenum: New York, 1977; Vol. 3.
- (14) Pai, S. C. *Anal. Chim. Acta* **1988**, *211*, 271-280.

RECEIVED for review July 26, 1989. Accepted November 22, 1989. S. C. Pai and G. T. F. Wong were supported by the National Science Council of the Republic of China (Grants NSC74-0407-M019-01 and NSC77-0209-M002a-15). G. T. F. Wong was also supported by Old Dominion University as a faculty on leave in 1988.

## Design for Field-Flow Fractionation Channels and Split-Flow Lateral-Transport Thin Separation Cells

Lori Koch

Central Analytical Department, CIBA-GEIGY Ltd., CH-4002 Basel, Switzerland

Although the mechanisms underlying separation diverge (1), the fundamental technical requirements associated with field-flow fractionation (FFF) channels and split-flow lateral-transport thin (SPLITT) cells are similar in many respects. Both techniques realize the goal of separation through the application of transverse driving forces to various particle populations carried by flow down a thin, unobstructed, ribbonlike channel of regular geometry. In FFF, the more well-established of the two methods, this criterion has usually been met by sandwiching a spacer, i.e., a thin (usually 0.05-0.5 mm) film of Mylar, Teflon, or stainless steel sheeting from which the channel volume has been cut out and removed, between two walls which are constructed such that they allow transmission of the driving force (2) (see ref 3 for a notable exception). This configuration has changed little from that used to carry out some of the first successful thermal FFF experiments more than 20 years ago (4). Split-outlet FFF (5) and SPLITT cell systems (6) have been based upon similar, although somewhat more complicated, configurations. The construction of these systems has been approached through the use of a three-layer channel system, with the layers subject to cut-outs of different geometries and the entire sandwich construction clamped between two appropriate walls.

In order to ensure that the channel area be well-defined, i.e., that a seal be maintained precisely at the channel boundaries and that the channel itself has a high degree of

geometrical integrity, these designs required secure, even clamping of the spacer with rows of bolts. The ideal spacer needed to be both rigid, to maintain the best geometry, and compressible, to maintain the best seal. A compromise serving neither purpose completely was found in Mylar or Teflon spacers, which sealed well when bolted with sufficient force (although the latter possessed little dimensional stability). Wall materials were thereby restricted to those that could withstand these forces of clamping.

This can have serious ramifications for flow FFF and SPLITT systems, which are preferentially constructed from Plexiglass or glass to allow visual monitoring of the channel geometry or contents. In the former, the problem is compounded by the necessity of a porous frit being embedded into the lower channel wall. These frits can be quite brittle and subject to easy breakage. Moreover, clamping of traditional spacers acts to compress the membrane at the channel edges, causing it to bulge slightly into the channel and resulting in uncertain system performance through distortion of the channel geometry. In SPLITT systems, the splitting edges of the necessarily thin splitting layer are insufficiently stable to assure that the passageways above and below remain equally open to flow.

This note describes an uncomplicated new approach to open parallel plate type channel construction which overcomes these obstacles by eliminating the need for a traditional spacer. It

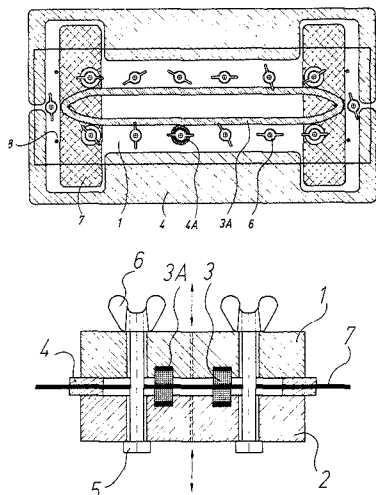


**Figure 1.** Schematic representation of the SPLITT system showing implementation of the new design: (1) upper channel wall, (2) lower channel wall, (3) silicone seal that defines the channel, (3A) Teflon underlay, (4) metal spacer, (4A) precision washer, (5) bolts, (6) wing nuts, (7) metal splitter, (8) alignment pins.

enables the rapid achievement of a seal that maintains its integrity even under high flow rate conditions and allows the adjustment of channel thickness without necessitating a complete disassembly of the system. Proven advantages for SPLITT and flow FFF systems are presented.

#### EXPERIMENTAL SECTION

The new design utilizes a seal that also serves to define the channel. Its implementation in a SPLITT cell system is schematically depicted in Figure 1. A channel-shaped groove, 3 mm deep and 6 mm wide, was milled with a high degree of accuracy out of each of the two Plexiglas walls (1 and 2) of a SPLITT system and filled with liquid silicone casting compound (Silicone Rubber RTV 56) from Wacker Chemicals (Munich). After vulcanization was complete, the solidified, cast silicone was removed from the grooves. With a specially designed template, Teflon sheeting possessing a thickness slightly greater than half of the desired channel thickness was cut to yield a pair of underlays (3A) which fit precisely into the base of each empty well (one in each). Therefore, when the two cast silicone pieces (3) were replaced, they were each raised to a level slightly above the surface of the wall by these underlays, thereby serving to define the channel's thickness and geometry.

The splitter consisted of two small, thin (0.02, 0.05, and 0.1 mm thicknesses were tested) spring stainless steel sheets (7) that were appropriately positioned at the ends of one wall before the system was closed. Their flatness was maintained with a special device (not shown) which held them to the external walls of the channel under tension. The two halves of the system were placed together lightly with alignment pins (8), and metal strips (4) having a thickness corresponding to the desired final channel thickness were inserted along the perimeter of the system, alongside the bolts. When the system was bolted together to complete the assembly procedure, these strips assured that the desired channel thickness was precisely maintained. Alternatively, precision steel washers (4A) of the correct thickness could be placed around the bolts (7) before the system was closed, but this results in a less flexible system, as will be described later. Wing nuts (6), tightened less than finger tight, assured that the silicone faces provided the necessary seal. The time required for system disassembly and reassembly (with attainment of a seal) was well under 3 min.

Two HPLC pumps with pulse dampeners (Sykam) provided the sample and carrier flows. The outlet flow rates were adjusted with needle valves. For the tests of seal strength, water was

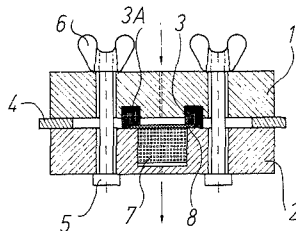


**Figure 2.** Cross sectional view of the flow FFF system showing implementation of the new design: (1) upper channel wall, (2) lower channel wall, (3) silicone seal that defines the channel, (3A) Teflon underlay, (4) metal spacer, (5) bolts, (6) wing nuts, (7) porous frit, (8) membrane.

pumped into the system at gradually increasing flow rates beginning at 0.2 and ending at 40 mL/min. The pressure in the channel during the high flow runs reached 12.3 bar. Even at these high flow rates and pressures, the seal was maintained. The geometrical integrity of the above-described system was verified by injection of a pigment solution into the upper flow stream and observation of the resulting flow profile.

It was possible to adjust the channel thickness at will, in a matter of seconds, within the range of thicknesses typical for these experiments, simply by loosening the wing-nuts slightly and slipping in the appropriate thickness of spacer strips (4). The need for opening the channel (and concomitant introduction of air) was eliminated, along with the need for interrupting the flow at flow rates below about 5 mL/min. The use of the precision washers (4A) required that the channel be opened to adjust the thickness.

The same sealing system was implemented in a Plexiglas, asymmetric flow FFF system, schematically depicted in Figure 2. In this case, however, only the upper (solid) wall (1) was machined to allow seating of the silicone seal (3) which defined the channel shape. As shown in the figure, the flexible nature of the seal also acts to prevent leakage from the edges of the membrane itself (8). The soft channel face reduces the forces placed on the membrane and the frit (7), which is seated in the lower wall (2).

#### RESULTS AND DISCUSSION

Other flow FFF system designs, previously tested in our laboratory, which utilized an O-ring oriented externally to the channel, ensured that no liquid escaped from the system as a whole but allowed leakage around the spacer and up to the sealing ring at flow rates above 5 mL/min. In addition, conventional spacers constructed of thin silicone sheeting, while possessing excellent sealing properties, proved to have insufficient dimensional stability to ensure the well-defined channel geometries necessary for FFF and SPLITT techniques, and their elasticity made their preparation and inclusion into the systems difficult.

In contrast, the design presented here has proven to be exceptionally effective and convenient to implement. Its advantages for open parallel plate channel systems are numerous. The most obvious of these is the significant reduction in down time afforded by the rapid, convenient sealing mechanism. Another is the ability to adjust the channel thickness at will with practically no related down time. The latter proved particularly useful for the unproblematic accommodation of larger-than-expected sample particles in the SPLITT system described above. In addition, it is this compressibility of the channel which enables the implementation of the simple splitter construction described earlier. These splitters were resistant to deformation even at the very high flow rates used in some of our studies.

This channel design also fulfills many of the special instrumental needs demonstrated by flow FFF systems. Just as the metal splitter sheets were easily accommodated in the



SPLITT system, the face of the channel molds itself around the membrane edges to ensure that the sides of the membrane are securely sealed in the flow FFF system. The implementation of this design allows the use of even very brittle ceramic or carbon frit materials. These frits produce a better result upon machining than plastic or sintered metal frits. However, our experiences showed that, without extreme care upon clamping, they can have a limited lifetime, particularly when a system is in the developmental stage and must necessarily undergo several opening and closing cycles for channel or membrane changes.

The reduction of pressure on the membrane itself appears to prevent problematic membrane deformations which previously occurred at the channel edges. Thus, although we had noted troubling "channeling", which led to a degradation of resolution, in earlier (traditional) designs, we do not observe this in our system based upon the new design described here. As a related consequence, membranes can be confidently replaced, even after repeated system disassemblies, since they retain their structural integrity throughout their entire length and width to such a large degree. The elimination of a true "sandwich" construction also means that there is only one part to position when the system is disassembled, i.e., the membrane itself. This, too, saves time.

It should be noted that, because the edges of the rubber channel are compressible, and since it is this compression (although extremely slight) that enables the system to seal, it must be expected that the channel edges bulge slightly into the interior of the channel upon completion of the seal. However, this effect (not visible to the naked eye) did not

produce any observable disturbances in the flow profile. In fact, the edges appeared to be considerably straighter and smoother than those of our conventional cut spacers.

Silicone casting compounds are available with various properties, for example, solvent or temperature resistance, to accommodate special needs, so this design should prove suitable for other FFF systems as well. Furthermore, although we described this new design applied to an asymmetric flow FFF system, it is anticipated that it would be similarly suited to a symmetric system. We are only beginning to investigate the benefits provided by this new construction, but we look forward, in particular, to a significant improvement in the function of flow FFF systems.

#### ACKNOWLEDGMENT

Special thanks are given to P. Jordi for generously sharing his technical expertise and for providing the AutoCAD drawings.

#### LITERATURE CITED

- (1) Giddings, J. C. *Sep. Sci. Technol.* **1985**, *20*, 749.
- (2) Giddings, J. C. *Chem. Eng. News* **1988**, *66* (41), 34.
- (3) Kirkland, J. J.; Dilks, C. H., Jr.; Yau, W. W. *J. Chromatogr.* **1983**, *255*, 255.
- (4) Thompson, G. H.; Myers, M. N.; Giddings, J. C. *Anal. Chem.* **1969**, *41*, 1219.
- (5) Giddings, J. C.; Lin, H. C.; Caldwell, K. D.; Myers, M. N. *Sep. Sci. Technol.* **1983**, *18*, 293.
- (6) Springston, S. R.; Myers, M. N.; Giddings, J. C. *Anal. Chem.* **1987**, *59*, 344.

RECEIVED for review September 29, 1989. Accepted December 18, 1989.

## Ultrasonic Hydrodynamic Modulation Voltammetry

Howard D. Dewald\* and Brock A. Peterson<sup>1</sup>

Department of Chemistry, Ohio University, Athens, Ohio 45701-2979

### INTRODUCTION

The effect of an ultrasonic field on electrochemical processes has been studied extensively. Moriguchi found that ultrasonic waves lowered the water decomposition voltage on platinum electrodes (1). Debye predicted that the propagation of longitudinal ultrasonic waves through an electrolytic solution should result in the generation of alternating-potential differences between points within the solution, separated by a phase distance other than an integral multiple of the wavelength, and proposed a method that would indicate the masses of solvated electrolytic ions directly (2). Yeager and co-workers modified Debye's equation and experimentally verified the prediction (3-5). Several studies have been undertaken relative to the effects of ultrasonic energy during electrolysis and electroplating processes (6). Ultrasonic radiation is also capable of facilitating electrochemical (7) and organic synthesis (8, 9), otherwise referred to as sonochemistry.

Ultrasonics primarily increase the rate of mass transfer to the electrode raising the limiting current density considerably and causing a reduction in the diffusion layer thickness (10, 11). Dutta and Sinha have proposed an expression for the enhanced rate of diffusion in terms of three dimensionless groups: amplitude number, diffusion length number, and cavitation damping number (12). Cavitation, the formation and sudden collapse of bubbles within the solution, is considered the most important factor. Cavitation at or near the

electrode surface creates microstreaming, which is more effective than stirring in disrupting concentration gradients.

Hydrodynamic modulation voltammetry (HMV) involves a variation in the convection rate of the solution at a solid electrode as a function of time. Either the electrode motion relative to the solution or vice versa produces a modulated current,  $\Delta i$ , that depends on the diffusing analyte concentration, and which is free from contributions that do not depend on the mass transfer rate (e.g., double-layer charging, surface transients, and electrolyte reactions). Thus HMV is applicable to trace analysis with detection limits several orders of magnitude better than conventional voltammetry. The theory and applications of HMV have been reviewed by Wang (13).

Sinusoidal hydrodynamic modulation about an average rotational velocity with the rotating disk electrode (HMV-RDE) has been developed and well-characterized by Bruckenstein and Miller and co-workers (14-25). Blaedel and Wang and co-workers have investigated several square-wave modulated techniques referred to as pulsed- and stopped-flow (26-30), pulsed- and stopped-rotation (31-35), and pulsed-stirring (36) voltammetry. HMV based on vibrating wire and microcylinder electrodes has been recently demonstrated (37-39).

The technique described in this work utilized ultrasonic radiation to modulate the mass transfer rate at a glassy carbon electrode in HMV. The modulation was controlled with the cycle time of an ultrasonic horn while the electrode potential was scanned linearly over a 1-V range. The characteristics and advantages of this study are elucidated by application

<sup>1</sup> Present address: E. I. du Pont de Nemours & Company, Experimental Station, Wilmington, DE 19898.

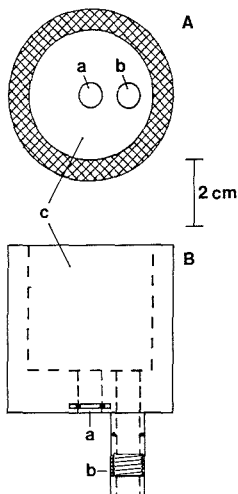


**Figure 1.** Ultrasonic modulation electrochemical cell: (A) top view, (B) front view; (a) working electrode, (b) reference electrode, (c) solution reservoir. Ultrasonic microtip probe (not shown) is centered over working electrode.

to the measurement of micromolar concentrations of ferrocyanide.

### EXPERIMENTAL SECTION

**Apparatus.** An ultrasonic horn (Branson Sonic Power Co., Danbury, CT, Model W-200P) operating at 20 kHz at power levels up to 54 W was used as the ultrasonic source for most experiments. It was equipped with a standard tapered microtip probe with a tip diameter of 3.2 mm.

The cell design used with the microtip probe is shown in Figure 1. The body was machined from an acrylic cylinder (5.0 cm diameter, 5.0 cm length). A solution reservoir (43-mL capacity) was milled into the center of the top face (3.8 cm diameter, 3.8 cm depth). One hole (6.35 mm diameter) was then drilled through the center of the bottom face and a groove was cut across the hole near the bottom face to accept an O-ring. The dimensions allowed for a snug-fit of the working electrode flush with the bottom of the reservoir. The reference electrode was connected to the reservoir through a second hole (6.35 mm diameter) drilled off to the side and was held in place with an O-ring seal threaded-connector attached to the bottom face of the cell. The microtip probe was positioned directly over the center of the working electrode surface at a distance that resulted in the largest current response. The cell and ultrasonic horn were clamped on different ring stands.

The electrochemical measurements were controlled with a EG&G PARC Model 174A polarographic analyzer. All potentials were measured against a Ag/AgCl (3 M NaCl) reference electrode (BAS, Inc., W. Lafayette, IN, Model RE-1). The working electrode was glassy carbon (3 mm diameter, BAS, Model GCE) and the auxiliary electrode was a Pt wire. The output was recorded on an X-Y recorder.

**Reagents.** Glass-distilled water was passed through a mixed-bed demineralizer cartridge (Barnstead D8902) and used to prepare all solutions. The supporting electrolyte was 1.0 M potassium nitrate. Potassium ferrocyanide solutions were prepared fresh and directly in supporting electrolyte before the start of each study.

**Procedure.** The glassy carbon electrode was polished with a 0.05- $\mu$ m alumina slurry on a Microcloth disk (Buehler, Lake Bluff, IL) and rinsed with water, dilute nitric acid, and again with water. Further pretreatment was performed by cycling the potential between  $\pm 1.0$  V and holding at the potential limit for 2 min with supporting electrolyte in the cell. Linear sweep voltammetry was used. A modulated response was obtained by

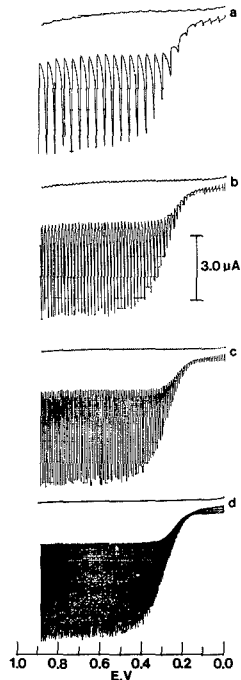


**Figure 2.** Linear sweep voltammograms for 0.5 M  $\text{KNO}_3$  and oxidation of  $100 \mu\text{M K}_4\text{Fe}(\text{CN})_6 \cdot 3\text{H}_2\text{O}$  in 0.5 M  $\text{KNO}_3$  at a glassy carbon electrode vs Ag/AgCl (3 M NaCl) with ultrasonic modulation for different potential scan rates: (a) 50 mV/s, (b) 20 mV/s, (c) 10 mV/s, (d) 2 mV/s; ultrasonic horn modulation cycle time, 1 s; duty cycle, 20%.

appropriate selection of the pulse mode cycle time of the ultrasonic horn.

### RESULTS AND DISCUSSION

**Effect of Potential Scan Rate and Ultrasonic Pulse Width on Ultrasonic Modulation Response.** Figure 2 shows a representative ultrasonic modulation voltammogram for 0.5 M  $\text{KNO}_3$  and for the oxidation of  $100 \mu\text{M}$  ferrocyanide at potential scan rates of (a) 50 mV/s, (b) 20 mV/s, (c) 10 mV/s, and (d) 2 mV/s between the potential range of 0.0 and 0.9 V. Five voltammograms were recorded at each scan rate. The wave for ferrocyanide oxidation rises sharply in the potential limited region and plateaus in the limiting current region. The modulation frequency of the ultrasonic horn was constant at a 1-s cycle time (20% duty cycle). The modulation response is smooth and reproducible. The limiting current measured at 0.7 V for all voltammograms ranged between 4.8 and  $5.2 \mu\text{A}$  with an average value of  $5.0 \mu\text{A}$  ( $n = 20$ ). The half-wave potential occurred at 0.28 V. A minimum current occurred at 0.16 V. This minimum was evident in many of the modulated voltammograms. Its exact origin is unknown but is thought to be related to the potential of zero charge (40). The duty cycle of the ultrasonic horn provides a continuously adjustable pulse width between 0.1 and 0.9 s. As the pulse width was increased from 0.1 to 0.8 s, a nonlinear increase in the limiting current was obtained (Table I). However, at the longer pulse widths ( $>0.6$  s) the noise at the limiting current plateau concomitantly increased and distorted the voltammogram. Therefore short pulse widths were used.

**Effect of Ferrocyanide Concentration on Ultrasonic Modulation.** Figure 3 shows linear sweep voltammograms for 0.5 M  $\text{KNO}_3$  and for oxidation of three (out of four

**Table I. Effect of Ultrasonic Pulse Width on Limiting Current Measurements by Ultrasonic Modulation<sup>a</sup>**

pulse width, s	av limiting current, <sup>b</sup> $\mu\text{A}$	pulse width, s	av limiting current, <sup>b</sup> $\mu\text{A}$
0.1	3.5	0.6	4.3
0.2	3.7	0.8	6.3

<sup>a</sup> 100  $\mu\text{M}$   $\text{K}_4\text{Fe}(\text{CN})_6 \cdot 3\text{H}_2\text{O}$  in 0.5 M  $\text{KNO}_3$  at 3 mm glassy carbon electrode vs  $\text{Ag}/\text{AgCl}$  (3 M  $\text{NaCl}$ ). Scan rate 5 mV/s. Pulse cycle time 1 s. <sup>b</sup> Measured at 0.7 V. Average of 5 voltammograms recorded at each pulse width.

measured) concentrations of ferrocyanide both with and without ultrasonic modulation. The current scales of the PARC 174A polarographic analyzer were adjusted with each concentration. Thus each limiting current would have the same height output at the recorder for a linear response. The nonmodulated peak potential was found at 0.28 V and the half-wave potential was 0.29 V for the ultrasonic modulated voltammograms. Linear calibration curves were obtained with and without ultrasonic modulation over the concentration range of 10  $\mu\text{M}$  to 1 mM. The average limiting currents measured at 0.7 V from five replicate ultrasonic modulated voltammograms were 0.54, 5.47, 27.8, and 55.6  $\mu\text{A}$ , at 10, 100, 500, and 1000  $\mu\text{M}$ , respectively. Least-squares treatment of the data resulted in a slope of  $55.7 \pm 0.06$  nA/ $\mu\text{M}$  and intercept of  $-49 \pm 31$  nA;  $S_Y = 43$ . The correlation coefficient,  $r$ , was 0.9999. On the basis of the signal-to-background characteristics of the response, the detection limit for  $S/B = 2$  would be  $7.4 \times 10^{-7}$  M. The increase in sensitivity with ultrasonic modulation was 15–20-fold that without modulation.

**Ultrasonic Horn as Modulation Source.** The cavitation effect of ultrasound was notably evident with the use of the ultrasonic horn. With each pulse a stream of bubbles was observed emanating from the microtip probe. The largest current response was obtained with the microtip probe centered at a height of 1 cm above the glassy carbon working electrode surface. Additionally, solution heating was not a problem. The variation in temperature in the results reported above was generally 0.5  $^\circ\text{C}$  and no more than 2  $^\circ\text{C}$ .

The automated ultrasonic pulse cycle time overcomes a serious drawback encountered in the manual switching used with most square-wave modulation techniques (26–36). Additionally, the instrumentation is relatively simple, and the experiment is easy to perform. (Initial experiments were performed using an ultrasonic cleaner as the modulator.) The attainment of both qualitative and quantitative data on electroactive materials has been shown. The ultrasonic modulation frequency (1 Hz) is intermediate to values used in HMV (13, 38). Both the detection limit ( $\approx 10^{-7}$  M) and sensitivity ( $\approx 50$  nA/ $\mu\text{M}$ ) are comparable to those attained by using other hydrodynamic techniques. The reproducibility of voltammograms obtained by HMV has not been reported widely (35); the average limiting current values given above range between 0.88 and 3.58% relative standard deviation and indicate the feasibility of obtaining reproducible voltammetric data.

Clearly, ultrasound, long used in electrolysis, can be applied to analytical voltammetry. Ultrasonic modulation has been demonstrated in attaining sensitive voltammograms for micromolar solutions at glassy carbon electrodes. Cavitation bubbles at or near the electrode surface raise the limiting currents attainable as a result of reduction in the diffusion layer thickness, similar to other modulation voltammetries. A potential advantage of ultrasonic modulation voltammetry lies in the unraveling of electrode mechanisms by using ultrasonic energy intense enough to disrupt solvation spheres. Additionally, since the modulation is not intrinsic to the electrochemical cell, other geometries (especially membrane

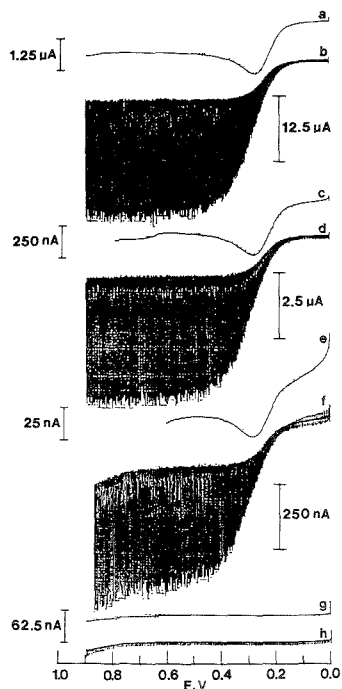


**Figure 3.** Linear sweep voltammograms with and without ultrasonic modulation for 0.5 M  $\text{KNO}_3$  and oxidation of different concentrations of  $\text{K}_4\text{Fe}(\text{CN})_6 \cdot 3\text{H}_2\text{O}$  at a glassy carbon electrode vs  $\text{Ag}/\text{AgCl}$  (3 M  $\text{NaCl}$ ):  $\text{K}_4\text{Fe}(\text{CN})_6$ , (a, b) 500  $\mu\text{M}$ , (c, d) 100  $\mu\text{M}$ , (e, f) 10  $\mu\text{M}$ ;  $\text{KNO}_3$  supporting electrolyte (g, h); voltammograms without modulation, a, c, e, g; voltammograms with modulation, b, d, f, h; ultrasonic horn modulation cycle time, 1 s; duty cycle, 10%; scan rate, 5 mV/s.

and flowthrough cells) and electrode dimensions (porous or microelectrode) could be incorporated into a design for their beneficial applications.

#### ACKNOWLEDGMENT

We thank Dewey King for assisting us with the machining of the electrochemical cell and Jack Blazyk for the loan of the ultrasonic horn and microtip probe.

Registry No.  $\text{Fe}(\text{CN})_6^{4-}$ , 13408-63-4; C, 7440-44-0; Pt, 7440-06-4.

#### LITERATURE CITED

- Moriguchi, N. *J. Chem. Soc. Jpn.* **1934**, *55*, 751–754. *Chem. Abstr.* **1934**, *28*, 7120<sup>1</sup>.
- Debye, P. *J. Chem. Phys.* **1933**, *1*, 13–16.
- Bugosh, J.; Yeager, E.; Hovorka, F. *J. Chem. Phys.* **1947**, *15*, 592–597.
- Yeager, E.; Bugosh, J.; Hovorka, F.; McCarthy, J. *J. Chem. Phys.* **1949**, *17*, 411–416.
- Zana, R.; Yeager, E. B. In *Modern Aspects of Electrochemistry*; Bockris, J. O'M., Conway, B. E., White, R. E., Eds.; Plenum: New York, 1979; Vol. 14, Chapter 1.
- Ensminger, D. *Ultrasonics*; Dekker: New York, 1973; pp 511–512.
- Gautheron, B.; Tainturier, G.; Degrand, C. *J. Am. Chem. Soc.* **1985**, *107*, 5579–5581.
- Bremner, D. *Chem. Br.* **1986**, *22*, 633–638.
- Abdulla, R. *F. Aldrichim. Acta* **1988**, *21*, 31–42.
- Penn, R.; Yeager, E.; Hovorka, F. *J. Acoust. Soc. Am.* **1959**, *31*, 1372–1376.
- Kowalska, E.; Mizera, J. *Ultrasonics* **1971**, *9*, 81–84.
- Dutta, S. K.; Sinha, A. P. *Indian Chem. Eng.* **1981**, *23*(3), 19–24.
- Wang, J. *Talanta* **1981**, *28*, 369–376.
- Miller, B.; Bellavance, M. I.; Bruckenstein, S. *Anal. Chem.* **1972**, *44*, 1983–1992.
- Bruckenstein, S.; Bellavance, M. I.; Miller, B. *J. Electrochem. Soc.* **1973**, *120*, 1351–1356.

- (16) Miller, B.; Bruckenstein, S. *Anal. Chem.* **1974**, *46*, 2026-2033.  
 (17) Miller, B.; Bruckenstein, S. *J. Electrochem. Soc.* **1974**, *121*, 1558-1562.  
 (18) Tokuda, K.; Bruckenstein, S.; Miller, B. *J. Electrochem. Soc.* **1975**, *122*, 1316-1322.  
 (19) Bruckenstein, S.; Miller, B. *Acc. Chem. Res.* **1977**, *10*, 54-61.  
 (20) Tokuda, K.; Bruckenstein, S. *J. Electrochem. Soc.* **1979**, *126*, 431-436.  
 (21) Kansaki, Y.; Bruckenstein, S. *J. Electrochem. Soc.* **1979**, *126*, 437-441.  
 (22) Rosamilia, J. M.; Miller, B. *Anal. Chem.* **1983**, *55*, 1142-1145.  
 (23) Miller, B.; Rosamilia, J. M. *Anal. Chem.* **1983**, *55*, 1281-1285.  
 (24) Rosamilia, J. M.; Miller, B. *Anal. Chem.* **1984**, *56*, 2410-2413.  
 (25) Rosamilia, J. M.; Miller, B. *J. Electroanal. Chem. Interfacial Electrochem.* **1984**, *160*, 131-140.  
 (26) Blaedel, W. J.; Boyer, S. L. *Anal. Chem.* **1971**, *43*, 1538-1540.  
 (27) Blaedel, W. J.; Iverson, D. G. *Anal. Chem.* **1977**, *49*, 1563-1566.  
 (28) Blaedel, W. J.; Yim, Z. *Anal. Chem.* **1980**, *52*, 564-566.  
 (29) Blaedel, W. J.; Wang, J. *Anal. Chem.* **1981**, *53*, 78-80.  
 (30) Wang, J.; Deward, H. D. *Anal. Chim. Acta* **1982**, *136*, 77-84.  
 (31) Blaedel, W. J.; Engstrom, R. C. *Anal. Chem.* **1978**, *50*, 476-479.  
 (32) Blaedel, W. J.; Wang, J. *Anal. Chem.* **1980**, *52*, 1697-1700.  
 (33) Blaedel, W. J.; Wang, J. *Anal. Chim. Acta* **1980**, *116*, 315-322.  
 (34) Wang, J. *Anal. Chem.* **1981**, *53*, 1528-1530.  
 (35) Wang, J.; Freiha, B. A. *Analyst (London)* **1983**, *108*, 685-690.  
 (36) Wang, J. *Anal. Chim. Acta* **1981**, *129*, 253-257.  
 (37) Pratt, K. W., Jr.; Johnson, D. C. *Electrochim. Acta* **1982**, *27*, 1015-1021.  
 (38) Schuette, S. A.; McCreery, R. L. *Anal. Chem.* **1986**, *58*, 1778-1782.  
 (39) Schuette, S. A.; McCreery, R. L. *Anal. Chem.* **1987**, *59*, 2692-2699.  
 (40) Frumkin, A. N.; Petrii, O. A.; Damaskin, B. B. In *Comprehensive Treatise of Electrochemistry*; Bockris, J. O'M., Conway, B. E., Yeager, E., Eds.: Plenum: New York, 1980; Vol. 1, Chapter 5.

RECEIVED for review November 27, 1989. Accepted January 8, 1990. This work was supported in part by the Ohio University Research Committee and Research Challenge programs. H.D.D. acknowledges support from the Grasselli-Day summer faculty research fellowship.

## Construction of Submicrometer Voltammetric Electrodes

Bradford D. Pendley and Héctor D. Abruña\*

Department of Chemistry, Baker Laboratory, Cornell University, Ithaca, New York 14853-1301

### INTRODUCTION

As a result of several unique advantages of microelectrodes, there has been a great deal of interest in their development for electrochemical measurements. The enhanced rate of mass transport results in a steady-state current response at sufficiently slow sweep rates and the reduced capacitive charging current allows increased temporal resolution of electrochemical experiments. The small currents produced at microelectrodes lead to a reduction in the  $iR$  drop so that electrochemical measurements in highly resistive media can be performed. In addition, an improved faradaic to nonfaradaic current ratio enhances the signal to noise ratio. And finally, extremely small environments can be examined with microelectrodes whose total tip size is of the order of a few micrometers (1).

Structurally small electrodes can be used for electroanalysis in minute environments such as single cells. A variety of approaches for the construction of microelectrodes have been reported including electropolished platinum (2, 3) or carbon (4) sealed in glass pipets, electropolished tungsten dipped in lacquer (5), gold-filled micropipet tips (6), carbon ring (7), carbon fiber (8), bevelled carbon fiber (9), and platinum-iridium conical and hemispherical (10) electrodes. Although all of these procedures yield electrodes with diameters of several micrometers or less, in many cases the construction process is quite difficult and the success rate low.

We are interested in the fabrication of small metal disk electrodes that can be chemically modified with a multifunctional polymer and used as selective electrochemical probes for some species of interest (e.g. metal ions) in small environments (11). We require that these electrodes have a total tip diameter (i.e. electrode and insulating material) of a few micrometers or less and that they be easily and reproducibly made.

We describe a procedure for the fast and reliable construction of platinum microelectrodes sealed in glass. The procedure involves pulling annealed platinum wire (75  $\mu\text{m}$ ) placed inside a borosilicate pipet to give microelectrodes of 1-5  $\mu\text{m}$  in total tip diameter.

### EXPERIMENTAL SECTION

**Electrochemistry.** Cyclic and differential pulse voltammetry (DPV) were performed with an IBM EC 225 voltammetric analyzer. For DPV, the pulse amplitude and scan rate were 50 mV and 10 mV/s, respectively. Data were recorded on a Soltec

VP-6423S X-Y recorder. Chronocoulometry was performed with a BAS 100 electrochemical analyzer. Electrochemical cells of conventional, three-compartment design were employed. All experiments utilized a three-electrode configuration and all potentials are referenced to the sodium-saturated calomel electrode (SSCE) without regard for the liquid junction. All experiments were performed inside a Faraday cage.

**Microscopy.** Scanning electron micrographs were obtained by use of a JOEL JSM-35CF scanning electron microscope with an accelerating voltage of 25 kV. Light microscopy was done with a Nikon Optiphot Biological Microscope.

**Reagents.** Acetonitrile (Burdick and Jackson Distilled in Glass), methylene chloride (Fisher ACS certified, spectroscopic grade), and *N,N*-dimethylformamide (Fisher ACS certified) were dried over 4-Å molecular sieves. Tetrahydrofuran (Fisher ACS certified) was distilled from sodium/benzophenone. Tetra-*n*-butylammonium perchlorate (TBAP) (G. F. Smith) was recrystallized 3 times from ethyl acetate and dried under vacuum. Water was purified with a Millipore Milli-Q system. All other reagents were of at least reagent grade quality and were used without further purification.

**Microelectrode Fabrication.** A 3-4-cm piece of annealed platinum wire (75  $\mu\text{m}$  diameter) (Engelhard Industries) was cut and placed inside a 6-7-cm section of a borosilicate pipet (25  $\mu\text{L}$ ) (Fisher) so that about 1 mm of the wire protruded from one end. This end was then folded over the edge of the pipet to secure the wire. The pipet/wire assembly was placed through four loops of nichrome wire (18 gauge) on a pipet puller (Narishige, Type PF-2) and adjusted so that the distance between the chucks was precisely 1.9 cm. Pulling was carried out at a current of 15 A and a magnet setting of 6.7. The resulting two microelectrodes were inspected by light microscopy to determine whether the platinum wire extended to the very end of the tip and was less than 10  $\mu\text{m}$  in diameter. If this was the case and no cracks were present in the glass, electrical contact to the platinum wire was established with a copper wire and silver paint. Although some microelectrodes worked at this stage, more reproducible behavior was observed when the electrode tip was manually snapped back to expose a new platinum surface. This resulted in the total outer diameter of the tip being larger than originally made, but still less than 10  $\mu\text{m}$ . The electrodes were rinsed with water and acetone prior to use.

### RESULTS AND DISCUSSION

A scanning electron micrograph of a typical platinum microelectrode is shown in Figure 1. The image is a composite of secondary and backscattered electrons to show both the tip morphology and the platinum. The micrograph shows the

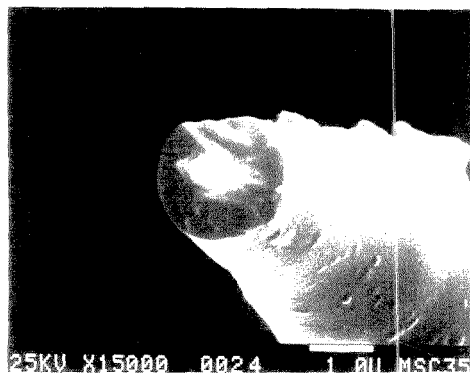


Figure 1. Scanning electron micrograph of the tip of a platinum disk microelectrode.

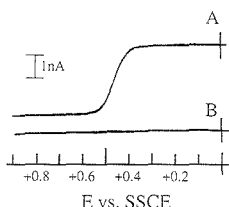


Figure 2. Cyclic voltammogram at a scan rate of 100 mV/s of (A) 3.4 mM ferrocene in 0.1 M TBAP/ $\text{CH}_2\text{Cl}_2$  at a 4.6  $\mu\text{m}$  total tip, 2.8  $\mu\text{m}$  platinum disk electrode, and (B) blank.

tip surface to be relatively defect free. The total outer diameter of the electrode is 2.1  $\mu\text{m}$  with a 0.48  $\mu\text{m}$  diameter platinum disk located in the center. The electrode can therefore be described as a disk in a finite insulating plane.

The integrity of the glass-platinum seal was investigated by using chronocoulometry. Under steady-state conditions, a time-independent chronocoulometric response was observed after application of a potential step, indicative of a good seal between the glass and the metal (12).

The microelectrodes are electrochemically well behaved. Figure 2 shows a cyclic voltammogram of ferrocene in methylene chloride and a very well developed sigmoidal voltammogram is observed. Similar steady-state voltammograms were also observed over the range of 50–1000 mV/s sweep rates in acetonitrile, tetrahydrofuran, and *N,N*-dimethylformamide. The results of the analysis of these steady-state voltammograms are shown in Table I. The wave slopes were calculated from plots of  $E$  vs  $\log(i/i_1 - i)$  and are expected to be 59 mV at 25 °C for a reversible, one-electron reaction (13). Reversible behavior was observed in all solvents except tetrahydrofuran, where the kinetics appear sluggish. Peaks in differential pulse voltammograms were well-defined and symmetric, with  $\Delta E_{\text{FWM}}$  between 105 and 110 mV.

The steady-state or limiting current for microelectrodes of a disk geometry is expected to follow the equation (1)

$$i_1 = 4nFDcr \quad (1)$$

where  $r$  is the electrode radius and all other symbols have their usual meaning.

Table II compares the predicted and measured limiting currents for five microelectrodes. The predicted current was calculated from eq 1, using  $D = (2.4 \pm 0.1) \times 10^{-5} \text{ cm}^2/\text{s}$  (14). In addition, the predicted current also takes into account that the platinum disk is present in a finite insulating plane of glass, and therefore, there is an enhancement in the observed cur-

Table I. Analysis of Steady-State Voltammograms<sup>a</sup>

solvent	wave slope, <sup>b</sup> mV	corr coeff
acetonitrile	60 ± 3	0.99 <sub>9</sub>
methylene chloride	61 ± 2	0.99 <sub>9</sub>
tetrahydrofuran	68 ± 3	0.99 <sub>9</sub>
<i>N,N</i> -dimethylformamide	59 ± 1	0.99 <sub>3</sub>

<sup>a</sup> For ferrocene in 0.1 M TBAP/solvent. <sup>b</sup> Wave slopes obtained from scan rates including 50, 100, and 200 mV/s and are reported as ±1 standard deviation

Table II. Comparison of Measured and Predicted Limiting Currents

electrode	current, nA		outside diameter, $\mu\text{m}$	
	measured <sup>a</sup>	predicted <sup>b</sup>	glass	platinum
1	4.11 ± 0.02	4.78 ± 0.50	6.9	2.3
2	1.84 ± 0.08	1.46 ± 0.29	5.1	2.3
3	2.39 ± 0.01	2.04 ± 0.30	4.6	3.0
4	3.21 ± 0.05	5.05 ± 0.87	4.6	2.8
5	2.13 ± 0.02	2.22 ± 0.25	9.2	4.6

<sup>a</sup> Measured from steady-state currents of voltammograms of ferrocene (1.3–3.5 mM) in 0.1 M TBAP/acetonitrile for three scans at rates from 50 to 1000 mV/s. Values are reported as ±1 standard deviation. <sup>b</sup> The predicted limiting current includes enhancement resulting from the platinum disk not being embedded in an infinite insulating plane (15). The uncertainty in the value reflects uncertainties in the measurement of the radius and in the value of the diffusion coefficient.

rent. Shoup and Szabo have used an explicit hopsotch algorithm to simulate the limiting current at a disk-shaped electrode that is not imbedded in an infinite insulating plane (15). Measurements of both the metal electrode and the outer glass diameters were made by using light microscopy. This allowed for correction of the predicted limiting current using the results of Shoup and Szabo. There is a large uncertainty in the predicted limiting currents listed in Table II and this is due to the fact that for electrodes of diameters such as presented here, the limit of resolution of conventional light microscopy is being approached. Even so, however, with the exception of electrode 4, agreement is quite good.

To ensure success in electrode preparation, it is essential that the platinum wire be annealed and not hard drawn. Hard-drawn platinum wire can be used to make microelectrodes, but there is no reduction in the wire's diameter upon pulling (16). Presumably, the increased ductility of the annealed platinum wire enables it to be drawn to very small diameters. This general idea has also been used in this laboratory to fabricate similar microelectrodes using gold wire instead of annealed platinum wire, although this has not been pursued extensively.

The method of microelectrode fabrication detailed here offers three significant advantages. First, it is extremely quick and easy to fabricate electrodes. Second, the method allows for the construction of very small microelectrodes (typically with total outer diameters between 1 and 5  $\mu\text{m}$ ) with smooth taper and excellent metal to glass seal. It should also be mentioned that platinum disk electrodes of extraordinarily small diameters can be prepared. For example, Figure 3 shows a cyclic voltammogram for a platinum electrode in contact with a 48.2 mM solution of ferrocene in 0.5 M TBAP/acetonitrile. From the magnitude of the limiting current, we estimate that the platinum disk has a diameter of about 27 Å. It should be noted that Morris et al. (17) have performed voltammetric measurements at platinum band electrodes with widths approaching molecular dimensions and have found that the limiting currents obtained at electrode widths less than

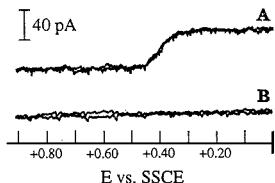


**Figure 3.** (A) Cyclic voltammogram of 48.2 mM ferrocene in 0.5 M TBAP/acetonitrile at a 1  $\mu\text{m}$  total tip, 27- $\text{\AA}$  platinum disk electrode at a scan rate of 50 mV/s. (B) Blank at a scan rate 100 mV/s.

200  $\text{\AA}$  are lower than theoretically predicted. They proposed that the diffusion coefficient of the electroactive species near the electrode may be lower than that in the bulk solution. Since the bulk value of the diffusion coefficient was used to estimate the electrode radius, it is likely that the true radius is actually larger. However, we believe the estimation to be good within a factor of 2 or 3. This represents the smallest platinum disk electrode ever reported and illustrates the capability of the method presented. Third, the success to attempt ratio of constructing electrodes whose total outer diameter is less than 10  $\mu\text{m}$  has been about 42%.

#### LITERATURE CITED

- (1) Wightman, R. M.; Wipf, D. O. In *Electroanalytical Chemistry*; Bard, A. J., Ed.; Dekker: New York, 1989; Vol. 15, pp 267-353.

- (2) Silver, A. *Med. Electron. Biol. Eng.* **1965**, *3*, 377-387.  
 (3) Ballintijn, C. M. *Experientia* **1961**, *17*, 523-526.  
 (4) Meulermans, A.; Poulain, B.; Baux, G.; Tauc, L.; Henzel, D. *Anal. Chem.* **1986**, *58*, 2088-2091.  
 (5) Hubel, D. H. *Science* **1957**, *125*, 549-550.  
 (6) Whalen, W. J.; Riley, J.; Nair, P. J. *Appl. Physiol.* **1967**, *23*(5), 798-801.  
 (7) Kim, Y.-T.; Scarnulis, D. M.; Ewing, A. G. *Anal. Chem.* **1986**, *58*, 1782-1786.  
 (8) Ponchon, J.-L.; Cespuoglio, R.; Gonon, F.; Jouvet, M.; Pujol, J.-F. *Anal. Chem.* **1979**, *51*, 1483-1486.  
 (9) Kelly, R. S.; Wightman, R. M. *Anal. Chim. Acta* **1986**, *187*, 79-87.  
 (10) Penner, R. M.; Heben, M. J.; Lewis, N. S. *Anal. Chem.* **1989**, *61*, 1630-1636.  
 (11) Hurrell, H. C.; Abruña, H. D. *Anal. Chem.* **1988**, *60*, 254-258.  
 (12) Thormann, W.; Bond, A. M. J. *Electroanal. Chem. Interfacial Electrochem.* **1987**, *218*, 187-196.  
 (13) Bard, A. J.; Faulkner, L. R. *Electrochemical Methods*; Wiley: New York, 1980.  
 (14) Kuwana, T.; Bublitz, D. E.; Hoh, G. J. *Am. Chem. Soc.* **1960**, *82*, 5811-5817.  
 (15) Shoup, D.; Szabo, A. J. *Electroanal. Chem. Interfacial Electrochem.* **1984**, *160*, 27-31.  
 (16) Johnson, M. W.; Manhoff, L. J., Jr. *Science* **1951**, *113*, 182-184.  
 (17) Morris, R. B.; Franta, D. J.; White, H. S. J. *Phys. Chem.* **1987**, *91*, 3552-3564.

RECEIVED for review November 10, 1989. Accepted January 3, 1990. This work was generously funded by the National Science Foundation. H.D.A. is a recipient of a Presidential Young Investigator Award (1984-1989) and an A. P. Sloan Fellow (1987-1991). B.D.P. acknowledges support as a Shell Doctoral Fellow (1989-1990).

#### CORRECTION

##### Random-Walk Theory of Nonequilibrium Plate Height in Micellar Electrokinetic Capillary Chromatography

Joe M. Davis (*Anal. Chem.* **1989**, *61*, 2455-2461).

On page 2458, second column, line 44, the text should read as follows: Quantity  $t_0/t_{\text{mic}}$  for the nucleic acids was equated to 0.47, the ratio of the elution times of the void peak and the final peak.

THE AMERICAN CHEMICAL SOCIETY PRESENTS . . .

# 25 Unique Sources of Archival-Quality Chemistry Research and News

## ACCOUNTS OF CHEMICAL RESEARCH

Editor, *Fred W. McLafferty*

*Cornell University*

12 issues a year. ISSN 0001-4842  
Member \$24 Nonmember \$127

## ANALYTICAL CHEMISTRY

Editor, *George H. Morrison*

*Cornell University*

24 issues a year. ISSN 0003-2700  
Member \$29 Nonmember \$59

## BIOCHEMISTRY

Editor, *Hans Neurath*

*University of Washington*

\*51 issues a year. ISSN 0006-2960  
Member \$85 Nonmember \$690

## BIOCONJUGATE CHEMISTRY

Editor, *Claude F. Meares*

*University of California, Davis*

The unifying medium of conjugation chemistry, **BIOCONJUGATE CHEMISTRY** will emphasize the joining of two different molecular functions by chemical or biological means.

6 issues a year. ISSN 1043-1802  
Member \$29 Nonmember \$249

## BIOTECHNOLOGY PROGRESS

Editor, *Jerome S. Schultz*

*University of Pittsburgh*

Jointly published with the American Institute of Chemical Engineers, this established journal offers *new, bimonthly access* to significant research in process development, product development, and equipment/instrumentation design for the biotechnology industry.

6 issues a year. ISSN 8756-7938  
Member \$25 Nonmember \$250

## CHEMICAL & ENGINEERING NEWS

Editor, *Michael Heylin*

*ISSN 0009-2347*

Nonmember \$60

## CHEMICAL RESEARCH IN TOXICOLOGY

Editor, *Lawrence J. Marnett*

*Vanderbilt University*

For the latest original findings, in primary research, on the toxicological effects of chemical agents.

6 issues a year. ISSN 0893-228X  
Member \$46 Nonmember \$269

## CHEMICAL REVIEWS

Editor, *Josef Michl*

*University of Texas, Austin*

8 issues a year. ISSN 0009-2665  
Member \$26 Nonmember \$225

## CHEMISTRY OF MATERIALS

Editor, *Leonard V. Interrante*

*Rensselaer Polytechnic Institute*

This new, international journal provides a molecular-level perspective at the interface of chemistry, chemical engineering, and materials science.

6 issues a year. ISSN 0897-4756  
Member \$49 Nonmember \$299

## CHEMTECH

Editor, *Benjamin J. Lubertoff*

*12 issues a year. ISSN 0009-2703*

Member \$39 Nonmember (Pers.) \$69  
Nonmember (Inst.) \$299

## ENERGY & FUELS

Editor, *John W. Larsen*

*Lehigh University*

A practitioner's guide to the chemistry of fossil fuels—from formation to methods of utilization.

6 issues a year. ISSN 0887-0624  
Member \$48 Nonmember \$294

## ENVIRONMENTAL SCIENCE & TECHNOLOGY

Editor, *William H. Glaze*

*University of North Carolina,*

*Chapel Hill*

12 issues a year. ISSN 0013-936X  
Member \$36 Nonmember (Pers.) \$67  
Nonmember (Inst.) \$276

## INDUSTRIAL & ENGINEERING CHEMISTRY RESEARCH

Editor, *Donald R. Paul*

*University of Texas, Austin*

12 issues a year. ISSN 0888-5885  
Member \$55 Nonmember \$372

## INORGANIC CHEMISTRY

Editor, *M. Frederick Hawthorne*

*University of California, Los Angeles*

26 issues a year. ISSN 0020-1689  
Member \$82 Nonmember \$612

## JOURNAL OF AGRICULTURAL AND FOOD CHEMISTRY

Editor, *Irvin E. Liener*

*University of Minnesota*

\*12 issues a year. ISSN 0021-8361  
Member \$25 Nonmember \$204

## JOURNAL OF THE AMERICAN CHEMICAL SOCIETY

Editor, *Allen J. Bard*

*University of Texas, Austin*

26 issues a year. ISSN 0002-7863  
Member \$75 Nonmember \$630

## JOURNAL OF CHEMICAL AND ENGINEERING DATA

Editor, *Bruno J. Zwiolski*

*Texas A&M University*

4 issues a year. ISSN 0021-9568  
Member \$30 Nonmember \$207

## JOURNAL OF CHEMICAL INFORMATION AND COMPUTER SCIENCES

Editor, *George W.A. Milne, N.I.H.*

4 issues a year. ISSN 0095-2338  
Member \$18 Nonmember \$108

## JOURNAL OF MEDICINAL CHEMISTRY

Editor, *Philip S. Portoghese*

*University of Minnesota*

12 issues a year. ISSN 0022-2623  
Member \$42 Nonmember \$329

## THE JOURNAL OF ORGANIC CHEMISTRY

Editor, *Clayton H. Heathcock*

*University of California, Berkeley*

26 issues a year. ISSN 0022-3263  
Member \$56 Nonmember \$428

## JOURNAL OF PHYSICAL AND CHEMICAL REFERENCE DATA

Editor, *David R. Lide, Jr.*

*National Institute of Standards &*

*Technology*

\*6 issues a year. ISSN 0047-2689  
Member \$70 Nonmember \$325

## THE JOURNAL OF PHYSICAL CHEMISTRY

Editor, *Mostafa A. El-Sayed*

*University of California, Los Angeles*

26 issues a year. ISSN 0022-3654  
Member \$70 Nonmember \$670

## LANGMUIR

Editor, *Arthur W. Adamson*

*University of Southern California*

\*12 issues a year. ISSN 0743-7463  
Member \$58 Nonmember \$429

## MACROMOLECULES

Editor, *Field H. Winslow*

*AT&T Bell Laboratories*

\*26 issues a year. ISSN 0024-9297  
Member \$57 Nonmember \$553

## ORGANOMETALLICS

Editor, *Dietmar Seyferth*

*Massachusetts Institute of Technology*

12 issues a year. ISSN 0276-7333  
Member \$59 Nonmember \$521

## For subscription information write:

American Chemical Society  
Marketing Communications Dept.  
1155 Sixteenth Street, N.W.  
Washington, D.C. 20036 U.S.A.

## Call toll free 1-800-227-5558.

In Washington, D.C. and outside the U.S.

call 202-872-4363.

Telex: 440159 ACSPU UI or 89 2582

ACSPUBS. FAX: 202-872-4615.

## For nonmember rates in Japan contact:

Maruzen Co., Ltd.,  
3-10 Nihonbashi 2-Chome, Chuo-ku,  
Tokyo 103, Japan

\*Frequency change in 1990.

Rates are valid through December 31, 1990.

# LECO® Introduces the Newest Technology for ICP Analysis

*The LECO® Plasmarray® ICP Spectrometer System with fully automatic, solid-state, dual frequency generator.*

Accuracy and precision in ICP analysis begins at the source. The LECO® Plasmarray® system incorporates a 2 kw, fully solid-state source that operates at either 27.12 or 40.68 Mhz. The comprehensive control and diagnostic interface permits fully automatic plasma ignition. While maintaining ease-of-operation, the software is designed to provide the analyst with the greatest latitude in user-defined parameters. Pre-stored operating conditions are effectively used to ensure stable and reproducible plasma excitation conditions.

The LECO® Plasmarray® combines high resolution echelle optics with polychromator preselection and photodiode array detection for the highest resolution available. This patented combination provides optimum wavelengths of 190 to 420 nm with optional coverage to 800 nm for the alkali elements.

The LECO® Plasmarray® Spectrometer is the world's first user-reprogrammable simultaneous/sequential system commercially available. These features allow the user to choose any set of elements in the simultaneous mode. The system also permits quantitative and semi-quantitative analysis to be carried out in a sequential manner.

The unique diode array detection system allows the user to record the entire spectral profile for all elements analyzed and permits simultaneous background correction. The powerful LECO® 386 computer can store the spectral data acquired allowing post processing of results.

For more information on how a LECO® Plasmarray® can improve your simultaneous ICP analysis, call or write today!



**LECO® Corporation**  
3000 Lakeview Avenue  
St. Joseph, MI 49085-2396

Phone: (616) 983-5531  
Facsimile: (616) 983-3850

CIRCLE 80 ON READER SERVICE CARD

